UNSTEADY HEAT TRANSFER MEASUREMENTS IN A ROTATING GAS TURBINE STAGE

Mary Anne Hilditch

St. John's College.

May 1989

A thesis submitted in partial fulfilment of the requirements of the degree of Doctor of Philosophy in the University of Oxford, Trinity Term 1989.

Department of Engineering Science
Parks Road
Oxford
OX1 3PJ

UNSTEADY HEAT TRANSFER MEASUREMENTS IN A ROTATING GAS TURBINE STAGE

Mary Anne Hilditch, St. John's College

A thesis submitted for the degree of Doctor of Philosophy in the University of Oxford, Trinity Term, 1989.

ABSTRACT

As the performance required of high pressure turbines continues to increase, there is a need to investigate many details of the flow which occur in a gas turbine stage that were previously overlooked. These include the effects of rotation and three-dimensional flow as well as unsteady effects due to the relative motion of the blade rows. In order to obtain a better understanding of the turbine flowfield a new transient facility has been commissioned in which aerodynamic and heat transfer measurements can be undertaken in a full stage turbine at engine representative conditions.

The previously used technique of measuring the heat transfer rate by mounting thin film gauges on models manufactured from machineable glass ceramic was not suitable for use on the rotor blade because of the high stress levels involved. An alternative technique has been developed in which a metal turbine blade is coated with an insulating layer of enamel and thin film gauges painted on top. The developments in signal processing and calibrations which were necessary for the use of this type of thin film gauge are discussed in detail.

Signal conditioning electronics have been developed which permit amplification of the thin film gauge output to a higher level within the rotating frame before transmission through a slipring. Extensive tests have been undertaken, in a purpose built spinning rig, to establish the effects of rotation on the performance and mechanical integrity of the instrumentation and associated electronics.

The heat transfer measurements recorded in the rotor facility to date are presented and compared with data from a previous two-dimensional simulation of wake passing flow on the mid-height section of the same blade.

CONTENTS

Page

Acknowledgements

Nomenclature

1 INTRODUCTION 1

2 THE TURBINE FLOWFIELD 5
- 2.1 Introduction
- 2.2 Heat Transfer to a Turbine Blade
- 2.3 Blade Row Interactions
- 2.4 The Effect of Freestream Turbulence on Heat Transfer
- 2.5 The Effect of Wake Passing on Turbine Heat Transfer
- 2.6 The Effect of Wake and Shock Passing on Heat Transfer
- 2.7 Three Dimensional Flow Mechanisms
- 2.8 Final Considerations

3 THE OXFORD ROTOR PROJECT 26
- 3.1 Introduction
- 3.2 Design of the Facility
- 3.3 Operation of the Facility
- 3.4 Choice of Profile and Operating Point
- 3.5 Instrumentation Requirements

4 MEASUREMENT OF HEAT TRANSFER RATE 37
- 4.1 Methods of Measuring Heat Transfer Rate
- 4.2 Thin Film Gauge on a Single Layer Substrate
- 4.3 Thin Film Gauge on a Two Layered Substrate

5 DEVELOPMENT OF INSTRUMENTATION 50
- 5.1 Manufacture of Blade for Heat Transfer Measurement
- 5.2 Design of In-shaft Electronics
- 5.3 Spinning Rig
- 5.4 Heat Transfer Instrumentation Tests in Spinning Rig
- 5.5 Pressure Transducer Tests

6 SIGNAL PROCESSING TECHNIQUES 61
- 6.1 Introduction
- 6.2 Processing Analogue Output to Obtain Heat Transfer Rate
- 6.3 Calculating Temperature Rise from the Analogue Output
- 6.4 Obtaining Temperature Rise from In-shaft Amplifier Output
- 6.5 Temperature to Heat Transfer Rate Conversion
- 6.6 Procedure for Obtaining the Mean Heat Transfer Rate
- 6.7 Procedure for Obtaining the Unsteady Heat Transfer Rate
- 6.8 Effect on Calculated Heat Transfer Rate of Variations in the Amplifier Transfer Function
- 6.9 Effect on Calculated Heat Transfer Rate of Varying the Gauge Parameters
- 6.10 Conclusions

7 CALIBRATION OF INSTRUMENTED BLADES 81
- 7.1 Distribution of Thin Film Gauges
- 7.2 Measurement of Temperature Coefficient of Resistance
- 7.3 Measurement of Enamel Thermal Product, $\sqrt{(\rho ck)_1}$
  - 7.3.1 Theory
  - 7.3.2 Experimental Technique
  - 7.3.3 Results
- 7.4 Laser Calibration - Measurement of a/k
  - 7.4.1 Introduction
  - 7.4.2 Theory
  - 7.4.3 Experimental Method
  - 7.4.4 Commissioning
  - 7.4.5 Actual Method of Calculating a/k
  - 7.4.6 Uncertainty in Measured Value
  - 7.4.7 Measurement of Enamel Thickness
  - 7.4.8 Discussion of a/k Calibration Results
- 7.5 Conclusions

8 HEAT TRANSFER MEASUREMENTS 101
8.1 Introduction
8.2 Commissioning of Instrumentation
8.2.1 Data Acquisition System
8.2.2 Noise Tests
8.3 Mean Heat Transfer Results
8.3.1 Introduction
8.3.2 Temperature History
8.3.3 Calculation of Nusselt Number
8.3.4 Results
8.4 Unsteady Heat Transfer Results
8.4.1 Introduction
8.4.2 Signal to Noise Ratio
8.4.3 Signal Processing
8.4.4 Results
8.4.5 Overall Nusselt Number
8.5 Mean Heat Transfer Results - Comparison with Doorly
8.5.1 Simulation of Wake Passing Flow
8.5.2 Scaling of Results
8.5.3 Results
8.6 Unsteady Heat Transfer Results - Comparison with Doorly.
8.7 Conclusions

9 CONCLUSIONS 125

References 128

Tables 135

Appendix I Prediction of Analogue Output 144

Appendix II Predicted Output from In-Shaft Electronics 145

Appendix III Uncertainty in Measured Heat Transfer Rate 147

Figures 149

ACKNOWLEDGEMENTS

The experimental work described in this thesis would not have been possible without the assistance that I received from numerous people.

First, I would like to thank all the staff and students at the Osney Laboratory for their friendship and their willingness to help and advise.

I am especially grateful to my supervisor, Dr. R.W. Ainsworth, for his support and guidance throughout my time in Oxford.

The Rotor Project was a team effort and the assistance of all members of the project team, past and present, especially that of Mr. A.G. Sheard is greatly appreciated.

Dr. M.L.G. Oldfield provided much useful advice on instrumentation and signal processing which is gratefully acknowledged.

Thanks are also due to Mr. N. Brett for his help with the spinning rig; to Mr. K.J. Grindrod for his expert assistance with the ILPT and to Mr. J.L. Allen for the manufacture of the thin film gauges and help with many of the instrumentation tests.

The Rotor Project was jointly funded by Rolls-Royce plc and the SERC under grants No. GR/D 21189 and GR/E 28062. Financial assistance was also provided by the MoD (Procurement Executive) under grant No. 2057/103.

Finally, I would like to thank my husband, James, for his support and encouragement, without which this thesis would not have been written.

NOMENCLATURE

a	Insulator thickness
A	Area
A	$\frac{\sqrt{(\rho ck)_1} - \sqrt{(\rho ck)_2}}{\sqrt{(\rho ck)_1} + \sqrt{(\rho ck)_2}}$
b	$\sqrt{\frac{2\omega a^2}{\alpha_1}} = \sqrt{2\omega}\sqrt{(\rho ck)_1}\left(\frac{a}{k_1}\right)$
b	Wake width
B(s)	Amplifier gain
c	Specific heat capacity
c	Capacitance per unit length
C_{ax}	Axial Chord
C_D	Drag coefficient
d	Diameter
f	Frequency
F_n	Nyquist Frequency
i	Current
i	Index in series
I	Constant current
I_0	Constant current
j	$\sqrt{-1}$
k	Conductivity
k	Index in series
K	Constant
K_a	Analogue Constant = $\frac{1}{R_1\sqrt{(c/r)}}$
m	Index in series
$\dot{m}$	Mass flow rate
M	Mach Number
M	Signal length, number of points
N	Turbine speed (rpm)
N	Signal length, number of points
p	Static pressure
P_0	Total pressure
$\dot{q}$	Heat transfer rate
Q	Constant heat transfer rate
r	Radius
r	Resistance per unit length
R	Resistance
R	Gas constant
R_1	Analogue input resistance
R_0	Initial resistance
Re	Reynolds Number
s	Laplace transform variable
s	Surface length
S	Total length along blade surface
t	Time

T	Temperature or temperature rise
T_0	Total temperature
T_0	Initial temperature
u	Unit step function
u	Velocity deficit in wake
U	Flow velocity
v	Voltage change
V_0	Initial voltage
V_a	Analogue output
V_B	Amplified output
x	Distance
x	Axial distance
X	Distance along blade surface

Greek

α	Inlet angle
α	Temperature coefficient of resistance
α_1	Thermal diffusivity of insulator = $k/\rho c$
α_2	Thermal diffusivity of metal layer
B	Mixing length constant
γ	Ratio of specific heats
Δ	Change in ...
Δt	Sample interval in time domain
$\Delta\omega$	Sample interval in frequency domain
λ	Constant
ρ	Density
τ	Time interval
τ_1	Breakpoint
T	Sample interval
ω	Frequency
ω_1	Breakpoint = $1/\tau_1$

Subscripts

1	Insulating layer
2	Metal layer
i	Initial condition
20	Conditions at 20° C
r	Conditions during run
B	Amplified signal
m	Measured value
rel	Relative conditions
D	Design value
w	Conditions at wall
g	Conditions in gas
s	Conditions at surface

Others

$\sqrt{(\rho ck)_1}$	Thermal product of enamel layer
$\sqrt{(\rho ck)_2}$	Thermal product of metal layer
–	Transformed variable
CALSPAN	Calspan Advanced Technology Center, Buffalo, NY 14225
DFT	Discrete Fourier Transform
FFT	Fast Fourier Transform
IDFT	Inverse Discrete Fourier Transform
MIT	Massachusetts Institute of Technology, Cambridge, MA 02139

CHAPTER 1

INTRODUCTION

The gas turbine has found many applications, but its greatest impact has been on aircraft propulsion. Since the introduction of the jet engine nearly 50 years ago, the quest for improved performance has been continuous, hastened in recent years by rising fuel costs. One parameter which directly affects the efficiency of a real turbine is the gas temperature at entry to the first turbine stage, with an increase in the turbine entry temperature resulting in an increase in cycle efficiency, **(Cohen, Rogers and Saravanmuttoo)**. This can be considered either as a reduction in specific fuel consumption (civil engines) or as an increase in specific thrust (military engines).

Developments in blade materials and cooling technology have made possible a continuous increase in turbine entry temperature throughout the evolution of the engine. This is illustrated in figure 1.1 (from **Hennecke**) and it can be seen that the operating temperature of the high pressure turbine stage is currently around 1800 K, which is above the melting point of metals used for blade manufacture.

The purpose of blade cooling is not merely to lower the overall temperature below that which would cause failure through excessive creep or oxidization, but also to minimize thermal stresses by the attainment of a uniform metal temperature. It has been recognized (**Sokolowski**) that the increases in turbine entry temperature have been accompanied by a decrease in the durability of the hot section components, namely the turbine and the combustor. An idea of the scale of the problem was given by **Hennecke** who stated that a further 15K increase in blade metal temperature would result in

halving the blade life. Consequently there is an increased emphasis on improving high temperature materials and developing more effective cooling techniques so as to improve the reliability and extend the life of these components.

In a cooled turbine a fraction of the total airflow is bled from the compressor and passed to the turbine blades, where it is typically fed through internal passages, cooling the blade by convection and finally expelled through holes in the blade surface, providing a film of cool air between the hot gas and the blade surface. Other components including the turbine disc, inner and outer annulus walls and seals are also cooled. The increase in percentage coolant flow that has been necessary to achieve the desired increase in turbine entry temperature is shown in figure 1.2 (from **Byworth**) and it can be seen that at present about 6% of the core flow is used in cooling.

The cooling capability could be improved by increasing the coolant mass flow rate, but the penalties arising from blade cooling must be considered. Work has been performed on the coolant by the compressor which is not all recovered when it enters the mainstream flow and there are also aerodynamic losses associated with mixing of the cooling air and hot gases. These contribute to a reduction in the cycle efficiency thus limiting the advantages of increasing the turbine entry temperature. Consequently more effective cooling techniques are being investigated.

A review of the developments in turbine cooling is presented by **Metzger** who also describes some of the research work directed at improving future designs. Two typical aerofoil cooling schemes were presented and these are reproduced in figure 1.3. The design shown in figure 1.3a is most often found in stationary vanes, while that shown in figure 1.3b is typical of

a cooled rotor blade. The midchord region is cooled with a multiple pass channel and the trailing edge portion incorporates a pedestal array to increase the coolant convection rate. At the leading edge cooling is accomplished by channel flow with wall roughness and augmented by injection of a portion of the coolant into the mainstream for film cooling. On many blades film cooling is also applied at locations other than those shown here. Coolant injection is provided at the blade tip to counteract the high heat load caused by tip leakage flow.

The design of an effective cooling system requires an accurate knowledge of the heat transfer rate to the blade surface. The numerical prediction of this data is common place, but there is an ever present need for improved accuracy. Differences are found in the performance of blades in engines to that predicted or measured in simplified environments, such as linear cascades and there are features in the flow which are beyond the scope of available prediction techniques.

Experimental data is needed to improve the capability of the numerical techniques. Fundamental investigations must be undertaken to gain a better understanding of the complex flow phenomena occuring in the turbine and hence to improve the modelling of these features. It also necessary to make detailed measurements to provide data for validation of the new predictions. This data must be recorded under conditions as representative of those found in the engine as possible.

The Oxford Rotor Project has been undertaken to provide a facility in which detailed aerodynamic and heat transfer measurements can be made in a full stage turbine operating at engine representative conditions. This thesis describes the developments in instrumentation which were necessary to enable unsteady heat transfer measurements to be made on the rotor blade.

A review of previous experimental work indicating the need for a fully rotating experiment is presented in chapter two and the design and operation of the Oxford Rotor Project is described in chapter three. Various methods of measuring the heat transfer rate in transient facilities are discussed in chapter four, followed by the theory of the method used in this project. The development work undertaken to prove the use of this technique in the rotating environment is the subject of chapter five. Chapter six contains details of the digital signal processing methods used to establish the heat transfer rate and the calibration of the instrumentation is described in chapter seven. Finally the results obtained in this facility are presented in chapter eight and the conclusions of the project to date are stated in chapter nine.

CHAPTER 2

THE TURBINE FLOWFIELD

2.1 Introduction.

The flow passing through the high pressure turbine stage of a gas turbine engine is complex. The combustion process results in a highly turbulent and spatially non-uniform flow entering the stator row of the first turbine stage. The flow is then further complicated by three-dimensional flow mechanisms and the relative motion of the blade rows.

The complexity of the flow and the hostile environment found in a real engine mean that the current understanding of the aerodynamic and heat transfer processes has arisen from simpler experiments devoted to specific aspects of the flow regime. This chapter aims to summarize these findings and then to consider the discrepancies between experimental results and the heat transfer distribution observed in engines.

2.2 Heat Transfer to a Turbine Blade.

Static cascade studies such as those of **Nicholson, Daniels** and **Consigny and Richards** have been widely used to investigate the factors affecting the heat transfer rate to turbine blades. These were listed by **Nicholson** to be :- Mach number, Reynolds number, freestream turbulence level, pressure gradient, surface curvature and acceleration parameter. For a given blade profile at a constant inlet angle, the last three are fixed and the others can be varied independently.

The heat transfer rate is governed by the state of the boundary layer around the blade. Typically the boundary layer development is as sketched in figure 2.1. For the suction surface the boundary layer is laminar at the leading edge and then thickens with increasing distance along the

surface until transition to a turbulent state takes place. The heat transfer rate is highest at the stagnation point due to the high local temperature and then falls off as the boundary layer thickens until a sudden change takes place caused by improved mixing in the turbulent boundary layer. The boundary layer state on the pressure surface is less predictable. Transition often occurs early and the resulting high heat transfer rates can be further increased by curvature effects. Under certain conditions the boundary layer may re-laminarize and though the boundary layer is not properly laminar, laminar levels of heat transfer are found. In general designers have found that it is more difficult to predict the heat transfer rate to the pressure surface than the suction surface.

Consigny and Richards investigated the effects of Mach number, inlet Reynolds number, inlet flow angle and turbulence level on the heat transfer rate to a turbine blade. The development of the boundary layer as described above was clearly shown.

The effect of increasing Reynolds number was to cause earlier transition on the suction surface. On the pressure surface a separation bubble had formed with turbulent reattachment. Increasing the inlet flow angle caused the separation bubble to disappear and for a short distance on the pressure surface a laminar boundary layer was present. Increasing the freestream turbulence level from 0.8% to 5.2% caused the start of transition on the suction surface to advance. Stagnation point, laminar and transitional heating were increased by turbulence, but the heat transfer level for an already turbulent boundary layer was unaffected.

A supersonic exit Mach Number resulted in shock induced transition on the suction surface for conditions where the boundary layer was not already turbulent.

2.3 Blade Row Interactions.

A gas turbine engine is made up of alternate rows of stationary and rotating blades. The blade rows are sufficently close together for the influence of one blade row on the flow through the adjacent rows to be important. For a subsonic stage there are two forms of interaction, the first due to the blades of one row cutting through the wakes shed by blades in previous rows and the second due to the potential flow field around each blade being modulated by the relative motion of both upstream and downstream blade rows.

Parker and Watson suggest that for a blade row spacing of 30% of blade chord the potential flow interaction has decreased so that it is insignificant compared with the wake interaction effect. In most engines the axial gap between blade rows is greater than this and hence it is the wake interaction effect which is most important. For highly loaded, low aspect ratio turbines, the blade row interactions are dominated by the secondary flows and associated vortices, rather than the wakes.

In cases where the flow reaches transonic velocity in the blade passages an additional source of unsteadiness arises through "shock wave passing". This is the unsteady flow produced by the blades of one row passing through the shock waves of the upstream blades.

Parker and Watson describe the wake immediately downstream of an unstalled aerofoil as consisting of a central core of very low velocity with a width of similar order to the trailing edge thickness and bounded by regions with very steep velocity gradients in which the flow is generally turbulent. As the wake is swept downstream in the main flow turbulent mixing causes the wake to broaden and at the same time become less intense.

In recent years detailed investigations of the wake structure have been undertaken (**Gostelow). Hah and Lakshiminarayana** have presented several studies of the wakes shed by turbo-machinery blading. They identify three areas; a) very near wake - confined to the trailing edge of the aerofoil, b) near wake - in this region the physical characteristics of the aerofoil and aerodynamic loading have substantial effects on the development of the wake and c) far wake - at some distance from the blade, the wake structure is almost symmetrical, the velocity defect is reduced and the effects of aerofoil shape and loading have vanished.

The description of **Parker and Watson** applies to the far wake region and is a realistic description of the wake at the distance downstream where interaction with the following blade row takes place.

Smith considered the progress of a wake shed by a stationary blade as it passes through the moving row downstream. Neglecting viscosity he showed both theoretically and experimentally that the wake is chopped into segments which are reorientated, so that they are not reunited at rotor exit.

These findings were confirmed by **Hodson (1985)** in a recent experiment. He measured the unsteady free-stream velocity and blade surface pressures at midspan on the rotor of a large scale, single stage air turbine and also undertook flow visualisation experiments in a small scale water turbine. The wake fluid was found to migrate across the blade passage from the pressure surface to the suction surface. The wake was also distorted as a result of the cross channel variation in the convection velocity. The wake segment became bowed in the downstream direction due to the higher convection velocity in mid-passage than at the blade surfaces. It was seen that the rate at which a fluid particle convected along the suction surface

was about twice the rate of one convecting along the pressure surface, causing the reorientation of the wake segment as noticed by **Smith**. The modulation of the wake was clearly seen in the water turbine experiments and it was noted that the wake was not a single entity after its passage through the rotor, but a series of individual segments which lie between the wakes of adjacent rotor blades. The flow onto a subsequent stator row would therefore contain both rotor wakes and wake-generated unsteadiness from the previous stator row. The stator wake segments do not rotate with the rotor wakes as they are convected downstream, but convect with the stationary frame flow. In a multi-stage machine the flow will become increasingly complex as the number of upstream stages increases.

The effect of unsteady wake passing flow on the boundary layer and consequently on the heat transfer rate had not been investigated until recently and attempts to allow for large scale periodic disturbances in design processes, normally resulted in simultating the unsteady flow as a higher level of homogenous turbulence.

2.4 The Effect of Freestream Turbulence on Heat Transfer.

Freestream turbulence has a major effect on the heat transfer rate to turbine blading because of its influence on the boundary layer state. The effect is not numerically predictable and much use has to be made of experimental data.

As explained by **Priddy and Bayley (1987)**, many parameters have been argued as being of significance in defining unsteady or turbulent flow. The amplitude or intensity of the velocity fluctuations is of major importance, but others such as the scale and frequency of the disturbance are less well understood. The importance of reproducing these parameters in

an experiment so as to truly represent the flow found in an engine is now understood, although the problem of making measurements in an engine to establish the conditions have not yet been fully overcome.

In the discussion of the paper by **Consigny and Richards** described earlier, it is stated that the turbulence level of the inlet gas stream in a turbine is usually of the magnitude of 15% or greater. **Goldstein et al** used a Laser Doppler Velocimeter to measure the velocity, turbulence intensity and temperature at the exit of various combustors. The results showed that the effect of combustion on turbulence intensity depended on the combustor design and on the mixing process of the secondary air entering the flow after combustion . The turbulence level of a combustor typical of those used in VTOL aircraft was found to be around 20%.

Investigators have found that the classical method of using a cascade of bars to generate turbulence does not allow these high levels of turbulence to be reproduced (**Consigny and Richards**). Alternative methods such as the two described below enable the generation of a wide range of turbulence levels as well as the independent variation of intensity, scale and frequency.

Krishnamoorthy used a turbulence generator consisting of a hollow cylinder upstream of a cascade. High pressure air was supplied to both ends of the cylinder which had holes drilled along its length so that two rows of jets 180 degrees apart issued perpendicular to the main flow. The interaction between the jets and the main flow produced high turbulence intensities at the cascade and by changing the injection pressure the intensity, but not the scale, of the turbulence was changed.

The results showed that for turbulence intensities in the range 5 to 21% an increase in turbulence resulted in an increase in local heat transfer

coefficient with the effect on a laminar boundary layer being larger than the effect of a turbulent one. The location of the transition point on the suction surface did not change appreciably with turbulence intensity and the boundary layer on the pressure surface was turbulent over the entire length under all flow regimes.

Priddy and Bayley (1985 and 1987) have used a rotating, spoked cylinder as a turbulence generator. The speed and number of bars in the assembly could be changed , enabling the frequency of the perturbation to be varied. For a fixed bar diameter the intensity depends on the distance between the generator and the cascade.

In early experiments **(Bayley and Priddy, 1981)**, the intensity was varied from 0.5% (no bars) to 31%. The heat transfer rate was found to increase with increasing turbulence intensity in all regions except on the downstream half of the suction surface beyond the normal laminar-turbulent transition region which was suppressed by the perturbations. The effects on the heat transfer coefficient were greatest on the pressure surface and the leading edge and rather less on the upstream suction surface. Increasing the frequency of the perturbation also resulted in a higher heat transfer rate.

In 1985 **Priddy and Bayley** reported experiments in which the turbulence intensity was kept below 20% and under these conditions the effect of perturbation frequency was not seen.

In 1987 they presented the results of a study using Laser Doppler Anemometry in which the variations in flow perturbations through the passages of a cascade of turbine blades had been measured. The variations in fluctuating velocity were observed to remain constant in absolute amplitude. This provides some confirmation of the common assumption that in passing through a cascade the perturbations in the flow are "frozen" and it is the

variation in local mean velocity which dictates the turbulence level.

As the leading edge was approached the velocity of the mainstream flow was observed to fall rapidly. The velocity of the perturbations fell too, but they were still present close to the leading edge where the local velocity was very low, resulting in a sharp rise in turbulence intensity. The high heat transfer levels in this region are thought to be a consequence of the persistence of the perturbations.

The acceleration of flow through the cascade had the effect of quickly reducing the turbulence level on the suction surface from a high value at inlet e.g. 17% to a low value e.g. 4%. This accounts for the relatively small increase in heat transfer with increase in turbulence intensity seen in this region.

2.5 The Effect of Wake Passing on Turbine Heat Transfer.

An investigation into the effects of wake passing on the laminar-turbulent transition of the boundary layer on a flat plate was reported by **Pfeil and Herbst,** and **Pfeil et al.** They used a large diameter, rotating, spoked cylinder to produce wake passing flow onto a flat plate. By taking measurements in the boundary layer they confirmed that as the wake impinged on the surface the boundary layer became turbulent for the duration of the disturbance. This behaviour forced transition to start after a shorter distance than with undisturbed flow.

Hodson (1984) measured the blade profile loss and the surface shear stresses at the midspan of a rotor blade in a slow speed, large scale turbine and in a rectilinear cascade of identical geometry. He found that the profile loss of the turbine rotor was approximately 50% greater than that of the cascade. Shear stress measurements, made with hot film gauges,

indicated that as the stator wake was convected through a rotor passage, the laminar boundary layers on the rotor underwent transition in the vicinity of the wake. Hodson attributed the increased profile loss to the unsteady, transitional nature of the rotor boundary layers.

Wittig et al (1985 and 1986) used a hot gas test facility to investigate the effect of wake flow on the heat transfer rate of a cascade of blades. The wake was generated from an uncambered blade in front of the cascade which could be moved both axially and pitch-wise relative to the cascade. The position of the wake had a strong influence on the heat transfer level, with the highest heating occuring when the wake was incident on the leading edge.

Dring et al (1982) reported an experimental study of the aerodynamic interactions between the rotor and stator blades of a large scale, axial turbine. Time averaged and instantaneous surface pressures were measured, thin film gauges were used to determine the state of the boundary layer and time averaged heat transfer coefficients at stator mid-height were also established. Changing the axial gap from 0.15 to 0.65 of the average axial chord, had virtually no effect on the steady pressures around the rotor and stator blade. Variation of the fluctuating pressure on the stator with axial gap could be predicted by a steady rotor potential flow calculation. The fluctuating pressure on the rotor was much larger than could be explained by stator potential flow and its decay with increased axial gap was of a form usually associated with wake flow.

The thin film measurements revealed that the rotor suction surface boundary layer changed, between laminar and turbulent states, as it passed in and out of the wake.

The stator heat transfer rate was found to be affected by the

presence of the rotor. On the suction surface the heat transfer rate was 25% higher with a 15% axial gap than with a 65% gap. The same pattern of laminar turbulent transition was evident with both gaps. The pressure surface was transitional over the entire surface at both axial gaps and only a small change in heat transfer rate with axial gap was noticed.

In a more recent experiment **(Blair et al, 1989)** in the same facility, it was found that changes in the stator-rotor axial spacing produced negligible effects on the heat transfer rate. This contrary result was considered to be due to the improved measurement techniques used in the later experiment and the second set of results was thought to be more reliable.

Large scale facilities, running at low rotational speeds, such as this one, can be extensively instrumented on both rotor and stator and consequently enable detailed study of flow phenomena to be undertaken. However, it must not be forgotten that the flow is virtually incompressible (in the experiments described above the exit Mach Number was 0.2) and the facility is limited to the the study of flow features which are insensitive to compressibility effects. This is a serious limitation when investigating the flow found in a modern high pressure turbine, as the blades in these machines are often operating in the transonic region.

A team at CALSPAN **(Dunn et al, 1984)** built a full stage rotating turbine which used a shock tube as a short duration source of heated air. The gas dynamics and physical parameters of the experiment were representative of typical engine operating conditions and detailed heat transfer measurements were made using miniature thin film gauges. The experimental technique was not intended to duplicate every known parameter important to heat transfer studies, but to define the flow conditions

sufficiently well, that the measured heat flux could be used to validate and improve confidence in the accuracy of full stage design data and predictive techniques.

Dunn and Hause, 1982, describe a series of tests where heat flux measurements for the full turbine stage were compared with previous results taken in the absence of the rotor. The Reynolds number for the with rotor tests was slightly higher than for the stator only tests (1.67×10^5 compared with 1.25×10^5), but the conditions were still considered comparable. The stator heat transfer rate was found to be consistently higher with the rotor present than without.

In a further investigation of this turbine **(Dunn 1984)**, heat transfer measurements were obtained for the full stage with and without injection and on the NGVs with and without the rotor present. The NGV heat transfer rate with no cooling, but rotor present was compared with the no rotor data described above. There was little difference, except in the suction surface, trailing edge region, where the with rotor data was higher by about 25%.

Cooling was achieved by slot injection on the pressure surface of the vane and on the cooled blades the surface downstream of the slot was instrumented. The presence of the rotor was found to have a disruptive effect on the cooling flow.

In **1986 Dunn** reported the effect that NGV cooling had on the blade heat transfer rate, for the same turbine described above. The results showed that cooling the NGV resulted in an increase in heat transfer rate at and close to the blade leading edge, as compared with the uncooled test.

Unsteady heat transfer measurements made on the rotor are reported by **Dunn et al, 1986**. The fluctuations resulting from the vane/blade interaction were found to be large in comparison with the time averaged heat

flux at the three suction surface, midheight locations which were investigated. More detailed measurements of the unsteady heat transfer rate were published by **Dunn et al, 1989.** In this paper they present phase resolved measurements which show the variation in heat flux on the rotor blade as it traverses each NGV passage. All data was for the suction surface and in each passage the peak heat flux occurred in the portion of the flow which was associated with the vane wake. There were passage to passage and revolution to revolution variations, but in each case the overall characteristics of the passage signature were reproduced. The effect of increasing the vane/blade spacing from 0.19 to 0.50 axial chords was to diffuse the character of the heat flux history and to lower the heat transfer level.

Dunn and his co-workers have made measurements of the heat transfer rate in several different turbines, under many different flow conditions. Their investigations have shown that there can be an upstream effect of the rotor on the stator heat transfer, as well as the downstream effect of the NGV wake on the rotor heat transfer. The influence of axial spacing and cooling configuration has also been seen. In interpreting these results the value of simpler experiments which address specific aspects of the flow field are realised.

Doorly and **Doorly et al (1985 a,c)** describe an experiment in which wakes were generated by rotating a bar in front of a cascade of blades. The mid-height velocity triangle was correctly simulated as shown in figure 2.2 and the design flow conditions were achieved. The objective was to determine both the nature of the unsteady boundary layer on the turbine blade in response to a range of wake passing regimes and the consequent implication for the mean and fluctuating heat transfer rate. The simplicity of the arrangement enabled the size and spacing of the wake to be varied and by

changing the rotor speed, wake passing with and without shock waves could be studied. Different turbulence levels were generated using grids.

Initial tests, reported by **Doorly**, showed that the NGV wakes were symmetrical at the rotor inlet plane and could be simulated by the wakes of small circular bars. Schlieren flow visualisation was used to chart the progress of the wake through the blade passages. The unsteady heat transfer rate was measured using high frequency thin film gauges which also showed the state of the boundary layer.

The results showed that the passing of the wake could result in a transient increase in the heat transfer rate of up to 500% of the freestream level. Detailed analysis of the heat transfer measurements and schlieren photographs revealed the nature of the boundary layer transition caused by wake passing. On a laminar boundary layer a turbulent patch is produced by each wake and swept along the blade surface causing unsteady transition. This may significantly affect the blade performance, both by increasing the mean level and by causing severe periodic fluctuations in the heat transfer rate.

The effect of wake passing on a transitional boundary layer was smaller, but still resulted in an increase in the mean heat transfer rate due to the fully turbulent patch generated by each wake. For a fully turbulent boundary layer the presence of wakes did not affect the mean heat transfer level, but there was a noticeable increase in the fluctuation level.

When the bars were run at near sonic speed, (**Doorly** and **Doorly and Oldfield (1985b)**, shock waves were produced which impinged on the suction surface initiating a leading edge separation which subsequently collapsed, leaving a turbulent patch which was convected downstream. In each wake passing cycle the effects due to the shock immediately preceeded

those due to the wake, and at conditions representative of those found in an engine, the wake and the shock wave (from the next cycle) impinged simultaneously on the blade surface. The character of the unsteady transition was found to be different to that produced by wake passing alone. The turbulent patches produced in rapid succession merged to form an unsteady turbulent boundary layer resulting in a heat transfer rate which approached that associated with a "steady" turbulent boundary layer.

The shock waves studied were comparatively weak, but it is clear that shock wave passing is a major source of flow unsteadiness in the first stage turbine. The contribution of shock wave passing to the unsteadiness increases with NGV exit Mach Number and will affect the stage power output as well as the heat transfer rate.

2.6 Effect of Wake and Shock Wave Passing on Turbine Heat Transfer.

In recent years Doorly's wake generator has been used to study the effects of wake and shock passing on the unsteady aerodynamic and heat transfer processes in a highly loaded rotor profile **(Ashworth , Ashworth et al, Schultz et al (1986)** and **Johnson et al).** The effect of wake and shock passing on a film cooled version of the same profile was studied by **Rigby.**

The diminished velocity in a wake results in an apparently reduced blade incident angle. **Ashworth et al** measured the Mach Number and heat transfer rate distributions around the blade at +5 deg. and -10 deg. incidence as well as at design. The suction surface and leading edge heat flux was affected, with negative incidence producing the lowest heat flux, (approximately 50% of that measured at design incidence on the suction surface and 80% of the design value at the leading edge). The Mach Number distribution showed that the pressure gradient on the suction surface was

strongly affected by incidence changes.

The effect of bar passing was to raise the mean heat transfer level, except for a short distance in the middle of the suction surface, where the mean level was reduced. Examination of the unsteady heat transfer records established that shock wave passing resulted in a boundary layer separation, which was signified by a very low heat transfer rate. A very sharp rise in heat flux followed as the boundary layer reattached turbulently.

The effect of freestream turbulence and wake/shock passing was examined. On the suction surface the wake disturbance was found to be weaker in the case of low (0.8%) turbulence, than in the moderate (4%) case. With low freestream turbulence the instantaneous heat transfer rate between disturbances was higher than in the corresponding no bar test, while with 4% turbulence the heat flux dropped down to the no bar level. On the pressure surface the wakes induced an oscillation around the mean level, which resulted in an average heat transfer level which was little changed from the no wake level.

The conclusion was that the increase in mean heat transfer rate caused by wake and shock interaction overrode any reduction due to transient changes in the angle of incidence.

The high heating rate caused by shock passing was investigated further by **Johnson** and reported by **Johnson et al**. The instantaneous drop in heat flux reported above was sometimes observed to fall to negative levels and it was apparent that a mechanism besides transient separation was responsible. **Dunn et al (1986)** also reported negative portions in unsteady heat transfer signals. He remarked that these could be due to flow phenomena or instrumentation noise, but did not investigate further.

Johnson made high frequency pressure measurements, which like

the instantaneous heat transfer rate gave large, rapidly varying signals. Schlieren photography showed that the bar recompression shock wave was impinging on the suction surface and being reflected. The drop in heat transfer rate was seen to be associated with an expansion wave.

A simple first order perturbation analysis of the boundary layer equations showed that the transient adiabatic heating of the boundary layer by shock waves and rarefactions gave rise to high temperature gradients near the surface, which in turn led to large conductive heat transfer rate fluctuations. Application of this theory to measured pressure signals gave predictions of fluctuating heat transfer rates in agreement with the measured levels.

The highly loaded profile tested in the experiments described above was the midheight section of the rotor blade tested in the MIT blowdown, turbine facility **(Epstein et al, 1984)**. This team have made heat transfer measurements on the rotor blade of the full stage turbine under engine representative conditions and **Guenette et al** have compared data from the midspan of the rotor blade with that obtained in the 2D cascade.

The agreement between the cascade data, with a low freestream turbulence level of 0.8%, and the rotor data (0.5% turbulence) was good, except in the region of the leading edge, where the cascade data was considerably higher and on the last 30% of the suction surface , where the cascade data was 50% higher. The cascade data with 4% turbulence was higher than the rotor data over the first 60% of the pressure surface, but otherwise agreed with the low turbulence data.

Examination of the unsteady heat transfer traces also produced similarities, although the relative magnitude of the wake and shock induced spikes were different in the two facilities. Generally the unsteady interactions

were stronger on the rotor than in the cascade.

The remarkable similarity of the results from the 2D cascade and full turbine stage implied that the heat transfer processes on this transonic turbine were largely two-dimensional at midheight.

2.7 Three-Dimensional Flow Mechanisms

In the discussion so far it has been assumed that the flow through the turbine is two-dimensional. In practice the flow in a turbo-machine can be highly three-dimensional due to secondary flow and rotational effects. **Moore and Adhye** suggest that secondary flow could be described as, "unplanned three-dimensional flow effects in a turbine which lead to unexplained (secondary) losses". A more classical description of secondary flow is given by **Gregory-Smith et al**, who say that "the term secondary flows is usually used to describe the transverse velocities which are generated when a shear flow is turned". Besides causing a large proportion of the total losses in a turbomachine, secondary flows are responsible for redistributing the boundary layer and modifying heat transfer patterns.

In recent years many experimental investigations of secondary flow have been undertaken, including those by **Langston et al, Gaugler and Russell** and **Zunino et al.** A comprehensive review of all the work in this field was published by **Sieverding** in 1985.

The secondary flow in a blade passage, whether in a linear cascade or an annular blade row, is dominated by two features, the passage and horseshoe vortices. These are shown schematically in figure 2.3. from **Moore**. The inlet, endwall boundary layer separates on interaction with the blade leading edge and rolls up to form the horseshoe vortex. It is wrapped around the leading edge forming two legs, one in each passage. Pressure gradients

exist across the passage due to the turning and acceleration of the mainstream flow. The boundary layer within the passage is driven across the passage by these pressure gradients and rolls up when it encounters the suction surface, to form the passage vortex. The pressure surface leg of the horseshoe vortex is also convected across the passage and absorbed into the passage vortex. The suction surface leg stays close to the vane as it is swept downstream. The vortex is rotating in the opposite sense to the passage vortex and the interaction of the two is not clearly known (**Sieverding**) and seems to depend on the cascade geometry and overall flow conditions.

Gaugler and Russell used various flow visualisation techniques to define the secondary flow near the endwall in a large scale turbine cascade. They compared the secondary flow patterns with the measured heat transfer distribution and found a local peak in heat transfer near the leading edge where the initial vortex roll up begins.

The secondary flow in an annular cascade is modified by the geometry of the passage and the high swirl found at exit. **Wedlake et al** made detailed aerodynamic and heat transfer measurements on a transonic Nozzle Guide Vane in an annular cascade at design conditions. They also found high heat transfer levels corresponding to the leading edge horseshoe vortex region. An area of moderate heat transfer was seen early in the passage with its major axis aligned with the pressure surface leg of the horseshoe vortex as it moves across the passage to the suction surface. There was no obvious evidence of the passage vortex itself creating high heat transfer levels as it passed across the endwall surfaces.

As part of a study into the effects of blade row interactions on the wake and secondary flows **Binder and Romey** made measurements of the

secondary flows behind the stator ring of a low aspect ratio turbine. Just down stream of the trailing edge, the high loss region in the wake was seen and also that due to the hub and tip secondary flows. It was noticed that the high loss region at the outer radius was some distance from the casing while the other was very close to the hub. This is a consequence of the radial pressure gradient due to centrifugal forces. This gradient is built up by deflection within the blade rows and results in higher pressure on the outer casing. Reduction of the gradient behind the stator requires a radial flow towards the hub causing the movement of the secondary flows as described above. Within the wake there is a stronger flow towards the hub because the tangential velocity is lower. As a consequence, low energy material from the wake migrates to the hub increasing the loss in this region.

Using a Laser-2-Focus Velocimeter, detailed flow data were taken near and within the rotor of a cold air turbine, with special emphasis on determining the movement of the stator wakes within the rotor blade passages (**Binder et al, 1985**). High turbulence regions were found within the wake and the regions associated with secondary flow. There was a marked increase in velocity fluctuations within the stator wake when it was chopped by the rotor. Two counter rotating circulation regions were seen either side of the chopped stator wake, which resulted from the differences in velocity within and outside of the wake.

Further investigations were undertaken (**Binder**) to establish a connection between the chopping of the secondary vortices and the increase in flow turbulence. The measurements suggest that the secondary flow vortices break down after being cut and deformed by the rotor blade. A definite explanation of the flow mechanism involved in vortex break down

could not be given, but two reasons were discussed: a) The stator vortex is cut by the rotor blade, the pressure inside the vortex is lower than outside causing the vortex to fill, thus the pressure differences inside the vortex decays and the vortex breaks up.

b) The vortex becomes bowed on entering the rotor passage leading to a considerable increase and deformation of the vortex cross sectional area also causing the vortex to break down.

The energy of the vortex motion is converted into random fluctuation energy by the break down and remains useless in the turbine, therefore contributing to an increase of losses in the rotor. The high fluctuation of the flow in the wake region coupled with the low relative velocities measured near the pressure surface of the rotor blade can lead to very high values of turbulence intensity, which significantly affect boundary layer behaviour and hence heat transfer.

There have been few experimental investigations of the effect of rotation on secondary flows and those that have been conducted were low speed studies. It is known that rotation induced centrifugal and Coriolis forces generate spanwise flows in the boundary layer resulting in a radial outflow on the rotor blade (**Reynolds et al** and **Lakshminarayana et al**).

Dring and Joslyn (1981) have observed strong radial flows on a rotor blade which were due to the "relative eddy". Consider a flow which is irrotational in the absolute frame of reference. The flow enters a rotor and when viewed from the rotor the fluid appears to be rotating in the opposite direction. This relative rotation seen in the rotating frame of reference is called the relative eddy. **Dring and Joslyn (1983)** have shown that for some blade designs the relative eddy would cause a significant radial redistribution of fluid from the rotor inlet to exit, resulting in considerable attenuation to

the radial profile of total temperature. The change of radial total temperature profile has been cited as a possible explanation for the differences in heat transfer patterns seen in engines and experimental facilities **(Guenette et al).**

2.8 Final Considerations.

A description of the flow in an axial flow turbine stage has been given. It was seen that the flow is highly three-dimensional and unsteady, with the flow through one row modified by the presence of adjacent rows which have relative motion. The flow through the stator row may differ from that found in a linear cascade due to the higher swirl at exit and the presence of the rotor.

The flow through the rotor row is affected by the wake and secondary flows shed by the NGV row. These are chopped and dispersed on entering the rotating frame causing an increase in rotor loss. The flow at the outer radius is strongly modified by leakage flows through the rotor-tip gap. Rotation also results in radial flows due to centrifugal and Coriolis forces.

These three-dimensional flow features have a major effect on the state and distribution of the boundary layer and consequently on the heat transfer patterns. Further experiments are needed to increase understanding of the turbine flow field, and hence to enable the heat transfer distribution to turbine blading to be accurately predicted.

CHAPTER 3

THE OXFORD ROTOR PROJECT

3.1 Introduction.

The experimental work described in the previous chapter has illustrated the complexity of the turbine flowfield and the need for detailed heat transfer measurements in a fully rotating stage. There is a particular need to investigate the effects of unsteady flow features on the time resolved heat transfer rate . The experiments of **Doorly** and **Johnson** showed periodic fluctuations in heat transfer rate, due to wake and shock interactions, of up to five times the mean value. The thermal stresses induced by such fluctuations can have a major effect on the fatigue life of the blade, especially in the case of ceramic blades or those with a thermal barrier coating.

The environment in a real engine is too harsh to enable measurements of the required detail to be made, although it is possible to establish the blade surface temperature using a variety of techniques including optical pyrometry and surface mounted thermocouples, **(Alwang).**

It has been realized for two decades that the measurement of heat transfer rate is more easily accomplished in a transient facility than in a continuous hot tunnel, **(Schultz and Jones, 1973)**. In the continuous facility the model must be internally cooled to establish the temperature gradient from which the heat transfer rate is deduced, it must be capable of withstanding the high temperatures involved and the test must be conducted over a long enough period to enable steady state conditions within the model to be achieved.

In a transient facility the sudden onset of a high temperature flow results in a rapid rise of the model's surface temperature and the heat

transfer rate can be deduced by recording the time-temperature history. The short flow period means that the model never reaches thermal equilibrium and only experiences a modest temperature rise. Consequently it is not necessary to manufacture the components from high temperature materials. The running costs are also small compared with those of a continuous facility. **Schultz et al (1987)** have shown that the results from the two types of facility are in good agreement.

There are currently three transient facilities in which heat transfer measurements on a full stage turbine can be made under engine representative conditions.

A team at CALSPAN, **(Dunn et al, 1984)** uses a shock tube to supply air at a high temperature to a single stage turbine for approximately 20ms. The results obtained by this team during the past few years were discussed in chapter two and have provided valuable information concerning the effects of blade row interactions on both the rotor and stator heat transfer.

A blowdown turbine facility has been built at MIT (**Epstein et al, 1984**). The test gas is heated before being suddenly expelled through the turbine working section. The run time is approximately 0.5-1.0 s and an eddy current brake is employed to hold the speed constant throughout the run. The mid-height profile of this turbine has also been the subject of cascade tests and the results from the two experiments were compared in chapter two.

The Oxford Rotor Project is a recently commissioned facility, **Ainsworth et al, 1988.** An Isentropic Light Piston Tunnel is used to provide a short duration flow (approximately 200ms) at temperatures up to 400K.

The heat transfer instrumentation in these three facilities is

described in chapter 4 and a more detailed description of the Oxford Rotor Project is given below.

3.2 Design of the Facility.

The facility is based on the Isentropic Light Piston Tunnel, (ILPT), which has been used successfully in Oxford for approximately 15 years to measure the heat transfer rate to stationary cascades of turbine blades, **(Jones 1988).**

The general arrangement of the facility is shown in figure 3.1. The turbine working section, figure 3.2, was designed to replace the linear cascade used previously with as few modifications as possible.

The operation of the ILPT is described in detail by **Schultz et al, 1977** and only a brief description will be given here. The device consists of a frictionless pump tube containing a light piston, which is linked through the working section to a dump tank. The pump tube is isolated from the working section by a fast-acting valve. At the beginning of a run the piston is positioned at the far end of the pump tube, the main valves are then opened and the driver gas flows into the pump tube, pushing the piston forward and compressing the test gas between the piston and the fast acting valve. When the desired pressure and hence temperature are reached (the compression being isentropic) the fast acting valve is opened. Correct matching of the flow rates of the driver gas into the pump tube and the test gas out of the tube ensures that the piston continues along the tube at a constant velocity. A steady uniform flow of heated gas flows through the working section from the time that the fast acting valve is opened until the piston reaches the end of the pump tube.

The turbine module consists of a rotor disc containing 60 blades

mounted on a hollow shaft which is cantilevered from two sets of bearings. Upstream of the rotor there are 36 NGVs with two groups of four mounted in removable cassettes allowing easy access for flow visualization studies and instrumentation purposes.

The bearing assembly is supported from a bolster plate mounted on top of an A frame. The fast acting, annular gate valve, designed to isolate the working section from the pump tube before a run, is bolted to the bolster plate and at the end of the run the piston comes to rest on the front face of the gate valve. The design of the annular gate valve and inlet annulus was a crucial part of the project, **Ainsworth et al, 1988** and **Sheard** as it is essential that the flow field at NGV inlet is uniform and of low turbulence.

An airmotor is used to spin the turbine to the required speed before the run is started and also when checking the mechanical performance. The air supply to the motor is taken through the spokes of the annular gate valve, as is the oil for the bearing system and leads from the instrumentation used to monitor bearing performance.

The hollow shaft contains electronic circuits which amplify the signals before they are transmitted through the slipring. The slipring is connected to the shaft using a flexible coupling (Helical Products Company, Inc.). The discs for the speed encoder are also mounted at this end of the shaft.

The upstream, inner annulus liner is supported by the bearing housing and downstream of the rotor the inner annulus is supported by three radial spokes. A second throat was mounted between the turbine and the dump tank to set the rotor exit Mach Number and suppress upstream interference from the dump tank.

A photograph of the facility is shown in figure 3.3. In figure 3.4 the outer casing of the working section has been taken off, the disc is being removed from the shaft and the bearing housing and NGV ring can just be seen behind.

Details of the mechanical commissioning of the facility and the aerodynamic proving tests are given by **Sheard**.

3.3 Operation of the Facility.

The operation of the ILPT is shown in figure 3.5. Once the annular gate valve is opened a constant flow of hot air passes through the turbine causing it to accelerate at a rate which depends on the operating point. For the experiments described in this thesis the design speed was 8434 rpm and the run time was 190ms. During this time the rotor accelerated by approximately 3000 rpm. Consequently the operating procedure was to spin the turbine up to 6500 rpm using the airmotor and then fire the tunnel causing the turbine to accelerate. The high speed data acquisition equipment was triggered as the speed passed through the design value. This is illustrated in figure 3.6 and further details of the operating point are given in section 3.4.

Predictions were made of the effect of incidence changes on the blade surface Mach Number distribution and these indicated that meaningful data could be achieved within +/- 0.5 deg. of design incidence. As explained in section 3.5 the high speed data acquisition is accomplished in 17.5ms during which time the incidence changes by 1 deg. The decision not to include a brake in the design was based on this acceptable incidence change and a desire to keep the design as simple as possible.

A micro-computer system was used to control the airmotor and to

record measurements of the rotating system, eg speed, oil temperature, vibration levels and bearing temperature. A schematic of the system is shown in figure 3.7. The HP 9836 computer was linked to a PCI 6380 which is a Z80 based intelligent microcomputer interface maunufactured by CIL Micro Systems containing 8 A/D channels, 4 D/A channels and 4 relays. The various parameters required to monitor the mechanical performance were logged on the A/Ds and recorded by the computer.

An airmotor was chosen to drive the turbine so as to avoid possible electrical interference effects. The performance of the motor depends on the mass flow rate which is limited by a pressure regulator upstream of the settling tank. The rate of acceleration is then controlled by changing the position of a modulating valve. The computer operator inputs the new position and a signal is sent to the valve.

A controlled procedure for operating the inlet and vent valves is included in the computer program and the rig is automatically shut down if any of the measured parameters exceed pre-set values. A second, independent speed encoder is connected to an overspeed trip and there is also a pressure switch set at the airmotor rating. Both of these will shut off the air supply independently of the computer. As a final overriding safety device a manual "panic" button is included.

Many spinning tests were undertaken before full operation of the turbine and IPLT were undertaken. The performance of the bearings and the vibration level was carefully monitored and the results are discussed in detail by **Sheard.** However, a brief description of the vibration levels will be given here because of the importance of this topic to the whole project.

The facility was designed so that instrumentation changes on the rotor could be made without dismantling the rotor assembly. However, to

make use of this advantage it must also be possible to balance the rotor in situ, so that out of balance forces introduced by the instrumentation changes can be corrected. Prior to initial assembly the shaft and disc were two-plane balanced and subsequently a simple field balancing technique, described by **Dietz (1988)**, was used.

Vibration levels were measured using a Schenk T77 velocity transducer attached to the bearing housing and weights were attached to the rotor disc. The output of the velocity transducer was recorded by the control program through the PCI. A series of 30 readings was taken and the rms average was calculated and stored.

During spinning tests it was discovered that the rotor exhibited complex dynamic characteristics. These are best illustrated using a vibration trace captured as the rotor decelerated. The vibration level of the bearing housing is plotted against speed in figure 3.8. Two traces are shown, one recorded when the balance level was good and the other when the rotor was out of balance. In both cases major resonances can be seen at 4750 and 4200 rpm and smaller resonances at 2250 and 2100 rpm.

Vibration traces recorded when the rotor was accelerating were less repeatable. Three different modes of behaviour were noticed depending on the state of balance. Below 4750 rpm the traces were similar to those observed during run down tests, but the behaviour at speeds greater than 4750 rpm was unstable and highly unlinear. At a high unbalance level, as shown in figure 3.9, the rotor dropped out of the resonance at 4750 rpm and then started a further excitation which increased rapidly and which the airmotor could not drive through. At better balance levels the rotor suddenly dropped out of this resonance, figure 3.10 and when well balanced the rotor did not see this last resonance at all, figure 3.11.

In order to be able to operate the turbine in the ILPT the balance level of the rotor had to be such that the resonance above 4750 rpm was not excited or ceased to be excited at a speed well below 6000 rpm. Many hours were spent trying to achieve a good balance level, a task which was frustrated by the non-linear behaviour of the rotor.

The balance level appeared to deteriorate with time and operation of the ILPT and it became increasingly difficult to achieve a low vibration level. Various reasons were postulated for this behaviour including rubbing of the blades or seals on the casing, misalignment of the disc on the shaft and possible deterioration of the bearings. Before the heat transfer tests were completed it was decided that the time spent balancing the rotor had become prohibitive and the decision was made to strip the rotor and investigate the cause of the non-linear vibration.

3.4 Choice of Profile and Operating Point.

The turbine used in this project is a 0.62 scale model of the first stage of a high pressure turbine, similar to those currently found in civil aircraft engines. It has been the subject of several cold flow tests **(Rolls-Royce, plc)** and the midheight blade and vane profiles have been extensively tested in cascade tests at Oxford. **Nicholson** and **Nicholson et al** made heat transfer and aerodynamic measurements on both profiles in the ILPT. **Horton et al** undertook film cooling studies on the rotor and **King** made detailed aerodynamic measurements on the uncooled rotor. The work by **Doorly** using rotating bars to simulate the NGV wakes was also undertaken on this profile.

One of the major objectives of this study was to make heat transfer measurements around the rotor midspan and compare the results with those of **Doorly** and **Nicholson**. The positions of the heat transfer

gauges used in this study are given in chapter 7 along with a diagram indicating the position of the B22 plane section used in the linear cascade tests.

The operating point of a turbine can be defined by several "non-dimensional" groups, **Horlock**. The values for this turbine are given in Table 3.1. These parameters were then used to calculate the required conditions in the working section. As demonstrated by **Ainsworth et al (1988)** these depend on the choice of gas to wall temperature ratio. For this series of tests, a temperature ratio of 1.3 was used, which resulted in the running conditions listed in table 3.2.

The total pressure was set by the required Reynolds and Mach Numbers, the total temperature by the temperature ratio and as the compression is isentropic, the initial tube pressure was easily calculated. The total temperature seen on the rotor blade was the rotor relative temperature, which is lower than the absolute value and falls with increasing speed. Consequently the gas to wall temperature ratio on the rotor blade was lower than 1.3. For heat transfer experiments the signal to noise ratio is improved by using a higher temperature ratio, but in this experiment the greater mass flow rate through the facility required at a higher temperature ratio, **(Schultz et al, 1977)**, could not be matched by the driver gas. Consequently this was the highest temperature ratio for which a matched run could be obtained,

Jones et al have derived the equations governing ILPT operation and using these the running time was calculated. To estimate the speed change during a run, the specific power was assumed to be unchanged away from the design point. The polar moment of inertia was determined experimentally to be 1.66 Kg/m^2. Knowing this and the power generated enabled the speed change during a run to be calculated.

Further details of the choice of design point and a discussion of how closely it was achieved in practice, are presented by **Sheard.**

3.5 Instrumentation Requirements.

The key aim of this project was to make unsteady heat transfer measurements on the rotor blade. The developments in instrumentation required to achieve this are the subject of this thesis and are also summarized by **Ainsworth et al, 1989**.

The instrumentation specification was dictated by the operating conditions of the facility. At design speed the wake passing frequency is 5kHz and to give adequate resolution a bandwidth of 100 kHz was considered necessary. Consequently to satisfy the Nyquist criterion the sampling rate must be at least 200 kHz. The memory of the transient recorder used for data acquistion is 3500 blocks, so at 200 kHz the data acquisition time is 17.5ms, long enough to capture data from two and a half revolutions (90 wake passing events). The fastest sampling rate possible on the transient recorder is 500kHz which would give greater definition to the signal and also reduce the incidence change, but would only enable data from one revolution to be captured.

The instrumentation mounted on the rotor blade had to be able to withstand the forces of rotation, which were calculated at a maximum of 32,000g.

A further complication of making measurements on the rotor blade was that a means of transmitting the signals to the stationary frame had to be found. Several methods were considered. Radio telemetry and optical fibre links were discounted on cost grounds and a possible method of using digital on-shaft storage is still at the development stage. The most common method

of data transmission across a rotating to stationary interface is to use a slipring and this was the chosen solution for the rotor project.

The particular slipring used was a 24 channel, air-cooled unit made by IDM (in Reading, U.K.), type PM-24-01TC. The rings were silver plated and the brush tips were made of silver graphite. In order not to loose any of the output signal in noise generated by the slipring, circuits in the shaft were used to amplify the signal before transmission, thus ensuring a high signal to noise ratio. The design of these circuits is discussed in chapter four. Tests to discover the effects of rotation and measurement of the noise generated by the slipring are described in chapter five. To avoid earth loop problems the outputs from the in-shaft electronics were of a differential form and after transmission through the slipring each was passed to an AMP-05 signal conditioning unit, described fully by **Ainsworth et al, 1989.**

The specification for the heat transfer instrumentation also applies to fast response pressure transducers mounted on the rotor blade and a project is underway to develop a suitable measurement technique, **(Dietz, 1990).**

Besides the fast response heat transfer data other measurements must be made so that the flow conditions can be ascertained. Total temperature and pressure were measured upstream of the NGVs. Static pressure tappings were located at various positions on the inner and outer annulus and at hub, mean and tip locations on the vane. The instrumentation for these measurements was as used in the linear cascade tests and is described by **Oldfield et al, 1978.**

Measurements of the heat transfer rate on the rotor blade of this turbine have been succesfully undertaken and are presented in Chapter 8. Details of the aerodynamic and mechanical performance are given by **Sheard.**

CHAPTER 4

MEASUREMENT OF HEAT TRANSFER RATE

4.1 Methods of Measuring Heat Transfer Rate.

There are many methods of measuring the rate of heat transfer to a body and the choice of method will depend on the test conditions, the complexity of the model and the nature of the phenomena under investigation. All instrumentation used must be compatible with the environment in which it is operating, i.e. be able to withstand the gas temperature, heat flux levels and pressure loading. Minimum interference with the boundary layer is also important. The advantages of making heat transfer measurements in transient facilities have already been discussed in chapter three, where it was seen that the short test time enables relatively simple materials to be used in the manufacture of the instrumentation.

In moving to the rotating frame further requirements of the instrumentation must be considered. The size of the instrumentation is more important as it is desirable to keep modifications to the blading to a minimum for stress reasons. The instrumentation has to be capable of withstanding the centrifugal loading as well as the blade loading.

A method of measuring heat transfer rate that has been used widely in short duration facilities **(Schultz and Jones, 1973)** is the thin film resistance thermometer. A gauge of a suitable metal such as platinum is deposited on an insulating surface and a constant current passed through it. As the temperature changes, so does the resistance of the gauge and hence the voltage across it. By recording and processing the voltage change across the gauge the heat transfer rate can be calculated. This method has been widely used in Oxford **(Jones)** and will be described more fully later. The

method can be used to give both the mean and unsteady (time varying) heat transfer signal.

The three research teams which have built short duration, turbine test facilities (CALSPAN, MIT and Oxford) all had the same instrumentation requirements, but have developed three different, yet loosely related, systems.

The team at CALSPAN used platinum thin film gauges which were painted onto a pyrex insert let into the surface of the blade, **(Dunn, 1986)**. The shape and size of the insert depended on the region of the blade of interest. Small button gauges, figure 4.1, were used to make very local measurements to investigate events which occurred during passage and wake cutting. These were manufactured by painting a platinum gauge on to a pyrex button 0.97mm in diameter. The gauges were 0.1mm wide by 0.51mm long and approximately 500-1000 nm thick. At room temperature the gauge resistance was intended to be in the range 50 - 100 Ω. A coating of magnesium fluoride was vapour deposited over the gauge to protect against abrasion. The button type gauges were flush mounted around the aerofoil surface, but at the leading edge a contoured insert was used with a number of gauges painted on it. Each insert was carefully contoured to the blade leading edge profile prior to painting the gauges, so that no surface discontinuities were present.

There are two main problems with this method, **(Dunn et al, 1984)** apart from the difficulty of ensuring that the surface is free from discontinuities. These arise because the substrate, being an insulator, heats up during the test. The temperature of the insert rises by about 38 deg. C while the blade remains at ambient temperature. It is not known what effect these "mini islands of heat" have on the boundary layer. **Schultz and Jones (1973)** have addressed the problem of errors in the measured heat transfer rate due to a temperature discontinuity caused by the presence of the thin

film gauge. Their analysis followed that of **Kays and Crawford** and solutions were obtained for both laminar and turbulent boundary layers, but not for the case where the boundary layer was transitional. These two-dimensional solutions provide some guidance to the above three-dimensional problem but not a quantitative solution and the approach taken by **Dunn et al (1984)** has been to minimize the ratio of gauge diameter to chord length.

The rise in temperature of the substrate also results in changes in the material properties which must be taken into account when calculating the heat transfer rate.

The heat transfer gauge designed by the team at MIT consists of a metal thin film resistance thermometer sputtered on both sides of a thin (25μm) polyamide sheet, figure 4.2 . The sheet containing 25 gauges is then bonded to the aerofoil surface completely covering it. The temperature difference across the insulator is a direct measure of the heat transfer to the surface at low frequencies. But above a certain frequency, which depends on the insulator thickness, the substrate appears semi-infinite to the upper sensor and a quasi-1D analysis can be used to infer the high frequency heat flux from the upper surface temperature history. This instrumentation is described in a very detailed paper by **Epstein et al (1985)**, which considers not only the manufacture of the gauge, but also the optimization of the design and the calibration procedure.

Although wrapping a flexible insulating layer around the blade does not introduce thermal or geometric discontinuities, there are other disadvantages to this method. The flexible film has to be applied carefully and care must be taken to ensure that there are no air bubbles in the glue layer and on a highly three-dimensional blade it is obvious that there will be a limit to the locations where the thin film thermometers can be placed. The

use of polyamide (or any other similar substance) restricts the maximum operating temperature to around 300 deg. C.

The resistance thermometers are fabricated by vapour deposition of pure nickel and problems occur with cracking of the metal element due to stresses introduced in deposition. The cracks are multiple and not visible even under high magnification, but only crack free gauges give usable results. Gauges manufactured in this way also have a limited tolerance to bending and will tend to crack when applied to highly curved surfaces such as the leading edge region.

Despite these difficulties this type of gauge has been used successfully to measure the heat transfer rate around the midspan of a turbine rotor blade and the results are reported by **Guenette et al.**

The approach used at Oxford in the Rotor Project is a development of the proven technique of painting platinum thin film gauges on models fabricated from a machineable glass ceramic (**Oldfield et al, 1978**). The stresses encountered in the rotating frame exclude the possibility of manufacturing the rotor blades from machineable glass and an alternative technique of coating a metal blade with an insulating layer was adopted. The early development work was reported by **J.E. Doorly (1985)** and **J.E.Doorly and Oldfield (1986)**. This thesis includes the details of subsequent work.

Calculation of the heat transfer rate involves solution of the one-dimensional conduction equations and the appropriate theory for the new gauge system will be laid out in the next section. Practical aspects of the gauge manufacture will be dealt with in chapter 5.

4.2 Thin Film Gauge on a Single Layer Substrate.

A thin film gauge is essentially a platinum resistance thermometer

with resistance, R_0, at a temperature, T_0, and temperature coefficient of resistance, α. The resistance, R, for a temperature of $T_0 + T$ is given by

$$R = R_0(1+\alpha T) \qquad (4.1)$$

A constant current, I, is passed through the gauge and the voltage change, v, for a temperature rise, T, is given by

$$v = I R_0 \alpha T \qquad (4.2)$$

Consider a thin film gauge mounted on a single layer substrate as shown in figure 4.3. The heat transfer rate to the surface is $\dot{q}$.

For short time and neglecting the thermal capacity of the film itself, the one-dimensional conduction equation governs the flow of heat into the substrate.

$$\frac{\partial^2 T}{\partial x^2} = \frac{1}{\alpha_1}\frac{\partial T}{\partial t} \qquad (4.3)$$

where T is the temperature of the substrate at a distance, x, from the surface, at time, t, and α_1 is the thermal diffusivity of the substrate, defined in terms of the density, ρ, the specific heat, c, and the thermal conductivity, k:-

$$\alpha_1 = \frac{k}{\rho c} \qquad (4.4)$$

The boundary conditions are

$$\dot{q} = -k\frac{\partial T}{\partial x} \qquad \text{at } x = 0 \qquad (4.5)$$

$$T = 0 \qquad \text{at } x = \infty \qquad (4.6)$$

with initial condition

$$T = 0 \qquad \text{at } t = 0 \qquad (4.7)$$

Taking the Laplace transform of equation 4.3, it may be shown **(Schultz and Jones, 1973)**, that

$$\bar{\dot{q}} = \sqrt{(\rho c k)_1}\sqrt{s}\,\bar{T} \qquad (4.8)$$

where $\bar{}$ denotes the Laplace Transform and s is the Laplace Transform Variable.

If the heat transfer rate is constant i.e. $\bar{\dot{q}} = \frac{Q}{s}$

Then $$\bar{T} = \frac{Q}{s^{3/2}\sqrt{(\rho ck)_1}} \qquad (4.9)$$

and $$T(t) = \frac{2Q}{\sqrt{(\rho ck)_1}}\left(\frac{t}{\pi}\right)^{1/2} \qquad (4.10)$$

i.e. the resulting surface temperature rise is parabolic with time.

For the more general case where the heat transfer rate is not constant, it can be shown **(Schultz and Jones, 1973)**, that

$$\dot{q}(t) = \frac{\sqrt{(\rho ck)_1}}{\sqrt{\pi}}\left[\frac{T(t)}{\sqrt{t}} + \frac{1}{2}\int_0^t \frac{T(t) - T(\tau)}{(t-\tau)^{3/2}}\, d\tau\right] \qquad (4.11)$$

It is possible to compute the heat transfer rate from a digitally recorded temperature signal using equation 4.11, but the numerical method used must be chosen so as to reduce the errors introduced by the singularity in the integral at $t=\tau$ **(Schultz and Jones, 1973).** Also the numerical error arising from digitizing the temperature signal results in noise on the calculated heat transfer rate which can be considerable, **(Oldfield et al, 1978).**

An alternative is to use an electrical analogue to perform the temperature to heat transfer rate transformation. As shown in figure 4.4, from **(Schultz and Jones, 1973),** the flow of heat in to a semi-infinite material is analogous to the flow of current into a R-C transmission line. Solving the two cases using Laplace Transforms produces the following equations

$$\bar{i} = \sqrt{\frac{c}{r}}\sqrt{s}\,\bar{v} \qquad (4.12)$$

and $$\bar{\dot{q}} = \sqrt{(\rho ck)_1}\sqrt{s}\,\bar{T} \qquad (4.13)$$

In practice an analogue consisting of discrete R-C blocks is used to approximate the electrical case. The design and operation of the HTA1 analogues used at Oxford is described fully by **Oldfield, Burd and Doe.**

Figure 4.5 is a schematic of a resistance-capacitance line which has

input resistance, R_1, resistance per unit length, r and capacitance per unit length, c. The constant current is altered until the voltage across the film for zero temperature rise is, V_0 , the set voltage. The voltage change, v, after a temperature rise, T, is then

$$v = V_0 \alpha T \tag{4.14}$$

It can be shown **(Oldfield et al, 1984)** that the analogue current is given by

$$\bar{i}_{in} = \sqrt{s}\sqrt{\frac{c}{r}}\bar{v} = \sqrt{s}\sqrt{\frac{c}{r}}V_0 \alpha \bar{T} \tag{4.15}$$

and substituting from equation 4.8 and taking the Inverse Laplace Transform

$$i_{in} = \sqrt{\frac{c}{r}}V_0 \alpha \frac{1}{\sqrt{(\rho ck)_1}}\dot{q} \tag{4.16}$$

Hence the analogue current is directly proportional to $\dot{q}$ and may be found from the voltage, V_a, across the input resistor.

$$V_a = R_1 i_{in} \tag{4.17}$$

Sustituting equation 4.16

$$V_a = R_1\sqrt{\frac{c}{r}}V_0 \alpha \frac{1}{\sqrt{(\rho ck)_1}}\dot{q} \tag{4.18}$$

Each analogue is calibrated to obtain the parameter $\frac{1}{R_1\sqrt{\frac{c}{r}}}$, which is known as the analogue constant, K_a.

Rearranging equation 4.18

$$\dot{q} = \frac{V_a K_a \sqrt{(\rho ck)_1}}{V_0 \alpha} \tag{4.19}$$

The analogue output is therefore directly proportional to the heat flux. Taking the Laplace Transform of equation 4.17 and substituting for $\bar{i}_{in}$ using equation 4.15 gives the relationship between the analogue output and the surface temperature rise.

$$\bar{V}_a = \frac{\sqrt{s}V_0 \alpha \bar{T}}{K_a} = \frac{\sqrt{s}\bar{v}}{K_a} \tag{4.20}$$

This general relationship is necessary when considering the analogue output from gauges not mounted on a single layer, semi-infinite substrate.

During experiments in the Oxford I.L.P.T. the temperature of the substrate may rise by as much as 70K **(Oldfield et al, 1978)** resulting in a drop in driving temperature and also changes in the thermal properties of the substrate. Therefore it is necessary to know the temperature rise during the experiment so that allowance for these two effects can be made. Recording the temperature signal (the voltage across the film) as well as the analogue output uses twice as many A/D channels and often results in electrical interference on the analogue output **(J.E. Doorly, 1985)**.

It has already been mentioned that calculating the heat flux from the temperature signal is a noisy process, however the converse process of calculating the temperature rise from the heat flux is not. A simple numerical routine which transforms a heat transfer rate trace into the corresponding temperature trace with excellent agreement between calculated and recorded temperature signals is given by **Oldfield et al (1978).**

The theory given in this section has been for a thin film gauge mounted on a semi-infinite substrate. The question of the thickness of insulator required for the semi-infinite assumption to hold has been addressed by **Schultz and Jones (1973).** They suggest a rule of thumb for the depth, x, at which the substrate can be considered to be semi-infinite after a time, t. This is given as

$$x = 4\sqrt{\alpha_1 t} \qquad (4.21)$$

So for the machineable glass ceramic (m.g.c.) commonly used in Oxford which has a thermal diffusivity (α_1) of 8.58 E-7 m^2/s, a substrate of 2.6mm thickness will remain semi-infinite for a time of 500ms.

A transient thermal analysis was performed by **Ashworth** to investigate the validity of the semi-infinite assumption for the heat transfer rate to a turbine blade manufactured from m.g.c.. He plotted the isotherms

within the blade for a prescribed heat transfer rate distribution and found that the isotherms were parallel to the surface as required by the semi-infinite analysis, except in the region of the trailing edge.

4.3 Thin Film Gauge on a Two Layered Substrate.

In this section only the behaviour of a gauge on a two layered substrate with semi-infinite backwall will be examined. The case of a gauge on a two layered substrate with finite backwall is considered by **J.E. Doorly (1985)** and **J.E. Doorly and Oldfield (1987). J.E. Doorly (1985)** also considers the conditions under which the metal substrate can be considered to be semi-infinite.

Consider a thin film gauge on a two layered substrate as shown in figure 4.6. For short time and neglecting the influence of the film itself, the governing equations to be solved are:

$$\frac{\partial^2 T_1}{\partial x^2} = \frac{1}{\alpha_1}\frac{\partial T_1}{\partial t} \qquad 0 \le x \le a \qquad (4.22)$$

$$\frac{\partial^2 T_2}{\partial x^2} = \frac{1}{\alpha_2}\frac{\partial T_2}{\partial t} \qquad a \le x \le \infty \qquad (4.23)$$

Where $_1$ refers to conditions in the insulating layer and $_2$ to conditions in the metal substrate.

With the boundary conditions

$$\dot{q} = -k_1\frac{\partial T_1}{\partial x} \qquad x = 0 \qquad (4.24)$$

$$T_1 = T_2 \qquad x = a \qquad (4.25)$$

$$k_1\frac{\partial T_1}{\partial x} = k_2\frac{\partial T_2}{\partial x} \qquad x = a \qquad (4.26)$$

$$T_2 = 0 \qquad x = 0 \qquad (4.27)$$

These equations can be solved in the Laplace domain, **(J.E. Doorly, 1985)** to give

$$\bar{\dot{q}} = \sqrt{(\rho ck)_1}\sqrt{s}\,\frac{\left(1 - A\exp\left(-2a\sqrt{(s/\alpha_1)}\right)\right)}{\left(1 + A\exp\left(-2a\sqrt{(s/\alpha_1)}\right)\right)}\,\bar{T} \qquad (4.28)$$

where $A = \dfrac{\sqrt{(\rho ck)_1} - \sqrt{(\rho ck)_2}}{\sqrt{(\rho ck)_1} + \sqrt{(\rho ck)_2}}$

and a is the thickness of the insulating layer.

Thus the heat flux may be established from the temperature signal either by purely numerical methods or the electrical analogue described previously may be used with an analytical correction to account for the presence of the metal layer. **J.E.Doorly (1985,1987)** describes various methods of calculating the heat flux from the temperature signal and from the analogue output. The methods that have been used in this study are described fully in chapter 6.

By transforming equation 4.28 to the frequency ($j\omega$) plane, it is possible to examine the sensitivity of the gauge/layer system as a function of the frequency of the heat flux perturbation, **Ainsworth et al, 1989**.

Consider the block diagram of the system shown in figure 4.7, the transfer function is given by $G(j\omega)$, where

$$G(j\omega) = \frac{T(j\omega)}{\dot{q}(j\omega)} \qquad (4.29)$$

So from 4.28 and substituting $s = j\omega$

$$G(j\omega) = \frac{1}{\sqrt{(\rho ck)_1}\sqrt{(j\omega)}} \frac{\left(1 + A \exp\left(-2a\sqrt{(j\omega/\alpha_1)}\right)\right)}{\left(1 - A \exp\left(-2a\sqrt{(j\omega/\alpha_1)}\right)\right)} \qquad (4.30)$$

The modulus of this function is given by :

$$\left|G(j\omega)\right| = \frac{1}{\sqrt{(\rho ck)_1}\sqrt{\omega}} \frac{\left(1 + 2A\exp(-b)\cos b + A^2 \exp(-2b)\right)^{1/2}}{\left(1 - 2A\exp(-b)\cos b + A^2 \exp(-2b)\right)^{1/2}} \qquad (4.31)$$

Where $b = \sqrt{\dfrac{2\omega a^2}{\alpha_1}} = \sqrt{2\omega}\sqrt{(\rho ck)_1}\left(\dfrac{a}{k_1}\right)$

Thus the behaviour of the gauge depends only on the thermal product of the insulating layer $\sqrt{(\rho ck)_1}$, the thermal product of the metal layer $\sqrt{(\rho ck)_2}$ and the ratio of thickness to conductivity of the insulating layer, a/k_1. The calibration methods for obtaining these parameters are

described in chapter 7.

In this study the thin film gauges were mounted on a vitreous enamel coat on a metal blade. The enamel layer was sprayed onto the blade and consequently its thickness and thermal properties were expected to vary from blade to blade and around the blade surface. The thermal product of the metal will not vary much and can be considered constant. The effect of varying the enamel thickness and $\sqrt{(\rho ck)_1}$ can be examined using equation 4.31.

Starting with the typical values for:

(i) Thermal product of the insulating layer - 1460 $J/m^2Ks^{1/2}$

(ii) Conductivity of the insulating layer - 1.36 W/mK

(iii) Thermal product of the metal substrate - 14190 $J/m^2Ks^{1/2}$

the thickness of the enamel layer was varied from 50 to 400μm. The nominal thickness is 200μm, so this is equivalent to varying a/k_1 by 25% to 200%. The resulting variation is shown in figure 4.8, with the reciprocal of the gauge sensitivity, $\dot{q}/T$ being plotted against frequency. As can be seen the gauge response is invariant above 100Hz for enamel thicknesses above 100μm, because at these frequencies the enamel layer behaves as if it were semi-infinite.

The thermal product of the enamel layer was varied by +/- 60%, figure 4.9. At frequencies above about 10Hz, the output is seen to depend only on the thermal product, as expected for a semi-infinite enamel layer, equation 4.8.

It can be observed from these plots that at the high frequency end of the spectrum, where the enamel layer appears semi-infinite, the sensitivity of the gauge ($T/\dot{q}$) falls as the square root of the frequency (as stated by equation 4.8). If the temperature signal were recorded directly, then the high frequency component of the signal could be swamped by the discretization

error resulting from A/D conversion. Also noise picked up before digital recording, e.g. that introduced by the slipring could reduce the signal to noise ratio for the high frequency components to an unacceptable level. Consequently there is an obvious advantage in preferentially amplifying the high frequency information before passing the signal through the slipring to the A/D recorder.

The analogue circuit **(Oldfield et al, 1984)** could be used as this amplifies the temperature signal by $\sqrt{f}$, (equation 4.20), but a post-recording digital filter must be applied to correct for the presence of the metal layer. The analogue uses a large number of components and as the amplifier was to be contained in the shaft, there was a need to keep the component count to a minimum, so a simpler circuit to amplify the temperature signal was built, figure 4.10. The circuit had four break points which were set so that the gain of the circuit closely followed the reciprocal of the gauge sensivity which had been examined in figures 4.8 and 4.9. The two responses are overplotted in figure 4.11 and the overall system gain, which is defined as the gauge sensitivity multiplied by the circuit gain, is shown in figure 4.12. It can be seen that there is only a small variation of signal level over the whole frequency range allowing efficient use of the A/D converters.

The design and development of the "in-shaft amplifier" circuit is described in more detail in chapter 5 and the digital processing routines used to establish the heat flux from the amplified temperature signal are explained in chapter 6.

The length of time for which a thin film gauge on a composite substrate consisting of an insulating layer on top of a finite metal layer can be considered as if the metal layer were semi-infinite was examined by **J.E.Doorly (1985)** and **J.E. Doorly and Oldfield (1987).** The surface temperature

rise for various metal/insulator combinations with both finite and semi-infinite metal layer was predicted. The results for a 200μm layer of quartz on a 3mm thick and semi-infinite nickel substrate are shown in figure 4.13. It can be seen that the effect of the finite backwall does not become significant until a time of 0.13 seconds. As the insulating properties of the top layer are improved the effects of the backwall diminish due to the increased temperature drop across the insulator.

The choice of metal/insulator combination used in this study is described in the next chapter along with details of the gauge manufacture and proving tests. The procedures for calibrating the gauges are the subject of chapter 7 as is a discussion of the parameter variations which were found. Finally, the results of both mean and unsteady heat transfer measurements, made on the rotor blade of a full stage turbine in a transient facility using these gauges, are presented in chapter 8 proving that this technique is suitable for use in this difficult environment.

CHAPTER 5

DEVELOPMENT OF INSTRUMENTATION

5.1 Manufacture of Blade for Heat Transfer Measurement.

The new generation of thin film heat transfer gauges mounted on enamel coated metal blades are applied by painting "Liquid bright platinum 05-X" (Englehard Industries Ltd) and firing at high temperatures. This is the same procedure as used previously with models fabricated from machineable glass ceramic (m.g.c.) or quartz.

The choice of metal/enamel combination is a potential problem area in manufacturing the new type of gauges. The metal is required to have sufficient strength to withstand the rotational forces and must be easily machined. The insulator must adhere well to the metal, provide a smooth or polishable surface and be impervious to gold and platinum. Experience has shown that the metal must have a low carbon content (**J.E. Doorly, 1985**) and that the thermal expansivity of the two materials must match over the temperature range encountered when firing.

The blades and vanes supplied for the Oxford Rotor Project were manufactured from Jethete which is a stainless steel. Despite extensive tests an insulator which fulfilled the requirements above could not be found for this metal. One possible reason for this is the variation of thermal expansivity of Jethete with temperature. This is plotted in figure 5.1 and it can be seen that there is an inflexion in the curve between 700 and 800 deg. C. None of the insulators could match this expansion rate with the result that cracks appeared in the coating when the insulator/metal combination was fired.

Consequently new blades had to be manufactured from a metal which could be coated. The material chosen was Inco 718 which is a nimonic

alloy and the insulating layer used was a vitreous enamel (WB5847 supplied by Ferro GB Ltd).

Before enamelling, the model must be thoroughly cleaned and the surface roughened using glass bead blasting. The enamel is supplied as a water based solution which is sprayed on to the blades and then dried to bisque stage at 125 deg. C. Final firing takes place for 15 minutes at 825 deg. C before the substrate is allowed to cool naturally.

The fabrication of thin film gauges is described in detail by **Schultz and Jones (1973)**. After painting the liquid bright platinum the blade is heated from 20 to 640 deg. C and then allowed to cool naturally. Further coats of platinum are applied and fired in this way until the resistance of the gauge is brought down to the required value (normally 50Ω). A photograph of thin film gauges painted on a rotor blade is shown in figure 5.2.

The heat treatment received during the enamelling and thin film gauge construction could have a detrimental effect on the strength of Inco 718 which is supplied in the fully annealed state ready for machining. The effect of the various firing processes on the yield strength was investigated in a series of tests. Four standard tensile test specimens were manufactured from a sheet of fully annealed Inco 718 and three of the specimens were given heat treatments representative of the thin film gauge construction process. The results are presented in table 5.1.

The fully annealed sample had the lowest yield strength. Comparison of tests 3 and 4 show that heating the specimen to 825 deg. C gave it a higher yield strength than heating it to 925 deg. C, which is very close to the annealing temperature. Cycling the sample from 20-640 deg. C four times was also seen to increase its strength more than cycling it twice. This is as expected as each cycle partially ages the specimen. Calculations of

the maximum stress expected in the blade gave an acceptable factor of safety for all three heat treatments.

Another series of tests was carried out to determine the performance of a thin film gauge under tensile loading. This was an important investigation as the heat transfer gauges on the rotor blade experience centrifugal forces of up to 32,000g.

Tensile test specimens were constructed from the same metal/enamel combination as the instrumented blades, figure 5.3. The specimens were placed in a tensile test machine and the gauge resistance was monitored as a load was applied. The results of a test in which the load was repeatedly applied are shown in figure 5.4. After some initial annealing the variation was quite repeatable up to a much higher level of strain than expected on the rotor blades. A change in resistance of 0.02Ω corresponds to a temperature change of approximately 0.5 deg. C.

Electrical leads to the gauges were formed by painting wide gold strips using "liquid bright gold KA6" from the thin film gauge on the aerofoil down to the root region. 0.25mm diameter holes were spark eroded through the platform and copper wires (0.11mm diameter) attached directly using a conductiving adhesive, (Eccobond 58C, Hiteck Electronic Materials Ltd). These led to a shoulder on the turbine disc where a set of soldered contacts permitted the blades to be interchanged readily. Bundles of copper wires leading from the outer radius to solder pads on the outside of the shaft were attached to the disc and leads from the electronics inside the shaft were brought out to these solder pads.

A photograph of an instrumented blade before the wires were attached at the platform is shown in figure 5.5 and the wiring on the disc is shown in figure 5.6. The connections at the outer radius proved to be the

most troublesome as there is a hollow area between the blade platform and the disc. Originally the wires were laid loosely across this gap, but the centrifugal forces pushed the wires outwards causing disconnections at the solder pads. The wires could not be rigidly fixed along their length as some flexibility had to be available to allow for radial growth due to rotation. The final successful arrangement is shown in figure 5.7. The wires were glued to the underside of the platform using a "superglue" gel with an activator, then to the front of the root and finally they were led to the solder pads. The small loop of wire which was left free was tucked under the mini-disc and embedded in silicon rubber.

5.2 Design of In-shaft Electronics.

The in-shaft electronic circuits have already been introduced in chapters 3 and 4. The function of these circuits is threefold:- to supply the thin film gauges with a constant current, select the output from given gauge using a multiplexer and then amplify the chosen signal by a factor depending on its frequency.

In previous cascade experiments in Oxford using machineable glass ceramic models the current supplied to the gauges had been set at 5mA. This limited the rise in temperature of the substrate caused by ohmic heating to an acceptable level. The effect of ohmic heating on a metal model is much smaller because the improved conductivity dissipates the heat far more effectively. Consequently a higher current could be used which would result in the same temperature rise, but an improved signal to noise ratio since the output is directly proportional to the current, but the noise generated is only proportional to the square root of the current **(Horowitz and Hill)**. These considerations led to a constant current of 30mA being chosen for the rotor

project.

The reasons for the frequency dependent amplifier and the choice of transfer function have already been discussed in chapter 4. The circuit was based on the OP-37, low noise, fast response operational amplifier which was configured in non-inverting mode with a variable impedance in the feed-back leg. The components used in the variable gain amplifier are clearly shown in figure 4.10, as is the constant current source. The two multiplexers are addressed in parallel, one selecting the thin film gauge to which the constant current should be supplied and the other selecting the output from that gauge and passing it to the amplifier. In this way 16 thin film gauges could be connected to each circuit with one sensor in operation at any one time. The multiplexers were not switched during the run.

In practice, the design of the inshaft electronics was constrained by the inside dimensions of the shaft and the number of slipring channels. There was room inside the shaft for two boards, each 62mm by 360mm. A locally available CAD package for printed circuit board development was used to design two double sided boards each carrying four of the circuits shown in figure 4.10. Much effort was expended on optimizing the layout for minimum vulnerability to pick up and oscillation problems. A close up of one of the boards used in the project is shown in figure 5.8.

By running the eight modules in parallel inside the shaft, it was possible to monitor eight thin film gauges simultaneously. Since 16 gauges could be connected to each module a total of 128 sensors could be accommodated on one build. Each signal had a separate earth, so of the 24 slipring channels available, 16 were used by the outputs from the thin film gauges, four as address select lines and three as power supply connections, leaving one spare.

Frequency response tests were carried out on prototype in-shaft circuits, before printed circuit board versions were produced. The values of the components in the gainshaping circuit were measured and are given in table 5.2 along with the calculated breakpoints. The measured frequency response for one of the circuits is shown in figure 5.9 and exhibits typically good agreement until the bandwidth of the amplifier is reached. The predicted frequency responses for four circuits on one of the boards are compared with that calculated from the nominal values in figure 5.10 and it is seen that there is only a small difference despite the variation in component values. Consequently it was decided that for numerical processing the nominal breakpoints could be used. Measurements of noise indicated values of order 0.5mV r.m.s. at output, with a thin film gauge connected and using a wide bandwidth voltmeter.

5.3 The Spinning Rig.

A simple rotating facility, named "The Spinning Rig", was designed and developed by the author. It was used as a test rig for the control and instrumentation systems used in the main rotor project. The principal components are drawn in figure 5.11. The airmotor was mounted on one plate with the slipring on another. The whole facility was housed in a thick steel tank which could be partially evacuated.

The primary aim of the experiment was to investigate the effects of centrifugal force on the in-shaft electronics, the wiring and on pressure transducers and thin film gauges mounted on the rotor blades. The rig was therefore designed with a rotating can of the same inside diameter as the rotor shaft in which versions of the in-shaft electronics could be placed. Fixed to the can were two aerofoil blades of the same outer radius as the

rotor blades which could be instrumented in the same way as the blades. The design speed of the facility was 8434 rpm, the same as that of the turbine. The facility was powered by an air turbine identical to that used in the rotor experiment and the control system described in chapter 3 was developed on this rig.

A prototype of the in-shaft electronics was built to fit in the can. Using some of the slipring channels a frequency response test was carried out on the in-shaft electronics whilst the rig was rotating. There was no discernable change in the performance of the circuit.

The noise characteristics of the slipring were tested using the system shown in figure 5.12. The r.m.s. noise level was recorded first with the rig stationary and then at various rotational speeds. In all cases the r.m.s. noise, measured with a wide bandwidth voltmeter was about 0.5mV. Examination of the noise trace on an oscilloscope suggested a slight variation of signal form with speed and a HP3562A Waveform Analyser was used to examine the frequency spectrum. On some occasions peaks at multiples of the rotational speed could be seen, figure 5.13, but this was not usually the case, figure 5.14. In all cases the peaks were of a very small magnitude and were not considered important.

5.4 Heat Transfer Instrumentation Tests in Spinning Rig.

The tips of the two bars were coated with enamel and two thin film gauges were painted on each, as shown in figure 5.15. Copper wires were glued down the length of the bar terminating at solder pads on the root and from here wires led to the in-shaft electronics which operated as described previously.

The noise levels from the thin film gauges were monitored during

rotation. The r.m.s. values varied between 0.8 and 1.1 mV and there did not seem to be any correlation between noise and speed. The increase in noise over that measured in bench tests was not unexpected considering the increased number of connections and lead length.

The d.c. output from the thin film gauge was monitored while the rig was spinning and output-time graphs and speed-time graphs could be plotted. A typical result is shown in figure 5.16 where it can be seen that the output increases with speed. There are several possible reasons for this:- strain, effect of rotation on the electronics and heating of the bar due to movement through the air.

The effect of strain was quantified in the tensile test experiment and a change in resistance of 0.08% was seen at the strain level to be expected on the blade when rotating at 8000 rpm. Consider the sharp fall in signal when the rig is shut down. 0.08% of the initial voltage is 5mV which is far smaller than the measured drop. Consequently a strain effect is not responsible for the change in output.

In order to examine the effect of rotation on the in-shaft electronics a 50Ω resistor was placed inside the can and connected to the circuit in place of a thin film gauge. The output during a run is plotted in figure 5.17 and can be compared with that recorded when the rig was stationary, figure 5.18 . The overall change follows a different pattern to that seen from a thin film gauge and is much smaller. As the speed increases the signal falls and on shut down rises to a level above the initial value. When the test was repeated in a better vacuum, figure 5.19, a smaller change was seen, but still in the opposite sense to that seen with a thin film gauge connected.

The motion of the bar through the air created a driving

temperature (recovery - ambient) of order 30 deg. C. This caused the bar to heat up and the temperature rise was monitored by the thin film gauge. The convective heat transfer coefficient was dependent on the pressure in the tank and at lower pressures, figure 5.20, the output of the gauge changed more slowly due to the reduced heat transfer coefficient. At the lowest pressure achieved in the tank (18mm Hg) the temperature rise monitored by the thin film gauge was of order 13 deg. C.

Such a temperature rise would have been unacceptable in the rotor experiment and every effort was made to limit the time taken to spin the turbine up to speed before the tunnel was fired. Also the working section in the rotor facility was able to withstand a lower vacuum level and as a result of these measures a temperature rise of only two or three deg. C was seen before the ILPT was fired (chapter 8).

The movement of the bars through the air dissipated heat resulting in a rise of the air temperature. This was monitored using a thermocouple and a typical result is shown in figure 5.21. It can be seen that the temperature rose with speed and the overall change was only two deg. C. The same effect had been experienced by **Doorly (1984)** when spinning wire bars in a partially evacuated working section.

The tests in the spinning rig using bars instrumented with thin film gauges gave valuable experience of the effects of rotation on the perfomance of the electronics and instrumentaion and enabled a sensible pre-run procedure for the rotor project to be drawn up.

5.5 Pressure Transducer Tests.

The unsteady pressure seen on the rotor blade is to be measured using miniature, flatpack pressure transducers (Kulite LQ-080 series). A

series of tests was performed to find a method of mounting the transducers in a strain-free way such that they withstood the rigours of rotation and could be removed and used again. Rotating tests were undertaken to establish the effects on the mechanical and electrical performance of the transducers.

Two transducers were mounted on standard tensile test specimens, figure 5.22, one with double-sided adhesive tape and the other using strain gauge cement. The output was monitored as a load was applied in small steps up to 6kN which previous calculations had shown to correspond to the centrifugal stress on a blade root in the rotor at design speed. The results of the two tests are shown in figure 5.23. The output from the transducer mounted using double-sided tape did not change with load, indicating that this method gave strain isolation. The output from the other showed a linear change with load.

Due to the high cost of a transducer spinning tests to test the mechanical integrity of the mounting arrangement and methods of securing the leads were first undertaken with a dummy shim which had no transducer chip. "Superglue" was used to stick the shim to a flat milled on one of the bars as it was known that when heated to 125 deg. C the glue broke down and the transducer could be easily removed. 0.15mm diameter wires were secured to the bar and can using adhesive tape. These wires were representative of those on a live transducer and very much smaller than those stuck to the bar in the thin film gauge tests. This arrangement was spun at design speed several times and no damage occurred. The live transducer was then mounted on another bar in the same way.

The noise level was recorded with the rig both stationary and rotating and was found to have a large high frequency component which was

reduced significantly when a 100 kHz low pass filter was introduced. The noise level at all rotational speeds was of order 0.5mV after filtering.

The output from the transducer was amplified by a factor of 30 using a Maywood Amplifer before being recorded. Output-time and speed-time graphs for the transducer with different vacuum levels in the tank are plotted in figures 5.24 and 5.25. The transducer measures the static pressure, p, which is given by:

$$p = p_0 - \frac{\rho u^2}{2} \qquad (5.1)$$

where p_0 is the total pressure, ρ the density and u the local velocity at the transducer. Assuming incompressible flow the local velocity is proportional to the bar speed

i.e. $$u = \lambda r \omega \qquad (5.2)$$

where ω is the rotational speed and λ is a constant.

Hence the change in transducer output should be proportional to the square of the rotational speed. Figure 5.26 is a graph showing the relationship between transducer output and speed squared and it is seen that for each vacuum level, i.e. ρ, a straight line was achieved.

The principal objective of these tests was to investigate the mechanical integrity of this type of pressure transducer under the adverse conditions to be experienced on the rotor blade. No problems were found and a method of mounting the transducer so that it could be recovered was developed. When rotating the mass of the transducer will result in a centrifugal force on the transducer itself, this was not investigated and should be quantified along with the strain effects before any measurements of surface pressure on the rotor blade are undertaken.

CHAPTER 6

SIGNAL PROCESSING TECHNIQUES

6.1 Introduction.

The theory of thin film heat transfer gauges was introduced in Chapter 4. It was explained that an electrical analogue could be used to establish the heat flux to a gauge on a single layer substrate, but for a gauge on a two layered substrate an analytical correction was necessary to account for the presence of the second layer.

The advantage of preferentially amplifying the high frequency component of the thin film gauge signal before digital recording was demonstrated. The electrical analogue, which exactly models the single layer case could be used for this, but for amplifying the signals in the rotating frame a new circuit was developed which had fewer components.

This chapter deals with the methods of processing the output from a thin film gauge on a two layered substrate when passed through either an analogue circuit or the new "in-shaft" amplifier. Only the methods used in this study are described and details of other methods are given by **J.E.Doorly, (1985 and 1987)**. The methods chosen were those most thoroughly documented by Doorly and are not necessarily the most efficient or accurate. Fast Fourier Transform, FFT, techniques were used where possible because of the speed of implementation. A detailed comparison of various methods some of which employ the FFT will be published soon **(J.E. Doorly, 1989)**.

The various routes for obtaining the heat transfer rate from a thin film gauge on a two layered substrate are shown in a block diagram, figure 6.1. Each step will now be described and supported by tests to prove the validity of the chosen method.

6.2 Processing the Analogue Output to Obtain Heat Transfer Rate.

The relationship between the heat transfer rate and the surface temperature rise was given in equation 4.28,

$$\bar{\dot{q}} = \sqrt{(\rho ck)_1}\sqrt{s}\,\frac{(1 - A\ \exp\ (-2a\sqrt{(s/\alpha_1)}))}{(1 + A\ \exp\ (-2a\sqrt{(s/\alpha_1)}))}\,\bar{T} \qquad (6.1)$$

and the relationship between the analogue output and surface temperature rise was given in equation 4.20,

$$\bar{T} = \frac{\bar{V}_a K_a}{\sqrt{s}\, V_0 \alpha} \qquad (6.2)$$

Hence $$\bar{\dot{q}} = \frac{\sqrt{(\rho ck)_1} K_a \bar{V}_a}{V_0 \alpha}\ \frac{(1 - A\ \exp\ (-2a\sqrt{(s/\alpha_1)}))}{(1 + A\ \exp\ (-2a\sqrt{(s/\alpha_1)}))} \qquad (6.3)$$

Let $$K = \frac{\sqrt{(\rho ck)_1} K_a}{V_0 \alpha} \qquad (6.4)$$

and expanding the term in brackets equation 6.3 can be rewritten as

$$\bar{\dot{q}} = K\,\bar{V}_a\left(1 + 2\sum_{m=1}^{\infty}(-A)^m \exp(-2ma\sqrt{(s/\alpha_1)})\right) \qquad (6.5)$$

Let $$\bar{g} = 2\sum_{m=1}^{\infty}(-A)^m \exp(-2ma\sqrt{(s/\alpha_1)})\Big) \qquad (6.6)$$

So $$\bar{\dot{q}} = K.\bar{V}_a(1 + \bar{g}) \qquad (6.7)$$

Taking the Inverse Laplace Transform of equation 6.7 gives

$$\dot{q}(t) = K(V_a(t) + g(t) * V_a(t)) \qquad (6.8)$$

where $$g(t) = 2\sum_{m=1}^{\infty}\frac{ma}{\sqrt{(\alpha_1 \pi t^3)}}(-A)^m \exp\left(\frac{-m^2a^2}{\alpha_1 t}\right) \qquad (6.9)$$

The analogue output $V_a(t)$ is a sampled waveform of length N. The function g(t) can be evaluated at each of the N points in time. The number of terms, m, that need to be taken in the series, depends on the value of t for the Nth point, i.e. the maximum time value. The exponential term quickly approaches zero as m increases. For the metal/enamel combination used in

this study typical values of the various parameters are given in table 6.1. and using these $a/\sqrt{\alpha_1}$ is calculated as having the value 0.104 s/m.

Let $$\exp\left(\frac{-m^2 a^2}{\alpha_1 t}\right) < 1.0\ E\text{-}9 \quad \text{be considered negligible} \qquad (6.10)$$

So the value of m required to satisfy the inequality is given by

$$\frac{-m^2 a^2}{\alpha_1 t} < -20 \qquad (6.11)$$

Substituting for a^2/α_1 gives:

$$m^2 > 1849\, t \qquad (6.12)$$

So for t = 0.1 s, m > 14 and for t = 1.0 s, m > 43.

In practice less terms need be used as the term $(-A)^m$ also decreases with increasing m.

The function g(t) has been evaluated for various values of m and is plotted in figure 6.2. The result of taking too few terms in the summation can be clearly seen, thereby illustrating the importance of considering the signal duration and then using equation 6.12 to evaluate m.

Evaluation of the time convolution in equation 6.8 can be accelerated using a Fast Fourier Transform algorithm (FFT). The infinite convolution in equation 6.8 is approximated by a discrete convolution using rectangular integration, (**Brigham**).

$$g(t)*V_a(t) = \int_{-\infty}^{+\infty} V_a(\tau)g(t-\tau).\ d\tau$$

$$\approx T\sum_{i=0}^{N-1} V_a(iT).g[(k-i)T] = g(kT)*V_a(kT) \qquad (6.13)$$

where T is the sample interval.

The summation term can be rapidly evaluated using the discrete convolution transform pair.

$$\sum_{i=0}^{N-1} V_a(iT).g[(k-i)T] = Fac\ .\ IDFT\{DFT(g).\ DFT(V_a)\} \qquad (6.14)$$

where Fac is a scale factor introduced by the particular FFT routine used. For this calculation the **NAG** routine CO6ECF was employed and Fac = $1/\sqrt{N}$.

To perform the discrete convolution in equation 6.14 the two sampled waveforms g(t) and $V_a(t)$ must be made periodic with length M, where

$$M \geq 2N-1 \qquad (6.15)$$

This is done by padding the original signal with extra zeros, and as explained by **Brigham** is necessary to avoid the convolution result of one period overlapping the result of the succeeding period.

This process was tested using the exact predicted analogue output from a gauge on a two layered substrate subject to a step in heat transfer rate of 25kW/m^2, figure 6.3. The prediction method is detailed in Appendix I and the parameters which are used are listed in table 6.1. The analogue output is extended to double its original length with extra zeros, figure 6.4, and the heat transfer rate is then calculated using equations 6.4, 6.8, 6.9, 6.13 and 6.14. The result is shown in figure 6.5 and is only valid over the original N points, so the remainder of the signal must be discarded. Closer examination, figure 6.6, reveals a maximum error of 0.07% in the reconstructed heat flux.

6.3 Calculating the Temperature Rise from the Analogue Output.

Sometimes the surface temperature rise is required from the analogue output as well as the heat transfer rate. A knowledge of the temperature rise is needed for the laser calibration technique (Chapter 7) and also if allowance is to be made for changes in substrate properties with temperature. As explained in chapter 4 the temperature signal can not be obtained by directly recording the thin film gauge output because of the numerical errors introduced by digitization. Instead the signal must be conditioned by a frequency dependent amplifier and then digitally recorded.

The actual temperature rise can be accurately calculated from the digitized signal due to the high resolution with which double precision numbers are stored in the computer. The heat transfer rate can also be obtained from the surface temperature rise (section 6.5), but for the case where the output is passed through an analogue it is preferable to calculate the heat transfer rate directly from the analogue output using the method described above as this is quicker and more accurate.

Rearranging equation 4.20

$$\overline{T} = \frac{\overline{V}_a K_a}{\sqrt{s} V_0 \alpha} \tag{6.16}$$

The analogue output can be considered to be the summation of a series of steps as in figure 6.7.

$$V_a(t) = \sum_{n=0}^{N-1} a_n . u(t-n\tau) \tag{6.17}$$

where τ is the time interval between steps, u is the unit step function defined as follows (**Kreyszig**):

$$u(t-a) = \begin{cases} 0 & \text{if } t < a \\ 1 & \text{if } t \geq a \end{cases} \tag{6.18}$$

and $$a_n = V_a((n+1)\tau) - V_a(n\tau) \tag{6.19}$$

Taking the Laplace Transform of equation 6.17 gives

$$\overline{V}_a = \sum_{n=0}^{N-1} \frac{a_n e^{-sn\tau}}{s} \tag{6.20}$$

Substituting equations 6.20 into equation 6.16

$$\overline{T} = \frac{K_a}{V_0 \alpha s^{3/2}} \sum_{n=0}^{N-1} a_n e^{-sn\tau} \tag{6.21}$$

which can be inverted

$$T(t) = \frac{K_a}{V_0 \alpha} \sum_{n=0}^{N-1} a_n \frac{2}{\sqrt{\pi}} (t-n\tau)^{1/2} . u(t-n\tau) \tag{6.22}$$

Let $t = m\tau$

$$T(m\tau) = \frac{2K_a\sqrt{\tau}}{\sqrt{\pi} V_0 \alpha} \sum_{n=0}^{N-1} a_n (m-n)^{1/2} u(m\tau-n\tau) \tag{6.23}$$

which can be also be written as

$$T(m\tau) = \frac{2K_a\sqrt{\tau}}{\sqrt{\pi}V_0\alpha}\sum_{n=0}^{m} a_n(m-n)^{1/2} \qquad (6.24)$$

Hence the surface temperature rise is calculated from a simple time series.

The temperature rise calculated from the predicted analogue output for a gauge on a two layered substrate subject to a step in heat transfer, figure 6.3, is shown in figure 6.8. When the temperature rise is plotted against $\sqrt{t}$, figure 6.9, it can be seen that it is made up of two parabolas. This is as expected as the insulating layer will initially appear semi-infinite, but after a certain time the influence of the metal layer will be seen and the gauge temperature will rise more slowly.

6.4 Obtaining Surface Temperature Rise from In-shaft Amplifier Output.

The electronic circuits mounted in the shaft were described in detail in chapter 5. The principal function of these circuits is to preferentially amplify the high frequency component of the thin film gauge output before transmission through the slipring.

The circuit also includes the constant current source which energizes the thin film gauges. This is used in a slightly different way to the constant current source which powers the gauges connected to an analogue. In the analogue circuit the constant current supplied to each gauge is adjusted so that the set voltage across each gauge is the same regardless of its resistance. The inshaft circuit supplies a constant current, I, to every gauge. For the tests reported in this thesis this was set at 30mA.

The gauge resistance at 20 deg. C, R_{20}, is known. Let the initial voltage be V_i at an initial temperature T_i.

Hence $$V_i = IR_{20}(1 + \alpha_{20}(T_i - 20)) \qquad (6.25)$$

Likewise, at some time into the run, let the temperature be T_r and the voltage V_r

$$V_r = IR_{20}(1 + \alpha_{20}(T_r - 20)) \qquad (6.26)$$

The change in voltage, v, is given by

$$v = V_r - V_i = IR_{20}\alpha_{20}T \qquad (6.27)$$

where $T = T_r - T_i$ is the temperature rise.

The inshaft amplifier amplifies the change in output, v, from the thin film gauge using a frequency dependent amplifier The circuit is shown in figure 6.10. Let the amplifier gain be B(s) and the amplifed output, V_B, where :-

$$\overline{V}_B = \overline{v}.\, B(s) \qquad (6.28)$$

The transfer function of the circuit is :-

$$B(s) = \left(\frac{R_1 + R_2 + R_3 + R_4}{R_1 + R_2 + R_3}\right) \frac{(1 + s\tau_1)(1 + s\tau_3)}{(1 + s\tau_2)(1 + s\tau_4)} \qquad (6.29)$$

where τ denotes a breakpoint and $\tau = \frac{1}{2\pi f}$ (f in Hz)

The asymptotes to the frequency response curve are shown in figure 6.11. The breakpoints were set at approximately 20Hz, 200Hz, 2kHz and 20kHz and the actual values for each circuit are given in table 5.2. The bandwidth of the amplifier is 100kHz and around this frequency the gain of the amplifier begins to fall off, figure 5.9. A fifth breakpoint can be added to the ideal analysis to account for this roll off, this is shown as a dotted line in figure 6.11.

The complete transfer function of the actual system then is:—

$$B(s) = \left(\frac{R_1 + R_2 + R_3 + R_4}{R_1 + R_2 + R_3}\right) \frac{(1 + s_1\tau)(1 + s\tau_3)}{(1 + s\tau_2)(1 + s\tau_4)(1 + s\tau_5)} \qquad (6.30)$$

Taking the Laplace Transform of equation 6.27 and substituting for $\overline{v}$ into equation 6.28

$$\overline{V}_B = IR_{20}\alpha_{20}\overline{T}.\, B(s)\,. \qquad (6.31)$$

Dividing throughout by $IR_{20}\alpha_{20}$ gives the amplified temperature signal, $\overline{T}_B$.

$$\overline{T}_B = \overline{T}.B(s) \qquad (6.32)$$

Equation 6.32 can be rearranged to give the actual temperature rise, in the Laplace Transform domain.

$$\overline{T} = \overline{T}_B \cdot \frac{1}{B(s)} \qquad (6.33)$$

Generally, for functions for which $f(t)=0$ for $t<0$, the Fourier Transform, $F(j\omega)$ and the Laplace Transform, $F(s)$, can be obtained from each other by replacing s by $j\omega$. Hence equation 6.33 can be written as

$$\overline{T} = \overline{T}_B \cdot \frac{1}{B(j\omega)} \qquad (6.34)$$

where $\overline{\ }$ denotes the Fourier Transform and

$$B(j\omega) = \frac{(R_1+R_2+R_3+R_4)}{(R_1+R_2+R_3)} \frac{(\omega_2\omega_4\omega_5)}{(\omega_1\omega_3)} \frac{(\omega_1+j\omega)(\omega_3+j\omega)}{(\omega_2+j\omega)(\omega_4+j\omega)(\omega_5+j\omega)} \qquad (6.35)$$

The temperature rise can be obtained by using the discrete Fourier Transform to invert equation 6.34 .

$$T(t) = IDFT\{ DFT(T_B). \frac{1}{B(j\omega)} \} \qquad (6.36)$$

As with the convolution operation described in section 6.2, the sampled signal T_B must be extended to at least twice its original length by zero padding and $\frac{1}{B(j\omega)}$ evaluated over a corresponding range. Also, the computer program uses a different FFT routine for this operation which has the additional restriction that the number of points N in the zero padded signal must be a power of 2.

This procedure for extracting the input temperature signal from the sampled amplifier output was tested as follows. A known input, figure 6.12, was applied to the inshaft amplifier using the anti-analogue, **(Carlini).** This was designed to supply a parabolic voltage (with time) to a conventional heat transfer analogue (**Oldfield et al, 1984**) which should then produce a step output, i.e. the anti-analogue simulates the response of a thin film gauge on a single layer, semi-infinite substrate to a step in heat transfer

rate. The output from the in-shaft amplifier is plotted in figure 6.13. This signal is 2048 points long and in order to satisfy the requirements of the FFT routine it was extended to 4096 points using extra zeros, figure 6.14. The input signal was reconstructed, figure 6.15, using the method described above, which is contained in the routine DB in the program DSIGPRO. Only the original 2048 data points are valid and these are plotted in figure 6.16 along with the input signal. It can be seen that the two curves lie on top of each other.

This exercise was repeated for several timescales and it was found that in some cases the reconstructed signal varied considerably from the actual input. In each case 2048 points were recorded and at sample intervals of 1.0E-3s and 1.0E-4s the agreement was good, but as the sample interval was decreased to 1.0E-5s and 1.0E-6s an increasing discrepancy was found, figures 6.17.

The process of extracting the actual temperature rise from the amplified temperature signal, involves multiplying, in the frequency domain, the reciprocal of the amplifier transfer function and the discrete Fourier Transform of the amplified temperature signal. The spacing of the samples when transformed to the frequency domain, $\Delta\omega$, is related to the number of points in the sample, N, and the sample interval, Δt, by the following equation **(Ramirez).**

$$\Delta\omega = \frac{1}{N\Delta t} \qquad (6.37)$$

and the highest frequency that can be defined is the Nyquist Frequency, given by

$$F_n = \frac{1}{2\Delta t} \qquad (6.38)$$

Consider the values of $\Delta\omega$ and F_n for signals of 2048 points captured at the sample intervals mentioned above.

Δt	$\Delta\omega$	F_n
1.0E-3	0.488Hz	500Hz
1.0E-4	4.88 Hz	5 kHz
1.0E-5	48.8 Hz	50 kHz
1.0E-6	488Hz	500 kHz

As stated earlier the breakpoints of the amplifier circuit are at approximately 20Hz, 200Hz, 2kHz and 20KHz. The sample interval in the frequency domain, $\Delta\omega$, must be small enough to define the breakpoints, ie. smaller than the lowest breakpoint. At sample intervals of 1.0E-3 and 1.0E-4 this requirement is satisfied, but at faster sample rates it is not. The effect of the shortfall can be illustrated by plotting the transfer function of the amplifier calculated at each point in the frequency domain according to equation 6.30. This is done for sample intervals of 1.0E-4s and 1.0E-5s in figures 6.18 and 6.19.

For each sample rate the upper frequency at which the transfer function is required is the Nyquist frequency, below this frequency all breakpoints must be defined. In figure 6.18 three breakpoints at 20Hz, 200Hz and 2kHz are obvious, while in figure 6.19 the first breakpoint at 20Hz is not reconstructed.

It is obvious from equation 6.37 that increasing the number of points in the sample will result in closer spacing of the points when transformed to the frequency domain. For a sample interval of 1.0E-5 extending the signal to 8 times its original length by zero padding, 16384 points, results in a frequency interval of 6.1 Hz which is small enough to define the amplifier frequency response as shown in figure 6.20. The input signal was then calculated from the zero-padded output trace and unlike the reconstruction shown in figure 6.17, gave excellent agreement with the original input, figure 6.21.

6.5 Temperature to Heat Transfer Rate Conversion.

The previous two sections have described the signal processing procedure for calculating the gauge surface temperature rise from the output of either the analogue or in shaft amplifier circuits. The remaining problem, especially in the case of the signal conditioned by the in-shaft electronics, is to obtain the heat transfer rate from the surface temperature rise.

Recalling equation 4.28

$$\bar{\dot{q}} = \sqrt{(\rho ck)_1}\sqrt{s}\ \frac{(1 - A\exp(-2a\sqrt{(s/\alpha_1)}))}{(1 + A\exp(-2a\sqrt{(s/\alpha_1)}))}\ \bar{T} \qquad (6.39)$$

As explained in the previous section this equation can be rewritten in the Fourier Transform domain by substituting $j\omega$ for s

$$\bar{\dot{q}} = \sqrt{(\rho ck)_1}\sqrt{(j\omega)}\ \frac{(1 - A\exp(-2a\sqrt{(j\omega/\alpha_1)}))}{(1 + A\exp(-2a\sqrt{(j\omega/\alpha_1)}))}\ \bar{T} \qquad (6.40)$$

where $\bar{}$ denotes the Fourier Transform.

Alternatively equation 6.40 can be written as

$$\bar{\dot{q}} = \bar{F}(j\omega).\bar{T} \qquad (6.41)$$

where $$\bar{F}(j\omega) = \sqrt{(\rho ck)_1}\sqrt{(j\omega)}\ \frac{(1 - A\exp(-2a\sqrt{(j\omega/\alpha_1)}))}{(1 + A\exp(-2a\sqrt{(j\omega/\alpha_1)}))} \qquad (6.42)$$

The heat transfer rate can be calculated from equation 6.41 using the discrete Fourier Transform.

$$\dot{q}(t) = \mathrm{IDFT}\{\mathrm{DFT}(F).\mathrm{DFT}(T)\} \qquad (6.43)$$

The discrete Fourier Transform of F is approximated by sampling the function $F(j\omega)$ at frequency intervals of $1/(M\,T)$, where T is the time interval at which the temperature signal is sampled and M is the record length.

The temperature signal of length N points must be made periodic with length M points before the DFT is calculated. As in the previous

section there are some limitations on the value of M, namely $M \geq 2N-1$ and that M must be a power of two.

The procedure for calculating the heat transfer rate is illustrated in figures 6.22 and 6.23. The predicted temperature rise for a step in heat flux of $25 kW/m^2$ applied to a gauge on a two layered substrate is shown in figure 6.22. The signal has been extended to twice its original length with zero padding. The DFT of the temperature signal was obtained and the heat transfer rate calculated from equations 6.42 and 6.43, figure 6.23. The applied heat flux is also shown and it can be seen that the two do not agree.

The presence of the large negative spike can be explained by considering the simple case of a gauge mounted on a single layer substrate. The zero padded temperature signal can be approximated by a series of steps, figure 6.24, i.e.,

$$T(t) = \sum_{n=1}^{N} a_n . u(t-n\tau) - A_N . u(t-(N+1)\tau) \qquad (6.44)$$

where $A_N = \sum_{n=1}^{N} a_n$ and $a_n = T(n\tau)-T((n-1)\tau)$

Taking the Laplace Transform of equation 6.44

$$\overline{T} = \sum_{n=1}^{N} a_n \frac{e^{-sn\tau}}{s} - A_N \frac{e^{-s(N+1)\tau}}{s} \qquad (6.45)$$

For the single layer case, from equation (4.8)

$$\overline{\dot{q}} = \sqrt{(\rho ck)_1}\sqrt{s}\ \overline{T} \qquad (6.46)$$

Hence $$\overline{\dot{q}} = \sqrt{(\rho ck)_1}\left(\frac{1}{\sqrt{s}}\sum_{n=1}^{N} a_n e^{-sn\tau} - \frac{1}{\sqrt{s}} A_N e^{-s(N+1)\tau}\right) \qquad (6.47)$$

which can be inverted (using the translation property of the Laplace Transform)

$$\dot{q}(t) = \sqrt{(\rho ck)_1}\left(\sum_{n=1}^{N} a_n \frac{1}{\sqrt{\pi(t-n\tau)}} u(t-n\tau) - \frac{A_N}{\sqrt{\pi(t-(N+1)\tau)}} u(t-(N+1)\tau)\right) \qquad (6.48)$$

For $t > N\tau$ $\quad u(t-n\tau) = 1$ and $u(t-(N+1)\tau = 1$

and equation 6.48 reduces to

$$\dot{q}(t) = \sqrt{(\rho ck)_1}\left(\sum_{n=1}^{N} a_n \frac{1}{\sqrt{\pi(t-n\tau)}} - \frac{A_N}{\sqrt{\pi(t-(N+1)\tau)}} \right) \qquad (6.49)$$

For $t > N\tau$

The second term, which arises from the sudden truncation of the temperature signal, does not apply until $t > N\tau$, equation 6.48 and results in an infinite negative impulse at $t = (N+1)\tau$ which then decays asymptotically.

In equation 6.43 the DFT is employed to carry out the operation described above and this assumes that all signals are sampled and periodic. Consider the temperature signal shown schematically in figure 6.25(a) and the heat transfer rate calculated from this signal, figure 6.25(b). It is obvious that problems will occur if the period of the temperature signal is such that the negative impulse seen in the calculated heat transfer rate has not decayed to a small value before the next period as shown in figure 6.26(a) and (b). The result for one period is shown in figure 6.27 and can be seen to resemble figure 6.23.

To minimize this problem the period of the temperature signal must be further extended by padding with zeros and the mean value of the signal made equal to zero. This can be done by extending the temperature signal with a negative portion of equal area and equal or shorter duration than the original signal. Removing the d.c. component in this way improves the resolution of the temperature signal in the frequency domain.

These modifications to the procedure are illustrated in figures 6.28 to 6.30. Again the theoretical temperature rise for a step in heat transfer of $25 kW/m^2$ applied to a gauge on a two layered substrate was calculated. A negative portion of equal area was added and the signal extended to a total length of 8N by padding with zeros, figure 6.28. The heat flux was calculated from equations 6.42 and 6.43. The result for the entire signal length is

shown in figure 6.29 and the portion corresponding to the original N points is plotted in figure 6.30. The impulse function caused by the sudden truncation of the temperature signal is still seen, but has decayed quickly to zero. Closer examination of the reconstructed heat transfer rate reveals a sharp spike or overshoot at the beginning and oscillation of the signal about a step of the correct value. The ringing is caused by truncating the Fourier series which specifies the ideal waveform, (**Brigham, Ramirez**). The overshoot at each end of the step is referred to as Gibb's Phenomena and always occurs where there is a discontinuity in the original waveform.

The waveform can be smoothed to round the discontinuities. **J.E. Doorly (1987)** recommended using a Hanning function for which the amount of smoothing can be specified by setting the filter half width. The effect of this smoothing on a square wave is shown in figure 6.31 for filter half widths of 2 and 4. For most actual signals there are no discontinuities and smoothing is not only unnecessary but also modifies the fluctuations which are of interest.

Using a rectangular area to give the signal a zero mean value adds discontinuities to the waveform resulting in the problems described above. A Hanning Function of the form

$$F(n) = k\left(1-\cos\frac{2\pi n}{N}\right) \qquad (6.50)$$

is a better choice for the offset function as its Fourier transform has very small side lobes, figure 6.32 and is therefore far less susceptible to truncation in the frequency domain.

The temperature signal was processed again. A plot of the eight times extended signal with a Hanning function used to create the negative area is shown in figure 6.33. The whole wave form was smoothed using a four point Hanning filter. The heat transfer rate for the complete signal is

shown in figure 6.34 and a portion of the step function from the original N points is shown in figure 6.35. The ringing has disappeared and the initial overshoot has been modified as can be seen when this area of the step is enlarged, figure 6.36. It is also apparent that there is an error of 0.5% in reconstructing the step. This error is reduced slowly as the number of points in the extended signal is increased and for a signal of length 16N the error is 0.3%, figure 6.37.

6.6 Procedure for Obtaining the Mean Heat Transfer Rate.

The purpose of this project was to measure the heat transfer rate to the rotor blade of a full stage turbine. Now that the theory of the signal processing method has been developed it will be applied to experimental data.

The mean heat transfer rate was obtained by sampling the output from the inshaft amplifier at the relatively slow rate of 435 samples per second. A typical result is shown in figure 6.38. The number of points in the useful part of the data depends on the run time and in this case was 85. The remainder of the signal was discarded and the useful portion was divided by $I\alpha_{20}R_{20}$ to give the amplified temperature signal, which was then offset so that the initial value was zero. The signal was next extended to 256 points by adding extra zeros, figure 6.39. Then the routine DB in the program DSIGPRO was called which calculates the actual temperature rise using equations 6.35 and 6.36. The result is shown in figure 6.40. Note that the deboosting process modifies the discontinuity at the end of the temperature signal, removing the need for smoothing. The signal was further extended to 1024 points (greater than eight times the original 85 points), the area under the curve between points 1-85 calculated and a Hanning function

with an equal but negative area added between points 86 and 170, figure 6.41. Finally the routine QM in DSIGPRO was called which calculates the heat transfer rate using equations 6.43 and 6.42. The result for the entire zero padded signal is shown in figure 6.42 and the original points are plotted in figure 6.43. Note that smoothing was not applied at any stage.

6.7 Procedure for Obtaining the Unsteady Heat Transfer Rate.

The unsteady heat transfer rate was obtained by sampling the output from the inshaft amplifier at a fast rate (200kHz). A typical record, of length 3500 points is shown in figure 6.44. Again the signal is first divided by $IR_{20}\alpha_{20}$ to give the the amplified temperature rise, figure 6.45. The transient recorder is set up so that a number of points are recorded before the trigger which initiates data sampling at the fast rate, consequently the 3500 point record may not start at zero and must be offset.

The 3500 point record is only a short portion of the actual unsteady record which occurred during the run. The signal prior to the period of fast data acquistion is not considered by the signal processing routine, even though events which happen in this period may influence the portion of the signal which is recorded. It is therefore important that the fast data acquisition occurs at a time in the run such that the initial transient has decayed and is not influencing the unsteady signal.

In order to reconstruct the actual temperature rise the signal must first be extended with extra zeros. The extended signal length, M, is chosen so that the sample spacing in the frequency domain, given by equation 6.37, is smaller than the lowest breakpoint. The signal length must also be a power of two. Consequently the extended signal length was set at 16384 points, giving a frequency spacing of 12.2Hz. The routine DB was called to

calculate the actual temperature rise as described before.

The original 3500 points showing the temperature rise were selected and are plotted in figure 6.46. The signal was padded with 29268 zeros to give a total of 32768 points (greater than 8 times the original signal length). As described above a Hanning Function with a negative area equal to the area under the first 3500 points was created between points 3501 and 7000. Now that the signal was prepared the routine QM was called to calculate the heat transfer rate as described in section 6.5. The portion corresponding to the original 3500 points is plotted in figure 6.47.

As was seen in figures 4.8 and 4.10 at high frequencies the enamel layer appears semi-infinite and the thin film gauge can be considered as if mounted on a single layer substrate. Consequently the electrical analogue could be used to give the heat transfer rate directly, without it being necessary to apply an analytical correction to account for the presence of the metal layer. For unsteady signals recorded on the rotor blade the in-shaft amplifier is needed to condition the signals before they are passed through the slipring, but for high frequency signals seen in the stationary frame of reference, e.g. on the NGV, the analogue could be used to give the unsteady heat transfer rate directly.

6.8 Effect on Calculated Heat Transfer Rate of Variations in the Amplifier Transfer Function.

In table 5.2 the breakpoints for each of the eight in-shaft circuits were listed along with the nominal values. The transfer function of each circuits was plotted and it was seen that the curves did not vary very much, figure 5.10. The assumption was made that the nominal breakpoints and the

average dc gain could be used to calculate the actual temperature rise from the output of any amplifier and this was used when processing all the heat transfer data using the method described in section 6.6 and 6.7.

A test has been conducted to check that the effect of using the nominal rather than the actual breakpoints was small. The mean heat transfer rate from gauge 20 was calculated using first the real breakpoints for circuit 2C05 and secondly the nominal breakpoints which are both given in table 5.2, The two traces are plotted in figure 6.48 and it can be seen that the effect on the change on the heat transfer rate was negligible. This exercise was repeated for the unsteady data, figure 6.49 and the difference between the two traces was again small.

6.9 Effect on Calculated Heat Transfer Rate of Varying the Gauge Parameters.

The predicted analogue output, Appendix I, can be used to examine the effect of changes in the gauge parameters on the measured heat transfer rate.

The output from a two layered gauge subjected to a step in heat transfer and passed through an analogue was predicted using the method described in Appendix I and using the parameters in table 6.1. The input heat flux was then calculated from this predicted signal using the method described in 6.2. The program DSIGPRO which calls the appropriate routines asks the operator to input the calibrated values α, $\sqrt{(\rho ck)_1}$, $\sqrt{(\rho ck)_2}$ and a/k. By suppling an incorrect value the effect of uncertainties in the calibrated values can be examined.

Changes of +/- 10% were made to the value of $\sqrt{(\rho ck)_1}$ and the effect of these on the reconstructed heat transfer rate are clearly seen in figure 6.50. At short time the enamel layer appears semi-infinite and the heat

transfer rate is directly proportional to $\sqrt{(\rho ck)_1}$, equation 4.8. Hence the +/-10% change in $\sqrt{(\rho ck)_1}$ results in the same change in the initial height of the step. As time increases and the metal layer comes into play the influence of the enamel layer becomes less important.

This behaviour is also seen with +/- 5% changes in the value of a/k, figure 6.51. At short time the thickness of the enamel layer has no influence and so the correct heat transfer rate is obtained, but as time increases the effect of the changes in a/k are seen. Closer examination of the reconstructed heat transfer rate shows that the maximum effect on the heat transfer rate is +/- 3.2%.

Finally the effect of +/- 10% changes in the thermal product of the metal layer is plotted in figure 6.52. Again this parameter has no effect at short time and an increasing effect with time. The thermal product of a metal is actually known very accurately, so examining the effect of a 10% change is of theoretical interest only.

6.10 Conclusions.

The signal processing procedures used in this experimental program have been explained and tested.

Methods of calculating both the heat transfer rate and the temperature rise for the two cases where the thin film gauge output has been conditioned either by an electrical analogue or by the in-shaft circuit have been considered. The theory of each has been set out and a procedure suitable for digital calculation has been developed.

Each procedure was verified by taking data captured or predicted under known circumstances and recreating the input signal. This also enabled the accuracy of each method to be quantified, which was found to be

satisfactory in each case.

The processing procedure used with actual experimental data recorded in the rotor facility has been demonstrated and the practical problems of selecting a suitable signal length for each operation have been discussed.

By creating and then processing the predicted output from a gauge under known circumstances the effect of variations in the gauge properties have been examined and quantified.

CHAPTER 7

CALIBRATION OF INSTRUMENTED BLADES

7.1 Distribution of Thin Film Gauges.

A total of five blades were instrumented with thin film heat transfer gauges. The fifth blade was intended for use during commissioning of the rotor and the data acquisition system and only had two gauges painted on it. The number of gauges on each of the other blades was limited to eight by the size and spacing of the holes drilled in the platform, through which the signal leads were taken.

The main object of the project was to measure the heat transfer rate at mid-span around the blade, and over half the gauges were painted at this height. The remainder of the gauges were distributed at 10% and 90% span and on the platform. The gauges on the aerofoil were positioned along streamlines. The distribution of these gauges is shown in figure 7.1. The position of the plane section known as the B22 profile, which was tested in linear cascades of different scales by **Doorly** and **Nicholson**, is clearly marked, as are the two sections which define the blade. The distribution of gauges amongst the five blades is shown in figure 7.2.

A diagram showing how the gauge position has been defined in this experiment is drawn in figure 7.3. All heights (y) are measured vertically from a plane passing through point E (which is marked on the side of the blade root and given on the manufacturing drawings). The axial distance (x) is defined as the distance from plane B, which is an axial plane bisecting the blade root and also marked on the base of the blade. A negative distance indicates a point lying nearer to the leading than the trailing edge.

The B22 plane section is drawn in figure 7.4 and the positions of all the midheight gauges are marked. Details of this section, taken from the Proconsel file are given in Table 7.1. The position of the gauges around this section can be expressed as a fraction of either the surface length from the axial leading edge (X/s) or as a fraction of the axial chord (x/Cax). These values are listed in Table 7.2 along with the x,y coordinates. The positions of the gauges at heights other than 50% span are listed in Table 7.3.

Each gauge was calibrated in three stages to obtain the parameters α, a/k and $\sqrt{(\rho ck)_1}$ which are the temperature coefficient of resistance, the ratio of the thickness to conductivity of the enamel layer and the thermal product of the enamel layer, respectively.

7.2 Measurement of Temperature Coefficient of Resistance.

The temperature coefficient of resistance (α) for each gauge was measured by suspending the instrumented blade in a de-ionized water bath. The gauge resistance was recorded at various temperatures as the water was heated to 80 deg. C. The water was allowed to cool and further readings taken. A least squares line fit was then applied to the data and α and the gauge resistance at 20 deg. C were calculated. The results of this test are listed in Table 7.4.

The gauge resistance is measured very accurately using a HP3478A multi-meter, but there is a +/-0.5% uncertainty in the temperature measurement causing the same uncertainty in the calculated value of α. A repeat test on eight gauges showed a +/-0.4% variation between the two sets of readings, in line with the estimated +/- 0.5% uncertainty.

7.3 Measurement of Enamel Thermal Product, $\sqrt{(\rho ck)_1}$.

7.3.1. Theory.

The inhomogeneous nature of the enamel layer makes it necessary to measure the thermal product by experiment, rather than calculating it from the thermal properties. The circuit shown in figure 7.5 is used to suddenly put a constant current through the gauge, causing ohmic heating. This is equivalent to applying a step in heat flux to the surface. The experiment is performed over a very short time so that the enamel layer appears "semi-infinite" throughout the test and the conduction is one-dimensional, hence the description by **Schultz and Jones (1973)** of this test on a gauge mounted on a single layered substrate is applicable.

Referring to figure 7.5, the procedure is as follows:-

Initially the bridge is balanced, so

$$R_1 R_0 = R_3 R_4 \qquad (7.1)$$

Passing the current through the gauge causes a rise in temperature, ΔT, resulting in a resistance change, ΔR_0.

$$\Delta R_0 = R_0 \alpha \Delta T \qquad (7.2)$$

putting the bridge out of balance by an amount ΔV

$$\Delta V = \frac{\Delta R_0 R_1 I_0}{\Sigma R} \qquad (7.3)$$

where $\Sigma R = R_1 + R_2 + R_3 + R_0$

If the test is performed in a vacuum, the heat produced by the film, $\dot{q}$, is all transferred to the substrate .

$$\dot{q} = \frac{I_0 R_0}{A} \quad \text{where A is the film area} \qquad (7.4)$$

and for a constant heat transfer rate (from equation 4.10)

$$\dot{q} = \frac{\sqrt{\pi}\sqrt{(\rho ck)_1}\,\Delta T}{2\sqrt{t}} \qquad (7.5)$$

Substituting equations 7.3 and 7.4 in 7.5 and rearranging

$$\sqrt{(\rho ck)_1} = \frac{2\alpha I_0^2 R_0^2 R_1 \sqrt{t}}{A\sqrt{\pi}\sum R \Delta V} \qquad (7.6)$$

By recording ΔV and plotting against $\sqrt{t}$ a straight line is obtained and $\sqrt{(\rho ck)_1}$ can then be determined provided that the film area is known.

In practice accurate measurement of the film area is not easy, especially on a curved surface and a double calibration method is employed which eliminates the film area. First the film is pulsed in air and the change in bridge voltage ΔV_1 is recorded. Then it is covered with a layer of glycerine, pulsed again and the change ΔV_2 recorded. It can be shown **(Schultz and Jones 1973)** that

$$\sqrt{(\rho ck)_{air}} = \frac{\sqrt{(\rho ck)_{gly}}}{\frac{\Delta V_1/\sqrt{t}}{\Delta V_2/\sqrt{t}} - 1} \qquad (7.7)$$

The thermal properties of glycerine are well known, hence $\sqrt{(\rho ck)_1}$ can be calculated from equation 7.7.

7.3.2 Experimental Technique.

Measuring $\sqrt{(\rho ck)_1}$ for all the gauges was a lengthy process and had to be conducted with care. For the first stage of this calibration, the air test, it was essential that the gauge surface was clean and grease free as a finger print or the slightest trace of glycerine produced a false result. A suitable solvent e.g. "ultraclean" was used to gently clean the gauge.

The procedure was to balance the bridge and then pulse the gauge. The change in voltage was captured on an Iwatsu storage oscilloscope and down loaded to a HP 9836 computer for processing. Each gauge was pulsed three times in air and three times in glycerine. The data from each air test was used with the data from all the glycerine tests to produce nine values

for $\sqrt{(\rho ck)_1}$, from which the mean value was found.

The data taken from gauge two is used to illustrate the calculation procedure. The voltage change for both tests is shown plotted against time in figure 7.6 and plotted against $\sqrt{t}$ in figure 7.7. A straight line should be achieved in each test, but after a short while lateral (2D) conduction may occur causing the curve to deviate from a straight line. Ideally the test should be conducted in a short time, such that the effects of 2D conduction are not seen . In this series of calibrations 2048 points were taken in 5.12 ms The value of $\Delta V_1 / \Delta V_2$ was calculated by plotting the output of the air test against the output of the glycerine test and applying a least squares line fit, figure 7.8. The points over which the line was fitted were chosen so as to eliminate the transient response which occurs at the beginning of the test and also any effects of 2D conduction at the end.

7.3.3 Results.

The thermal properties of glycerine have been measured by many researchers and the results are documented by **Touloukain**. Using this data the following value for the thermal product of glycerine is obtained.

$$\sqrt{(\rho ck)_{gly}} = 920.6 \text{ +/- } 2.4\% \text{ J/Ks}^{1/2}\text{m}^2$$

The output from the thin film gauge during the glycerine test was smaller than that of the air test. The storage oscilloscope used to capture the trace had 25 bytes/division and a typical glycerine trace spanned three divisions. Hence the uncertainty in the voltage measurement was +/- 0.5/75 = +/- 0.7%.

The uncertainty in the line fit is negligible, due to the large number of points used, so the the total uncertainty in the measurement of $\sqrt{(\rho ck)_1}$ is

$$\text{+/- } (0.7\% + 2.4\%) = \text{+/- } 3.1\%$$

The mean value obtained for each gauge is listed in Table 7.4. The nine values which were calculated for each gauge, exhibited a scatter of +/- 3.0% which is in agreement with the uncertainty analysis above. For the 32 gauges tested (gauge 24 was faulty), the values of $\sqrt{(\rho ck)_1}$ varied from 976.1 to 1760.4 $J/m^2Ks^{1/2}$. A variation was expected as the enamel layer is not of uniform composition and varies not only from blade to blade, but also around each profile.

7.4 Laser Calibration - Measurement of a/k.

7.4.1 Introduction.

The third parameter required to calculate the heat transfer rate is a/k, the ratio of the thickness to the conductivity of the enamel layer. Uncertainty concerning the structure of the enamel layer and hence its conductivity, and also the difficulty of measuring the enamel thickness, mean that finding a/k is not a simple matter of measuring a and establishing k by experiment. Instead the parameter must be measured directly.

7.4.2 Theory.

Consider the behaviour of a gauge on a two layered substrate when a step in heat transfer rate is applied.

The relationship between heat transfer rate and the surface temperature rise was given in equation 4.28.

$$\bar{\dot{q}} = \sqrt{(\rho ck)}_1 \sqrt{\bar{s}} \; \frac{(1 - A\exp(-2a\sqrt{(s/\alpha_1)}))\,\bar{T}}{(1 + A\exp(-2a\sqrt{(s/\alpha_1)}))} \qquad (7.8)$$

For a constant heat transfer rate, Q

$$\bar{\dot{q}} = \frac{Q}{s} \qquad (7.9)$$

So $$\bar{T} = \frac{Q}{s^{3/2}\sqrt{(\rho ck)_1}} \frac{(1+A\exp(-2a\sqrt{(s/\alpha_1)}))}{(1-A\exp(-2a\sqrt{(s/\alpha_1)}))} \quad (7.10)$$

Which can be expanded to give

$$\bar{T} = \frac{Q}{s^{3/2}\sqrt{(\rho ck)_1}}\left(1 + 2\sum_{m=1}^{\infty} A^m \exp(-2am\sqrt{(s/\alpha_1)})\right) \quad (7.11)$$

This can be inverted

$$T(t) = \frac{2Q}{\sqrt{(\rho ck)_1}}\left(\sqrt{\frac{t}{\pi}} + 2\sum_{m=1}^{\infty} A^m \left\{\sqrt{\frac{t}{\pi}}\exp\left(\frac{-a^2m^2}{\alpha_1 t}\right) - \frac{am}{\sqrt{\alpha_1}}\operatorname{erfc}\left(\frac{am}{\sqrt{\alpha_1 t}}\right)\right\}\right) \quad (7.12)$$

For long time as $t \to \infty$ **(J.E. Doorly and Oldfield, 1987)**

$$T = 2Q\left(\frac{\sqrt{t}}{\sqrt{(\rho ck)_2}\,\pi}\right) + Q\frac{a}{k}\left(1 - \frac{\sqrt{(\rho ck)_1}}{\sqrt{(\rho ck)_2}}\right) \quad (7.13)$$

which is essentially the temperature rise for a gauge on the metal alone with an offset to account for the presence of the insulator.

For short time , as $t \to 0$

$$T(t) = 2Q\left(\frac{\sqrt{t}}{\sqrt{(\rho ck)_1}\,\pi}\right) \quad (7.14)$$

which is the temperature rise for a gauge on insulator alone.

Therefore if a step in heat transfer is applied to a gauge on a two layered substrate, initially only the insulating layer is seen and the temperature follows equation (7.14). As time increases the enamel layer ceases to be semi-infinite and the temperature rise follows equation (7.13). Figure (7.9) shows this behaviour.

The time of intersection of equations (7.13) and (7.14) is given by -

$$\sqrt{t} = \frac{\sqrt{\pi}}{2}\frac{a}{k}\frac{\sqrt{(\rho ck)_1}}{\sqrt{(\rho ck)_2}}\left(\sqrt{(\rho ck)_1} + \sqrt{(\rho ck)_2}\right) \quad (7.15)$$

and the ratio of the slope of the two lines is given by-

$$\frac{\text{Slope 1}}{\text{Slope 2}} = \frac{\sqrt{(\rho ck)_2}}{\sqrt{(\rho ck)_1}} \quad (7.16)$$

$\sqrt{(\rho ck)_1}$ is known from a standard air/glycerine test, hence by fitting

lines to the first and second parts of the curve, $\sqrt{(\rho ck)_2}$ can be calculated from equation (7.16). The fitted lines can also be used to find the time of intersection and then a/k can be evaluated using equation (7.15) .

7.4.3 Experimental Method.

J.E. Doorly used the electrical discharge method described above to provide a step in heat transfer rate. The duration of the pulse had to be considerably longer than in the $\sqrt{(\rho ck)_1}$ calibration test in order to see the effect of the metal layer and consequently the effects of 2D conduction were significant and had to be taken into account.

A thermal radiation technique was also used by **J.E Doorly**. The element from a car cigarette lighter was used as the heat source and a mechanically operated camera shutter was placed between it and the gauge being tested. Unfortunately the opening time of the shutter was too slow and the early response of the gauge was obscured. Consequently a value for a/k could not be achieved from this test, but the output could be reprocessed, using the value obtained from the discharge test, to reconstruct the input step in heat transfer, thus providing a check on the calibrated parameters.

During the course of this project a new experimental technique has been designed and commissioned. Doorly's work made it clear that a thermal radiation technique was required as this reduces the effects of 2D conduction by providing a "spot" of heat covering both the gauge and the surrounding area. It is also necessary that the switching or rise time of the heat source is short, (less than 10μs).

Several heat sources were considered such as a mercury or xenon arc lamp, but the only solution was found to be an Argon ion laser

modulated using a Pockels cell. The optical arrangement is shown in figure 7.10. The laser is made by Spectra Physics and has a power output of 4W. It is operated in single mode on the green line (540 nm). The beam is modulated using the polarizer/Pockels cell arrangement and a beam expander is used to obtain a spot of light of the required size at the gauge.

The Pockels cell is the key component in the apparatus and its operation will be briefly described. A more detailed description is given by **Wilson and Hawkes**. The device depends on the Pockels electro-optic effect in crystals which essentially results in a change in the polarizing properties of the crystal when an electrical field is applied. To modulate the laser output, the beam is first polarized before passing through the Pockels cell, figure 7.10. The direction of polarization is changed by 90° when a set voltage is applied across the device. An analysing polarizer is mounted after the Pockels cell at 90° to the original polarizer, so that the beam is only transmitted when the voltage is applied.

The voltage required to activate the Pockels cell is provided by a UHT supply, which in turn is triggered by a pulse generator, the duration and frequency of the pulse being easily changed.

7.4.4 Commissioning.

Commissioning the system involved checking out several points of concern. The first was the rise time of the heat pulse and another was that the power density of the Pockels cell was not sufficient to transmit the required laser power without absorbing some of the incident beam.

A photodiode (R.S. Part no.308-067) was positioned in place of the blade with the laser beam incident on it. The output which is proportional to the intensity of the incident light was monitored. The rise time of the heat

pulse was found to be less than 10μs and a constant output was recorded over a period of time showing that the Pockels Cell was not absorbing any of the beam, figure 7.11.

The first gauge to be radiantly tested using this apparatus was mounted on machinable glass ceramic (m.g.c.). The output from the gauge was passed through a HTA1 Analogue before being recorded on an Iwatsu digital storage oscilloscope. The analogue output for a gauge on a single layered substrate subject to a step in heat flux is also a step (equation 4.19) and the temperature rise is parabolic.

The results of the first test are shown in figures 7.12 and 7.13. It can be seen that the analogue output is not constant and that the temperature v $\sqrt{t}$ plot is not a straight line. This is due to two-dimensional conduction; the gauge has a higher emissivity than the surrounding m.g.c., consequently it absorbs more heat which is then conducted laterally to the substrate. The emissivity of the two surfaces can be made more uniform by blackening the surface and a water soluble overhead projector pen has been found suitable for this purpose **(Epstein et al, 1985)**. The results of a test on a blackened m.g.c. sample are shown in figures 7.14 and 7.15 and it can be seen that the output is a step and that the temperature rise is directly proportional to $\sqrt{t}$.

Machinable glass ceramic samples were also used to examine the effect of signal averaging, pulse length and pulse interval. A pulse pattern of 100ms on and 900ms off was found to produce a repeatable output of sufficient length, figure 7.16 and averaging 64 consecutive pulses resulted in an acceptable signal to noise ratio.

The first tests of gauges mounted on enamel coated blades were performed with the gauge blackened and the results, figures 7.17 and 7.18

were very encouraging. Tests on an un-blackened gauge gave an output of similar shape, figure 7.19 , showing that the emissivity of the enamel was close to the emissivity of the gauge. The lower temperature rise of the un-blackened gauge, figure 7.20, illustrates the improved emissivity of the blackened surface. The values for the point of intersection calculated from the two tests were in good agreement and it was concluded that it was not necessary to blacken gauges on the enamelled substrate.

Another parameter which could be varied in the test was the diameter of the incident beam. In the tests reported so far it was 10mm, but subsequently it was reduced to 5mm. This resulted in a larger output because of the higher heat concentration, figures 7.21 and 7.22.

7.4.5 Actual Method of Calculating a/k.

Consider the results shown in figures 7.19 and 7.20. To establish the value of a/k, lines were fitted to the curve in figure 7.20 between times 0.03 and 0.06 $s^{1/2}$ and 0.25 and 0.29 $s^{1/2}$. The slope of each part was calculated along with the point of intersection. $\sqrt{(\rho ck)_2}$ was established from equation 7.16 and then a/k determined to be 80.4E-6 m^2K/W using equation 7.15.

When all the parameters were known it was possible to calculate the applied heat flux directly from the analogue output (chapter 6.2). This was done (figure 7.23) and it can be seen that the recovered signal was not a sharp step function. The analogue output was reprocessed using a value of 95 E-6 m^2K/W and a better step function was obtained, figure 7.24.

In order to examine the process of calculating a/k in more detail a program was written which predicted the analogue output for a two layered gauge subject to a step in heat flux (Appendix I). The predicted analogue output for a time and sample rate identical with those used in the laser calibration is shown in figure 7.25. The values used in the prediction are

listed in Table 6.1 and were typical of the gauges being calibrated. The temperature rise was calculated as before and is shown plotted against $\sqrt{t}$ in figure 7.26. The slopes of the two parts of the curve were established between times 0.03, 0.06 $s^{1/2}$ and 0.25, 0.29 $s^{1/2}$ and the point of intersection evaluated. The value of a/k was calculated to be 74.5 E-6 m^2K/W whereas it was actually 80.0E-6 m^2K/W. Further examination of the line fit data showed that while the initial slope had the correct value (equation 7.14) the slope of the second part of the curve was too steep resulting in an early time of intersection and a small value of a/k.

A second prediction was made over longer time, figures 7.27 and 7.28 and it can be seen from the temperature rise that the curve does not flatten out until a time greater than $\sqrt{t} = 0.3\ s^{1/2}$. The slope of the second part of the curve was calculated over short intervals of time from 0.29 $s^{1/2}$ to 1.0 $s^{1/2}$ and the results are plotted in figure 7.29. As can be seen the slope of the predicted curve is asymptotic to the line of slope given by equations 7.13 and 7.16 and will therefore always result in a low value of a/k.

In view of this problem an alternative technique was tried. For a metal the thermal product $\sqrt{(\rho ck)_2}$ can be calculated very accurately from the individual properties ρ, c and k. Hence the slope of the second part of the curve at long time can be calculated from equation 7.16 . A line of this slope is then drawn through a point on the curve, the time of intersection calculated and a/k established. The percentage error in the value of a/k is plotted against the value of $\sqrt{t}$ at which the second line was fitted in figure 7.30. Also plotted is the value obtained by the previous method. The improvement in accuracy is clearly shown. Even so the modified method will still tend to underpredict a/k by 5-10%.

The result of this investigation was that the modified processing

technique was adopted and it was also considered reasonable to increase the value of a/k obtained by 5-10% if this resulted in a sharper or flatter step in reconstructed heat flux. The best a/k value for each gauge is listed in table 7.4.

7.4.6 Uncertainty in Measured Value.

The measurement of a/k is not a single stage process and both α and $\sqrt{(\rho ck)_1}$ must be known before a/k can be established.

The temperature rise is calculated from the analogue output and is known to the uncertainty with which α is known, +/-0.5%. The standard error in the line fit through the first part of the curve can be easily calculated **(Chatfield)** and from the Students t-test the 95% confidence limit can be determined. This was found to be +/-0.25% for several gauges.

The slope of the second part of the curve is calculated from equation 7.16 and will depend on the uncertainty in slope 1, $\sqrt{(\rho ck)_1}$ and $\sqrt{(\rho ck)_2}$. These have been found to be +/-0.25%, +/-3.1% and 0.5% respectively, which gives a total uncertainty in slope 2 of +/-4.0%.

The effect of the uncertainties in the slopes of the two parts of the curve on the time of intersection is shown in figure 7.31 and was found to be +/- 1.0%.

A worst case estimate of the uncertainty in a/k can be obtained from the sum of the uncertainties in $\sqrt{t}$, $\sqrt{(\rho ck)_1}$, $\sqrt{(\rho ck)_2}$ and α which gives the total uncertainty in a/k as +/-5.0%.

The parameter which has most effect on a/k is $\sqrt{(\rho ck)_1}$ as the uncertainty in this value is directly responsible for the large uncertainty in the slope of the second part of the curve, leading to the uncertainty in $\sqrt{t}$. $\sqrt{(\rho ck)_1}$ also appears in equation 7.15 from which a/k is calculated.

7.4.7 Measurement of Enamel Thickness.

The profiles of the four blades OX1, 3, 5 and 6 (i.e. those with serial numbers 1, 3, 5 and 6) were measured at several heights before and after enamelling, using a Renishaw machine. A program, THICK, was written to calculate the perpendicular distance between the surfaces, i.e. the enamel thickness, from the two sets of coordinate data.

The results for the sections at a radius of 255mm from the turbine centreline (midheight) are plotted against axial position in figures 7.32 - 7.35. The enamel thickness varies around the blade profile and from blade to blade. The coating on blade OX1 is the thickest at around 0.2mm and is also the most uniform. The thinnest enamel occurs near the trailing edge, pressure surface of blade OX6 and on the leading edge, pressure surface of OX5 and is approximately 0.04mm.

All the blades show a very uneven coating at the leading and trailing edges. A detailed plot of the measurement points in these two regions for blade 0X5 is shown in figure 7.36. The build-up of enamel at the leading edge was seen on all blades. The shortage of points at the trailing edge, which causes an apparently "bald" patch, is a fault of the measuring machine and occurred on two of the blades making the coating appear more irregular than it is.

The thickness of enamel under each mid-height gauge is listed in table 7.5 and varies from 0.051mm to 0.143mm a change of 280%. This compares with a 330% change in a/k from $0.0000577 m^2K/W$ to $0.0001927 m^2K/W$.

7.4.8. Discussion of a/k Calibration Results.

Once a/k and $\sqrt{(\rho ck)_1}$ have been established the analogue output can

be reprocessed to give the input heat flux. This provides a check on the calibrated parameters, as the correct values will result in a step function. This procedure was demonstrated in section 7.4.5 where it was shown that in most cases increasing the value of a/k, which was initially obtained, improved the shape of the step function by shortening the rise time.

For some gauges there was no value of a/k for which a steady input heat flux could be reconstructed. There are several possible reasons for this. If the spot of heat were too localised, the effects of lateral conduction, i.e. heat being passed to the surrounding area, could cause the heat flux at the gauge to drop off. Tests on two gauges using both 5mm and 10mm diameter spot sizes found no suggestion that this was happening. Lateral conduction could also arise from non-uniform emissivity of the gauge and the surrounding substrate resulting in heat being transferred to or from the gauge by the substrate. This could be prevented by blackening the gauge and surrounding area. Calibration of gauges with and without blackening gave very similar results, as illustrated in figures 7.18 and 7.20 and it was concluded that blackening was not necessary for gauges painted on this type of enamel. However, both this test and the investigation of the effect of beam diameter were only carried out on a couple of gauges and a more thorough investigation should now take place.

It was assumed when developing the theory that the heat spot is incident on a flat surface. In many positions around the aerofoil this is approximately so, but in highly curved areas such as near the leading edge this is obviously not the case and the surface profile may cause non-uniform heating. However of the gauges in the leading edge region only gauges 18 and 20 gave problems and satisfactory step functions were achieved for gauges 2, 19 and 21.

A further assumption was that the metal layer appeared semi-infinite throughout the experiment. The effect of a finite backwall on the surface temperature rise is shown in figure 7.37 (from **J.E. Doorly and Oldfield, 1986**). Once the heat pulse has reached the backwall the temperature of the body increases more rapidly, curve (a) deviating from the semi-infinite behaviour shown by curve (b). The length of time for which the metal of an enamel coated turbine blade appears semi-infinite depends not only on the metal thickness but also on the enamel thickness. There is a larger temperature drop across a thick layer of enamel than across a thin one and the effects of a finite backwall are delayed for longer. The increase in slope of the temperature versus $\sqrt{t}$ graph resulting from the finite backwall would cause the wrong value of a/k to be calculated. Consequently the results for each gauge were examined for deviations of this type, but no significant changes were seen.

When all the a/k results were studied along with the reconstructed input heat flux trace for each gauge it was found that in general the gauges producing the best step functions were those with large a/k values eg. gauges 2, 10, 11, 12 and 22. This would imply that the enamel under the problem gauges was thin or had a high conductivity. The problem gauges included gauge 5 which was mounted on the thinnest layer of enamel of all the gauges (Table 7.5). The analogue output from this gauge is shown in figure 7.38 and the temperature rise in figure 7.39. The calculated a/k value was 60.2E-6m^2K/W which gave the reconstructed input plotted in figure 7.40. Using a smaller value of a/k increased the rise time and the peak became more pronounced, figure 7.41. The opposite effect was seen when a/k was increased, figure 7.42.

Besides having the thinnest enamel layer gauge 5 also had one of

the largest $\sqrt{(\rho ck)_1}$ values. Refering to equation 7.15, for a certain time of intersection and metal substrate (i.e. $\sqrt{(\rho ck)_2}$), a/k is inversely proportional to $\sqrt{(\rho ck)_1}$. Hence a large $\sqrt{(\rho ck)_1}$ value can be expected to result in a low value for a/k. Also an incorrect value for $\sqrt{(\rho ck)_1}$ results in an incorrect value for a/k. If figure 7.41 is compared with figure 6.50 in which the effect of a +10% error in $\sqrt{(\rho ck)_1}$ was investigated it can be seen that the shapes of the two are similar, suggesting that an incorrectly high value of $\sqrt{(\rho ck)_1}$ may have been measured.

In the electrical pulse test to establish $\sqrt{(\rho ck)_1}$ care has to be taken to ensure that the enamel layer appears semi-infinite throughout the experiment and that the conduction remains one-dimensional. The thinner the enamel layer the shorter the time for which these two criteria are satisfied. The duration of the pulse could be made shorter to avoid the onset of these problems, but the occurrence of the initial transient imposes a minimum time limit on the test.

The dimensions of the gauge will also affect the time for which the assumptions made in the electrical discharge test are valid. A preliminary check has indicated that the gauges used in this study were all of similar dimensions, and so this should not be the cause of problems with only some of the gauges, but a more detailed investigation may reveal otherwise.

Epstein et al, (1985) describe an alternative technique for establishing $\sqrt{(\rho ck)_1}$ which was adopted because the width of the thin film gauges they were using was of the same order as the insulator thickness and thus violated the uniform heating assumption. The method is similar to the technique described in section 7.3.1 except that instead of providing a pulse of heat by suddenly passing a current through the gauge, a radiant pulse is supplied using a laser. In both cases the test is conducted over a short time

such that insulator remains semi-infinite throughout. The thermal product of the insulator is given by:

$$\sqrt{(\rho ck)_{ins}} = \frac{\sqrt{(\rho ck)_{liq}}}{\frac{\Delta V_{air}/\sqrt{t}}{\Delta V_{liq}/\sqrt{t}} - 1} \qquad (7.17)$$

where ΔV_{air} is the output during the air test and ΔV_{liq} is the output when the sensor is covered with a reference liquid of known $\sqrt{(\rho ck)}$.

If further investigations reveal that the thickness of the enamel layer is making it difficult to conduct the electrical discharge test satisfactorily then use of the technique described by **Epstein et al (1985)** should be considered.

Two of the gauges on the platform behaved in a strange way. The analogue output for gauge 30 only fell a little with increasing time, figure 7.43 and the temperature rise, figure 7.44, was not made up of two separate curves. Consequently it was thought that the enamel layer under this gauge was thicker than that under the aerofoil gauges and remained semi-infinite throughout the experiment.

7.5 Conclusions.

The data presented in this chapter are the calibration results for a large number of thin film gauges mounted on enamel coated turbine blades. A total of 33 gauges were calibrated. The temperature coefficient of resistance was easily and accurately established for each gauge. The experimental calibration of the thermal product was a time consuming operation and had to be carried out carefully so as to ensure that the gauge was clean and that conduction remained one-dimensional. A wide variation in $\sqrt{(\rho ck)_1}$ was found amongst the gauges tested.

A new technique for measuring the parameter a/k has been

developed in which a laser is used to radiantly heat the gauge. The rise time has proved to be sufficiently short to enable the semi-infinite behaviour of the gauge to be captured and by using a radiant heating method problems of lateral conduction have been eliminated allowing the long time response to be clearly seen. 32 gauges have been calibrated using this method and a wide variation in the value of a/k was found.

The calibration of a large number of gauges indicates that viable methods of establishing the various parameters have been developed. A check on the parameters was made by calculating the applied heat flux from the analogue output captured during the laser pulse test and for many gauges satisfactory step functions were obtained. However, this was not always the case and problems were encountered with some gauges. In general these had low a/k values and measurement of the enamel thickness showed that the enamel under these gauges was thin.

The influence of the enamel layer thickness on the assumptions made in the electrical discharge and laser pulse tests has been discussed and it was seen that a thin enamel layer could lead to incorrect calibration of the parameters a/k and $\sqrt{(\rho ck)_1}$. The shape of the gauge and the curvature of the model could also influence the results of the $\sqrt{(\rho ck)_1}$ and a/k calibrations respectively.

In view of the problems encountered with some gauges it is recommended that a series of controlled experiments should be conducted in which various samples are calibrated using the methods described in this chapter. The samples should be made out of the same enamel/metal substrate as used for the instrumented turbine blades and different combinations of enamel thickness and gauge dimensions should be fabricated. The shape of the models should also be varied to represent the different

surfaces found on a turbine blade.

A systematic investigation of the effects of conducting the electrical discharge test over a shorter period of time should be undertaken, accompanied if possible by a back to back calibration using the method described by **Epstein et al, (1985).** A more detailed study of the effects of blackening, beam diameter and pulse duration on the laser calibration experiment should also be carried out. In this way not only will the accuracy of the calibrations be improved, but a better understanding of the behaviour of a thin film gauge on a two layered substrate will also be achieved.

CHAPTER 8

HEAT TRANSFER MEASUREMENTS

8.1 Introduction.

The aim of the experimental work was to measure the mean and unsteady heat transfer rate to the turbine blade using the 33 gauges detailed in chapter seven. Ultimately, due to various mechanical problems, only five tunnel runs were made, in which data was collected from a total of seven midheight gauges. The data was thoroughly analysed with particular attention to noise levels and the errors introduced by calibration and signal processing. As described in chapter three, temperature and pressure measurements were made so that coupled with a record of the speed, the flow conditions during the run could be established. Corrections have been made for off-design conditions and where appropriate scaling was applied to enable the results to be compared with those of **Doorly (1984).**

8.2 Commissioning of Instrumentation.

8.2.1 Data Acquisition System.

A block diagram of the signal chain for each gauge is shown in figure 8.1. Up to eight gauges were monitored during each run. The electronic circuits mounted inside the rotor shaft which amplified the signals before they were transmitted through the slipring were described in chapters four and five.

In the stationary frame of reference each signal was passed to two AMP-05 units, **(Ainsworth et al, 1989)** one of which was ac coupled and the other dc coupled. The ac signal was filtered and then recorded in two different ways to obtain the mean (time averaged) and unsteady heat transfer rates. The mean signal was conditioned by a CAS-8 amplifier and then

recorded on the computer controlled A/D system, as described by **Oldfield et al (1978).** The unsteady signal was recorded using a DATALAB Transient Recorder operating in split timebase mode. 596 points were recorded at a slow rate immediately before the trigger and then 3500 samples were taken at 200 kHz as the rotor passed through design speed. These signals were transferred to the PDP 11/34A computer for storage after the run.

The dc signal enables the actual temperature of the gauge to be ascertained and not just the temperature rise. This signal was also conditioned by a CAS-8 amplifier and sampled by the computer controlled A/D system. In addition the signal from one of the gauges was recorded by the HP 9836 computer used to control the rotor speed prior to a run. Data was taken at a very slow rate of approximately one sample per second, but was sufficient to provide a record of the gauge voltage during the time immediately before firing the tunnel when the rotor was spinning up to speed. Tests in the spinning rig and the rotating bar experiment **(Doorly, 1984)** had shown the need for monitoring the gauge temperature during this time.

The speed signal was recorded throughout the run on the UV chart recorder and this data was analysed by **Sheard** to give the initial and final rotor speed during the run. Timing signals of one and 36 times rotational speed were captured on the transient recorder along with the unsteady heat transfer signal.

All data was transferred from the PDP to a DEC Vax Station II for processing.

8.2.2 Noise Tests.

The signals were carried from the blades to the in-shaft electronics

via small diameter copper wires attached to the disc as described in chapter five. This wiring was a major area of concern, not only because it had to withstand the high rotational forces involved, but also because the various connections and the long lengths of wire were potential sources of electrical noise.

Noise measurements were made during bench tests on the in-shaft electronics as reported in chapter five and further tests were made as the instrumentation chain was built up, so that any problems could be identified as they occurred. When the wiring on the disc was completed the fifth blade, which had been specifically manufactured for the purpose of commissioning the instrumentation chain, was slotted in place on the disc. Connections were made from gauges 32 and 33 to circuits of the in-shaft electronics which were mounted inside the carrier. A 47 ohm resistor was connected to a third circuit for comparison. The gauge resistance, dc output and noise levels were measured using a wide bandwidth multi-meter (HP 3478A). Readings were taken using two different filter units and the results are listed in tables 8.1 and 8.2. The first filter was an eight pole, 100kHz low pass unit built by Barr and Stroud and the second was a two pole, low pass Butterworth filter incorporated into the AMP-05 unit and also set at 100kHz. The noise levels were similar in all cases and compared well with those measured in earlier tests on the in-shaft electronics.

Next the disc was mounted on the shaft and the signals from gauges 32 and 33 were fed through the slipring to the AMP-05s and subsequent signal conditioning and recording units. The noise level at each junction was measured and found to be less than 1 mV rms, in agreement with that measured in the bench tests.

No problems with noise and interference on the thin film gauges

were encountered until the main phase of the project, when all five instrumented blades were installed and 32 gauges connected simultaneously. All eight in-shaft circuits and 16 AMP-05 units were used. The source of the noise was not easily identified and various precautions were taken:- the case of each AMP-05 unit was earthed through the mains (a standard procedure which had been overlooked in making up the units); the gain of the ac coupled AMP-05 amplifiers was changed from 1 to 10, so that the signals were passed from the working section to the data acquistion equipment at a high level and finally, it was noticed that a few gauges were considerably noisier than the others or had bad connections. The outputs from these gauges were shorted at the point where they passed through the casing of the working section. These actions resulted in the noise levels listed in table 8.3, which when referenced to the input, gave values in agreement with those measured in bench tests.

During the commissioning tests using the fifth blade only, a series of noise measurements were taken from gauges 32 and 33 with the rotor turning at various speeds and no air flow. The noise levels at 0, 2000 and 8000 rpm were compared, figure 8.2 and it was found that at high speed, the noise level was much greater than when stationary. More data was recorded with the rotor spinning at 8000 rpm using a faster sampling rate, figure 8.3 and it was seen that distinct features of the trace were repeated every revolution. The data was plotted again on an expanded time scale and examined in more detail, figure 8.4. The frequency with which a particular rotor blade passes the NGVs was known and it was noticed that some of the disturbances appeared to occur at NGV passing frequency, indicating that the presence of the NGVs was causing a disturbance on the thin film gauge signal.

A simple investigation with a pocket compass established that some of the NGVs were quite strongly magnetic. No attempt had been made to demagnetize them when the facility was assembled and it was very probable that the instrumentation on the rotor was picking up the e.m.f. generated by cutting the magnetic field around the NGVs. It was not a trivial task to dismantle the NGV ring and demagnetize all the vanes, but it was possible to remove the eight in the two cassettes and spin the rotor without a full complement of NGVs. This was done, but the difference to the noise test, figure 8.5, was not immediately obvious. The large spikes were still present and it was only by establishing at what times the rotor blade was passing the cassettes, that the difference could be seen. The intervals in which the cassettes were passed are ringed in figures 8.3 and 8.5. When the two were compared, a periodic disturbance was found in the earlier trace which was not seen when the NGVs were removed.

The expected output from the thin film gauges and inshaft electronics was calculated (Appendix II) to be about 30mV peak to peak. This was larger than the average noise level at 8000 rpm but comparable with the largest spikes. When the first heat transfer measurements were recorded it was seen, figure 8.6, that the signal level was indeed approximately +/- 15mV and the magnetic disturbances could not be seen.

Having gained confidence that the signal to noise ratio was satisfactory and that it was not necessary to dismantle the NGV ring and demagnetize the vanes, two tunnel runs took place in which both mean and unsteady heat transfer measurements were recorded from the two gauges. These runs were successful and the results are discussed below. The rotor was then removed to enable the NGV exit surveys reported by **Iszak** to be carried out.

All five instrumented blades were installed in the rotor when it was rebuilt. After remedying the noise problems described above, attempts were made to make more heat transfer measurements. Unfortunately, after only two runs during which no meaningful data was recorded, only a few thin film gauges remained connected. The wiring was inspected and note taken of the manner of failure. It was repaired by studying the portions of wiring which were still attached and securing the rest using a "superglue" gel with an activator. This proved successful and two further tunnel runs were achieved before, as discussed in chapter three, the state of balance of the rotating assembly deteriorated to a level where it was considered prudent to strip the facility and establish the cause of the recurring vibration problems.

8.3 Mean Heat Transfer Results.

8.3.1 Introduction.

A list of the gauges for which mean heat transfer data is available, is presented in table 8.4. The positions of the gauges were shown in figure 7.4 and a listing of the coordinates was given in table 7.1. The procedure for processing the data has been described in chapter 6 and will be illustrated here using the data from gauge 4 captured during run 6448.

The ac voltage sampled on the computer data acquistion system is shown in figure 8.7. The initial peak which quickly dies away was caused by the tunnel starting processes. The disturbances at the end of the run were thought to be due to the piston hitting the front face of the gate valve and the oscillations during the run are caused by the finite mass of the piston. In previous investigations in this tunnel, these have been eliminated by compensation as described by **Schultz et al (1977)**, but the greatly increased mass flow rate required in the rotor facility meant that the previously used

compensation system had to be removed. The piston oscillations result in varying inlet conditions which cause small deviations from the design conditions during the run. As part of the analysis of the results described below, the piston oscillations were taken into account and the periodic variations in mean heat transfer level virtually eliminated.

The amplified temperature signal during the run time was obtained by scaling the raw output by $1/(\alpha_{20} I R_{20})$ and is shown in figure 8.8. The amplifier frequency response was then used to establish the actual temperature rise, figure 8.9, and finally from this the heat transfer rate is calculated, figure 8.10.

8.3.2 Temperature History.

Consider the temperature rise plotted in figure 8.9. After an initial rise of 25K the level fell back to 15K and then continued to fall more slowly whilst at the same time rising and falling with the piston oscillations. This pattern of temperature rise was expected. The initial peak and oscillations were explained above and the subsequent slow fall will be explained here.

The theoretical temperature rise for a gauge subjected to a step in heat transfer, as happens in the ILPT if the starting processes are ignored, is shown in figure 8.11. The gauge temperature rises quickly for the short time that the enamel layer appears semi-infinite, then the effect of the metal layer is seen and the temperature rises more slowly as heat is rapidly conducted through the metal. If the internal conduction were greater than the heat convected to the surface of the blade then it is conceivable that the gauge temperature could fall until a steady state was reached.

During the course of each experiment the driving temperature, which is the difference between the rotor relative total temperature and the

wall temperature fell due to two factors. The first was the surface heating up and the second, the fall in relative total temperature caused by the acceleration of the rotor. To quantify these effects:

Initial driving temperature (at 6500 rpm) = 334 - 288 K
= 46 K

Surface heats up 15K

Driving temperature now = 31 K.

Accelerate from 6500 to 8500 rpm

Relative total temperature falls by 6.5 K

Final driving temperature = 24.5 K

The temperature ratio (relative total temperature to blade surface temperature) at the end of the run was therefore 1:1.09 compared with 1:1.15 at the start of the run.

The temperature history of the gauge can also be obtained from the dc measurements recorded on the PDP and HP computers. The temperature rise calculated from the PDP dc record for gauge 8 is shown in figure 8.12 and after the initial transient shows good agreement with the temperature rise obtained from the ac signal which is also shown.

The output from one gauge was recorded by the HP computer for the whole time that the rotor was spinning. One such record is shown in figure 8.13 and it can be seen that there was a 2 deg.C rise before firing and a 10 deg. C rise during the tunnel run. It must be remembered that the HP computer acquisition system only took one reading per second and some detail of the speed and temperature during the run will have been lost. The temperature rise experienced by the rotor in the pre-run spinning period is much smaller than that recorded in the spinning rig tests (chapter 5). There are a variety of reasons for this favourable finding including the shorter spinning time and better vacuum level obtained in the working section of the turbine facility.

8.3.3 Calculation of Nusselt Number.

The heat transfer rate can be expressed in non-dimensional form as a Nusselt Number, which may be defined as follows:

$$Nu = \frac{\dot{q}_m C_{ax}}{\Delta T_m k} \qquad (8.1)$$

where $\dot{q}_m$ = measured heat transfer rate

C_{ax} = rotor axial chord = 24.35mm

ΔT_m = measured driving temperature = $T_{gas} - T_{wall}$

k = conductivity, based on the local surface temperature.

This definition of Nusselt Number is identical to that used by **Guenette et al** when processing the data from the MIT turbine facility. It has been adopted because of the ease with which $\dot{q}_m$ and ΔT_m are found, not only in this experiment, but also from other research, enabling comparisons to be readily made.

The heat transfer rate, $\dot{q}_m$, varied throughout the run due to the piston oscillations and change in driving temperature as explained above. By calculating the Nusselt Number the change in driving temperature is taken into account and corrections for variations in Reynolds Number can be made.

Consider the variation in driving temperature. The total temperature varied due to the piston oscillations and can be calculated, assuming an isentropic compression, from the initial pressure in the piston tube and the measured total pressure, equation 8.2.

$$T_0 = T_{initial}\left[\frac{P_0}{P_{initial}}\right]^{\frac{\gamma-1}{\gamma}} \qquad (8.2)$$

The driving temperature was the difference between the gas temperature as seen by the rotor blade, i.e. the relative total temperature, and the surface temperature. The latter was measured by the thin film gauge

and the first calculated from the total temperature and the rotor speed. The speed change during each run was evaluated by **Sheard** from the once per revolution signal captured on the UV chart recorder. He found that the variation was approximately linear and gave an initial and final speed for each run, table 8.5.

Assuming the design static temperature of 317.4 K, the blade speed was calculated as a Mach number, M_ω. The velocity triangle for the rotor blade is shown in figure 8.14. As the rotor accelerated the absolute flow vector incident on the rotor did not change, but the relative flow velocity and angle did. The relative Mach number, M_{rel}, was calculated from the triangle;

$$M_{rel}^2 = M_\omega^2 + 0.946^2 - 2\cos\alpha\, M_\omega \qquad (8.3)$$

and the relative total temperature is given by:

$$T_{o\,rel} = \frac{1 + 0.2\, M_{rel}^2}{1 + 0.2 \times 0.946^2} T_o \qquad (8.4)$$

The variation of relative Mach number and relative total temperature with rotor speed is shown in figure 8.15 for constant absolute total temperature. The total temperature calculated from equation 8.2 can be used in equation 8.4 to obtain the relative total temperature during the run and knowing the gauge temperature the driving temperature during the run can be calculated. The driving temperature during run 6383 for gauge 32 is plotted in figure 8.16 and it can be seen that the oscillations are quite considerable.

The varying inlet conditions resulted in a variation of Reynolds Number which can be taken into account. The design Reynolds Number at the NGV exit is 2.7 E+6 based on the NGV axial chord and isentropic exit Mach Number. Assuming that the NGVs were choked the Reynolds number can be expressed as a function of the mass flow rate through the NGV throat,

$$Re = \frac{\rho U C}{\mu} \qquad (8.5)$$

The mass flow rate at NGV exit is given by:

$$\dot{m} = \rho U A \qquad \text{where A is the area at NGV exit.} \qquad (8.6)$$

This is of course equal to the mass flow rate through the throat which was only dependent on the throat area and the upstream total conditions and is given by the following equation, **(Massey)**.

$$\rho U A = \rho^* U^* A^* = A^* \sqrt{\rho_o P_o \gamma_o} \left(\frac{2}{\gamma+1}\right)^{\frac{\gamma+1}{2(\gamma-1)}} \qquad (8.7)$$

where * denotes conditions at the throat.

For γ=1.4 it can be seen that

$$\rho U = \frac{A^*}{A} P_o \sqrt{\frac{\gamma}{RT_o}} \times 0.578 \qquad (8.8)$$

Hence

$$Re = \frac{A^*}{A} P_o \sqrt{\frac{\gamma}{RT_o}} \times 0.578 \times \frac{C}{\mu} \qquad (8.9)$$

At the design conditions the NGV exit Mach number is 0.946 for which isentropic flow tables give an area ratio A/A^* of 1.0025.

Using the following values:-

μ = 1.9369 E-5 N/s.m^2

R = 287 J/Kg.K

γ = 1.4

C = 0.0312 m (NGV axial chord)

equation 8.9 can be written as

$$Re = 64.87 \frac{P_0}{\sqrt{T_0}} \qquad (8.10)$$

The variation in Reynolds Number during run 6383 was calculated and is plotted in figure 8.17. The mean level agrees well with the design value of 2.7E+6, but the oscillations are about +/- 10% of the mean level. It has been shown, **Kays and Crawford**, that for a laminar boundary layer

$$Nu = \text{constant.}\ Re^{0.5} \qquad (8.11)$$

and for a turbulent boundary layer

$$Nu = \text{constant}.\ Re^{0.8} \qquad (8.12)$$

Knowing the measured and design Reynolds Number it was possible to scale the measured Nusselt Number to obtain the Nusselt Number under design conditions.

$$Nu_D = Nu_M \left(\frac{Re_D}{Re_M}\right)^{0.8} \qquad (8.13)$$

Where D denotes design value and M the measured value.

8.3.4 Results.

The heat transfer results from gauges 32 and 33 are plotted in figures 8.18 and 8.19 and results from the five gauges obtained during run 6448 are shown in figure 8.20. The data of figures 8.18 and 8.19 does not have an initial flat portion as seen in figure 8.20. This is because the data acquisition system was not timed correctly during these first tests, consequently there is no certainty that the beginning of the run was captured. The small spikes seen on some of the data in figure 8.20 were due to a once per revolution disturbance which will be explained later.

The Nusselt Number can be calculated using equation 8.1 and the result for gauge 32, run 6383 is shown in figure 8.21. The spike at the beginning, which can be ignored, is a consequence of the starting processes and the different rise times of the temperature and pressure instrumentation. The curve can be seen to be much flatter than the corresponding heat transfer trace, shown inset, indicating that most of the oscillations were due to variations in the driving temperature.

The effect of Reynolds Number scaling on the results of gauge 32, run 6383 is shown in figure 8.22. The correction for a turbulent boundary layer (0.8 power) produced the flattest trace and was consequently applied to all the measured data. **Guenette et al** also used a correction of $Re^{0.8}$ when

comparing data from two experiments at different Reynolds numbers.

The data from gauges 32 and 33 are plotted in figures 8.23 and 8.24 to show the variation in Nusselt number during runs 6383 and 6384. The results from run 6448 are plotted similarly in figure 8.25. The time at which design speed was reached during the run is shown on each plot. The Nusselt number at the design point is plotted against axial distance in figure 8.26. The agreement between the two results for gauges 32 and 33 is good. A comparison with the results of **Doorly** will be carried out in section 8.5.

8.4 Unsteady Heat Transfer Results.

8.4.1 Introduction.

As explained earlier, transient recorders were used to capture the unsteady heat transfer rate as the rotor passed through its design point. A list of the data obtained is given in Table 8.6. There are several repeat measurements enabling run to run comparisons to be made.

8.4.2 Signal to Noise Ratio.

Before the processed results are discussed, some of the raw signals will be presented and compared with the noise levels described earlier. The intention was to capture a noise trace at design speed for each gauge to provide a check on the signal to noise ratio and the magnitude of any periodic disturbances caused by NGV magnetism. This was not achieved for all gauges, but comparisons are possible for gauges 33, 17 and 8. The unsteady heat transfer signal from gauge 8 was clipped by the transient recorder, but still provides useful data. In figures 8.27, 8.28 and 8.29 the raw output and noise levels are plotted on the same scale. In each case the signal level was greater than the noise level and periodic disturbances such

as those in figure 8.27, which had been attributed to magnetic pickup, were not visible in the heat transfer signal. These results gave confidence that the signal to noise ratio was adequate.

8.4.3 Signal Processing.

The procedure for processing the high frequency signals was essentially the same as that for the mean heat transfer rate, but as discussed in chapter 6, care had to be taken to ensure that there were sufficient points in the time domain to completely define the amplifier frequency response in the frequency domain.

The signal processing chain will be illustrated using the data from gauge 20, run 6447. The raw signal is plotted in figure 8.30. The time for one revolution is indicated and it can be seen that there is a large disturbance once per revolution. This occurred as the blade passed top dead centre and was caused by the blade rubbing the outer casing at this point. The disturbance is thought to be responsible for the small spikes seen on some of the mean heat transfer data. The disturbances were slightly worse during run 6448, when the vibration problem was most severe and not seen at all on the early runs 6382-6384.

The raw signal was first scaled by $1/(\alpha_{20} IR_{20})$ to obtain the ampified temperature signal, figure 8.31. The amplifier transfer function was then used to obtain the actual temperature rise, figure 8.32 and from that the unsteady heat transfer rate was obtained, figure 8.33.

8.4.4 Results.

As explained in chapter three the record length and sample interval were such that in each case data was captured over at least two revolutions.

The position of each gauge at any time in the run was known, so it was possible to plot a portion of the record starting from the time that the gauge passed a reference point. The reference point was chosen as NGV 7, figure 8.34 and the selected portions were 1024 points long, which is the time for 26 NGV passing events. Hence the time when the blade passed top dead centre was not included.

A portion, as described above, of the unsteady trace from each gauge is shown in figures 8.35-8.36. The positions of the gauges are listed in table 7.2 and shown in figure 7.4. The timing signal indicates NGV passing frequency and it can be seen that on the suction surface, gauges 20, 32 and 33 (figure 8.35) show large disturbances of irregular height and shape at the NGV passing frequency. Less obvious fluctuations at the NGV passing frequency are seen on the output from gauge 8 and the two pressure surface gauges, figure 8.36, show rapid fluctuations with no apparent component at the NGV passing frequency.

8.4.5. Overall Nusselt Number.

The unsteady signal is only the a.c. component and to put the fluctuations into perspective the mean and unsteady signals must be added together. The mean heat transfer rate has been expressed as a Nusselt Number in section 8.3 to take account of the piston oscillations and the Nusselt number at the design point has been plotted in figure 8.26. In order to add the two components the unsteady heat transfer rate must also be expressed as a Nusselt Number.

The definition of Nusselt Number was given in equation 8.1

$$Nu = \frac{\dot{q}_m C_{ax}}{\Delta T_m k}$$

The unsteady signal was taken over a short period of time around

the design point, so, to be consistent with the mean data, ΔT_m in the above equation is the driving temperature at the design point and k, the conductivity, is evaluated at the gauge temperature at that time. This gives a scale factor which when multiplied by the measured heat transfer rate yields the unsteady Nusselt Number.

A typical combined heat transfer signal, mean plus unsteady from each gauge is plotted in figures 8.37 -8.39. It can be seen that in each case, the unsteady component is a fairly significant proportion of the mean signal.

The fluctuations on gauges 20, 32 and 33 do not appear to form a regular pattern. By comparing the output from different runs and also from subsequent revolutions, it is possible to establish whether the irregularities are a physial phenomenon or due to random noise. In each comparison the records plotted are 1024 points long, i.e. the time for 26 NGV passing events and start at the same angular position.

The output from gauge 20 during two successive part revolutions is plotted in figure 8.40 and the output during two different runs is shown in figure 8.41. The repeatability of the flow features in magnitude and pattern is excellent in both cases and is also seen for gauges 32 and 33 in figures 8.42-8.45.

The output from two adjacent gauges during the same run can be compared using the data from gauges 32 and 33. The output during run 6383 is shown in figure 8.46 and some of the flow features on gauge 32 are seen a short while later on gauge 33, albeit in a modified state.

The repeatable pattern seen on the thin film gauge outputs confirms that the irregular shapes of the periodic features are due to physical phenomena and are related to the angular position. Possible causes of such variations around the NGV ring are differences in NGV height and spacing,

causing a variation in passage size; differences in rotor over-tip gap, which would modify the flow over the rotor blade and variations in the magnetic properties of the NGVs. The precise reason for the irregularities cannot be determined for these results, but the discrepancies in magnetic field and tip spacing will be investigated and eliminated before further experiments are undertaken. Manufacturing tolerances in real engines mean that some variation in NGV spacing is inevitable and it is important to know the influence of this variation on the heat transfer rate. One of the reasons for presenting the data in this unaveraged form is that any passage to passage variation is not seen if the signal is ensemble averaged.

Dunn et al, 1989 recorded phase-lock averaged heat transfer measurements on a rotating turbine stage and found significant variations from passage to passage and smaller variations for revolution to revolution comparisons of the same passage.

8.5 Mean Heat Transfer Results - Comparison with Doorly.

8.5.1 Simulation of Wake Passing Flow.

A major objective of the rotor project was to obtain heat transfer data from the rotor blade and compare it with the results of **Doorly**, who used a rotating wake generator in front of a cascade of the same rotor blade profile, to simulate the wake interaction. The object of Doorly's experiment, which is described more fully in chapter two, was to create a simple two-dimensional simulation of the turbine flow field so that fundamental studies of the wake interaction process could be undertaken. The experiment was conducted at the same Mach Number and Reynolds Number as the rotor experiment, but at a higher temperature ratio. The velocity triangle achieved by Doorly, figure 8.47, can be seen to be in good agreement with the rotor

mid-height velocity triangle..

Doorly undertook extensive tests to establish the shape and size of body required to produce a wake representative of that shed from the NGV. Figure 8.48 (from **Doorly, 1984**) is the result of a total pressure traverse at the exit of a cascade containing a 0.9mm diameter bar mounted between two NGVs. It can be seen that the shape of the pressure loss curves are similar, showing that a round bar produces a wake of the required form. However, it also appears that the bar produced a wake which was much larger than that shed by the NGVs, thus invalidating the wake modelling experiment. But what is not made clear in Doorly's thesis, is the fact that the rotor cascade used in the heat transfer experiments was 1.935 times the scale of the NGV cascade used in these wake proving tests. The data in figure 8.48 can be used to establish the size of bar required to simulate the wake produced by an NGV of the correct scale.

Schlichting considers the development of a two-dimensional wake at a large distance downstream, figure 8.49 and gives the following results for the variation of wake width, b and velocity decrease, u, with distance downstream, x and diameter of the body, d.

$$b = \text{constant}.(\beta.x.C_D.d)^{1/2} \qquad (8.14)$$

$$\frac{u}{U_\infty} = \text{constant}.\left(\frac{C_D\, d}{\beta\, x}\right)^{1/2} \qquad (8.15)$$

where β is the mixing length constant and C_D is the drag coefficient of the body.

The problem, summarized in figure 8.50, is to find the size of bar, d_2 which produces the same wake as that shed by the NGV. For geometrically similar bodies at the same distance downstream, equations 8.14 and 8.15 become dependent only on the bar diameter.

Considering the velocity deficit, produced by bars of diameter d_1 and

d_2, from equation 8.15:

$$\frac{u_2}{u_1} = \left(\frac{d_2}{d_1}\right)^{1/2} \tag{8.16}$$

Hence $$d_2 = d_1\left(\frac{u_2}{u_1}\right)^2 = d_1\frac{\Delta P_{o1}}{\Delta P_{o2}} \tag{8.17}$$

and d_2 can be found using the data displayed in figure 8.48.

$$d_2 = 0.9 \times \frac{95}{40} = 0.4 \text{ mm.}$$

Similarly, considering the wake width

$$d_2 = d_1\left(\frac{b_2}{b_1}\right)^2 = 0.9 \times \left(\frac{7.2}{14.4}\right)^2 \tag{8.18}$$

and $d_2 = 0.23$ mm

The wake strength was probably more correctly captured by the traverse, than the wake width, making the first result a more reliable estimate of the required bar size. Hence, at the scale of the rotor cascade, the size of bar which would have correctly simulated the NGV wake, was:

$d = 0.4 \times 1.935 = 0.774$mm

which is 14% smaller than the diameter of the bar used in the experiment (0.9mm).

Doorly could generate low or high frequency wake passing by installing two or eight bars in the disc, with eight bars approximating engine conditions. In order to correctly model the wake interaction effects, it is necessary to match the velocity triangles, as shown in figure 8.47, and also the reduced frequency parameter, which is defined as follows:

$$k = \frac{f C_{ax}}{2U_{ax}} \tag{8.19}$$

where f = wake passing frequency (rad/s)

C_{ax} = axial chord

U_{ax} = axial velocity

Substituting the appropriate values for the two experiments, it was found that for the rotor project, $k = 3.6$ and for Doorly's wake passing experiment

k = 3.0, indicating that the wake passing frequency of the rotating bar experiment was 17% lower than required for ideal matching. Most of his tests were carried out at a freestream turbulence level of 0.2% or 5%, with a few at 2%. The turbulence level at inlet to the NGV plane in the rotor facility, has been measured (**Izsak**) and found to be 2.5%. The turbulence level at inlet to the rotor will be lower than this due to the acceleration of the mainstream flow, hence the low turbulence level used by Doorly can be considered to be the most representative.

8.5.2 Scaling of Results.

Doorly presented his results as heat transfer rate to an isothermal wall at ambient temperature. The conditions he used are listed in table 8.7. Knowing these values the results from the rotor project can be scaled as if they were measured under the conditions of Doorly's experiment.

Previous work in Oxford, **Fitt et al**, has shown that Nusselt number is a slight function of temperature ratio:

$$Nu = \text{constant}.\left(\frac{T_w}{T_g}\right)^{-0.25} \tag{8.20}$$

So for similar models

$$\left\{\frac{Nu}{\left(\frac{T_w}{T_g}\right)^{-0.25}}\right\}_{Doorly} = \left\{\frac{Nu}{\left(\frac{T_w}{T_g}\right)^{-0.25}}\right\}_{Rotor} \tag{8.21}$$

In the rotor project the gas temperature, T_g, is the relative total temperature, T_{0rel}, and the wall temperature, T_w, is the surface temperature, T_s. Doorly used a temperature ratio of 1.5, so equation 8.21 can be written

$$Nu_{Doorly} = Nu_{Rotor}\left(\frac{T_{o\,rel}}{T_s}.\frac{1}{1.5}\right) \tag{8.22}$$

and hence

$$\dot{q}_{Doorly} = \left(\frac{\Delta T.k}{C}\right)_{Doorly}.\ Nu_{Rotor}\left(\frac{T_{o\,rel}}{T_s}.\frac{1}{1.5}\right) \tag{8.23}$$

8.5.3 Results.

The mean heat transfer rate under these conditions was calculated for each gauge and the value at the design speed was recorded. Plotted in figure 8.51 are the rotor results at the design point, scaled according to equation 8.23 so as to be comparable to the heat transfer measurements made by Doorly. Two sets of results from his experiments are shown, (i) High frequency wake passing with 0.9 mm bars and low free stream turbulence and (ii) 5% turbulence with no wake passing. The second case was reported to result in a turbulent boundary layer on the suction surface beyond X/s = 0.2.

The agreement between the rotor results and the measurements of Doorly with low turbulence and wake passing is very encouraging. The high value seen at gauge 14 may be significant as it is in this region that engine tests frequently show a higher heat transfer level than that given by predictions or cascade tests.

The heat transfer level at gauge 20 seems very low compared with Doorly's results and this may be due to an inaccurate measurement of the gauge position, which was difficult to establish. Also the location of the leading edge stagnation point will change as the rotor accelerates. When comparing the MIT rotor experiments with the Oxford cascade data **Guenette et al** noted that the rotor leading edge heat transfer was lower than that measured in the cascade. It was pointed out that the level in this region is very sensitive to the location of the gauge and the position of the stagnation point relative to the nose of the blade. It was also suggested that the difference could be caused by the larger spanwise extent of the MIT gauges compared with those used in the cascade tests.

The results presented for gauges 14, 17, 20, 4 and 8 are the results

from a single run and for gauges 32 and 33 the results from two runs are shown. With such a small quantity of data it is not practicable to draw many conclusions from the results and further analysis must wait for repeat measurements and data from other gauges.

An estimate of the uncertainty in the mean heat transfer rate has been made in Appendix III and was seen to be approximately +/- 5%. This uncertainty is represented as error bars on figure 8.51 and it is immediately obvious that the two results from gauges 32 and 33 are within the uncertainty of the experiment.

8.6 Unsteady Heat Transfer Results - Comparison with Doorly.

The unsteady heat transfer results measured by Doorly on the suction surface are presented in figure 8.52 (from **Doorly 1984**). These plots show the total heat transfer signal and should be compared with the rotor results shown in figures 8.37-8.39. The most striking feature is the magnitude of the unsteady signal compared with the mean level. In Doorly's results the excursions from the mean level are often of the same order as the mean value, whereas in the results from the rotor the largest excursions are only about a third of the mean level.

Neglecting this discrepancy, the results do show some similarities. The unsteady component for X/s in the region 0.1 - 0.3 on the suction surface, is greater than that at the leading edge in both sets of results. On the rotor at an X/s of 0.42, only slight evidence of regular wake passing can be seen, whereas Doorly's results show massive fluctuations.

In figure 8.53, the results of high frequency bar passing with 5% turbulence are plotted, i.e. the effect of wake passing on a boundary layer which is turbulent over most of the surface. Fluctuations at wake passing

frequency can just be made out at the leading edge, but are quickly lost, with increasing surface distance, in the random fluctuations. The signal at X/s = 0.4 is very similar to that from gauge 8 on the rotor, figure 8.41. This suggests that the boundary layer on the rotor blade has become turbulent by this location, but this is not supported by the mean heat transfer level, which is very low.

Doorly's results, showing the effects of wake passing on the pressure surface, are presented in figure 8.54. As found in the rotor facility, no evidence of wake passing is seen at X/s locations of 0.2 - 0.64.

8.7 Conclusions.

Unsteady heat transfer measurements have been made on the rotor blade of a single stage turbine under engine representative conditions. The new instrumentation which has been developed to withstand the rotating environment has performed well.

It was shown that by presenting the data in non-dimensional form as a Nusselt Number the effects of piston oscillations on the heat transfer rate could be taken into account. The data could then be scaled so as to be comparable with the heat transfer measurements made by **Doorly** under slightly different conditions in a linear cascade using a rotating bar to simulate the wake shed by an NGV.

From the limited data available, it appears that there are both similarities and differences between the rotor data and that of Doorly. The mean level from both experiments showed excellent agreement and unsteady effects due to wake passing were seen at the same locations. The most interesting feature of the mean heat transfer results was the result from gauge 14, at an X/s of 0.64 on the pressure surface, where a higher level

was seen on the rotor blade than in the cascade tests. This result is compatible with observations made in engine tests of higher than expected heat transfer rates on the pressure surface.

The magnitude of the unsteady signal, in relation to the mean, seems to be much smaller than that seen in the cascade with wake passing. Checks were made to determine that the wake generator produced wakes representative of those shed by NGVs and it was found that the 0.9mm bar which was used, produced wakes which were slightly too large. The frequency parameter was 0.8 of that occuring in the rotor, and the axial spacing was slightly larger. However, the overall conclusion was that the rotating bar wake generator should have been a good two-dimensional simulation of the NGV wakes.

While these experiments were being carried out in the rotor, there was a recurring oil leak, which resulted in the instrumentaion being covered with a very thin film of oil. This will have reduced the frequency response of the gauges a little, thus smoothing out the unsteady signal.

As the noise tests at design speed were not completed, the effects of NGV magnetism, although thought to be small, are not quantitatively known for all gauges and are very likely to be responsible for some of the irregularities seen in the unsteady signal.

The oil, vibration and magnetism problems which were present throughout this series of tests and which compromised the results, are being corrected and further tests using these gauges will be presented by **Allan**.

CHAPTER 9

CONCLUSIONS

A full stage turbine has been installed in a transient windtunnel and measurements of both mean and unsteady heat transfer rates on the rotor blade have been recorded at engine representative conditions.

The mode of operation of the facility was such that the correct operating conditions were achieved as the rotor accelerated through the design speed. Transient recorders were used to record the unsteady signal at this time and the incidence change during the high speed data acquisition period was reported to be negligible.

The widely used technique of measuring the heat transfer rate by mounting a thin film gauge on an insulating substrate has been successfully adapted for use in the rotating environment. Metal turbine blades were coated with a layer of vitreous enamel on which thin film gauges were painted.

A major feature of the rotor instrumentation scheme was the installation of electronic circuits in the shaft to preferentially amplify the high frequency component of the signal before transmission through a slipring.

The effect of rotation on the performance and mechanical integrity of the in-shaft electronics and the thin film gauges was examined in a purpose built test facility and found to be negligible. The noise generated by the slipring was measured and very low levels were recorded. The effect of strain on the thin film gauge performance was examined statically and found to be insignificant up to the maximum loading expected on the rotor blade.

The amplified output from the thin film gauge was passed to a

differential amplifier after transmission through the slip ring and then digitized. The theory and application of the digital signal processing routines used to obtain the heat transfer rate have been presented. Each method was verified using data predicted or captured under known circumstances and the accuracy of each was quantified.

Details of the three stage calibration process to establish the gauge parameters was given. A new method for measuring the ratio of thickness to conductivity, a/k, of the enamel layer was developed. This involved using a laser to subject the thin film gauge to a step in heat transfer.

A total of 33 thin film gauges distributed amongst five blades were calibrated and as expected wide variations in the value of the enamel thermal product, $\sqrt{(\rho ck)_1}$, and the ratio a/k were found.

A check on the calibrated parameters was made by reconstructing the input heat pulse from the laser test. In most cases a satisfactory response was obtained, however problems were observed with a few gauges and measurements showed that the enamel layer under these gauges was thin.

It was recommended that a systematic investigation of the various parameters that affect the calibration process is undertaken, with special attention paid to the effect of enamel thickness on the calibration process.

The new type of thin film gauge has been used to measure both the mean and unsteady heat transfer rate around the midheight profile of the rotor blade. The data was presented in non-dimensional form as a Nusselt Number and corrections for off design conditions were made where necessary.

The data was scaled so as to be comparable with the results of a previous experiment in which a rotating bar, wake generator was placed in

front of a two-dimensional cascade of the midheight profile to simulate the wakes shed by the NGVs.

The mean heat transfer rate from the rotor project was found to be in reasonable agreement with that recorded in the previous two-dimensional simulation of wake passing flow, although on the pressure surface at a X/s of 0.64 the mean level recorded on the rotor was higher than that seen in the cascade experiment. This is consistent with the high heat transfer rates observed in this region in engine tests.

Fluctuations in heat transfer rate at NGV passing frequency were seen at the same locations in both experiments. However the magnitude of the unsteady signal in the two-dimensional simulation was considerably greater than that seen on the rotor.

These first heat transfer results from the rotor project have shown that a viable instrumentation scheme for making detailed heat transfer measurements on the rotor blade has been developed. The next phase in the project is to repeat the measurements reported here and to make others around the midheight section and at hub, tip and on the blade platform. This will enable a more detailed comparison with the midheight, two-dimensional simulation to be made, thus contributing to a better understanding of the rotor blade heat transfer distribution.

REFERENCES

Ainsworth, R.W., Schultz, D.L., Davies, M.R.D., Forth, C.J.P., Hilditch, M.A., Oldfield, M.L.G. and Sheard, A.G., "A Transient Flow Facility for the Study of Thermofluid-Dynamics under Engine Representative Conditions", A.S.M.E. Paper 88-GT-144, 1988

Ainsworth, R.W., Allen, J.L., Davies, M.R.D., Doorly, J.E., Forth, C.J.P., Hilditch, M.A., Oldfield, M.L.G. and Sheard, A.G., "Developments in Instrumentation and Processing for Transient Heat Transfer Measurement in a Full Stage Model Turbine", Journal of Turbomachinery, pp 20-27, Vol. 111, January 1989

Allan, W.D.E., D.Phil Thesis, Oxford University, to be published, 1990.

Alwang, W.G., "Problems in the Measurement of Metal Temperature, Gas Temperature, Heat Flux and Strain in Combustors and Turbines", AGARD CP-281, Brussels, Belgium, 1980.

Ashworth, D.A., "Unsteady Wake and Shock Interactions on a Transonic Turbine Blade", D.Phil. Thesis, University of Oxford, 1987.

Ashworth, D.A., LaGraff, J.E., Schultz, D.L. and Grindrod, K.J., "Unsteady Aerodynamic and Heat Transfer Processes in a Transonic Turbine Stage", A.S.M.E. Paper No. 85-GT-128

Bayley, F.J. and Priddy, W.J., "Effects of Free-Stream Turbulence Intensity and Frequency on Heat Transfer to Turbine Blading", Journal of Engineering for Power, pp 60-64, Vol. 103, January 1981.

Binder, A., "Turbulence Production Due to Secondary Vortex Cutting in a Turbine Rotor", A.S.M.E. Paper 85-GT-193.

Binder, A., Forster, W., Kruse, H. and Rogge, H., "An Experimental Investigation into the Effect of Wakes on the Unsteady Turbine Rotor Flow", Journal of Engineering for Gas Turbines and Power, pp. 458-466, Vol. 107, April 1985.

Binder, A. and Romey. R., "Secondary Flow Effects and Mixing of the Wake Behind a Turbine Stator", Journal of Engineering for Power, pp. 40-46, Vol. 105, January 1983.

Blair, M.F., Dring, R.P. and Joslyn, H.D., "The Effects of Turbulence and Rotor/Stator Interaction on Turbine Heat Transfer: Part I - Design Operating Conditions", Journal of Turbomachinery, pp. 87-96, Vol. 111, January 1989.

Brigham, E.O., "The Fast Fourier Transform", Prentice Hall, Inc., 1974.

Byworth, S., "Design and Development of High-Temperature Turbines", The Rolls-Royce Magazine, Number 29, June 1986.

Carlini, A.R., "Design and Construction of a Calibration Device for Electrical Analogues of the Heat Transfer Conduction Process in a Transient Cascade", Third Year Project, Department of Engineering Science, University of Oxford, 1984.

Chatfield, C., "Statistics for Technology", Chapman and Hall, 1983

Cohen, H., Rogers, G.F.C. and Saravanmuttoo, H.I.H., "Gas Turbine Theory", Longmans, 1987.

Consigny, H. and Richards, B.E., "Short Duration Measurements of Heat-Transfer Rate to a Gas Turbine Blade.", Journal of Engineering for Power, pp. 542-551, Vol. 104, July 1982.

Danels, L.C., "Film Cooling of Gas Turbine Blades", D.Phil Thesis, Oxford University, 1978

Dietz, A.J., "Unsteady Aerodynamic Studies on a Three Dimensional Rotating Turbine Stage in a Transient Facility", First Year Report, Department of Engineering Science, Oxford University, 1988

Dietz, A.J., D. Phil Thesis, Oxford University, to be published, 1990

Doorly, D.J., "A Study of the Effect of Wake-Passing on Turbine Blades." D.Phil Thesis, Oxford University, O.U.E.L. Report 1515/84, 1984.

Doorly, D.J. and Oldfield, M.L.G., "Simulation of Wake Passing in a Stationary Turbine Rotor Cascade", Journal of Propulsion, pp. 316-318, Vol. 1, No. 4, July 1985(a).

Doorly. D.J. and Oldfield, M.L.G., "Simulation of the Effects of Shock Wave Passing on a Turbine Rotor Blade", Journal of Engineering for Gas Turbines and Power, pp. 998-1006, Vol. 107, October 1985(b).

Doorly, D.J., Oldfield, M.L.G. and Schrivener, C.T.J., "Wake-passing in a Turbine Rotor Cascade", AGARD CP-390, Bergen, Norway, 1985(c).

Doorly, J.E., " The Development of a Heat Transfer Measurement Technique for Application to Rotating Turbine Blades." D. Phil Thesis, Oxford University, 1985.

Doorly, J.E., "Procedures for Determining Surface Heat Flux Using Thin Film Gauges on a Coated Metal Model in a Transient Test Facility". A.S.M.E. Paper No. 87-GT-95.

Doorly, J.E., OUEL Report, No. 1697, 1989

Doorly, J.E. and Oldfield, M.L.G., " New Heat Transfer Gauges for Use on Multi-layered Substrates", A.S.M.E. Paper 86-GT-96.

Doorly, J.E. and Oldfield, M.L.G., "The Theory of Advanced Multi-layer Thin Film Heat Transfer Gauges", International Journal of Heat and Mass Transfer, pp. 1159-1168, Vol. 30, No. 6, 1987.

Dring, R.P. and Joslyn, H.D., "Measurement of Turbine Rotor Blade Flows", Journal of Engineering for Power, pp. 400 - 405, Vol. 103, April 1981.

Dring, R.P. and Joslyn, H.D., "The Relative Eddy in Axial Turbine Rotor Passages", A.S.M.E. Paper 83-GT-22.

Dring, R.P., Joslyn, H.D., Hardin, L.W. and Wagner, J.H., "Turbine Rotor-Stator Interaction," Journal of Engineering for Power, pp. 729-742, Vol. 104, October 1982

Dunn, M.G., "Turbine Heat Flux Measurements: Influence of Slot Injection on Vane Trailing Edge Heat Transfer and Influence of Rotor on Vane Heat Transfer", A.S.M.E. Paper No. 84-GT-175

Dunn, M.G., "Heat Flux Measurements for the Rotor of a Full-Stage Turbine: Part 1, Time Averaged Results." A.S.M.E. Paper No. 86-GT- 77

Dunn, M.G. and Hause, A., "Measurement of Heat Flux and Pressure in a Turbine Stage", Journal of Engineering for Power, pp. 215-223, Vol. 104, January 1982.

Dunn, M.G., Rae, W.J. and J.L. Holt, "Measurement and Analyses of Heat Flux Data in a Turbine Stage: Part 1 —Description of Experimental Apparatus and Data Analysis." Journal of Engineering for Gas Turbines and Power, pp. 229-240, Vol. 106, January 1984.

Dunn, M.G., George, W.K., Rae, W.J., Woodward, S.H., Moeller, J.C. and Seymour, P.J., "Heat Flux Measurements for the Rotor of a Full-Stage Turbine: Part II - Description of Analysis Technique and Typical Time Resolved Measurements", Journal of Turbomachinery, pp. 287-293, Vol. 108, 1986.

Dunn, M.G., Seymour, P.J., Woodward, S.H., George, W.K. and Chupp, R.E., "Phase-resolved Heat-Flux Measurements on the Blade of a Full-Scale Rotating Turbine", Journal of Turbomachinery, pp. 8-19, Vol. 111, January 1989.

Epstein, A.H., Guenette, G.R. and Norton, R.J.G., "The M.I.T. Blowdown Turbine Facility", A.S.M.E. Paper 84-GT-116

Epstein, A.H., Guenette, G.R., Norton, R.J.G. and Cao Yuzhang, "High Frequency Response Heat Flux Gauge for Metal Blading." AGARD CP-390, Bergen, Norway, 1985.

Fitt, A.D., Forth, C.J.P., Robertson, B.A and Jones, T.V., "Temperature Ratio Effects in Compressible Turbulent Boundary Layers", International Journal Heat and Mass Transfer, pp. 159-164, Vol. 29, 1986.

Gaugler, R.E. and Russell, L.M., "Comparison of Visualized Turbine Endwall Secondary Flows and Measured Heat Transfer Patterns", Journal of Engineering for Gas Turbines and Power, pp. 168-172, Vol 106, January 1984.

Goldstein, R.J., Lau, K.Y. and Leung, C.C., "Velocity and Turbulence Measurements in Combustion Systems", Experiments in Fluids, pp. 93-99, 1983.

Gostelow, J.P., "Cascade Aerodynamics", Pergamon Press, 1984.

Gregory-Smith, D.G., Graves, C.P. and Walsh, J.A., "Growth of Secondary Losses and Vorticity in an Axial Turbine Cascade", A.S.M.E. Paper 87-GT-114.

Guenette, G.R., Epstein, A.H., Giles, M.B., Haimes, R. and Norton, R.J.G., "Fully Scaled Transonic Turbine Rotor Heat Transfer Measurements," Journal of Turbomachinery, pp. 1-7, Vol. 111, January 1989.

Hah, C. and Lakshminarayana, B., "Measurement and Prediction of Mean Velocity and Turbulence Structure in the Near Wake of an Airfoil", Journal of Fluid Mechanics, pp. 251-282, Vol. 115, 1982.

Hennecke, D.K., "Heat Transfer Problems in Aero-Engines", Metzger, D.E. and Afgan, N.H., eds. Heat and Mass Transfer in Rotating Machinery, Hemisphere Publ. Corp. N.Y., 1984.

Hodson, H.P., "Boundary Layer and Loss Measurements on the Rotor of an Axial Flow Turbine", Journal of Engineering for Gas Turbines and Power, pp. 391-399, Vol. 106, April 1984.

Hodson, H.P., "Measurements of Wake-Generated Unsteadiness in the Rotor Passages of Axial Flow Turbines", Journal of Engineering for Gas Turbines and Power, pp. 467-476, Vol. !07, April 1985.

Holman, J.P., "Experimental Methods for Engineers", McGraw-Hill, Inc., 1984.

Horlock, J.H., "Axial Flow Turbines", Kruger Publishing Co., 1973

Horowitz, P. and Hill, W., "The Art of Electronics", Cambridge University Press, 1984

Horton, F.G., Schultz, D.L., and Forest, A.E., "Heat Transfer Measurements with Film Cooling on a Turbine Blade Profile in Cascade", A.S.M.E. Paper 85-GT-117.

Izsak, M.S., "Wakes and Transition in a Rotating Turbine Stage", M.Sc. Thesis, Oxford University, 1988

Johnson, A.B., "The Aerodynamic Effects of Nozzle Guide Vane Shock Wave and Wake Passing on a Transonic Turbine Rotor", D. Phil Thesis, Oxford University, 1988

Johnson, A.B., Rigby, M.J.G., Oldfield, Ainsworth, R.W. and Oliver, M.J., "Surface Heat Transfer Fluctuations on a Turbine Rotor Blade Due to Upstream Shock Wave Passing," A.S.M.E. Paper No. 88-GT-172

Jones, T.V., "Gas Turbine Studies at Oxford 1969-1987", A.S.M.E. Paper 88-GT-112

Jones, T.V., Schultz, D.L. and Hendley, A.D., " On the Flow in an Isentropic Light Piston Tunnel", ARC, Reports and Memoranda No. 3731, January 1973.

Kays, W.M. and Crawford, M.E., "Convective Heat and Mass Transfer", McGraw-Hill Book Company, 1980.

King, P., "Aerodynamics of High Performance Turbine Blading", D.Phil. Thesis, University of Oxford, 1986.

Kreyszig, E., "Advanced Engineering Mathematics", John Wiley and Sons, Inc., 1983.

Krishnamoorthy, V., "Effect of Turbulence on the Heat Transfer in a Laminar and Turbulent Boundary Layer over a Gas Turbine Blade", A.S.M.E. Paper 82-GT-146.

Lakshminarayana, B., Govindan, T.R. and Reynolds, B., "Effects of Rotation and Blade Incidence on Properties of Turbomachinery Rotor Wake", AIAA Journal, pp. 245-253, Vol. 20, No. 2, February 1982.

Langston, L.S., Nice M.L. and Hooper, R.M., "Three-Dimensional Flow Within a Turbine Cascade Passage", Journal of Engineering for Power, pp. 21-28, January 1977.

Metzger, D.E., "Developments in Air Cooling of Gas Turbine Vanes and Blades", A.S.M.E. Paper 83-GT-160.

Moore, J., "Lecture Notes on 3-D Flows in Turbomachinery Blade Rows", Turbomachinery Research Group Report No. JM/83 - 4, Mechanical Engineering Department, Virginia Polytechnic Institute and State University, Blacksburg, Virginia, 24061.

Moore, J. and Adhye, R.Y., "Secondary Flows and Losses Downstream of a Turbine Cascade", A.S.M.E. Paper 85-GT-64.

N.A.G., Numerical Algorithms Group, 7 Banbury Road, 0X2 6NN.

Nicholson, J.H., " Experimental and Theoretical Studies of the Aerodynamic and Thermal Performance of Modern Gas Turbine Blades." D.Phil Thesis, Oxford University, 1981.

Nicholson, J.H., Forest, A.E., Oldfield M.L.G. and Schultz, D.L., "Heat Transfer Optimized Turbine Rotor Blades - An Experimental Study Using Transient Techniques" Journal of Engineering for Gas Turbines and Power, pp. 173-182, Vol. 106, January 1984.

Oldfield, M.L.G., Burd, H.L. and Doe, N.G., "Design of Wide-Bandwidth Analogue Circuits for Heat Transfer Instrumentation in TransientTunnels", Metzger, D.E. and Afgan, N.H. eds. Heat and Mass Transfer in Rotating Machinery, Hemisphere Publ. Corp. N.Y., 1984.

Oldfield, M.L.G., Jones, T.V. and Schultz, D.L. "On-line Computer for Transient Turbine Cascade Instrumentation", IEEE Transactions on Aerospace and Electronic Systems, pp. 738-749, Vol. AES—14, No. 5, September 1978.

Parker, R. and Watson, J.F., "Interaction Effects Between Blade Rows in Turbomachines" Proceedings I.Mech.E. pp. 331-340, Vol. 186 21/72

Pfeil, H. and Herbst, R., "Transition Procedure of Instationary Boundary Layers", A.S.M.E. Paper No. 79-GT-128.

Pfeil, H., Herbst, R. and Schröder, T., "Investigation of the Laminar-Turbulent Transition of Boundary Layers Disturbed by Wakes", Journal of Engineering for Gas Turbines and Power, pp. 130-137, Vol. 5, January 1983.

Priddy, W.J. and Bayley, F.J., "Effects of Free-Stream Turbulence on the Distribution of Heat Transfer Around Turbine Blade Sections", International Journal of Heat and Fluid Flow, pp. 181-192, Vol.6, No. 3, September 1985.

Priddy, W.J. and Bayley, F.J., "Turbulence Measurements in Turbine Blade Passages and Implications for Heat Transfer", A.S.M.E. Paper 87-GT-195.

Reynolds, B., Lakshminarayana, B. and Ravindranath, A., "Characteristics of the Near Wake of a Compressor of a Fan Rotor Blade", AIAA Journal, pp 959-967, Vol. 17, No. 9, September 1979.

Rigby, M.J., D.Phil Thesis, Oxford University, to be published, 1989

Rolls-Royce, plc., Private Communication

Schlichting, H., "Boundary Layer Theory", McGraw-Hill, Inc., 1979.

Schultz, D.L., Ainsworth, R.W. and Scrivener, C.T.J., "The Role of Short Duration Facilities in Gas Turbine Research", Paper No. 87-7031, 8th Symposium of ISABE, Cincinnati, 1987.

Schultz, D.L., Johnson, A.B., Ashworth, D.A., Rigby, M.J. and LaGraff, J.E., "Wake and Shock Interactions in a Transonic Turbine Stage", AGARD CP-401, Munich, Germany, 1986.

Schultz, D.L. and Jones, T.V., "Heat Transfer Measurements in Short-Duration Hypersonic Facilities." AGARDograph No. 165, 1973.

Schultz, D.L., Jones, T.V., Oldfield, M.L.G. and Daniels, L.C., "A New Transient Cascade Facility for the Measurement of Heat Transfer Rates", AGARD CP-229, 1977.

Sheard, A.G., "The Aerodynamic and Mechanical Performance of a High Pressure Turbine in a Transient Wind Tunnel", D. Phil Thesis, Oxford University, 1989

Sieverding, C.H., "Recent Progress in the Understanding of Basic Aspects of Secondary Flows in Turbine Blade Passages", Journal of Engineering for Gas Turbines and Power, pp. 248-257, Vol. 107, April 1985.

Smith, L.H., "Wake Dispersion in Turbomachines", Journal of Basic Engineering, pp. 688-690, September 1966.

Sokolowski, D.E., "Toward Improved Durability in Advanced Aircraft Engine Hot Sections", A.S.M.E., 1988.

Touloukian, Y.S., "Thermophysical Properties of Matter", TRPC Data series, IFI/Plenum, New York, 1970.

Wedlake, E.T., Brooks, A.J. and Harasgama, S.P., "Aerodynamic and Heat Transfer Measurements on a Transonic Nozzle Guide Vane", Journal of Turbomachinery, pp. 36-42, Vol. 111, January 1989.

Wilson, J. and Hawkes, J.F.B., "Optoelectronics: An Introduction. Prentice – Hall International Inc.

Wittig, S., Dullenkopf, Schulz, A. and Hestermann, R., "Laser-Doppler Studies of the Wake-Effected Flow Field in a Turbine Cascade", A.S.M.E. Paper No. 86-GT-160.

Wittig, S., Schulz, A., Bauer. H.J. and Sill, K.H., "Effects of Wakes on the Heat Transfer in Gas Turbine Cascades.", AGARD CP-390, Bergen, Norway, 1985.

Zunino, P., Ubaldi, M. and Satta, A., "Measurements of Secondary Flows and Turbulence in a Turbine Cascade Passage", A.S.M.E. Paper 87-GT-132.

Table 3.1

TURBINE OPERATING POINT

Specific Speed	$\frac{N}{\sqrt{T_0}}$	436 rpm/$K^{1/2}$
Mass Flow Number	$\frac{\dot{m}\sqrt{T_0}}{P_0}$	7.04 E-4
Reynolds Number	(Based on NGV exit conditions and axial chord at midheight)	2.7 E+6
NGV exit Mach Number	(Isentropic, midheight)	0.946
Rotor relative exit Mach Number	(Isentropic, midheight)	0.959
NGV Axial Chord		0.0312m

Table 3.2

TUNNEL OPERATING PARAMETERS

Initial Tube Pressure	3.21 E+5 N/m^2
Initial Tube Temperature	288K
Final Tube Pressure	8.04 E+5 N/m^2
Final Tube Temperature	374K
Blade Relative Total Temperature	328K
Blade Relative Temperature Ratio	1.14
Run Time	0.213s
Turbine Output Power	2.36MW
Turbine Speed Change (during a run)	3300 rpm
Turbine Design Speed	8434 rpm

Table 5.1

THE EFFECT OF HEAT TREATMENT ON THE STRENGTH OF INCO 718

Specimen	Heat Treatment from Fully Annealed State	σ yield
1	Heat at 825 deg. C for 15 minutes. Air cool. Cycle from 20 - 640 deg. C twice. Air cool.	695.0 N/mm^2
2	None	352.9 N/mm^2
3	Heat at 825 deg. C for 15 minutes. Air cool. Cycle from 20 - 640 deg. C four times. Air cool.	781.3 N/mm^2
4	Heat at 925 deg. C for 15 minutes. Air cool. Cycle from 20 - 640deg. C four times. Air cool.	595.2 N/mm^2

Table 5.2

COMPONENT VALUES FOR IN-SHAFT CIRCUITS

Component	Nominal	Circuit 1A	Circuit 1B	Circuit 1C	Circuit 1D
R1	200Ω	198.1	199.94	200.2	198.7
R2	1800Ω	1779	1793	1793	1787
R3	22000Ω	21980	21948	21994	22195
R4	100kΩ	99924	99925	99927	99928
C2	47nF	47.73	46.84	44.29	44.88
C3	470nF	459.6	440.7	440.1	449.0
Breakpoints					
1st	18.71	91.15	20.00	19.99	19.62
2nd	170.75	175.97	181.88	182.85	179.96
3rd	1915.12	1907.70	1929.06	2040.12	2019.92
4th	20350.55	20294.55	20543.38	21591.69	21451.77
d.c.gain	5.17	5.17	5.17	5.17	5.13

Component	Nominal	Circuit 2A	Circuit 2B	Circuit 2C	Circuit 2D
R1	200Ω	200.1	200.0	199.2	200.3
R2	1800Ω	1803	1790	1798	1792
R3	22000Ω	21980	22050	21950	21940
R4	100kΩ	99870	99740	99820	99870
C2	47nF	48.1	46.7	49.4	49.1
C3	470nF	455.0	465.0	463	458
Breakpoints					
1st	18.71	19.35	18.88	19.04	19.25
2nd	170.75	175.37	173.30	172.69	174.94
3rd	1915.12	1868.31	1938.09	1824.13	1841.30
4th	20350.55	19959.73	20497.65	19533.97	19567.60
d.c. gain	5.17	5.16	5.15	5.17	5.17

Table 6.1

TYPICAL VALUES USED IN PREDICTION OF ANALOGUE OUTPUT

V_0	1.0V
K_a	0.3
α	$0.0015\,K^{-1}$
$\sqrt{(\rho ck)_1}$	1300 $J/Ks^{1/2}m^2$
$\sqrt{(\rho ck)_2}$	6491 $J/Ks^{1/2}m^2$
Q	$25kW/m^2$
a/k	$0.00008m^2K/W$

Table 7.1

DETAILS OF B22 PROFILE*

Section Name:	GY1
Radius to section from engine centreline:	253.7mm
Leading Edge Circle Radius:	0.85498mm
Trailing Edge Circle Radius:	0.32364mm
Axial Chord:	24.2536 mm
Tangent Chord:	31.65421mm
Axial Distance from Plane B to Leading Edge :	11.54mm
Height of definitive section 1 from engine centreline :	240mm
Height of definitive section 2 from engine centreline :	270mm

*All dimensions are listed at 0.62 engine scale which is the size of the turbine in the Oxford Rotor Project.
Doorly tested this profile at 1.3236 engine scale and **Nicholson** at 0.8577 engine scale.

Table 7.2

POSITION OF THIN FILM GAUGES NOMINALLY AT MIDHEIGHT

Gauge No.	X mm	Y mm	Blade Serial No.	x/Cax* %	X/s* %
Suction Surface					
21	- 12.01	32.55	3	0.0	0.0
1	- 11.19	32.66	5	1.7	3.0
2	- 10.86	32.16	1	3.0	5.0
3	- 10.40	32.75	3	4.9	7.0
32	- 10.08	35.45	9	6.2	8.0
4	- 9.66	32.82	6	8.0	10.0
5	- 9.30	32.66	5	9.4	11.0
6	- 5.62	32.92	6	24.6	22.0
33	- 3.73	33.60	9	32.3	26.0
7	- 1.68	33.98	5	40.7	31.0
8	+ 2.01	32.90	6	55.9	41.0
9	+ 5.78	33.90	5	71.4	58.0
10	+ 8.25	34.56	1	81.5	71.0
11	+ 11.49	34.90	1	94.8	91.0
Pressure Surface					
12	+ 10.86	34.79	5	92.2	89.0
13	+ 9.74	34.49	3	87.6	82.0
14	+ 6.64	34.46	5	74.9	64.0
15	+ 4.04	34.50	3	64.2	52.0
16	- 0.42	33.89	5	45.9	35.0
17	- 4.34	32.77	3	29.8	22.0
18	- 8.27	33.18	5	13.7	11.0
19	- 9.94	32.13	6	6.8	6.0
20	- 11.06	33.33	1	2.2	4.0

* x/Cax and X/s are calculated for the B22 plane section, defined in table 7.1 and figure 7.1 and drawn in figure 7.4.

Table 7.3

POSITION OF THIN FILM GAUGES NOT AT MIDHEIGHT

Gauge No.	X mm	Y mm	Z mm	Blade Serial No.	Surface	Nominal Height (% span)
22	-8.21	50.26		1	Suction	90
23	+4.09	51.92		6	Pressure	90
24	-0.21	51.65		3	Pressure	90
25	-9.35	19.93		1	Suction	10
26	-6.24	19.14		6	Suction	10
27	+4.39	16.53		6	Pressure	10
28	-0.51	17.20		6	Pressure	10
29	+11.74		-1.93	3	Suction	Platform
30	+5.55		+12.93	1	Pressure	Platform
31	-9.43		+7.12	1	Pressure	Platform

Table 7.4

CALIBRATED PARAMETERS

Gauge No.	R_{20} Ω	α K^{-1}	$\sqrt{(\rho ck)_1}$ $J/m^2Ks^{1/2}$	a/k m^2K/W
1	51.30	1.69504 E-3	1760.4	0.0000577
2	65.28	1.87646 E-3	1063.7	0.0001663
3	49.96	1.83899 E-3	1267.3	0.0000858
4	41.41	1.94974 E-3	1122.5	0.0000920
5	53.35	1.71828 E-3	1524.3	0.0000602
6	56.59	1.89770 E-3	1483.5	0.0000673
7	37.18	1.37571 E-3	1266.3	0.0001100
8	61.44	1.92295 E-3	1392.7	0.0000850
9	66.30	1.64821 E-3	1356.9	0.0000850
10	60.89	1.91000 E-3	1222.0	0.0000940
11	62.35	1.86929 E-3	1113.8	0.0001300
12	51.74	1.54922 E-3	1341.3	0.0001260
13	63.68	1.85360 E-3	1195.3	0.0001170
14	38.38	1.55886 E-3	1211.3	0.0001074
15	44.02	1.83715 E-3	1288.2	0.0001090
16	45.54	1.71699 E-3	1398.1	0.0000798
17	55.67	1.83138 E-3	1594.6	0.0000982
18	49.39	1.72550 E-3	1397.1	0.0000583
19	37.69	1.88590 E-3	1139.0	0.0000910
20	58.82	1.93654 E-3	1089.9	0.0001927
21	47.70	1.73860 E-3	1261.4	0.0001110
22	58.82	1.93654 E-3	1163.7	0.0001340
23	42.03	2.0585 E-3	1069.1	0.0001400
24	54.32	1.76544 E-3	-	-
25	60.56	1.85916 E-3	1147.6	0.0001240
26	47.65	1.90314 E-3	1197.8	0.0000827
27	40.45	1.77621 E-3	1391.9	0.0000747
28	41.27	1.82230 E-3	1245.2	0.0000900
29	68.68	1.83979 E-3	1485.5	0.0001118
30	58.41	1.64784 E-3	1388.1	-
31	61.24	1.56994 E-3	976.1	-
32	42.22	1.66940 E-3	1170.0	0.0000850
33	51.73	1.51340 E-3	1280.0	0.0000930

Table 7.5

MEASURED ENAMEL THICKNESS UNDER MID-HEIGHT GAUGES

Gauge No.	Blade Serial No.	$\sqrt{\rho ck_1}$	a/k	a (mm)
1	5	1760.4	0.0000577	0.066
2	1	1063.7	0.0001663	0.126
3	3	1267.3	0.0000858	0.066
4	6	1122.5	0.0000920	0.104
5	5	1524.3	0.0000602	0.051
6	6	1483.5	0.0000673	0.093
7	5	1266.3	0.0001100	0.073
8	6	1392.7	0.0000940	0.052
9	5	1356.9	0.0000940	0.088
10	1	1222.0	0.0001300	0.124
11	1	1113.8	0.0001317	0.111
12	5	1341.3	0.0001260	0.131
13	3	1195.3	0.0001170	0.085
14	5	1211.3	0.0001074	0.115
15	3	1288.2	0.0001090	0.094
16	5	1398.1	0.0000798	0.130
17	3	1594.6	0.0000982	0.111
18	5	1397.1	0.0000583	0.100
19	6	1139.0	0.0000910	0.065
20	1	1089.9	0.0001927	0.143
21	3	1261.4	0.0001110	0.095

Table 8.1

NOISE TESTS USING BARR AND STROUD FILTER

Gauge	Resistance (Ohms)	V_{out} (V)	No Filter V_{noise}(rms) (mV)	With Filter V_{noise}(rms) (mV)
Gauge 32	43.047	6.7590	0.982	0.900
Gauge 33	52.533	8.2602	0.994	0.916
47 Ω	47.313	7.3591	0.944	0.867

Table 8.2

NOISE TESTS USING AMP-05 FILTER

	Input to AMP-05		AMP-05 Output		
				Filter off	Filter on
	V_{in} (V)	V_{noise} (mV)	V_{out} (V)	V_{noise} (mV)	V_{noise} (mV)
Gauge 32	6.7147	0.970	6.7289	1.095	0.875
Gauge 33	8.2466	0.979	8.2244	1.110	0.890
47 Ω	7.3684	0.935	7.3555	1.050	0.845

Table 8.3

FINAL NOISE MEASUREMENTS

Multiplexer Channel	3		4		5		6	
	V (d.c) (V)	V_{noise} (mV)	V (d.c) (V)	V_{noise} (mV)	V (d.c) (V)	V_{noise} (mV)	V(d.c) (V)	V_{nois} (mV
Output								
0	-	-	7.745	7.495	-	-	9.743	8.880
1	8.204	8.126	7.182	7.719	8.640	8.423	8.305	8.702
2	6.870	6.795	9.466	8.315	8.072	7.373	7.020	6.903
3	7.962	7.459	7.387	7.445	10.145	9.131	6.819	7.134
4	6.973	9.201	8.947	6.870	9.415	7.030	9.749	7.581
5	-	-	-	-	-	-	9.761	7.875
6	-	-	-	-	5.959	6.209	5.945	6.155
7	7.562	10.144	-	-	9.337	7.340	7.709	7.068

Noise levels measured at input to transient recorder.
- indicates that gauge was malfunctioning.

Table 8.4

MEAN HEAT TRANSFER DATA FROM ROTOR EXPERIMENT

Run / Gauge	6383	6384	6448
4	-	-	√
8	-	-	√
14	-	-	√
17	-	-	√
20	-	-	√
32	√	√	-
33	√	√	-

Table 8.5

TURBINE SPEED (RPM)

Run No.	Initial	Final
6383	5950	8800
6384	5900	8900
6447	6900	9400
6448	6700	9200

Table 8.6

UNSTEADY HEAT TRANSFER DATA FROM ROTOR EXPERIMENT

Run Gauge	6382	6383	6384	6447	6448
8	–	–	–	–	√
14	–	–	–	√	√
17	–	–	–	√	√
20	–	–	–	√	√
32	–	√	√	–	–
33	√	√	√	–	–

Table 8.7

DOORLY EXPERIMENTAL CONDITIONS

Axial chord	51.9mm
Total Temperature	432 K
Ambient Temperature	288 K
Driving Temperature	144 K
Conductivity (at 288K)	25.26 E-3 W/mK
Reynolds Number (based on true chord and M_{exit})	2.02 E+6
M_{exit} (Isentropic)	0.959

APPENDIX I

PREDICTED ANALOGUE OUTPUT FROM THIN FILM GAUGE ON A TWO LAYERED SUBSTRATE SUBJECT TO STEP IN HEAT TRANSFER RATE

For a gauge on a two-layered substrate it was shown, equation 4.28, that

$$\bar{T} = \frac{\bar{\dot{q}}}{\sqrt{(\rho ck)_1}\sqrt{s}} \frac{(1 + A\exp(-2a\sqrt{(s/\alpha_1)}))}{(1 - A\exp(-2a\sqrt{(s/\alpha_1)}))} \quad (1)$$

The term in brackets can be expanded

$$\bar{T} = \frac{\bar{\dot{q}}}{\sqrt{(\rho ck)_1}\sqrt{s}} \left[1 + 2 \sum_{m=1}^{\infty} A \exp\left(-2 a m \sqrt{s/\alpha_1}\right) \right] \quad (2)$$

The change in film voltage, v, for a rise in temperature, T, is given by equation 4.14

$$v = V_0 \alpha T \quad (3)$$

where V_O is the initial voltage and α is the temperature coefficient of resistance.

The analogue output V_a can be written in the Laplace Transform domain, equation 4.20

$$\bar{V}_a = \frac{\sqrt{s}\,\bar{v}}{K_a} = \frac{V_0 \sqrt{s}\,\alpha \bar{T}}{K_a} \quad (4)$$

A step in heat transfer rate is given by:-

$$\bar{\dot{q}} = \frac{Q}{s} \quad (5)$$

Combining (2), (4) and (5) gives

$$\bar{V}_a = \frac{V_0 \alpha Q}{K_a s \sqrt{(\rho ck)_1}} \left[1 + 2 \sum_{m=1}^{\infty} A \exp\left(-2 a m \sqrt{s/\alpha}\right) \right] \quad (6)$$

This can be inverted to give:-

$$V_a(t) = \frac{V_0 \alpha Q}{K_a \sqrt{(\rho ck)_1}} \left[1 + 2 \sum_{m=1}^{\infty} A^m \operatorname{erfc}\left(\frac{ma}{\sqrt{\alpha_1 t}}\right) \right] \quad (7)$$

Hence the analogue output for a thin film gauge subjected to a step in heat flux can be calculated as a function of time. The program ANALOP was written to do this which uses the routine S15ADF from the **NAG** Library to evaluate the Complimentary Error Function (erfc).

APPENDIX II

PREDICTED OUTPUT FROM IN-SHAFT ELECTRONICS

The gain of the in-shaft amplifier varies with frequency, figure 4.11 . Let this gain be represented by $F(\omega)$.

The change in output, v, from a thin film gauge of resistance, R_{20}, supplied with a constant current, I, for a temperature rise , T, was given in equation 6.27.

$$v = IR_{20}\alpha_{20}T \qquad (1)$$

The output measured by the data acquisition system, V, is the output from the thin film gauge amplified by the in-shaft electronics.

$$V = v.\,\text{gain}$$

$$= IR_{20}\,\alpha_{20}T.F(\omega) \qquad (2)$$

The gauge sensitivity, figure 4.8 is expressed as $T/\dot{q}$ and is also frequency dependent. Let it be represented by $G(\omega)$.

Hence $T = \dot{q}.G(\omega)$ (3)

Substituting in (2)

$$v = IR_{20}\alpha_{20}\,\dot{q}\,.\,G(\omega).F(\omega) \qquad (4)$$

The overall system gain $G(\omega).F(\omega)$ was designed to be as constant with frequency as possible. It is plotted in figure 4.12 and varies between 2.5E-3 and 5.0E-4. Typical values for I, R_{20} and α_{20} are 30mA, 50Ω and $0.0015K^{-1}$ respectively. Hence the output per unit heat flux can be calculated.

If $G(\omega).F(\omega) = 2.5E\text{-}3$ then $V/\dot{q} = 5.6mV/kWm^{-2}$ (5)

If $G(\omega).F(\omega) = 5.0E\text{-}4$ then $V/\dot{q} = 1.1\ mV/kWm^{-2}$ (6)

In a cascade test of the blade used in the rotor project **Doorly** measured fluctuations in the heat transfer rate of around $50kW/m^2$ peak to peak. The Nusselt Number for the two experiments should be the same,

(ignoring temperature ratio effects)

$$\text{i.e.} \qquad Nu = \left(\frac{\dot{q}\, C_{ax}}{T\, k}\right)_R = \left(\frac{\dot{q}\, C_{ax}}{T\, k}\right)_D \tag{7}$$

where R represents conditions in the rotor experiment and D conditions in Doorly's experiment.

$$\text{Hence} \quad \dot{q}_R = \frac{Cax_D\, T_R}{Cax_R\, T_D}\dot{q}_D \tag{8}$$

The axial chord in Doorly's experiment was 51.9mm and in the rotor experiment it was 24.35mm. The driving temperature in the rotor experiment was 42K, whereas in Doorly's experiment it was 144K. Using these values in equation 8 the estimated heat flux is calculated to be 31kW/m^2.

The output from the inshaft electronics is therefore predicted to be of the order of 34mV peak to peak, using (6).

APPENDIX III

UNCERTAINTY IN MEASURED HEAT TRANSFER RATE

A first order error analysis has been undertaken on a commonsense basis, **(Holman).** The uncertainty of individual measurements has been established and the effect of each on the heat transfer rate has been considered.

Each gauge was calibrated to obtain the parameters α, $\sqrt{(\rho ck)_1}$ and a/k as described in chapter 7. The uncertainty in the measurements and hence in each calibrated parameter was also addressed in this chapter and only the results will be listed here.

Parameter	Uncertainty (+/- %)
α	0.5
$\sqrt{(\rho ck)_1}$	3.5
a/k	5.0
$\sqrt{(\rho ck)_2}$	0.5
Temperature	0.5

The uncertainties in the measured temperature and α both result in a +/- 0.5% uncertainty in the measured heat transfer rate.

The behaviour of a thin film gauge on a two layered substrate, is such that the influence of $\sqrt{(\rho ck)_1}$ and a/k depends on the time scale of the experiment. It was seen in chapter 6 that changes in $\sqrt{(\rho ck)_2}$ have a very small effect on the heat transfer rate and so any uncertainty arising from this parameter will be considered to be negligible.

At short time the enamel layer appears semi-infinite and hence the parameter a/k has no meaning. The effect of a 3.5% uncertainty in $\sqrt{(\rho ck)_1}$ is to produce a 3.5% uncertainty in the heat transfer rate.

The effect of a/k and $\sqrt{(\rho ck)_1}$ at long time was investigated in chapter 6. In figure 6.50 a 10% change in $\sqrt{(\rho ck)_1}$ was seen to produce a 0.6% change in the heat transfer rate, hence the effect of a 3.5 % uncertainty in

$\sqrt{(\rho ck)_1}$ can be estimated to result in an uncertainty of 0.2% in the heat transfer rate.

The result of a 10% change in a/k on the heat transfer rate was shown in figure 6.51. Similarly a 5% change in a/k was found to result in a 3.2 % change in the heat transfer rate.

A worst case estimate of the uncertainty is obtained by summing the individual uncertainties.

	Uncertainty in Heat Transfer Rate (+/-%)	
Parameter	Short Time	Long Time
α	0.5	0.5
Temperature	0.5	0.5
$\sqrt{(\rho ck)_1}$	3.5	0.2
a/k	0.0	3.2
Total	4.5	4.4

Expressing the heat transfer rate in a non-dimensional form as a Nusselt Number requires the total temperature as well as the ambient temperature to be measured, adding a further 0.5% to the uncertainty.

Consequently the uncertainty in the measured Nusselt Number is estimated as +/-5% over all timescales.

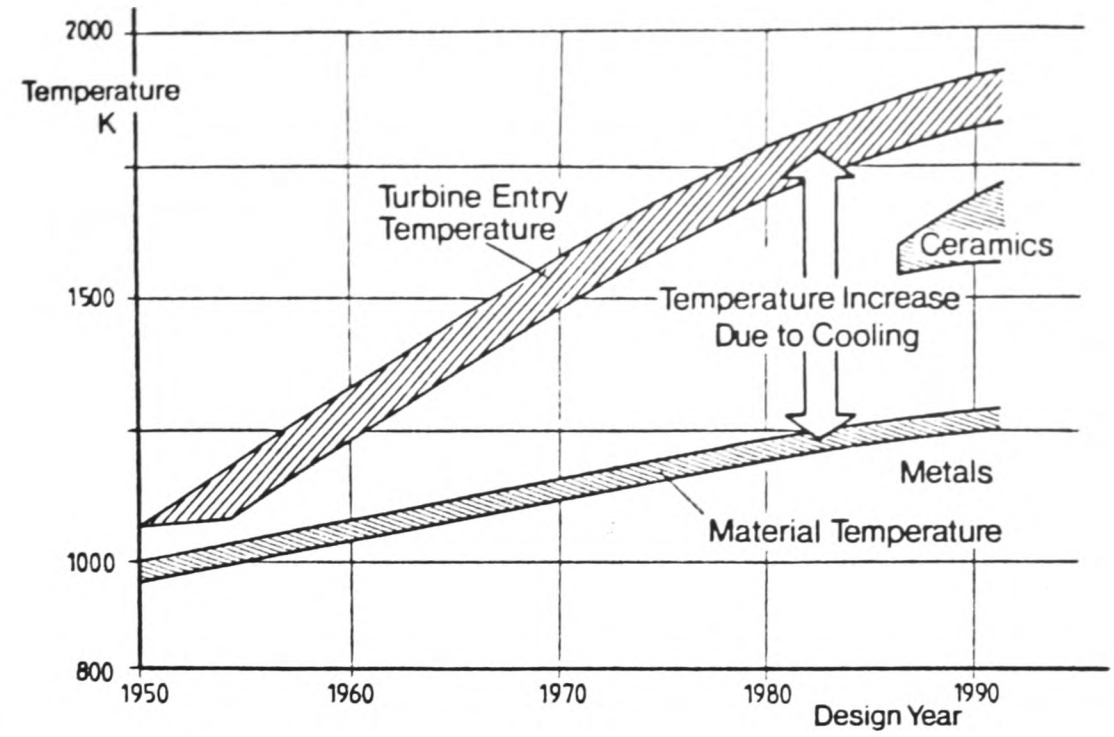

Figure 1.1: Development of Turbine Entry Temperature (from Hennecke)

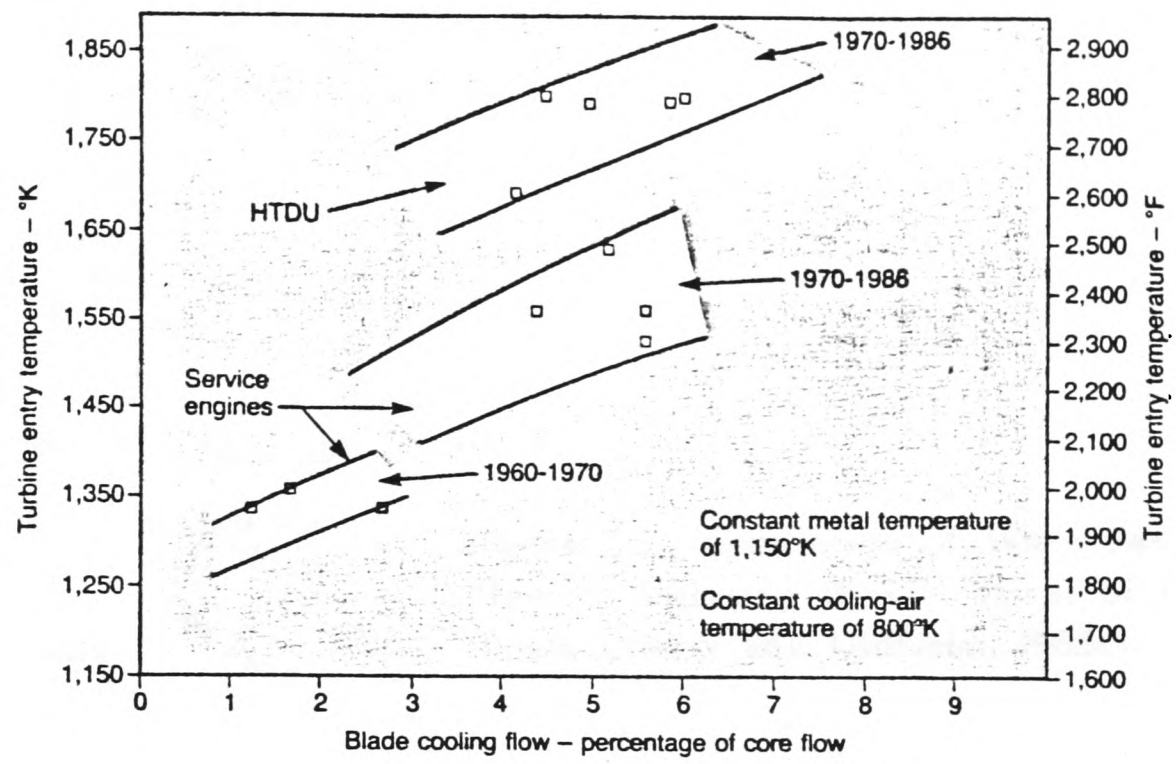

Figure 1.2: Advances in Turbine Cooling Technology Achieved with Service Engines and the High Temperature Demonstrator Unit (from Byworth)

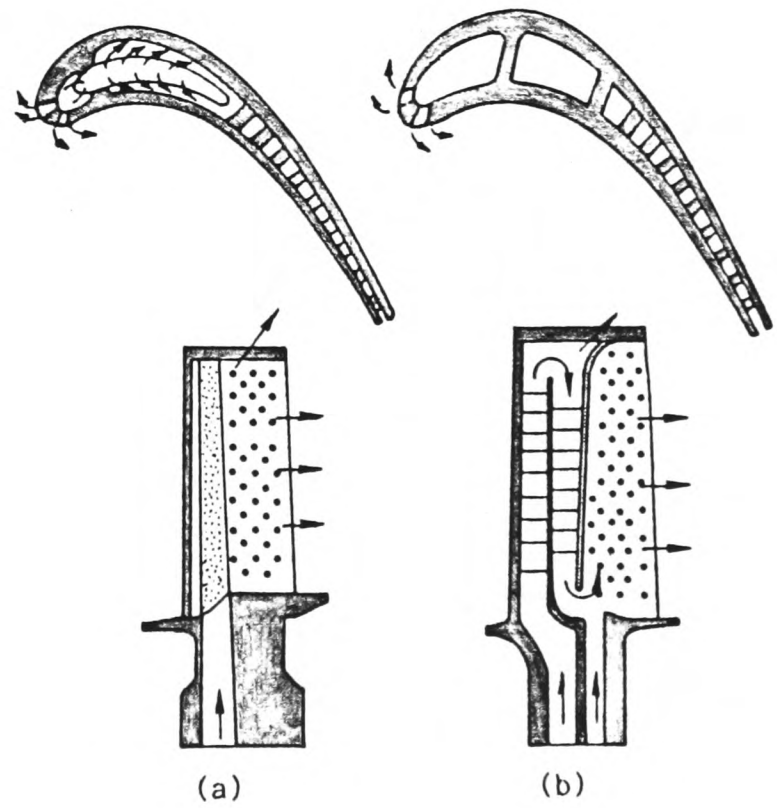

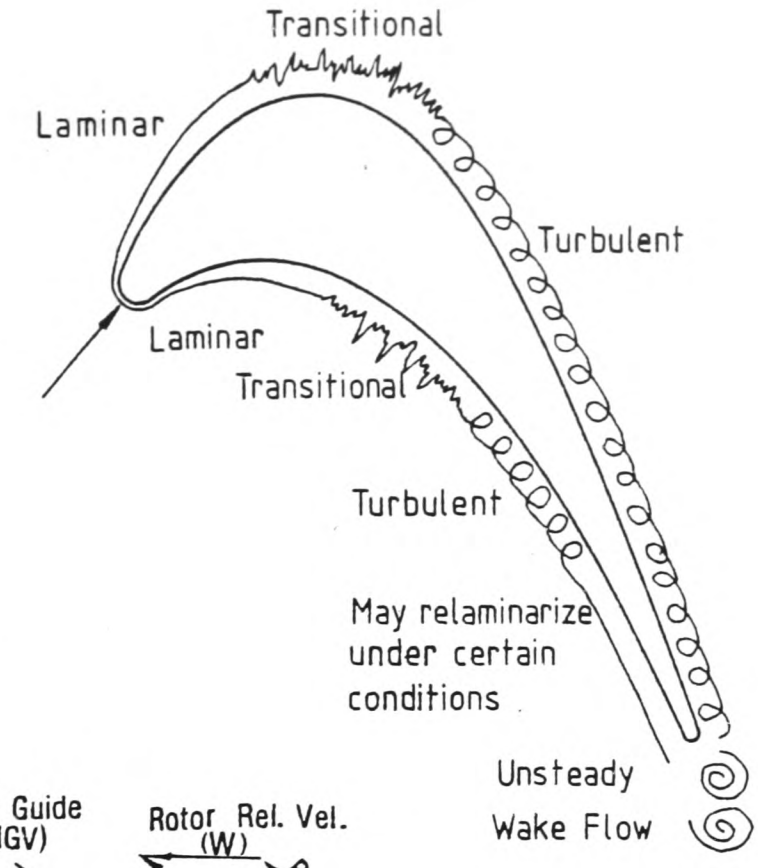

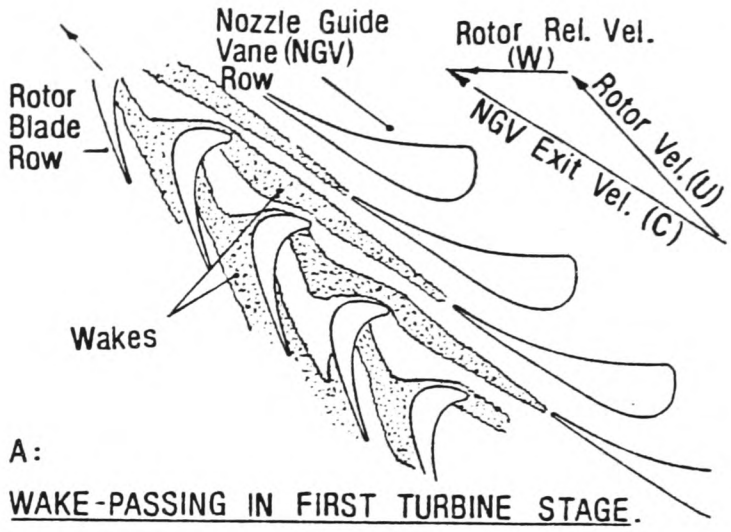

A:
WAKE-PASSING IN FIRST TURBINE STAGE.

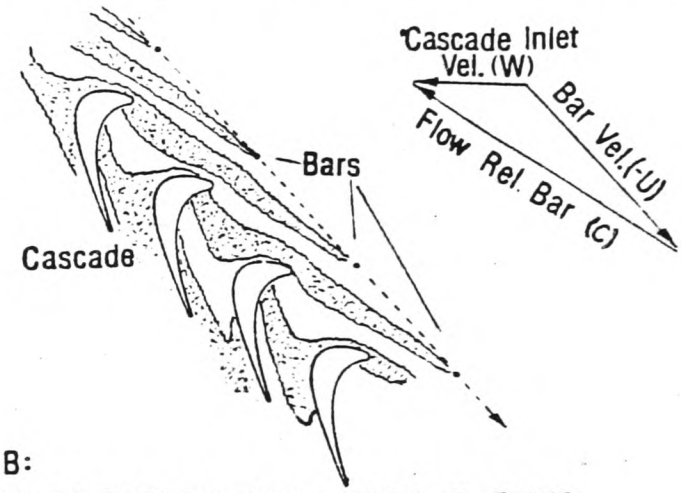

B:
WAKE-PASSING SIMULATION IN FIXED CASCADE OF TURBINE BLADES.

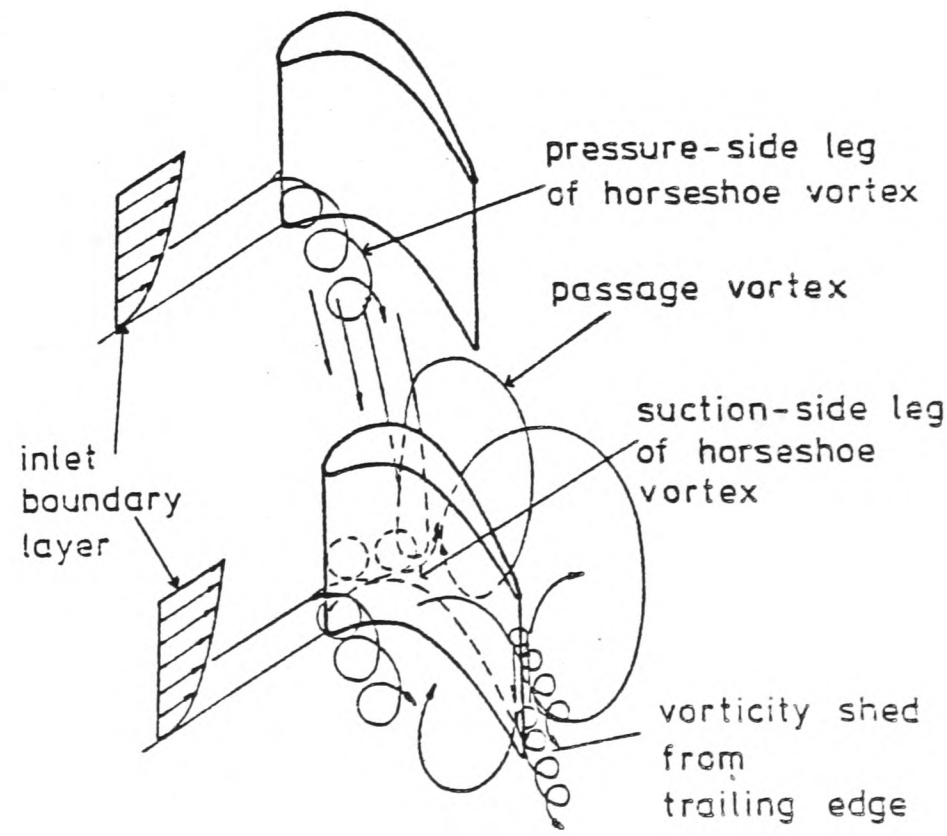

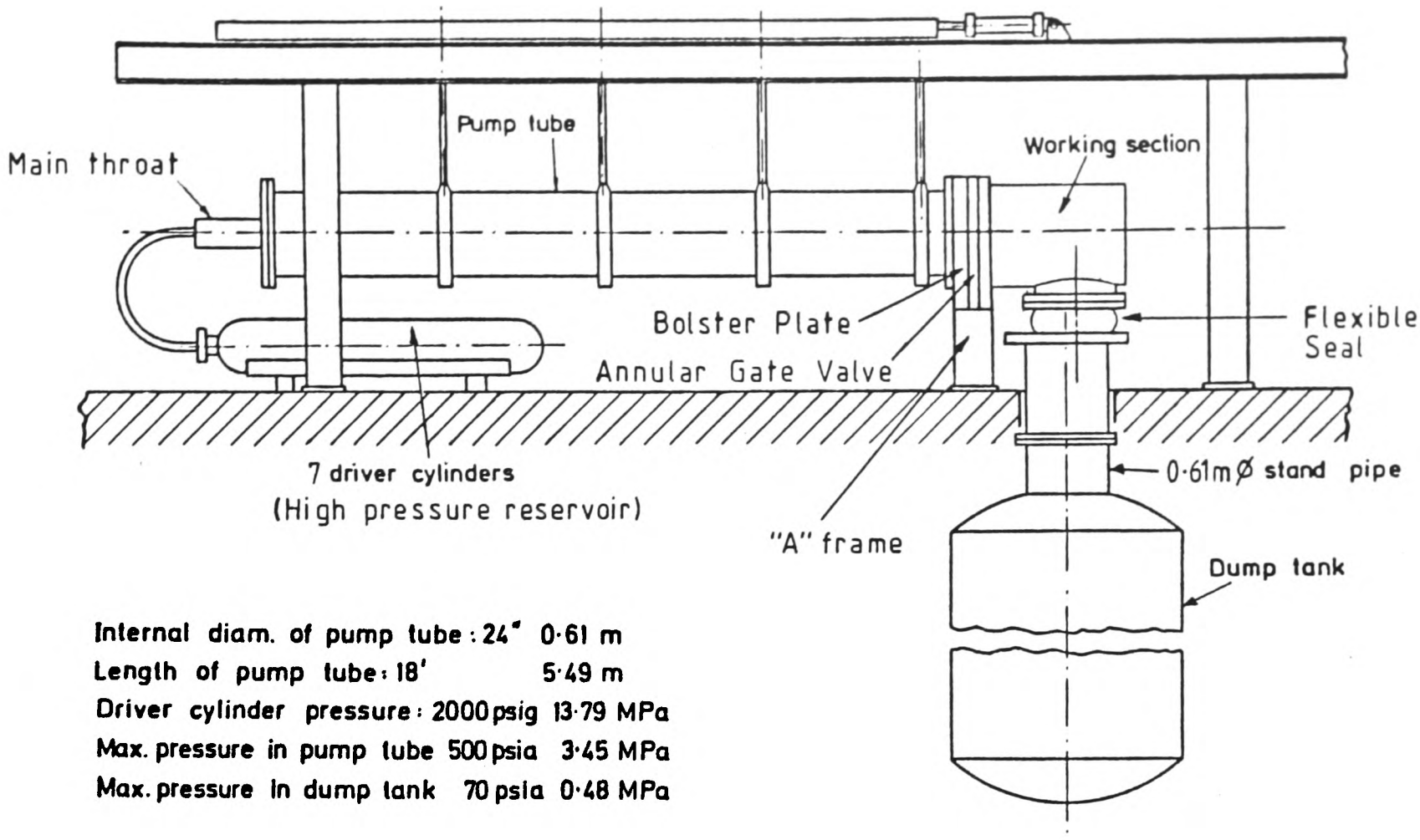

Figure 3.1: General Assembly of Rotor Facility

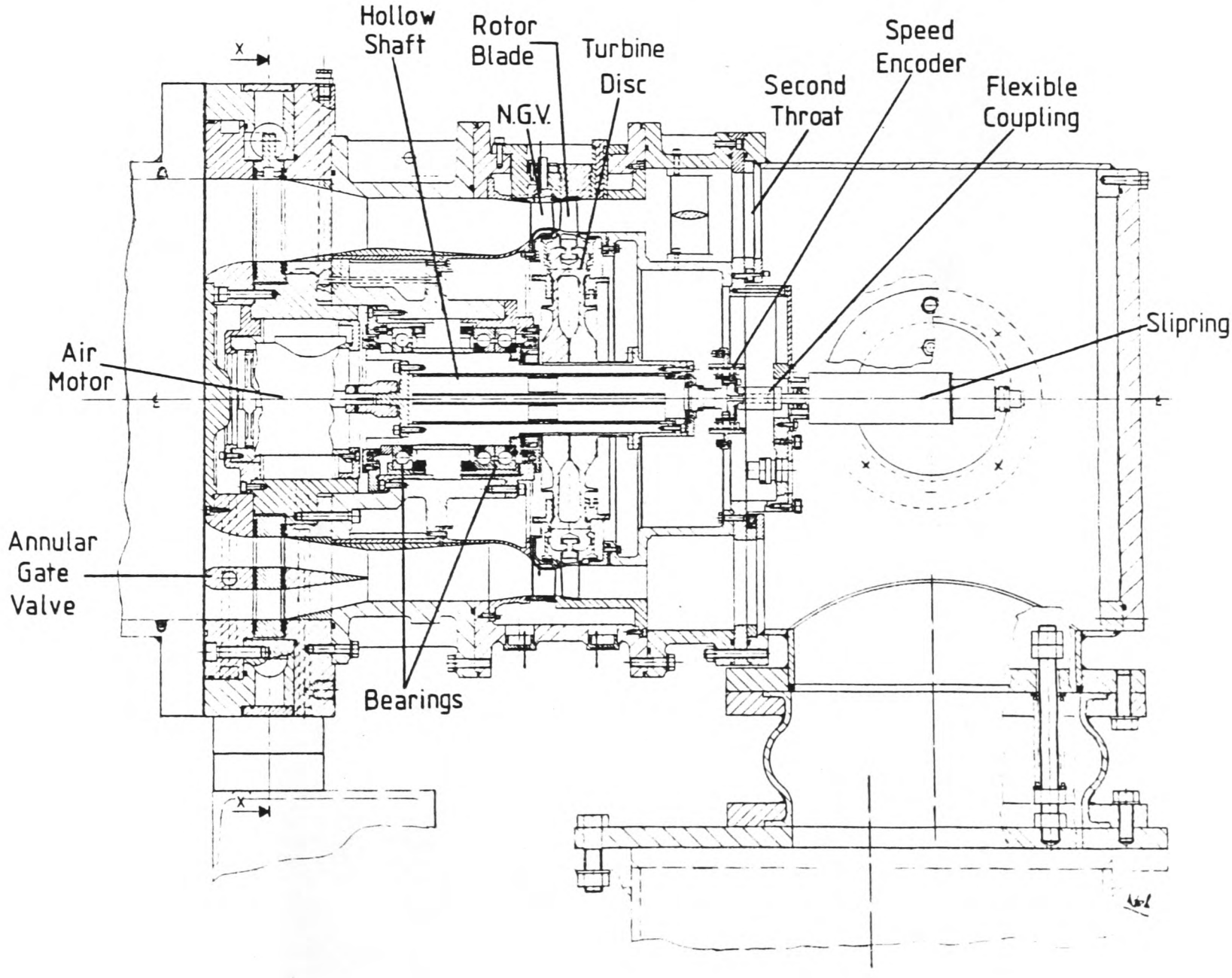

Figure 3.2: The Turbine Working Section

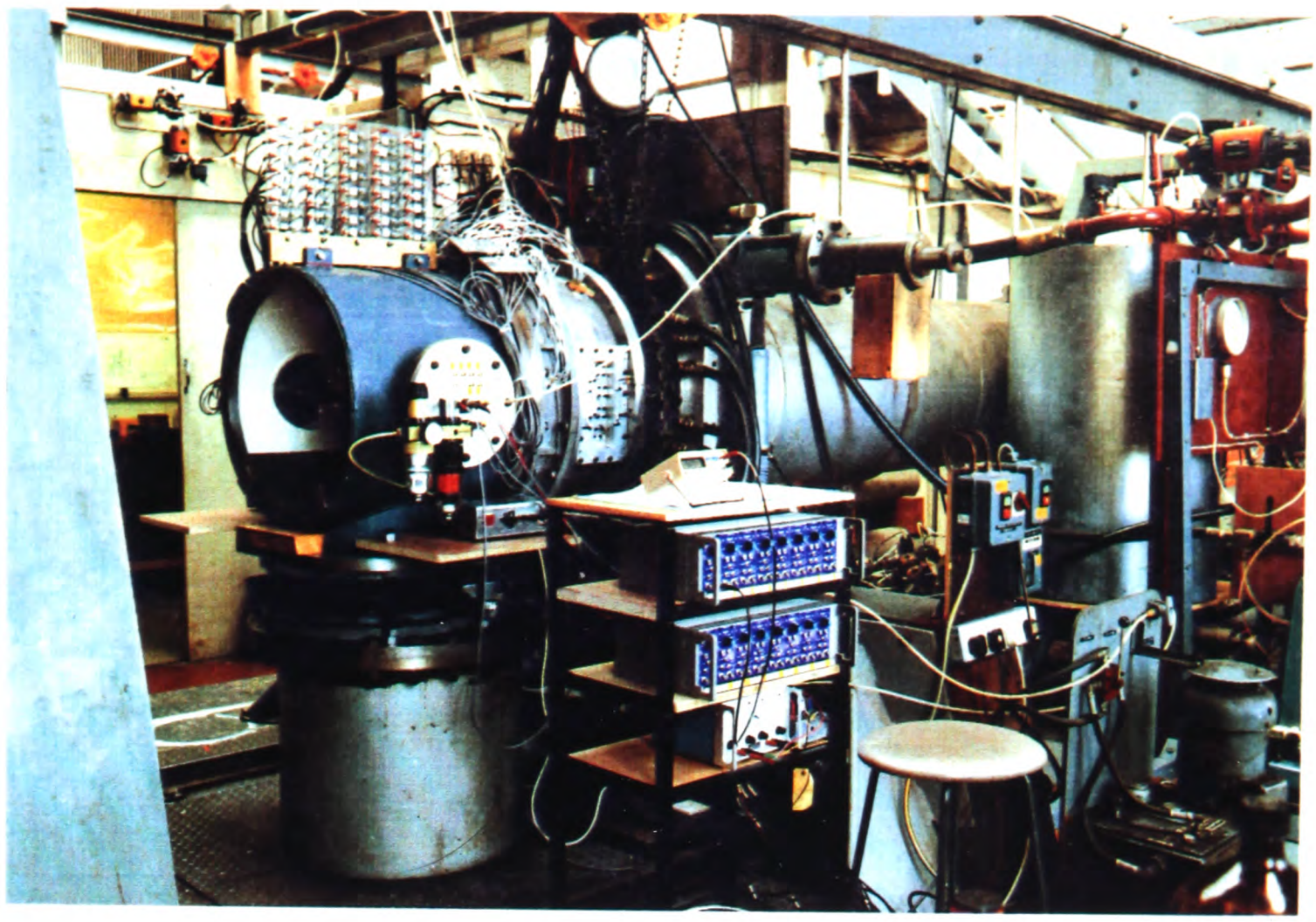

Figure 3.3: The Rotor Facility

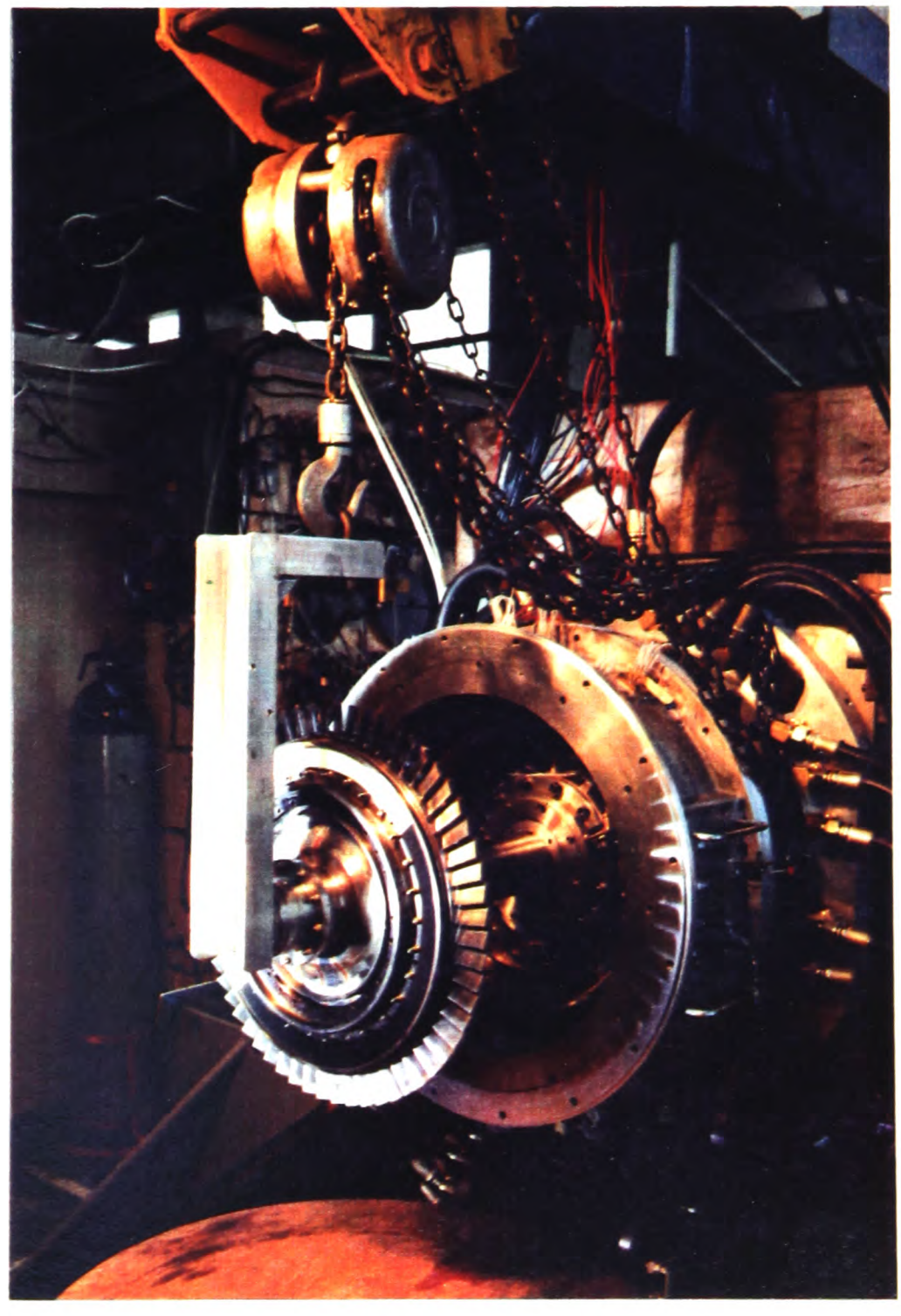

Figure 3.4: Removing the Rotor Disc

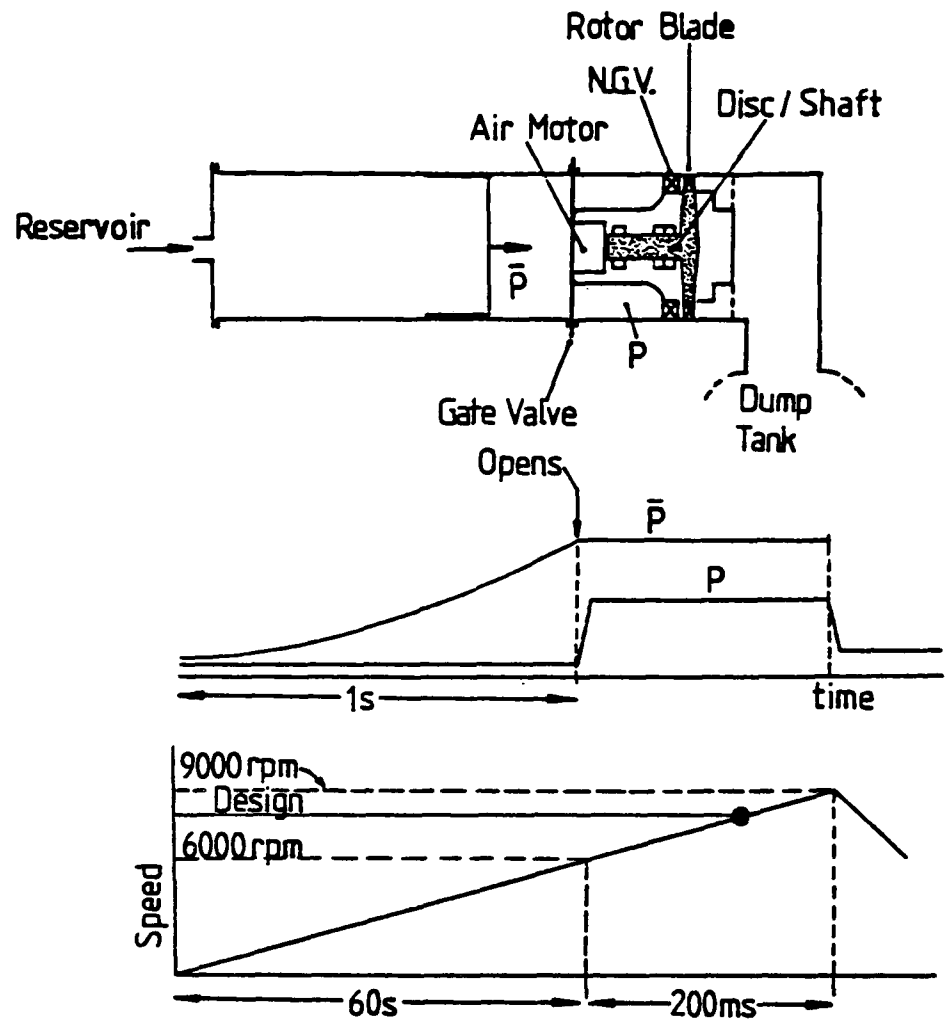

Figure 3.5: Operation of Turbine in the I.L.P.T.

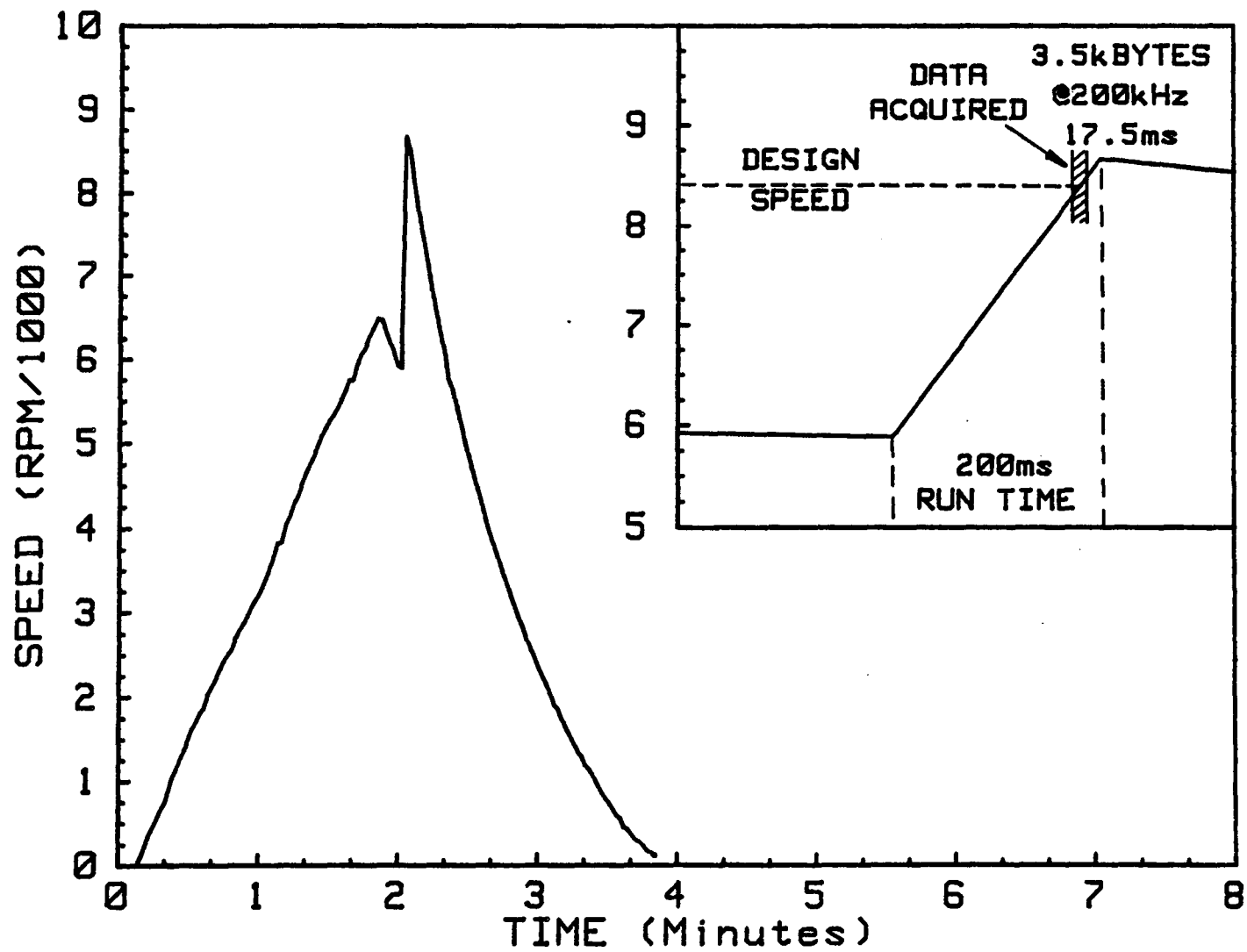

Figure 3.6: Operation of Rotor Facility

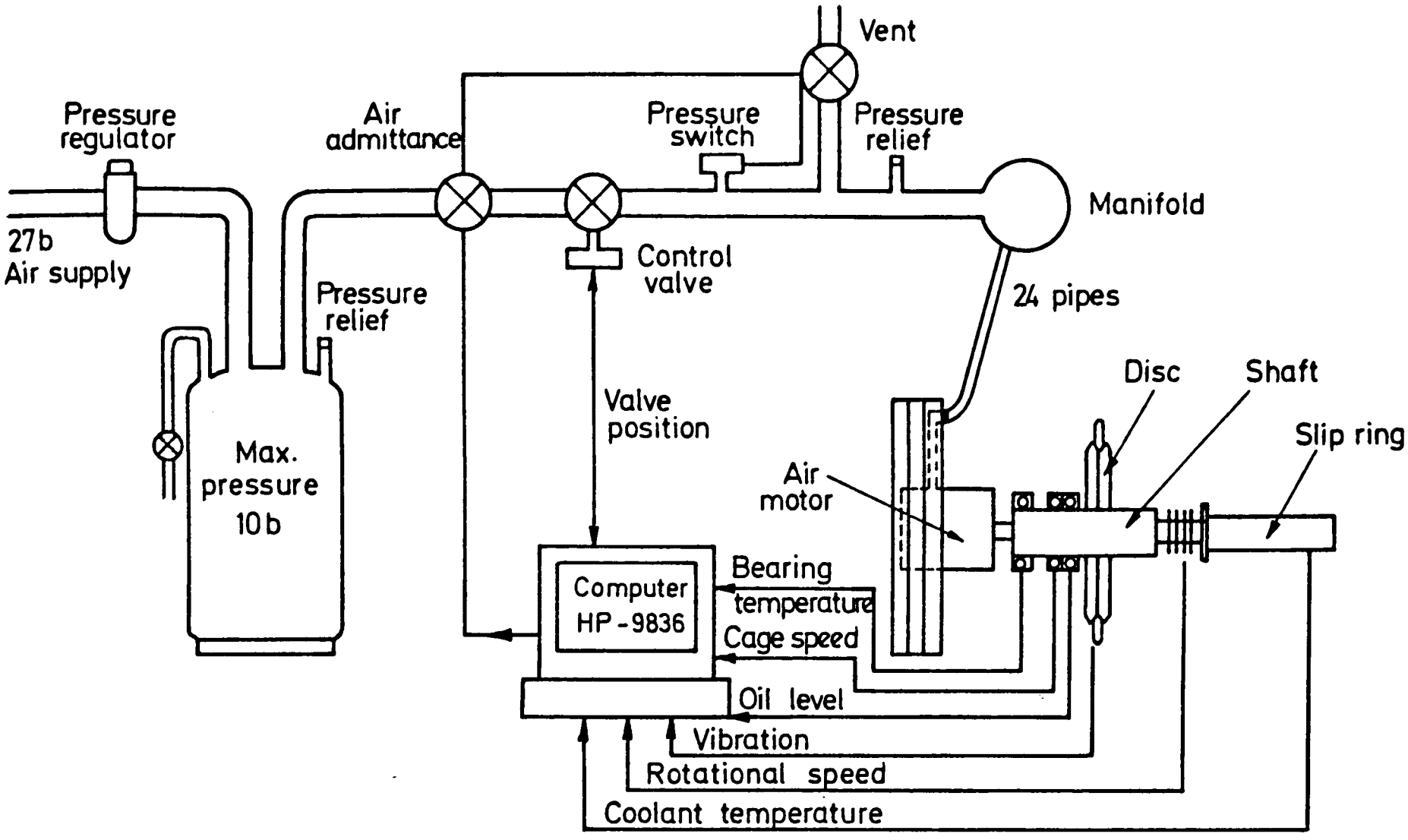

Figure 3.7: Rotor Control System

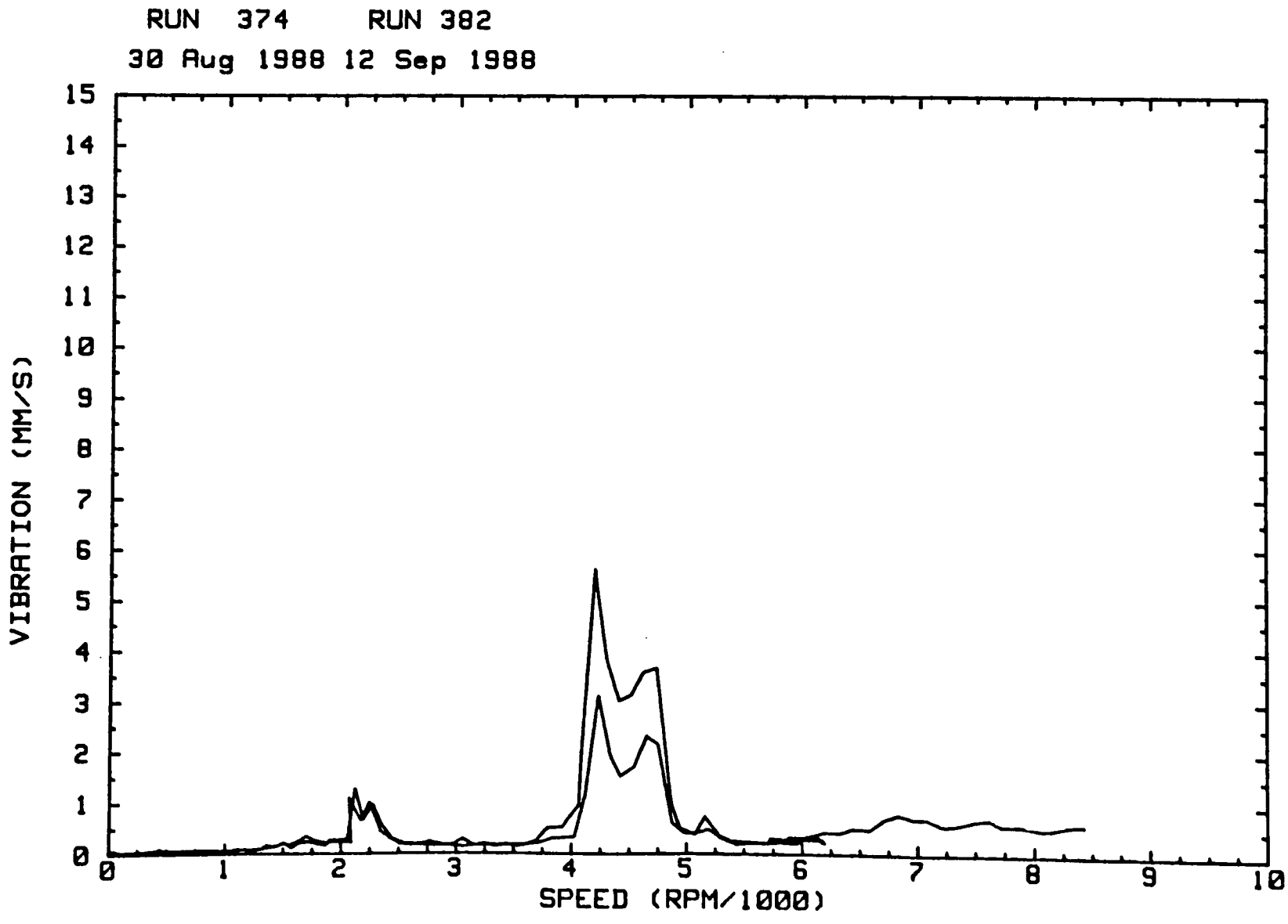

Figure 3.8: Vibration Level During Run Down Tests

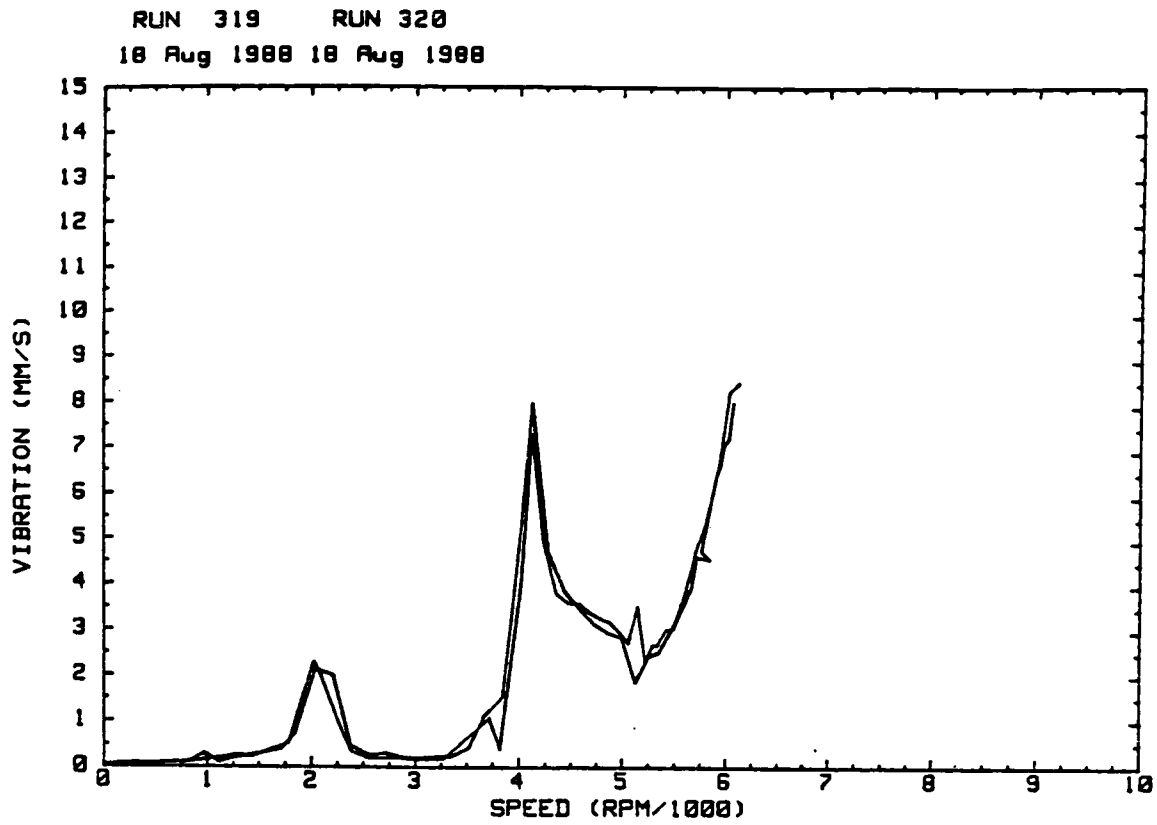

Figure 3.9: Vibration Trace from Run Up Tests - High Out of Balance Level

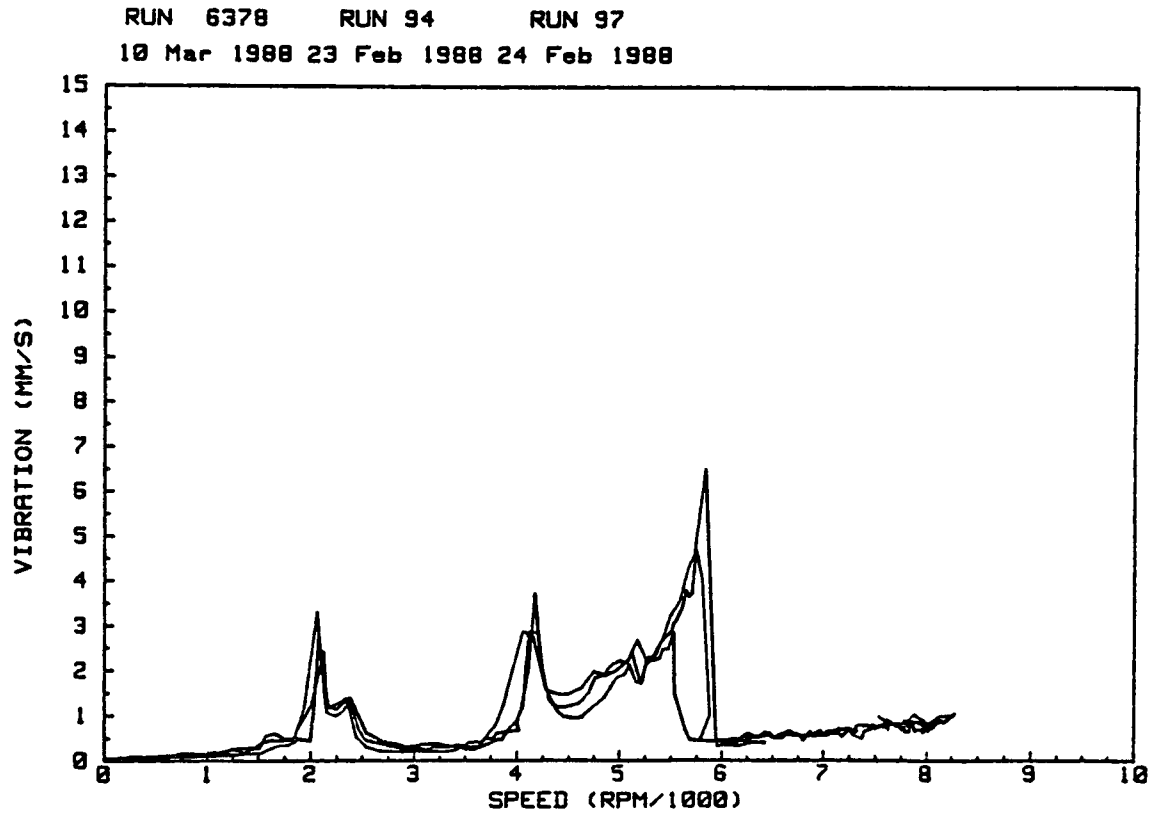

Figure 3.10: Vibration Trace from Run Up Tests - Medium Out of Balance Level

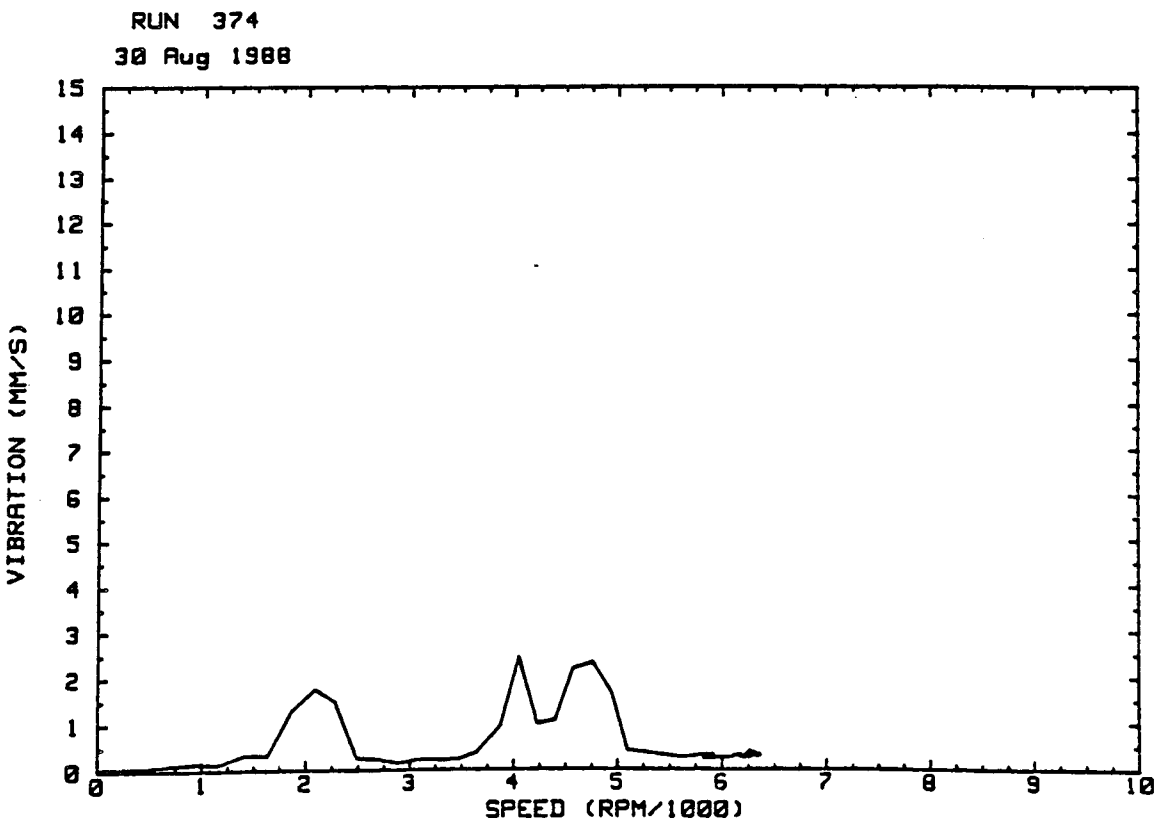

Figure 3.11: Vibration Trace from Run Up Test - Rotor Well Balanced

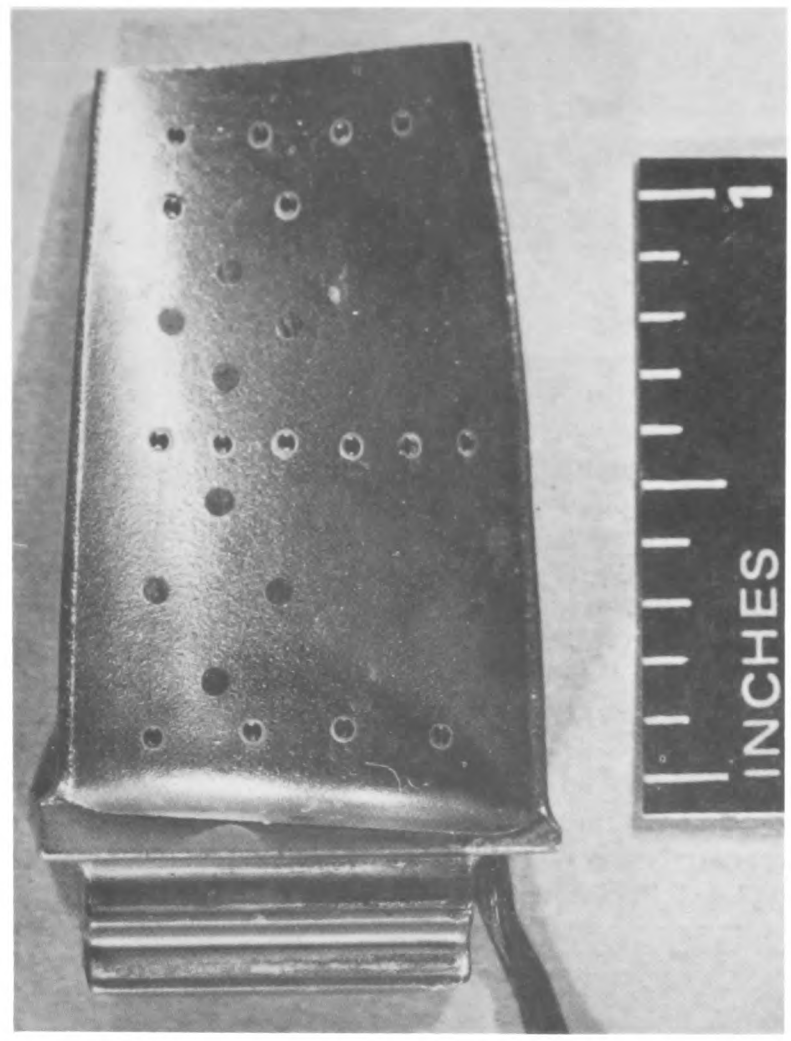

Figure 4.1: Blade Instrumented with Button Gauges (from **Dunn, 1986**)

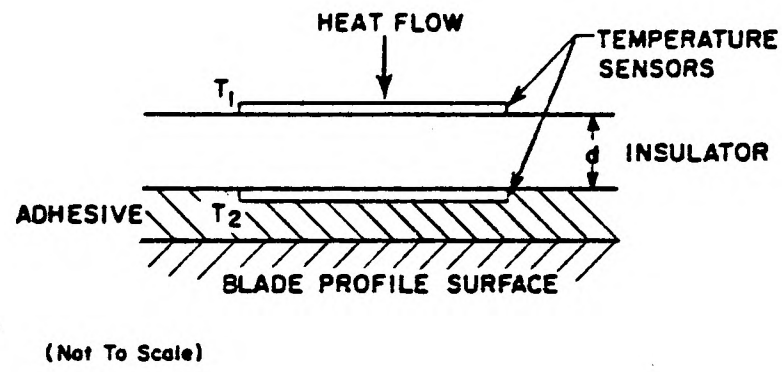

Figure 4.2: Schematic Cross-section of Multi-layer Heat Flux Gauge (from **Epstein et al, 1985**)

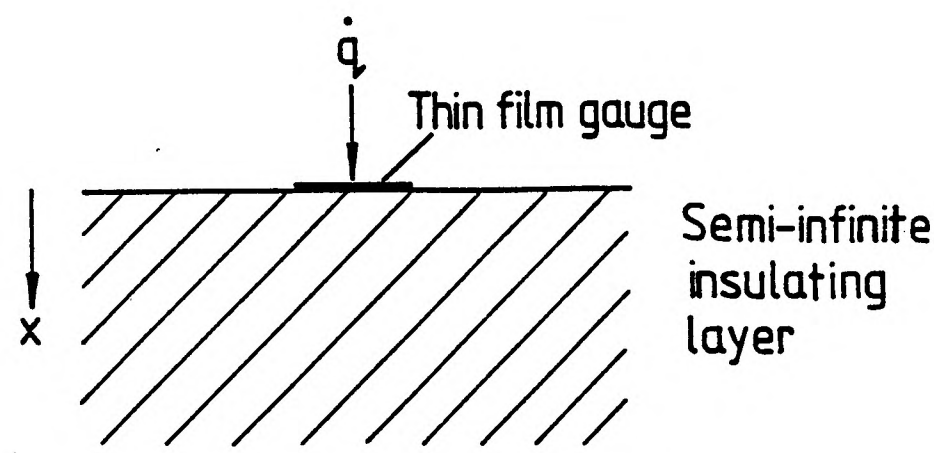

Figure 4.3: Thin Film Gauge on a Single Layer Substrate

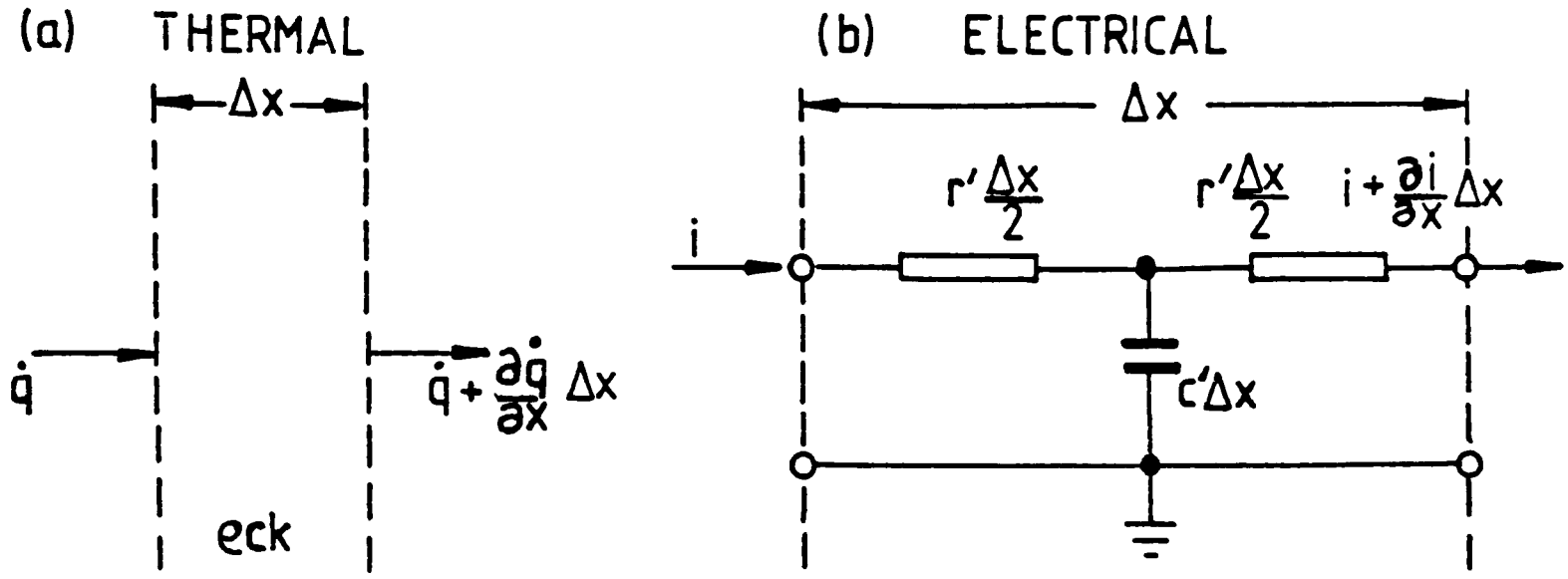

Rate of change of energy in element Δx

$$= -\frac{\partial \dot{q}}{\partial x}\,\Delta x$$

which by conservation of energy

$$= \rho c\,\Delta x\,\frac{\partial T}{\partial t}$$

Thus

$$\frac{\partial \dot{q}}{\partial x} = -\rho c\,\frac{\partial T}{\partial t}$$

The conduction equation is

$$\dot{q} = -k\,\frac{\partial T}{\partial x}$$

Combining the above equations the diffusion equation is obtained

$$\frac{\partial^2 T}{\partial x^2} = \frac{\rho c}{k}\,\frac{\partial T}{\partial t}$$

Rate of change of charge in element Δx

$$= -\frac{\partial i}{\partial x}\,\Delta x$$

which by conservation of charge

$$= c'\Delta x\,\frac{\partial V}{\partial t}$$

Thus

$$\frac{\partial i}{\partial x} = -c'\cdot\frac{\partial V}{\partial t}$$

Ohm's law is

$$i = -\frac{1}{r'\Delta x}\,\frac{\partial V}{\partial x}\,\Delta x = \frac{1}{r'}\,\frac{\partial V}{\partial x}$$

Combining the above equations the transmission line equation is obtained

$$\frac{\partial^2 V}{\partial x^2} = r'c'\cdot\frac{\partial V}{\partial t}$$

Figure 4.4: Derivation of the Electrical Analogue of Heat Conduction

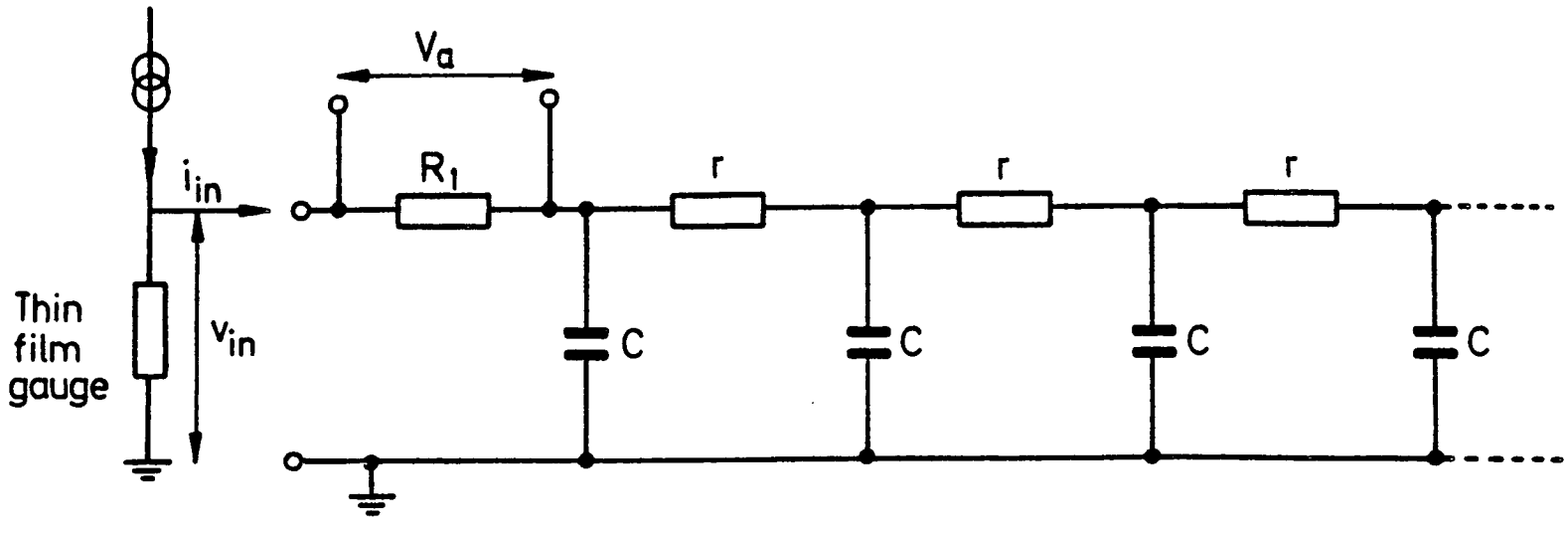

Figure 4.5: Schematic Diagram of Electrical Analogue

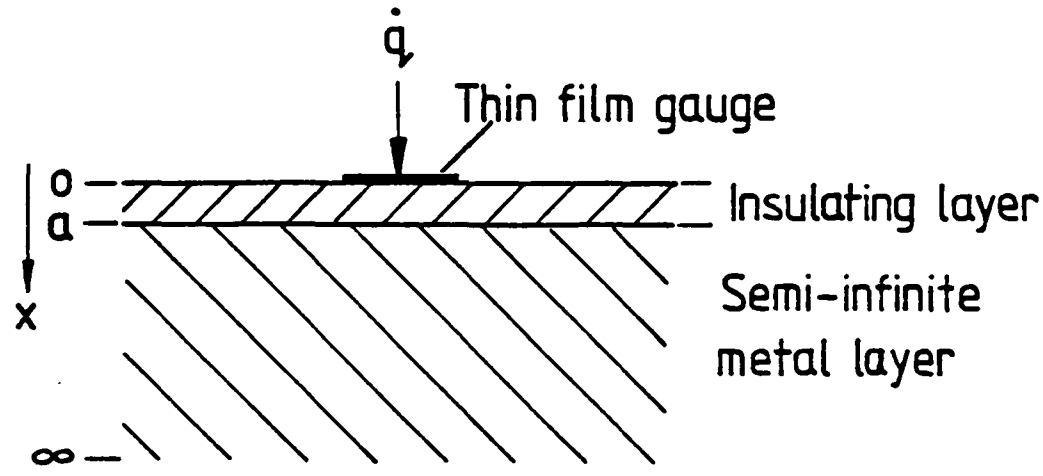

Figure 4.6: Thin Film Gauge on a Two Layered Substrate

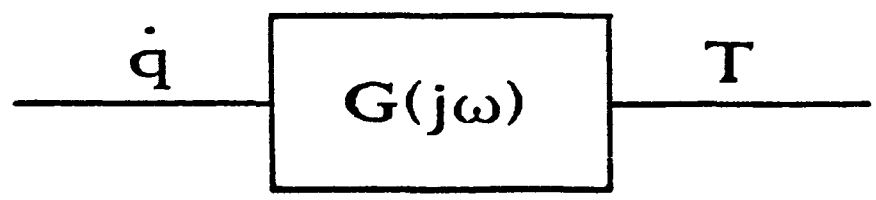

$$G(j\omega) = \frac{T(j\omega)}{\dot{q}\,(j\omega)}$$

Figure 4.7: Block Diagram of Thin Film Gauge

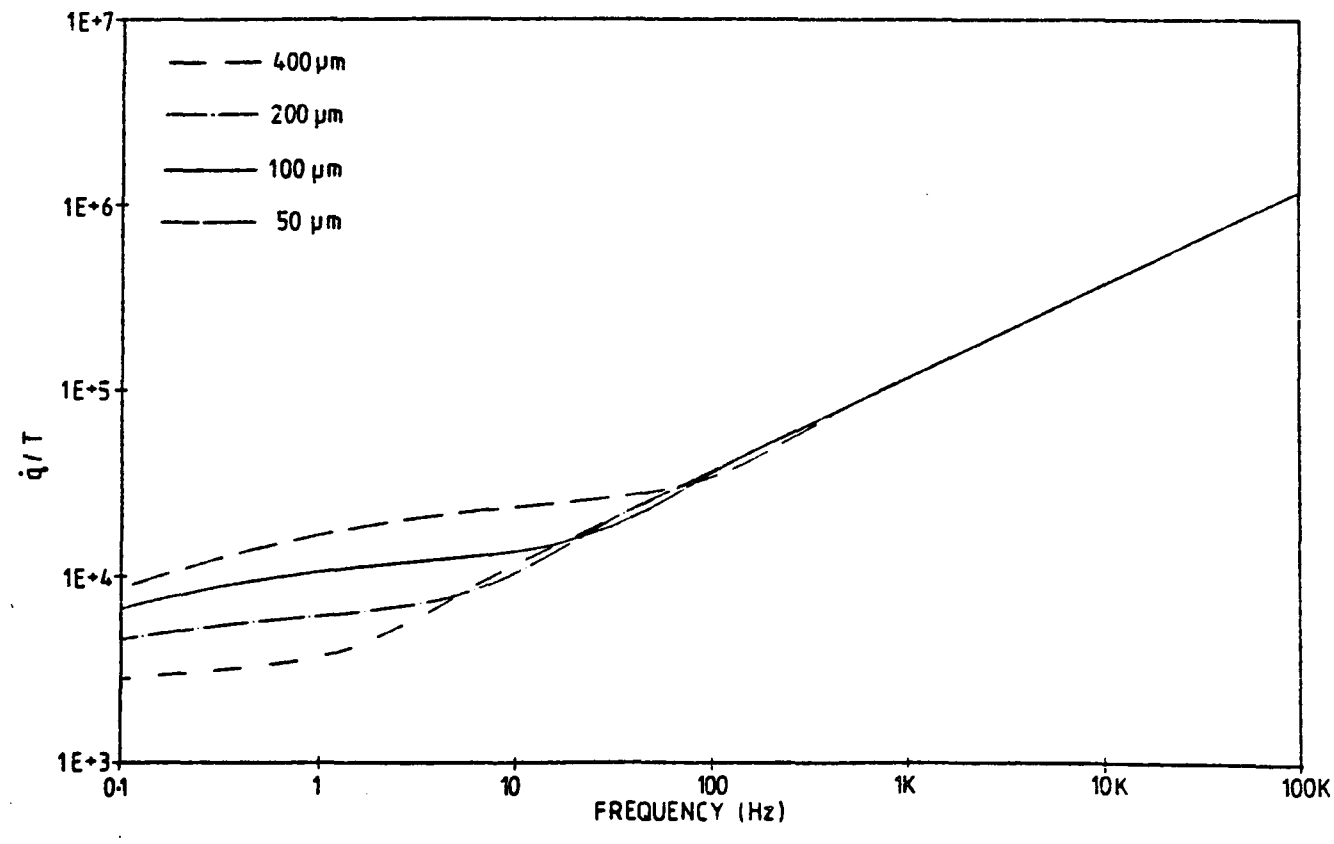

Figure 4.8: Effect of Enamel Thickness on Gauge Frequency Response

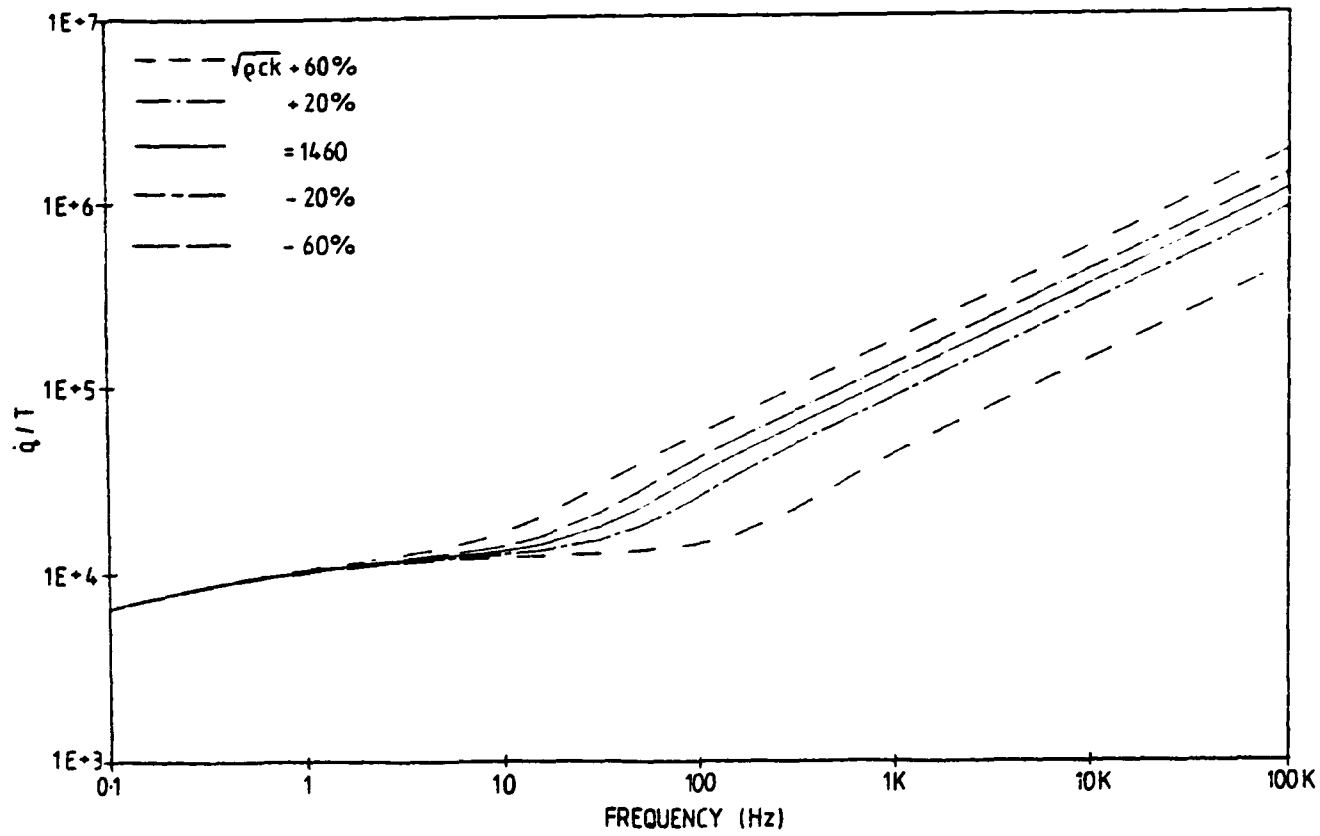

Figure 4.9: Effect of Enamel Thermal Product on Gauge Frequency Response

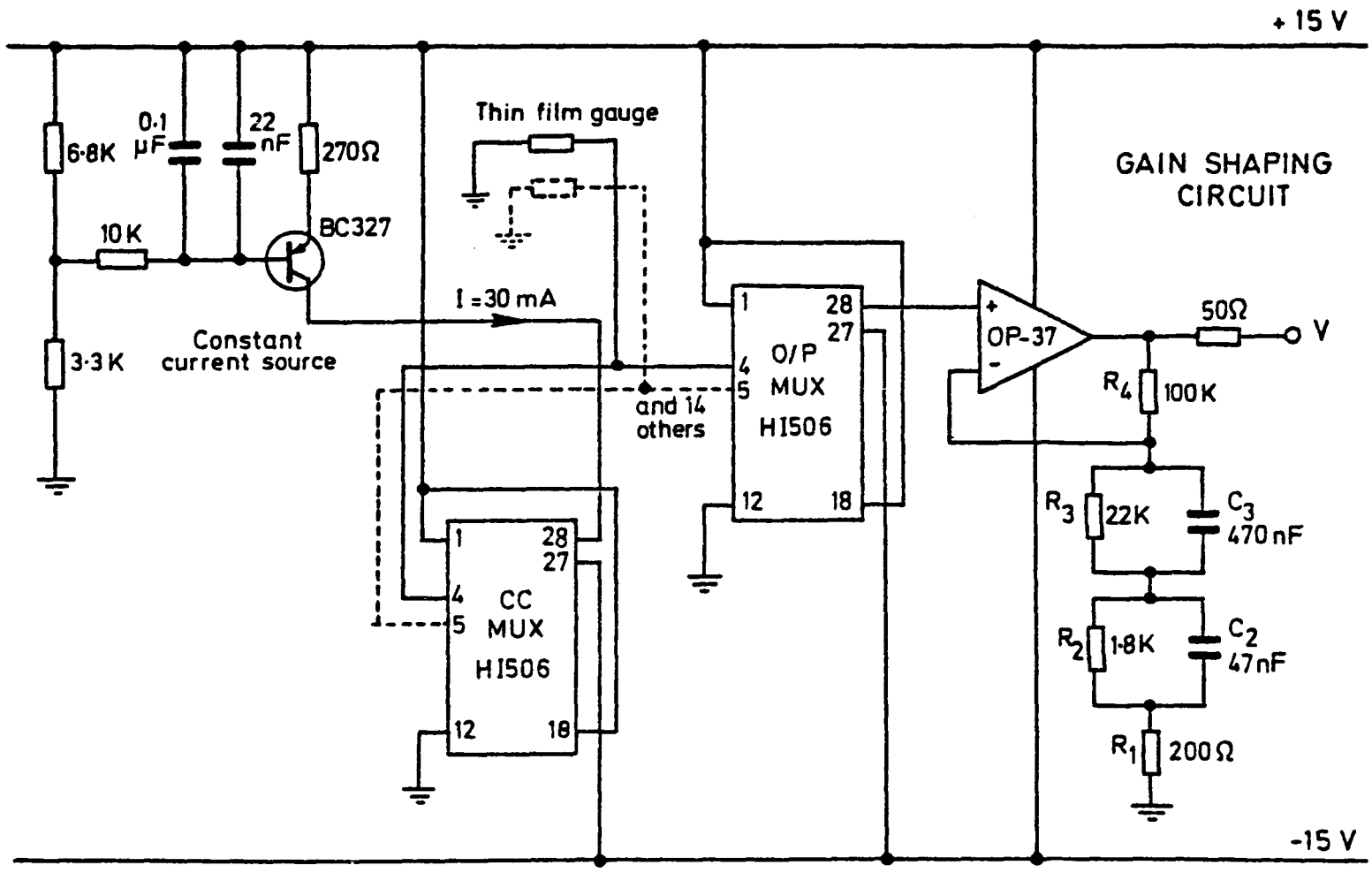

Figure 4.10: Circuit Diagram for In-Shaft Amplifier Unit

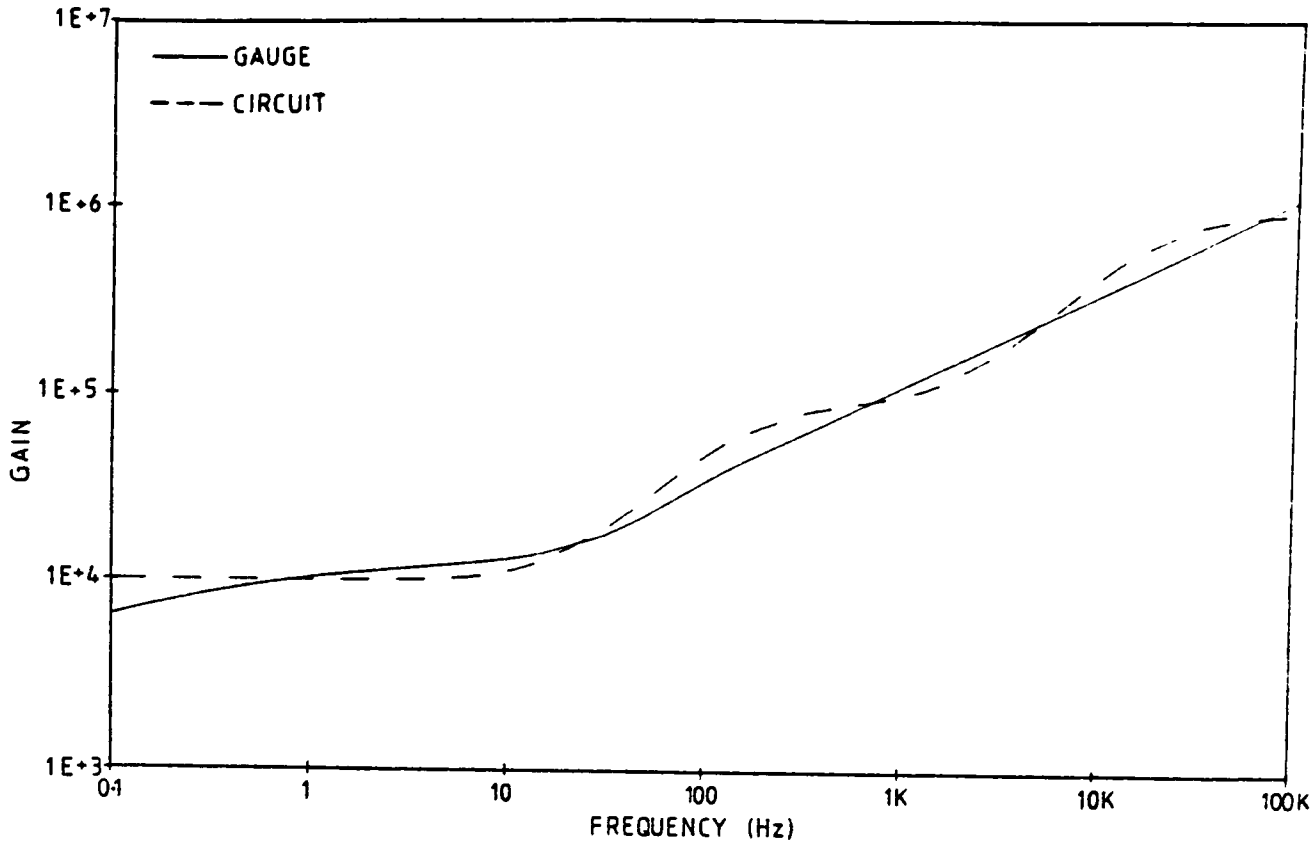

Figure 4.11: Superposition of Gauge and Circuit Frequency Response

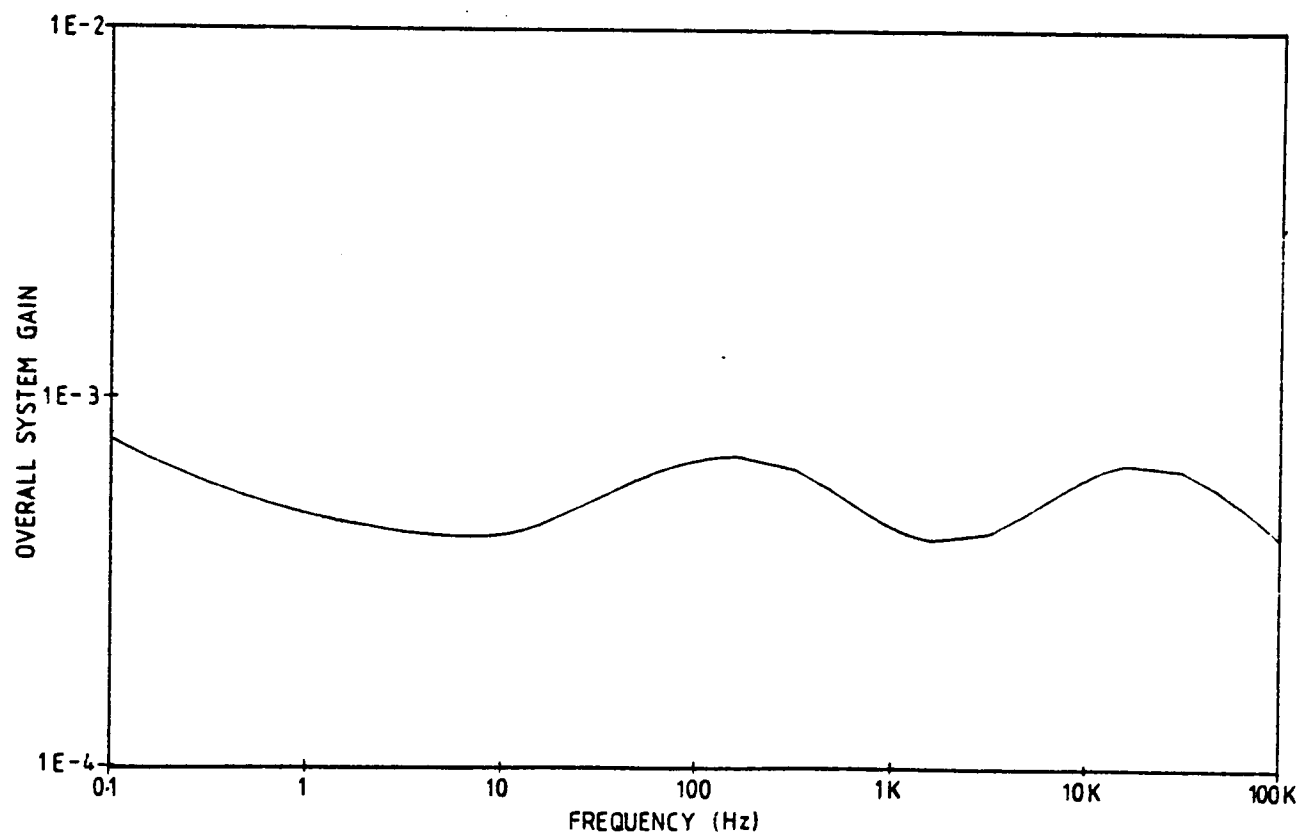

Figure 4.12: Product of Gauge and Circuit Gain

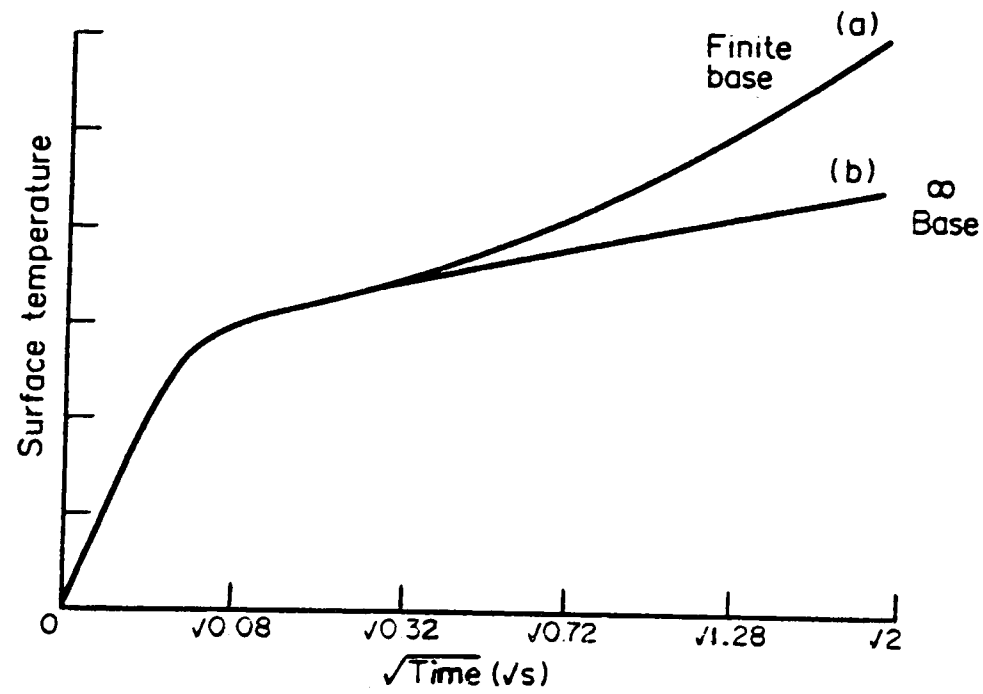

Figure 4.13: Surface Temperature Rise of Thin Film Gauge Subject to Step in Heat Transfer Rate at the Surface : (a) 200μm Quartz on 3mm Nickel; (b) 200μm Quartz on Semi-infinite Nickel (From **J.E. Doorly and Oldfield, 1987**)

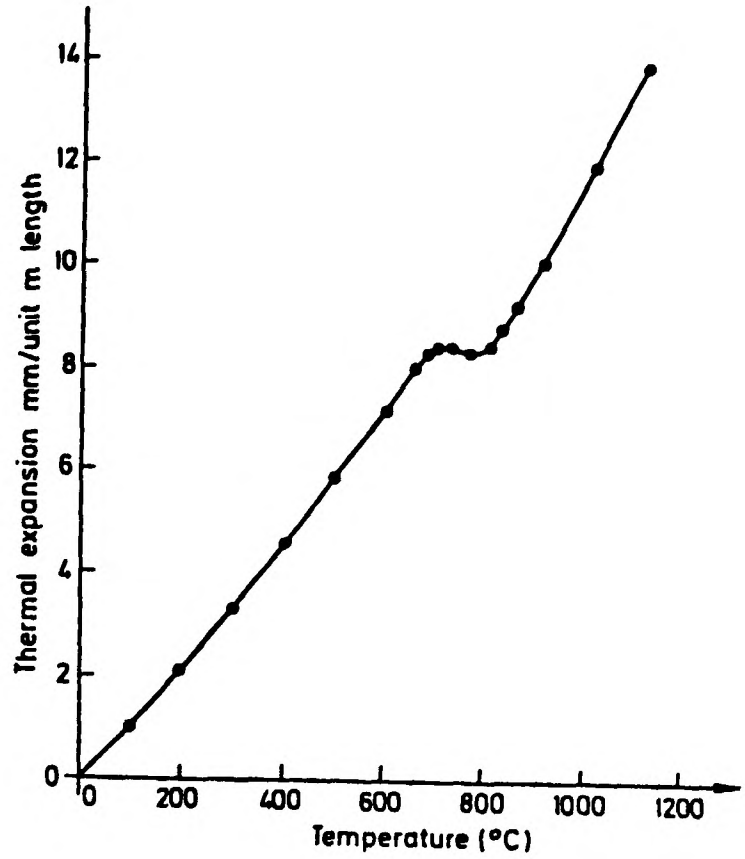

Figure 5.1: Thermal Expansion of Jethete.

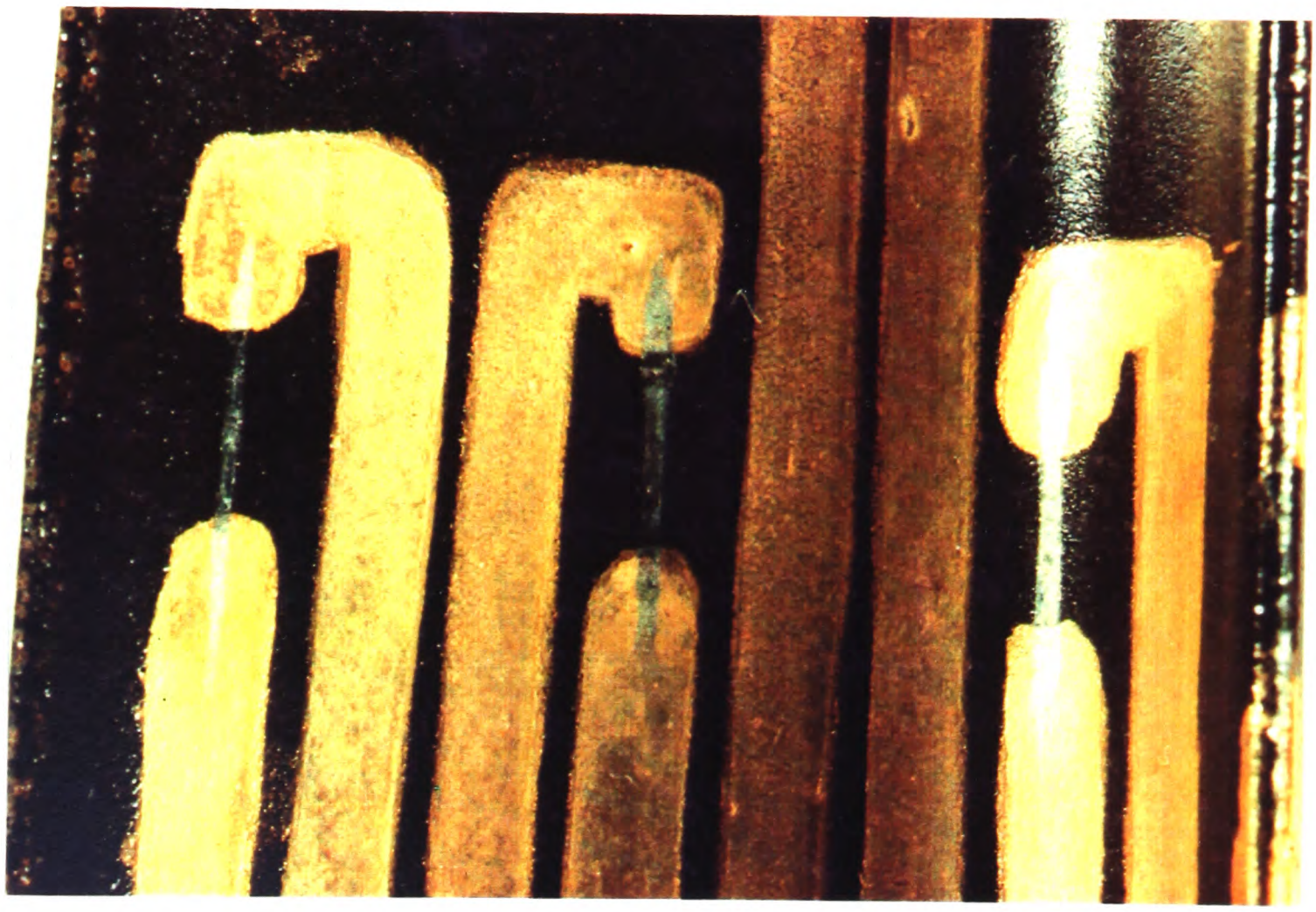

Figure 5.2: Thin Film Gauges Painted on Enamel Coated Turbine Blade

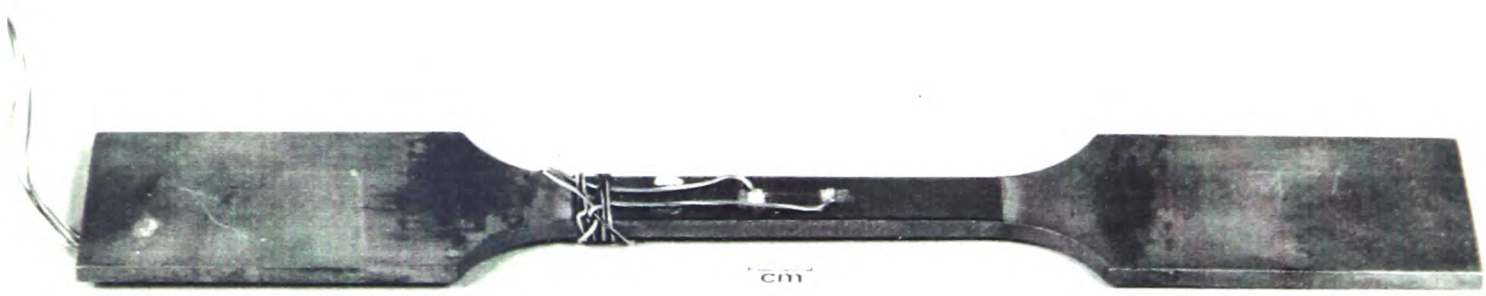

Figure 5.3: Tensile Test Specimen Instrumented with Thin Film Gauge.

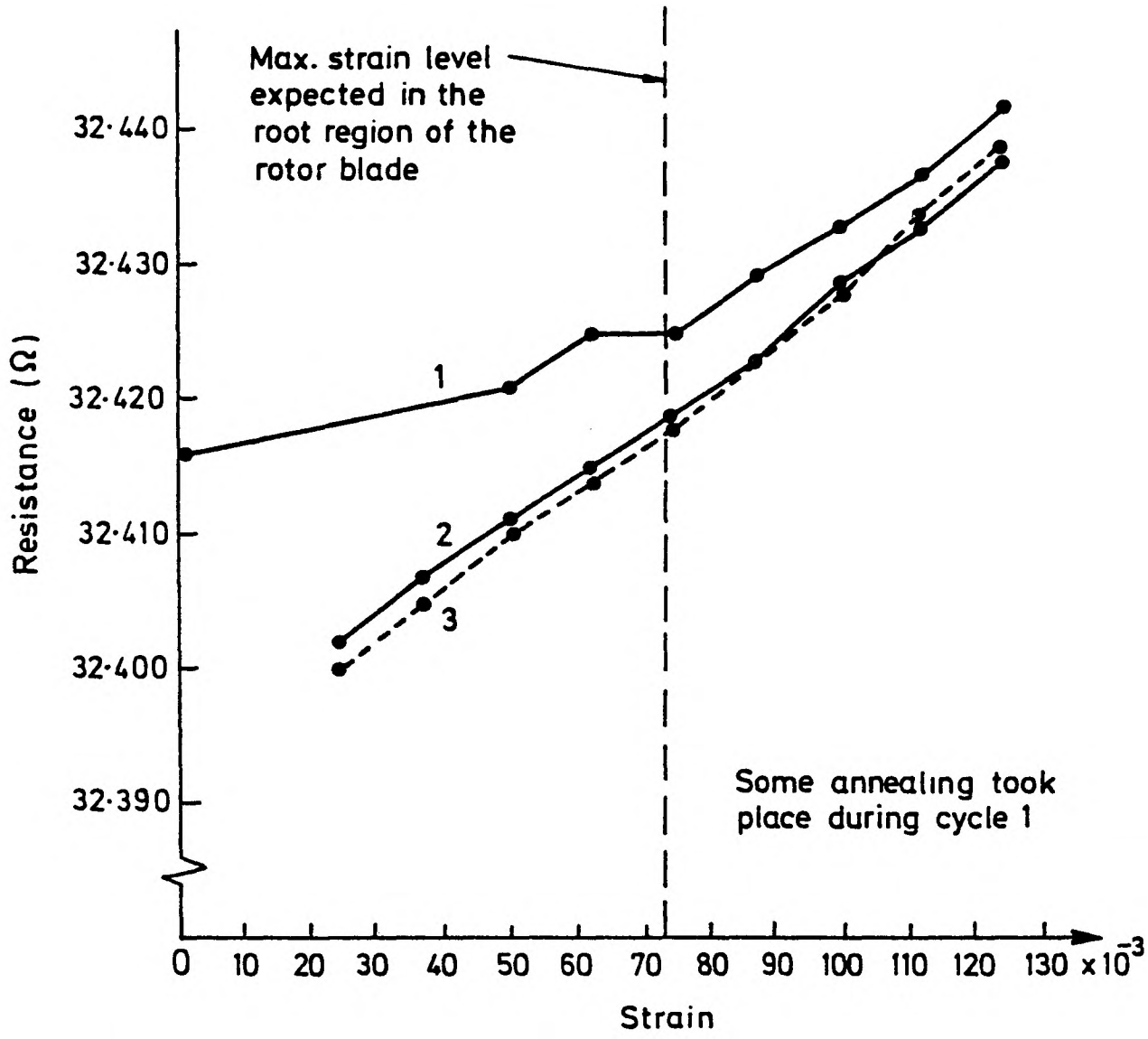

Figure 5.4: Variation of Gauge Resistance with Applied Strain.

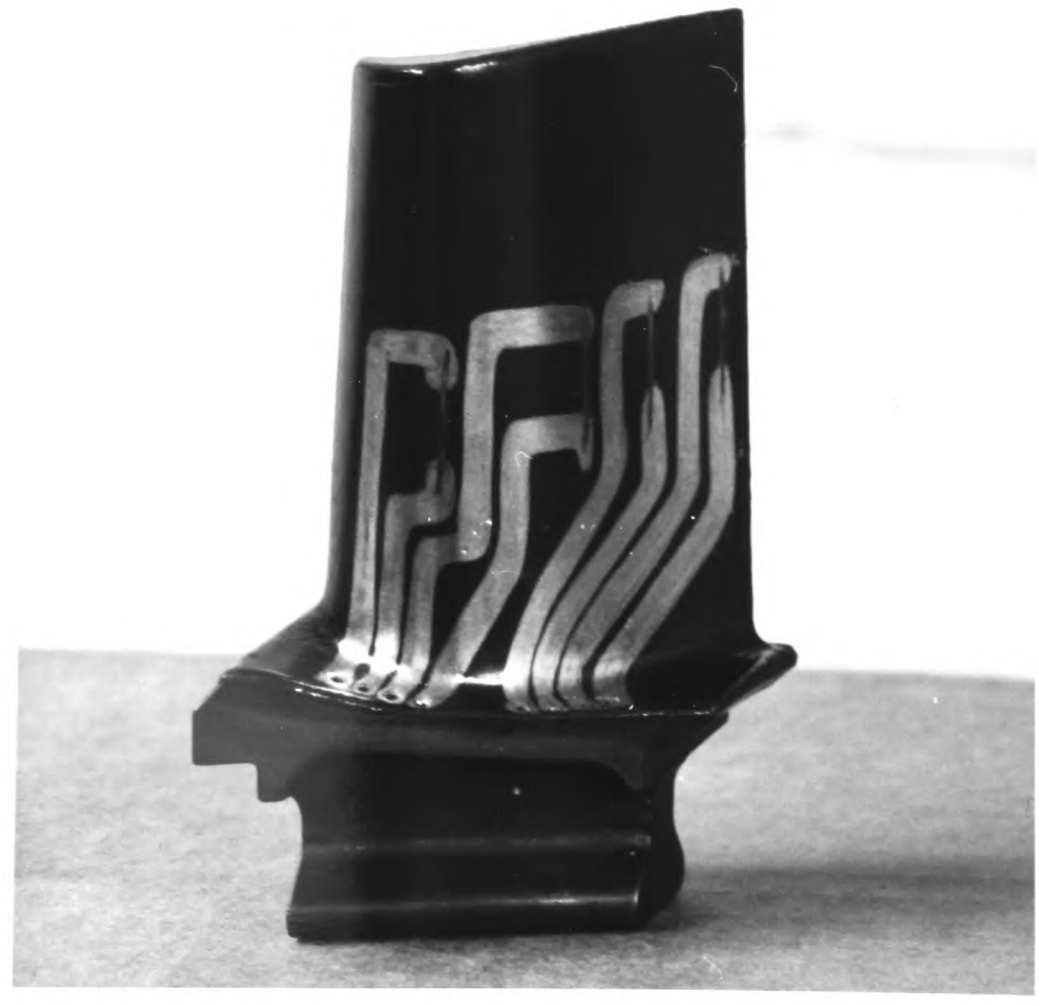

Figure 5.5: Instrumented Rotor Blade

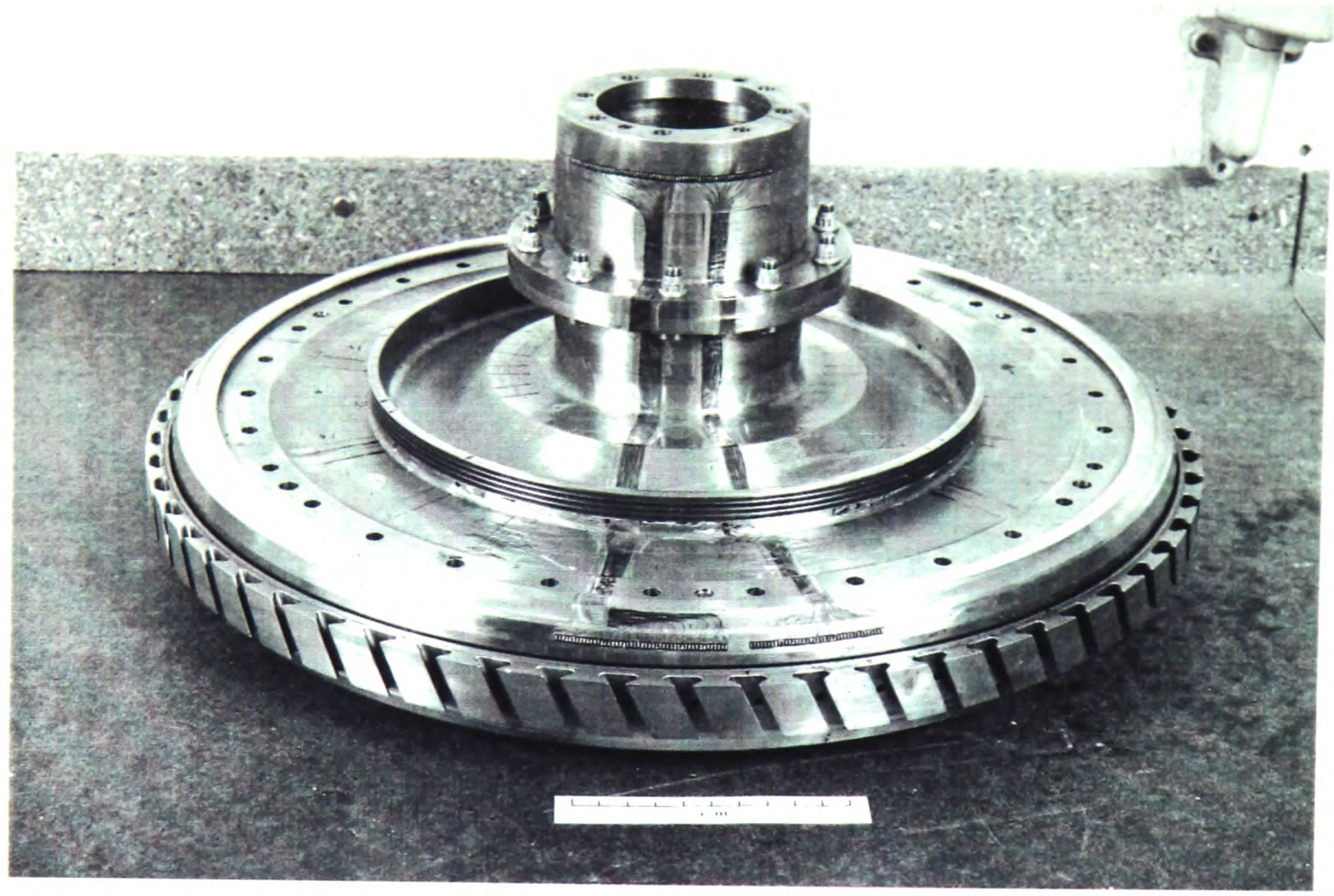

Figure 5.6: Arrangement of Wiring on Rotor Disc.

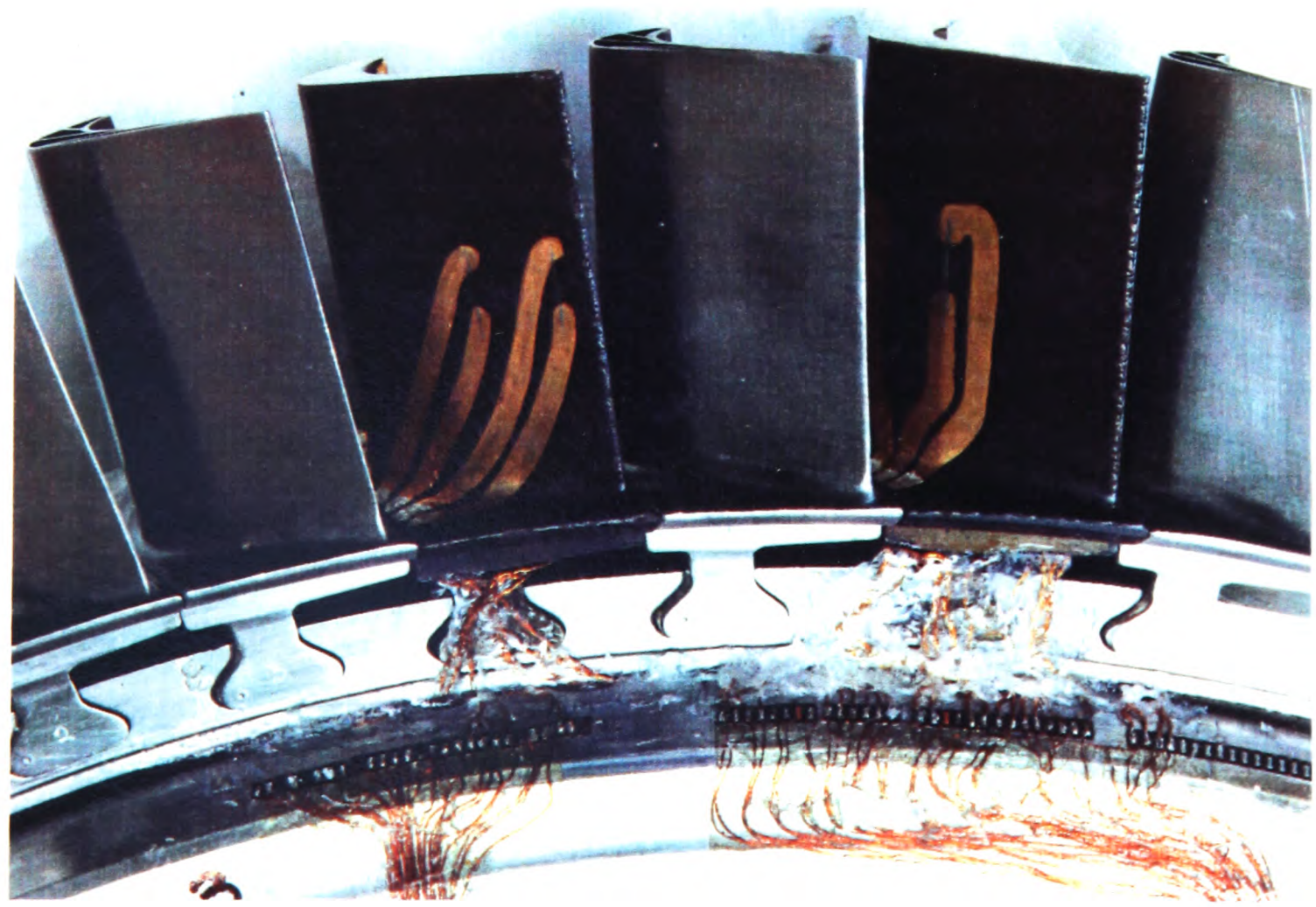

Figure 5.7: Detail of Wiring in Root Region

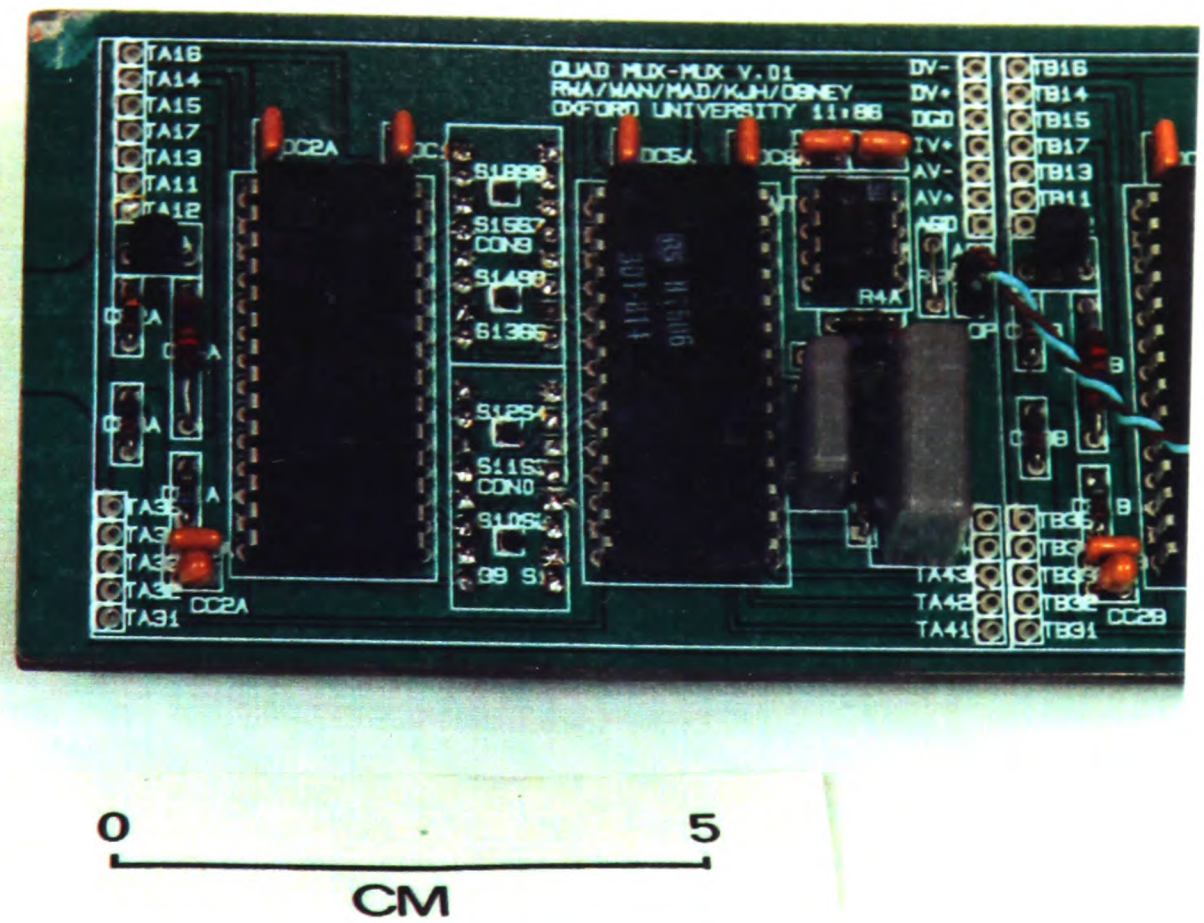

Figure 5.8: Close-up of Inshaft Circuit Board

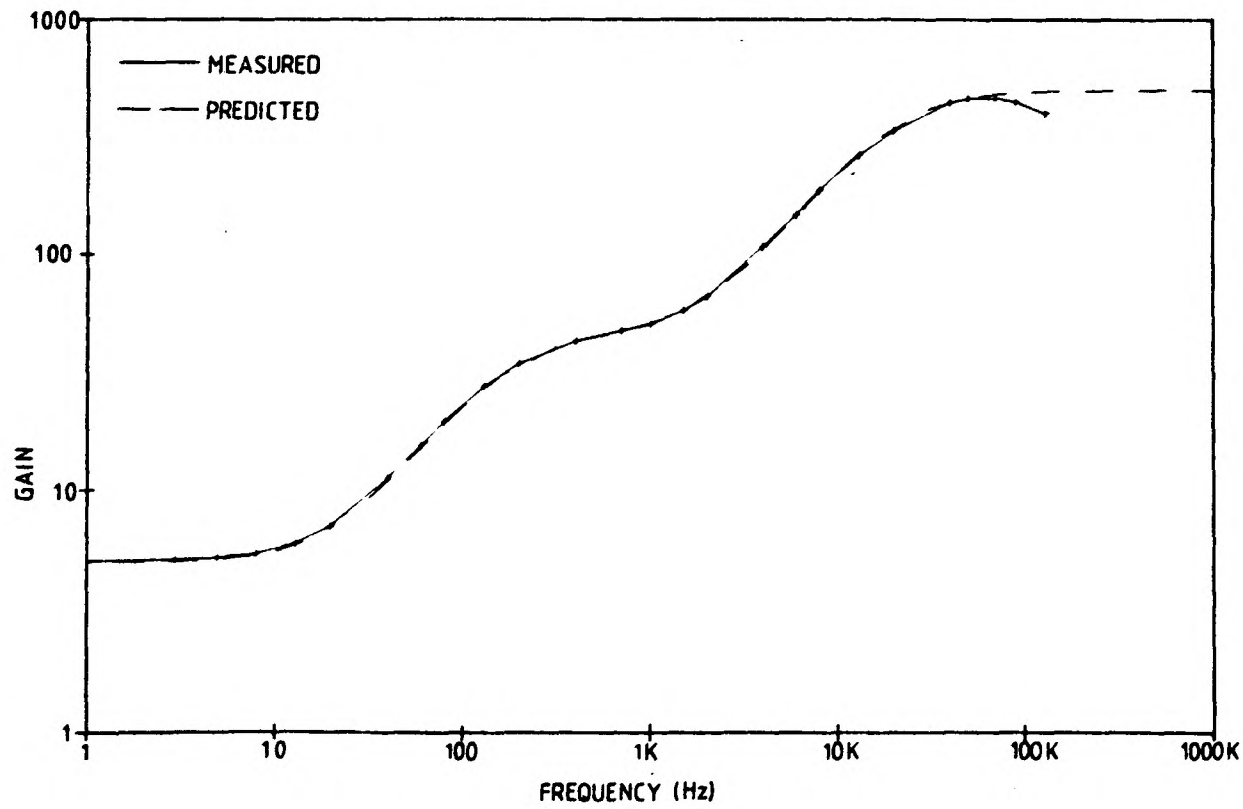

Figure 5.9: Measured and Predicted Frequency Response for Inshaft Circuit

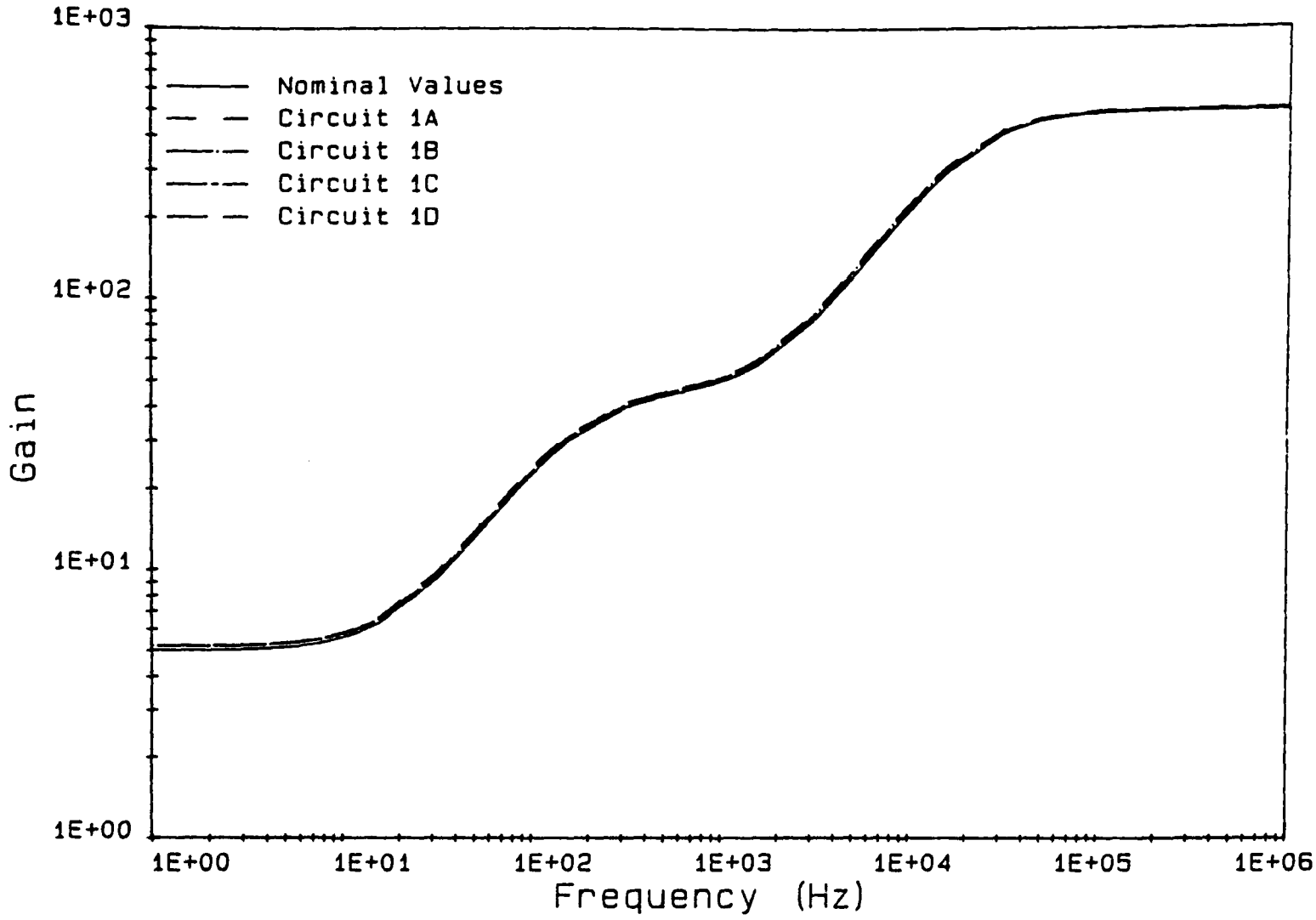

Figure 5.10: Frequency Response of In-shaft Circuit Calculated from Measured and Nominal Component Values

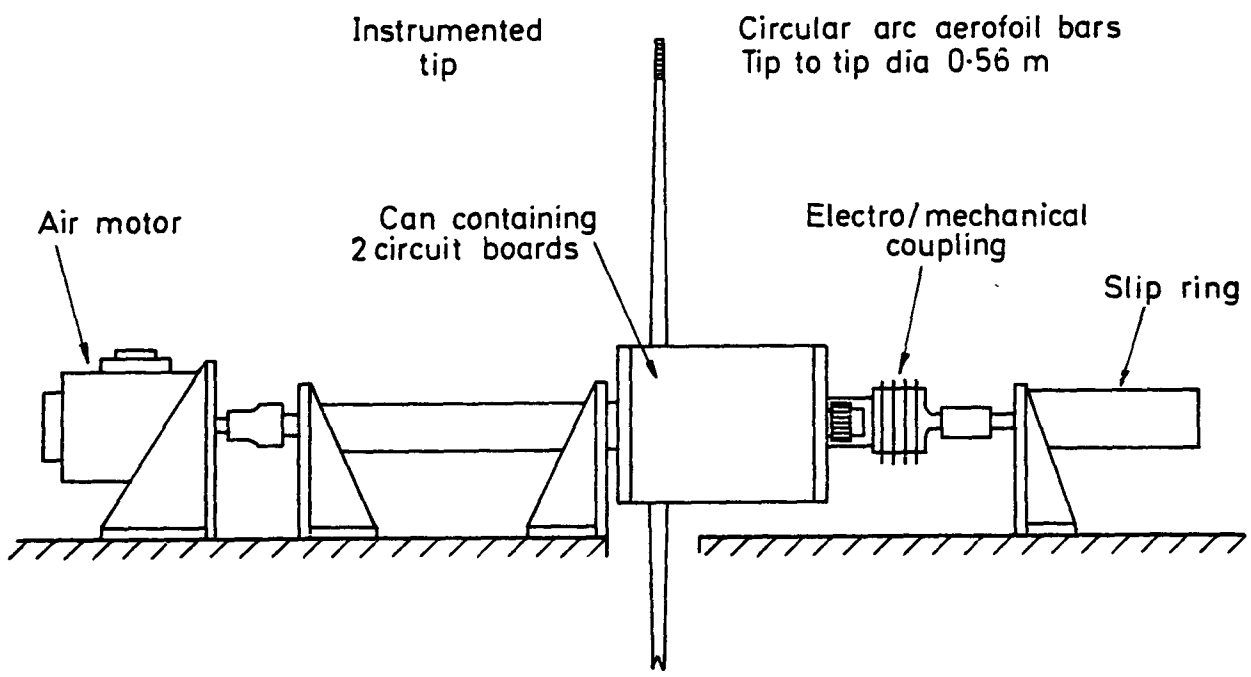

Figure 5.11: The Spinning Rig

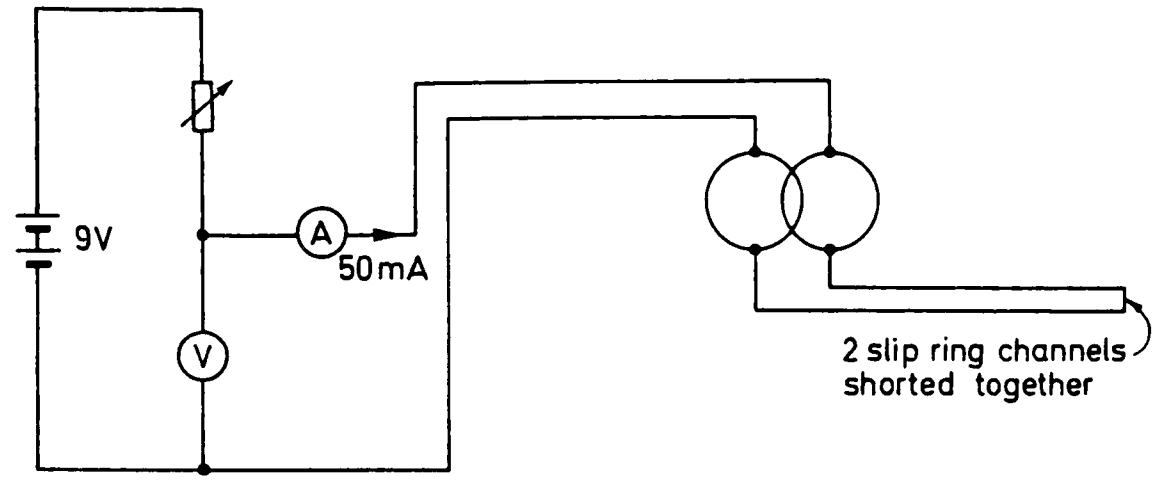

Figure 5.12: Circuit for Slipring Noise Tests

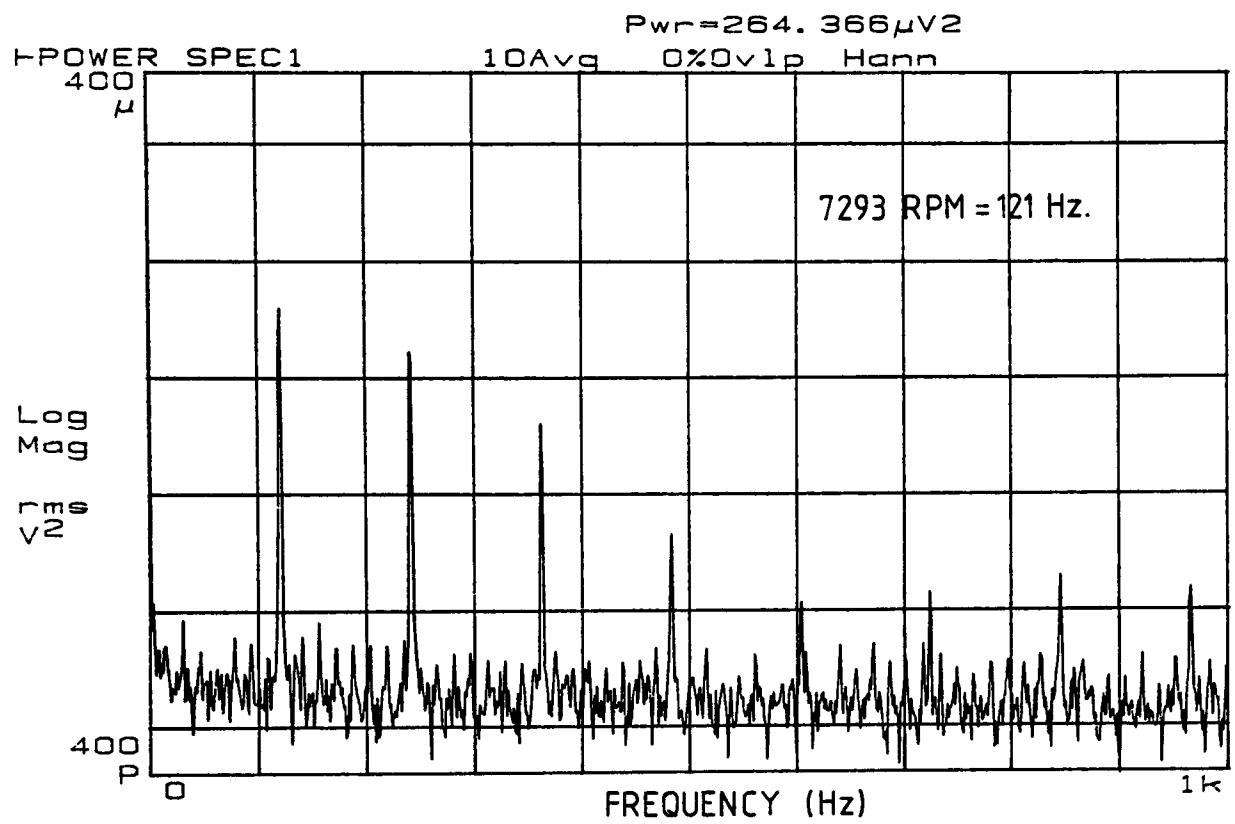

Figure 5.13: Noise Power Spectrum from Slipring Tests, Showing Peaks at Multiples of the Rotational Speed.

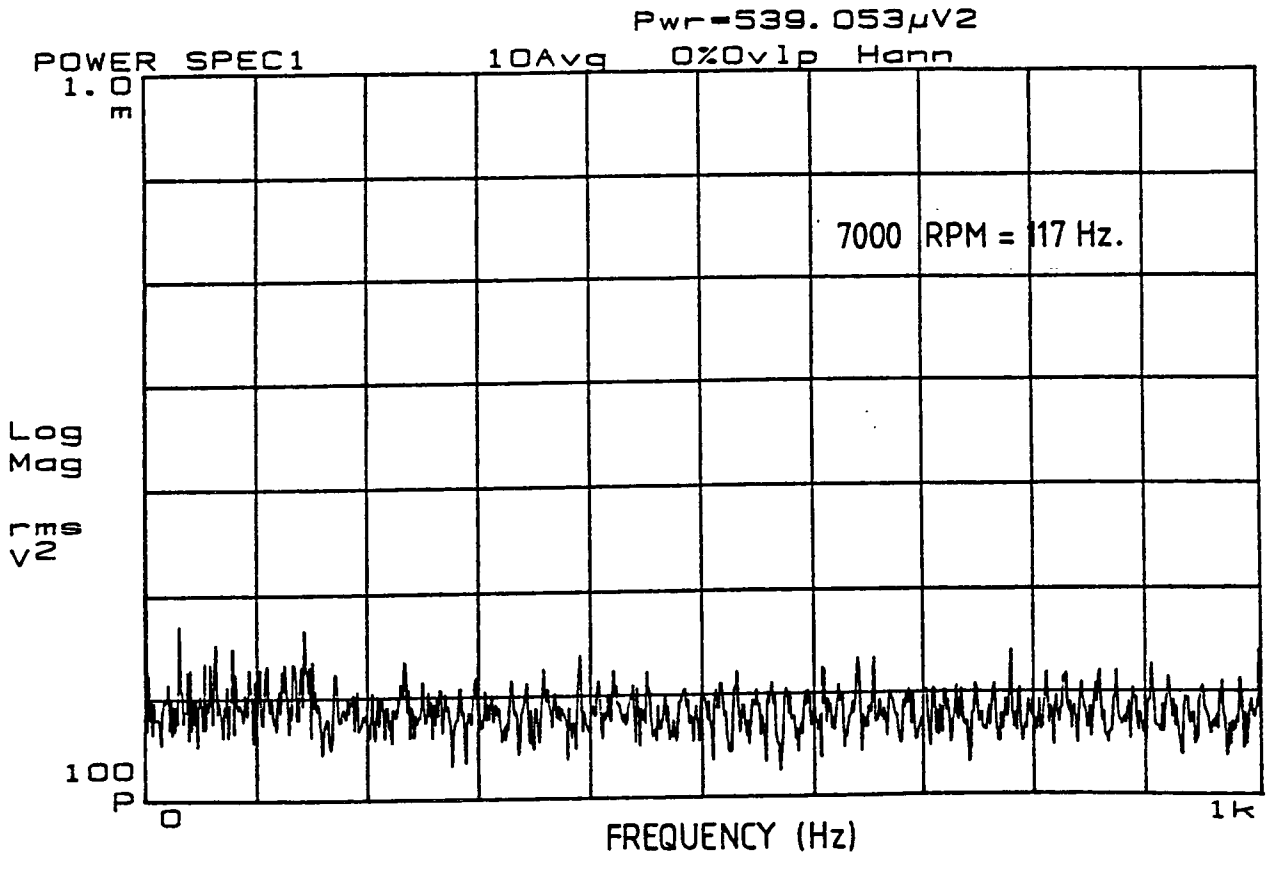

Figure 5.14: Noise Power Spectrum from Slipring Tests

Figure 5.15: Bar from Spinning Rig Instrumented with Thin Film Gauges.

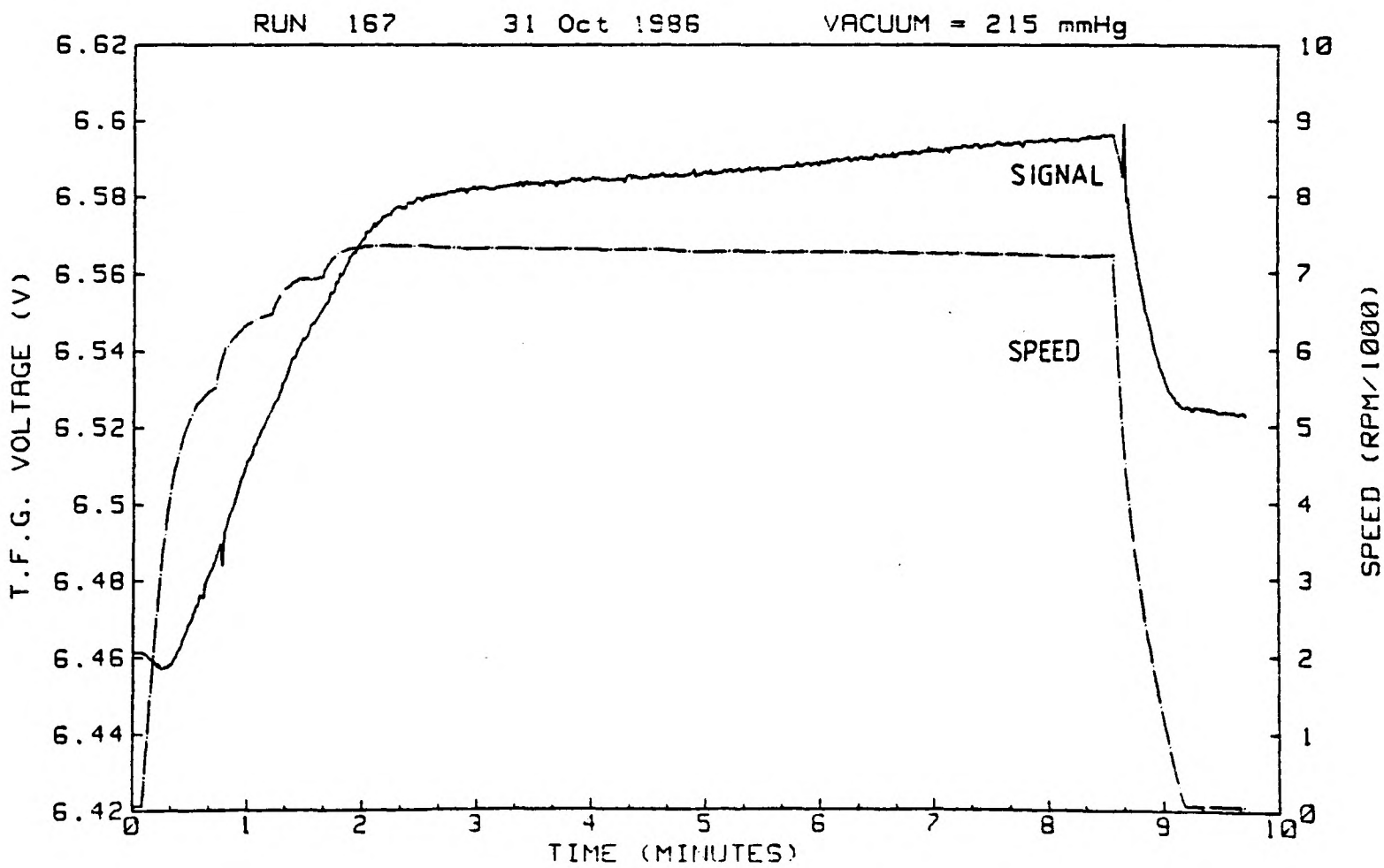

Figure 5.16: DC Shift in Signal from Thin Film Gauge - Vacuum 215 mmHg.

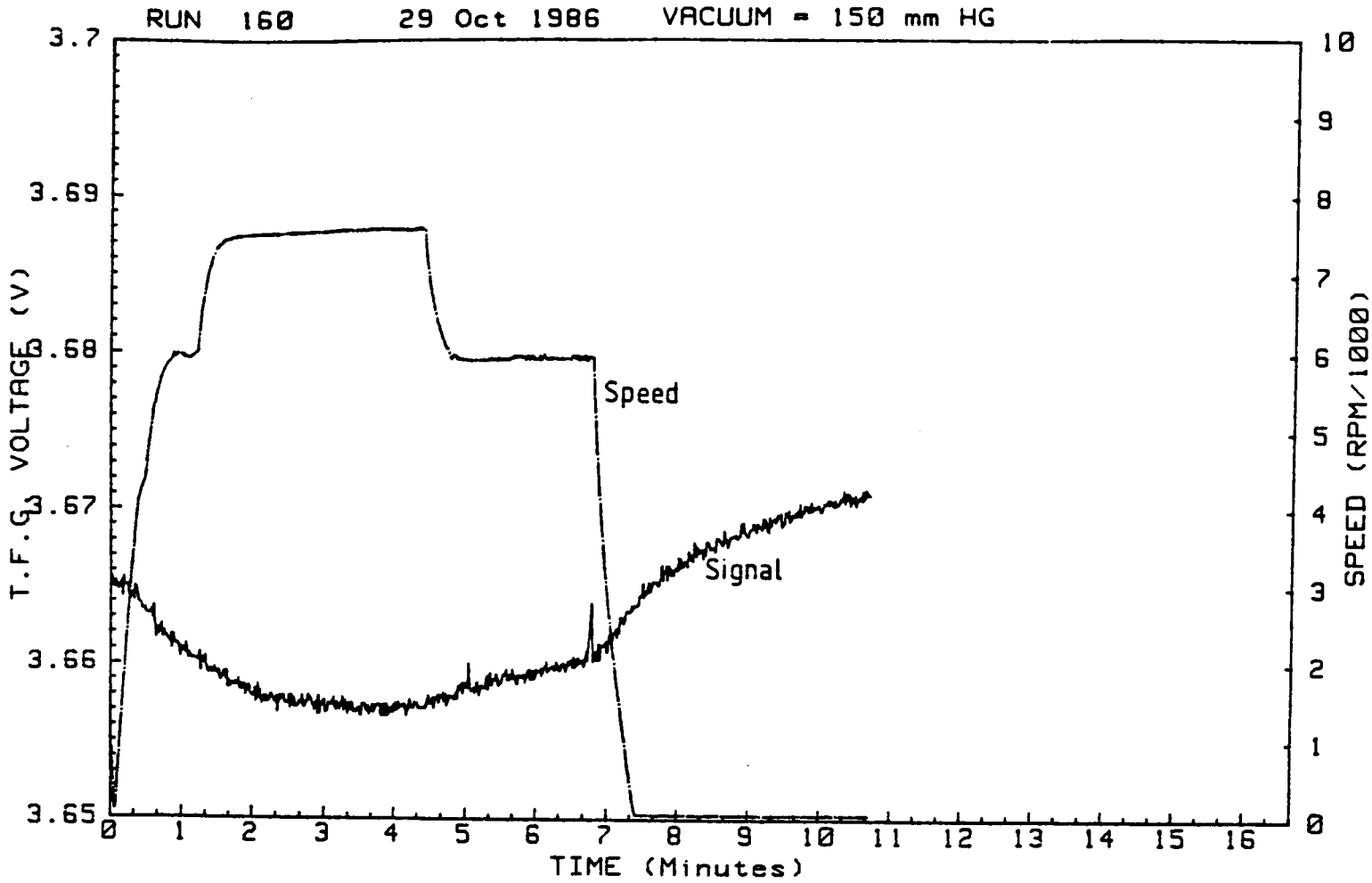

Figure 5.17: DC Shift in Signal from 50Ω Resistor - Vacuum 150 mmHg.

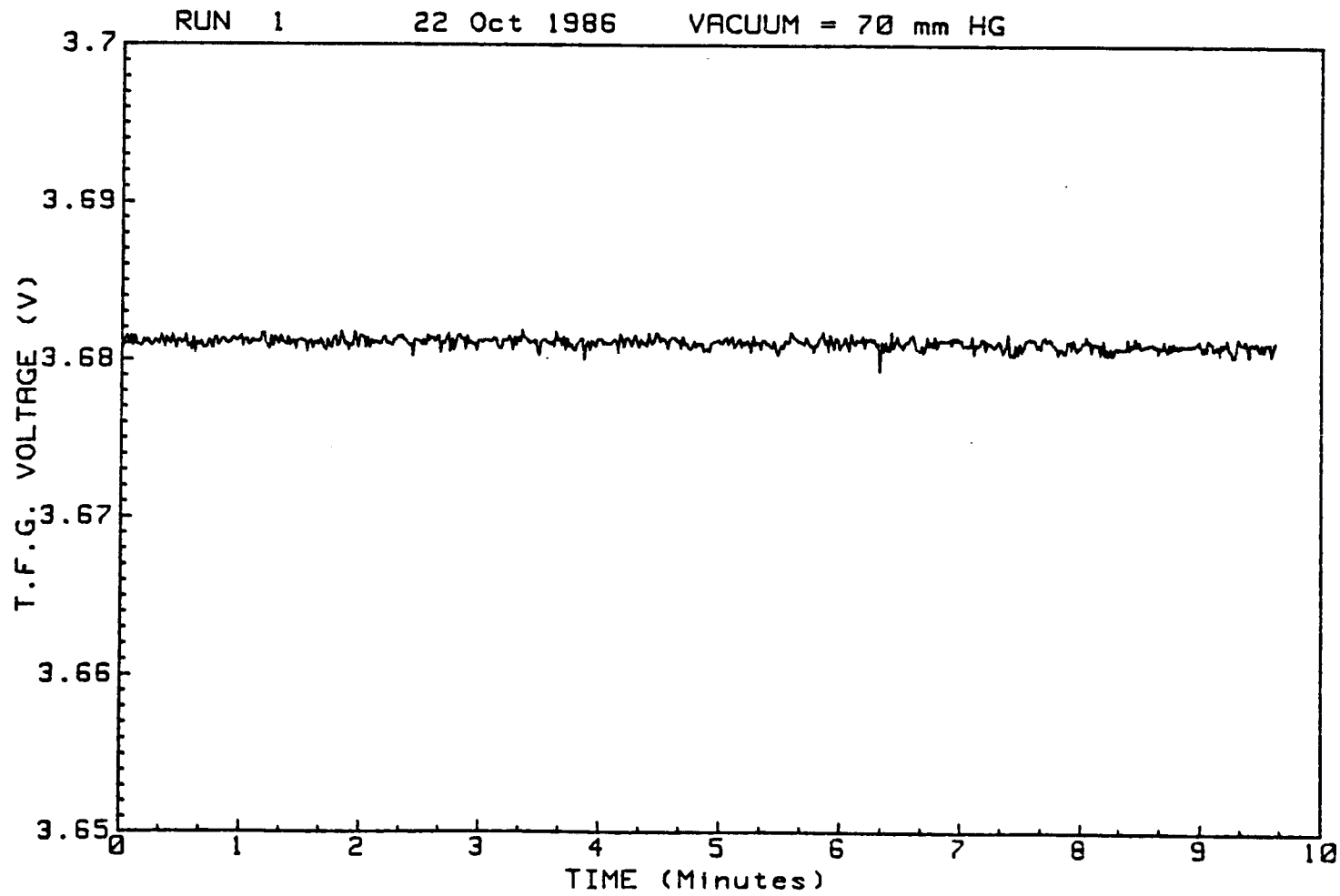

Figure 5.18: DC Shift in Signal from Stationary 50Ω Resistor - Vacuum 70 mmHg.

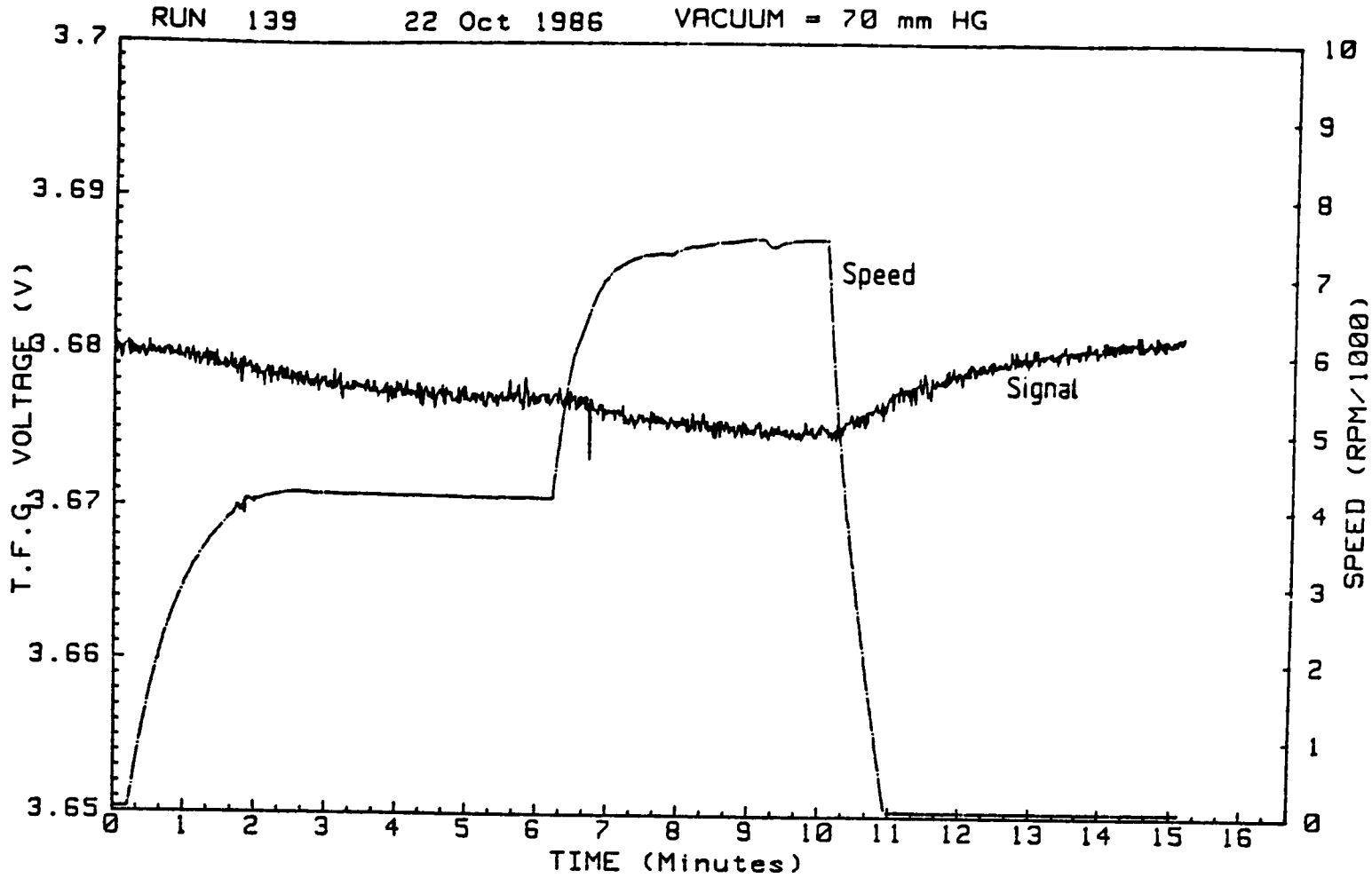

Figure 5.19: DC Shift in Signal from 50Ω Resistor - Vacuum 70 mmHg.

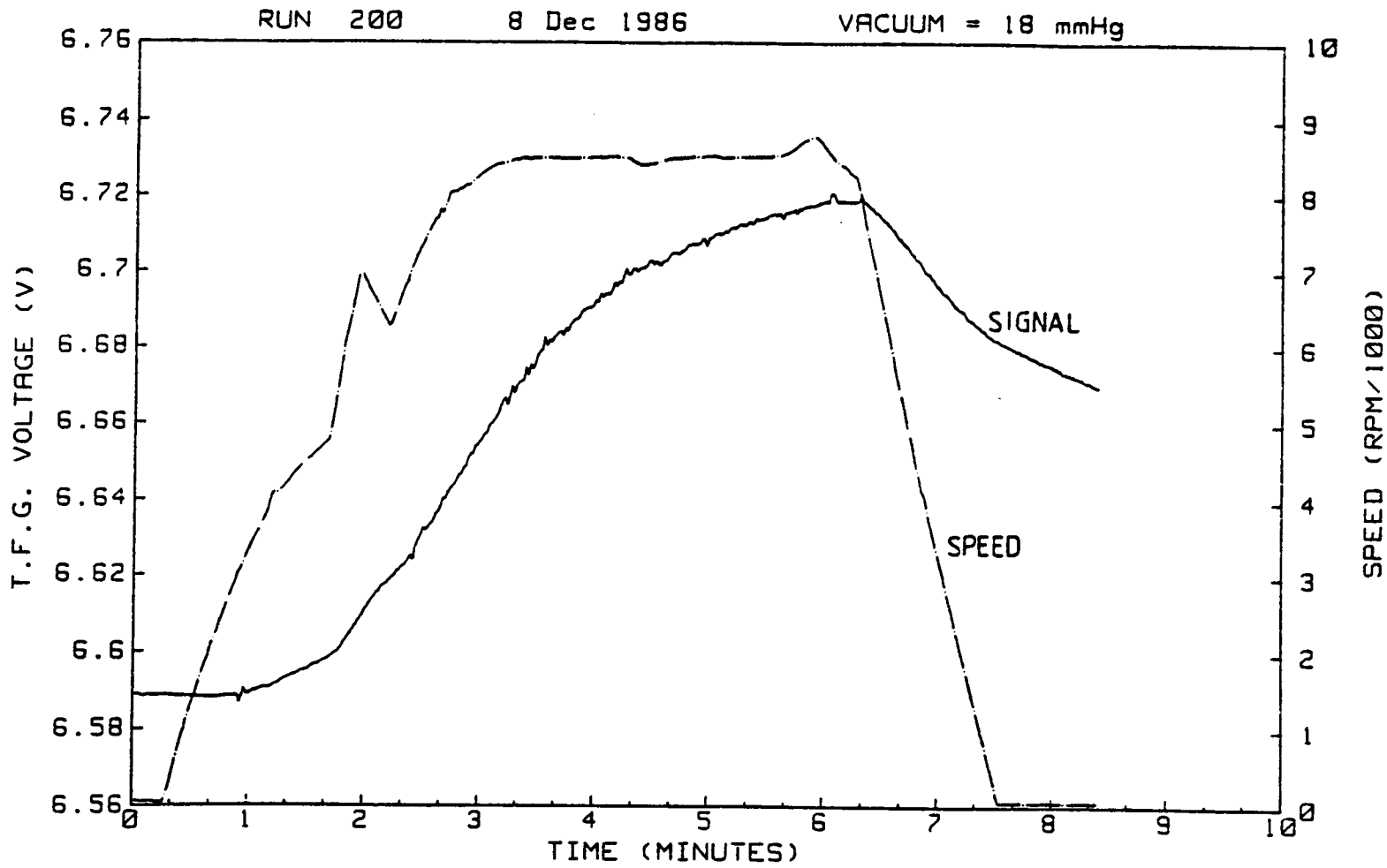

Figure 5.20: DC Shift in Signal from Thin Film Gauge - Vacuum 18 mmHg

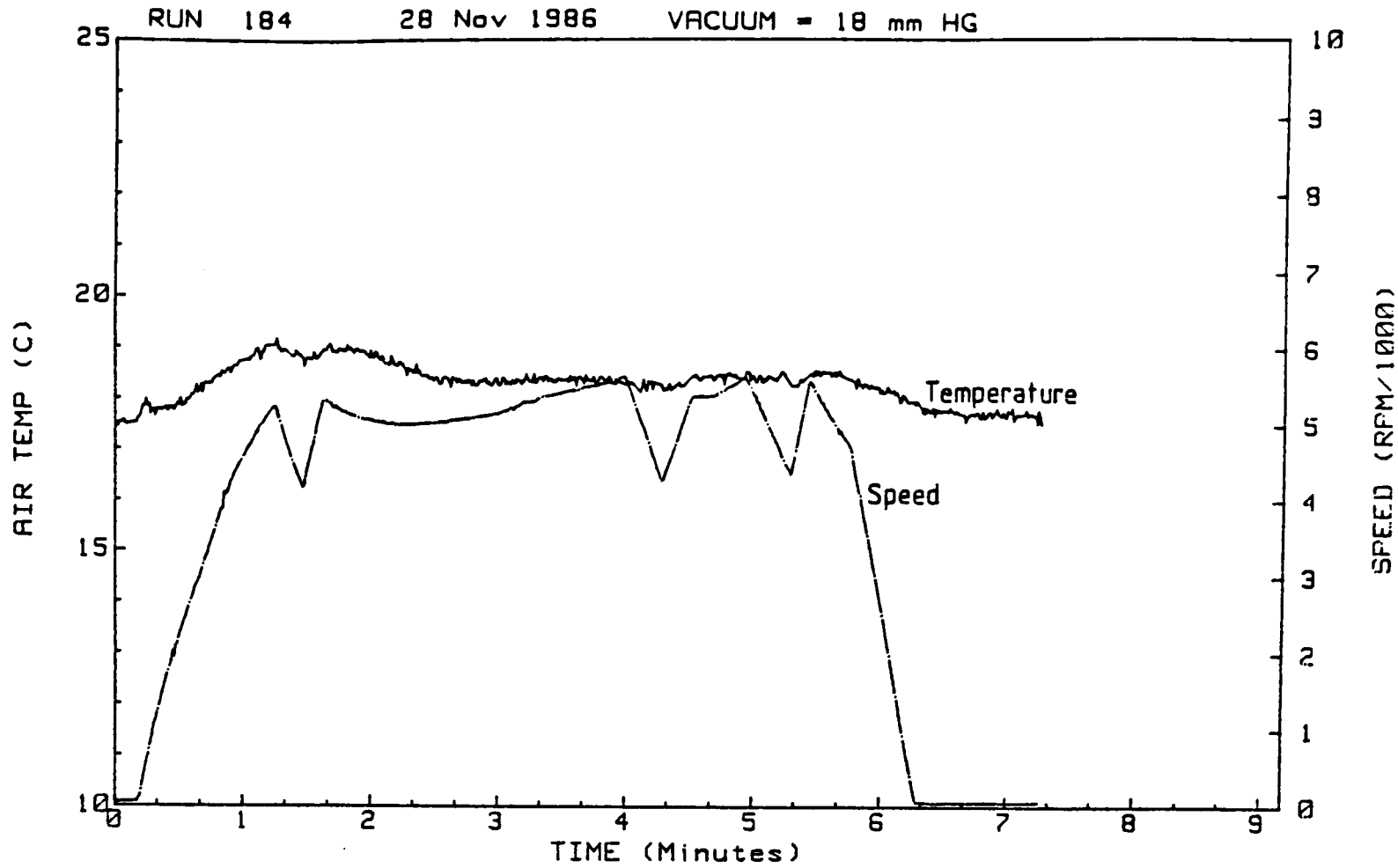

Figure 5.21: Variation of Air Temperature in Tank With Rotational Speed

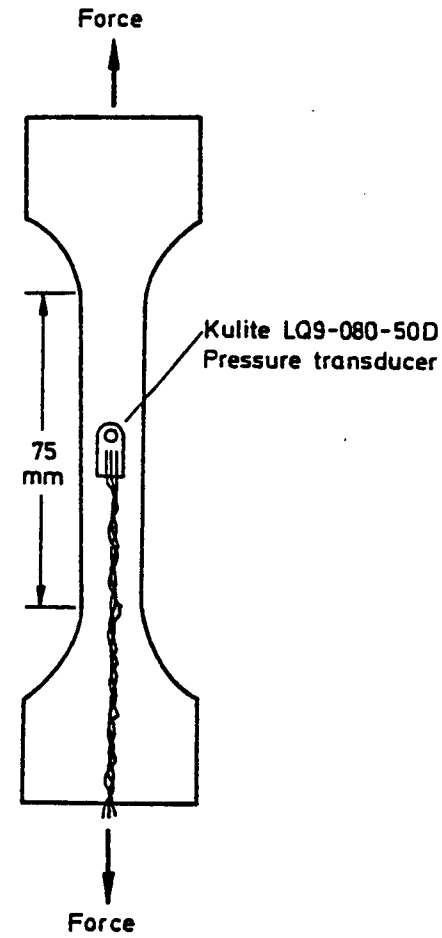

Figure 5.22: "Flat Pack" Pressure Transducer Mounted on Tensile Test Specimen

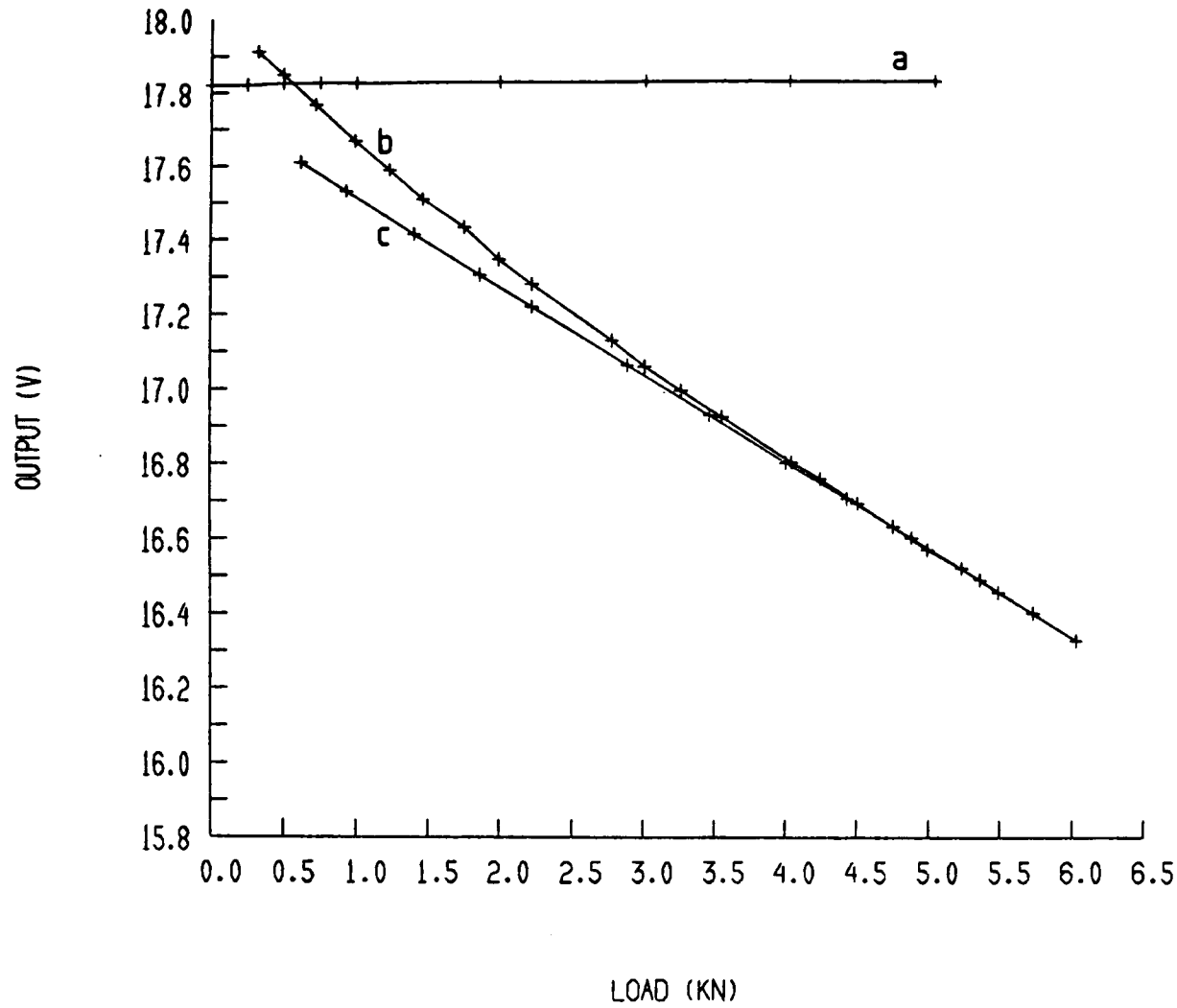

Figure 5.23: Variation of Pressure Transducer Output with Tensile Load.
(a) Transducer Mounted With Double-sided Adhesive Tape
(b) Gauge Mounted with "Super Glue" - Load Increasing
(c) Gauge Mounted with "Super Glue" - Load Decreasing

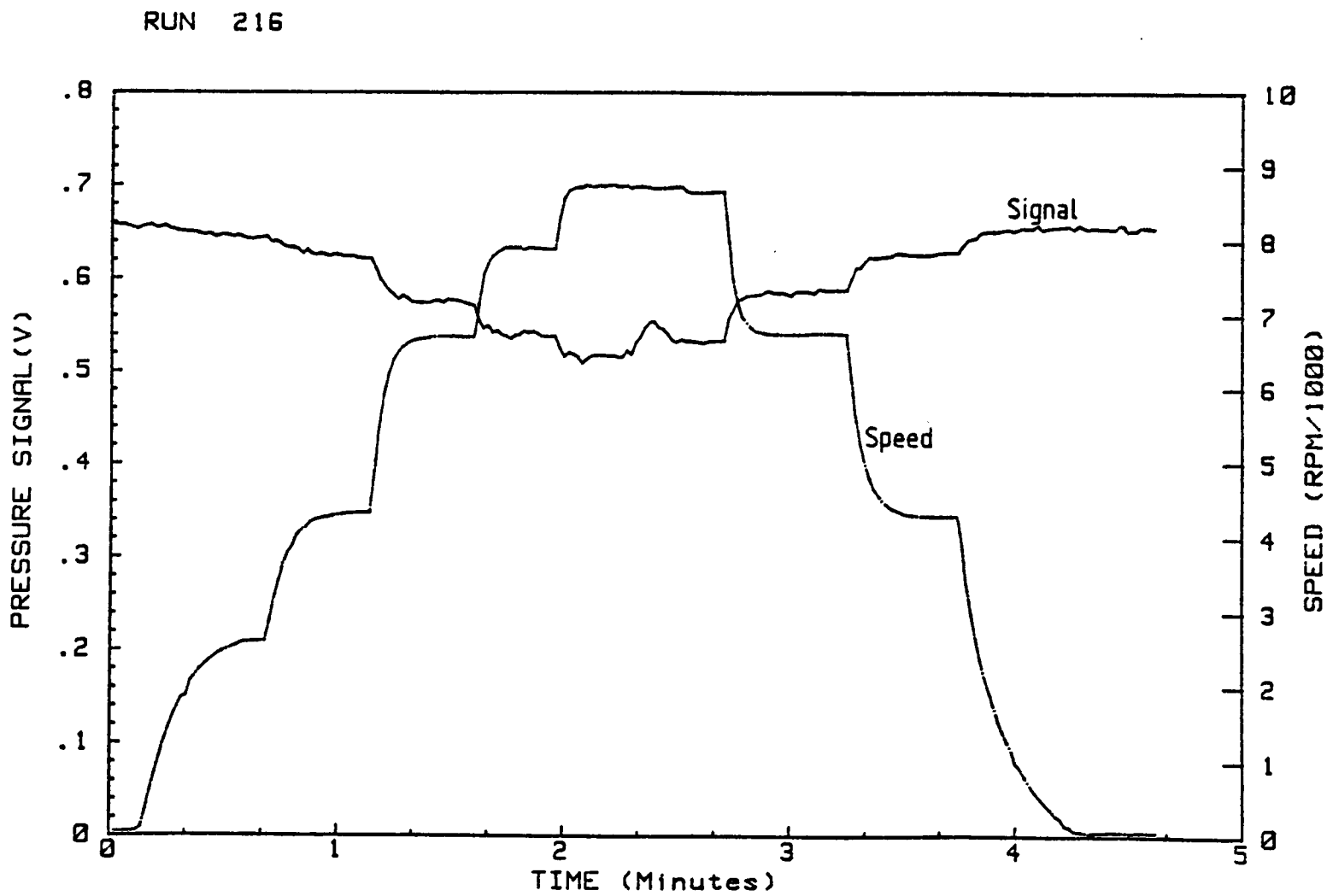

Figure 5.24: Variation of Output from Pressure Transducer with Rotational Speed - Atmospheric Pressure

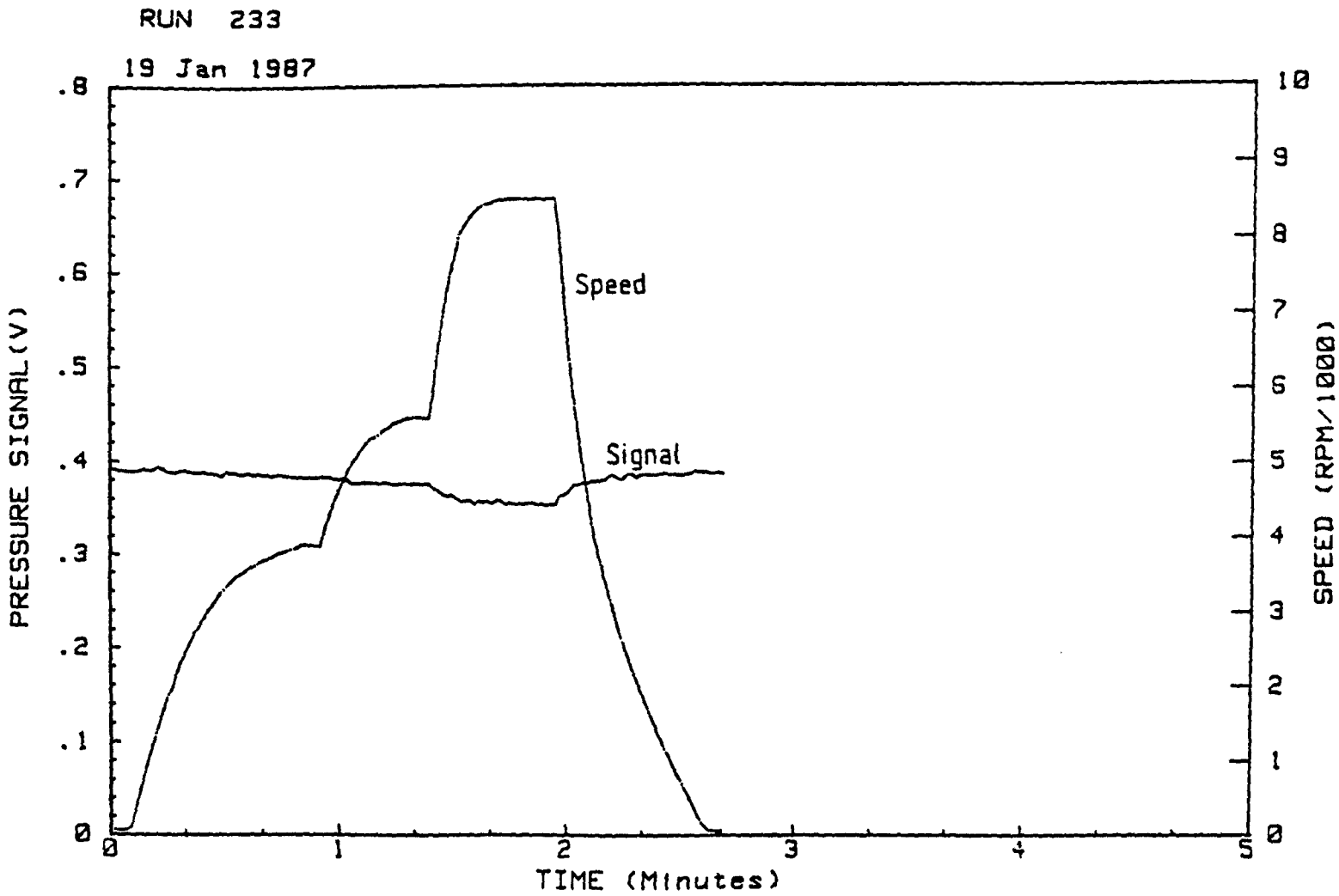

Figure 5.25: Variation of Output from Pressure Transducer with Rotational Speed - Vacuum 250 mmHg

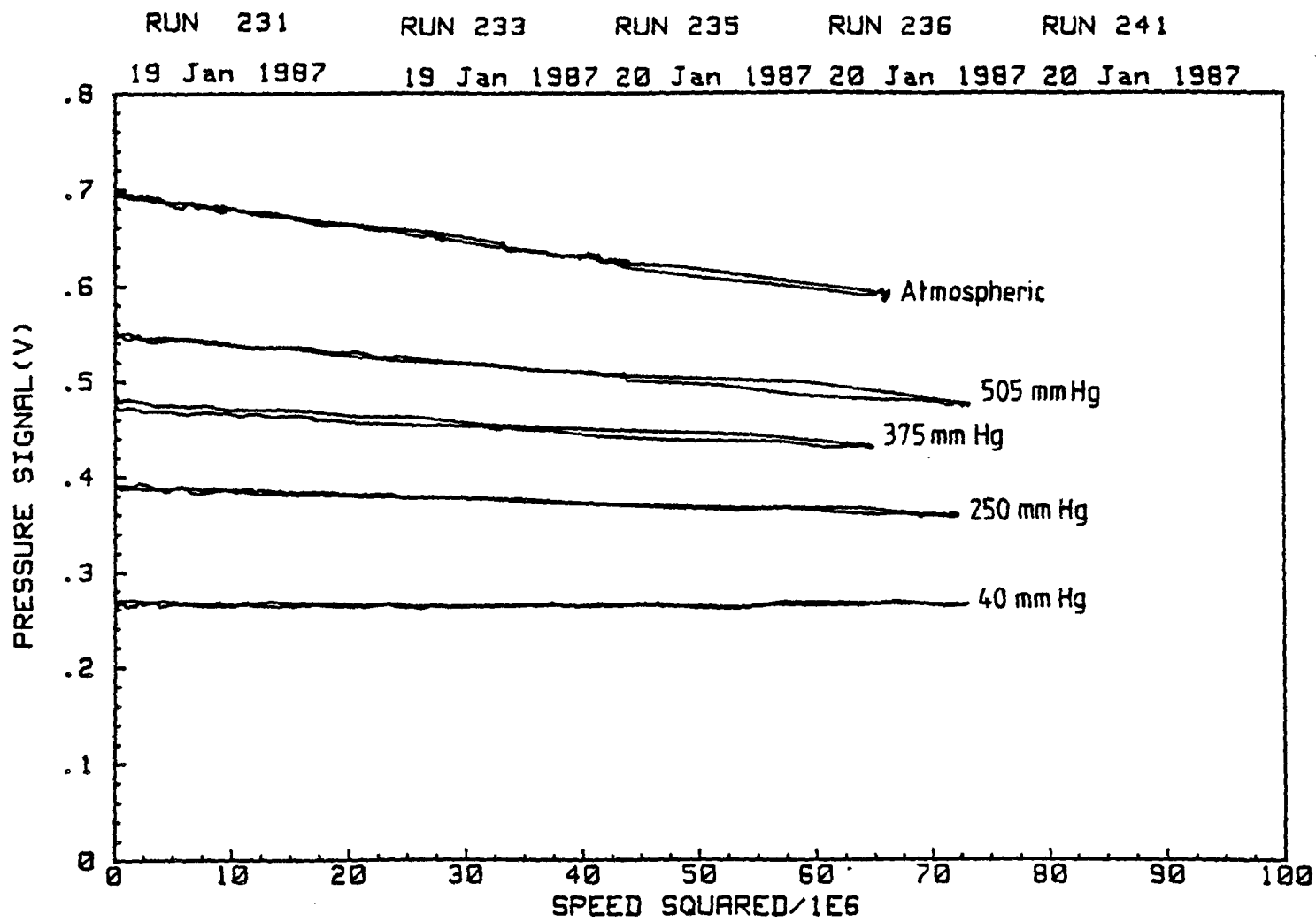

Figure 5.26: Variation of Output from Pressure Transducer with Square of Rotational Speed

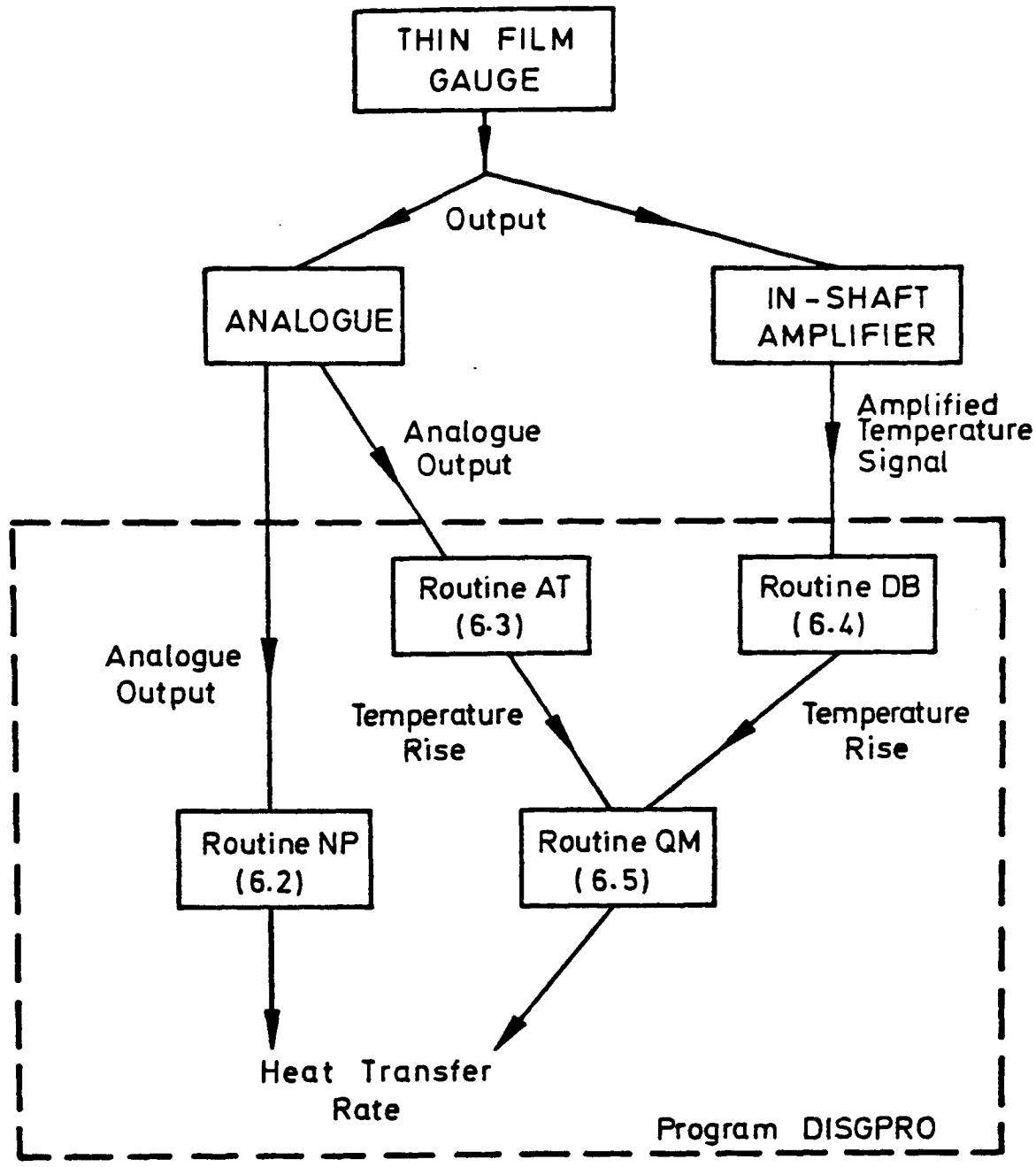

Figure 6.1: Methods of Processing the Output from a Thin Film Gauge on a Two Layered Substrate

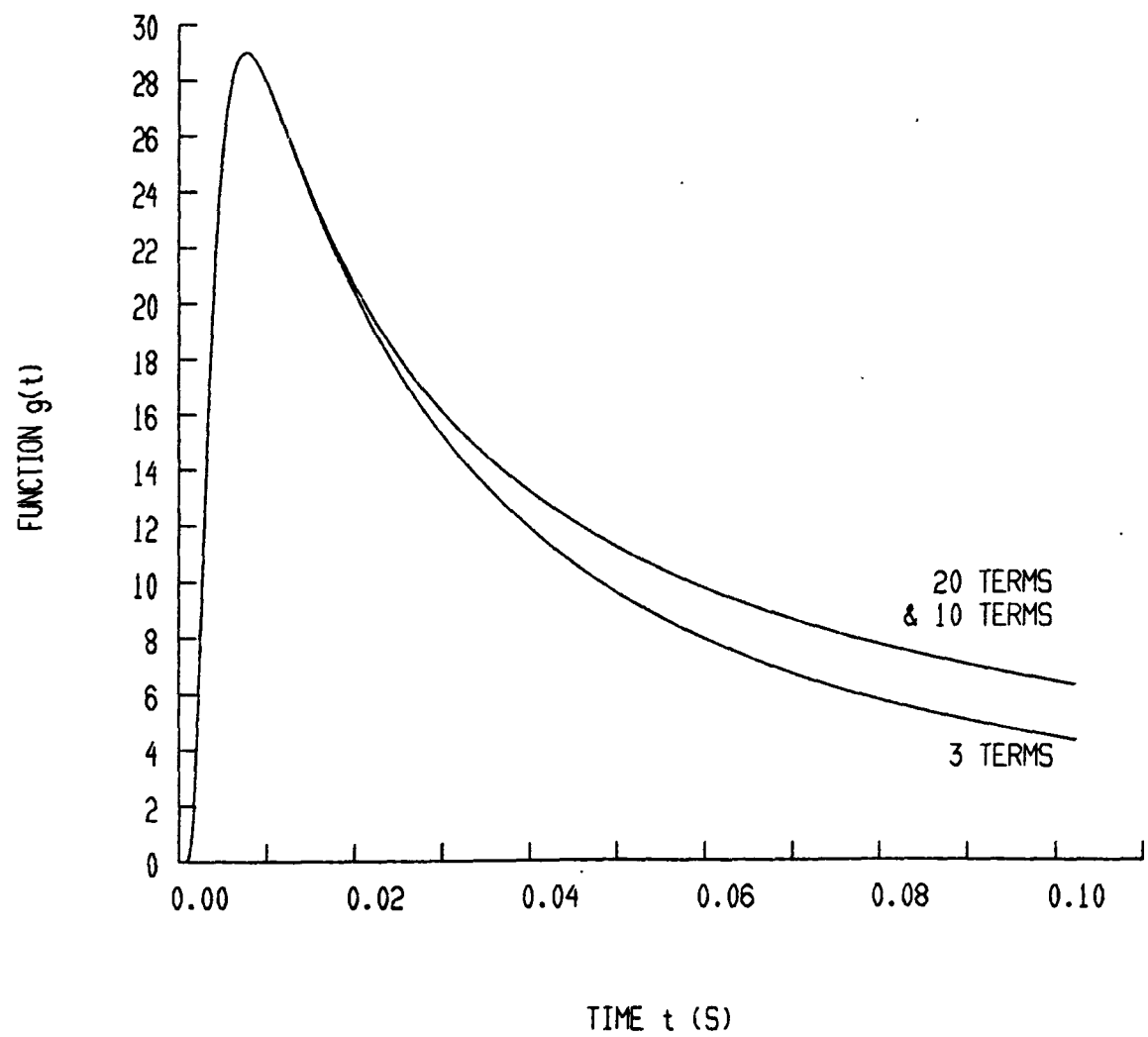

Figure 6.2: The Function g(t) (Equation 6.9)

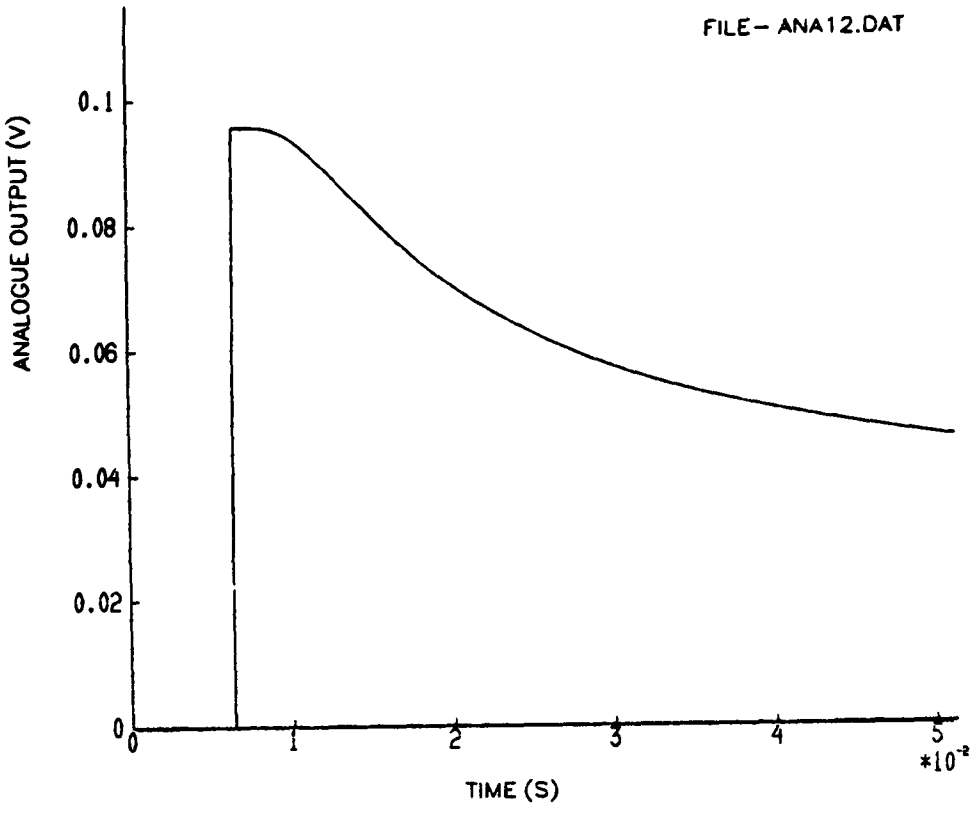

Figure 6.3: Predicted Analogue Output from Thin Film Gauge on Two Layered Substrate Subject to Step in Heat Transfer Rate

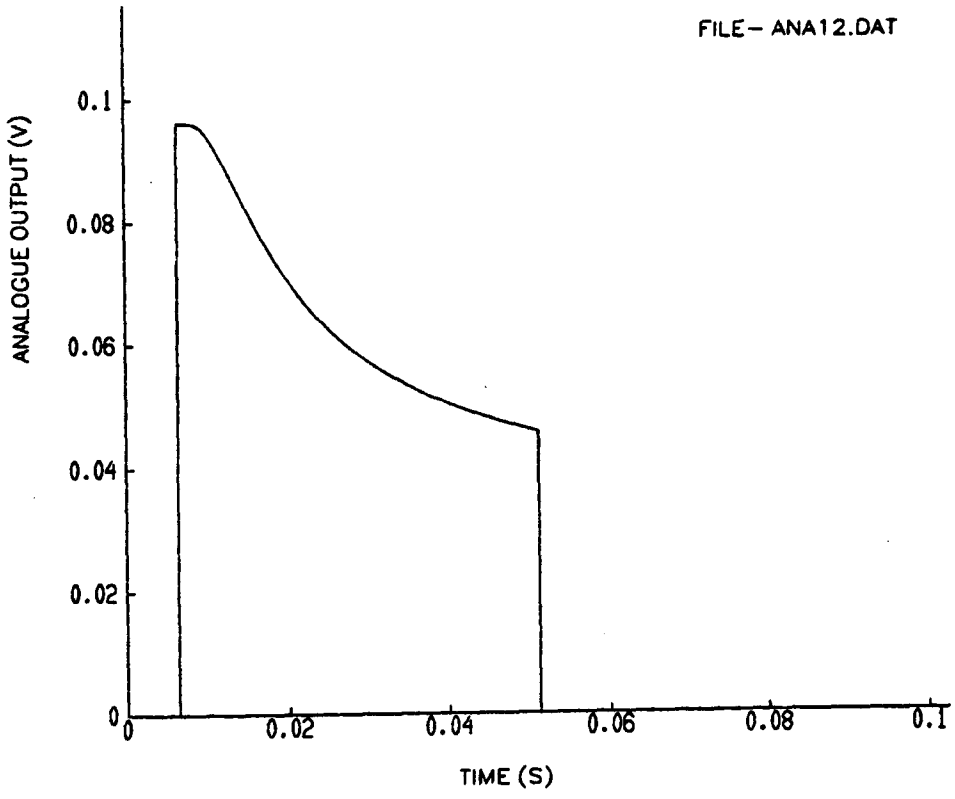

Figure 6.4: Predicted Analogue Output from Thin Film Gauge on two Layered Substrate Extended to Twice Original Length with Zero Padding

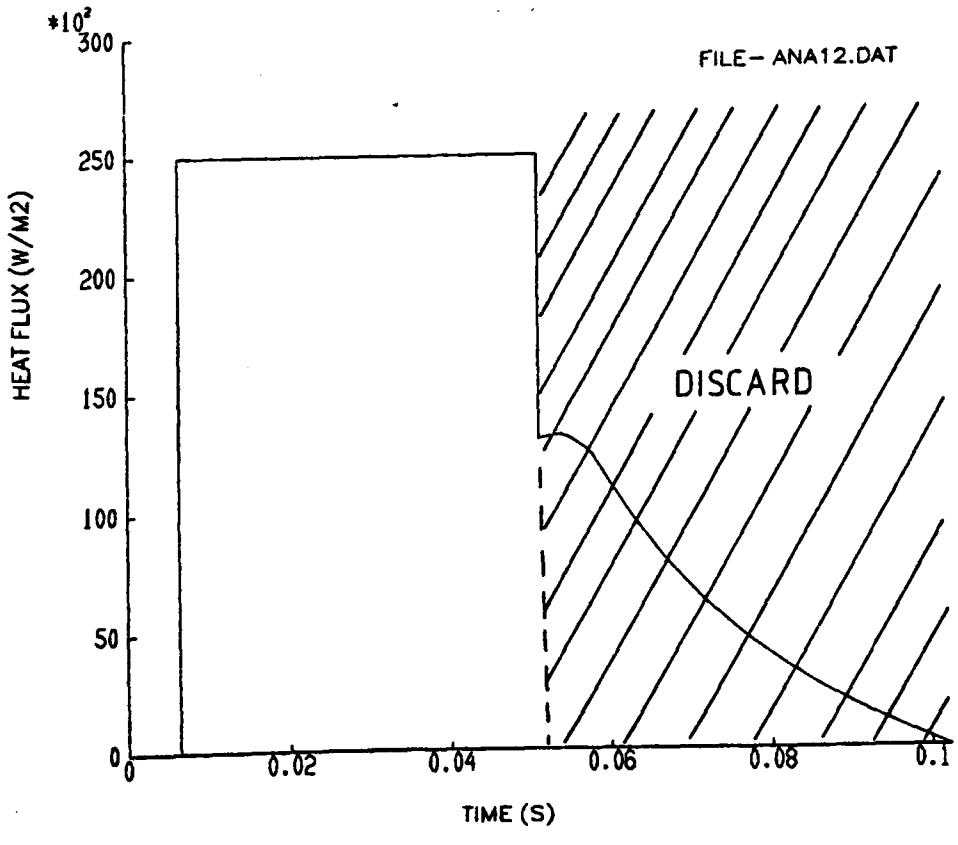

Figure 6.5: Heat Flux Calculated from Analogue Output Shown in Figure 6.4

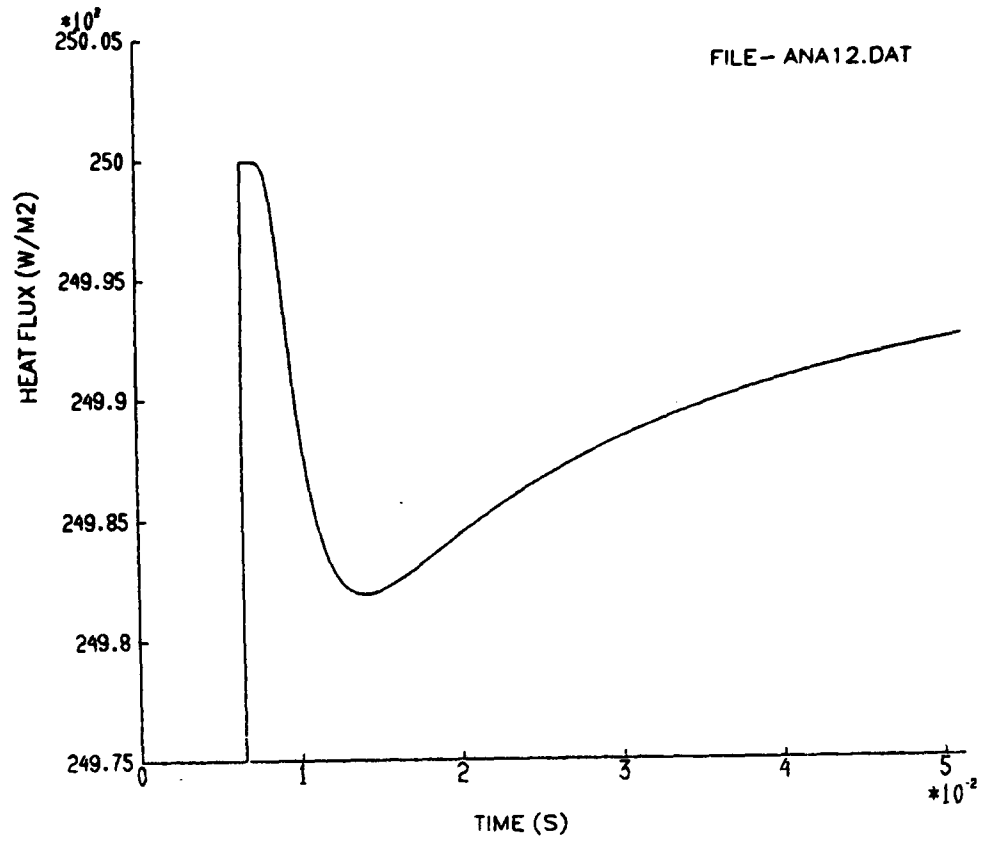

Figure 6.6: Expanded View of Figure 6.5, Showing Error in Reconstructed Heat Transfer Rate

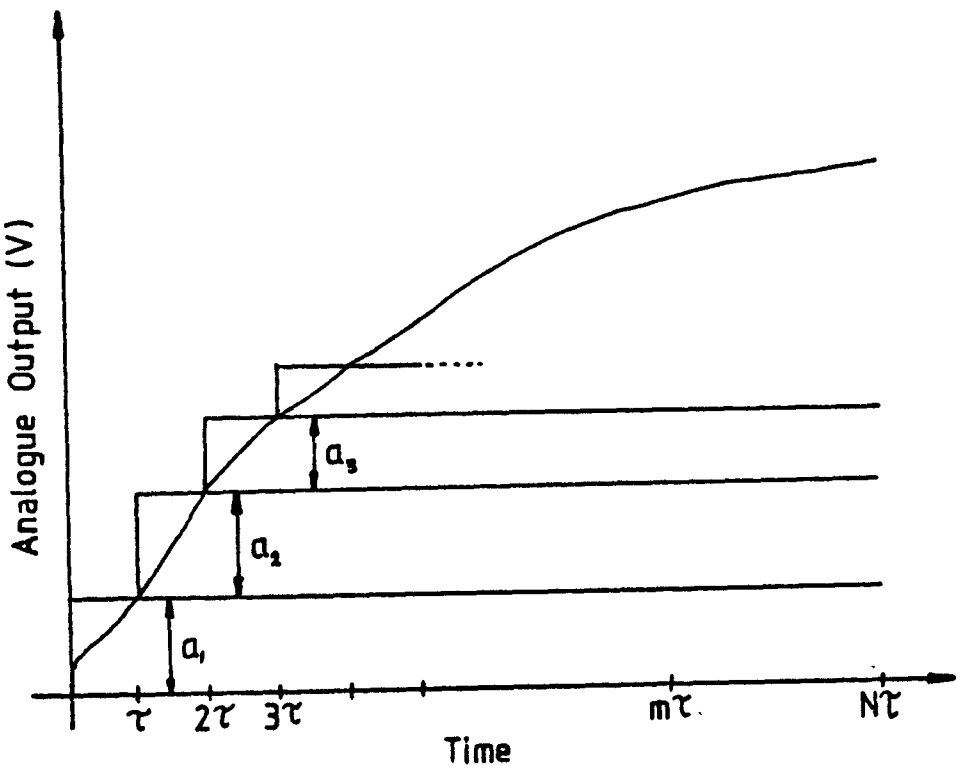

Figure 6.7: Representation of Analogue Output as a Series of Steps

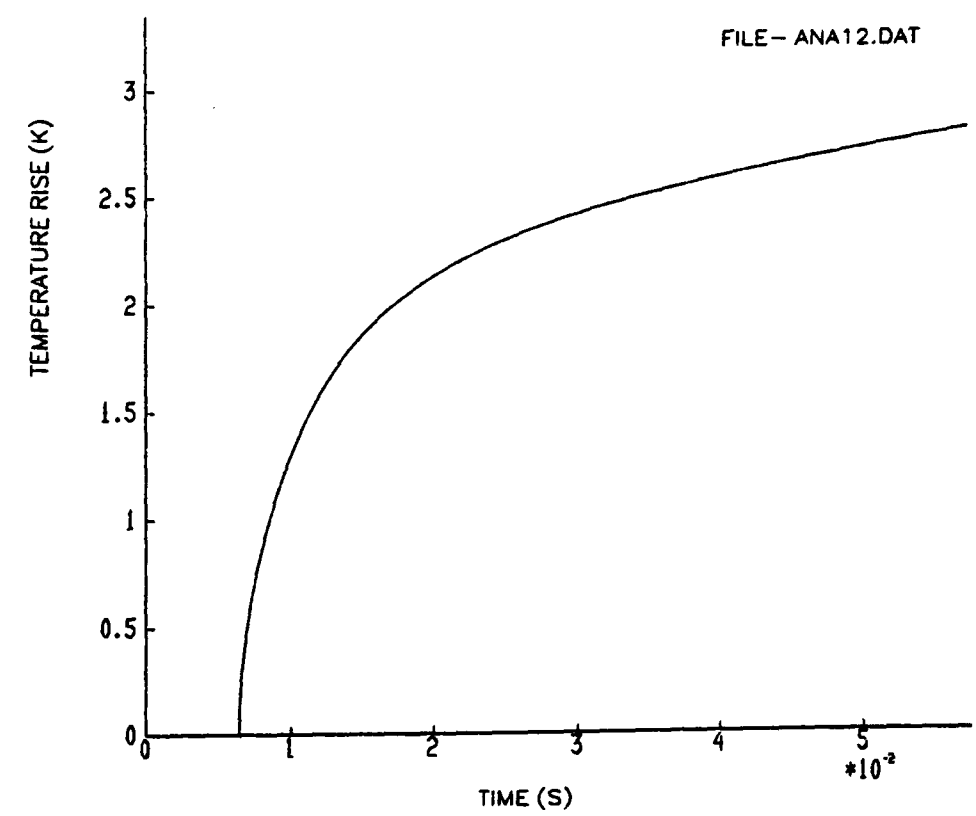

Figure 6.8: Temperature Rise Calculated from Predicted Analogue Output Shown in Figure 6.3

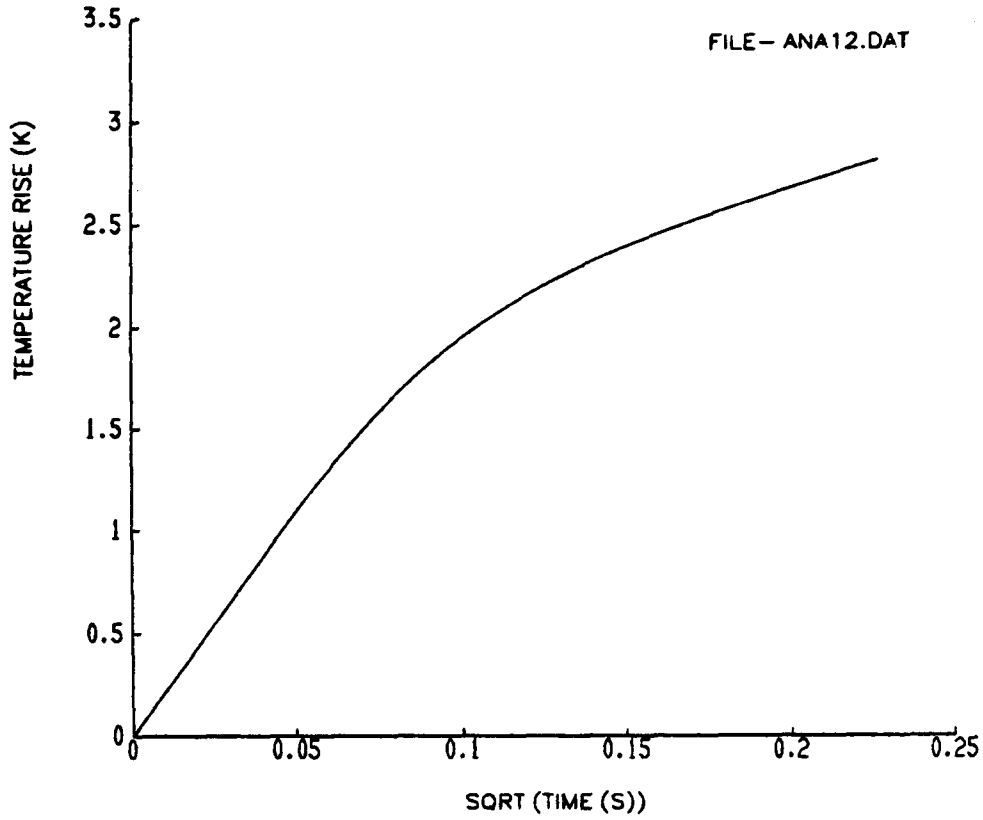

Figure 6.9: Temperature Rise Calculated from Predicted Analogue Output Shown in Figure 6.3, Plotted Against Square Root of Time

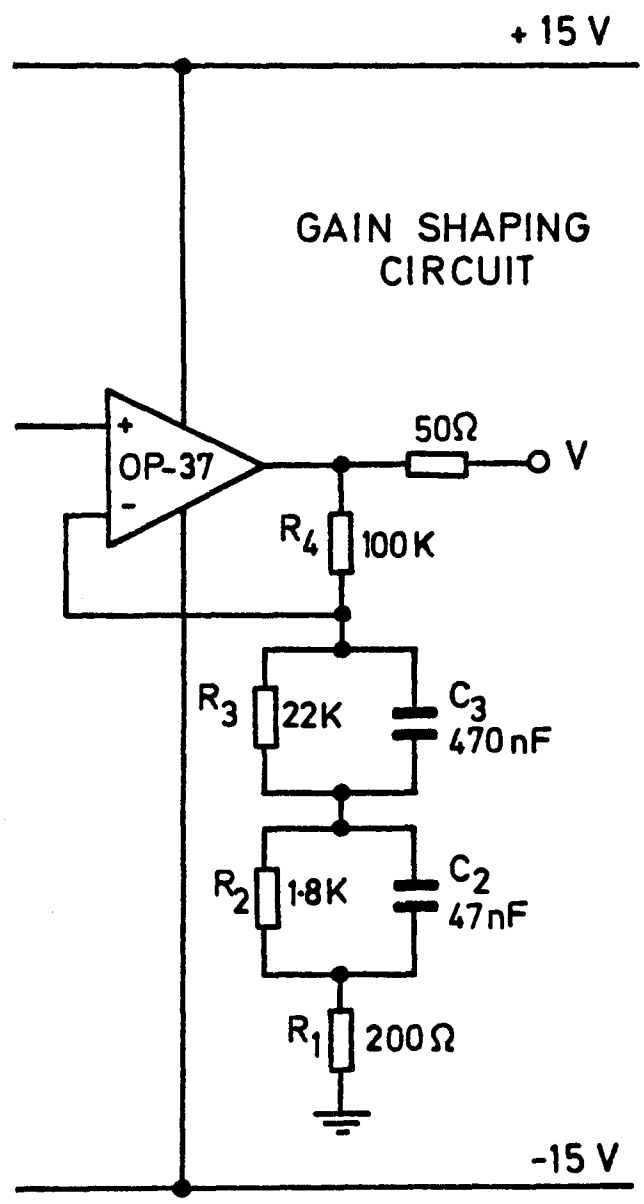

Figure 6.10: Circuit Diagram of Frequency Dependent Amplifier

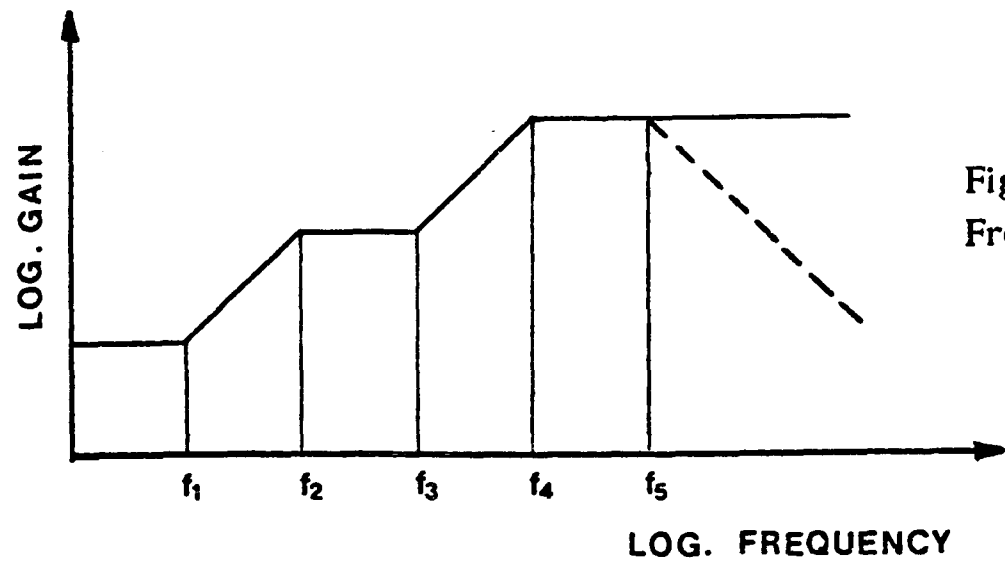

Figure 6.11: Asymptotes to Amplifier Frequency Response

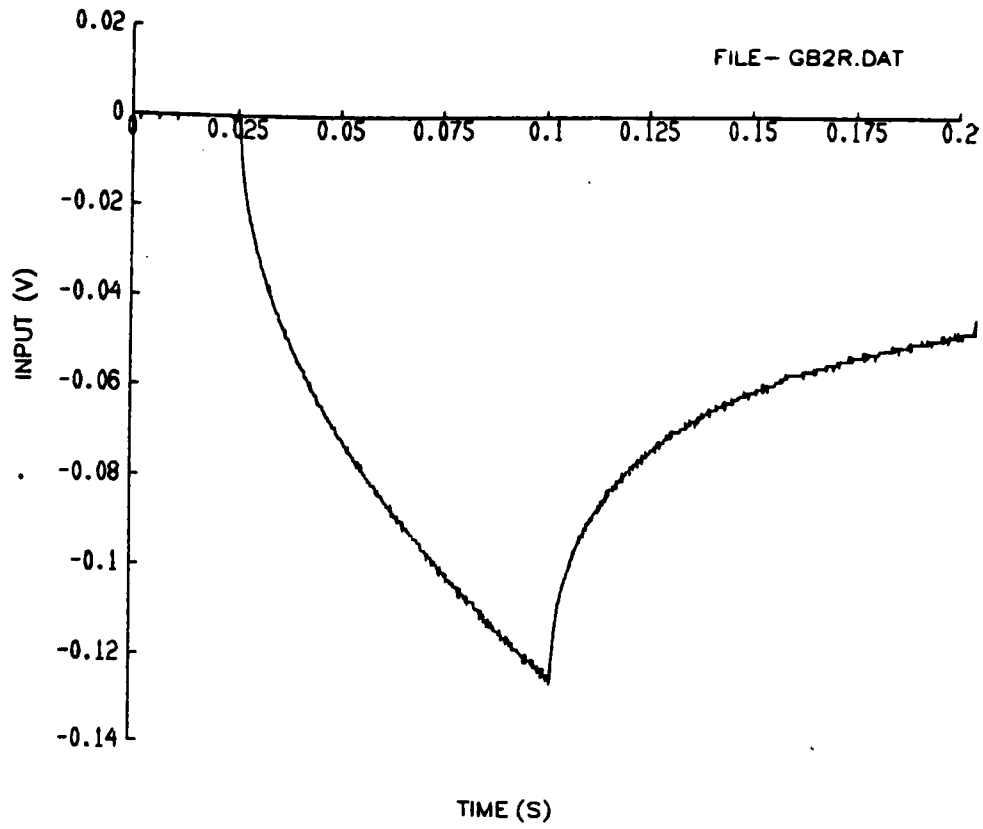

Figure 6.12: Parabolic Input

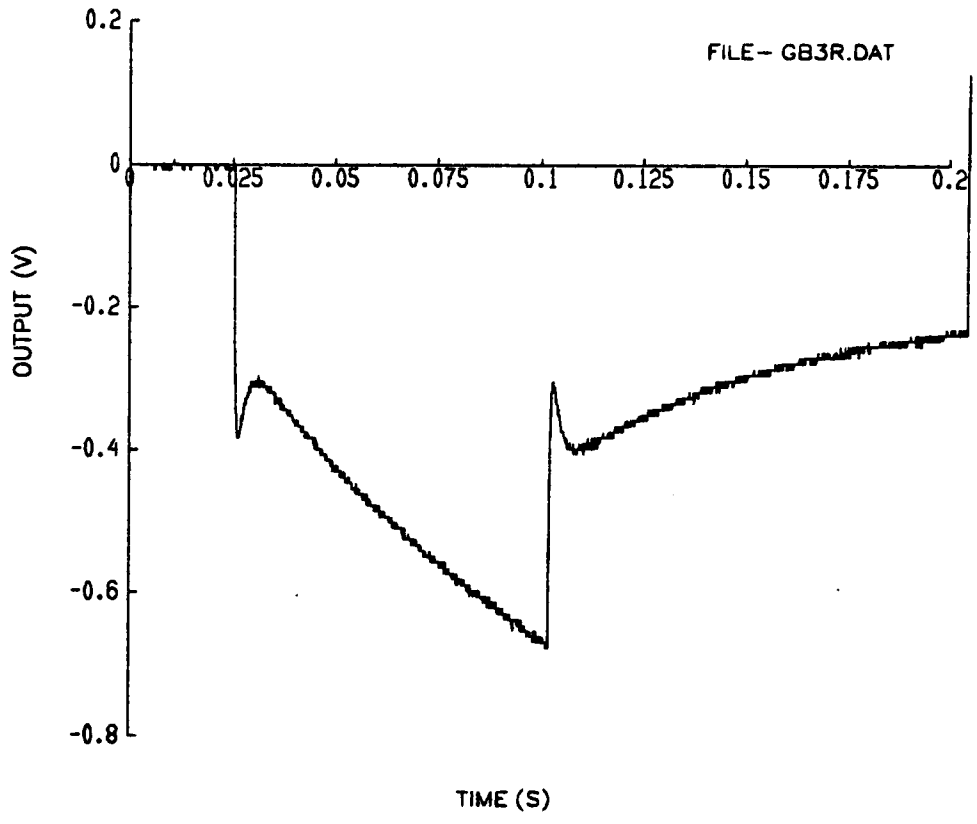

Figure 6.13: Output from In-shaft Amplifier When Parabolic Signal Applied at Input

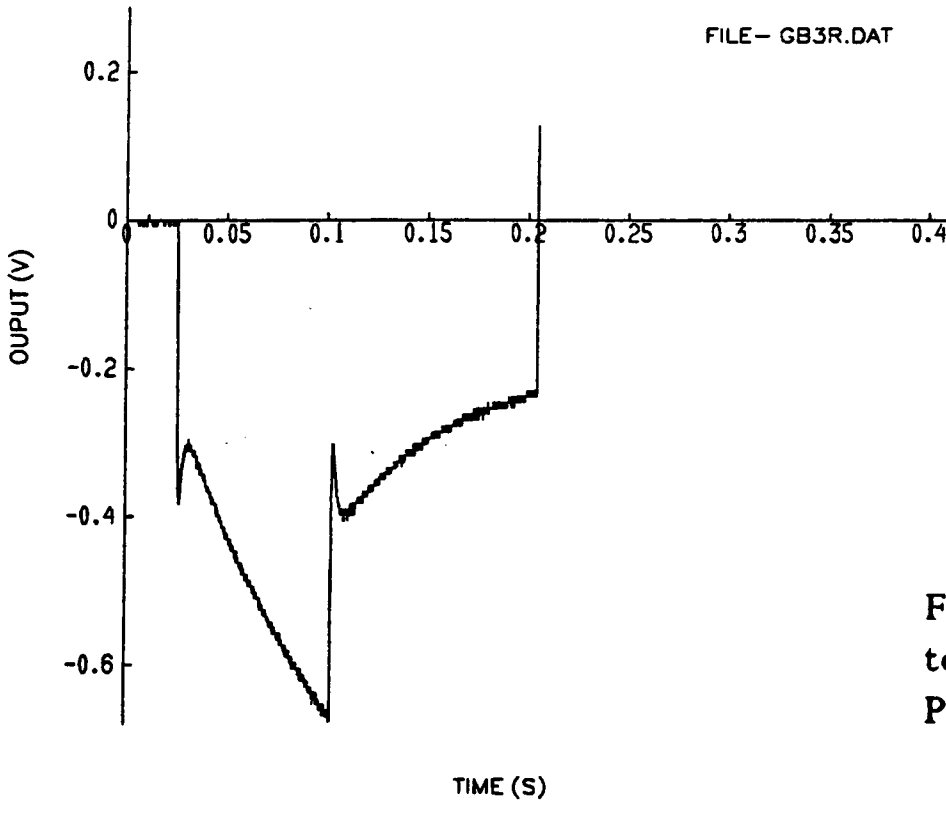

Figure 6.14: Output Signal Extended to Twice Original Length with Zero Padding

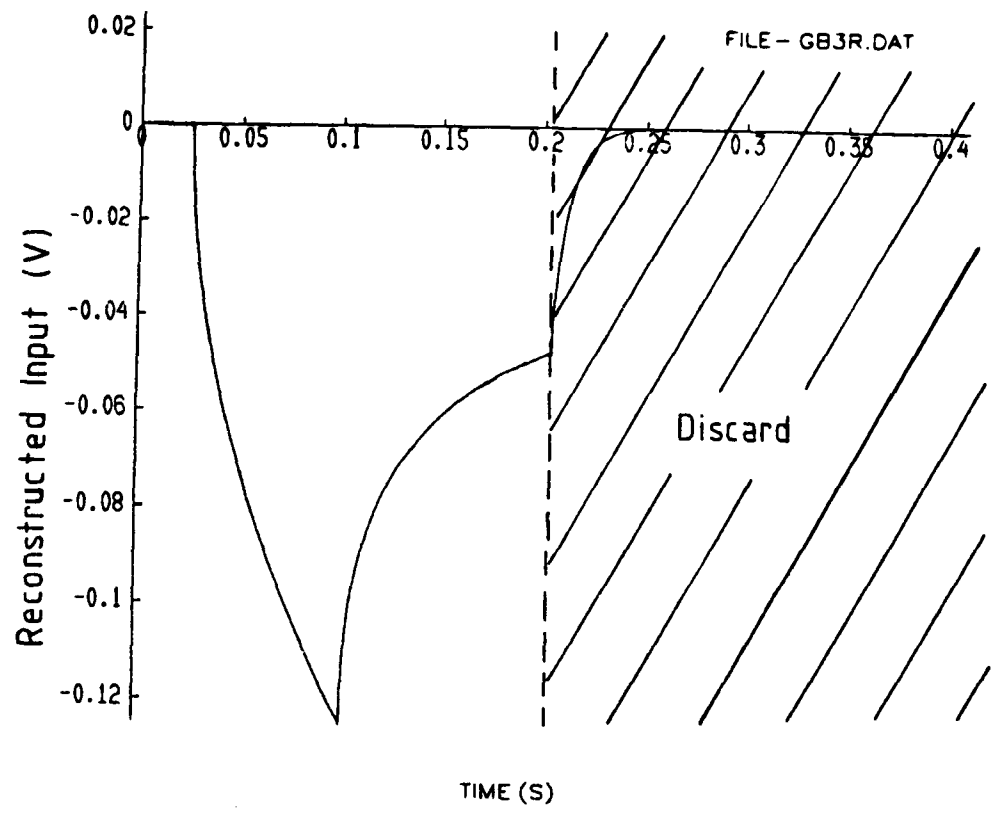

Figure 6.15: Reconstructed Input Signal

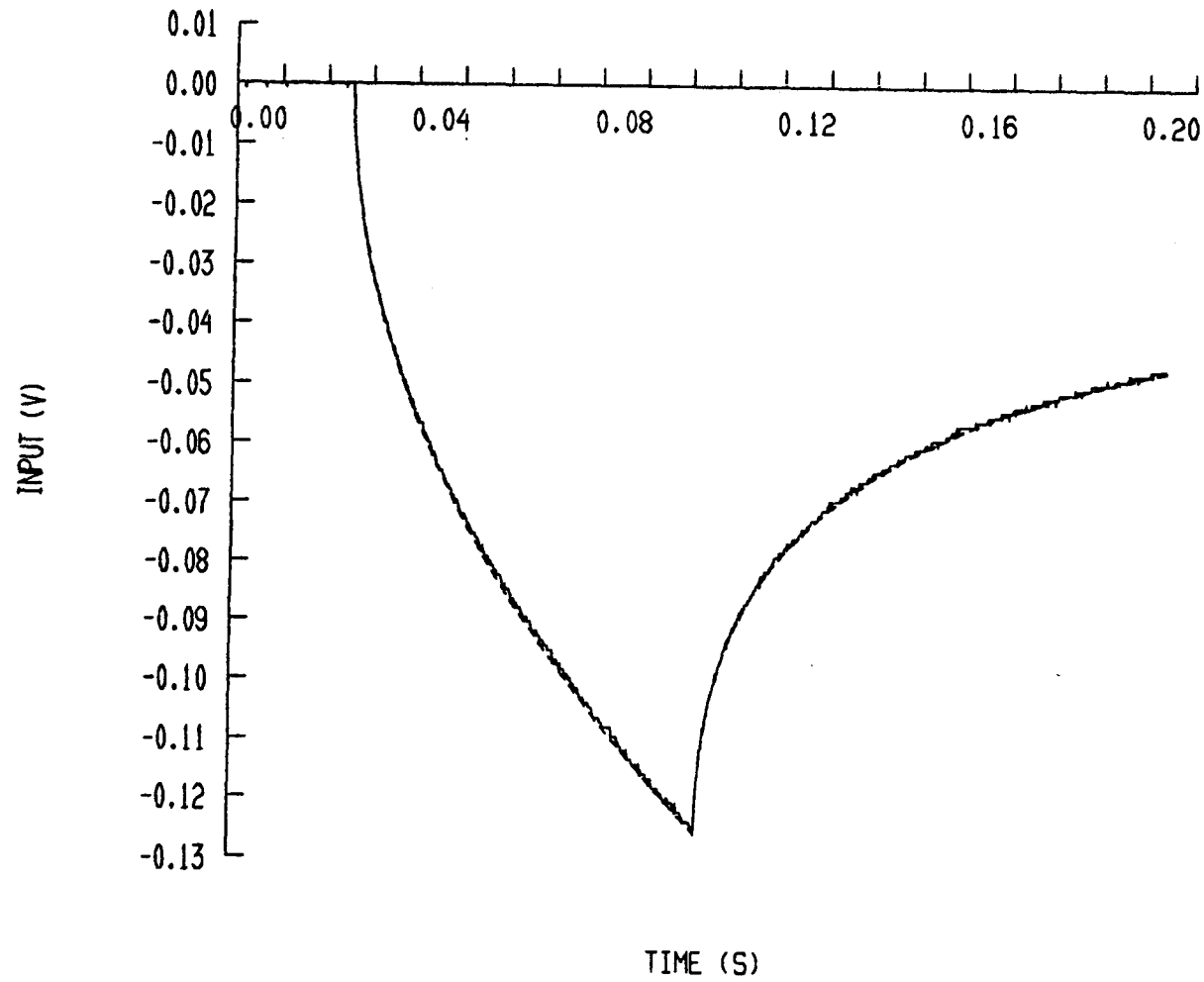

Figure 6.16: Reconstructed Signal Plotted Over Actual Input Signal

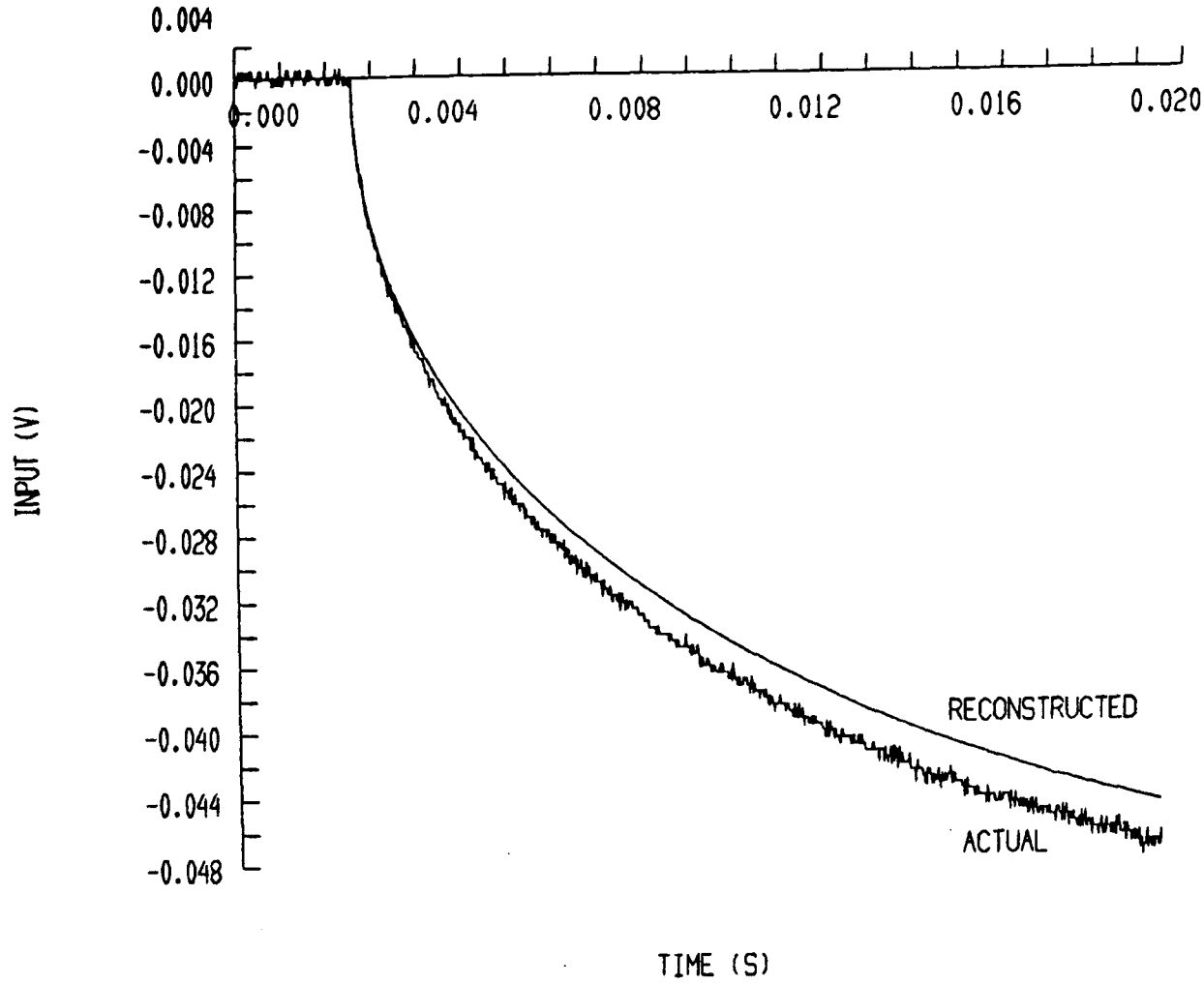

Figure 6.17: Reconstructed and Actual Input Signal (Sample Interval = 1.0E-5 s)

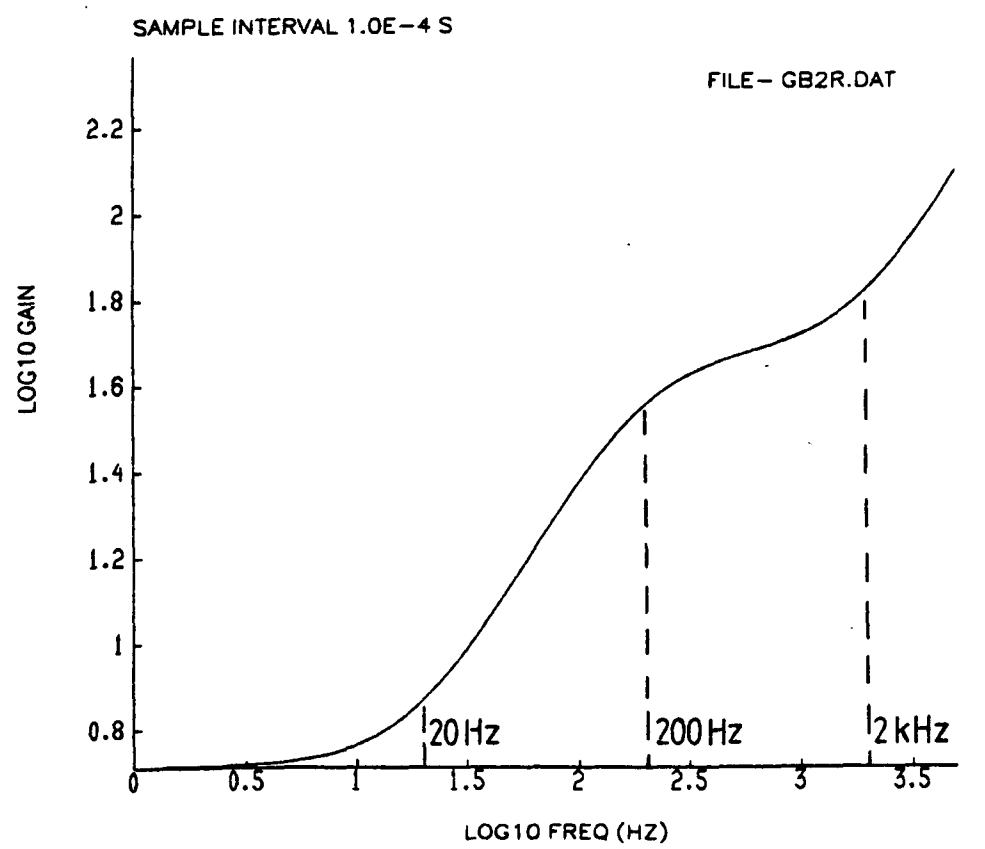

Figure 6.18: Calculated Amplifier Transfer Function (Sample Interval = 1.0E-4s)

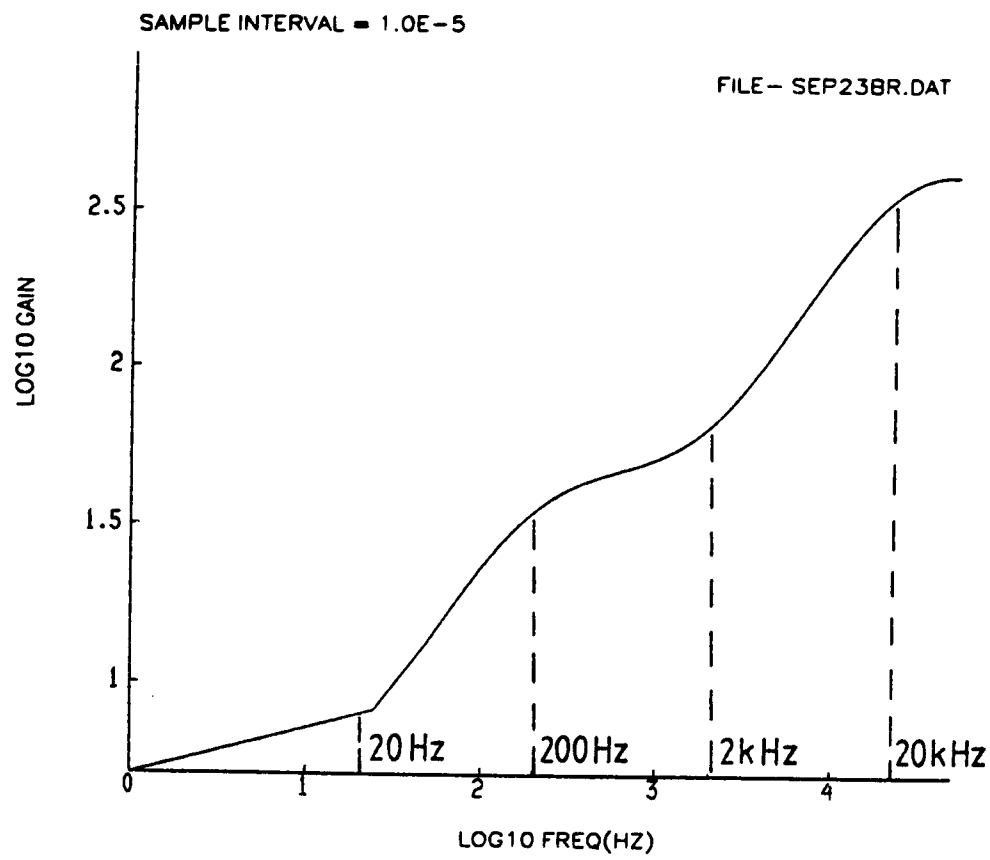

Figure 6.19: Calculated Amplifier Transfer Function (Sample Interval = 1.0E-5s)

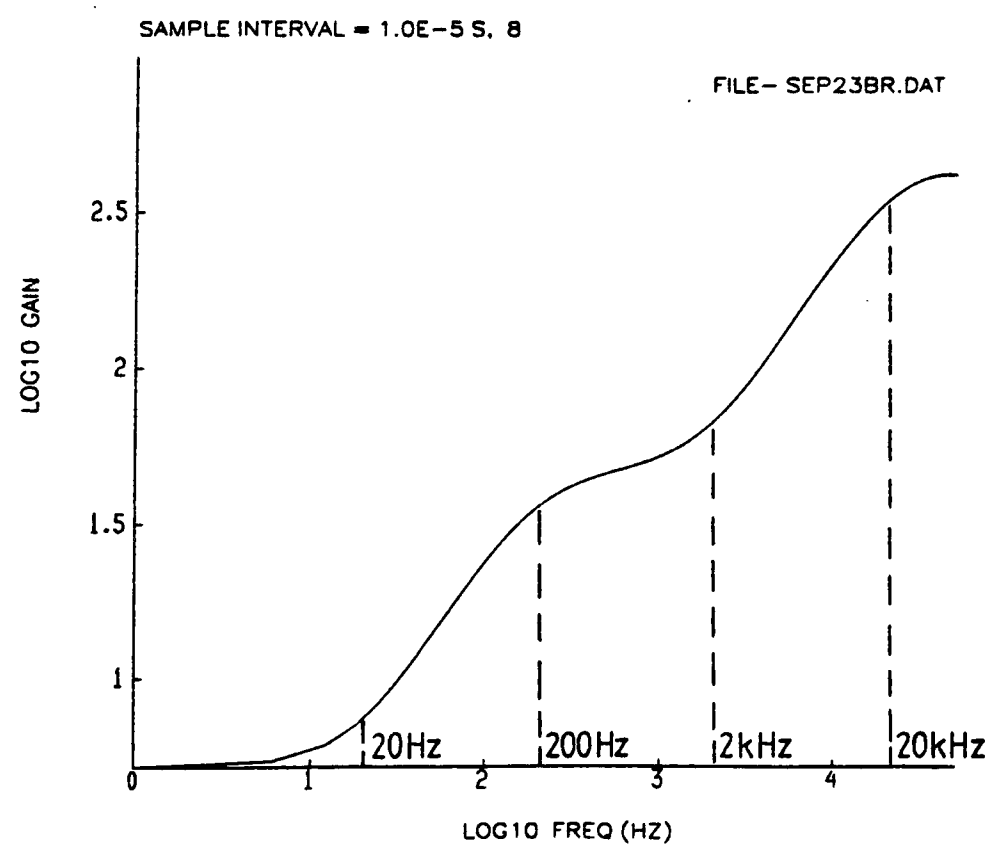

Figure 6.20: Amplifier Transfer Function Calculated for Signal Extended to 8 Times Original Length (Sample Interval = 1.0E-5s)

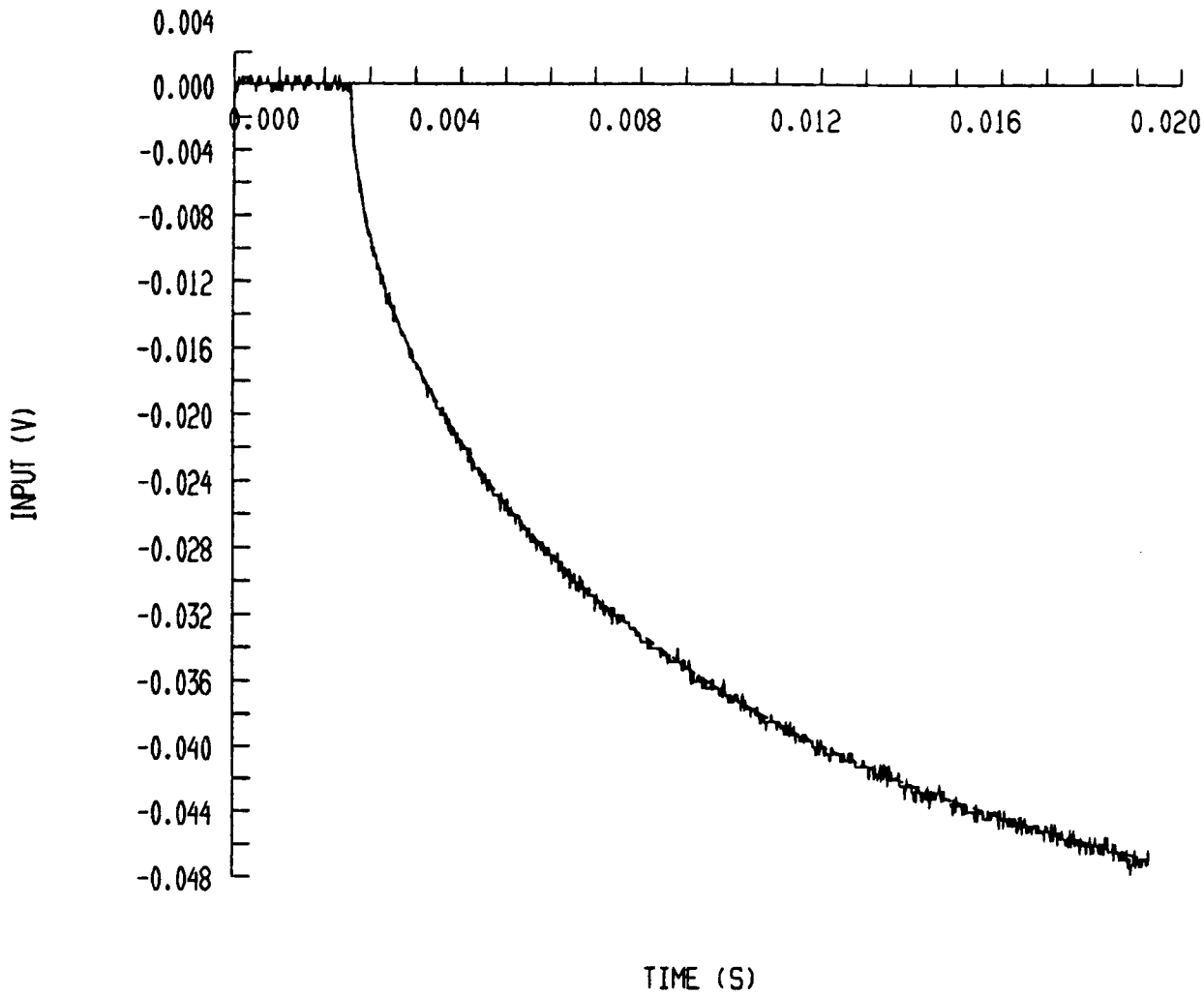

Figure 6.21: Reconstructed Input Signal Plotted Over Actual Input Signal (Sample Interval = 1.0E-5s)

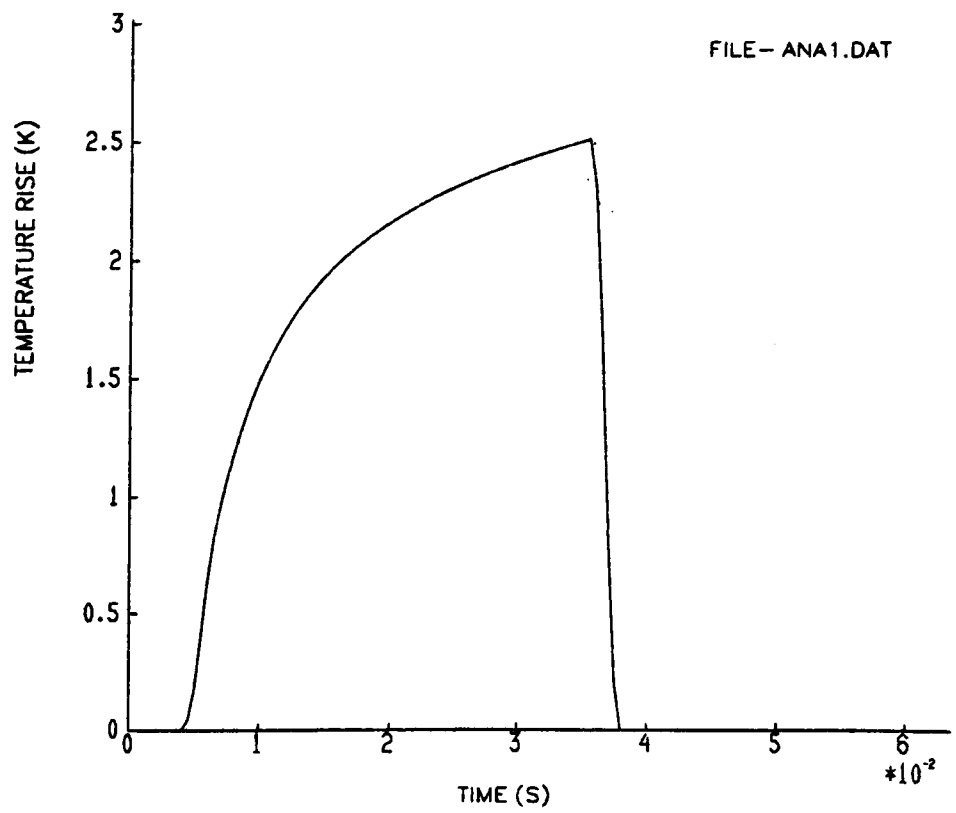

Figure 6.22: Predicted Temperature Rise for a Step in Heat Transfer Rate Applied to a Gauge on a Two Layered Substrate

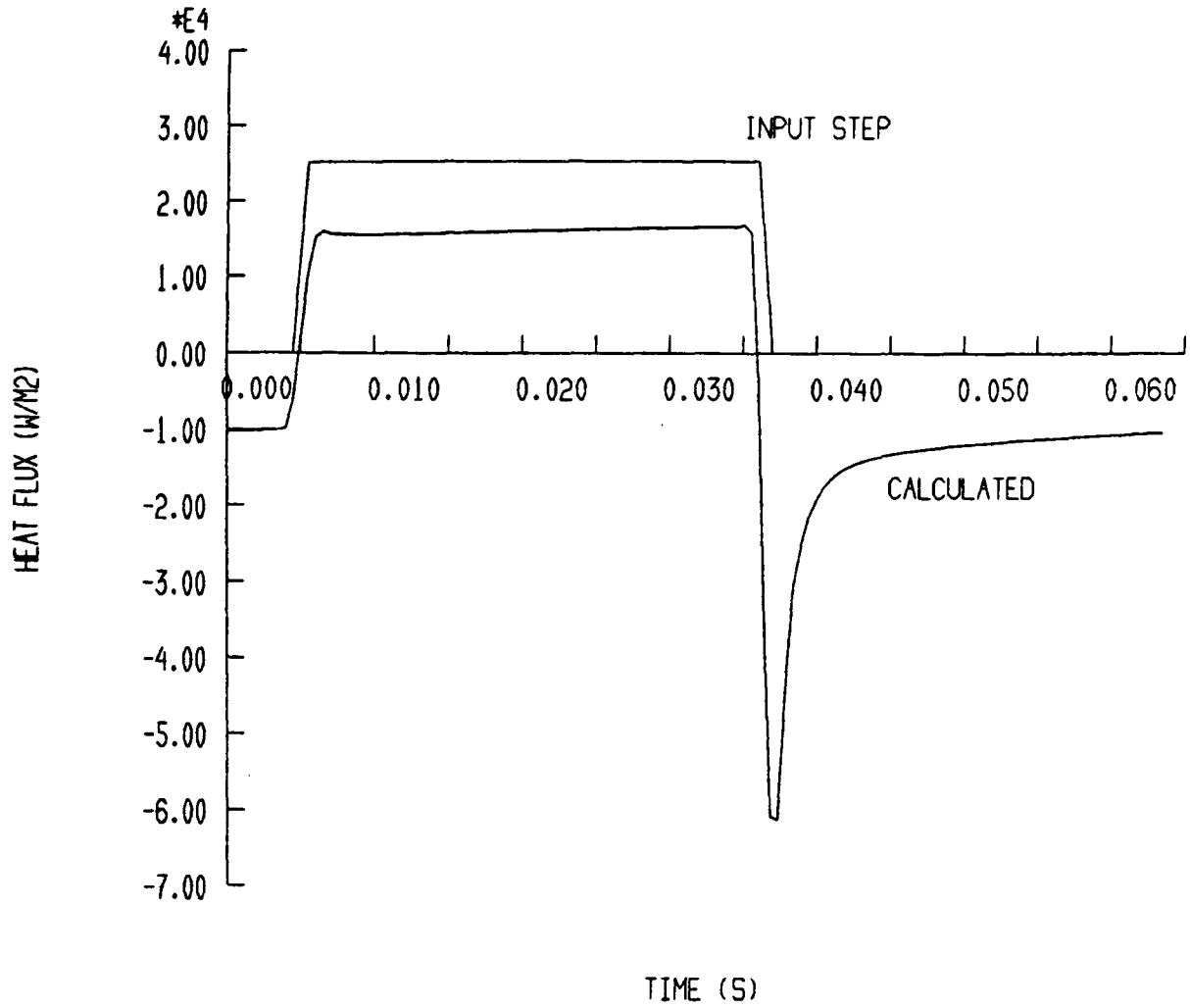

Figure 6.23: Comparison of Applied and Calculated Heat Transfer Rate

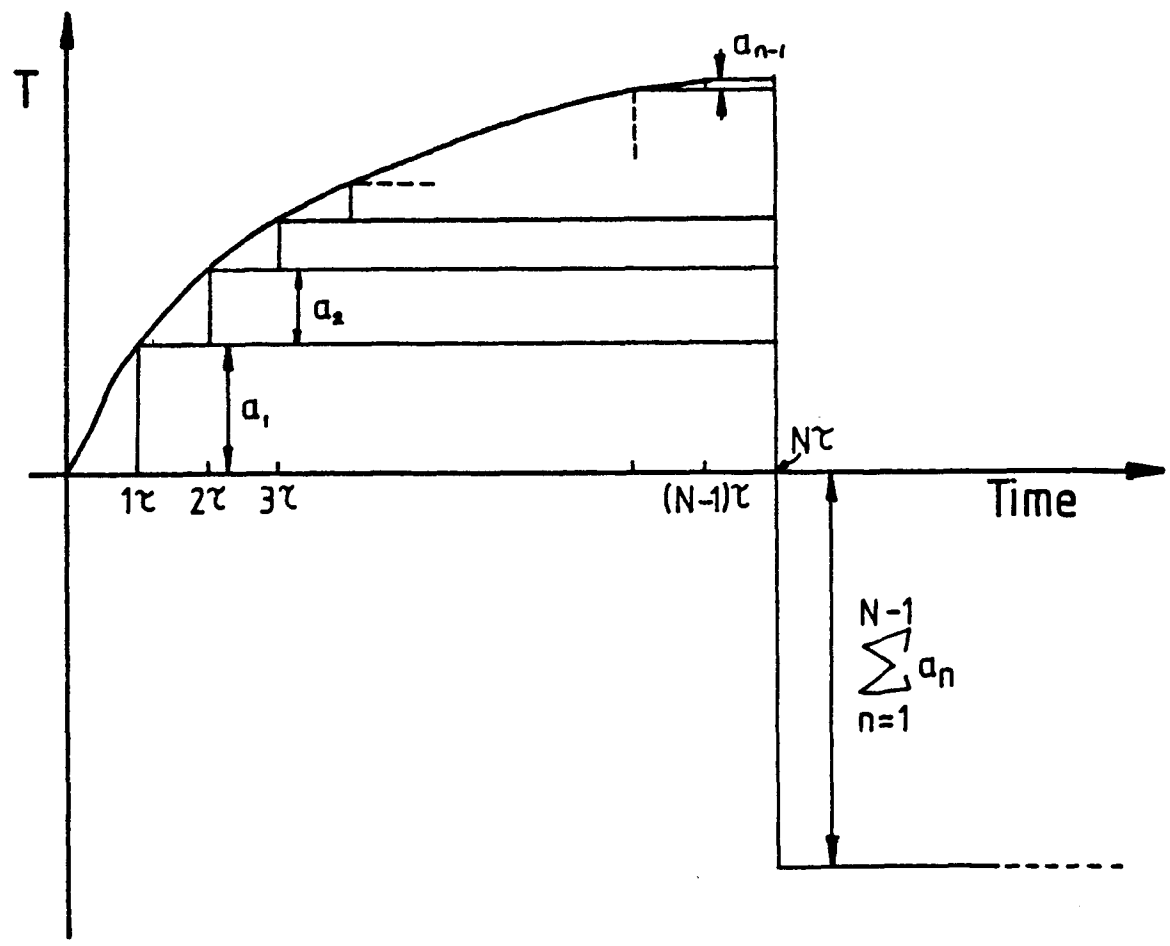

Figure 6.24: Temperature Rise Represented as a Series of Steps

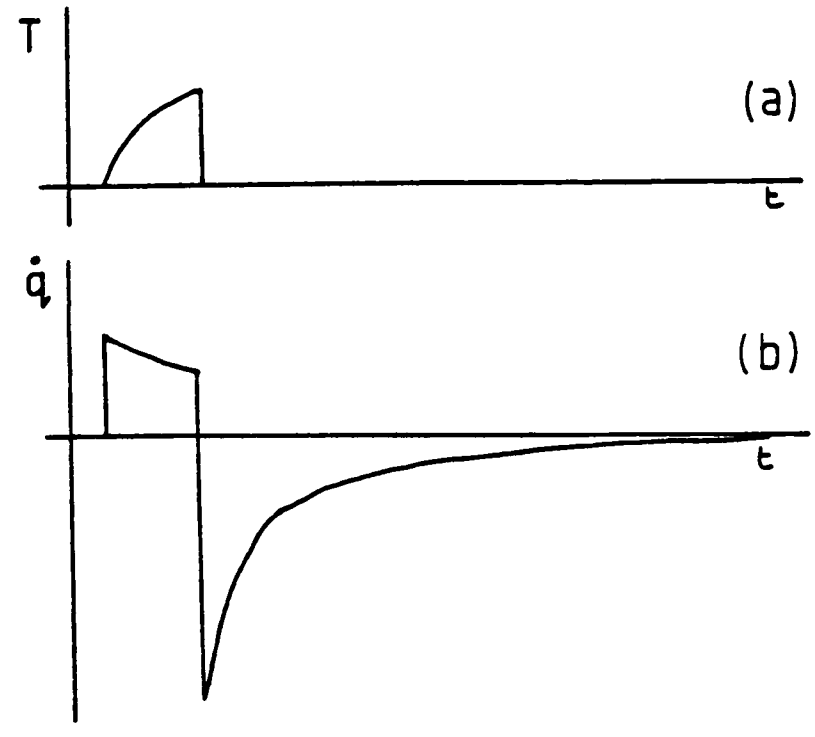

Figure 6.25: Schematic Diagram Showing :
(a) Temperature Rise for Thin Film Gauge on Single Layer Substrate
(b) Corresponding Heat Transfer Rate

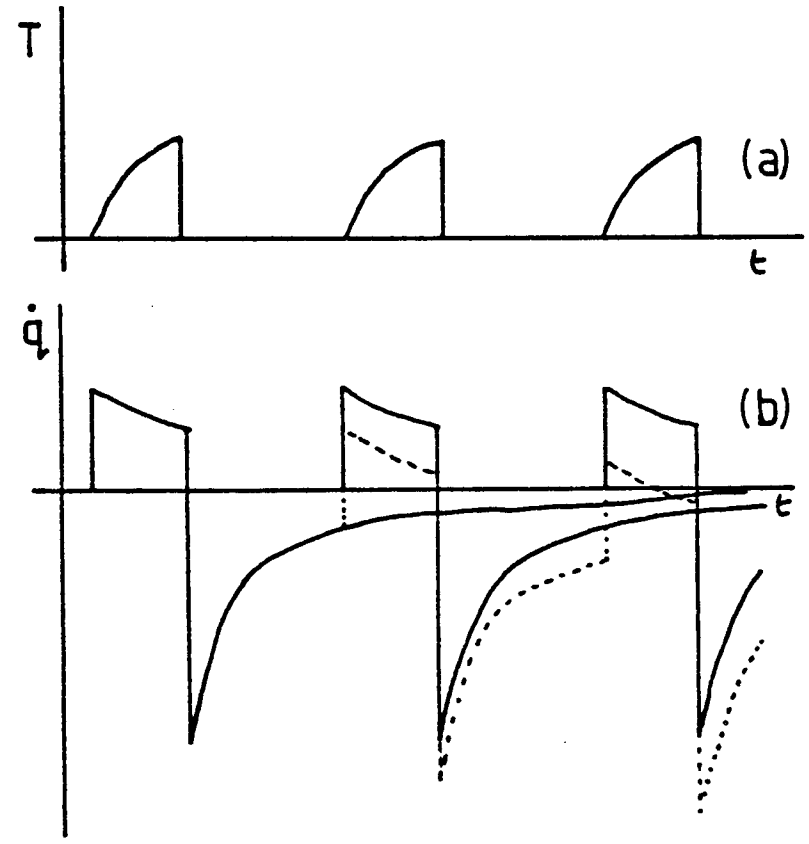

Figure 6.26: Schematic Diagram Showing:
(a) Periodic Temperature Signal
(b) Corresponding Heat Transfer Rate Signal

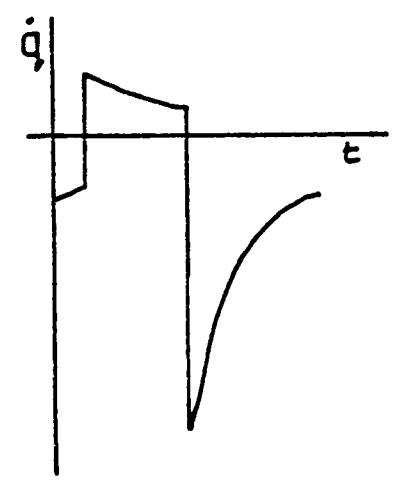

Figure 6.27: Resultant Heat Transfer Rate Signal Over One Period

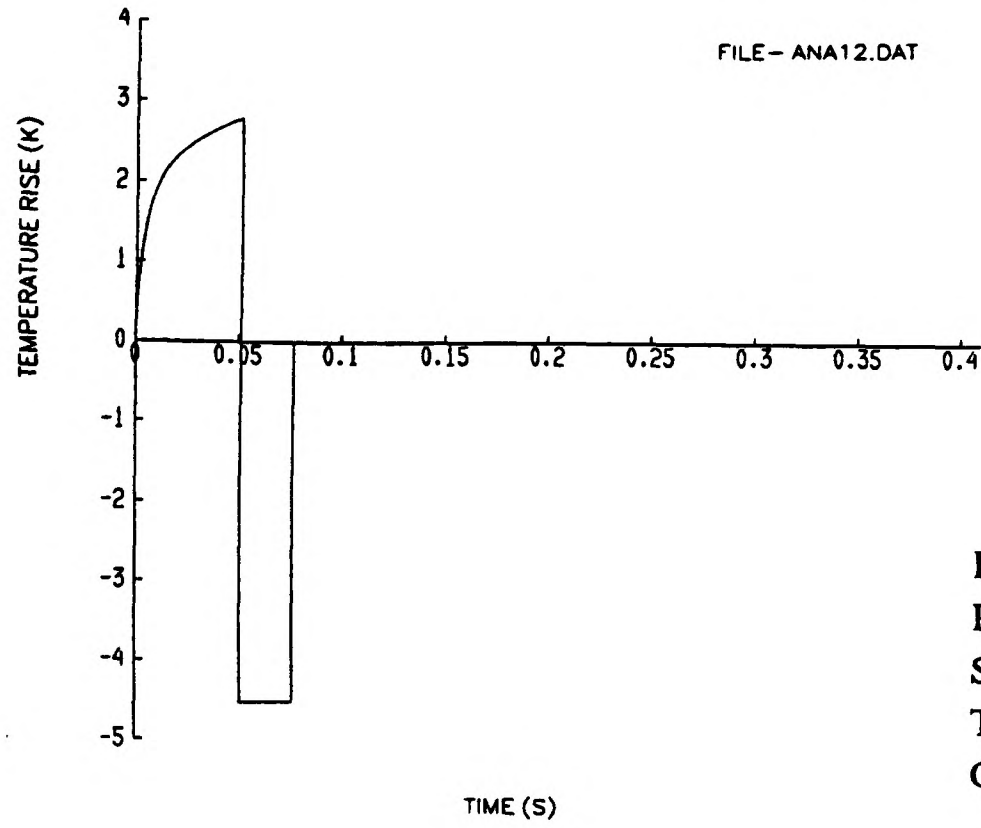

Figure 6.28: Theoretical Temperature Rise from Gauge on Two Layered Substrate Subject to Step in Heat Transfer Rate Extended to 8 Times Original Length

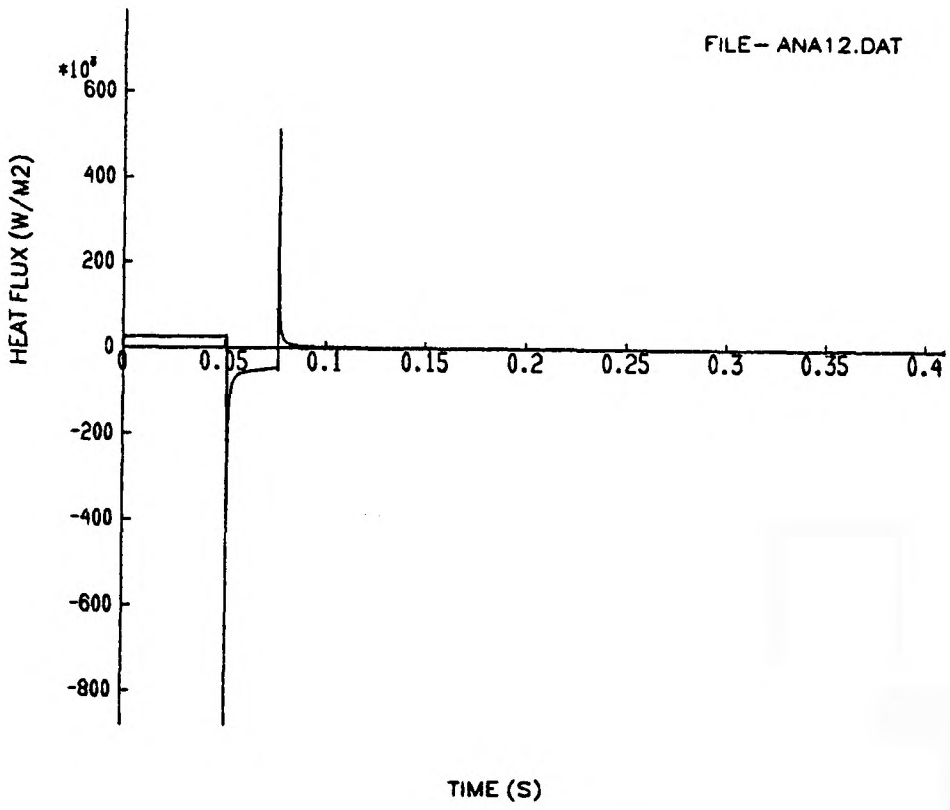

Figure 6.29: Heat Transfer Rate Calculated from Temperature Signal Shown in Figure 6.28.

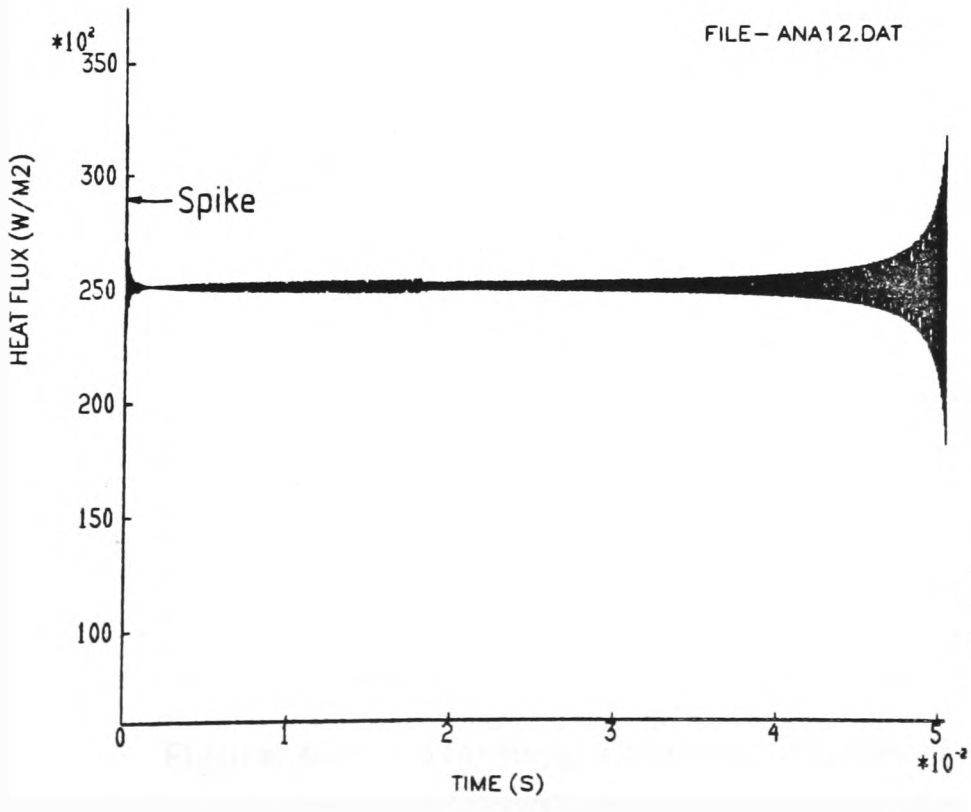

Figure 6.30: Heat Transfer Rate Corresponding to Original N Points.

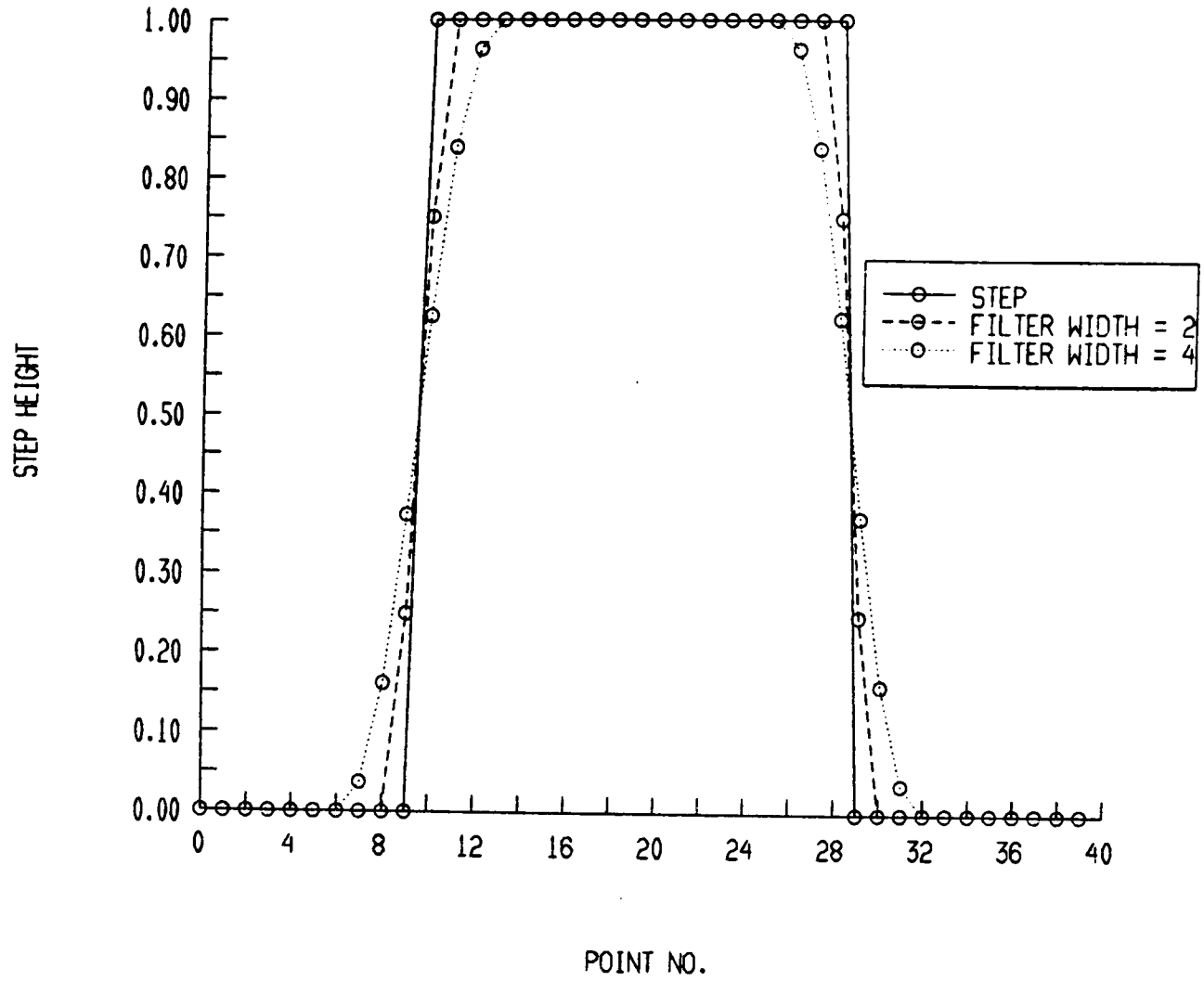

Figure 6.31: Effect of Smoothing on Square Wave

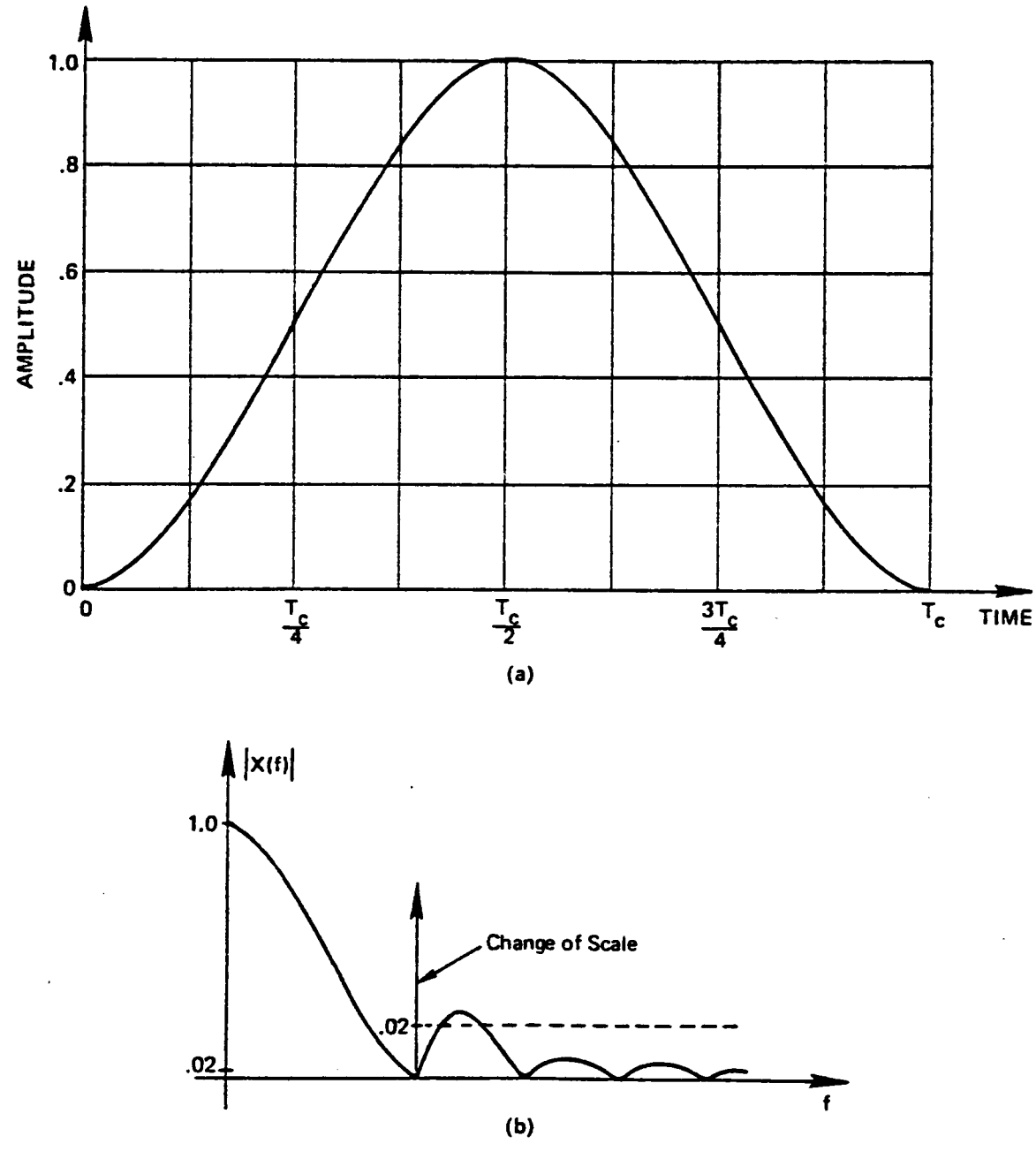

Figure 6.32: Hanning Function Fourier Transform Pair (from **Brigham**)

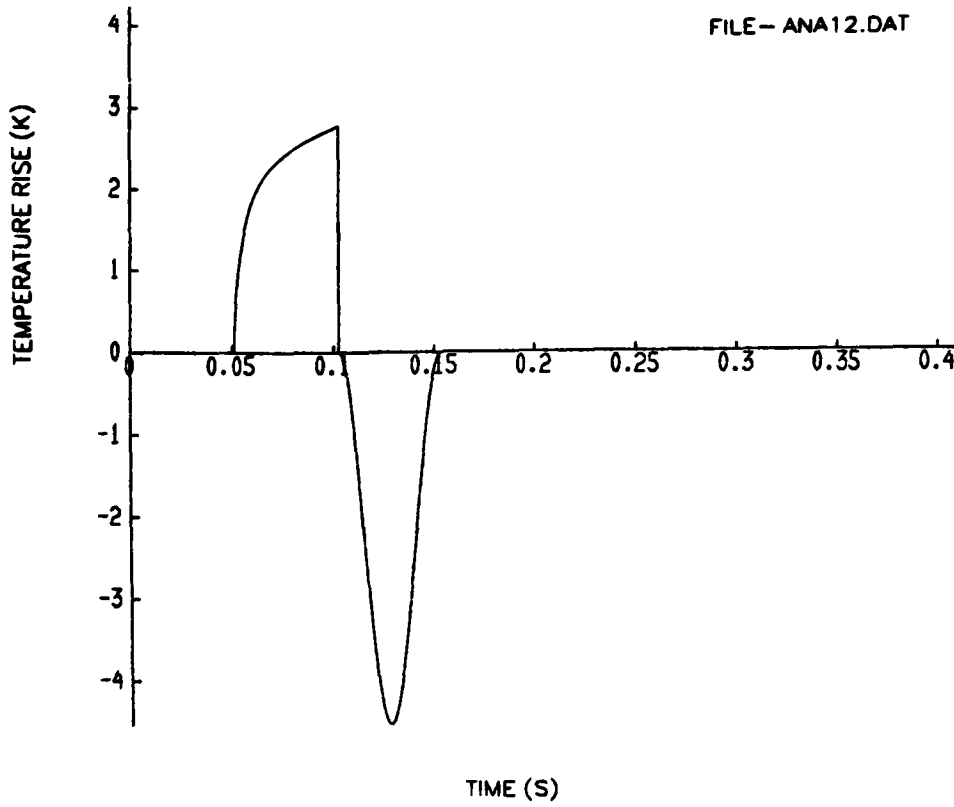

Figure 6.33: Smoothed Temperature Rise for Thin Film Gauge on Two Layered Substrate Subject to Step in Heat Transfer Rate Extended to 8 Times Original Length with Extra Zeros

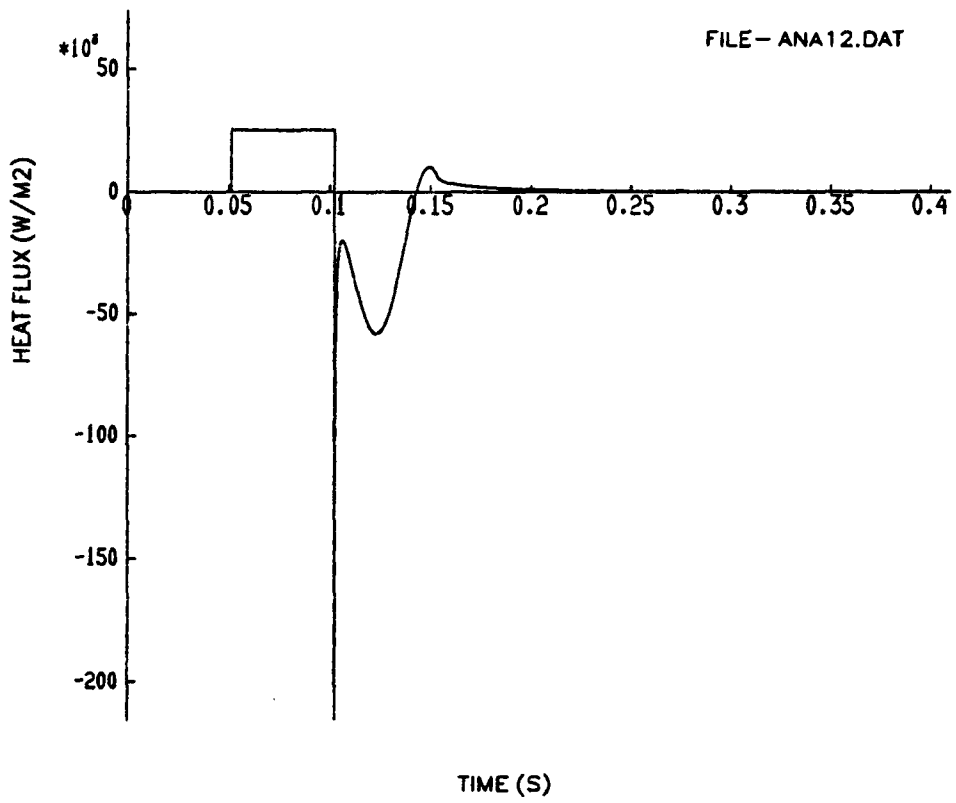

Figure 6.34: Heat Transfer Rate Calculated From Temperature Rise Shown in Figure 6.33

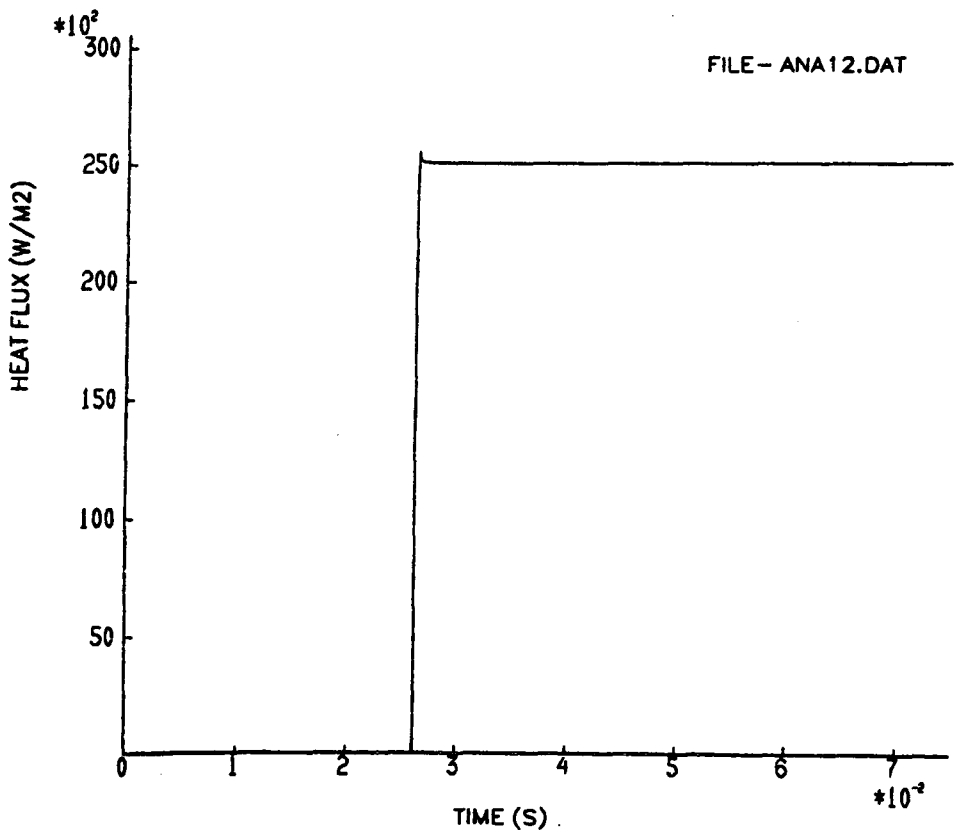

Figure 6.35: Enlargement of Step in Heat Transfer Rate Shown in Figure 6.34

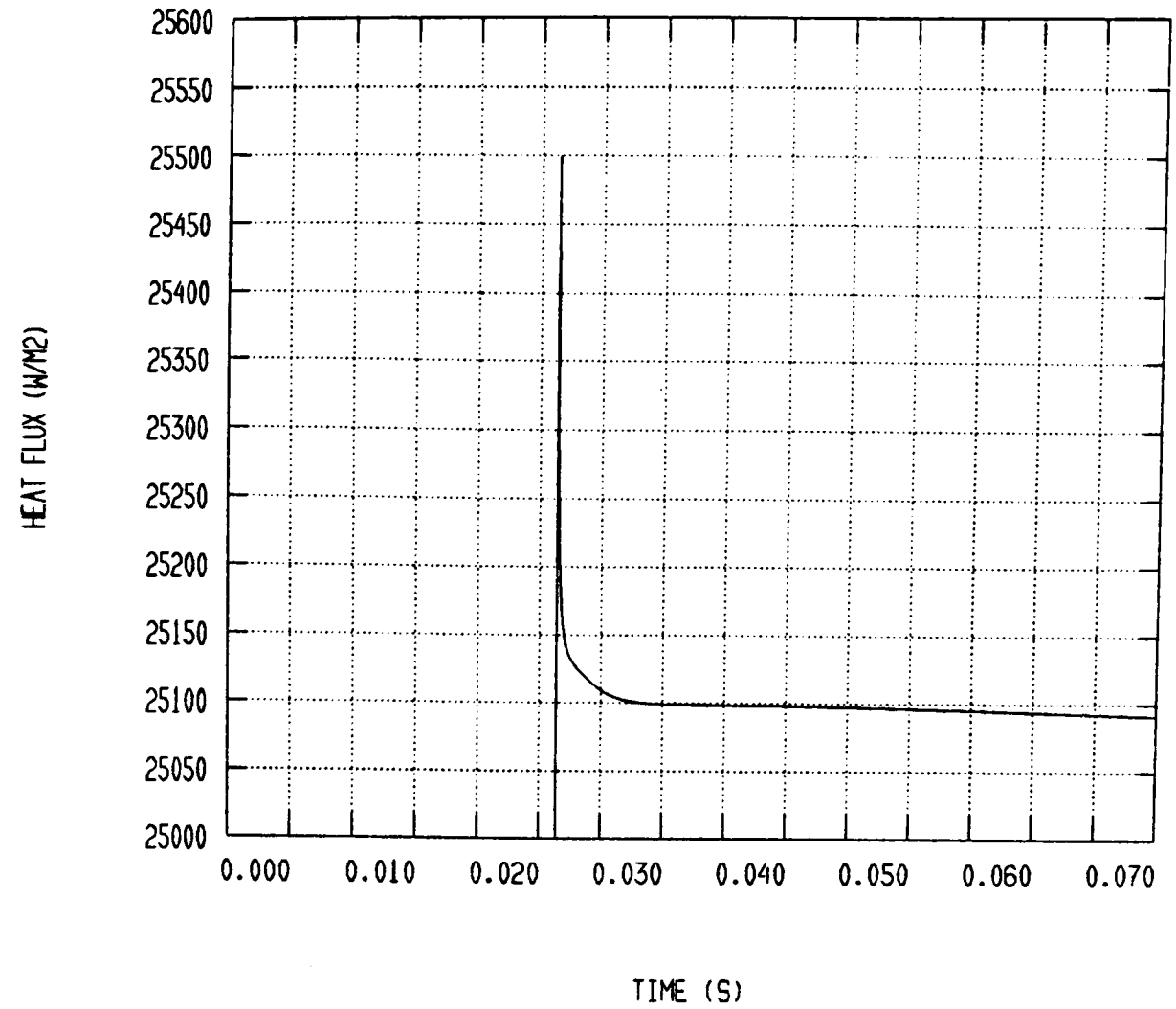

Figure 6.36: Expanded Plot of Data in Figure 6.34 Showing Error in Reconstructed Heat Transfer Rate (Actual Heat Transfer Rate = 25kW/m^2)

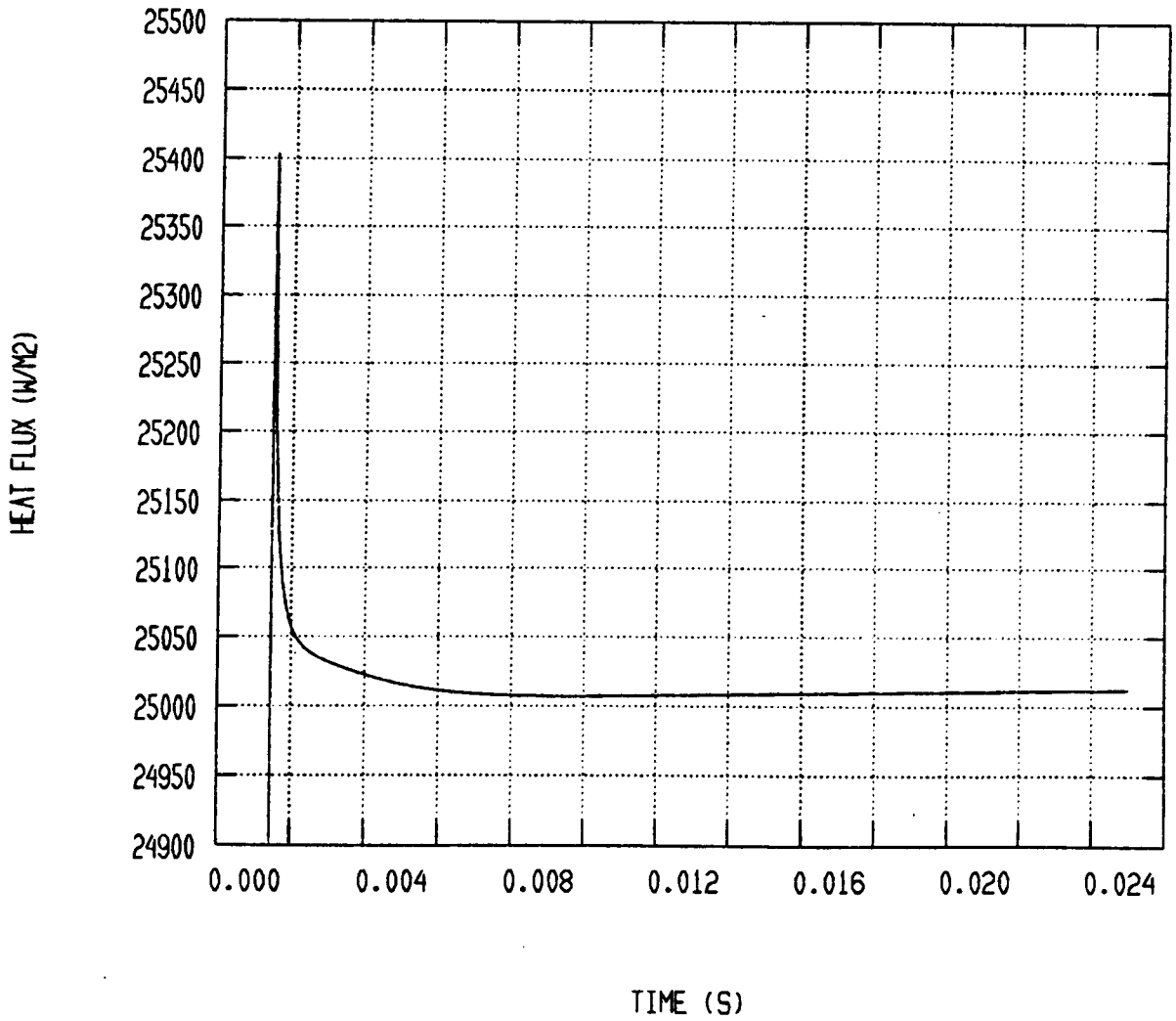

Figure 6.37: Reconstructed Heat Transfer Rate for Signal Extended to 16 Times Original Length (Actual Heat Transfer Rate = 25kW/m^2)

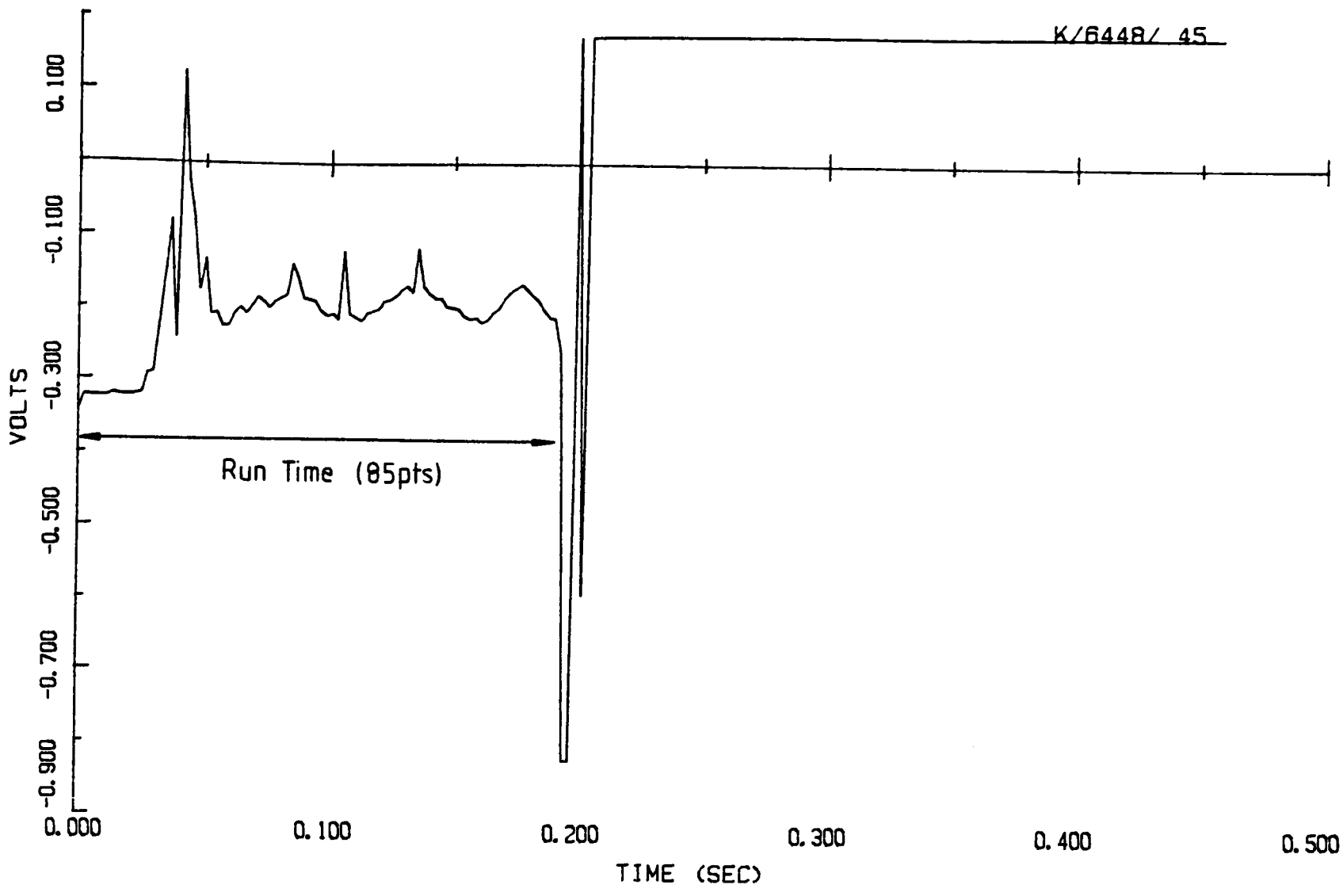

Figure 6.38: Output from Gauge 8 During Run 6448

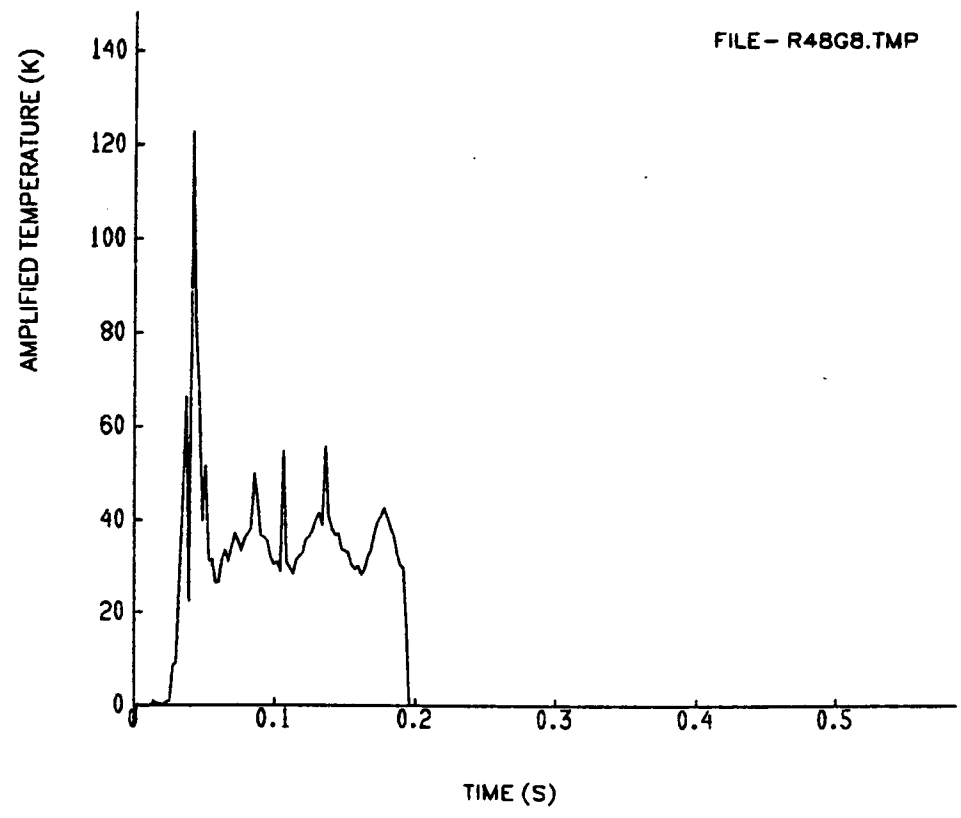

Figure 6.39: Amplified Temperature Signal from Gauge 8, Run 6448

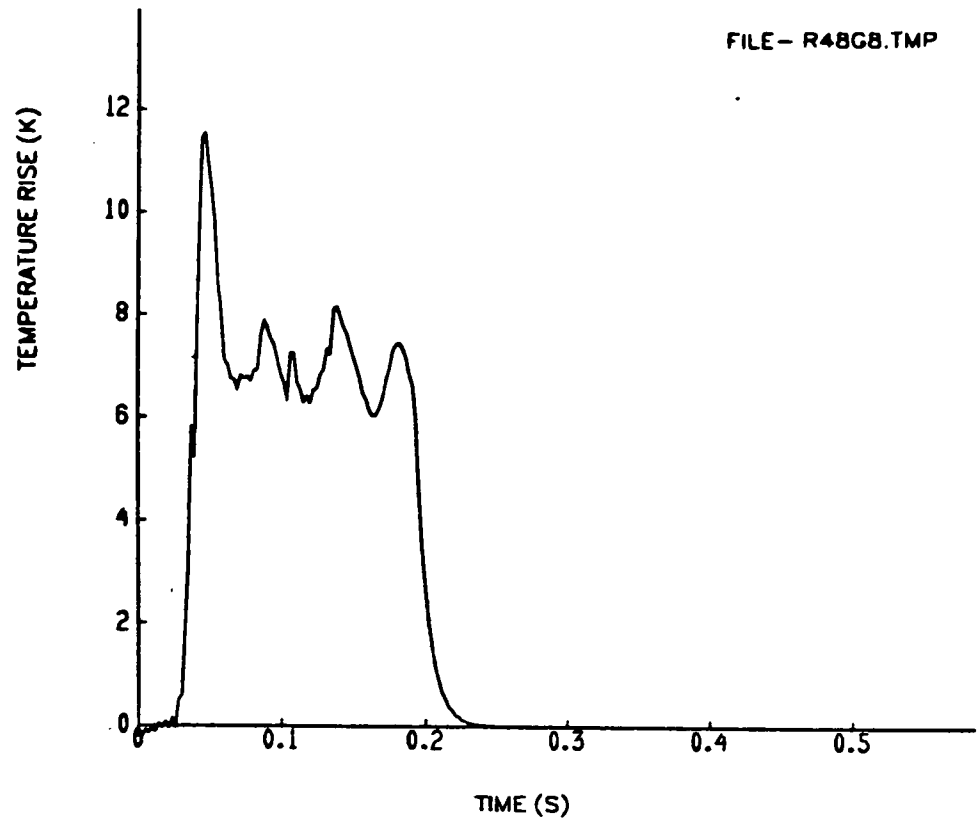

Figure 6.40: Temperature Rise from Gauge 8, Run 6448

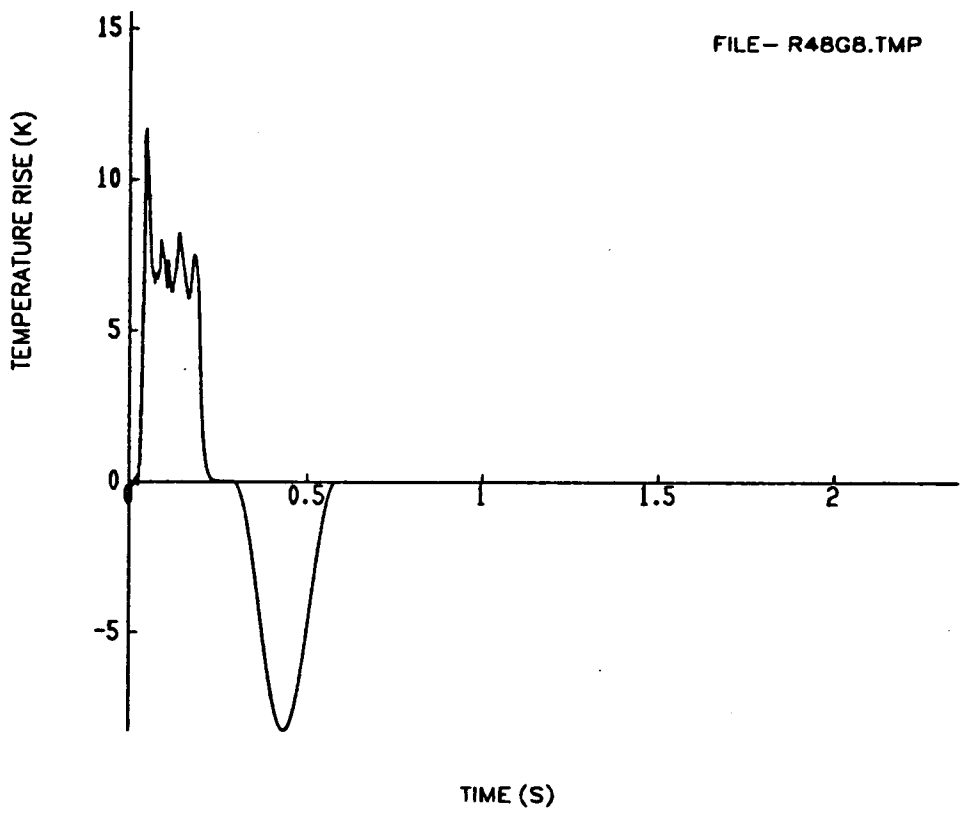

Figure 6.41: Extended Temperature Signal with Zero Mean Value, Gauge 8, Run 6448

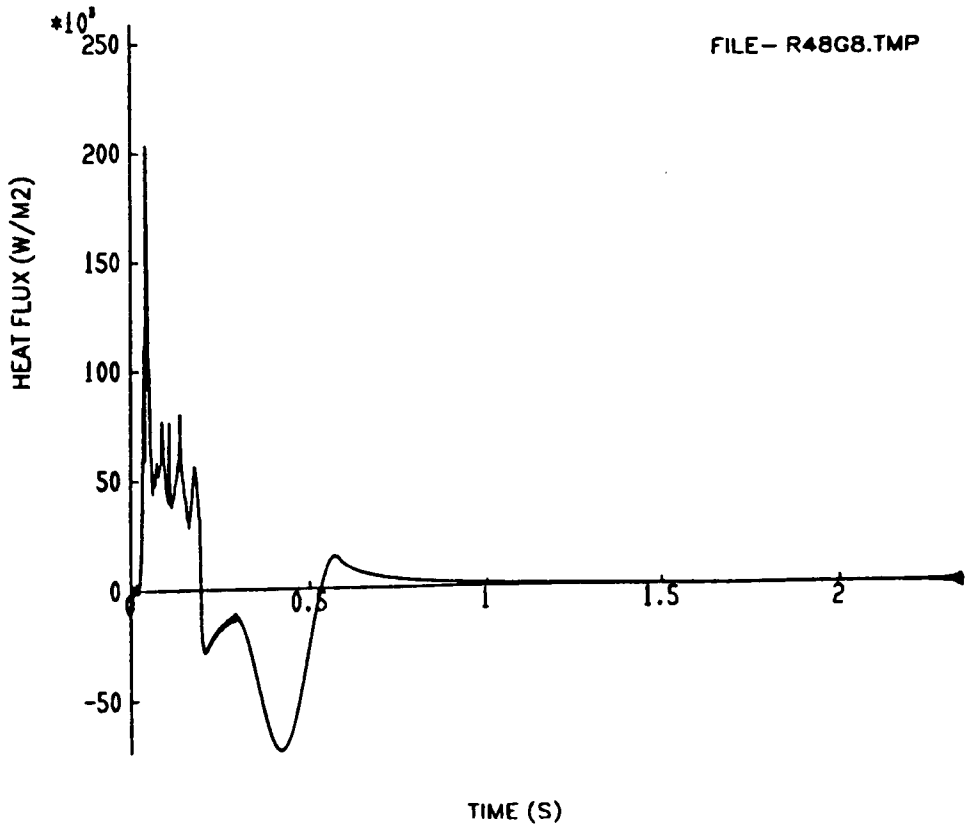

Figure 6.42: Heat Transfer Rate Calculated from Temperature Signal Shown in Figure 6.41

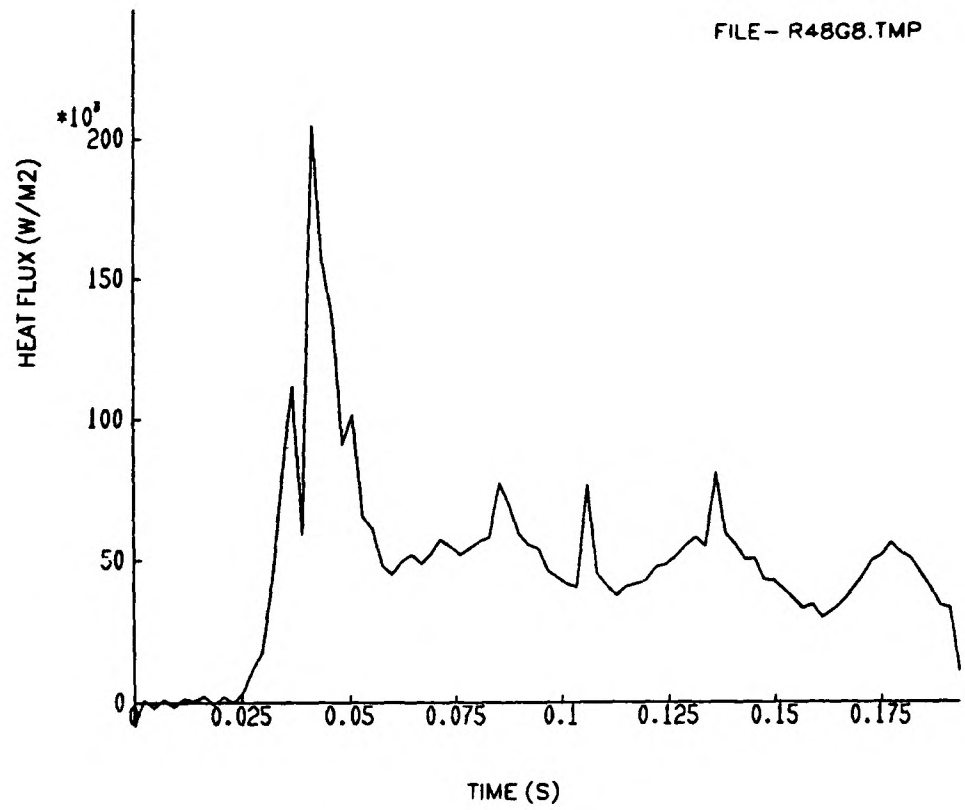

Figure 6.43: Mean Heat Transfer Rate from Gauge 8, Run 6448.

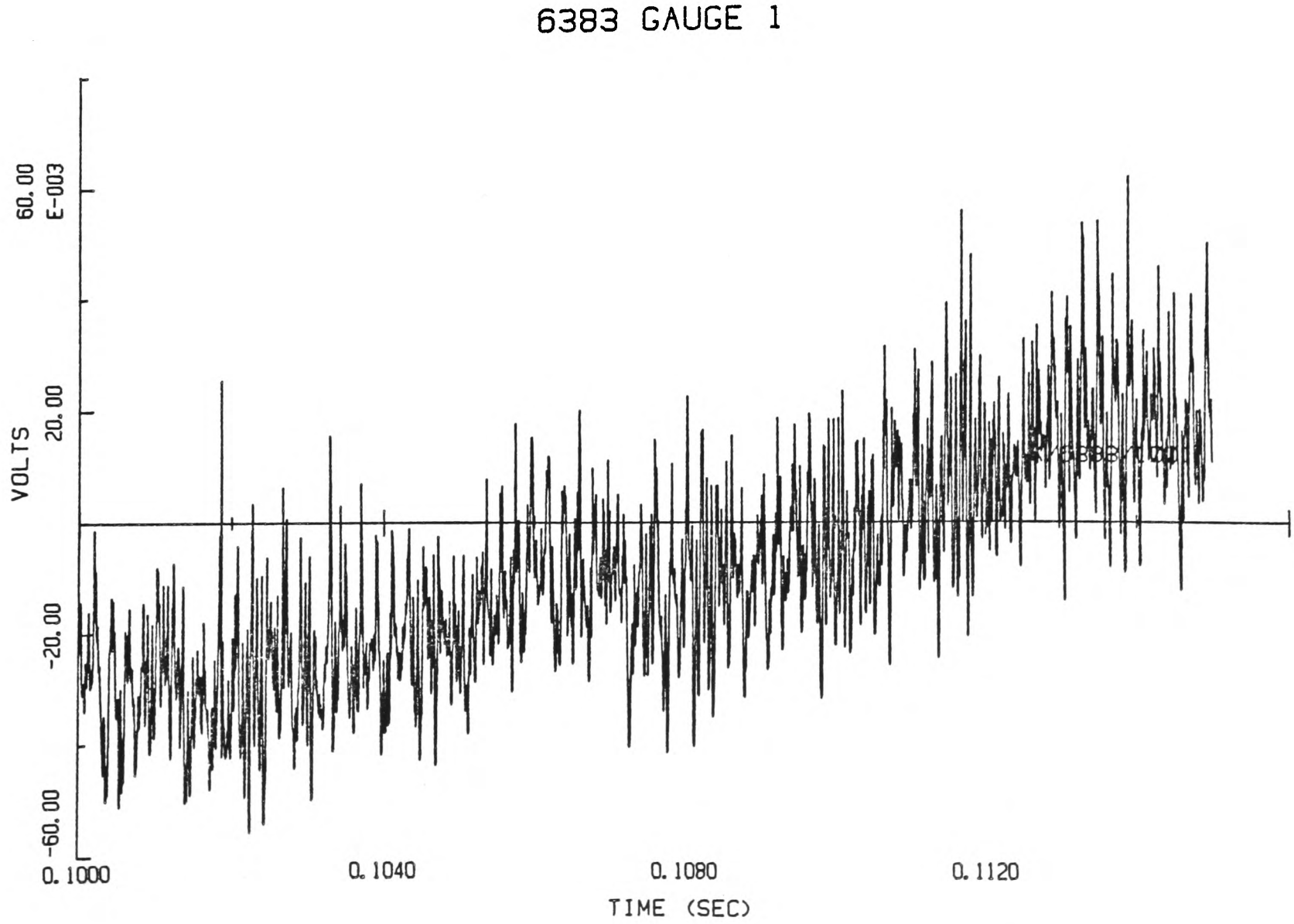

Figure 6.44: Unsteady Output from Gauge 32, Run 6383

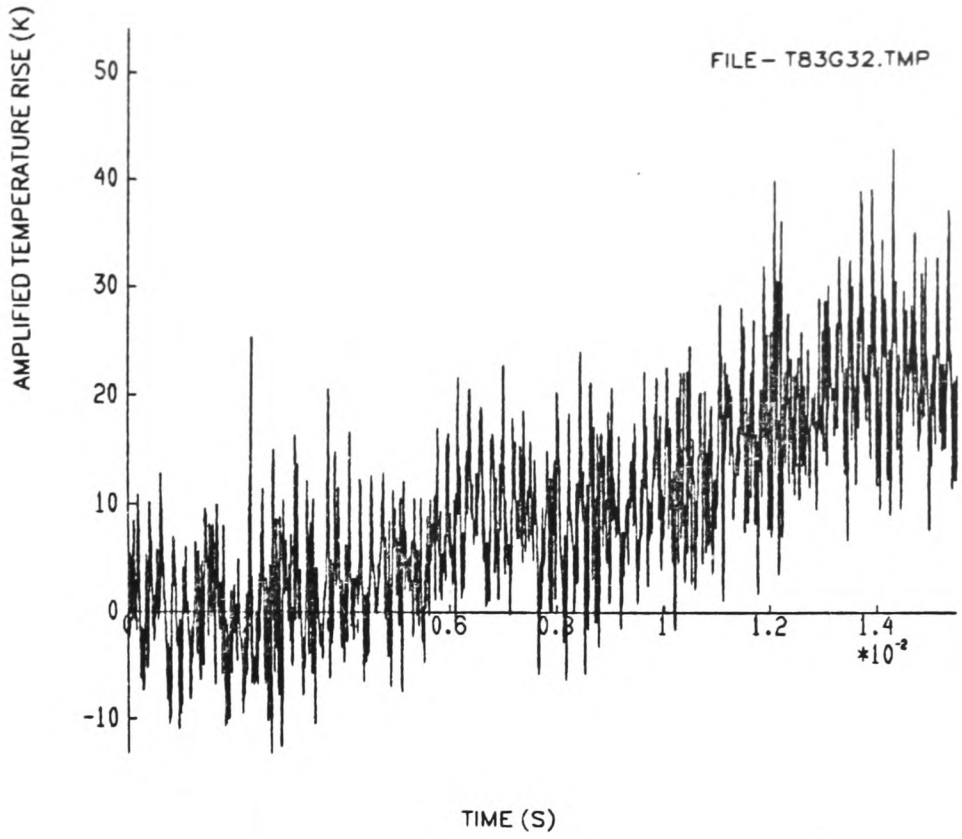

Figure 6.45: Amplified Unsteady Temperature Signal from Gauge 32, Run 6383

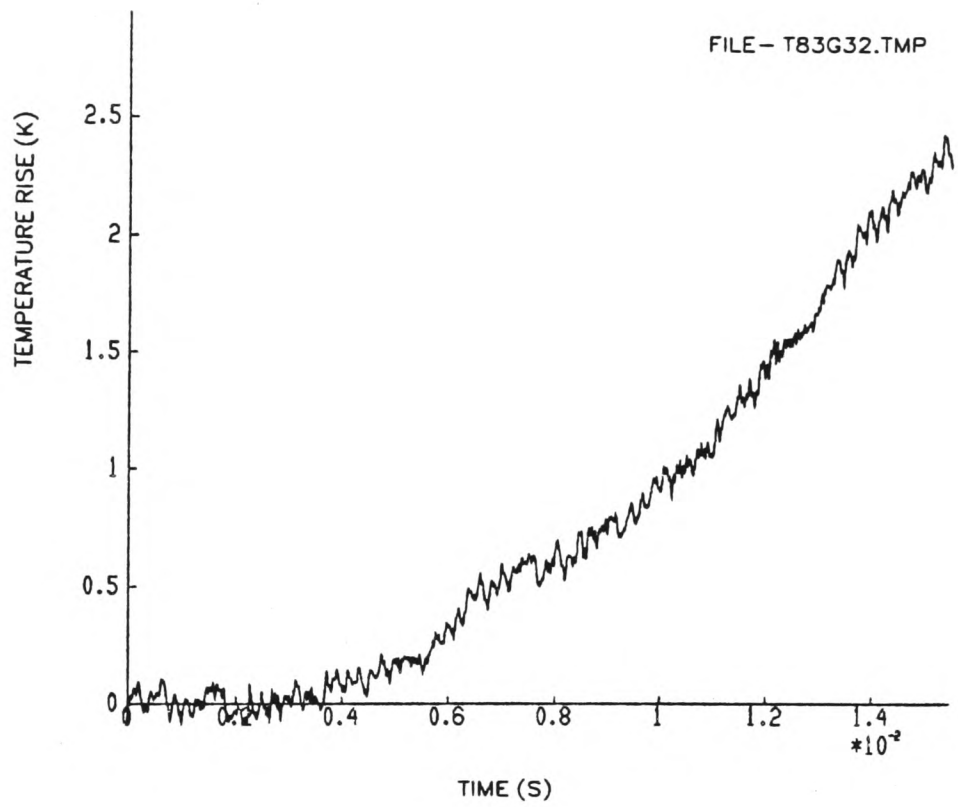

Figure 6.46: Unsteady Temperature Signal from Gauge 32, Run 6383

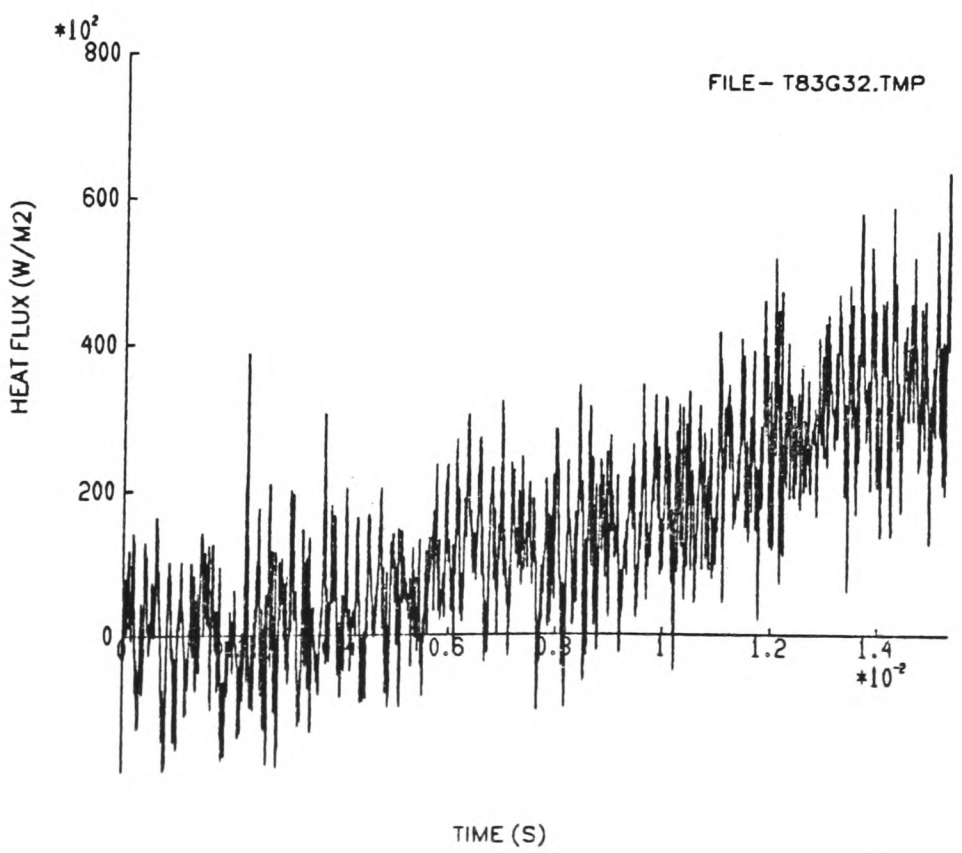

Figure 6.47: Unsteady Heat Transfer Rate from Gauge 32, Run 6383

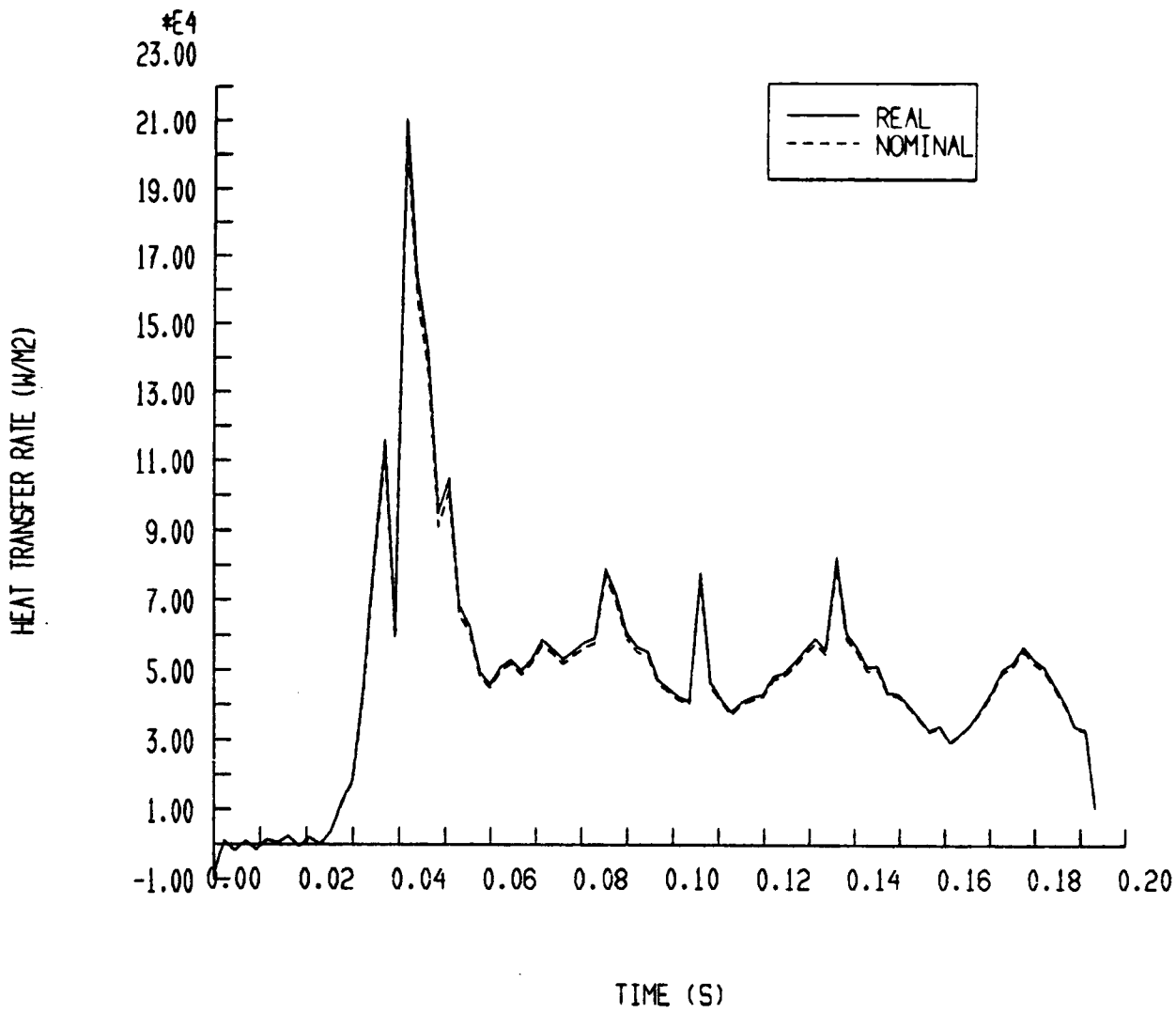

Figure 6.48: Mean Heat Transfer Rate from Gauge 20, Run 6448, Calculated using Real and Nominal Breakpoints

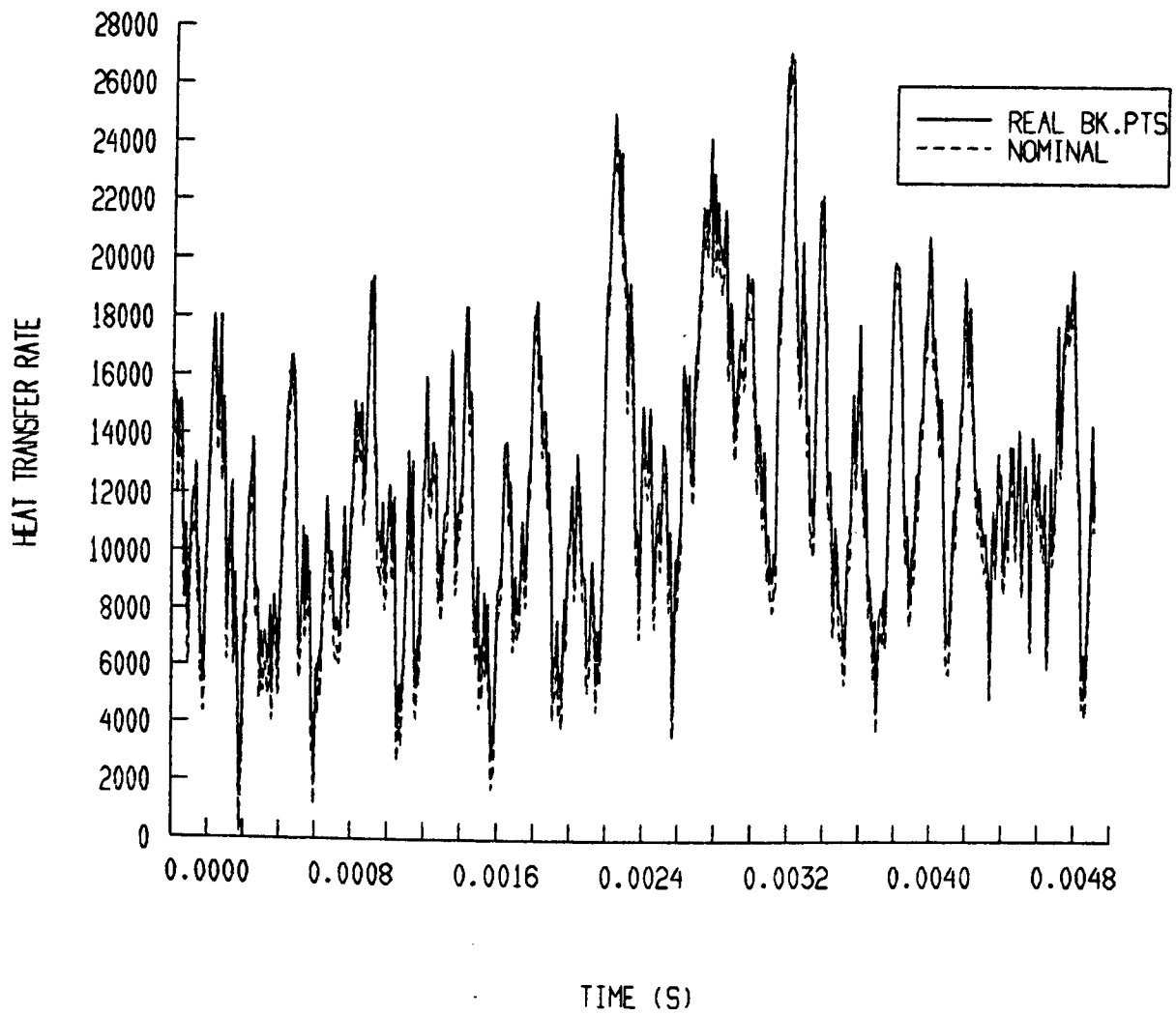

Figure 6.49: Unsteady Heat Transfer Rate from Gauge 20, Run 6448, Calculated using Real and Nominal Breakpoints

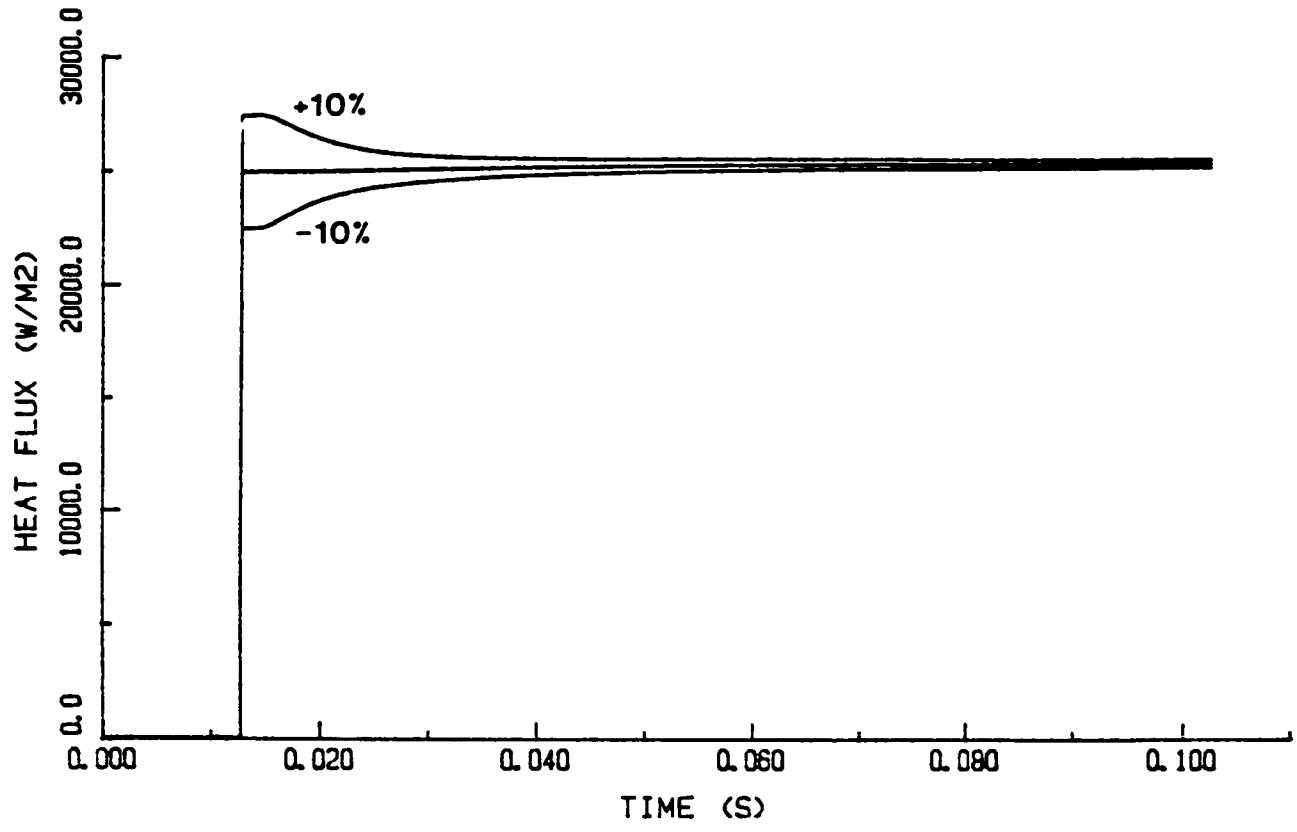

Figure 6.50: Effect on Heat Transfer Rate of 10% Variation in $\sqrt{(\rho ck)_1}$

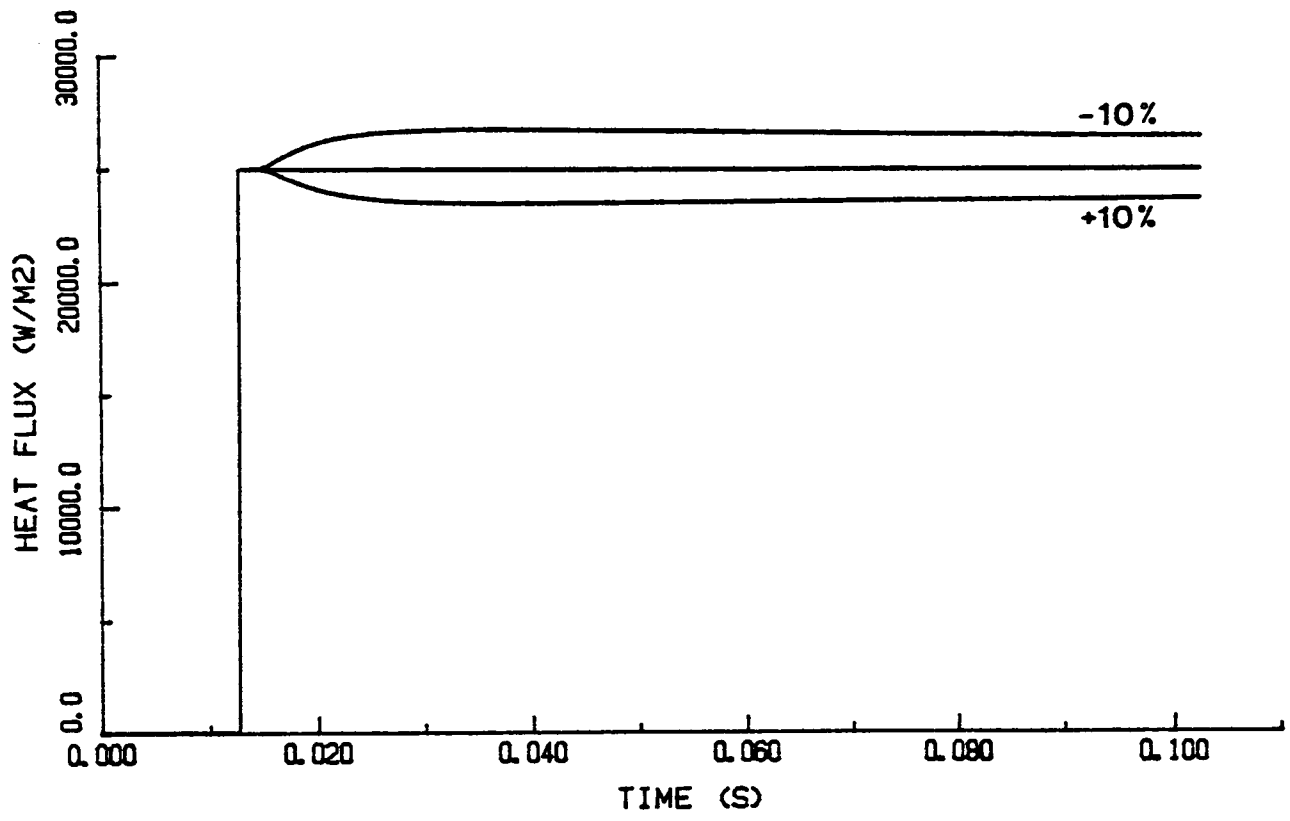

Figure 6.51: Effect on Heat Transfer Rate of 10% Variation in a/k

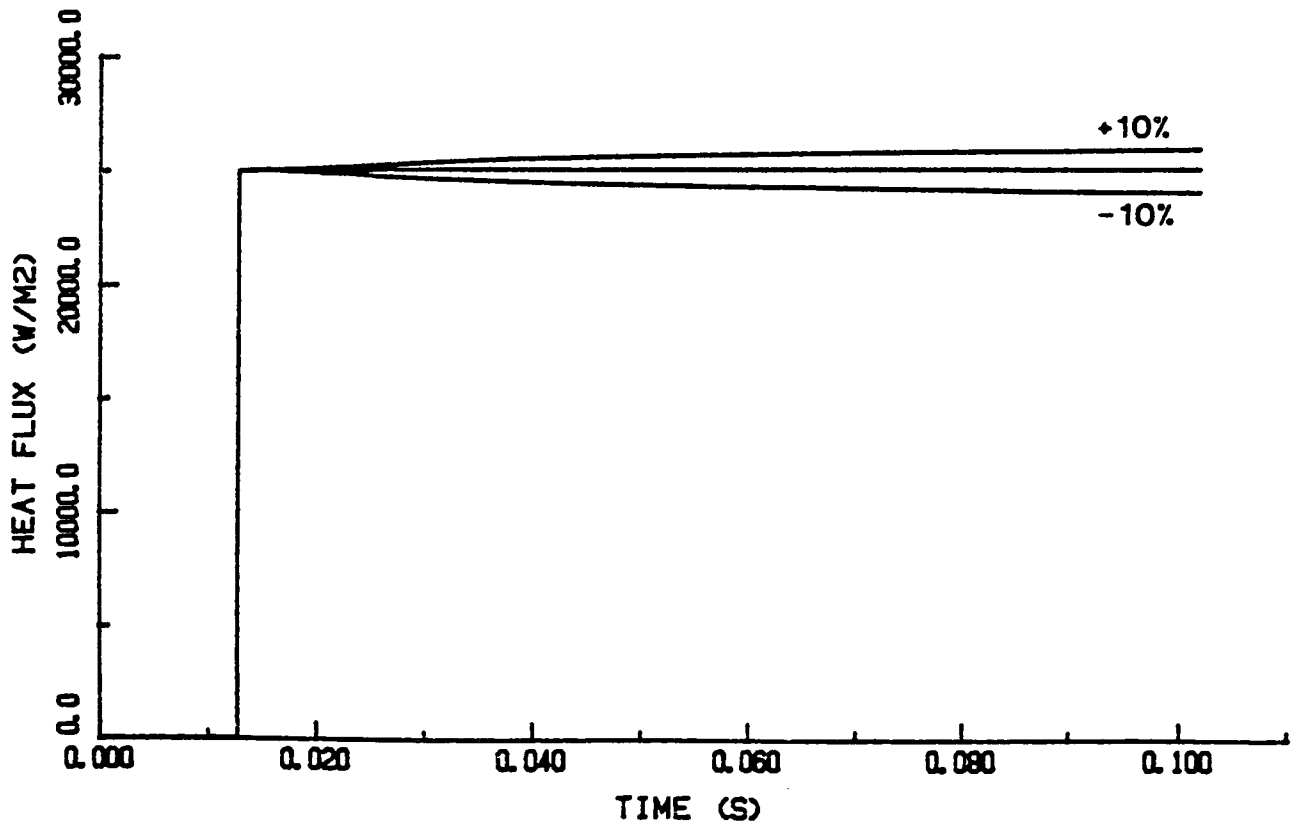

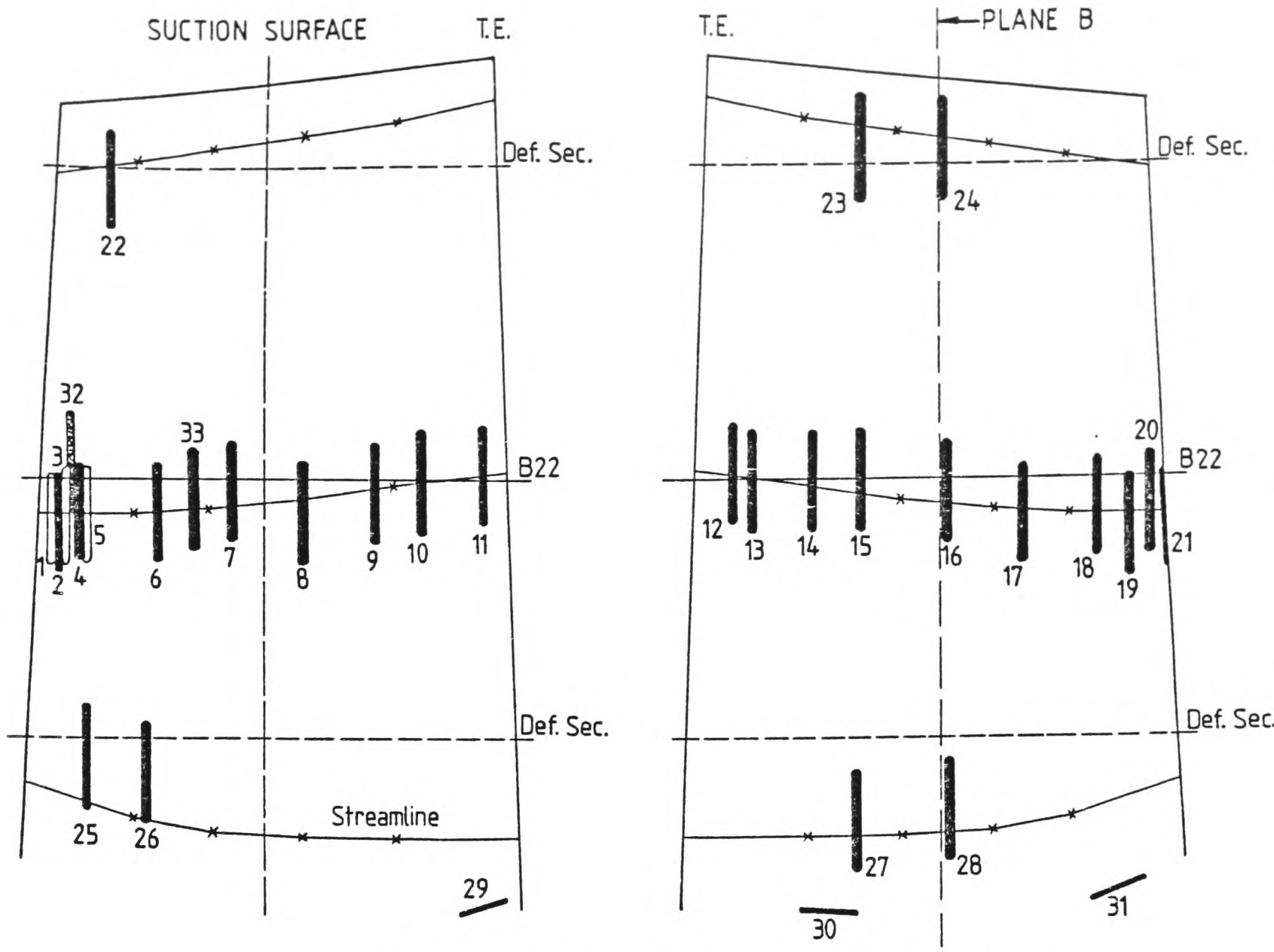

The heights from the engine centre-line to the B22 section and the two definitive sections are given in Table 7.1.

Figure 7.1: Overall Distribution of Thin Film Gauges

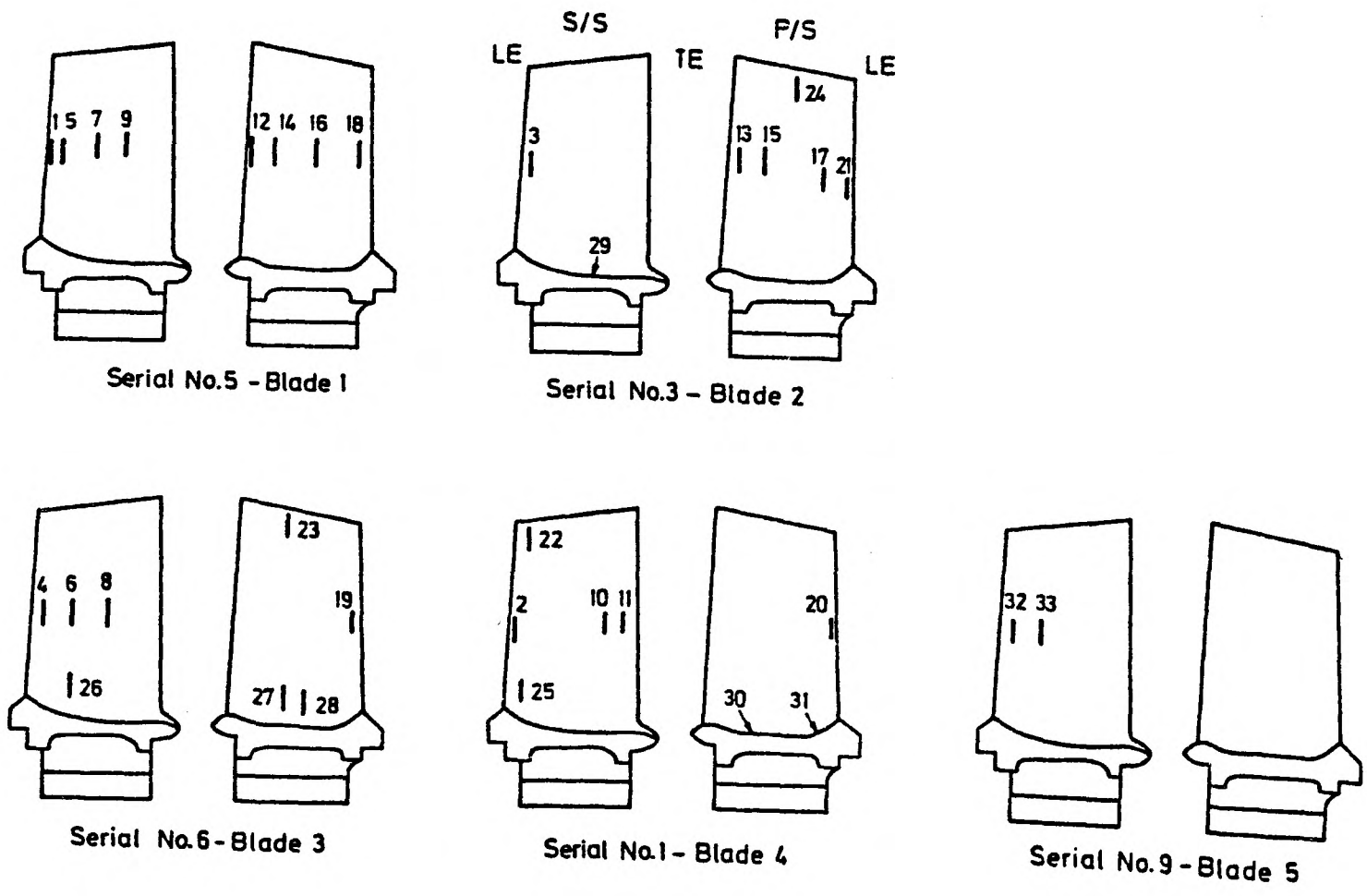

Figure 7.2: Schematic Diagram Showing the Distribution of Thin Film Gauges Amongst the Five Blades.

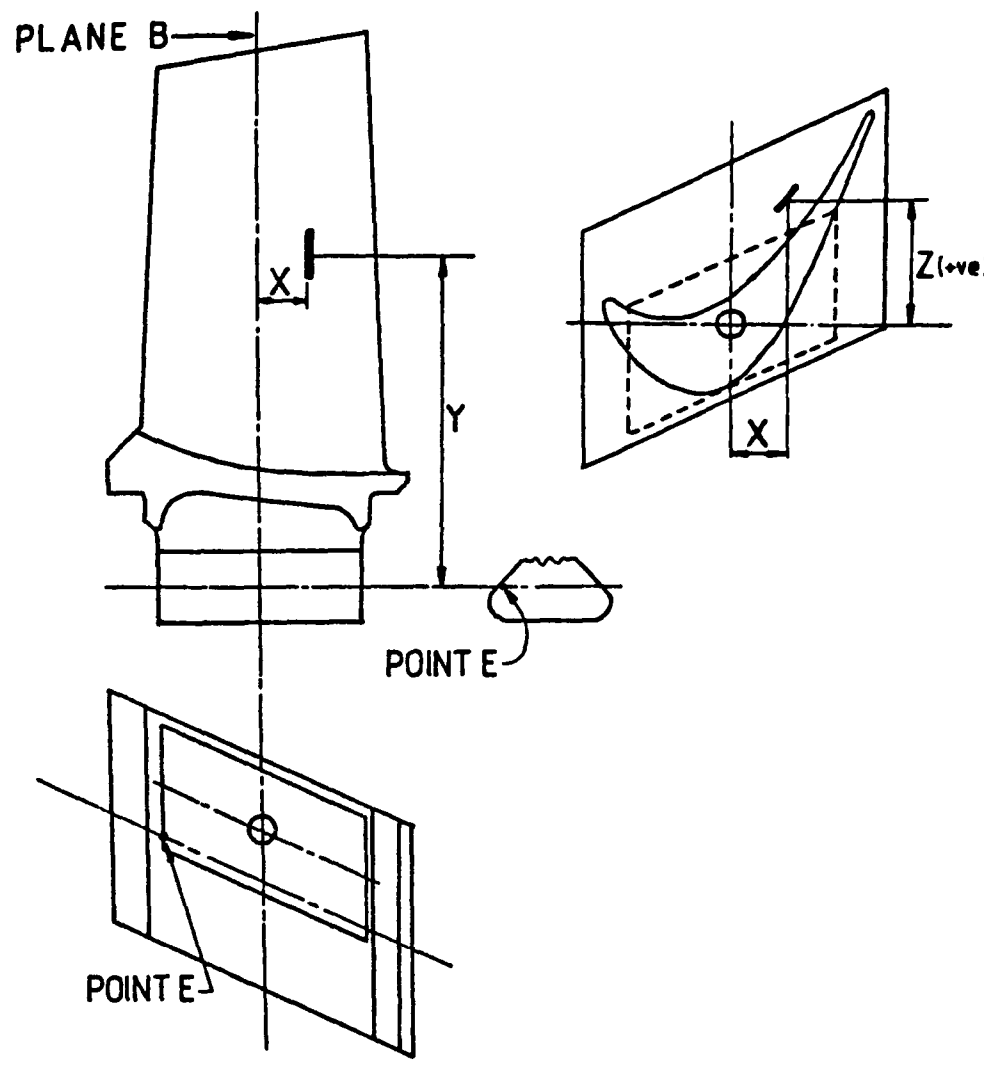

Figure 7.3: Definition of Thin Film Gauge Position.

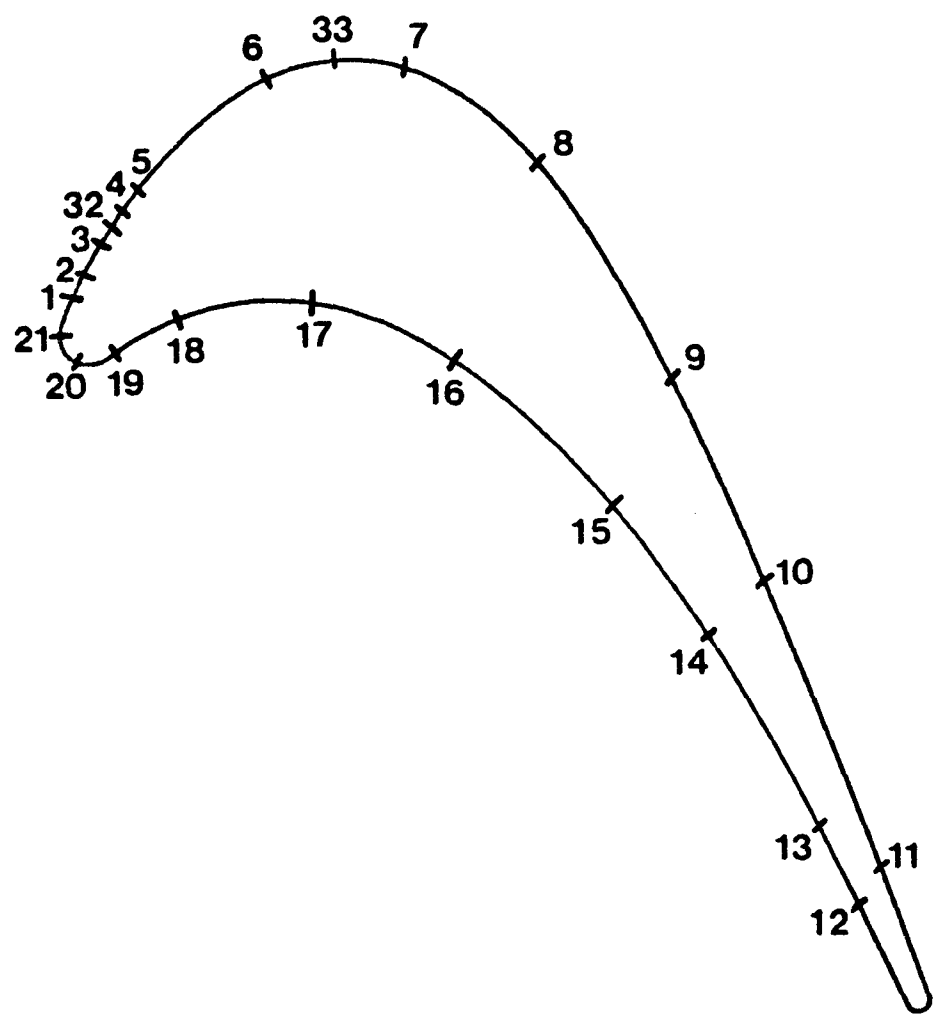

Figure 7.4: Position of Thin Film Gauges Around the B22 Profile.

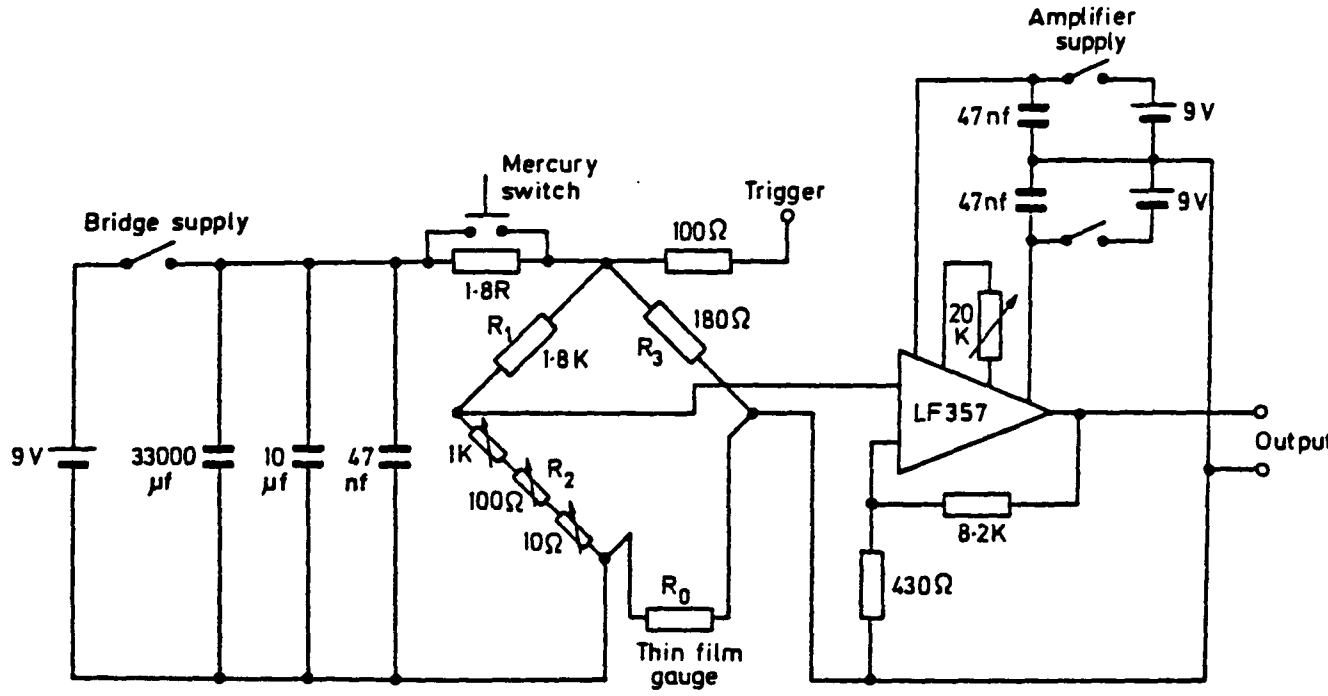

Figure 7.5: Circuit for Electrical Discharge Test.

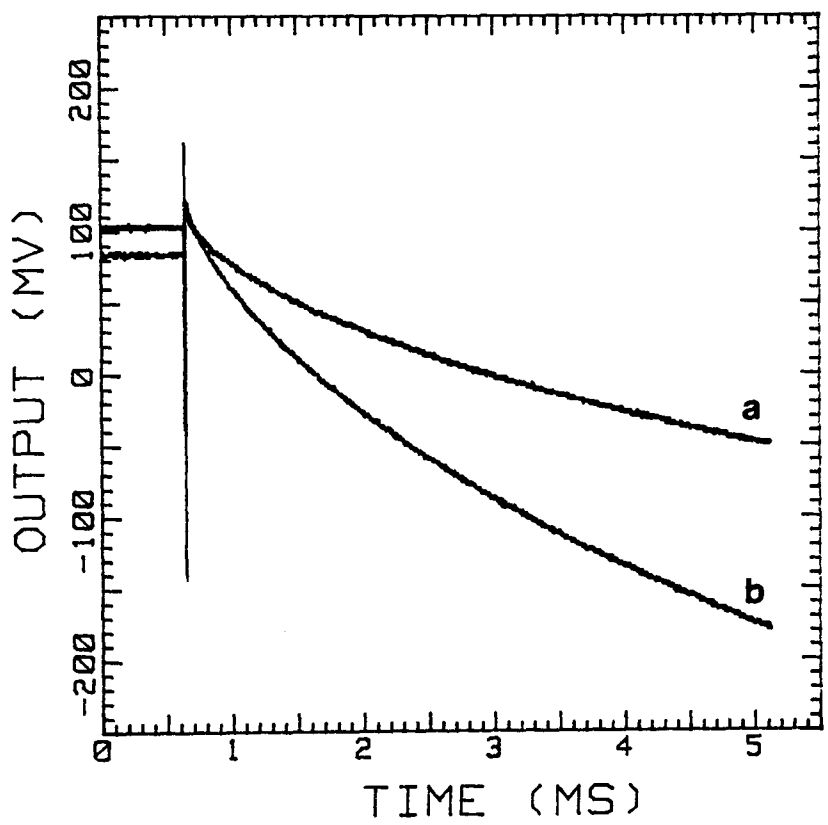

Figure 7.6: Thin Film Gauge Output during Electrical Discharge Test
(a) Gauge in Air
(b) Gauge Covered with Glycerine

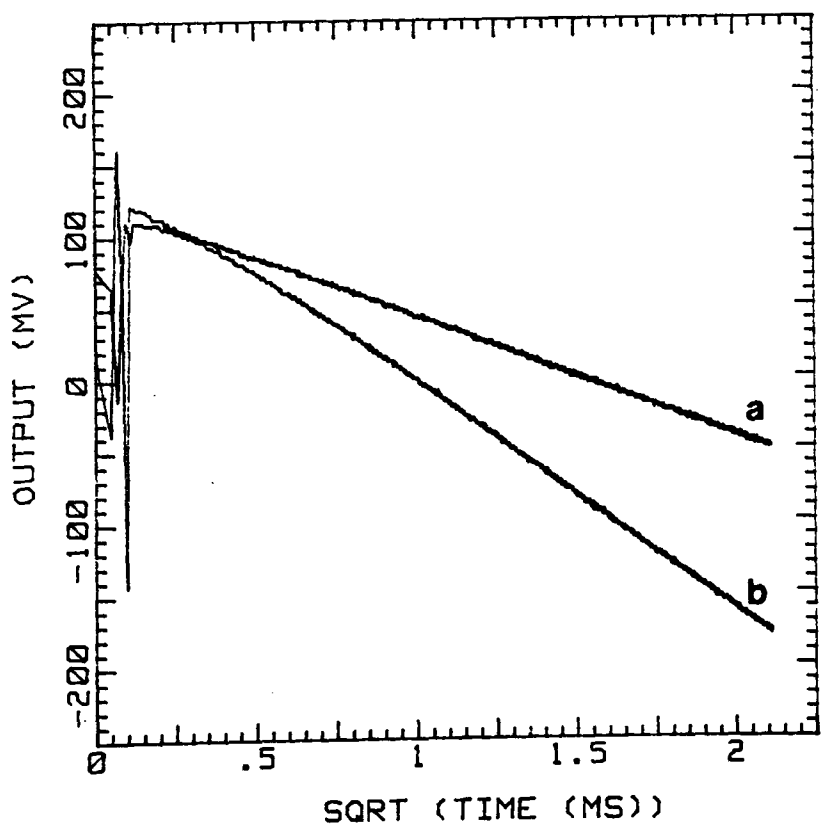

Figure 7.7: Thin Film Gauge Output during Electrical Discharge Test Plotted against Square Root of Time.
(a) Gauge in Air
(b) Gauge Covered with Glycerine

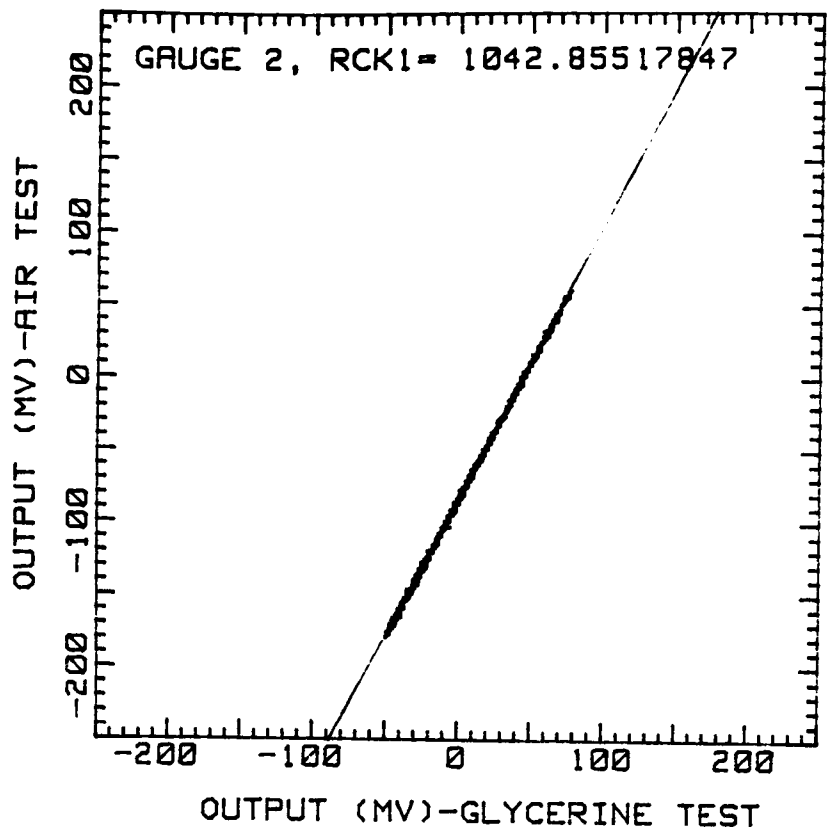

Figure 7.8: Calculation of $\sqrt{(\rho ck)_1}$ from the Ratio of Thin Film Gauge Outputs During the Air and Glycerine Tests, (equation 7.7).

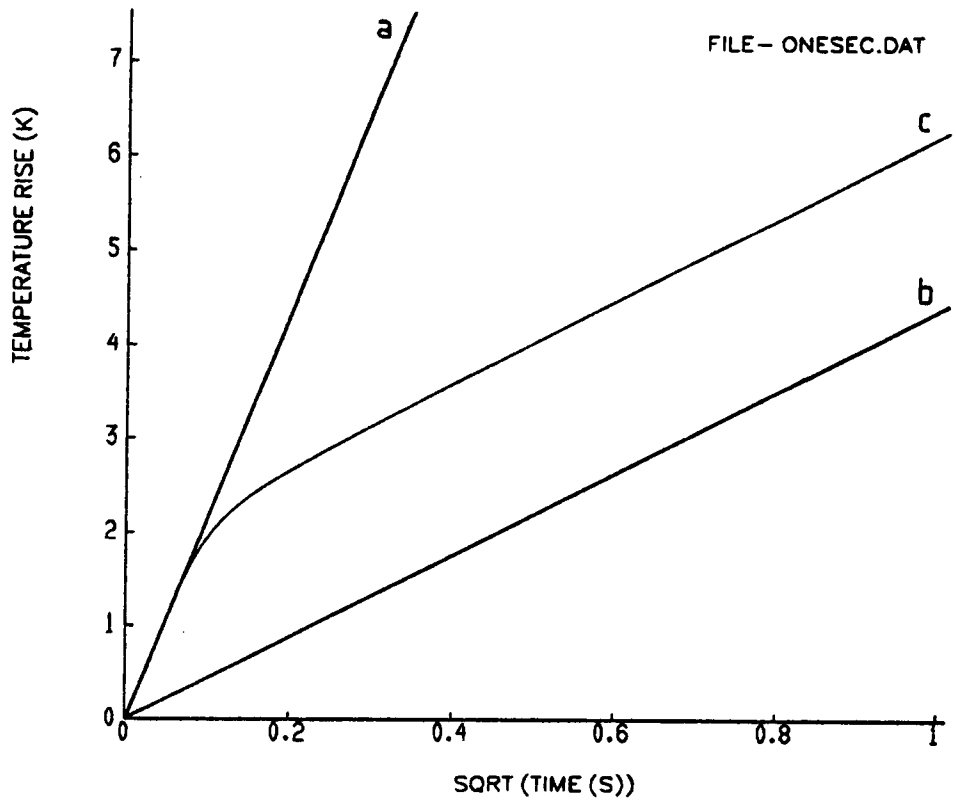

Figure 7.9: Predicted Surface Temperature Rise for Step in Heat Transfer Rate at the Surface of: (a) Insulator Alone; (b) Metal Alone; (c) Insulator Coated Metal.

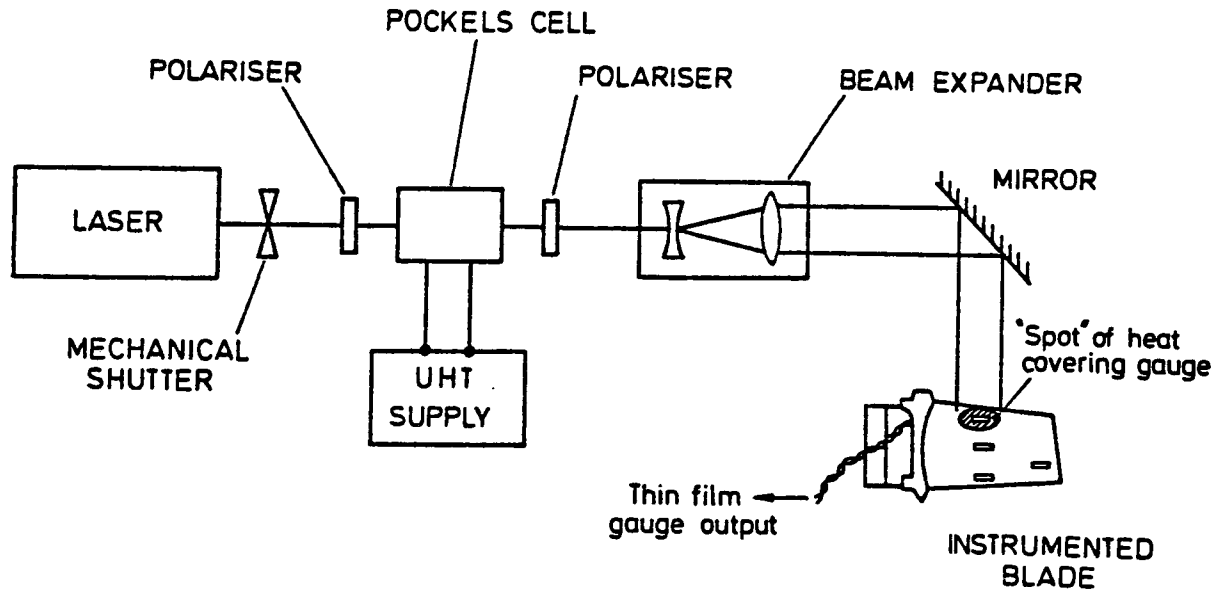

Figure 7.10: Apparatus for Laser Calibration of a/k.

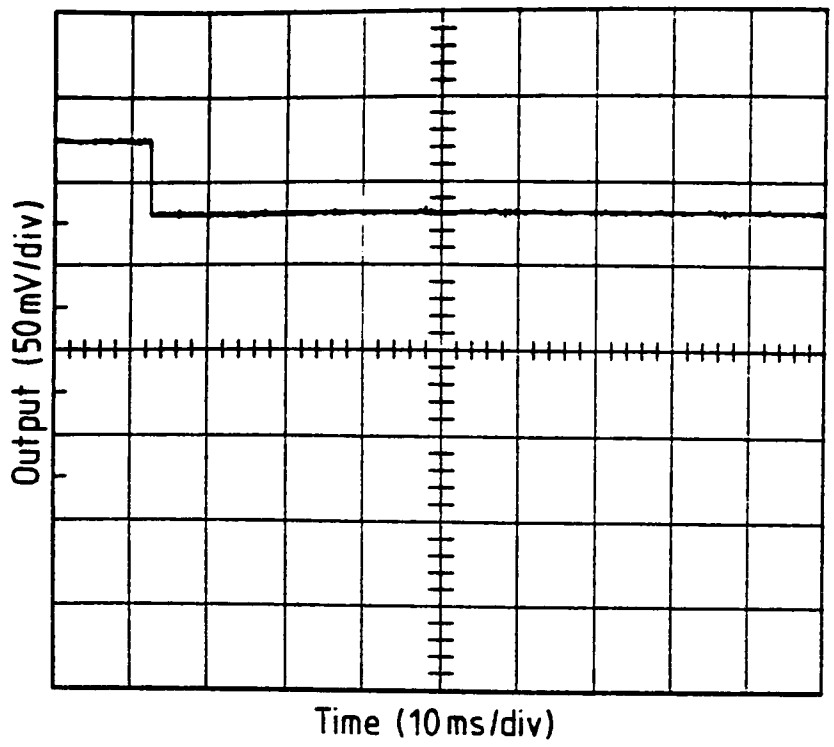

Figure 7.11: Photodiode Test.

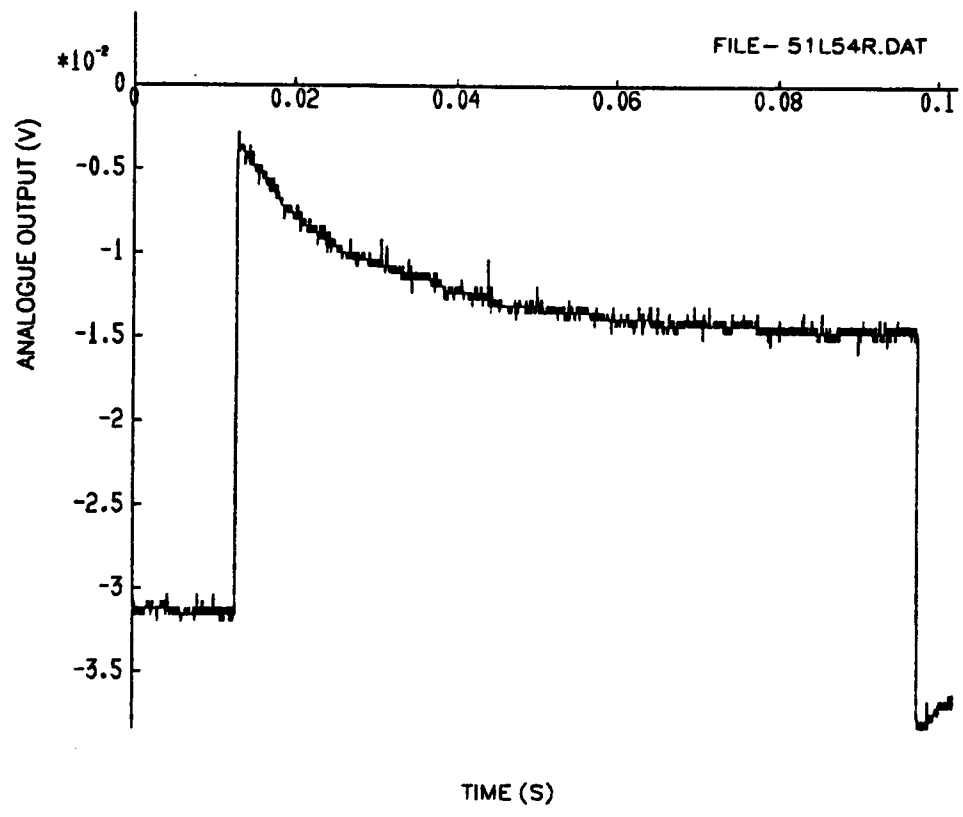

Figure 7.12: Analogue Output from Thin Film Gauge Mounted on M.G.C. Subject to Step in Heat Transfer Rate at the Surface.

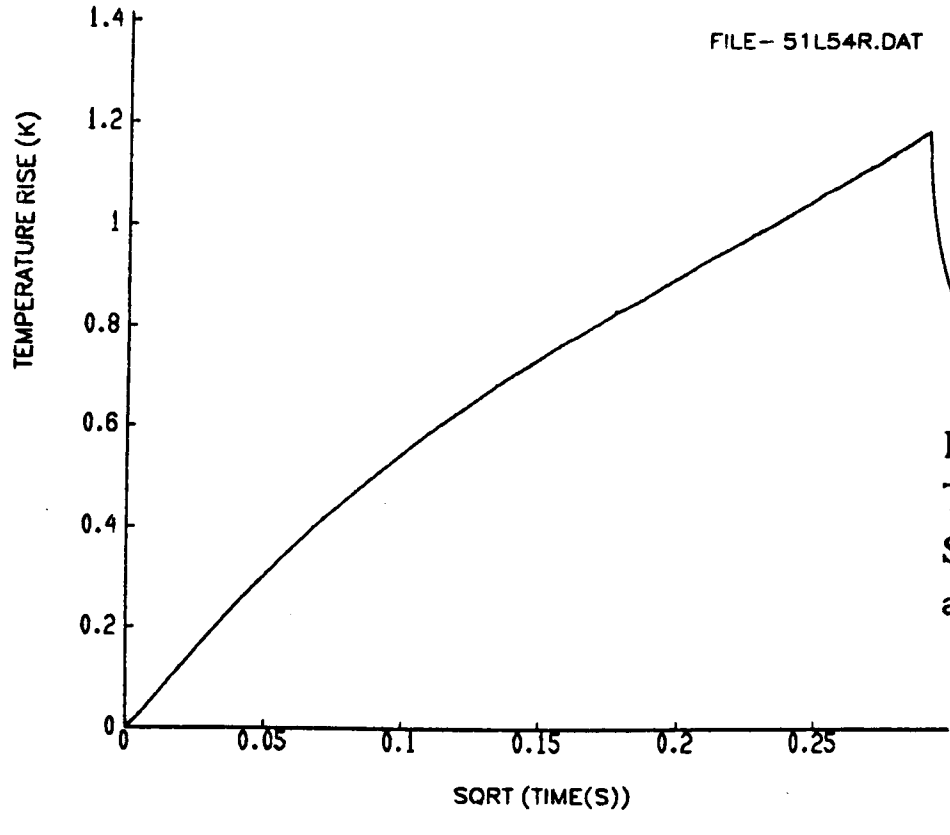

Figure 7.13: Temperature Rise of Thin Film Gauge Mounted on M.G.C. Subject to Step in Heat Transfer Rate at the Surface.

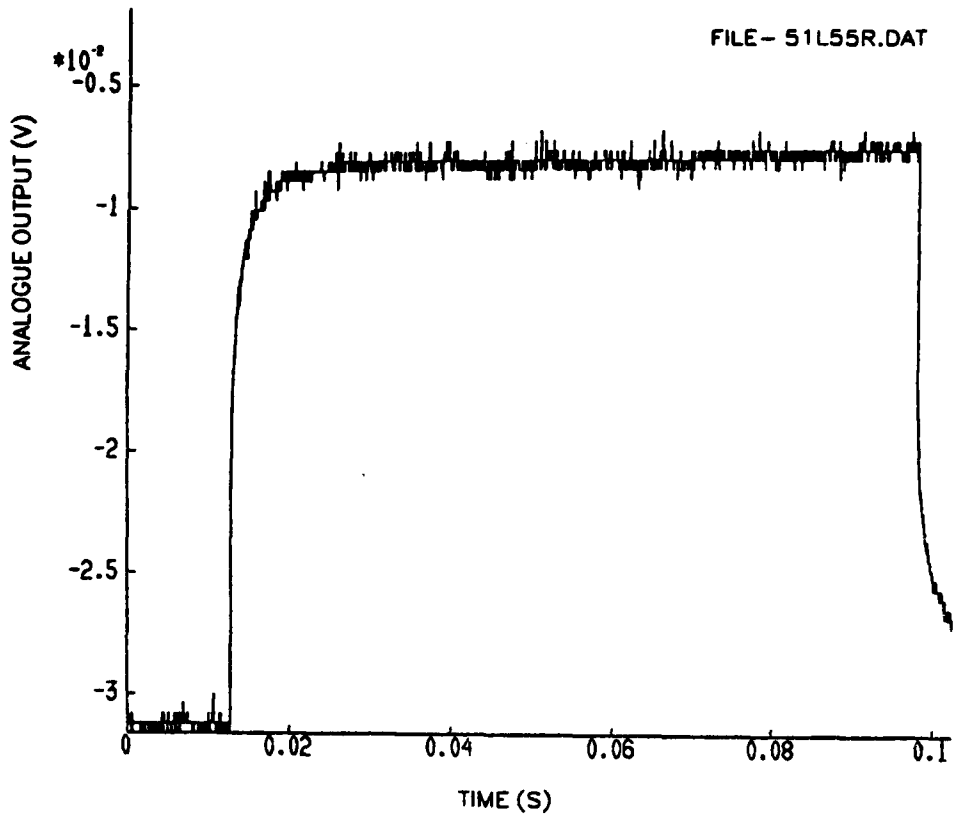

Figure 7.14: Analogue Output from Blackened Thin Film Gauge Mounted on M.G.C. Subject to Step in Heat Transfer Rate at the Surface.

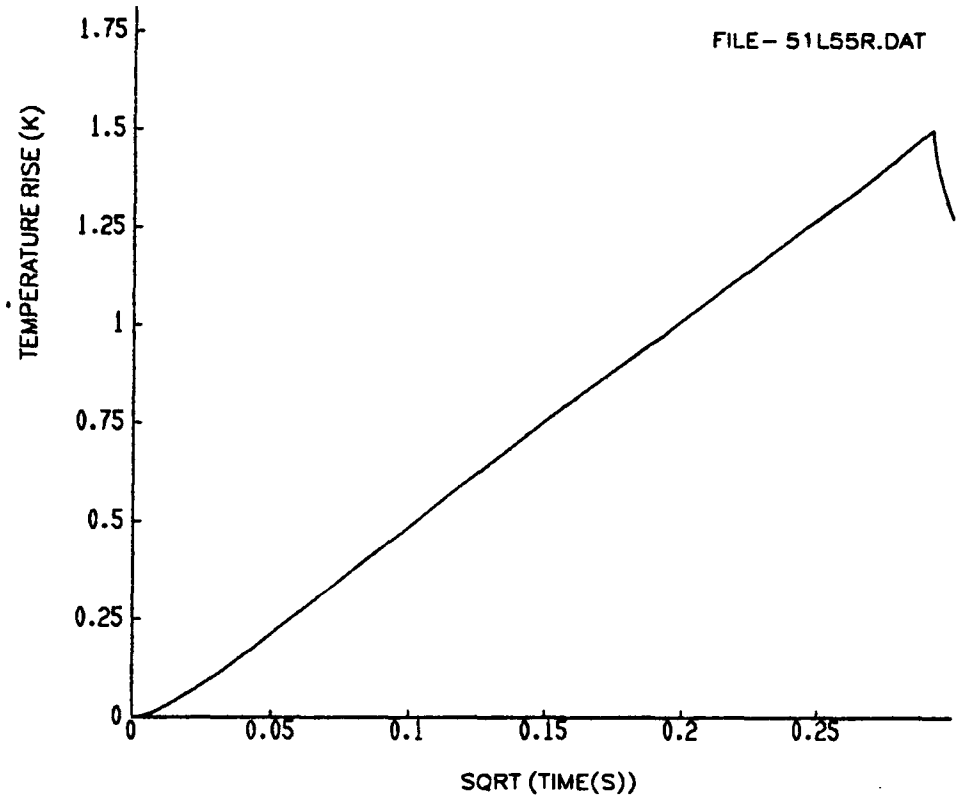

Figure 7.15: Temperature Rise of Blackened Thin Film Gauge Mounted on M.G.C. Subject to Step in Heat Transfer Rate at the Surface.

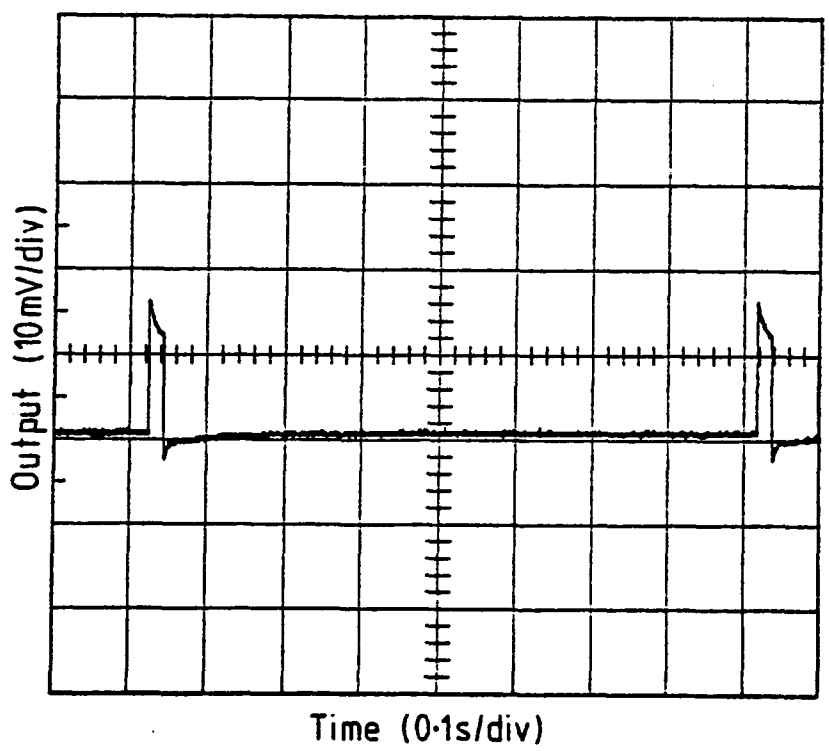

Figure 7.16: Repeat Pulsing of Gauge Mounted on M.G.C.

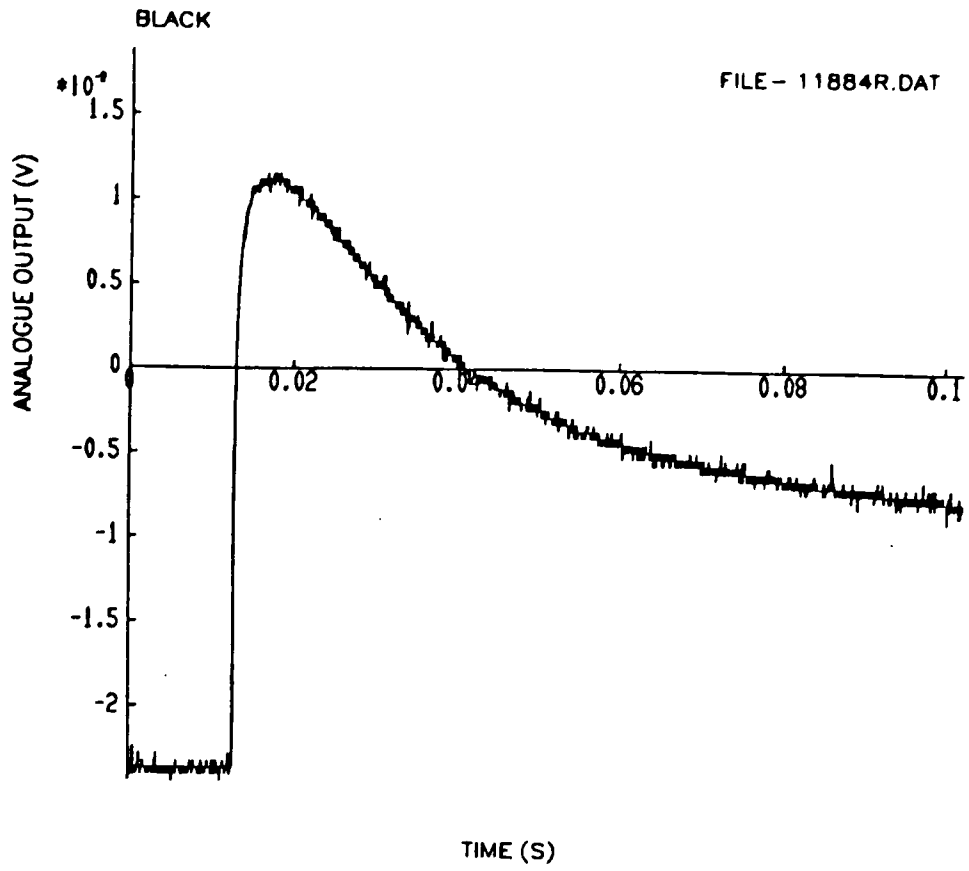

Figure 7.17: Analogue Output from Thin Film Gauge Mounted on Two Layered Substrate Subject to Step in Heat Transfer Rate at the Surface. (Beam Dia. 10mm, Gauge Blackened).

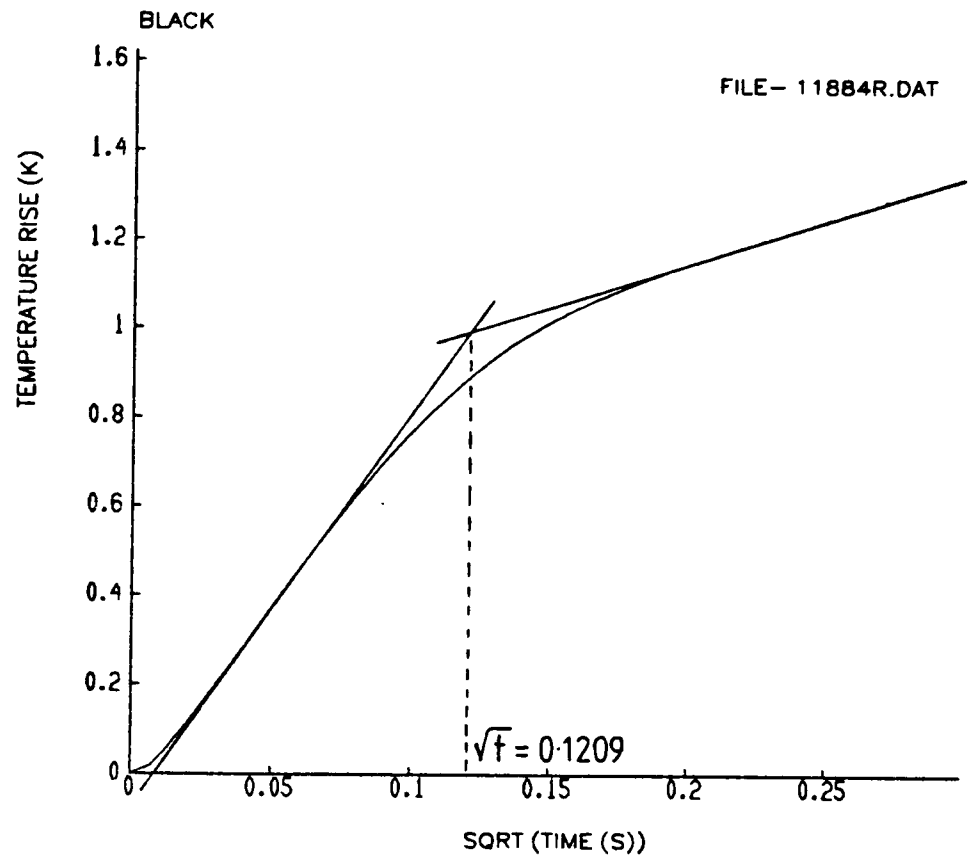

Figure 7.18: Temperature Rise from Thin Film Gauge Mounted on Two Layered Substrate Subject to Step in Heat Transfer Rate at the Surface. (Beam Dia. 10mm, Gauge Blackened).

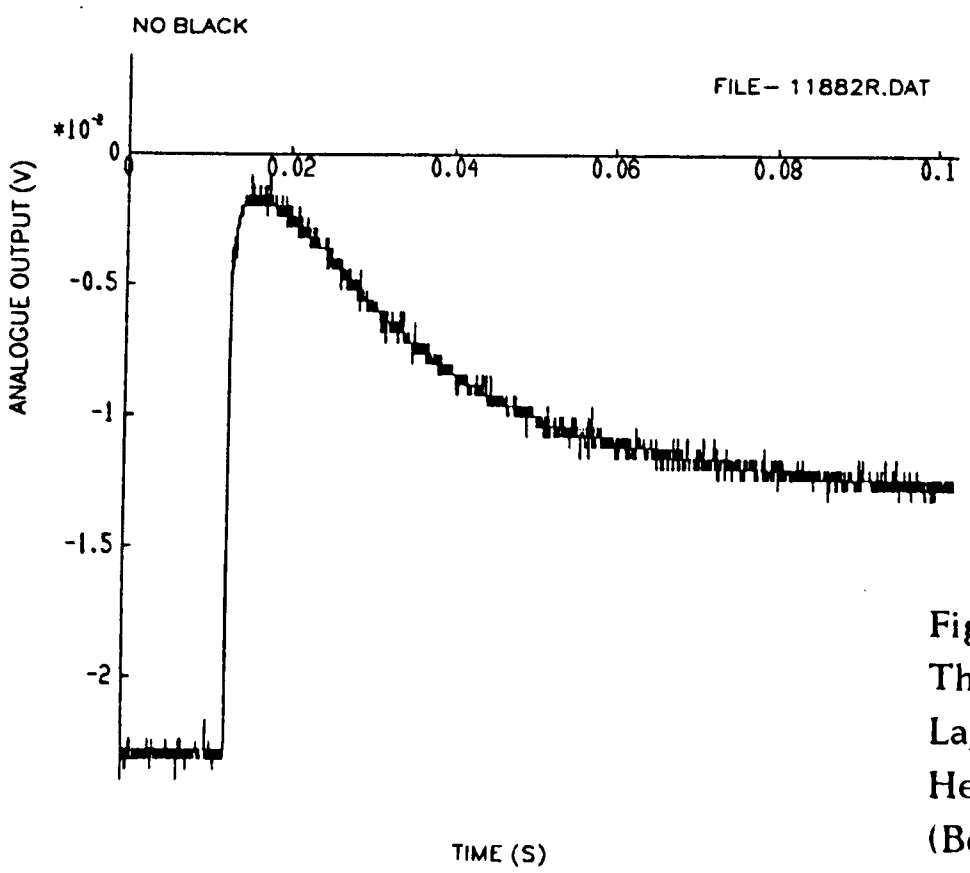

Figure 7.19: Analogue Output from Thin Film Gauge Mounted on Two Layered Substrate Subject to Step in Heat Transfer Rate at the Surface. (Beam Dia. 10mm, Gauge Not Blackened)

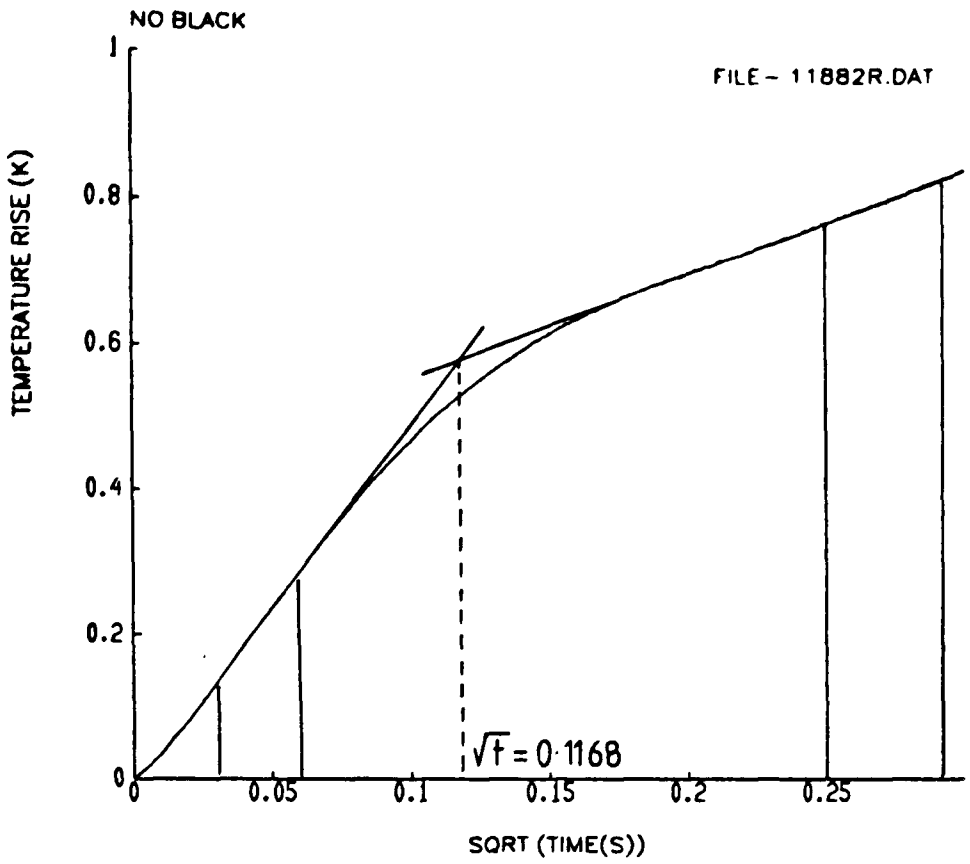

Figure 7.20: Temperature Rise from Thin Film Gauge Mounted on Two Layered Substrate Subject to Step in Heat Transfer Rate at the Surface. (Beam Dia. 10mm, Gauge Not Blackened)

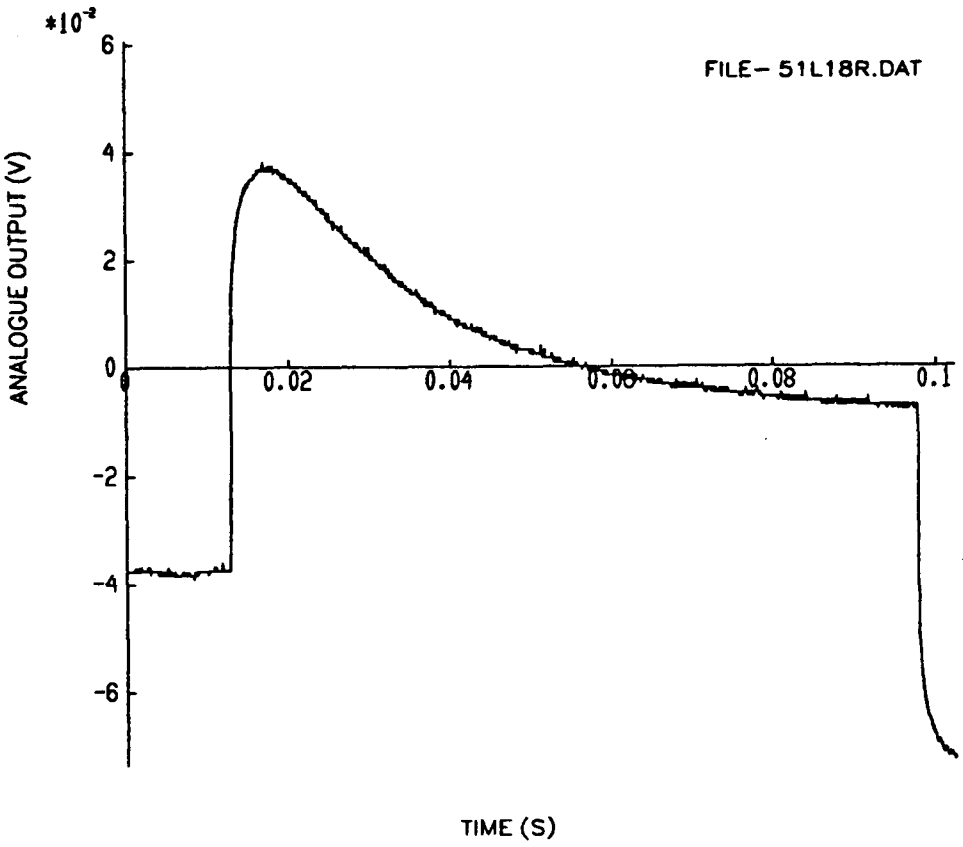

Figure 7.21: Analogue Output from Thin Film Gauge Mounted on Two Layered Substrate Subject to Step in Heat Transfer Rate at the Surface. (Beam Dia. 5mm, Gauge Not Blackened)

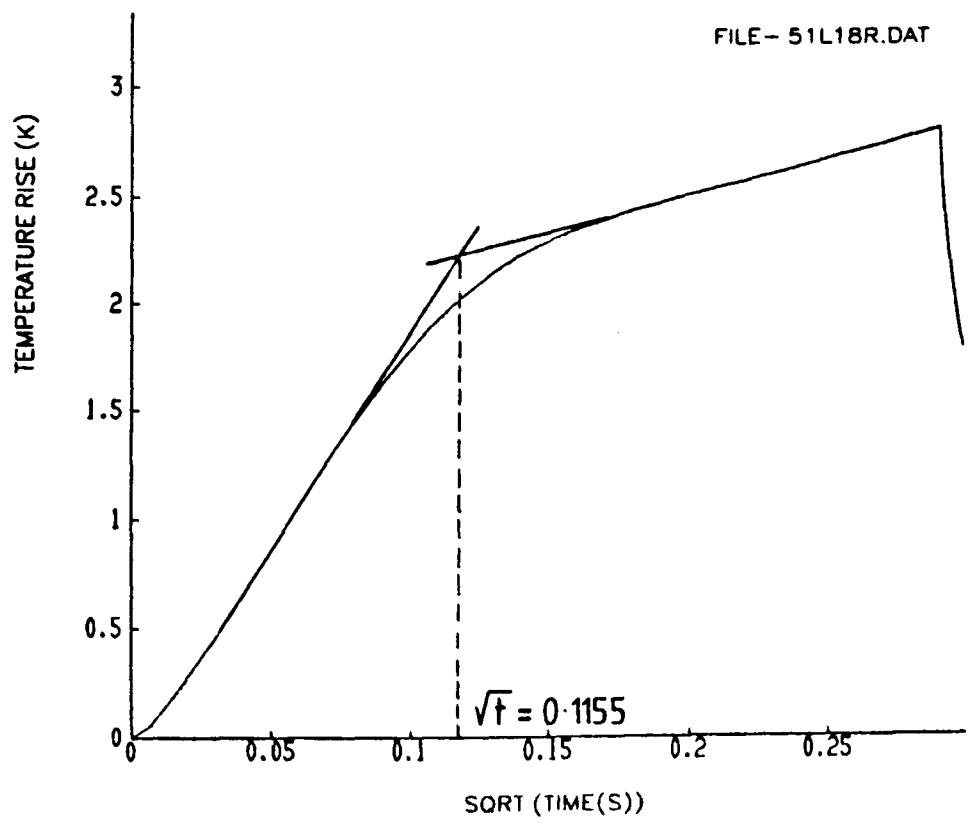

Figure 7.22: Temperature Rise from Thin Film Gauge Mounted on Two Layered Substrate Subject to Step in Heat Transfer Rate at the Surface. (Beam Dia. 5mm, Gauge Not Blackened)

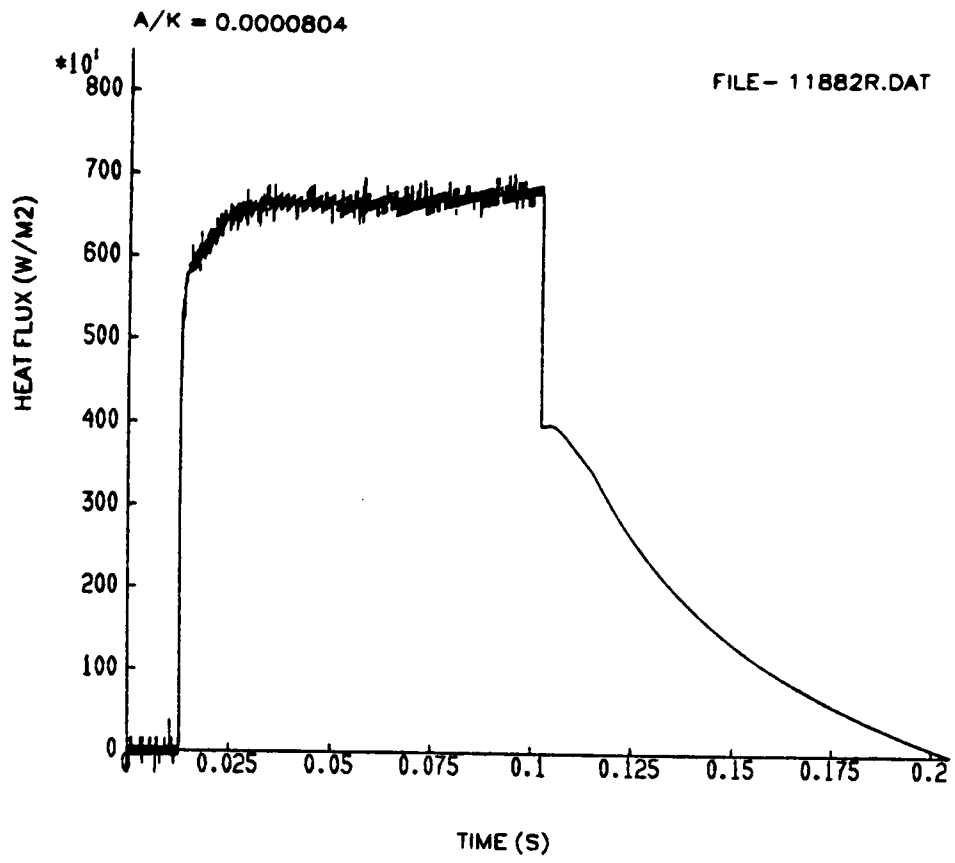

Figure 7.23: Heat Transfer Rate Calculated from Analogue Output Shown in Figure 7.19 ($a/k = 80.4E\text{-}6\,m^2K/W$).

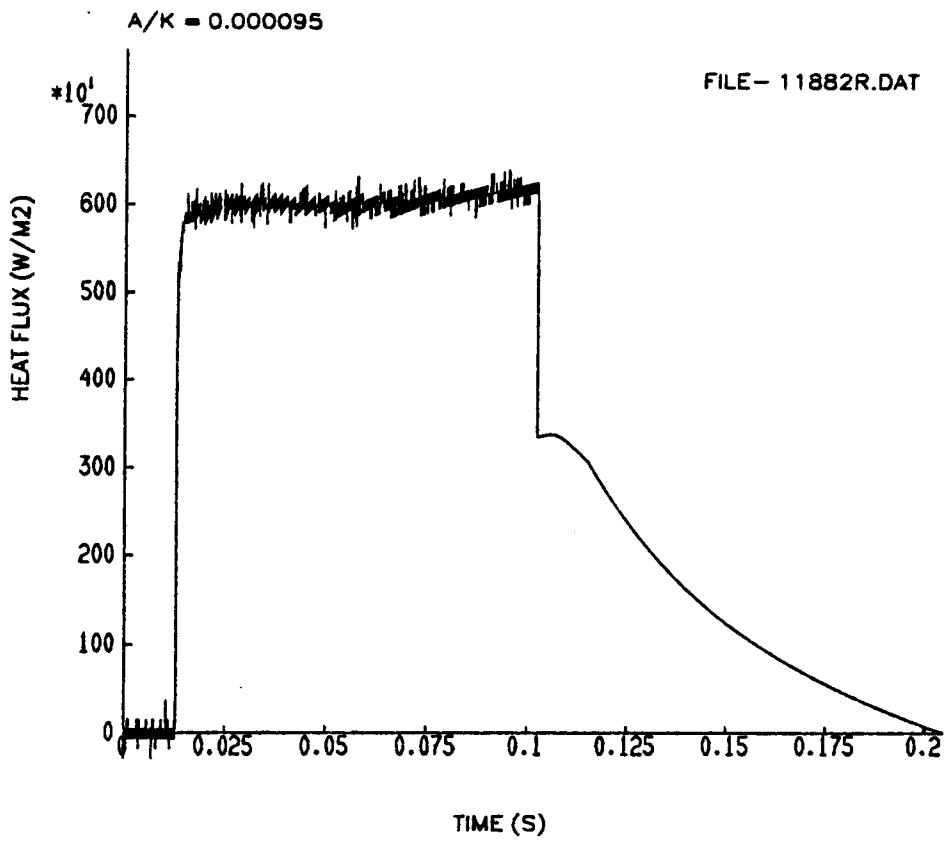

Figure 7.24: Heat Transfer Rate Calculated from Analogue Output Shown in Figure 7.19 ($a/k = 95.0E\text{-}6\,m^2K/W$).

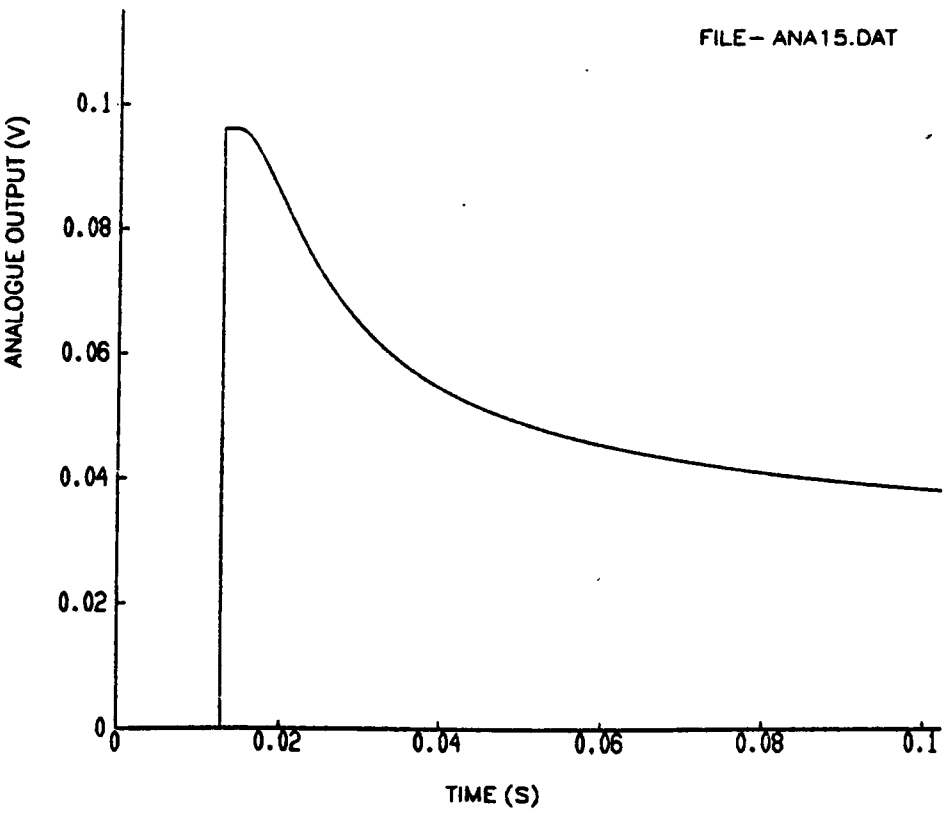

Figure 7.25: Predicted Analogue Output From Thin Film Gauge Mounted on Two-Layered Substrate Subject to Step in Heat Transfer Rate at the Surface.

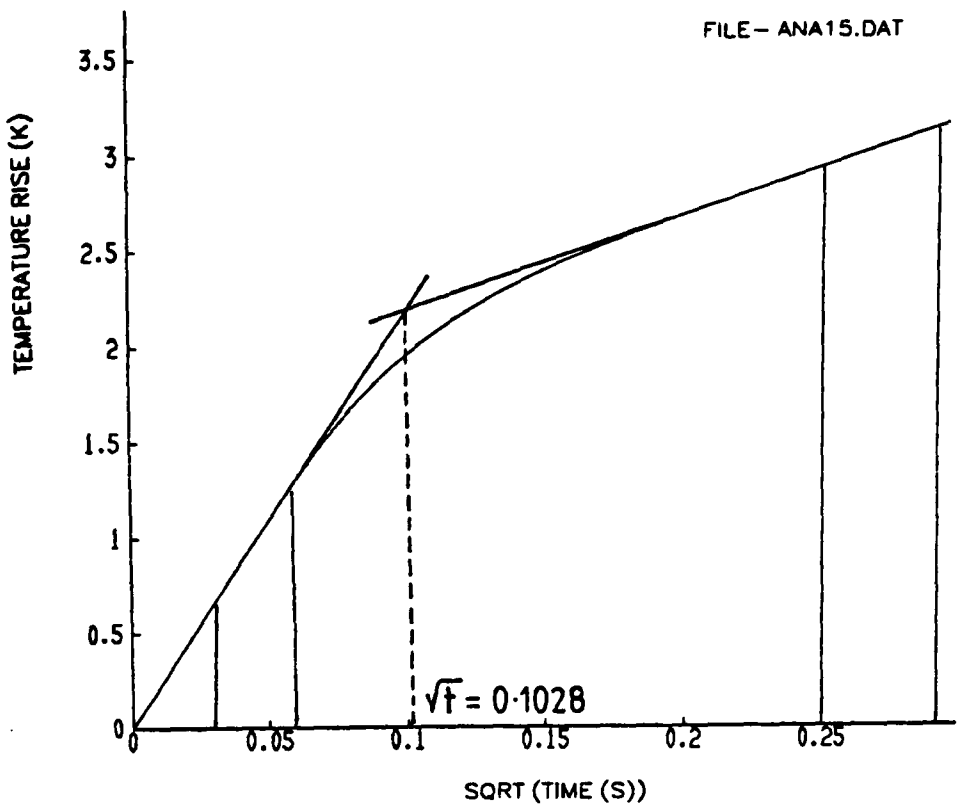

Figure 7.26: Predicted Temperature Rise from Thin Film Gauge Mounted on Two-Layered Substrate Subject to Step in Heat Transfer Rate at the Surface.

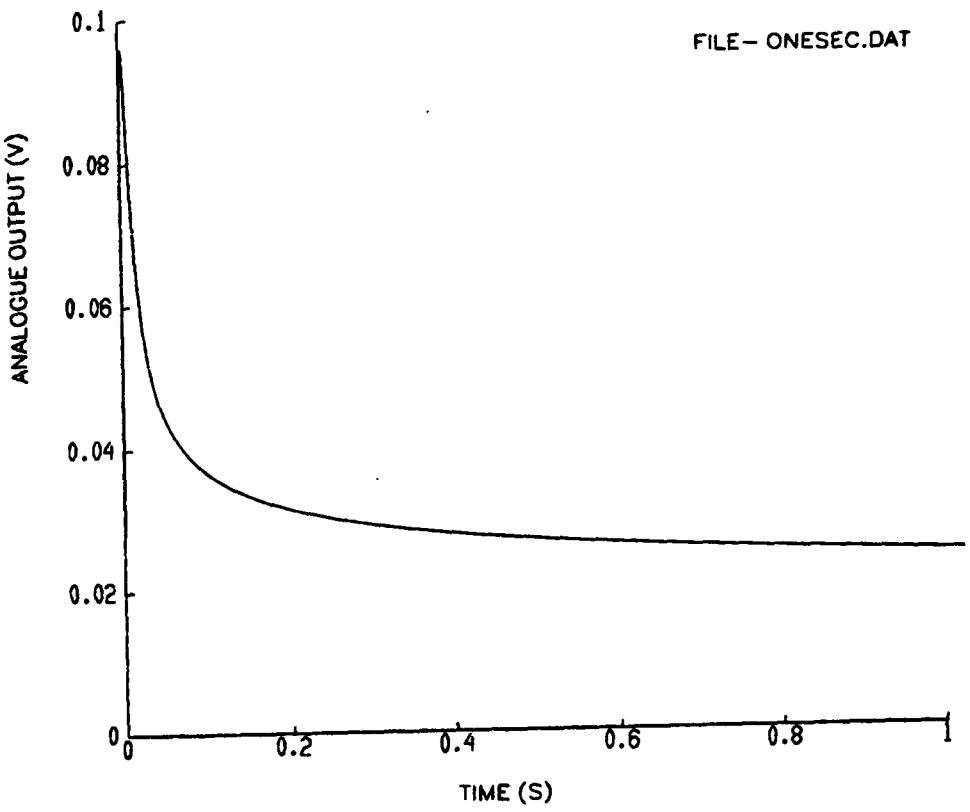

Figure 7.27: Predicted Analogue Output From Thin Film Gauge Mounted on Two-Layered Substrate Subject to Step in Heat Transfer Rate at the Surface.

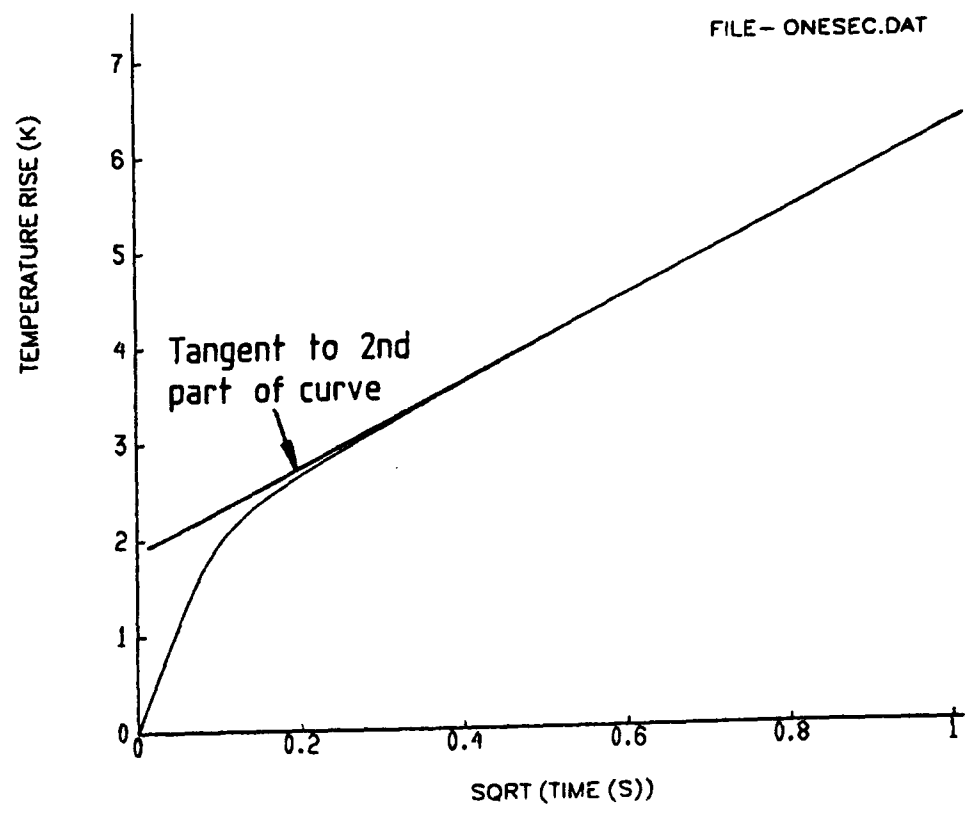

Figure 7.28: Predicted Temperature Rise from Thin Film Gauge Mounted on Two-Layered Substrate Subject to Step in Heat Transfer Rate at the Surface.

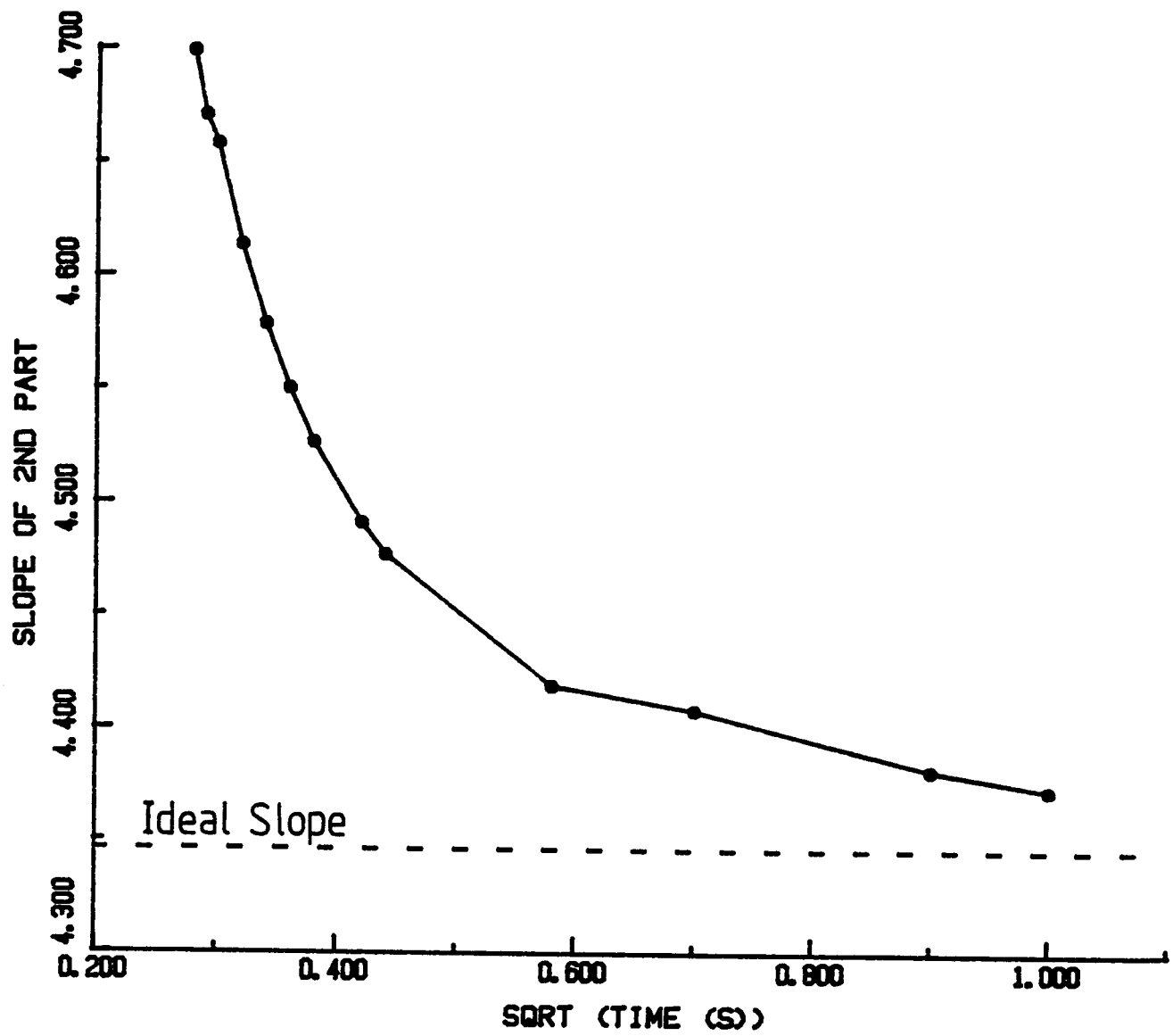

Figure 7.29: Variation of Slope of Second Part of Curve with Square Root of Time of Calculation.

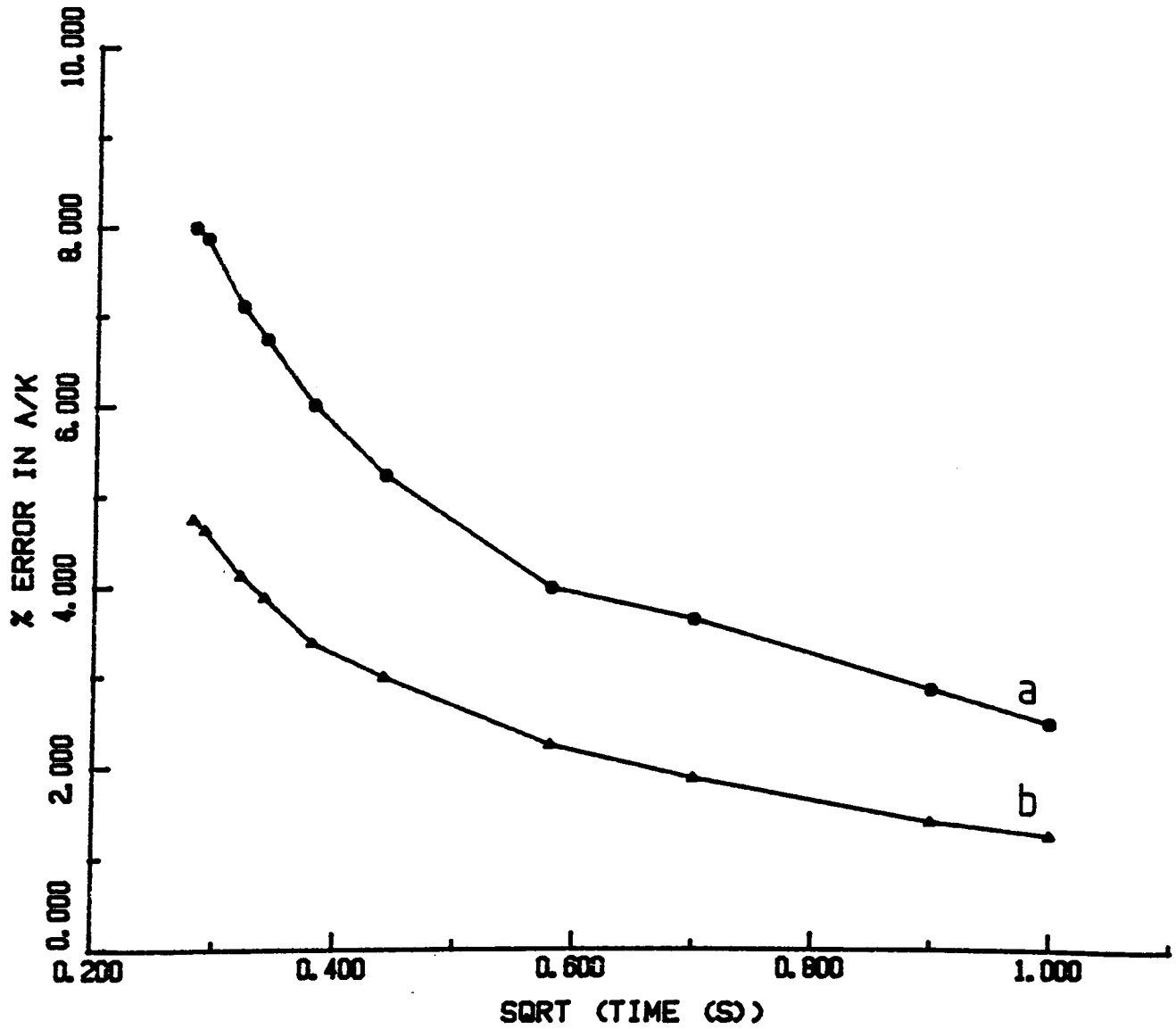

Figure 7.30: Variation of Error in Calculated Value of a/k with Square Root of Time at Which Slope of Second Part of Curve was Evaluated.
(a) Slope Calculated from Line Fit
(b) Slope Calculated from Equation 7.16 and $\sqrt{(\rho ck)_2}$

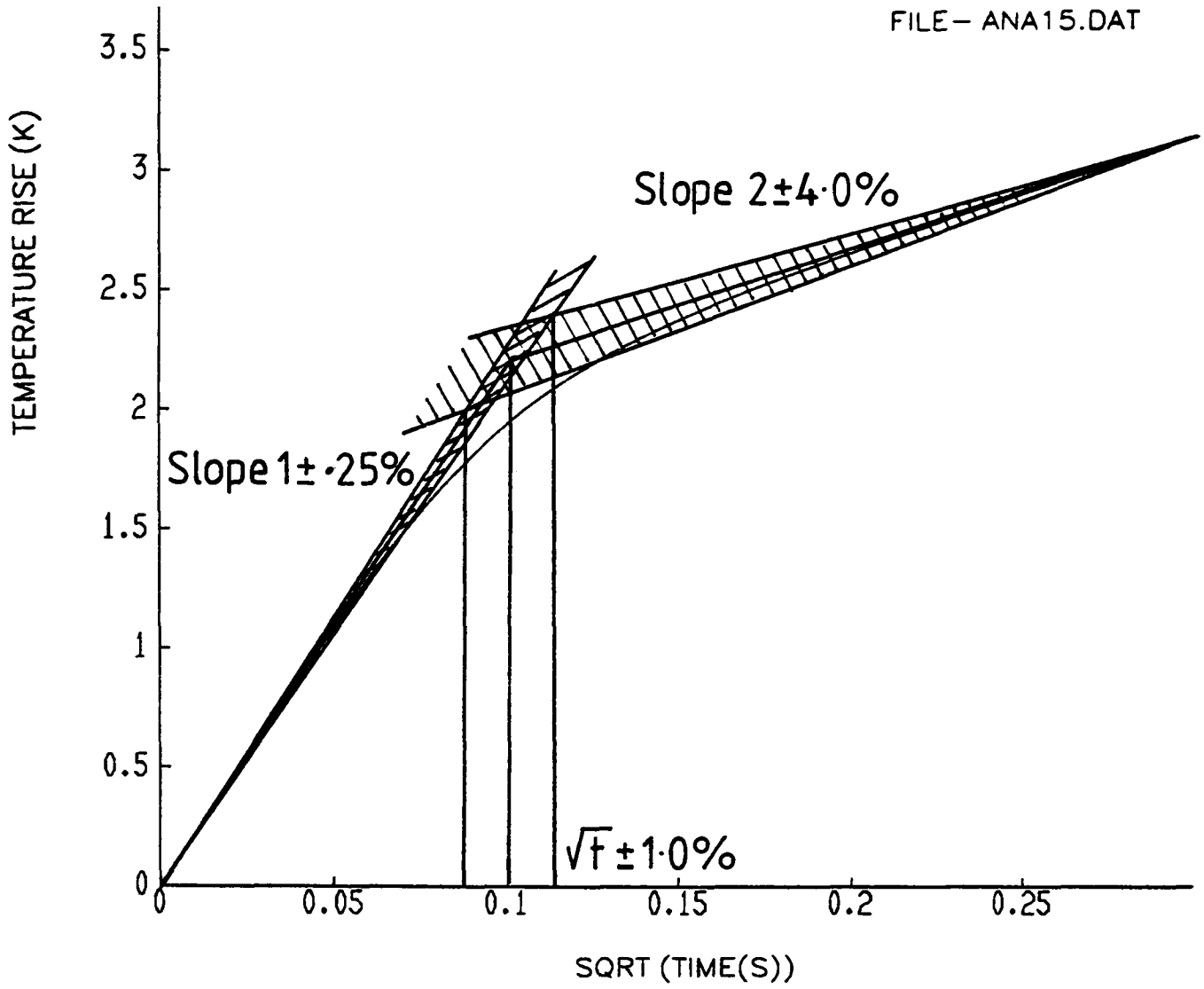

Figure 7.31: Effect of Uncertainty in Slopes 1 and 2 on Time of Intersection

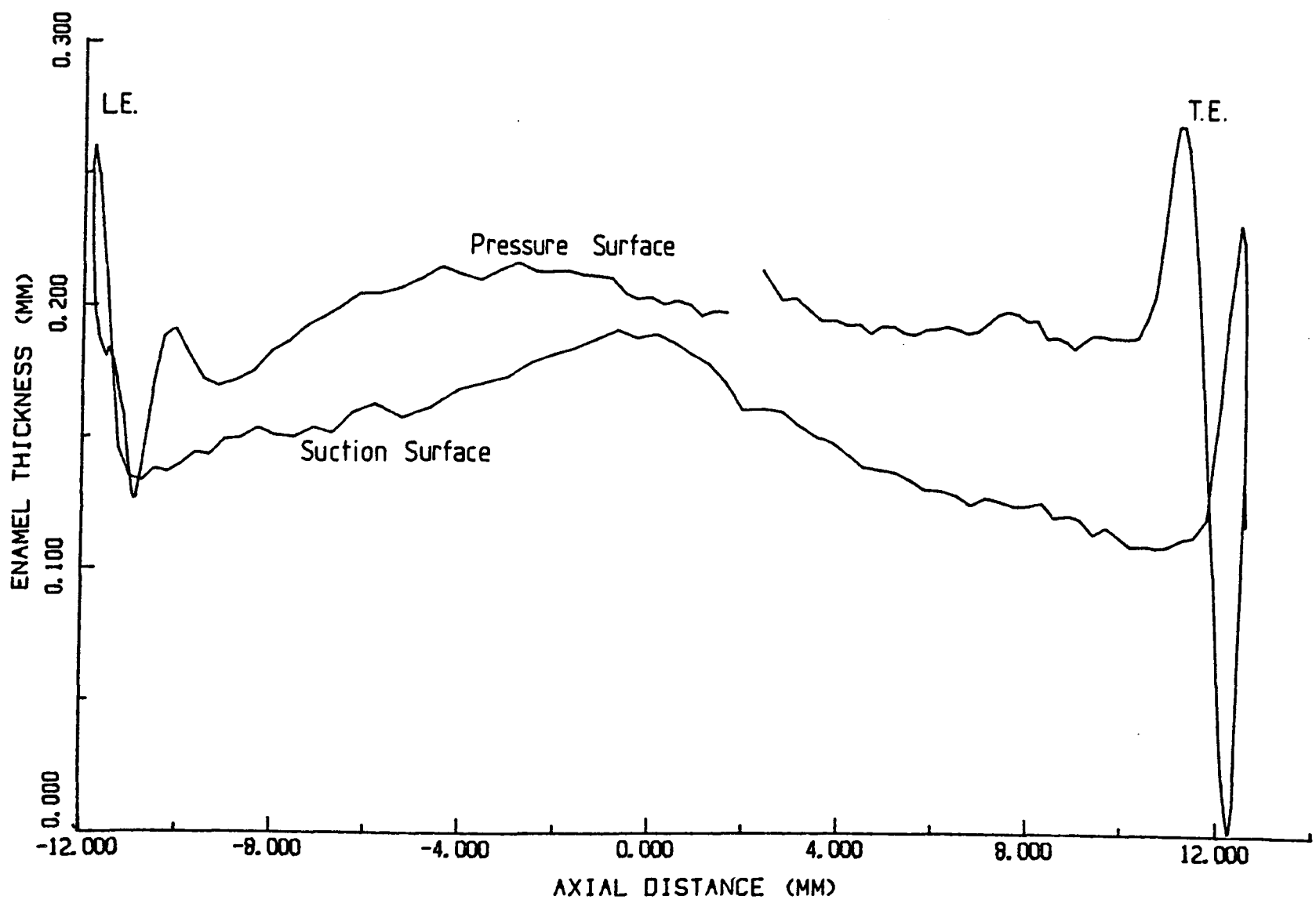

Figure 7.32: Variation of Enamel Thickness Around Blade Surface

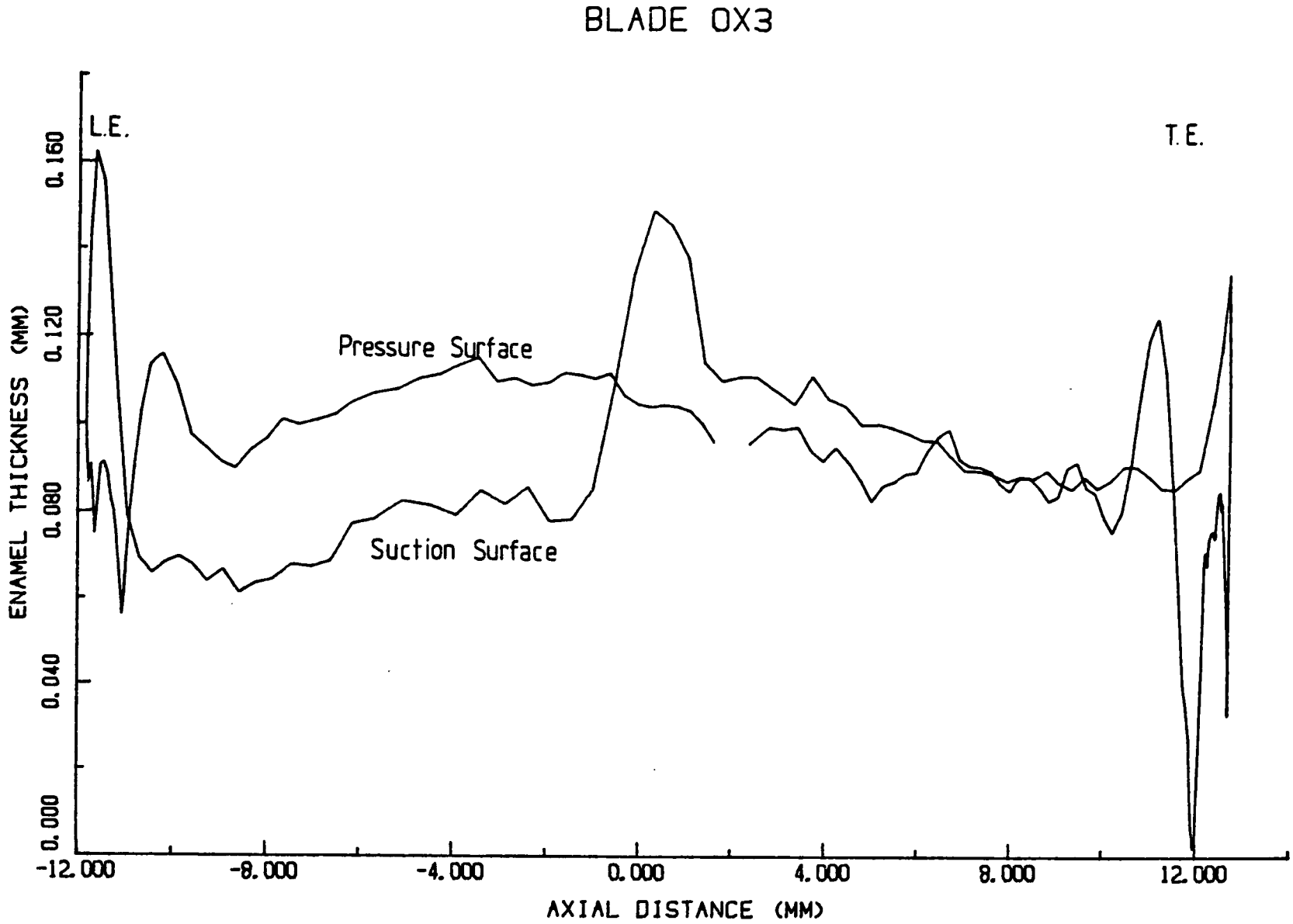

Figure 7.33: Variation of Enamel Thickness Around Blade Surface

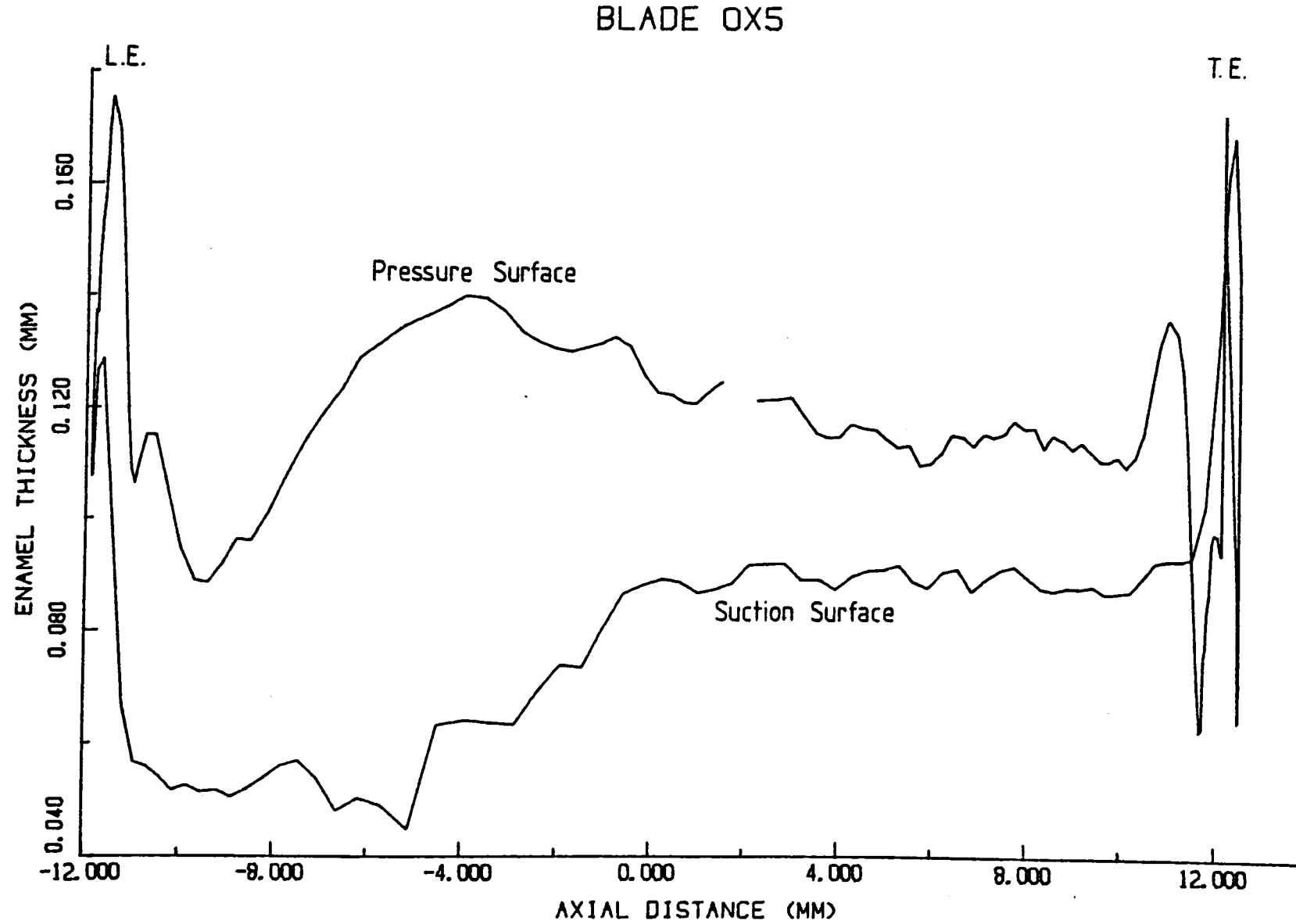

Figure 7.34: Variation of Enamel Thickness Around Blade Surface

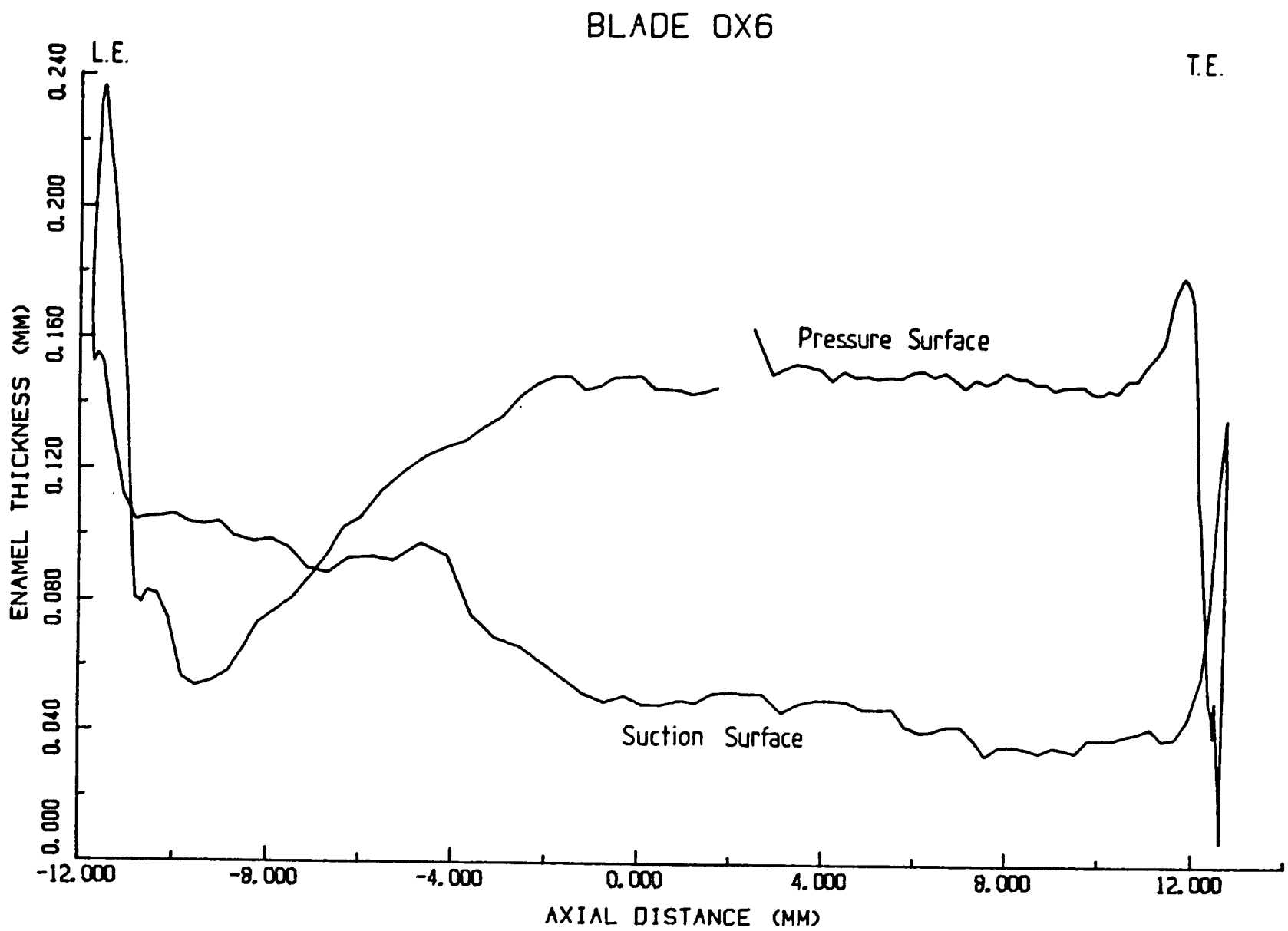

Figure 7.35: Variation of Enamel Thickness Around Blade Surface

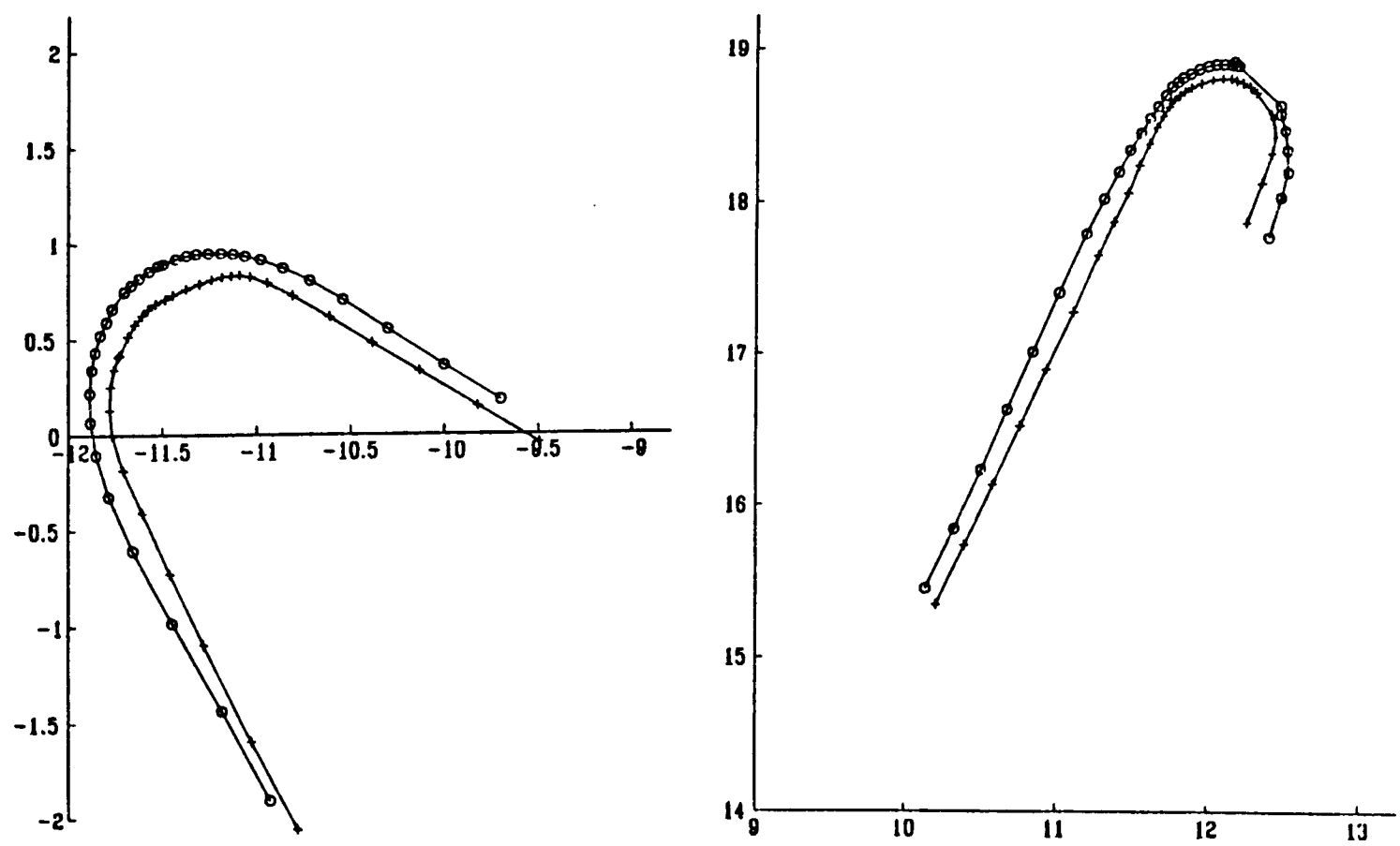

Figure 7.36: Detail of Measurement Points Around Leading and Trailing Edges

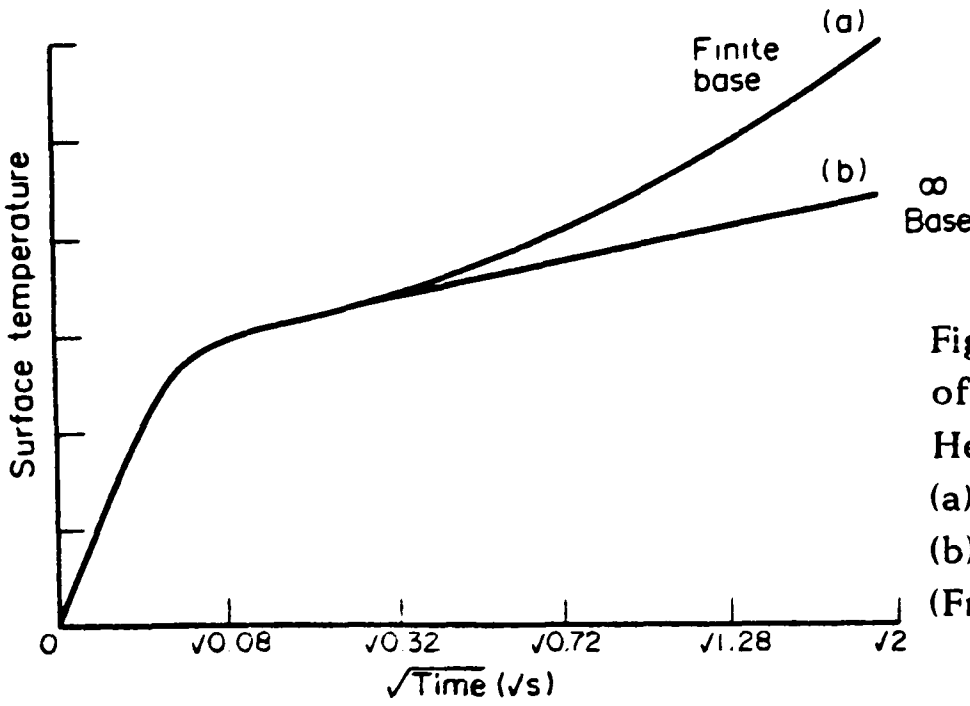

Figure 7.37: Surface Temperature Rise of Thin Film Gauge Subject to Step in Heat Transfer Rate at the Surface:
(a) 200μm Quartz on 3mm Nickel;
(b) 200μm Quartz on Semi-infinite Nickel
(From **J.E.Doorly and Oldfield, 1987**).

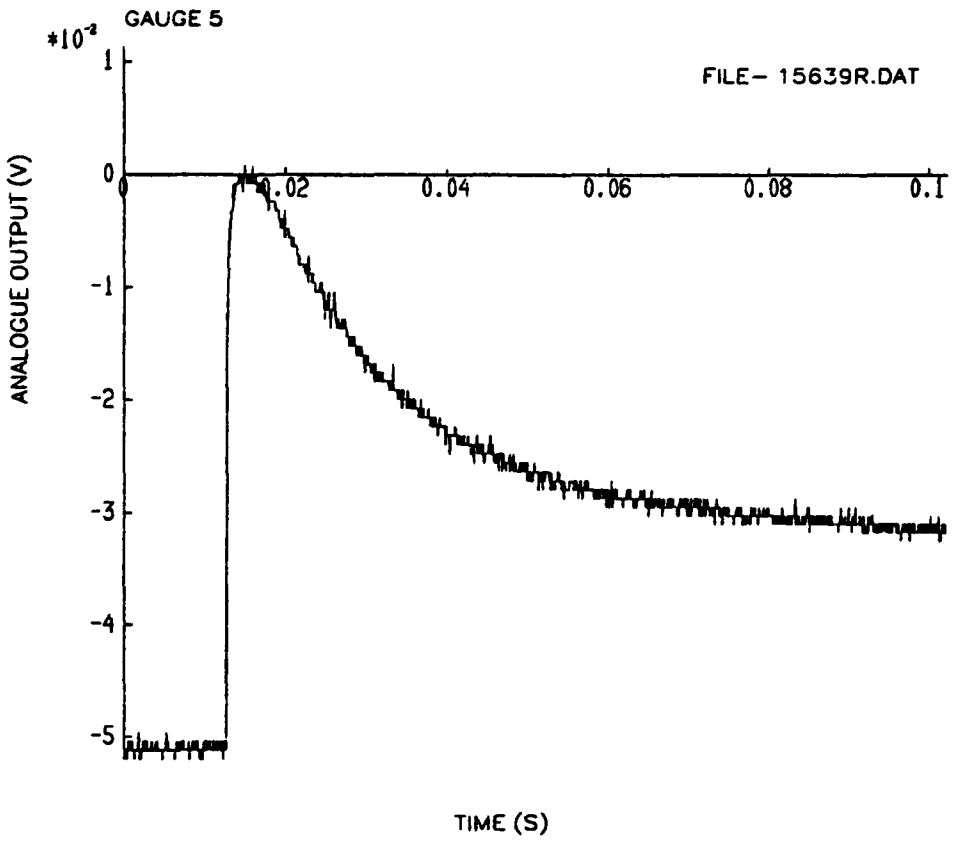

Figure 7.38: Analogue Output from Gauge Five - Step in Heat Transfer Rate Applied at the Surface.

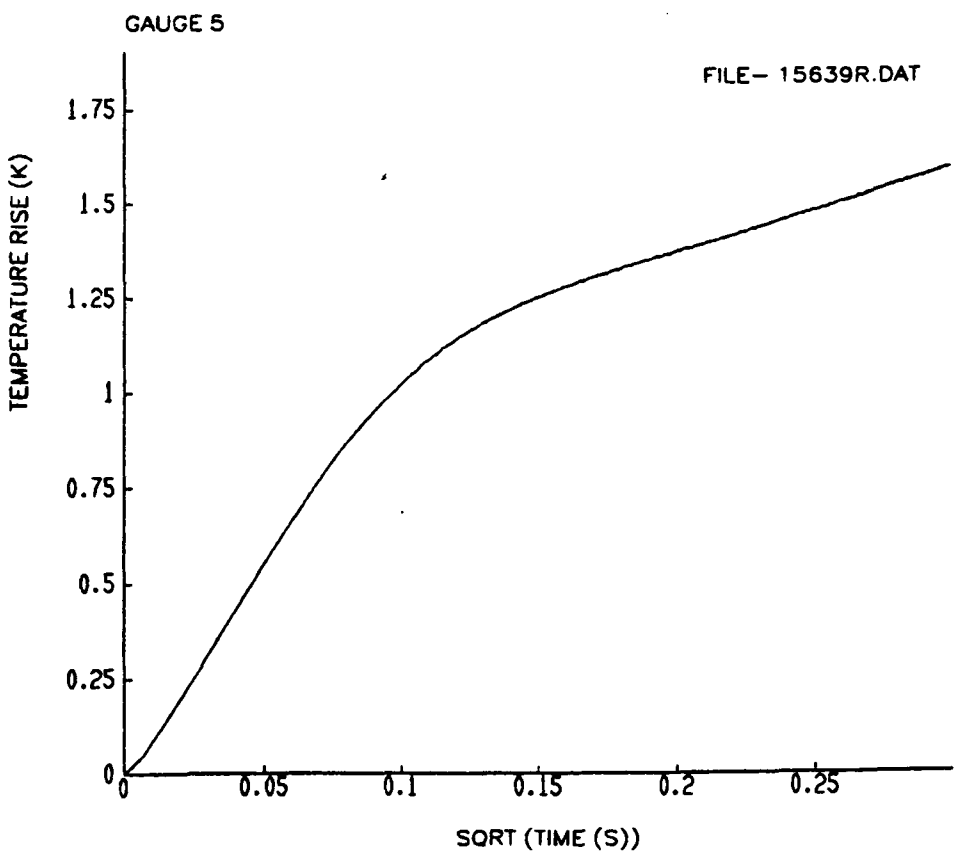

Figure 7.39: Temperature Rise from Gauge Five - Step in Heat Transfer Rate Applied at the Surface.

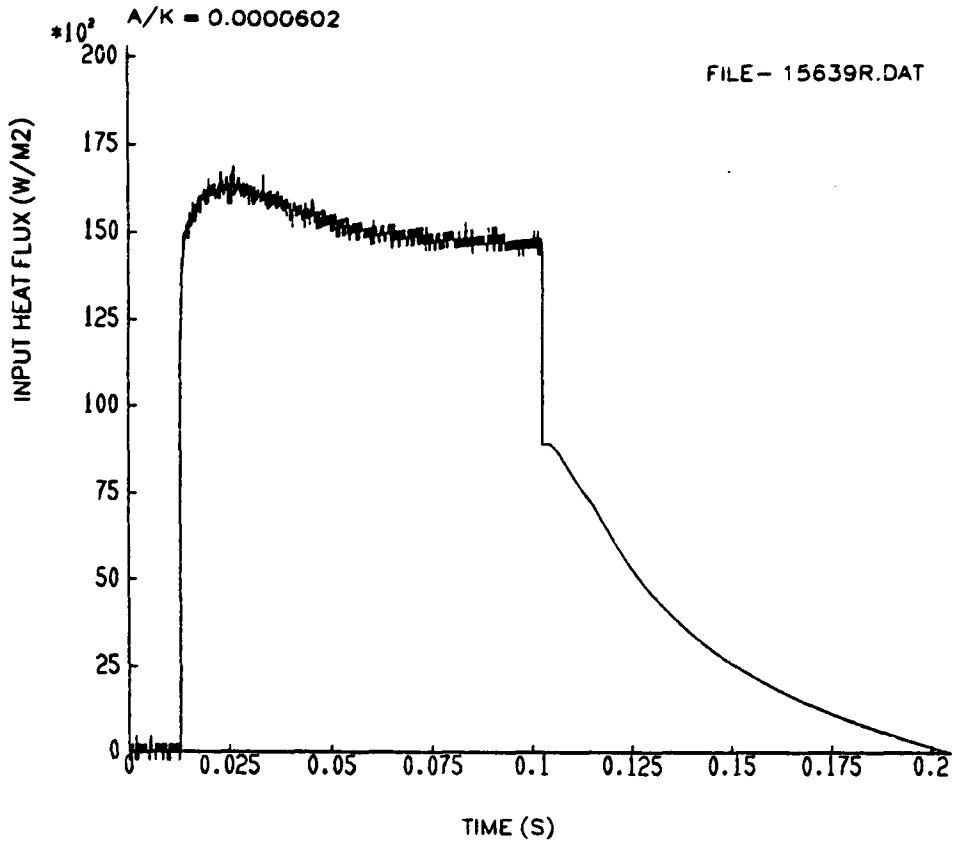

Figure 7.40: Heat Transfer Rate Calculated from Analogue Output Shown in Figure 7.38, (a/k = 60.2E-6 m^2K/W)

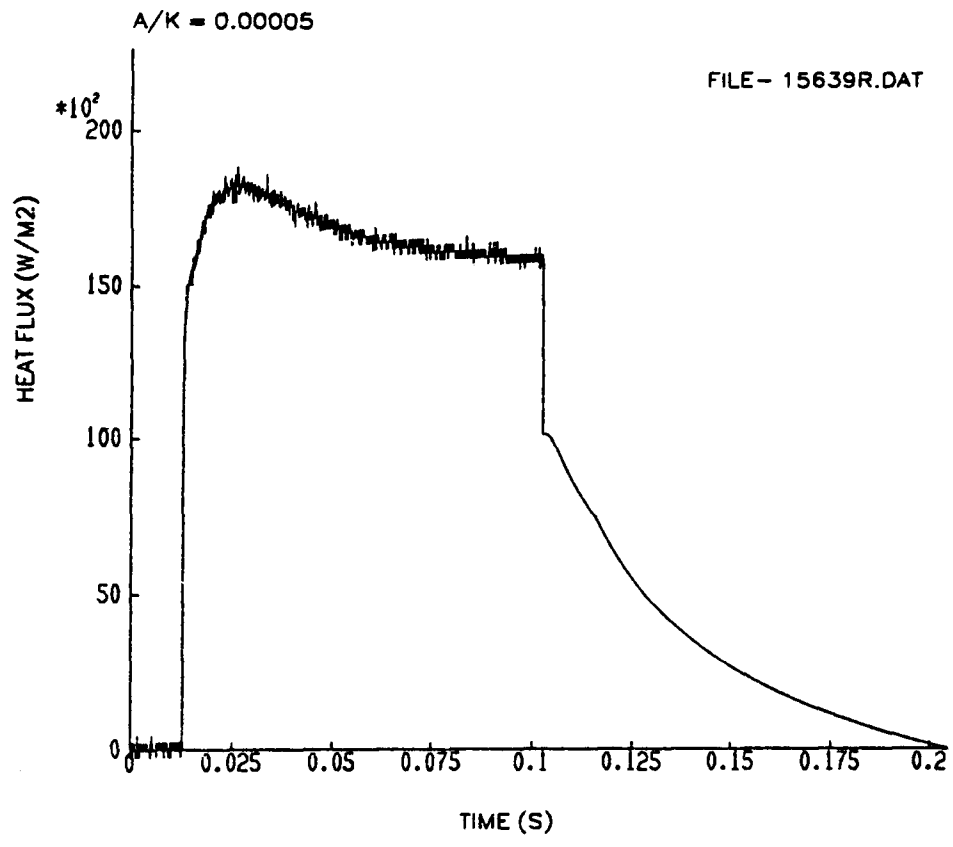

Figure 7.41: Heat Transfer Rate Calculated from Analogue Output Shown in Figure 7.38, (a/k = 50.0E-6 m^2K/W)

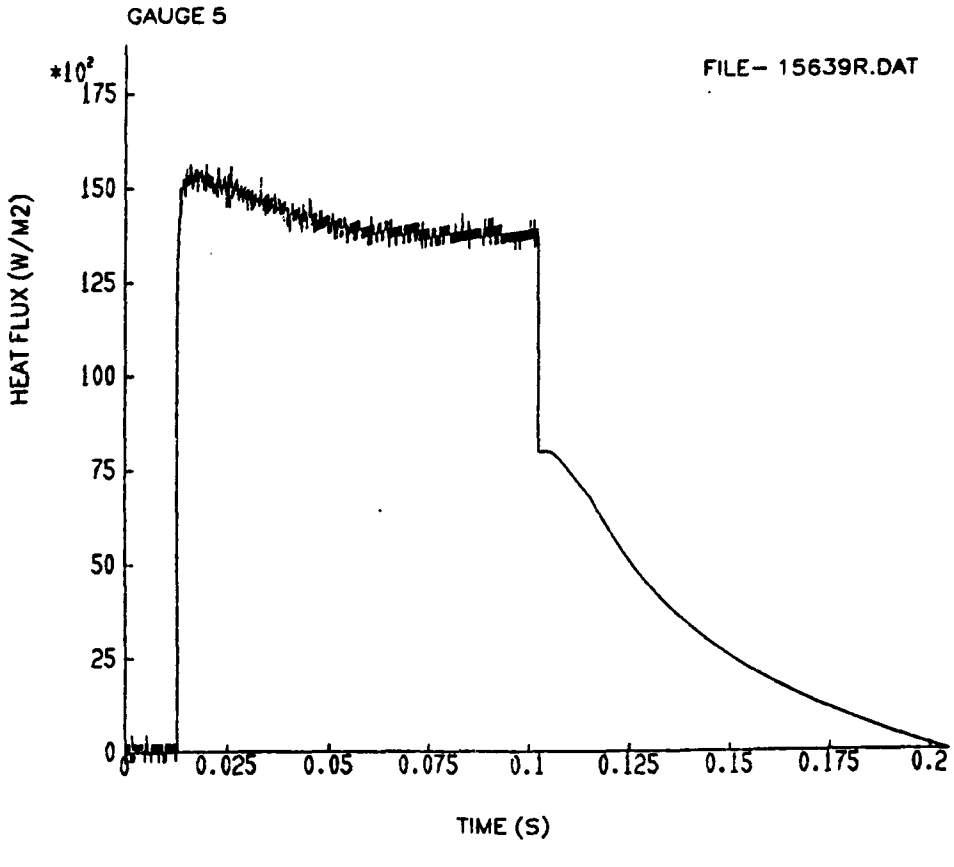

Figure 7.42 : Heat Transfer Rate Calculated from Analogue Output Shown in Figure 7.38, (a/k = 70.0E-6 m^2K/W)

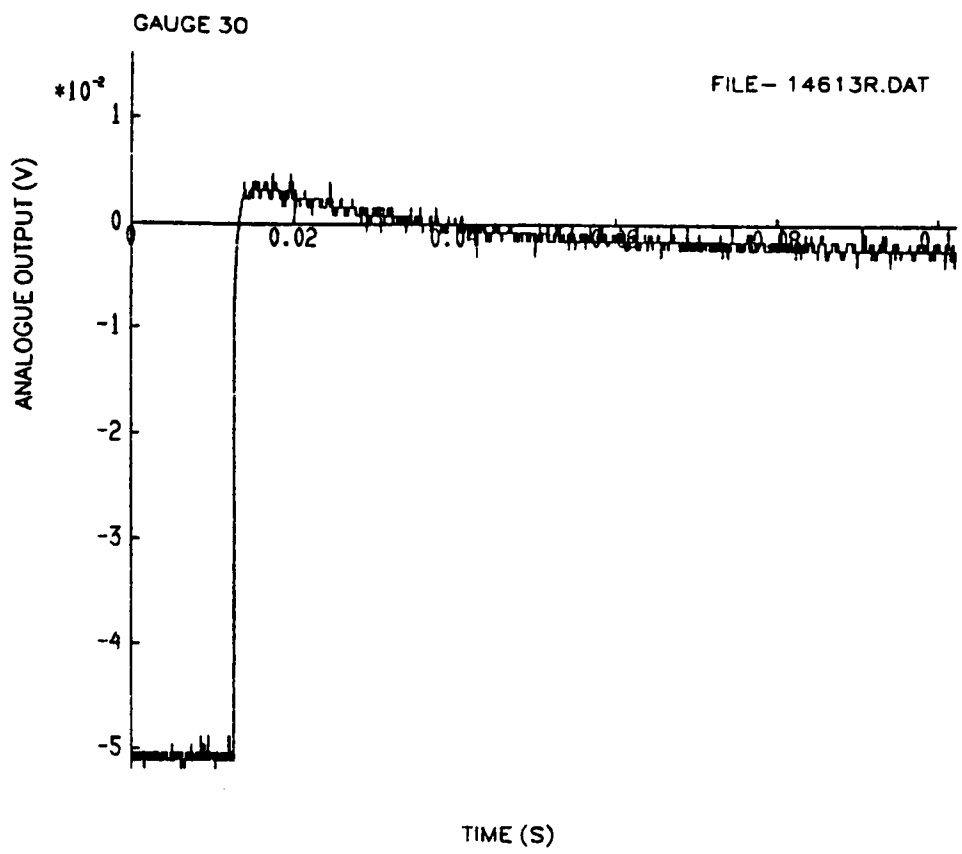

Figure 7.43: Analogue Output from Gauge 30, Mounted on Platform and Subject to a Step in Heat Transfer Rate at the Surface

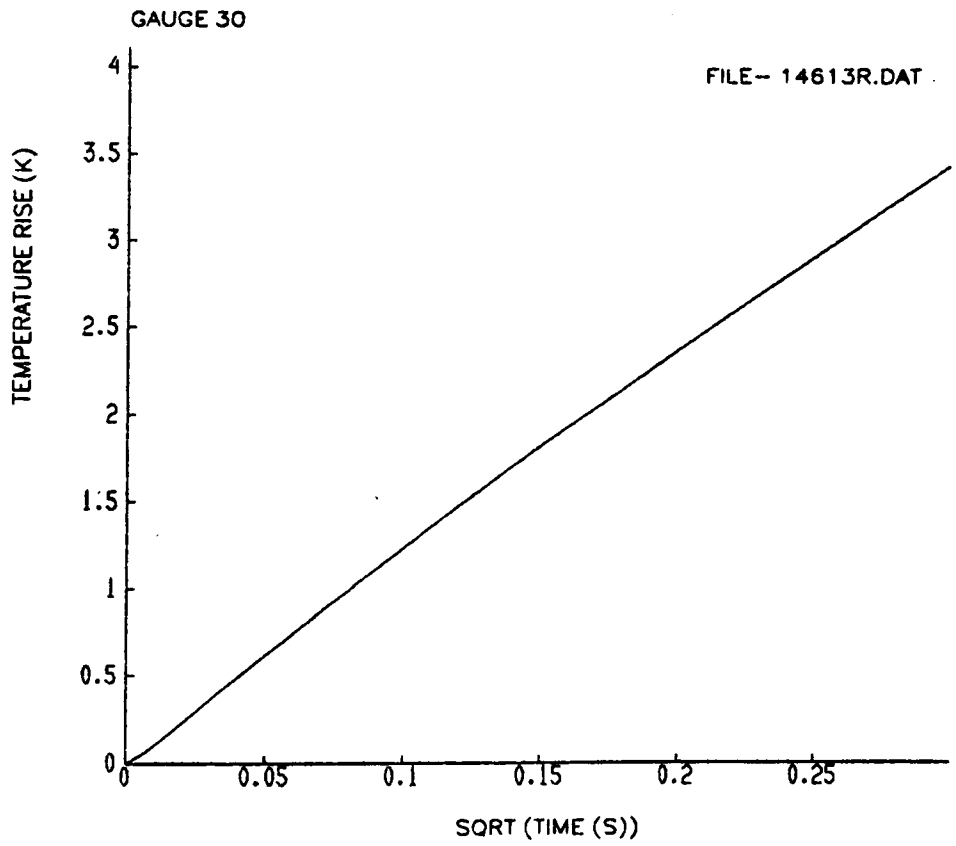

Figure 7.44: Temperature Rise From Gauge 30, Mounted on Platform and Subject to a Step in Heat Transfer Rate at the Surface.

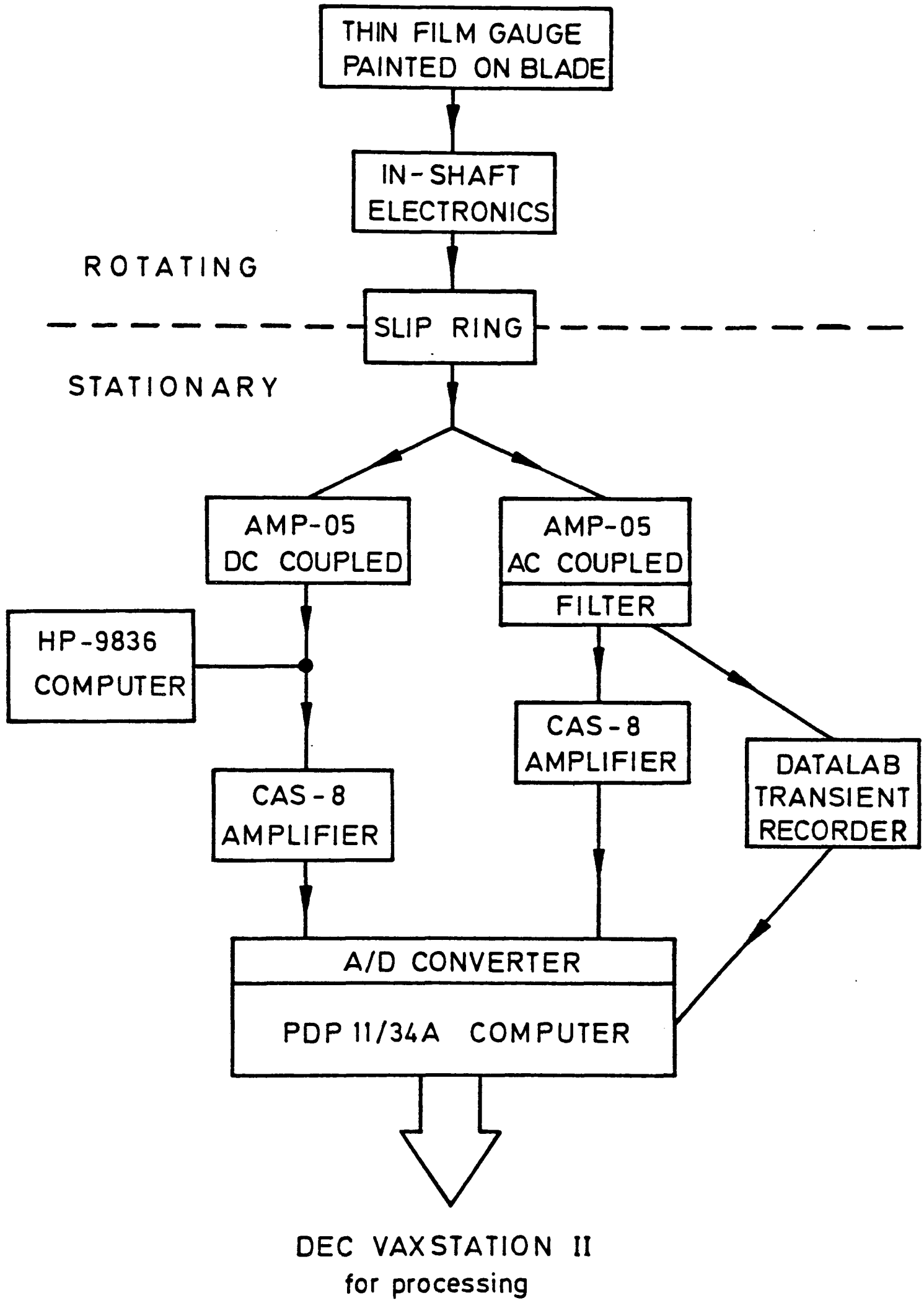

Figure 8.1: Data Acquisition System

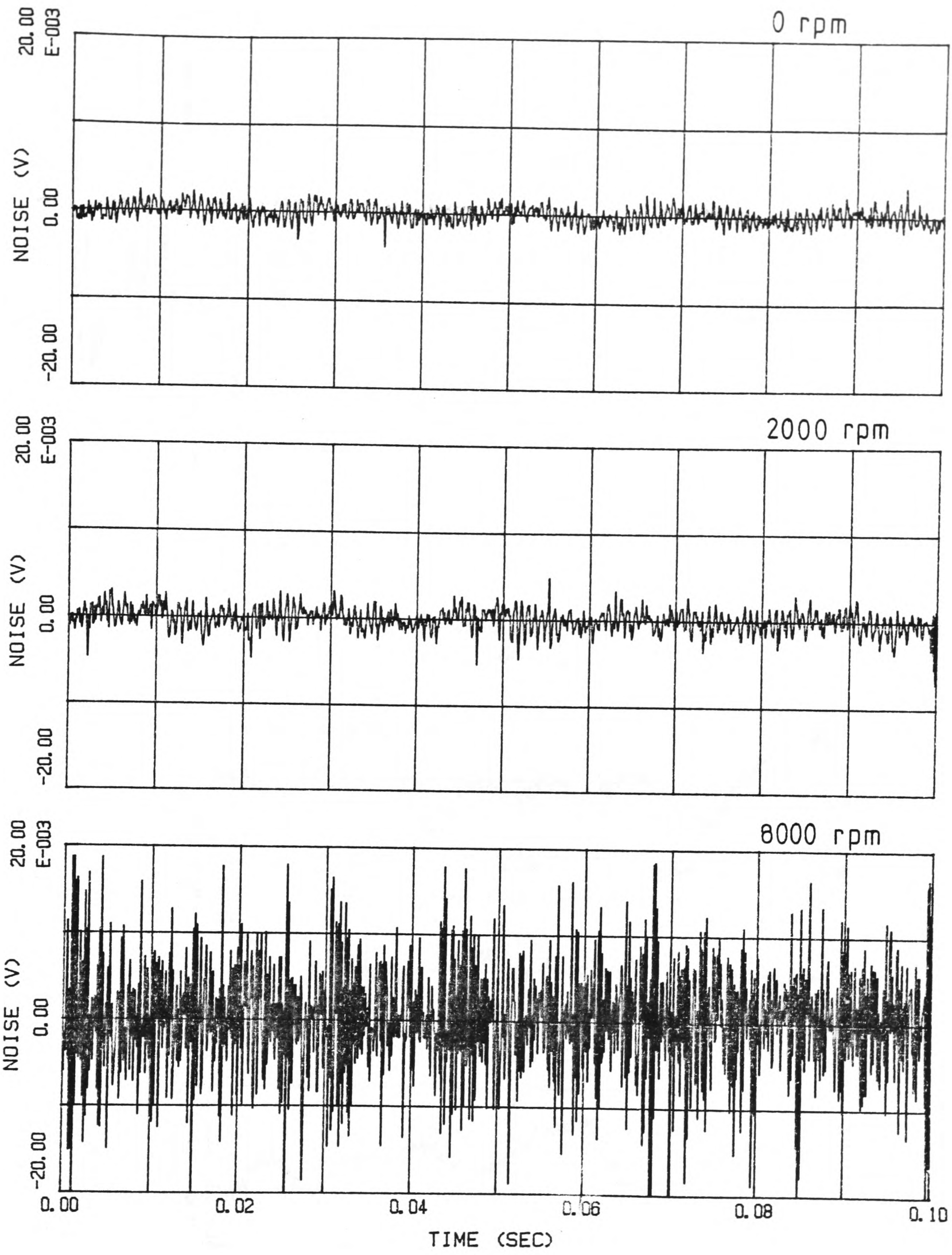

Figure 8.2: Noise Signals Captured with Rotor Turning at Speeds of 0, 2000 and 8000 rpm.

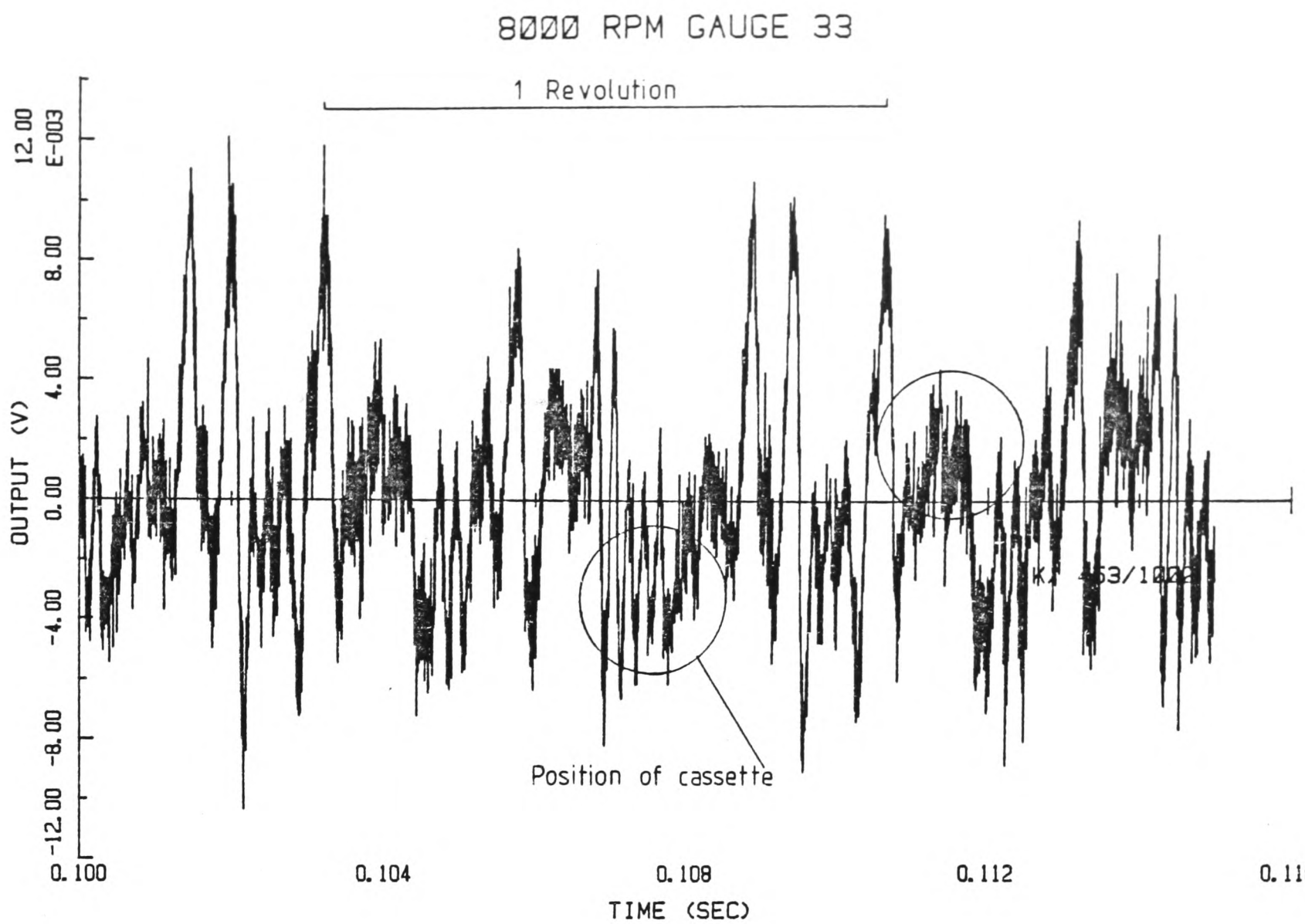

Figure 8.3: Noise Signal Captured at 200 kHz Sampling Rate - Rotor Turning at 8000 rpm.

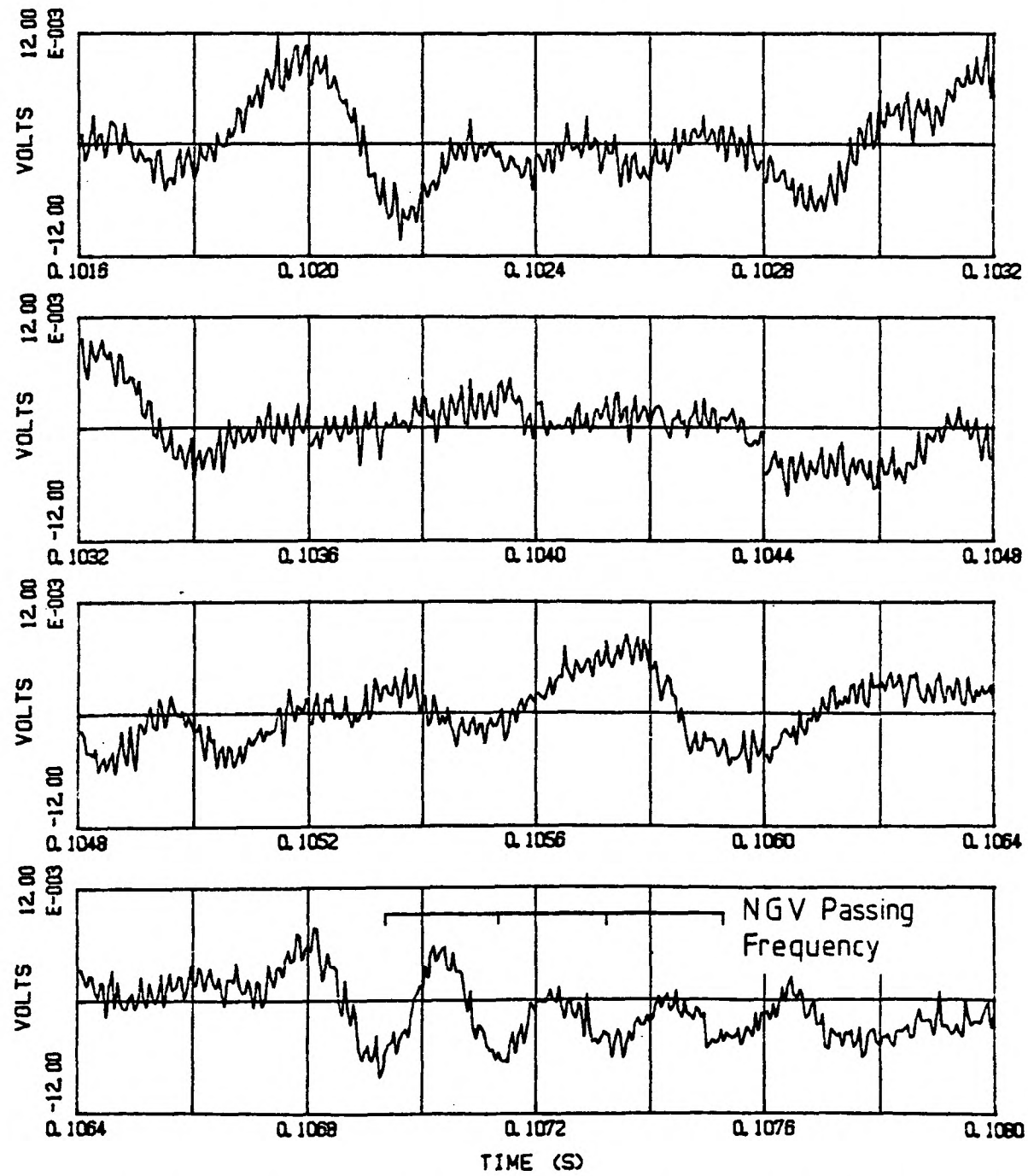

Figure 8.4: Noise Signal Captured at 200 kHz Sampling Rate -

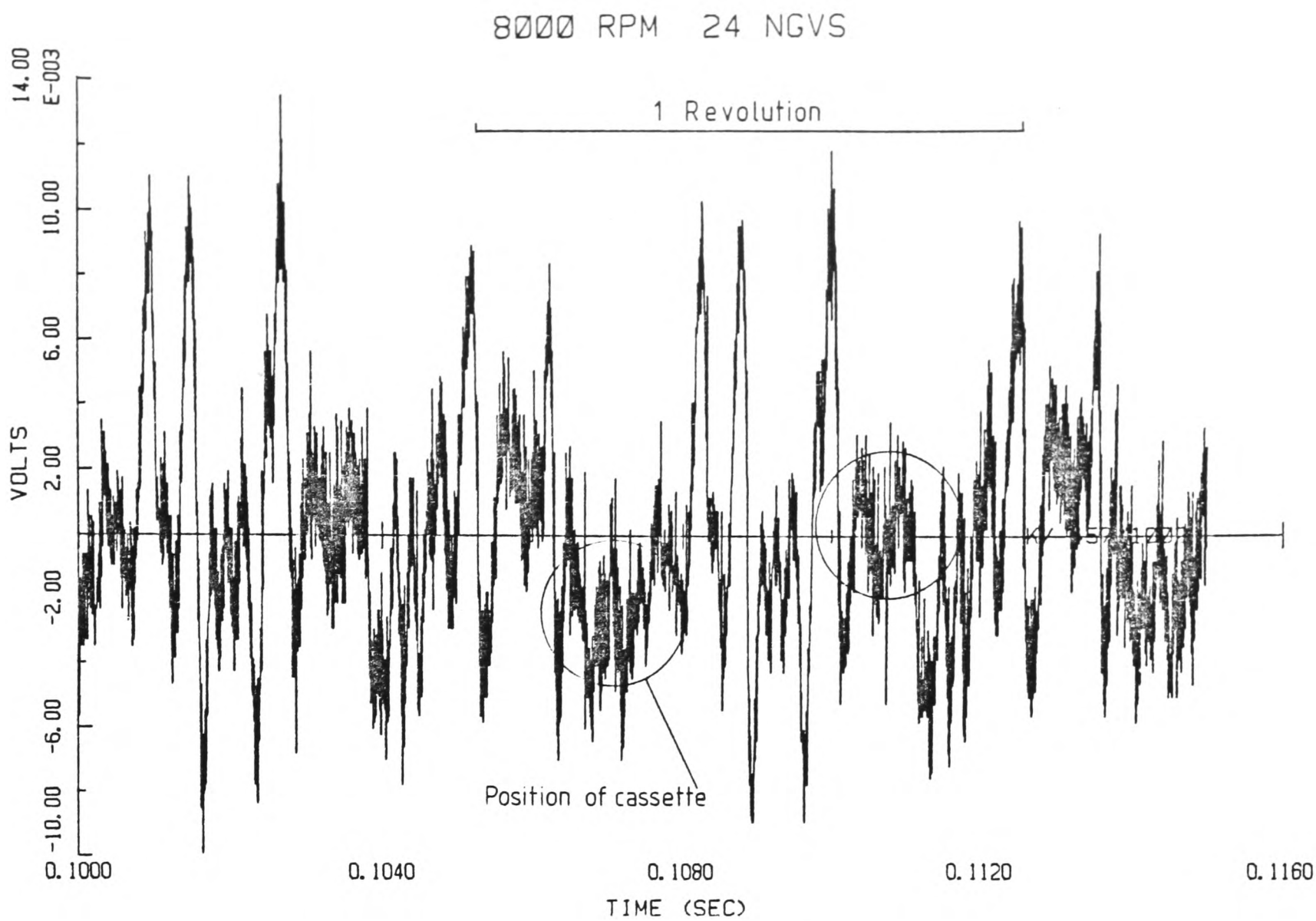

Figure 8.5: Noise Signal Recorded with NGVs Removed from Cassettes - Sampling Rate 200kHz, Rotor Turning at 8000 rpm.

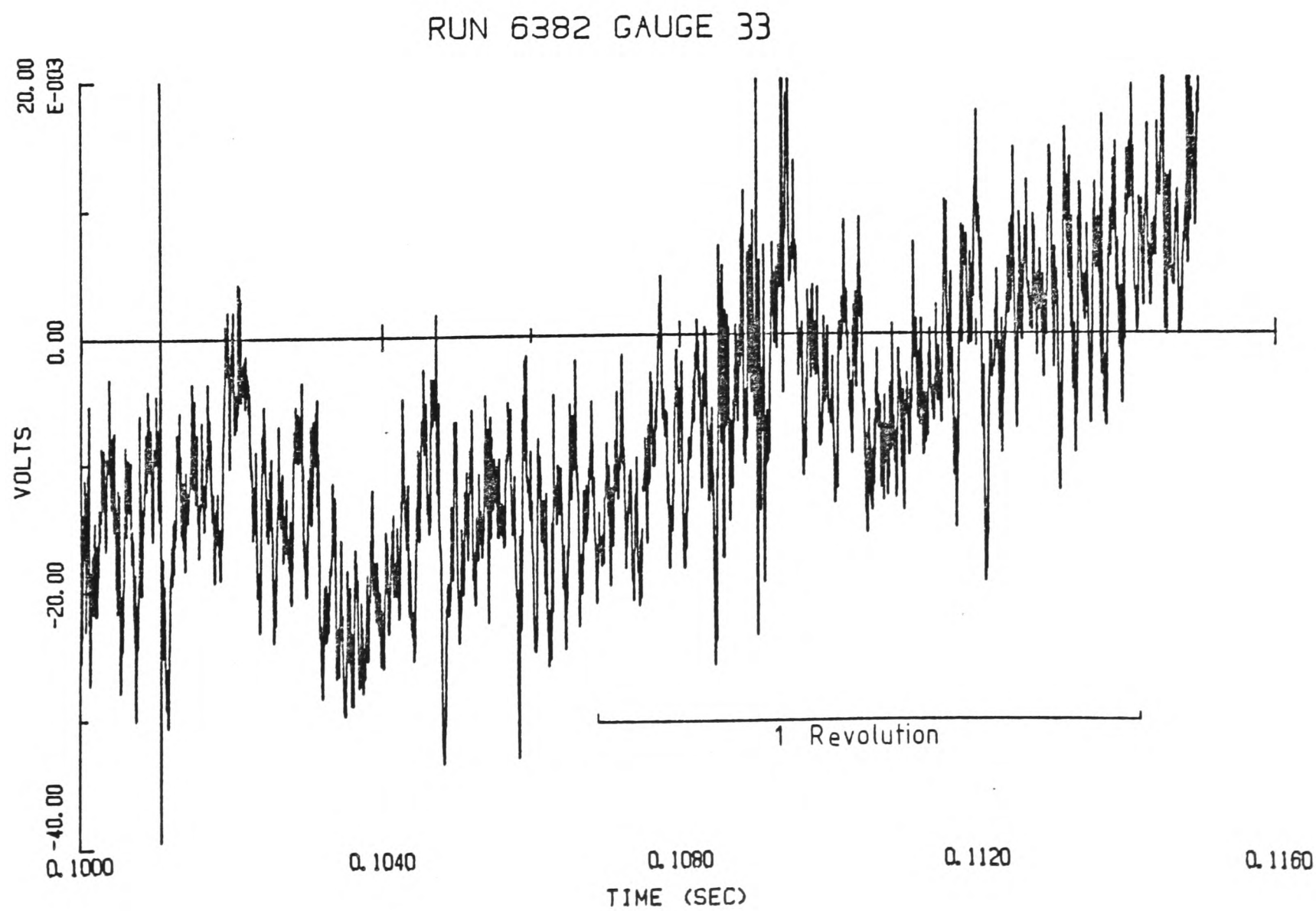

Figure 8.6: Output from Thin Film Gauge During First Heat Transfer Test (Sampling Rate 200 kHz)

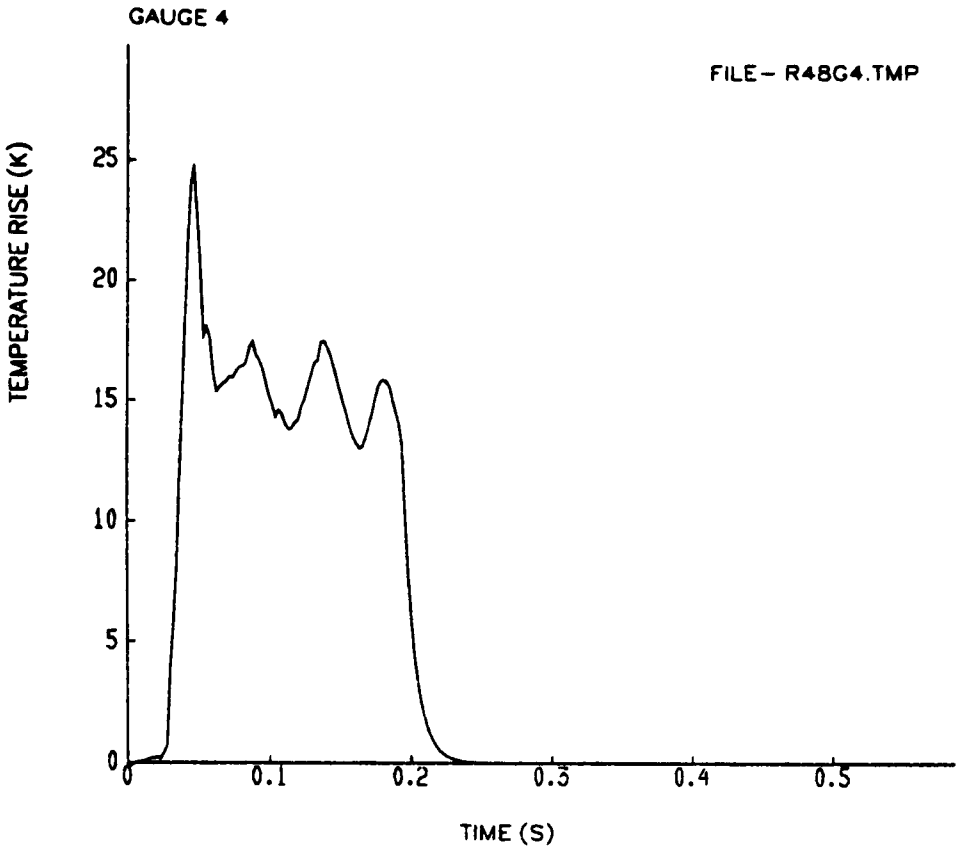

Figure 8.9: Temperature Rise Gauge 4, Run 6448

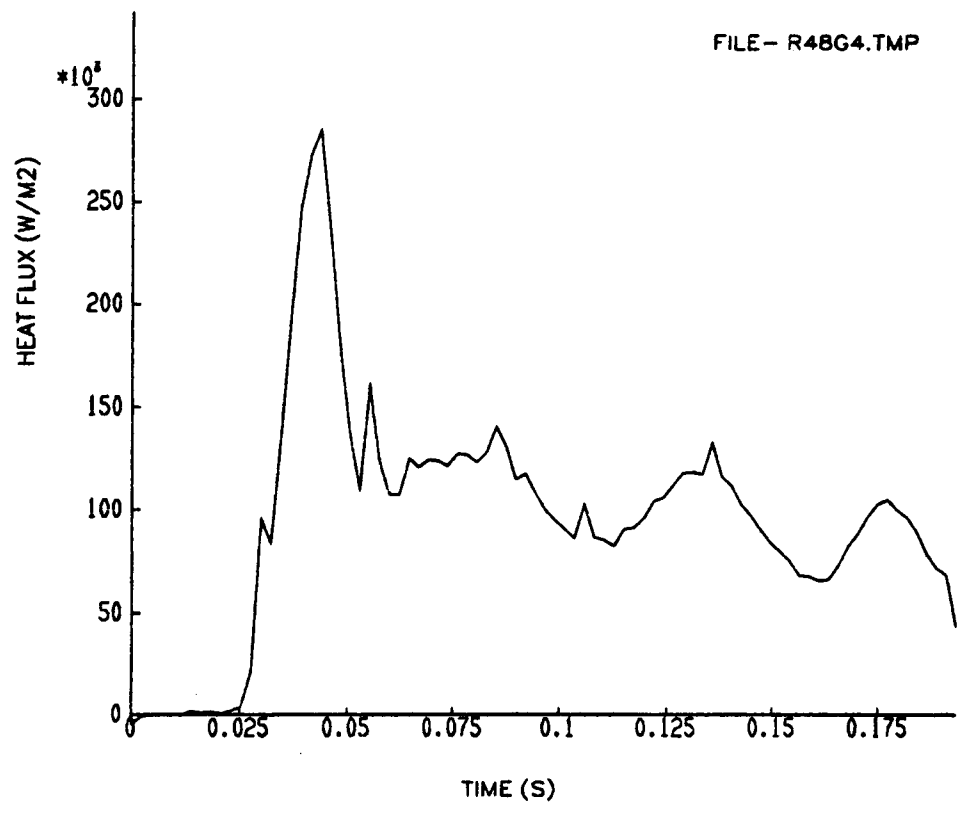

Figure 8.10: Heat Transfer Rate Gauge 4, Run 6448

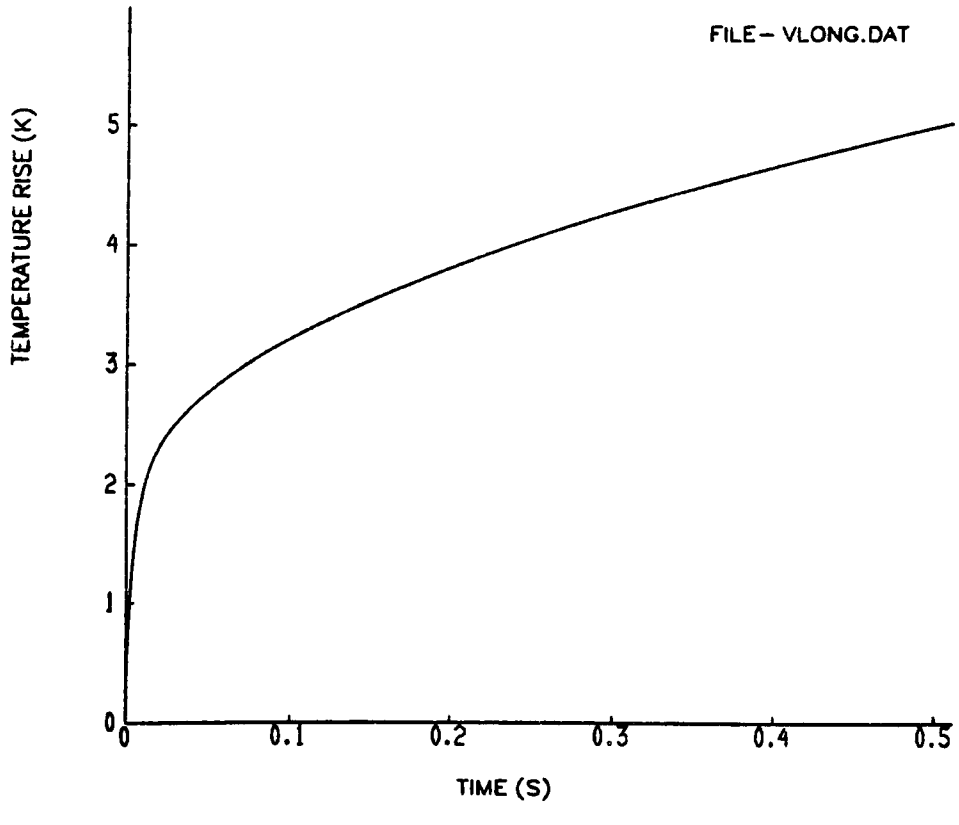

Figure 8.11: Predicted Temperature Rise for Thin Film Gauge on Two-Layered Substrate Subject to Step in Heat Transfer Rate

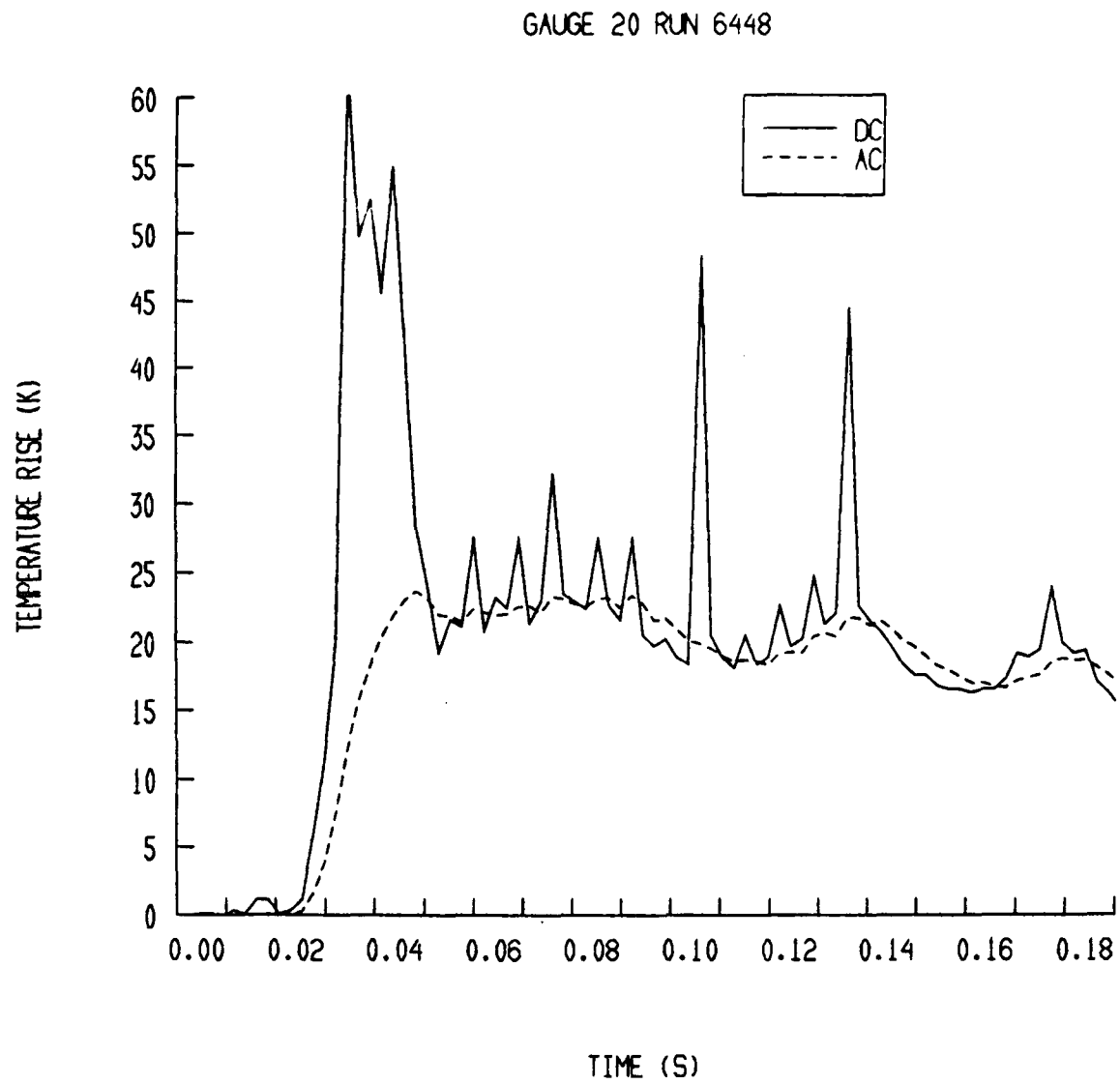

Figure 8.12: Temperature Rise for Gauge 20, Run 6448, Calculated from A.C. and D.C. Outputs

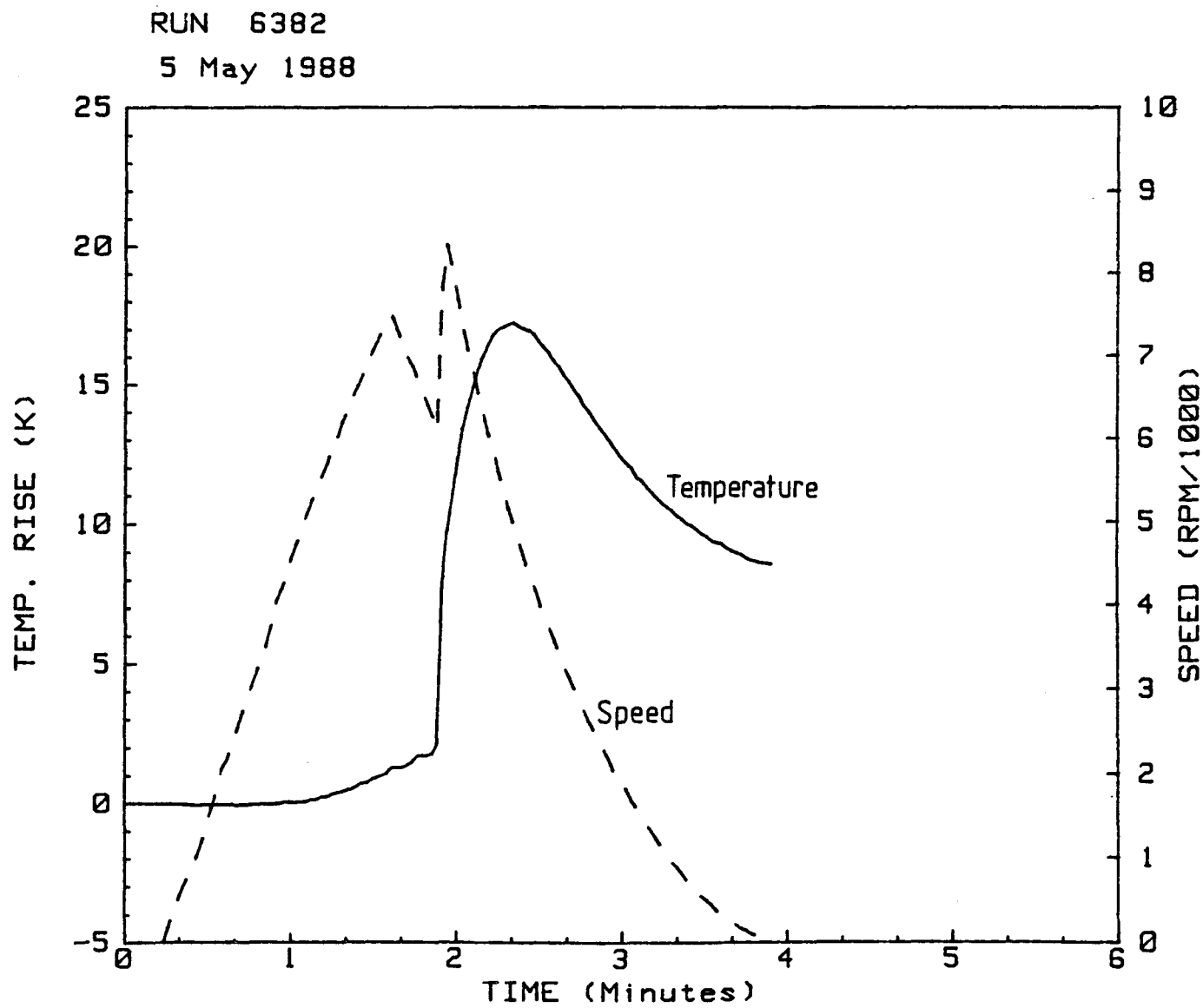

Figure 8.13: Temperature Rise Recorded on HP Computer, Gauge 33, Run 6382

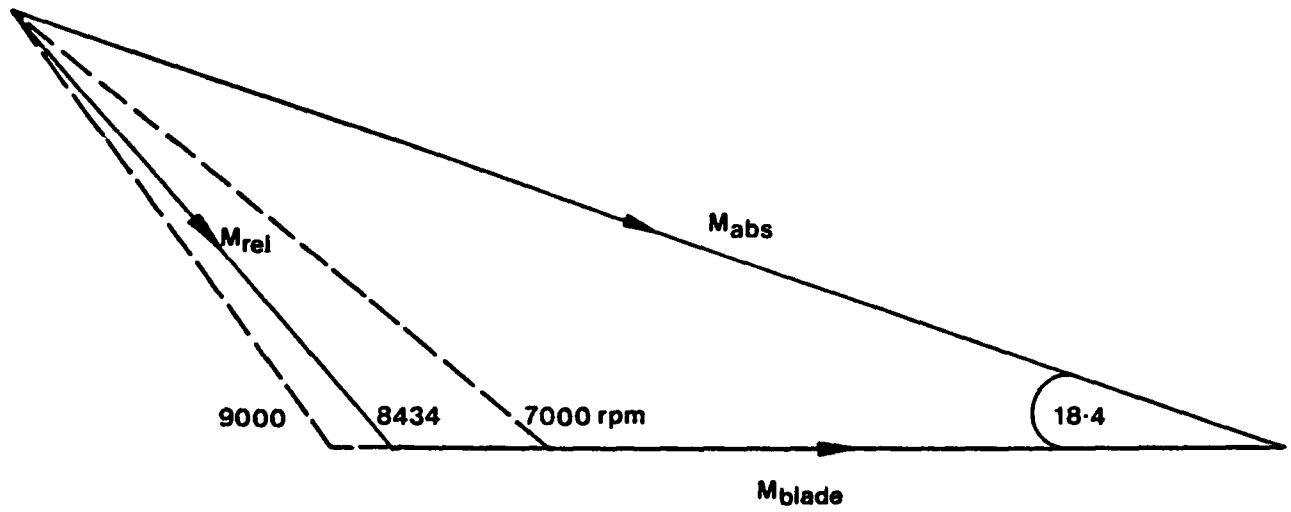

Figure 8.14: Effect of Rotor Speed on Rotor Inlet Velocity Triangle

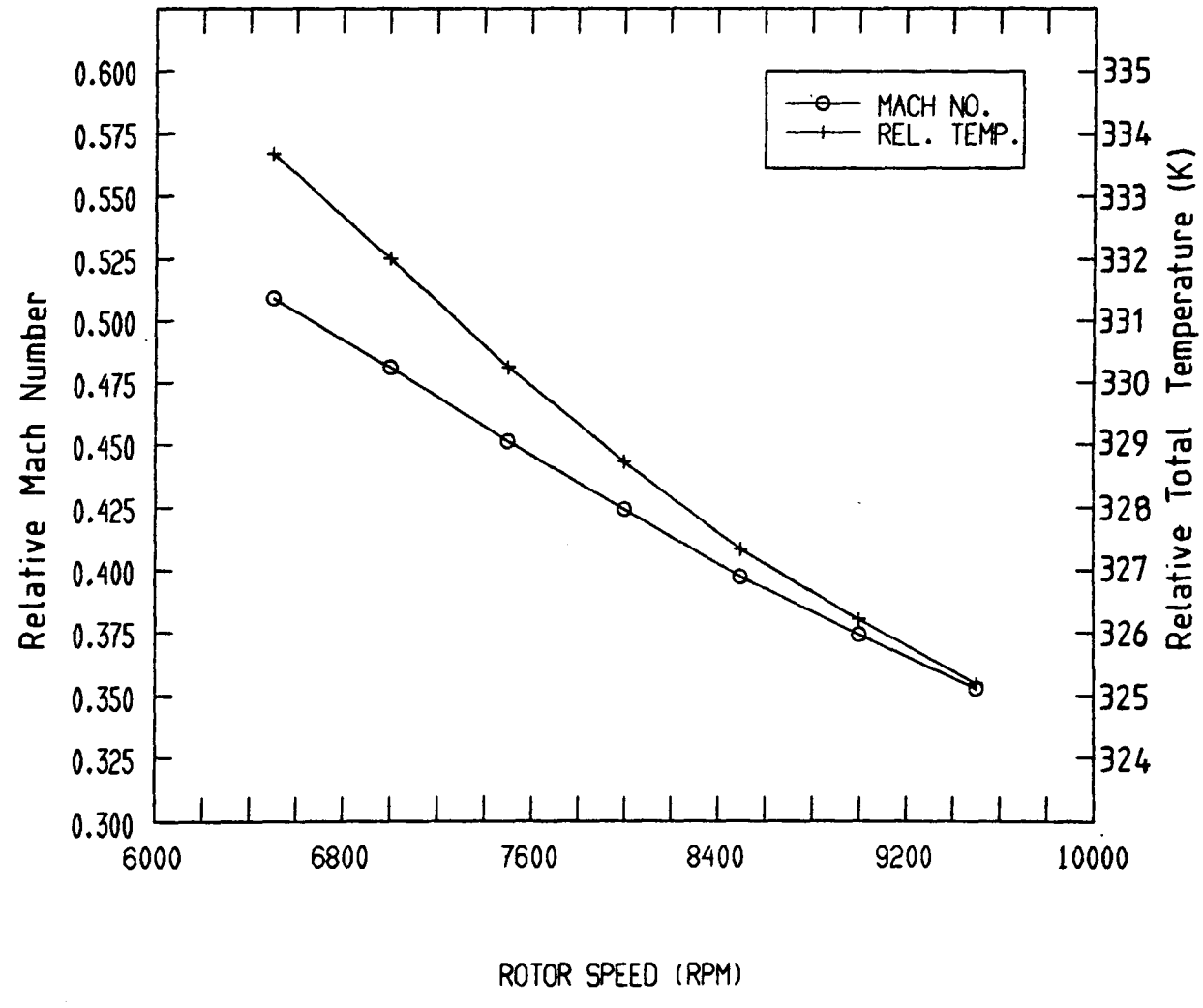

Figure 8.15: Effect of Rotor Speed on Relative Inlet Mach Number and Relative Total Temperature

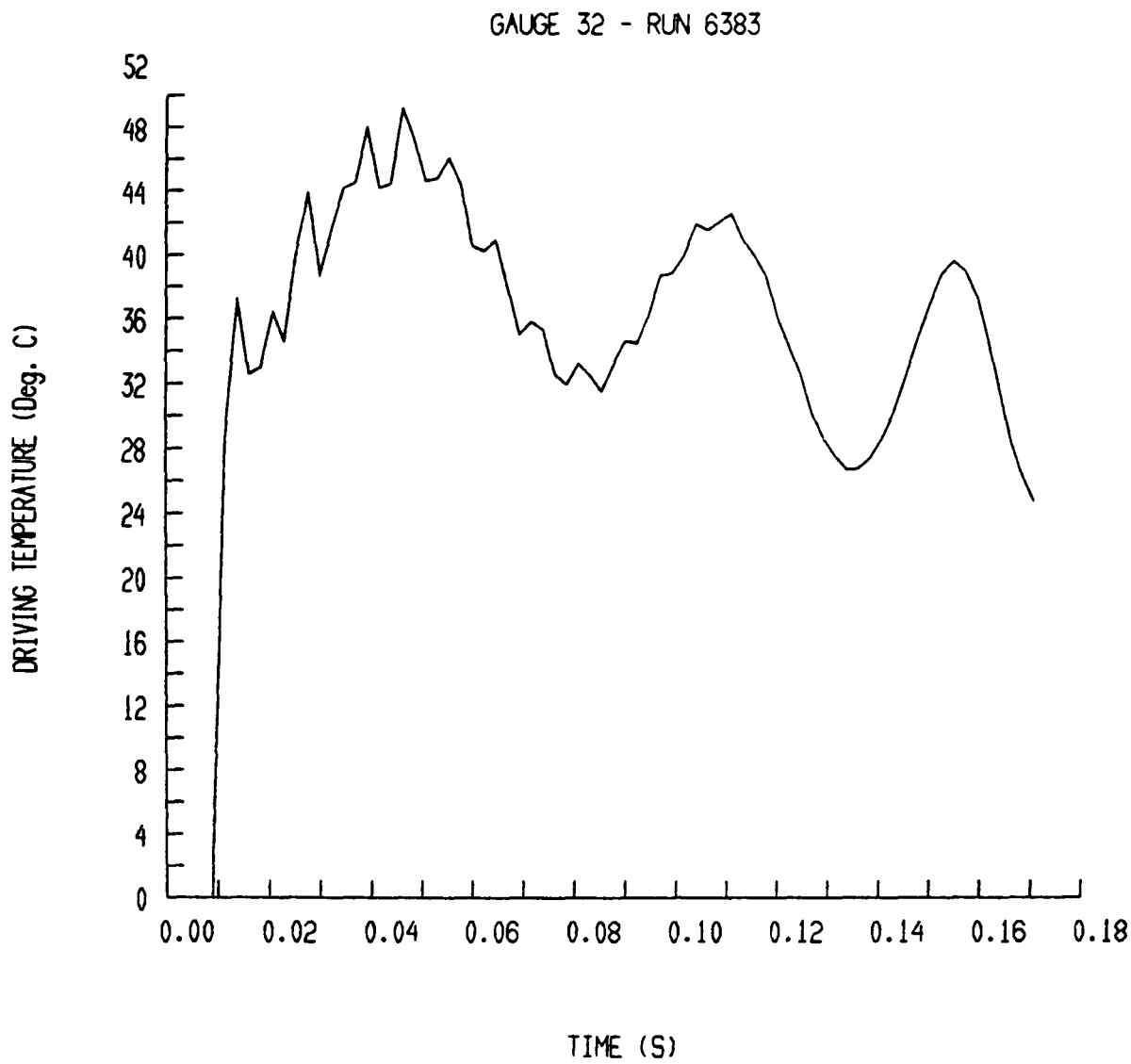

Figure 8.16: Driving Temperature for Gauge 32, Run 6383

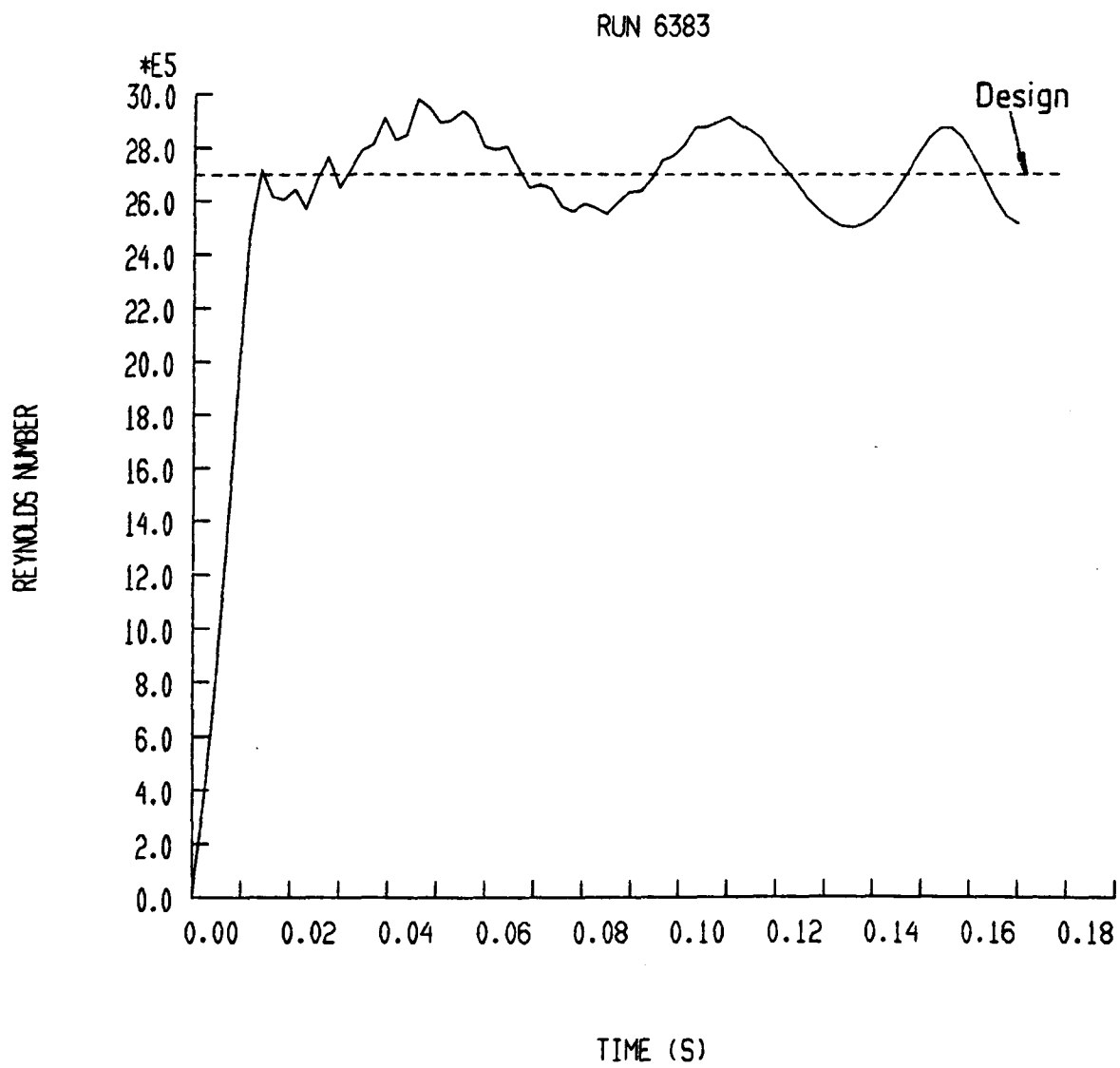

Figure 8.17: Variation in Reynolds Number during Run 6383

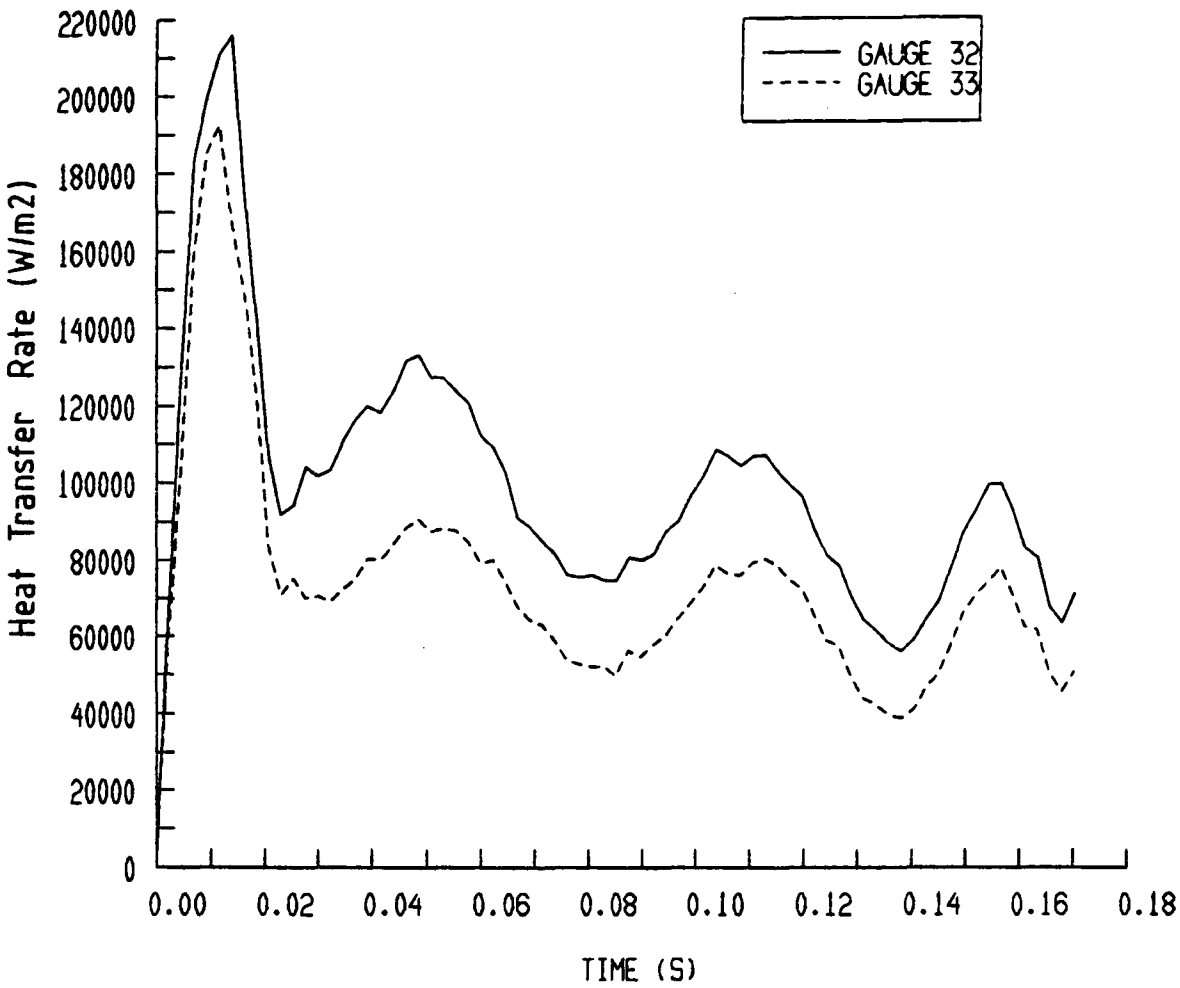

Figure 8.18: Measured Heat Transfer Rate from Run 6383

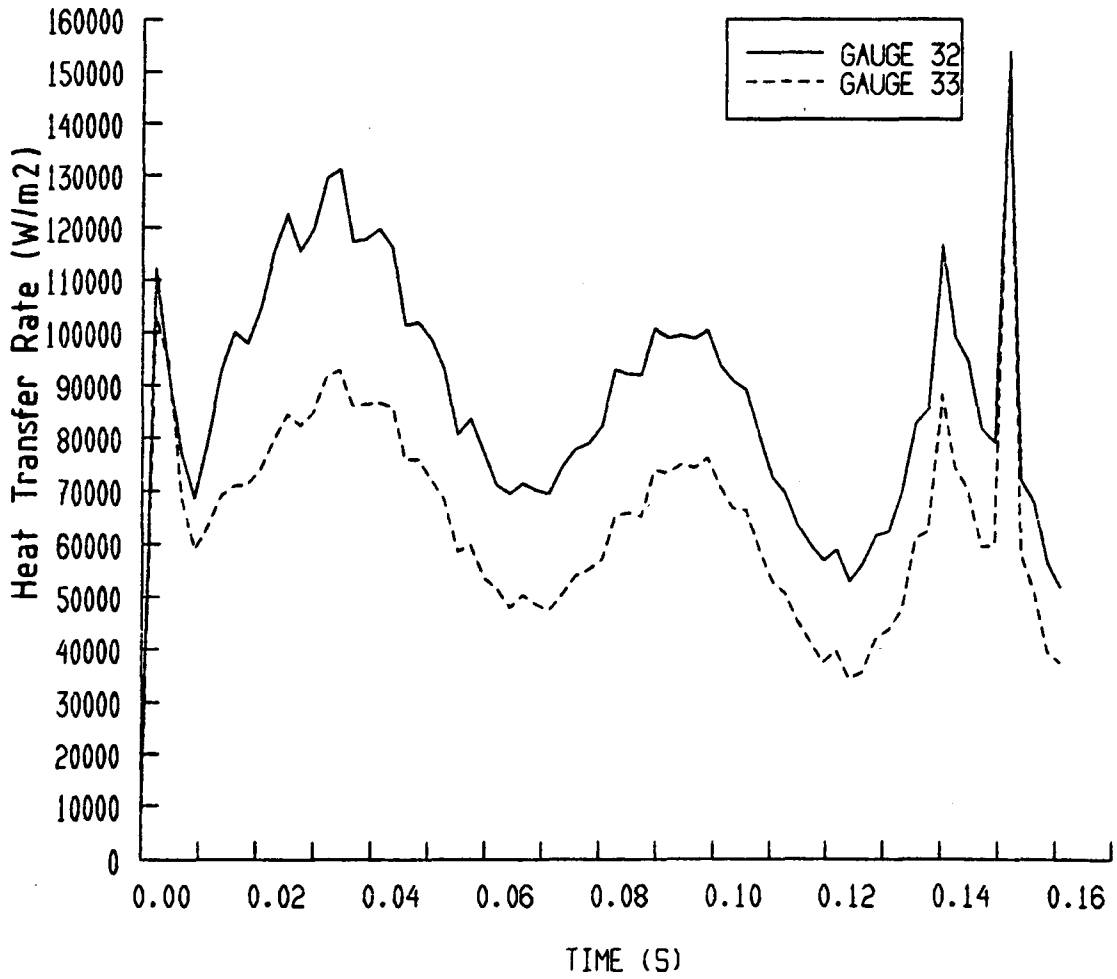

Figure 8.19: Measured Heat Transfer Rate from Run 6384

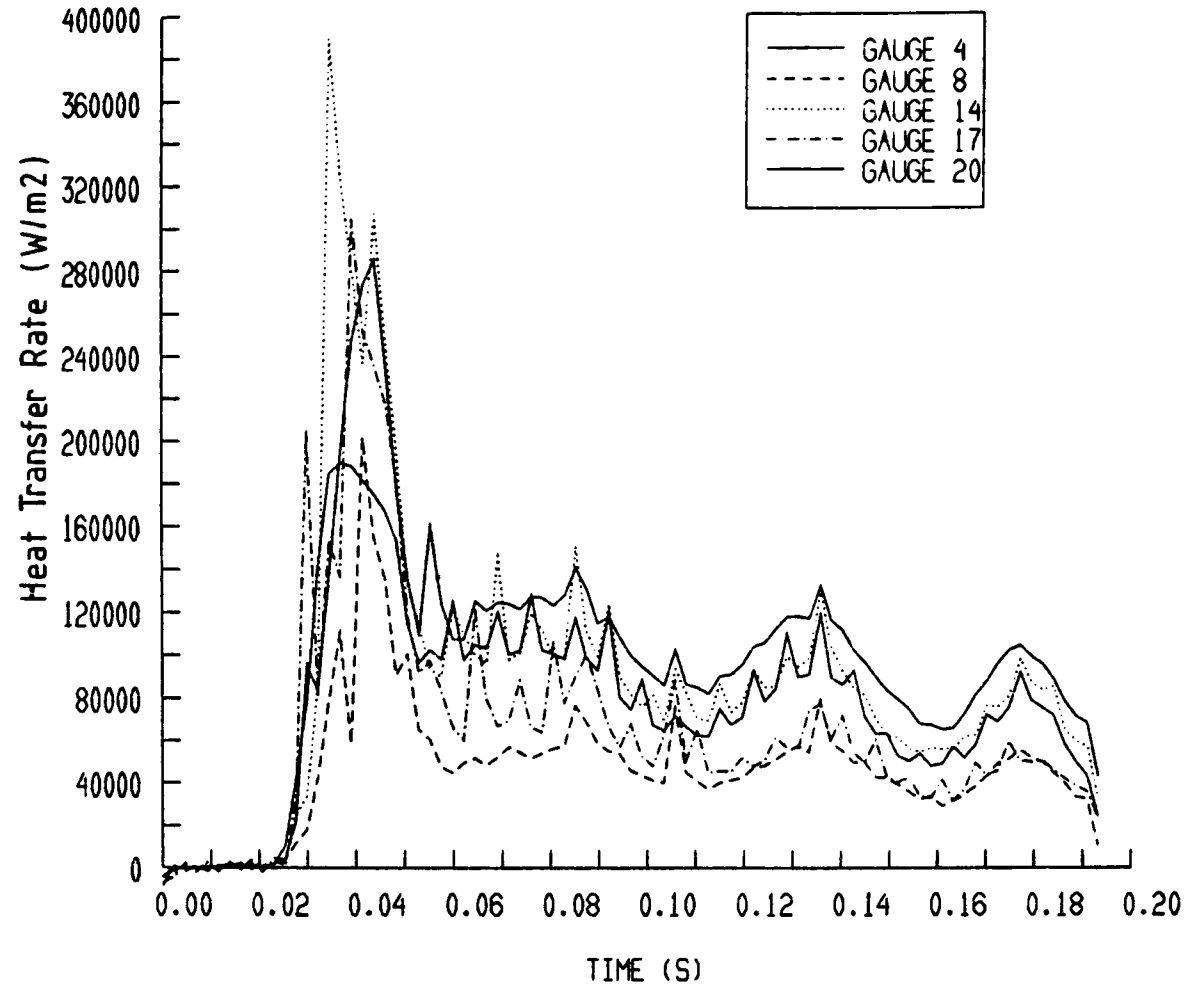

Figure 8.20: Measured Heat Transfer Rate from Run 6448

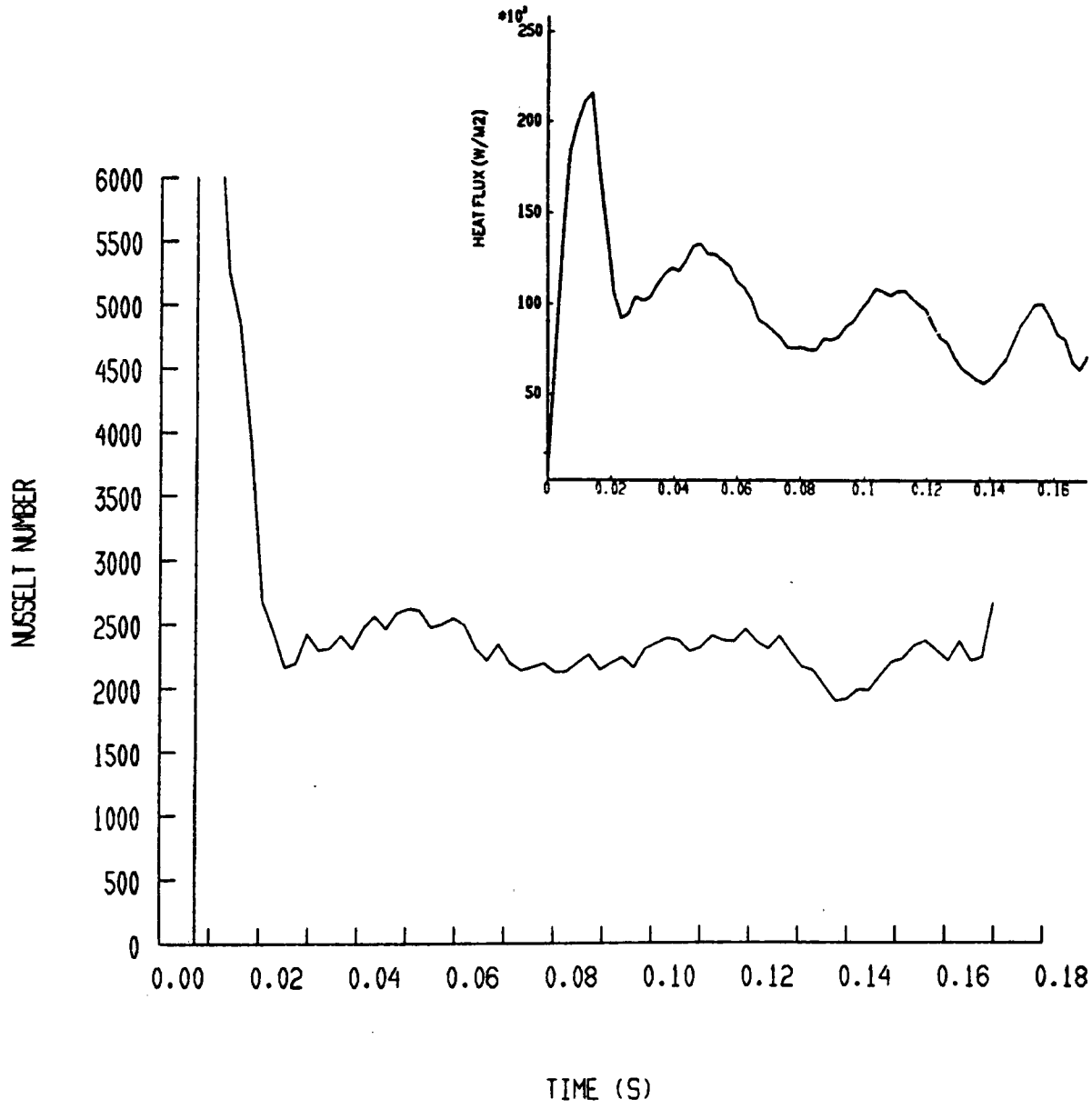

Figure 8.21: Nusselt Number for Gauge 32, Run 6383

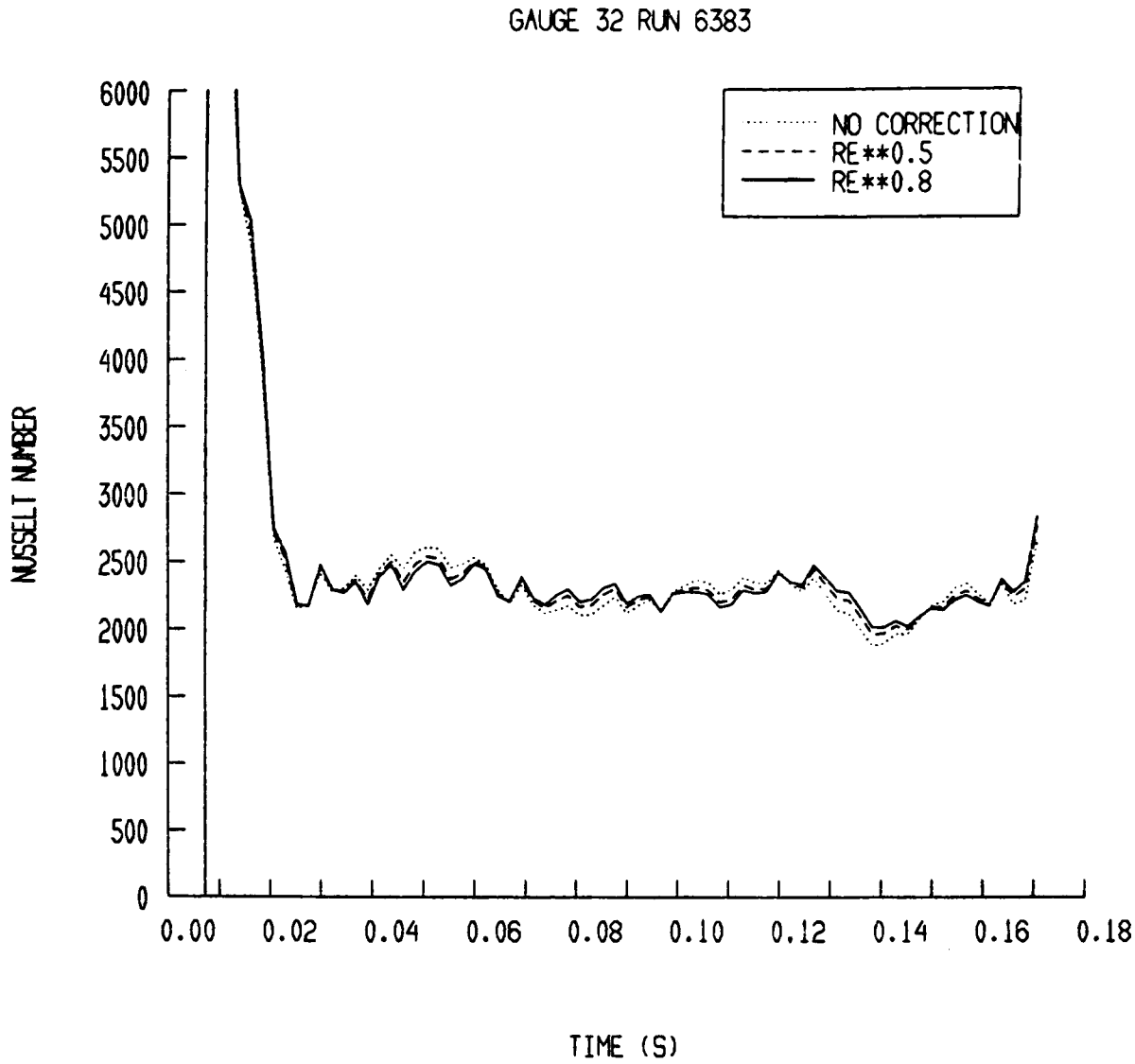

Figure 8.22: Effect of Reynolds Number Correction on Nusselt Number Run 6393, Gauge 32

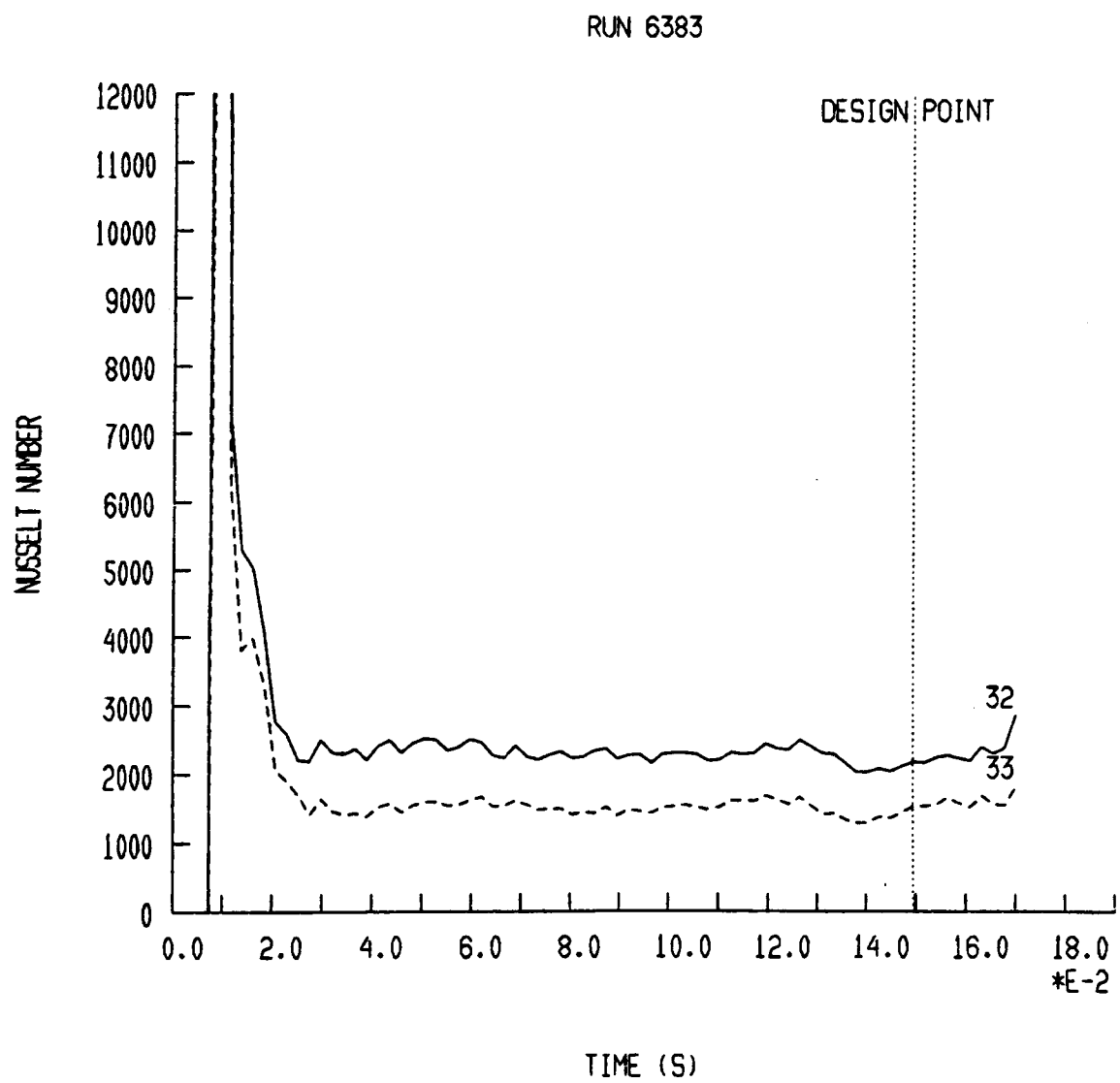

Figure 8.23: Mean Nusselt Number - Gauge 32 and 33, Run 6383

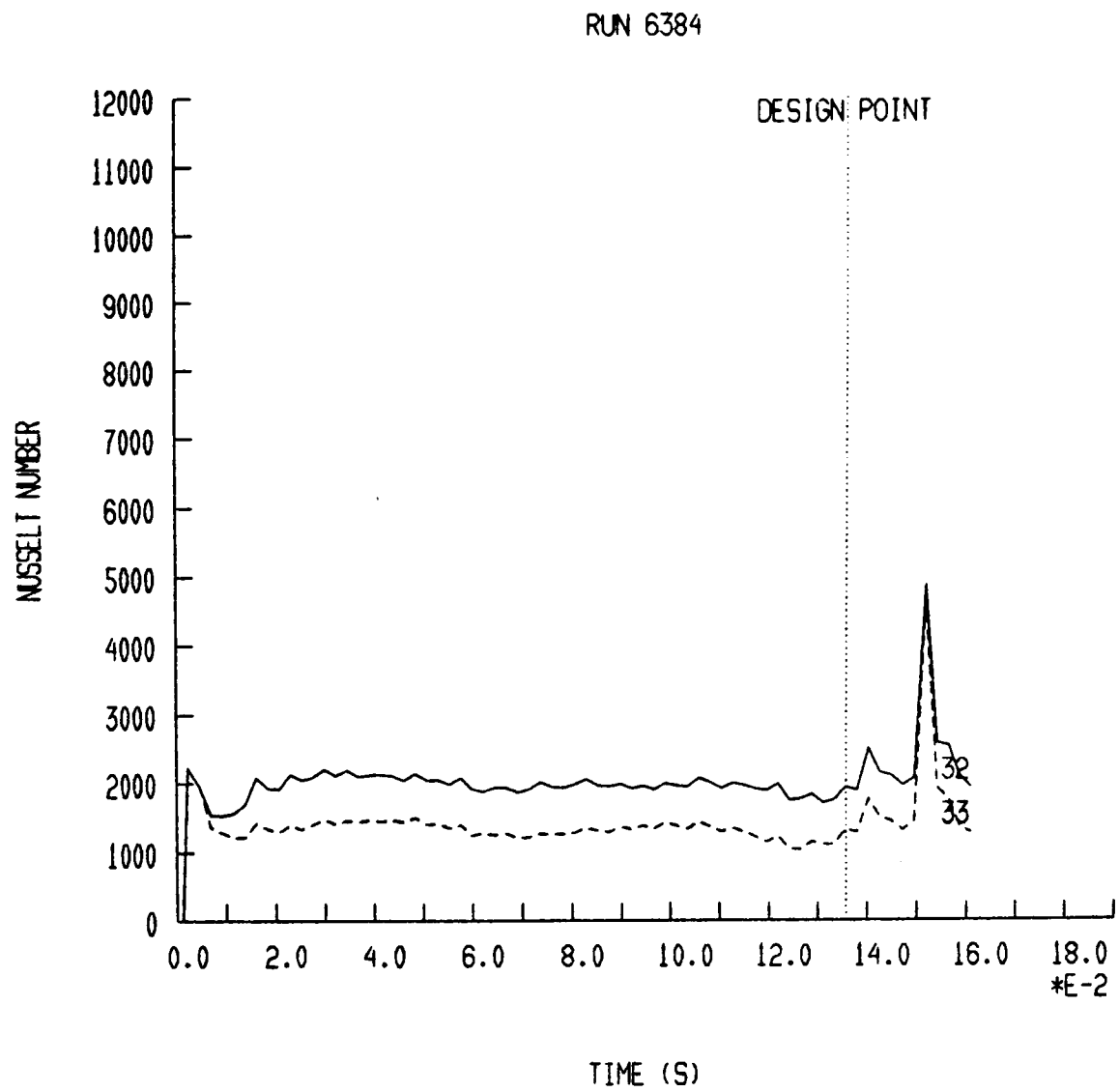

Figure 8.24: Mean Nusselt Number - Gauge 32 and 33, Run 6384

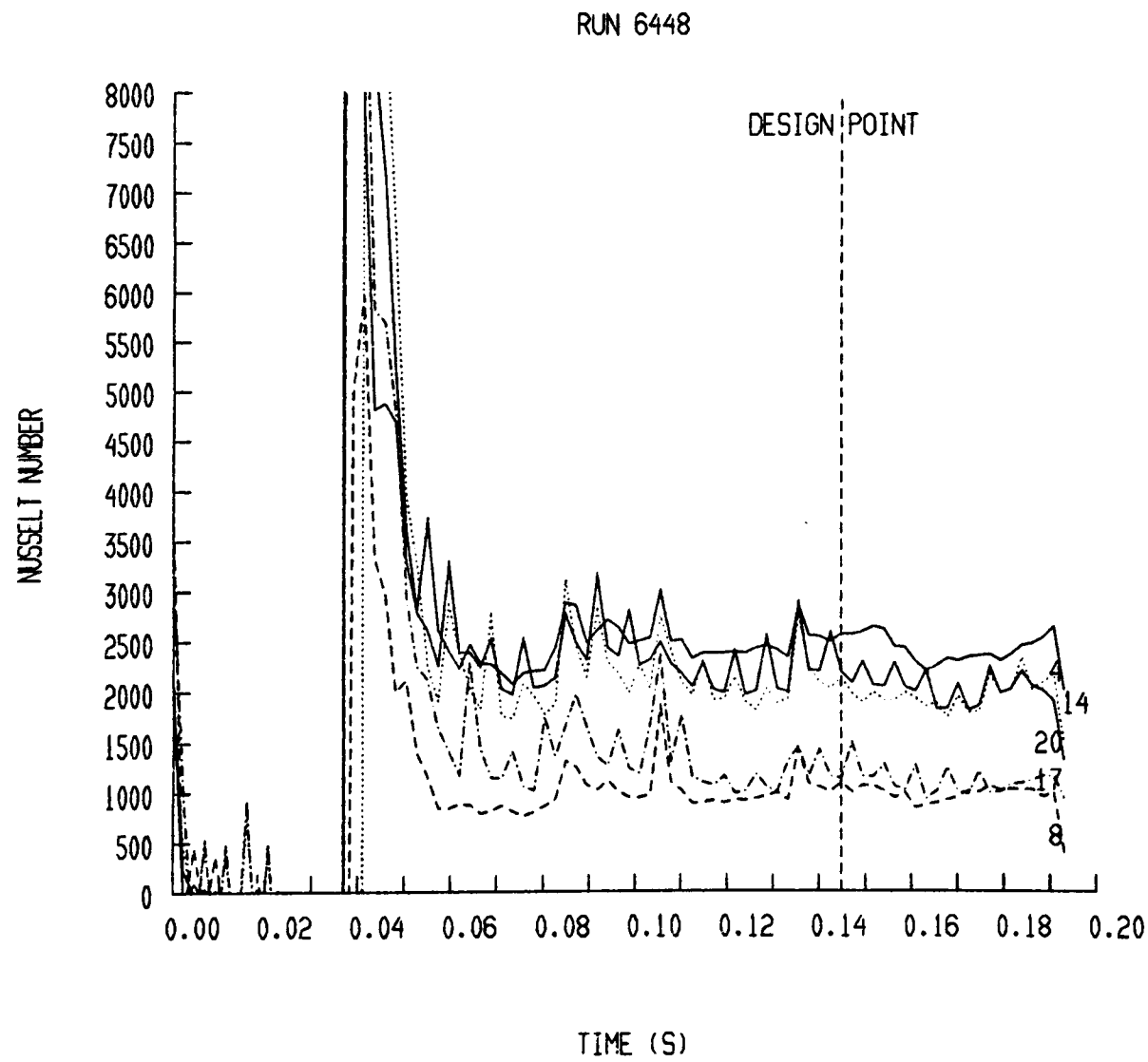

Figure 8.25: Mean Nusselt Number - Run 6448, Gauges 4, 8, 14, 17 and 20.

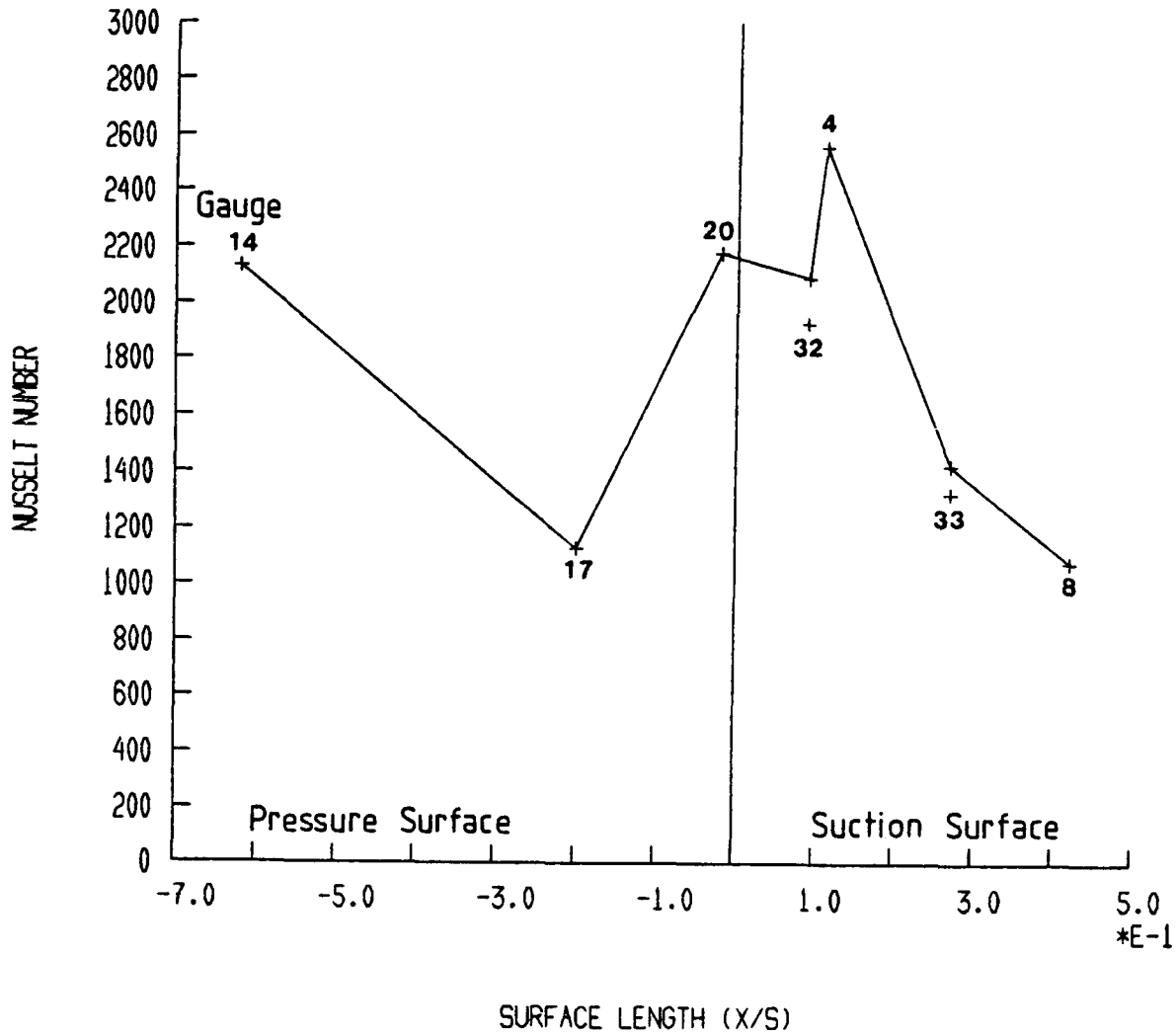

Figure 8.26: Measured Midheight Nusselt Number Distribution

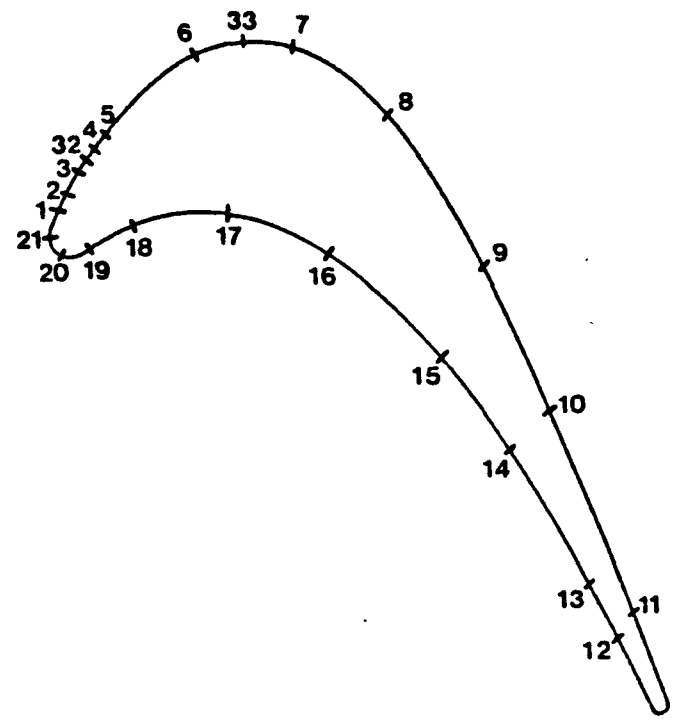

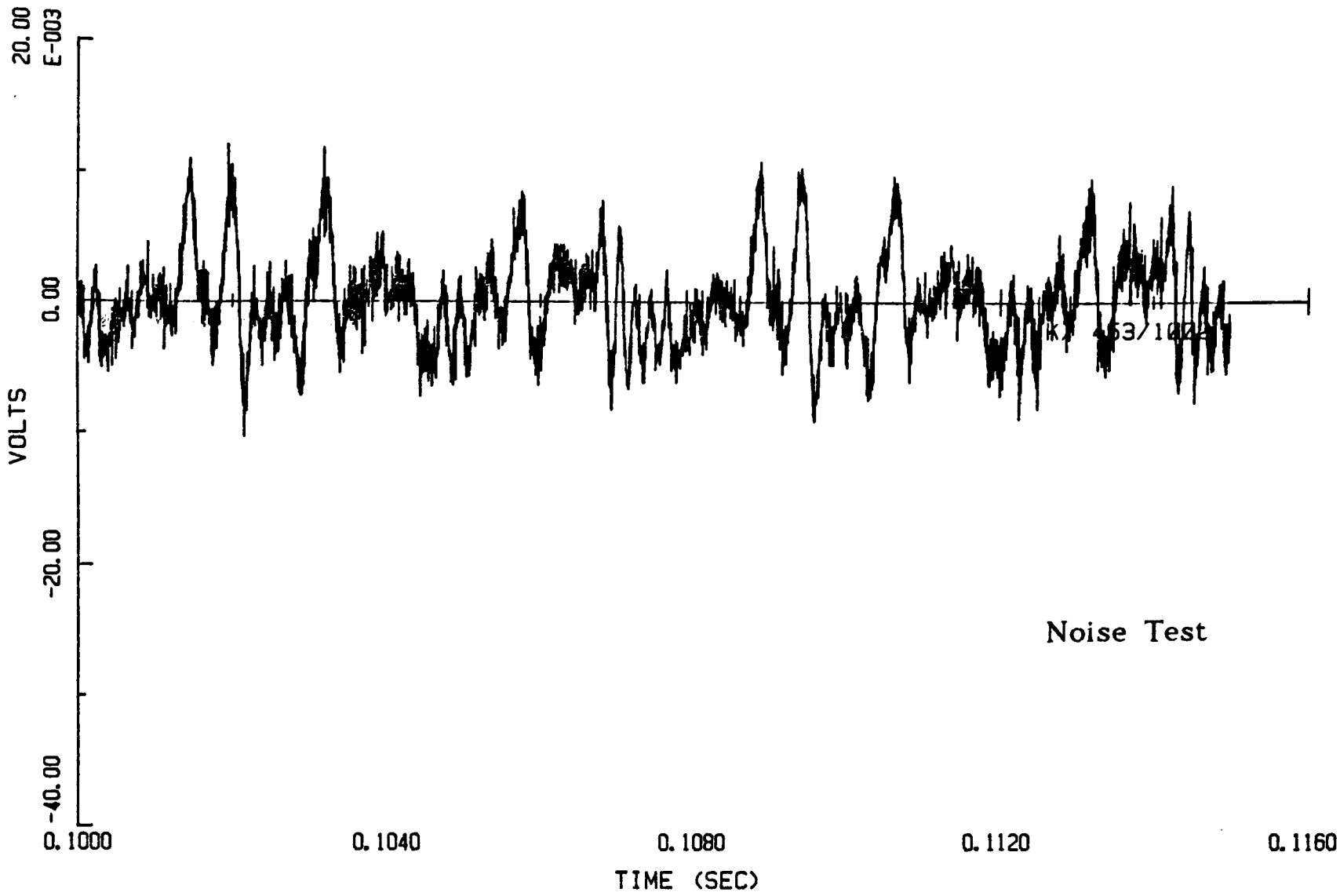

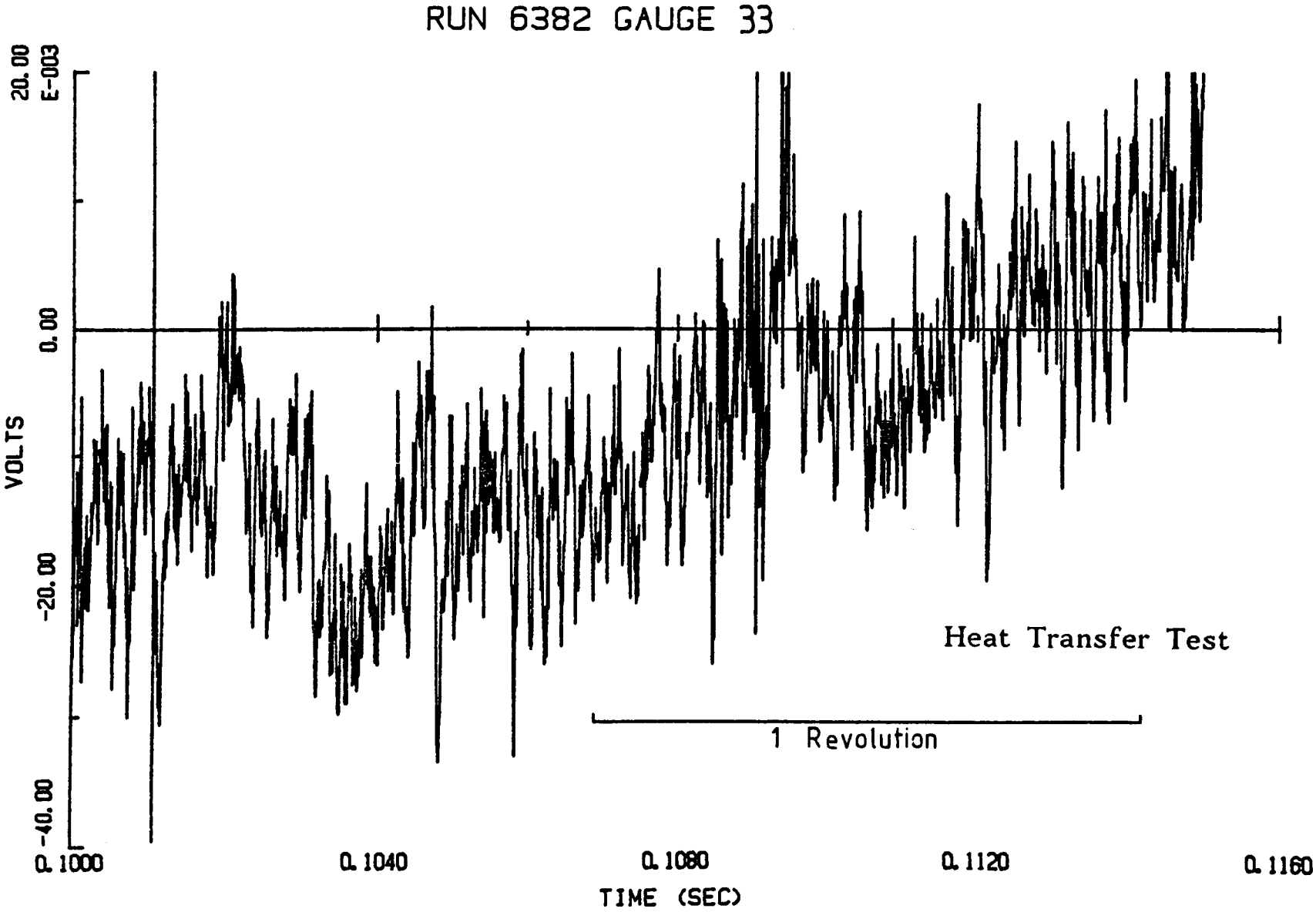

Figure 8.27: Comparison of Heat Transfer and Noise Signals- Gauge 33

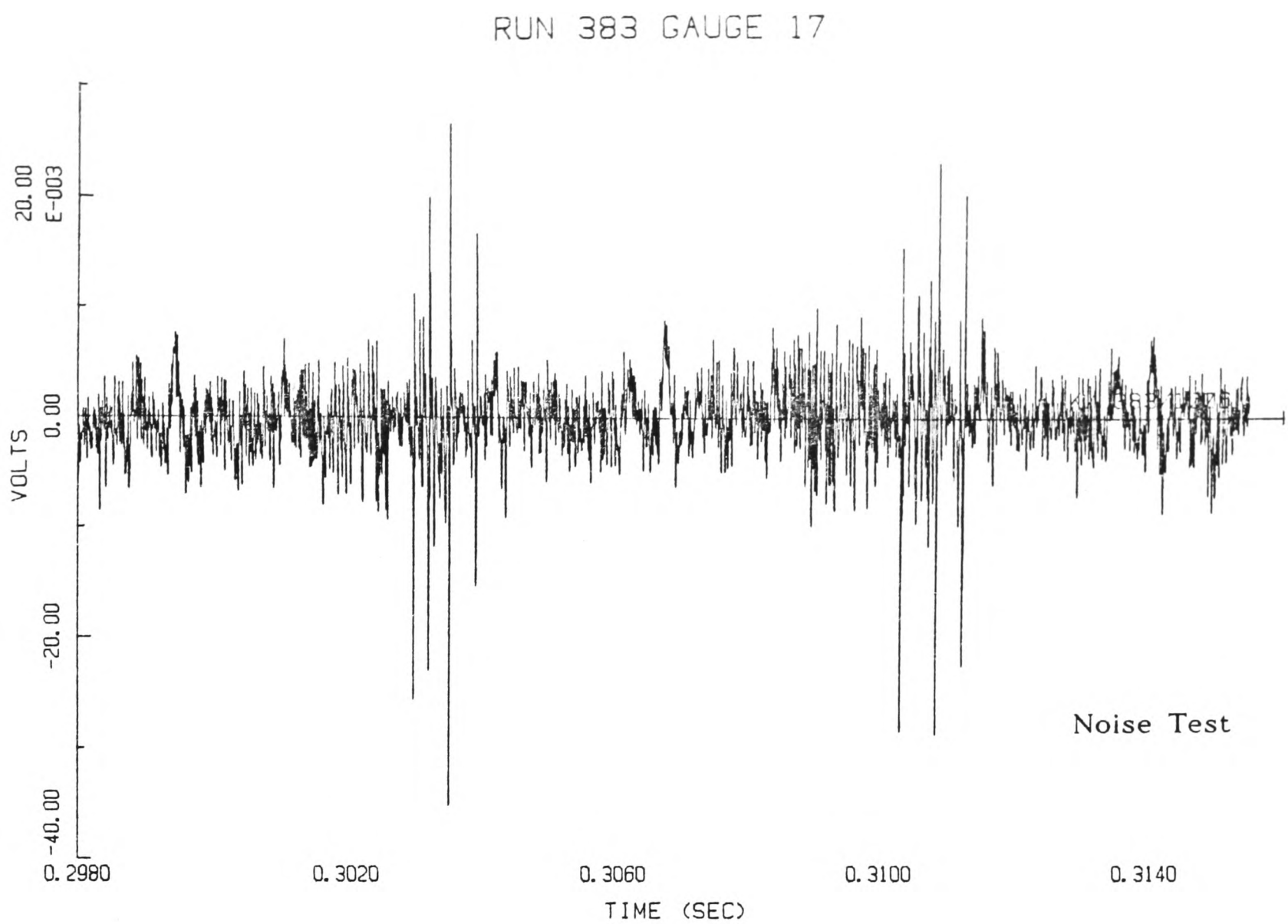

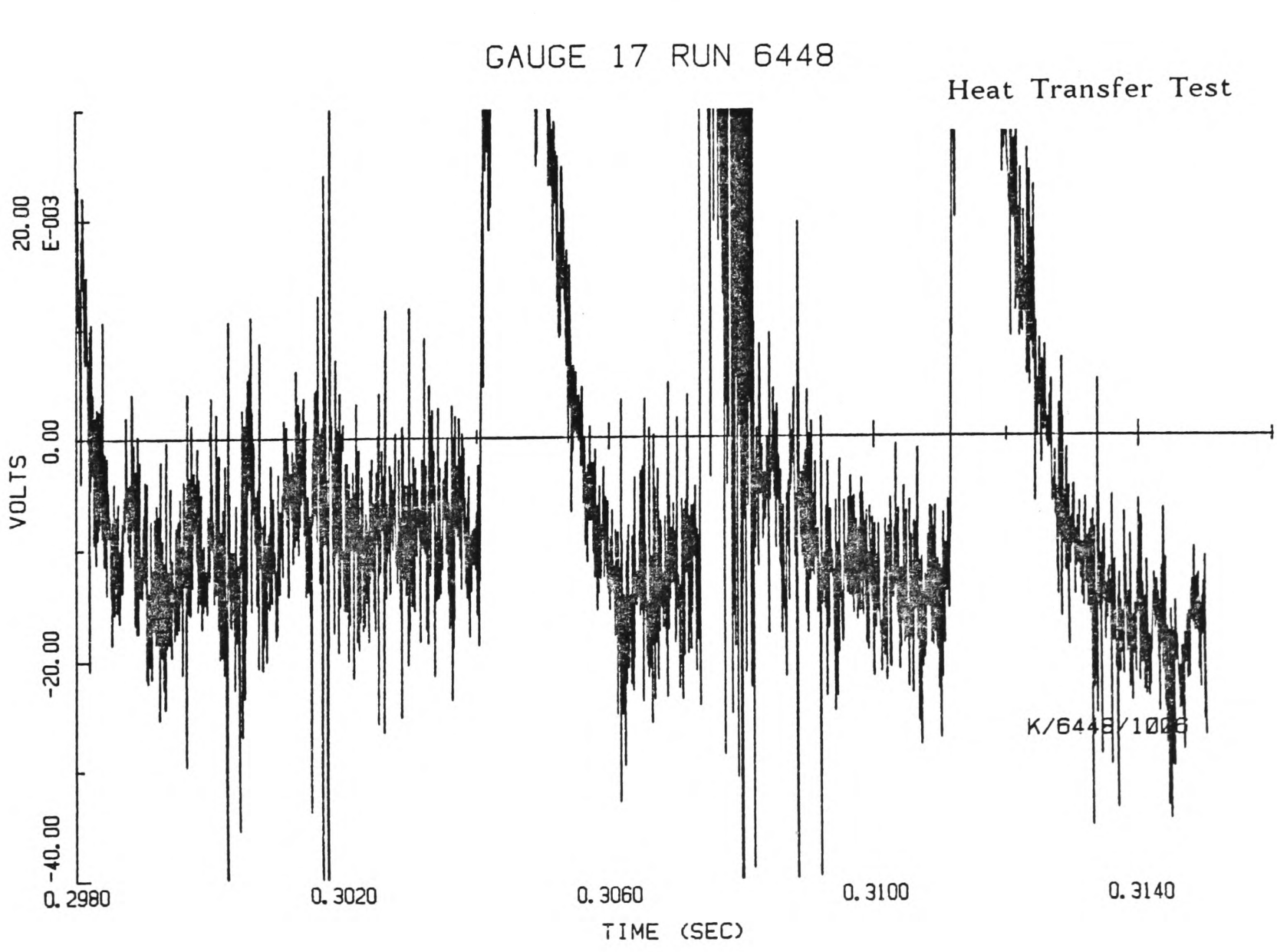

Figure 8.28: Comparison of Heat Transfer and Noise Signals- Gauge 17

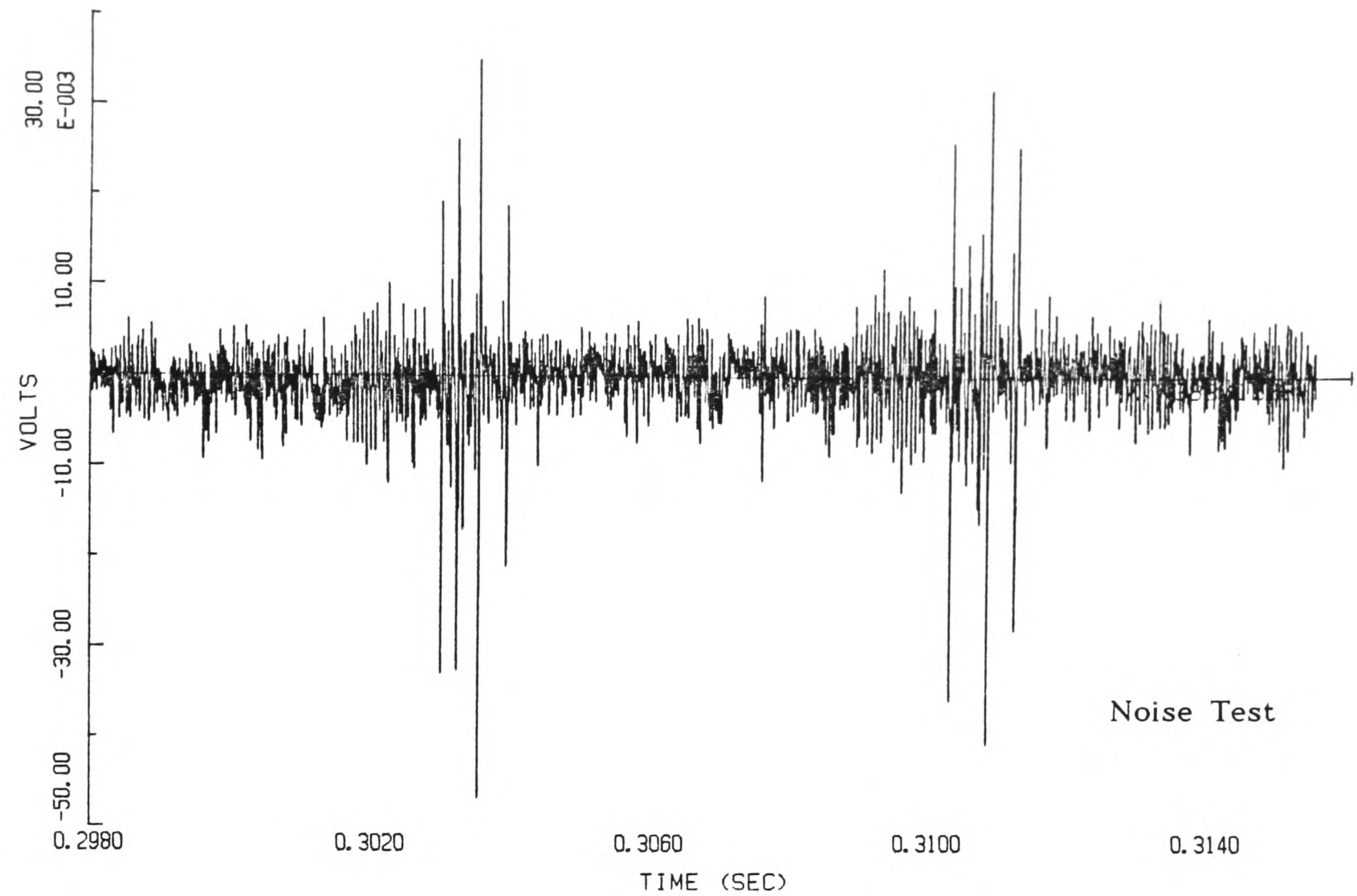

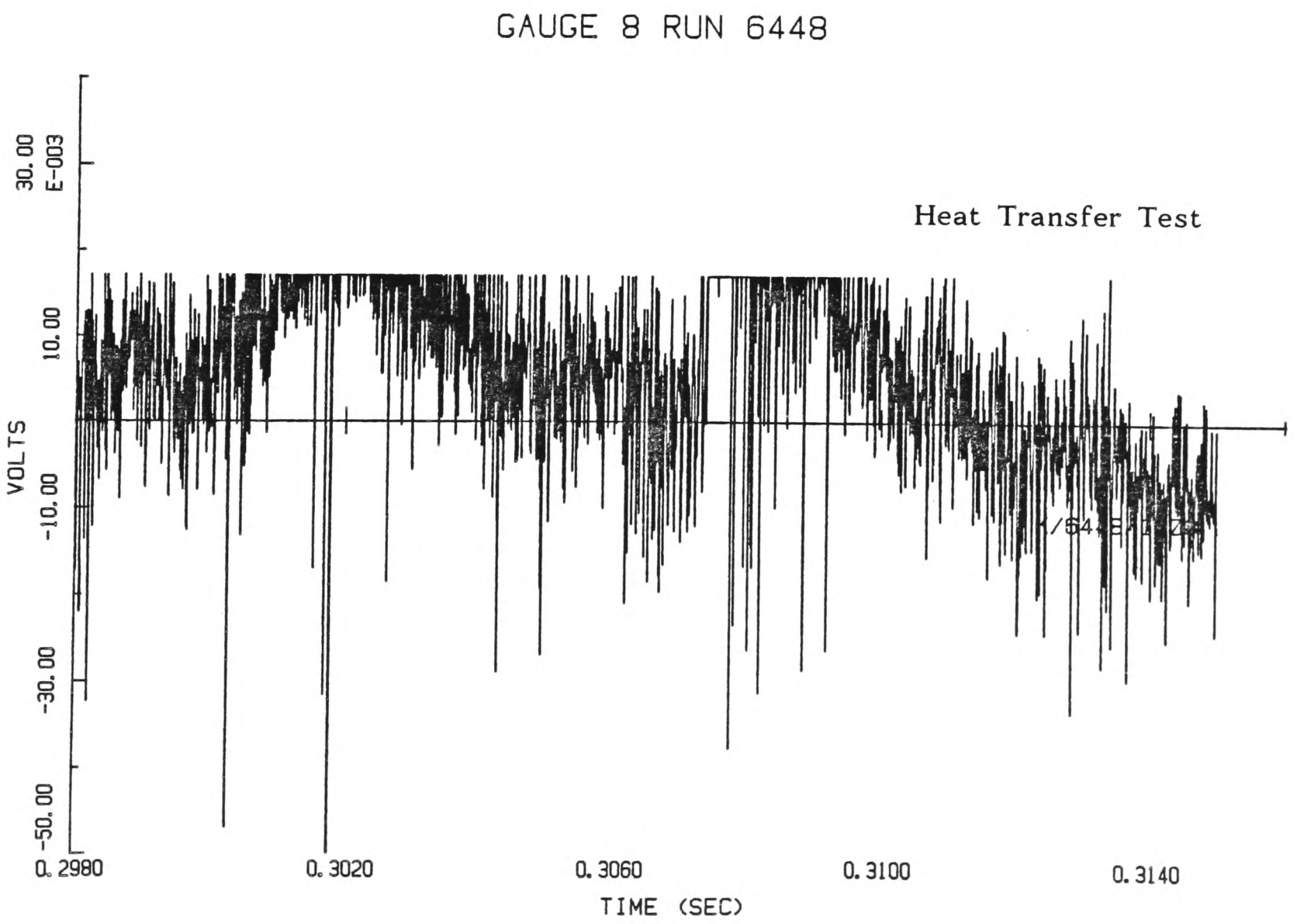

Figure 8.29: Comparison of Heat Transfer and Noise Signals- Gauge 8

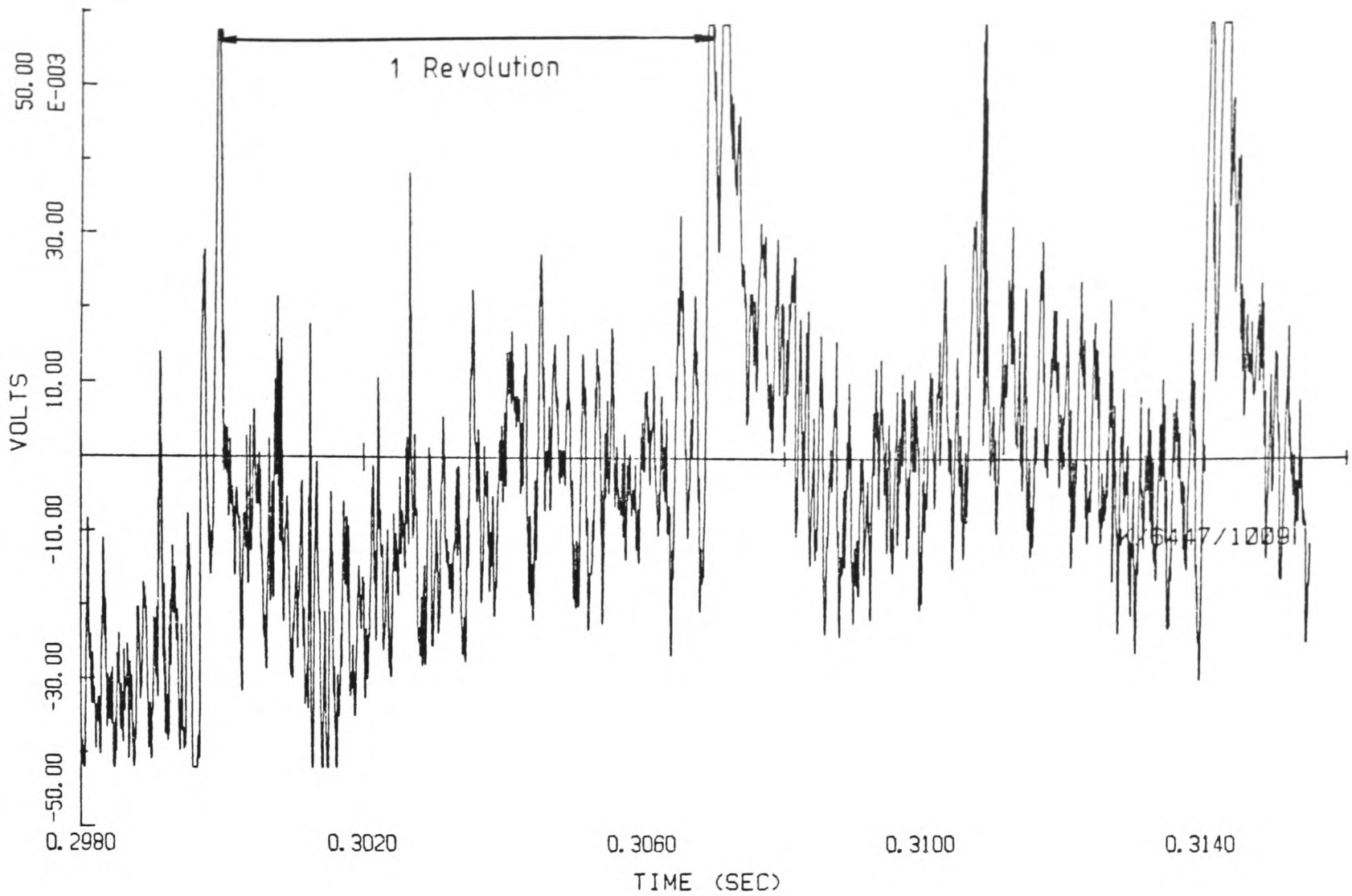

Figure 8.30: Raw Output from Gauge 20, Run 6447

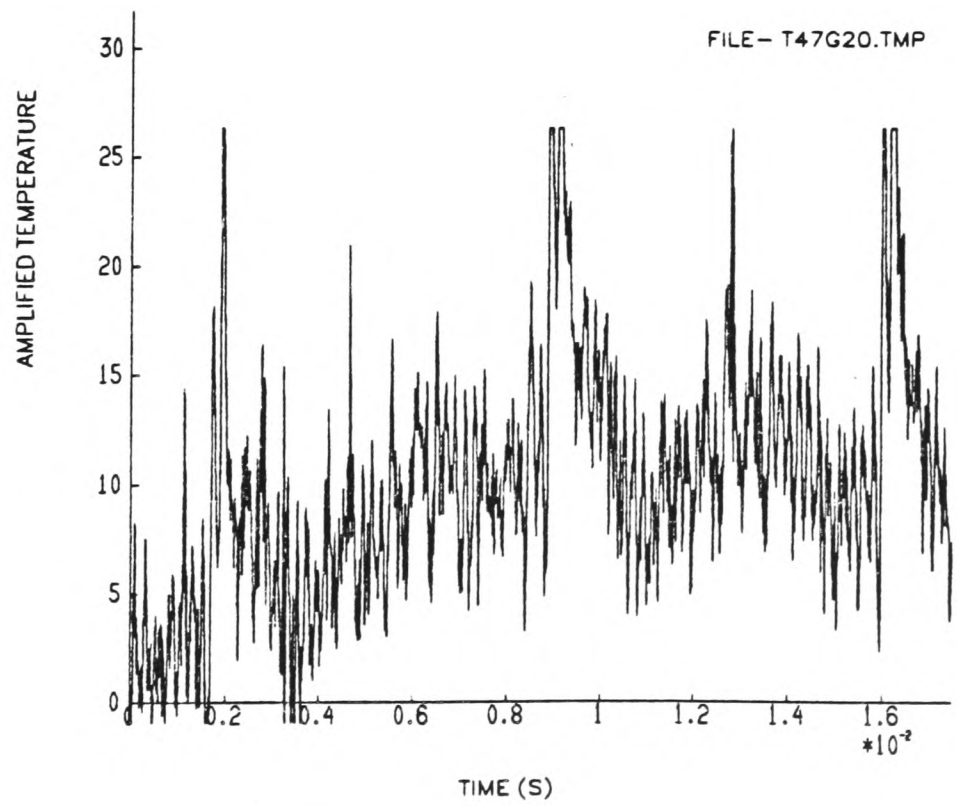

Figure 8.31: Amplifed Temperature Rise,
Gauge 20, Run 6447

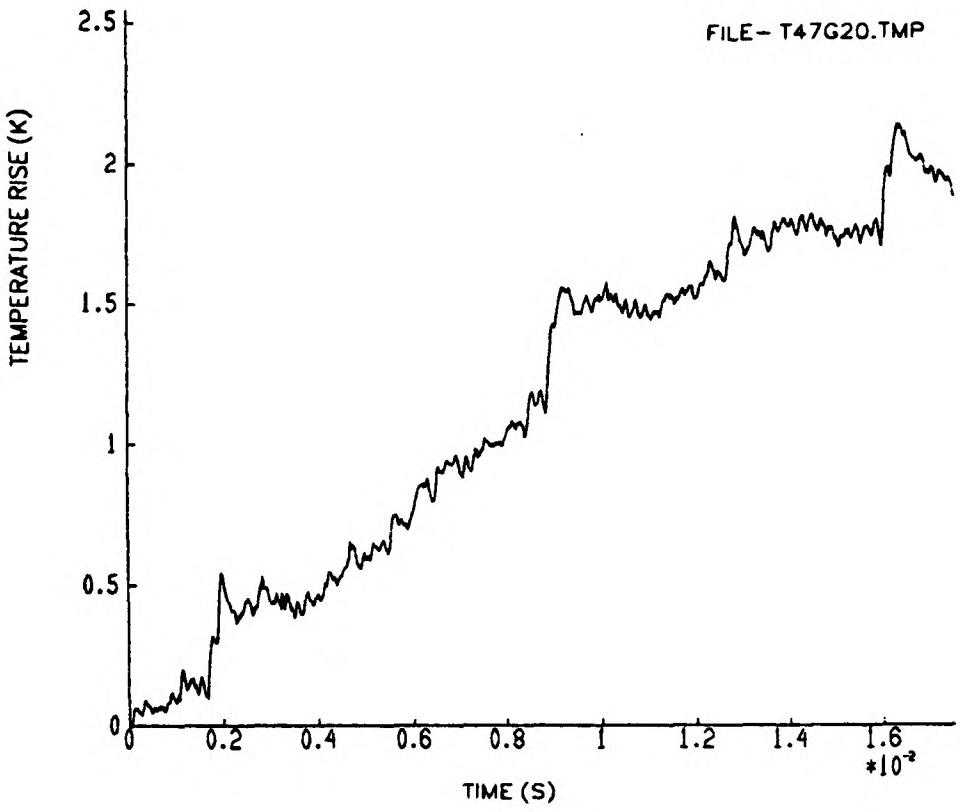

Figure 8.32: Temperature Rise Gauge 20, Run 6448

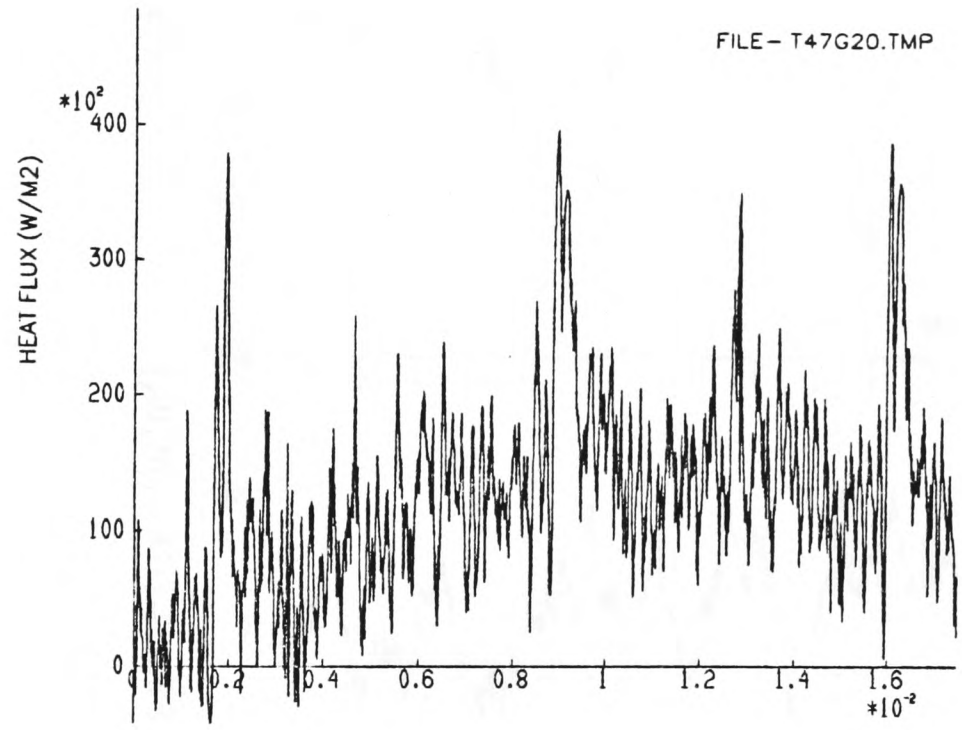

Figure 8.33: Heat Transfer Rate Gauge 20, Run 6448

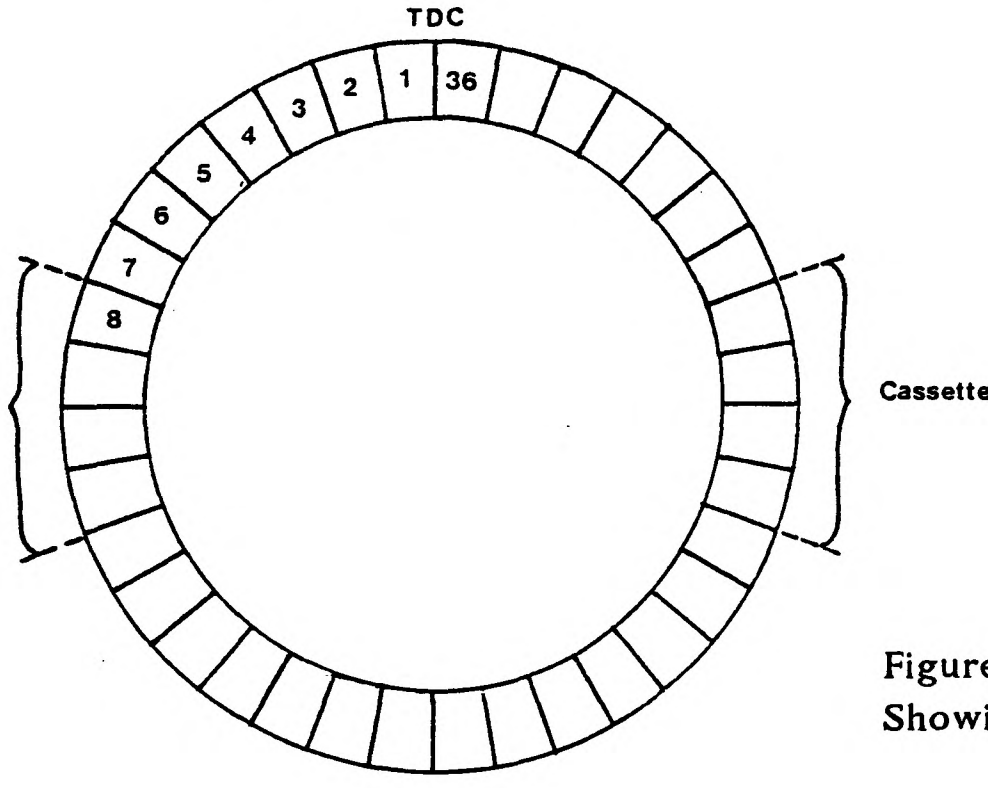

Figure 8.34: Schematic of NGV Ring, Showing Position of Cassettes

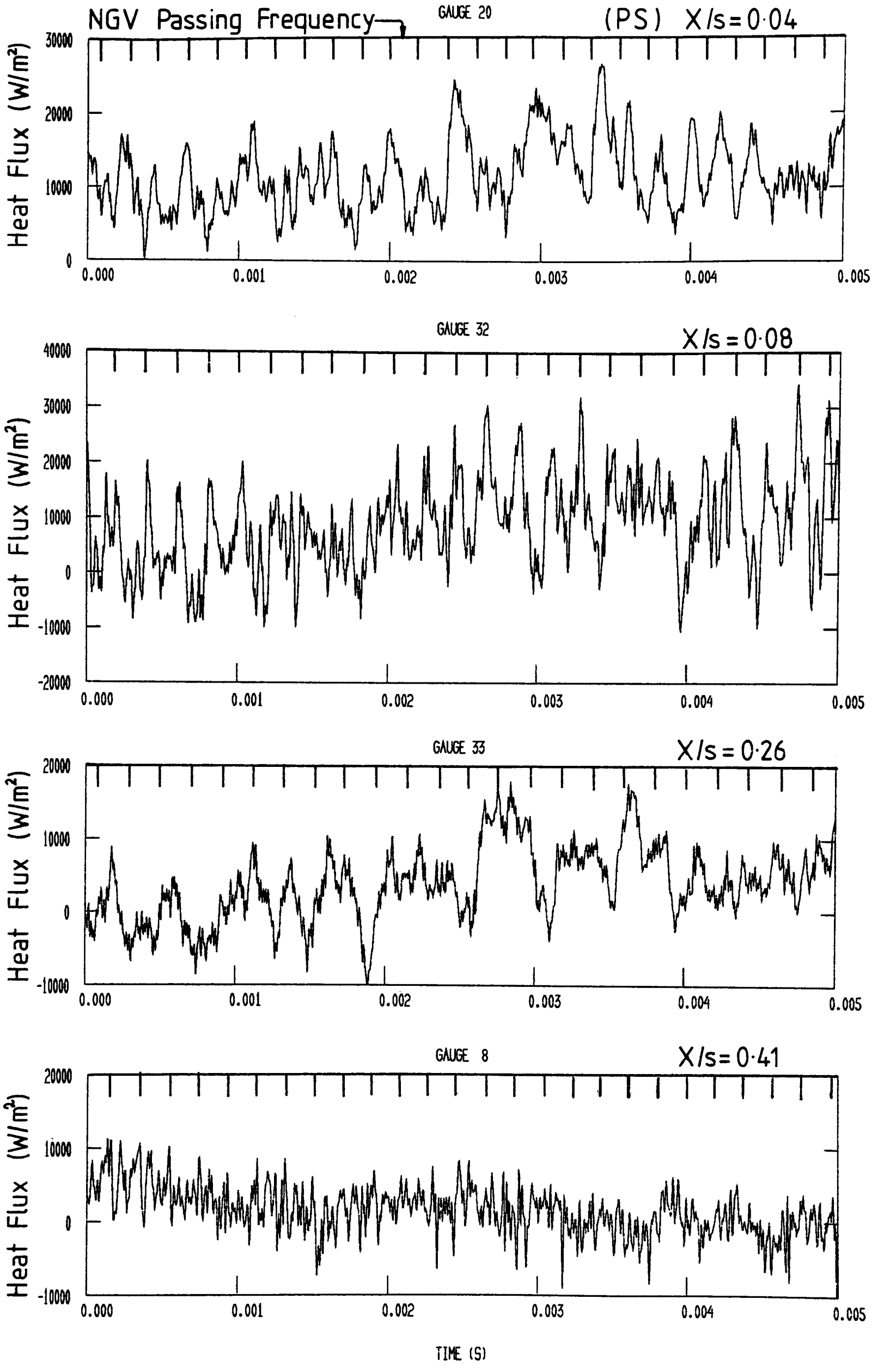

Figure 8.35: Unsteady Heat Transfer Rate - Suction Surface

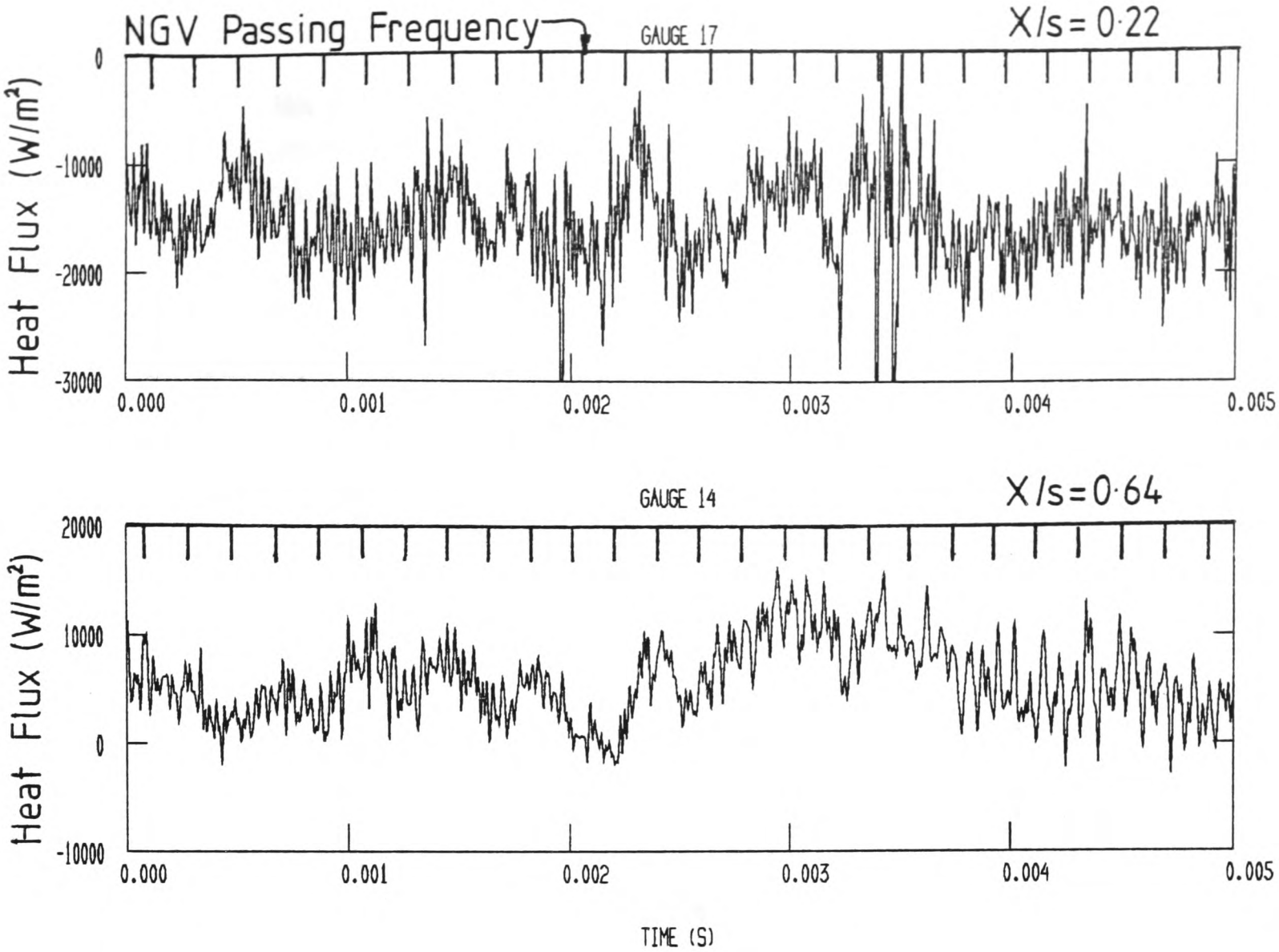

Figure 8.36: Unsteady Heat Transfer Rate - Pressure Surface

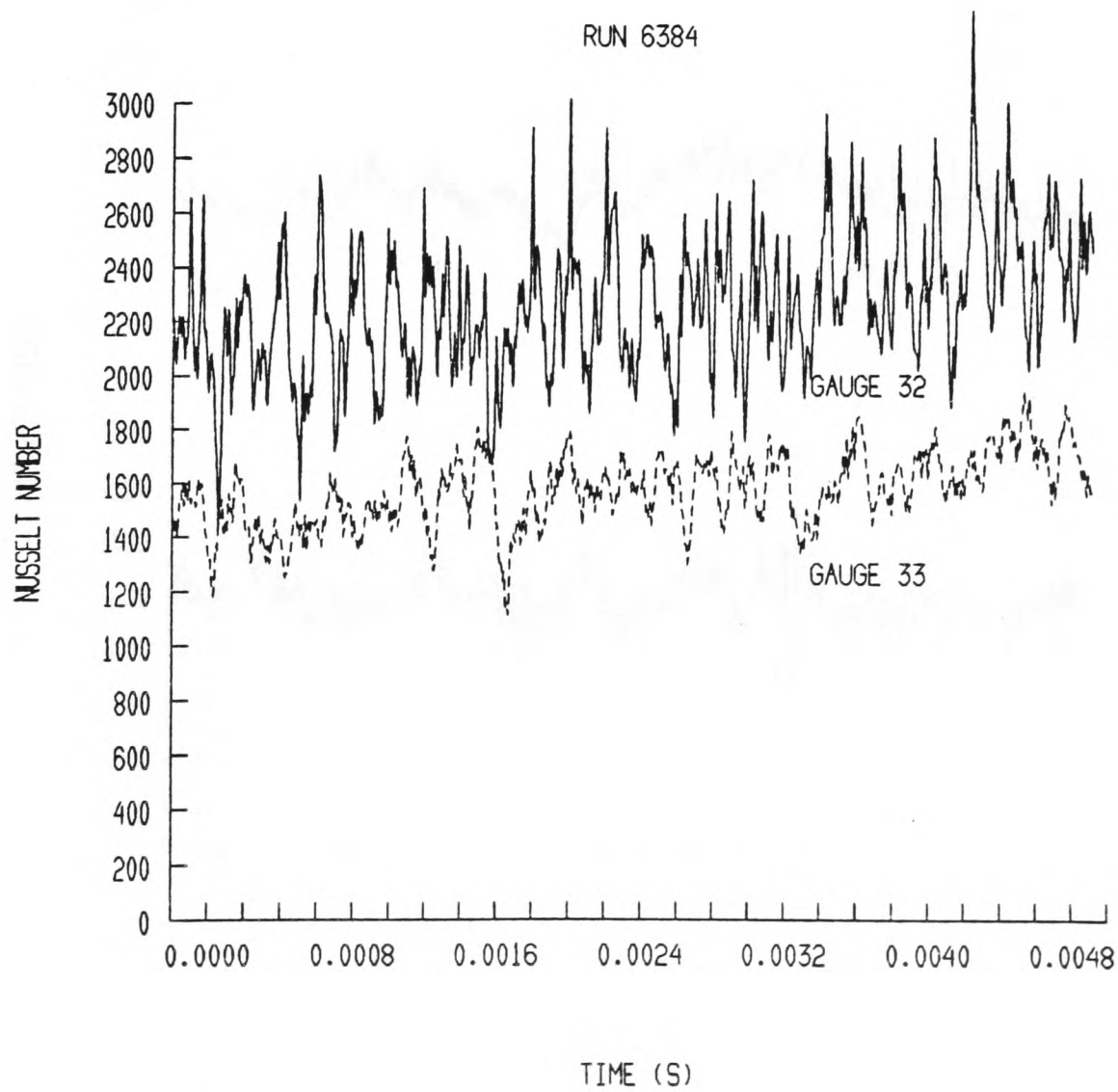

Figure 8.37: Nusselt Number - Gauges 32 and 33

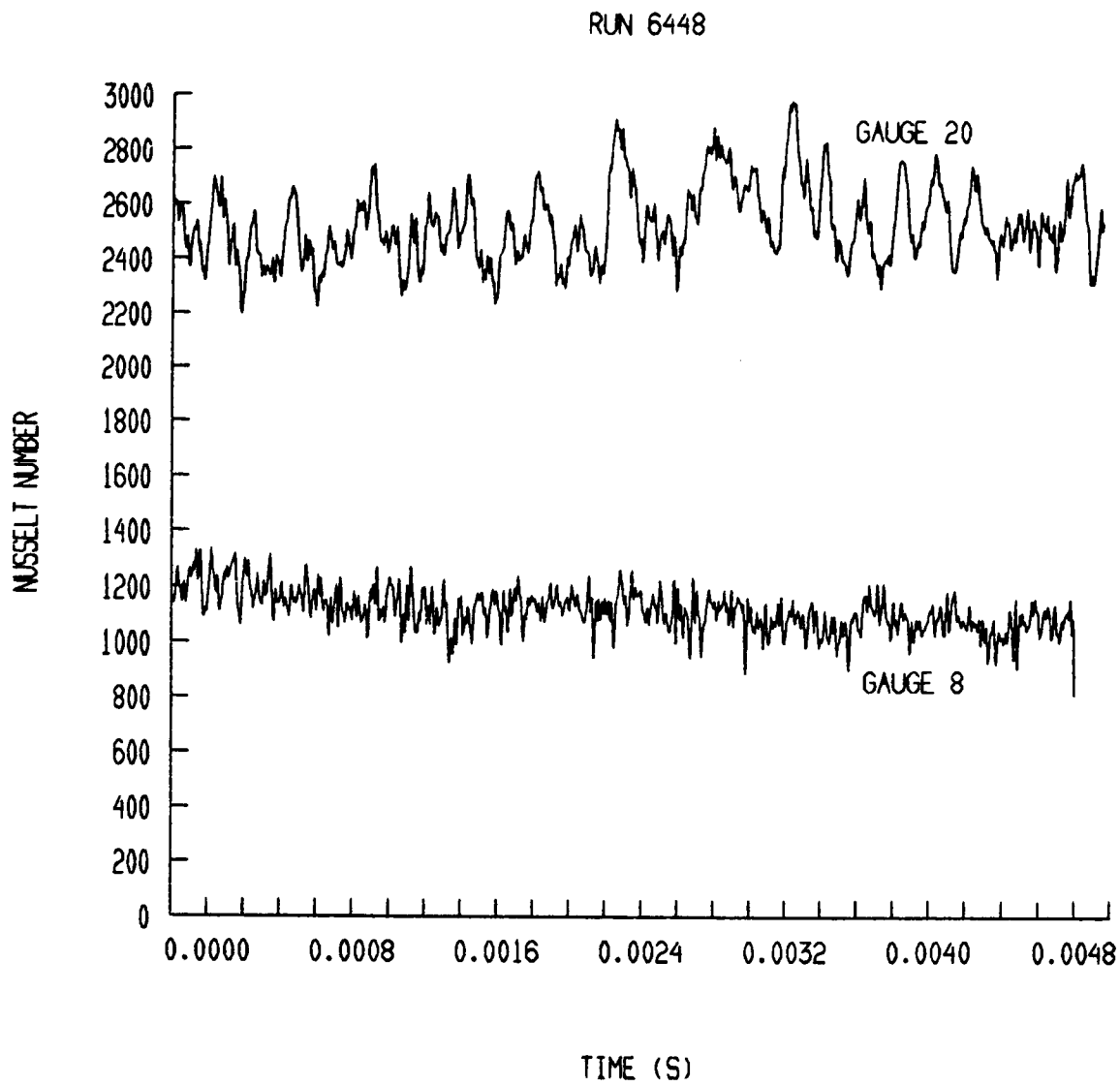

Figure 8.38: Nusselt Number - Gauges 20 and 8

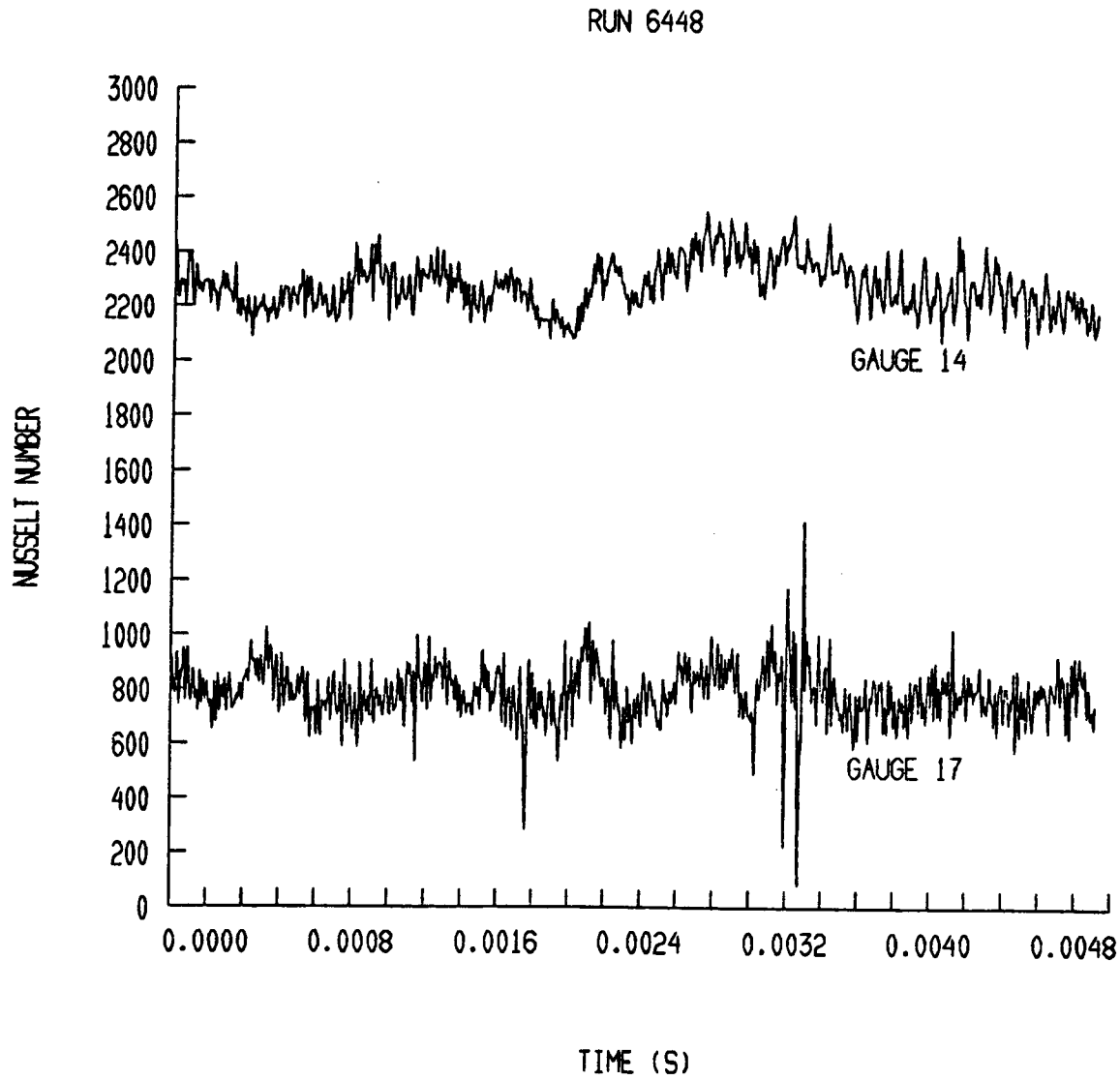

Figure 8.39: Nusselt Number - Gauge 14 and 17

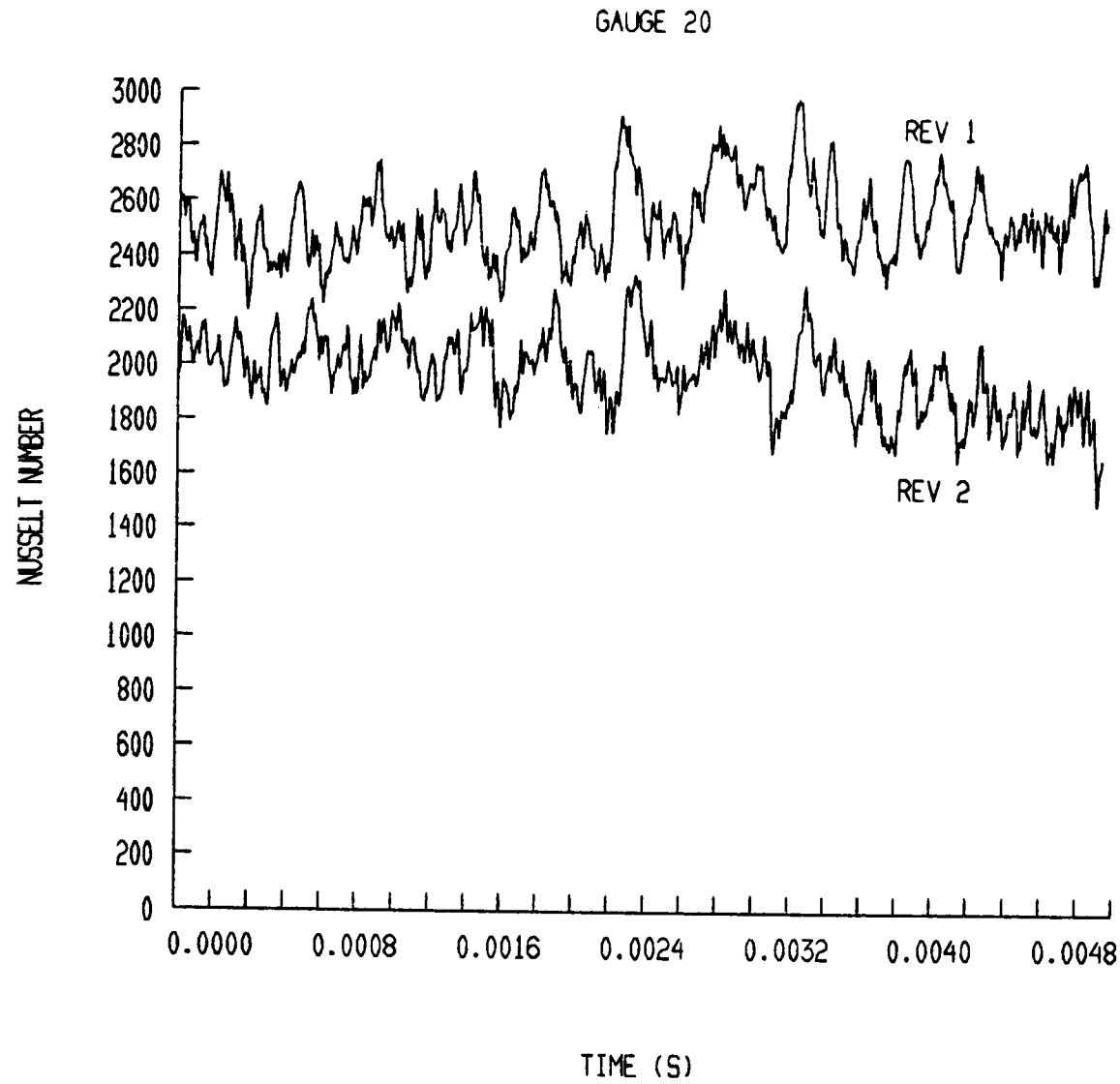

Figure 8.40: Gauge 20 - Nusselt Number From Two Successive Part Revolutions (Lower Trace Offset)

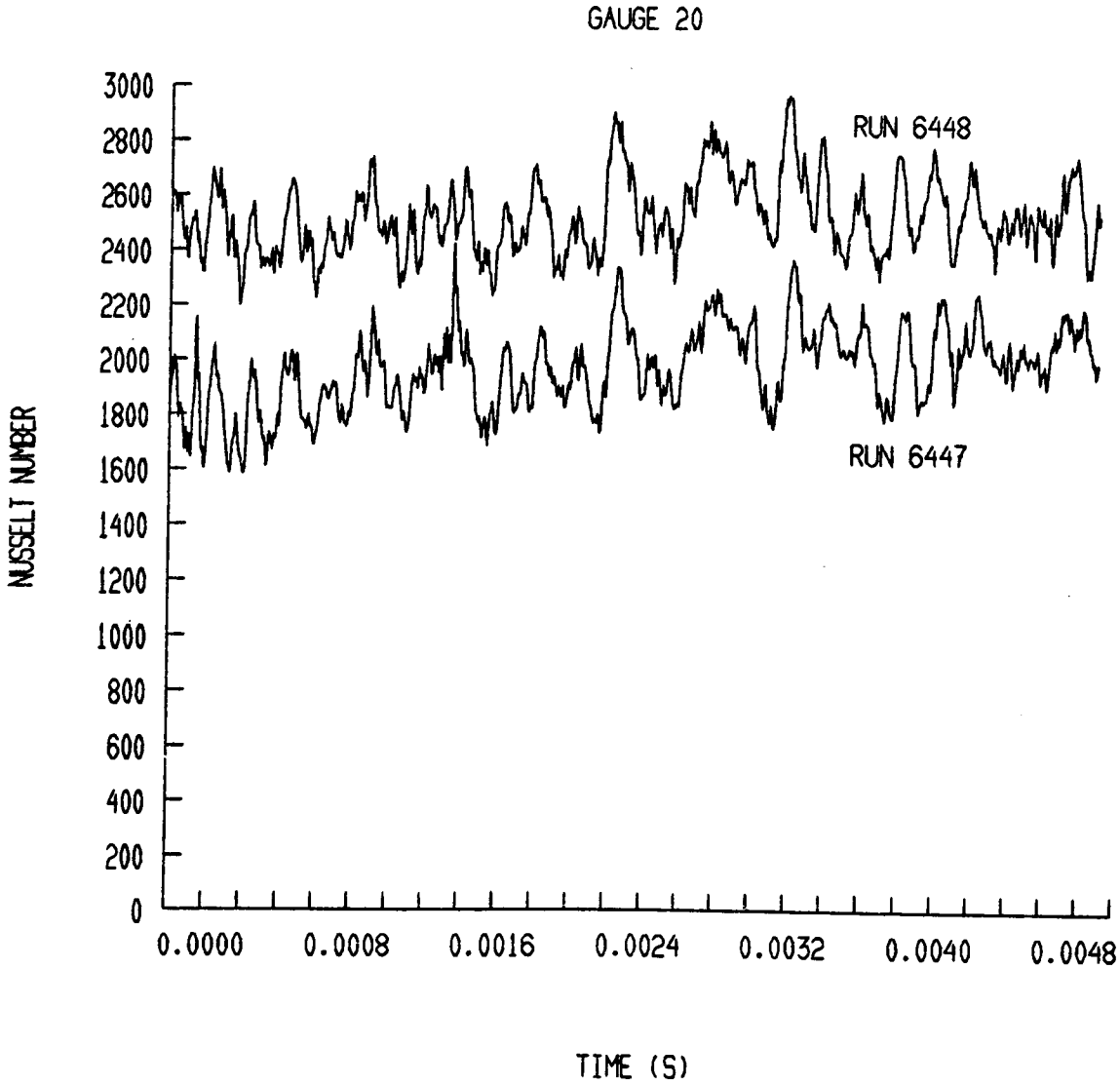

Figure 8.41: Gauge 20 - Nusselt Number from Two Runs (Lower Trace Offset)

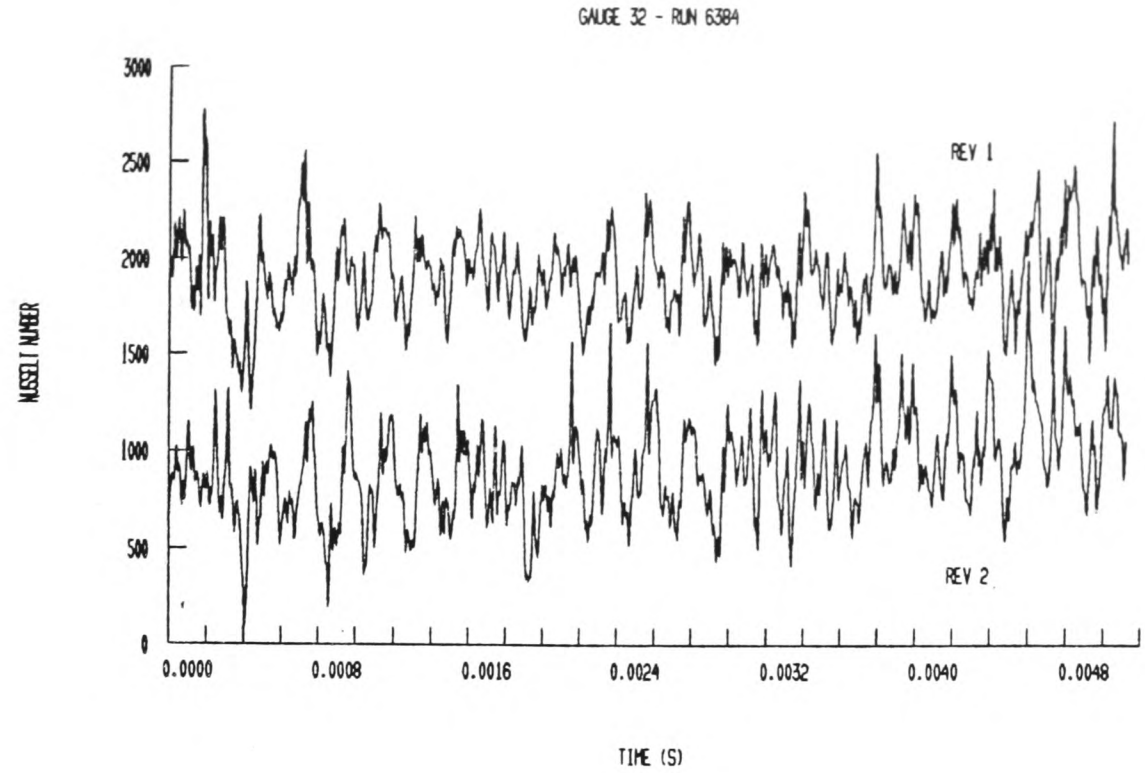

Figure 8.42: Gauge 32 - Nusselt Number From Two Successive Part Revolutions (Lower Trace Offset)

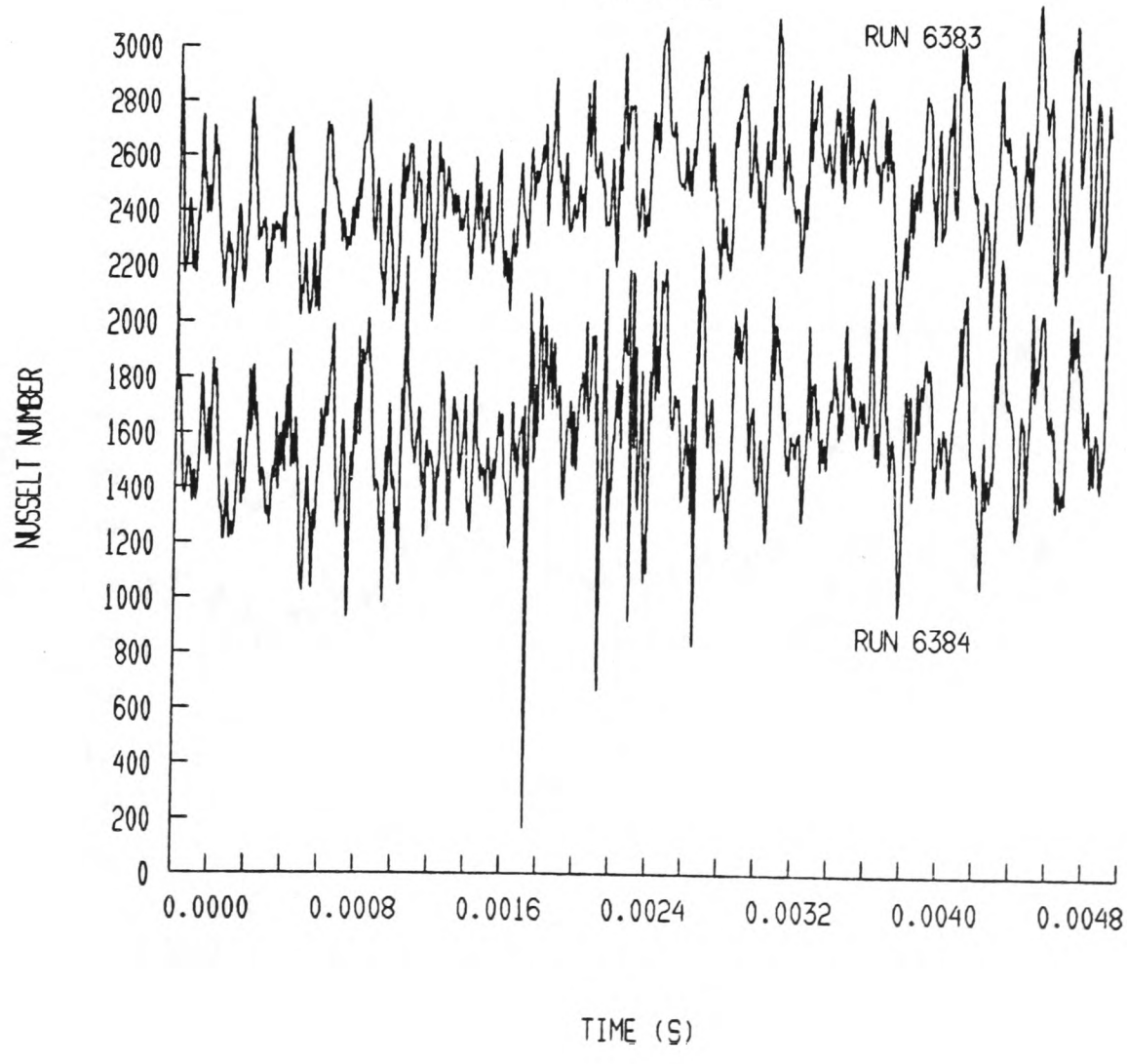

Figure 8.43 Gauge 32 - Nusselt Number from Two Runs (Lower Trace Offset)

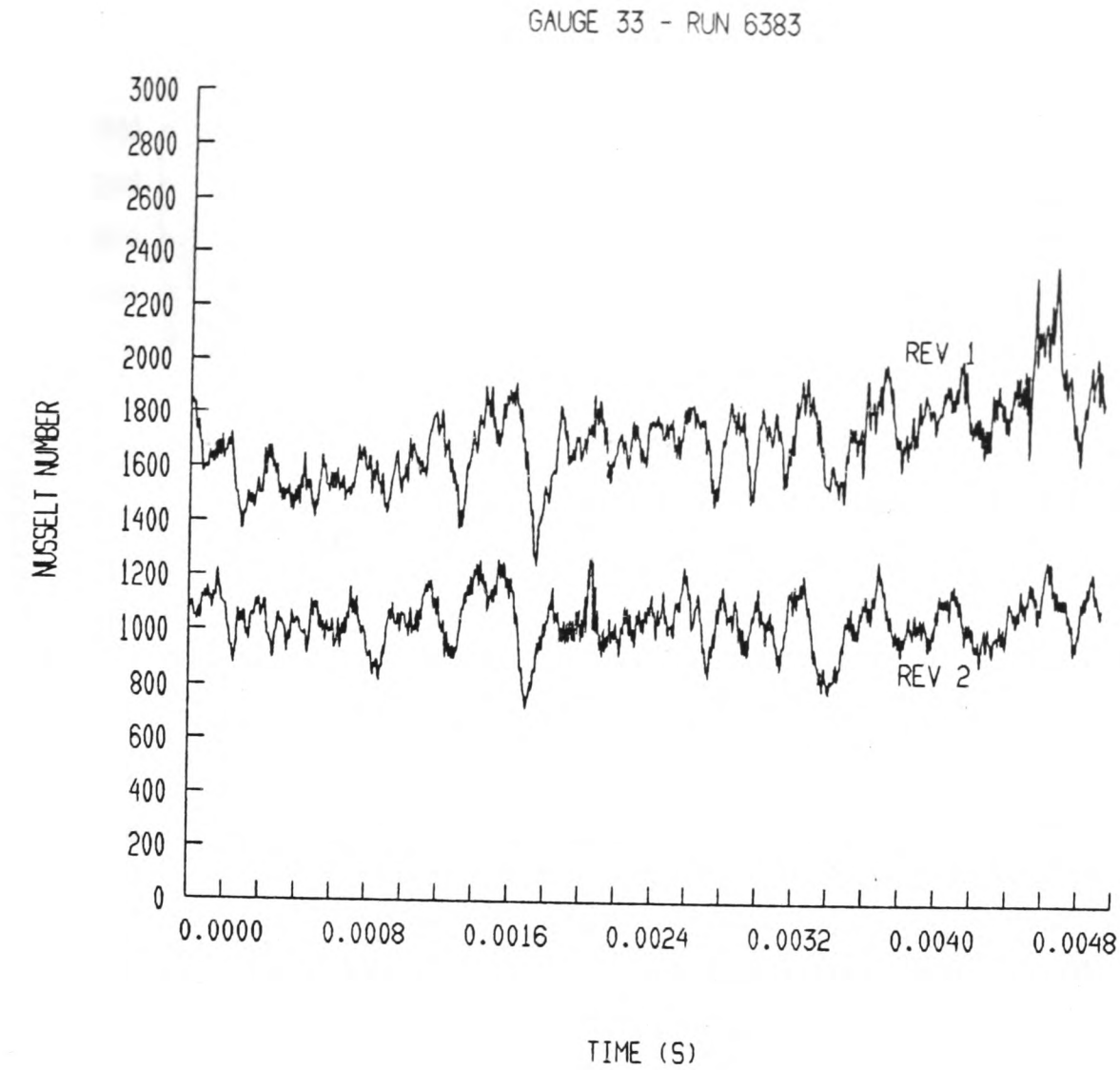

Figure 8.44: Gauge 33 - Nusselt Number from two Successive Part Revolutions (Lower Trace Offset)

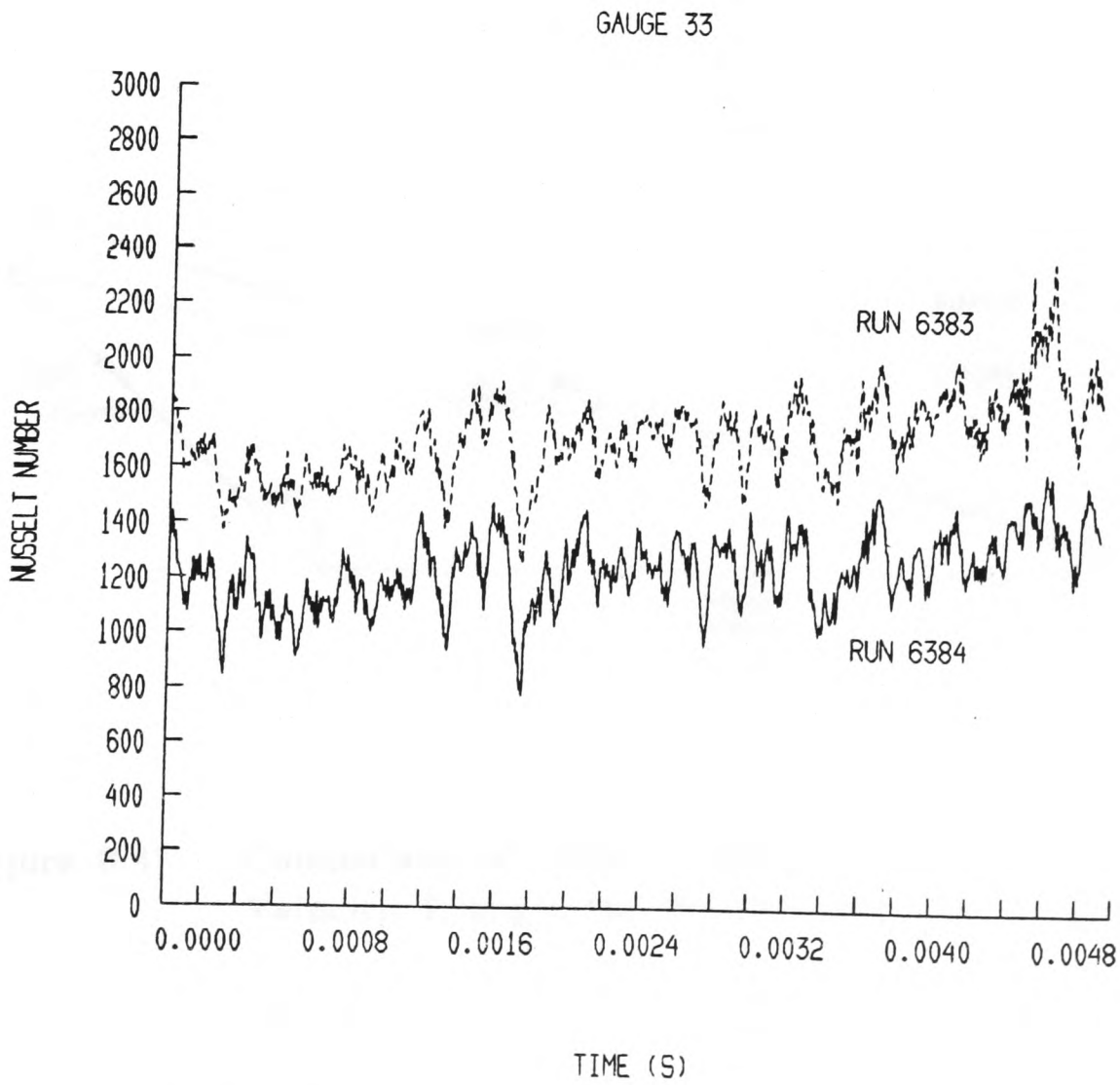

Figure 8.45: Gauge 33 - Nusselt Number from Two Runs (Lower Trace Offset)

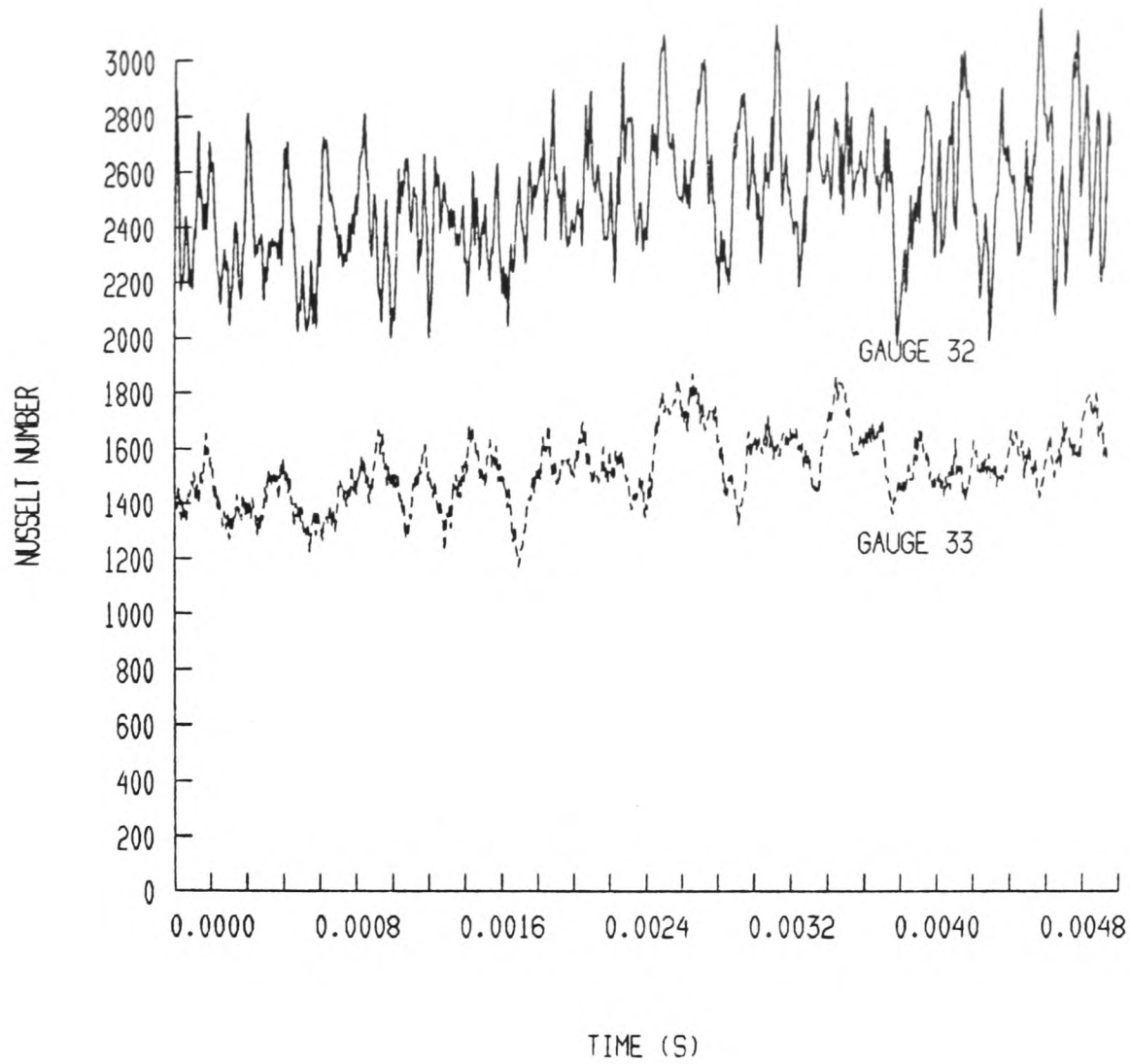

Figure 8.46: Nusselt Number from Gauges 32 and 33 - Run 6383

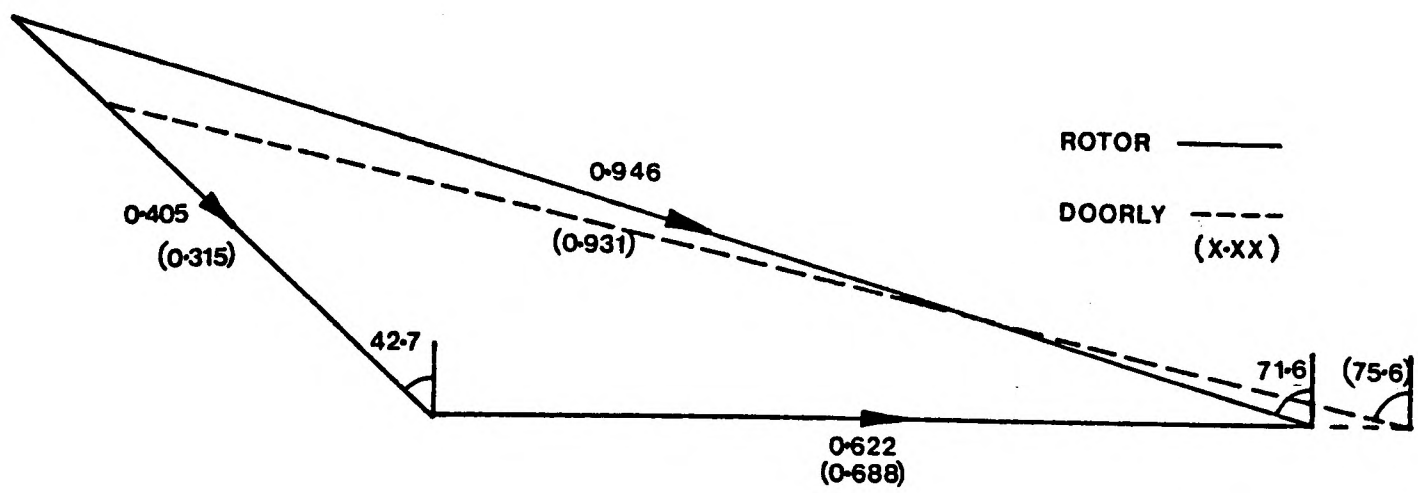

Figure 8.47: Comparison of Rotor Midheight Velocity Triangle and Velocity Triangle for Doorly's Bar Passing Experiment

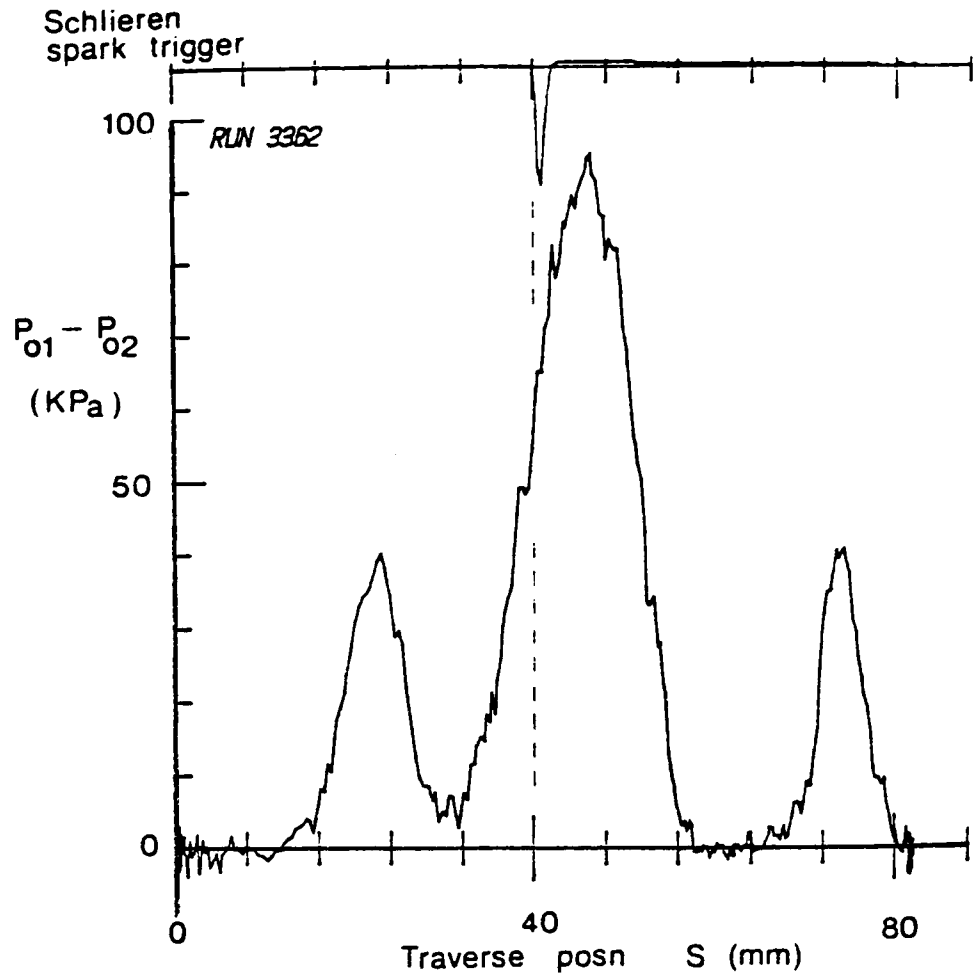

Figure 8.48: Wake Traverse of NGV Cascade with 0.9mm Bar Mounted in Mid-Passage (from **Doorly, 1985**)

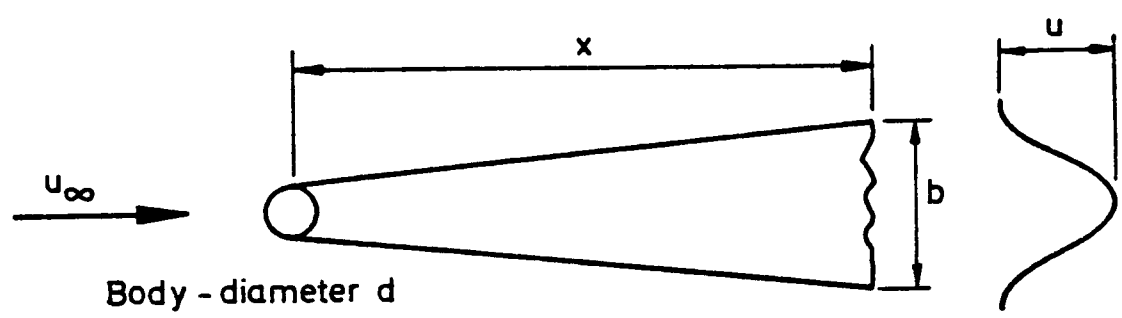

Figure 8.49: Development of a Two-Dimensional Wake

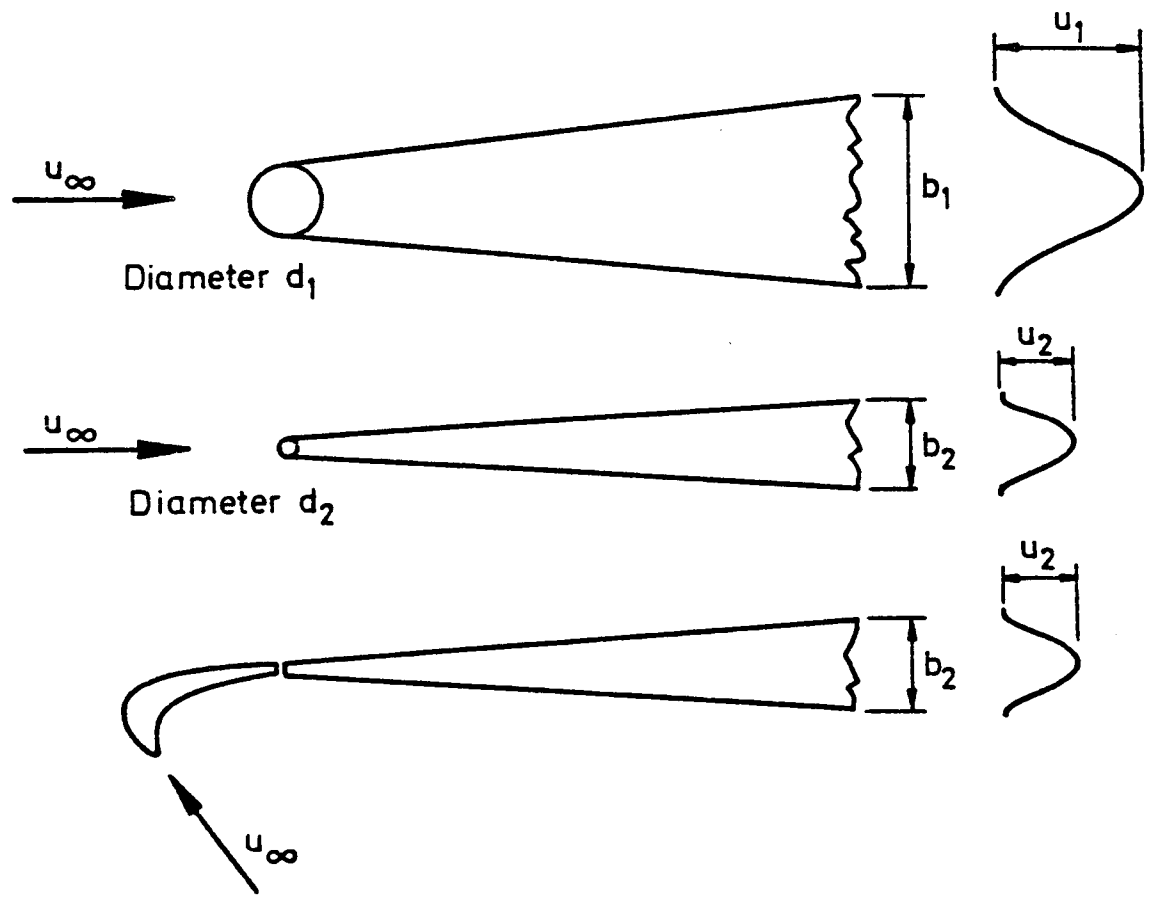

Figure 8.50: Use of a Small Diameter Bar to Represent the Wake Shed from an NGV

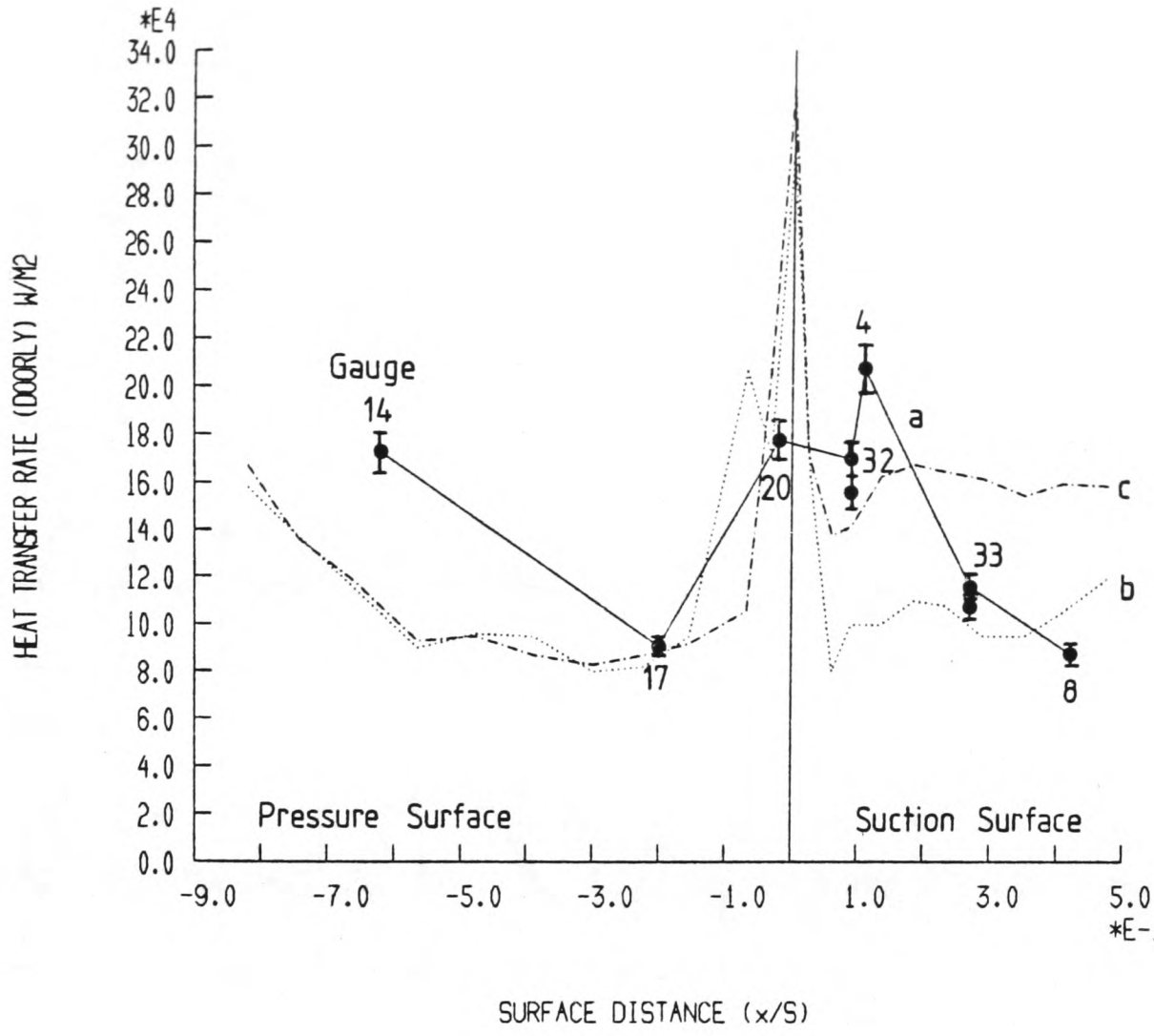

Figure 8.51: Mean Heat Transfer Rate Distribution
(a) Rotor Results Scaled as if Measured at the Conditions of Doorly's Experiment
(b) Doorly's Results - Eight 0.9mm Bars, 0.2% Turbulence
(c) Doorly's Results - No Bars, 5% Turbulence

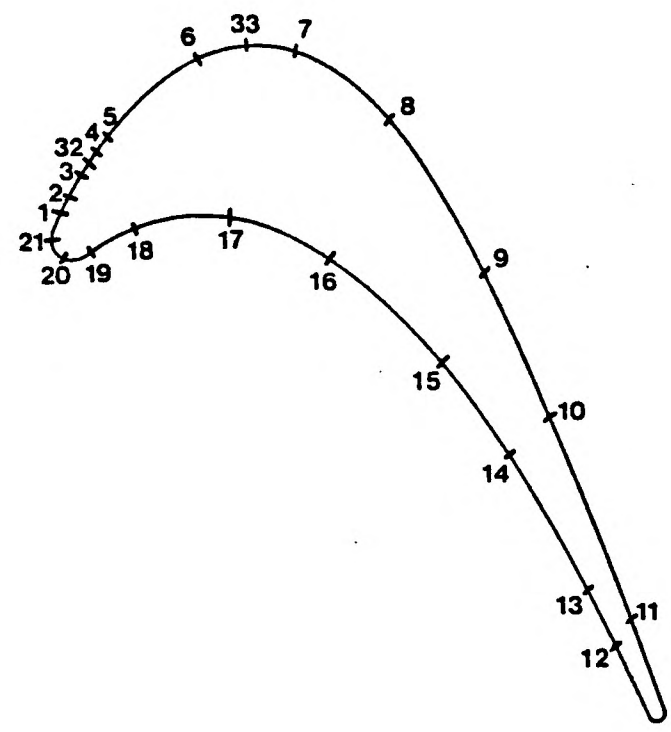

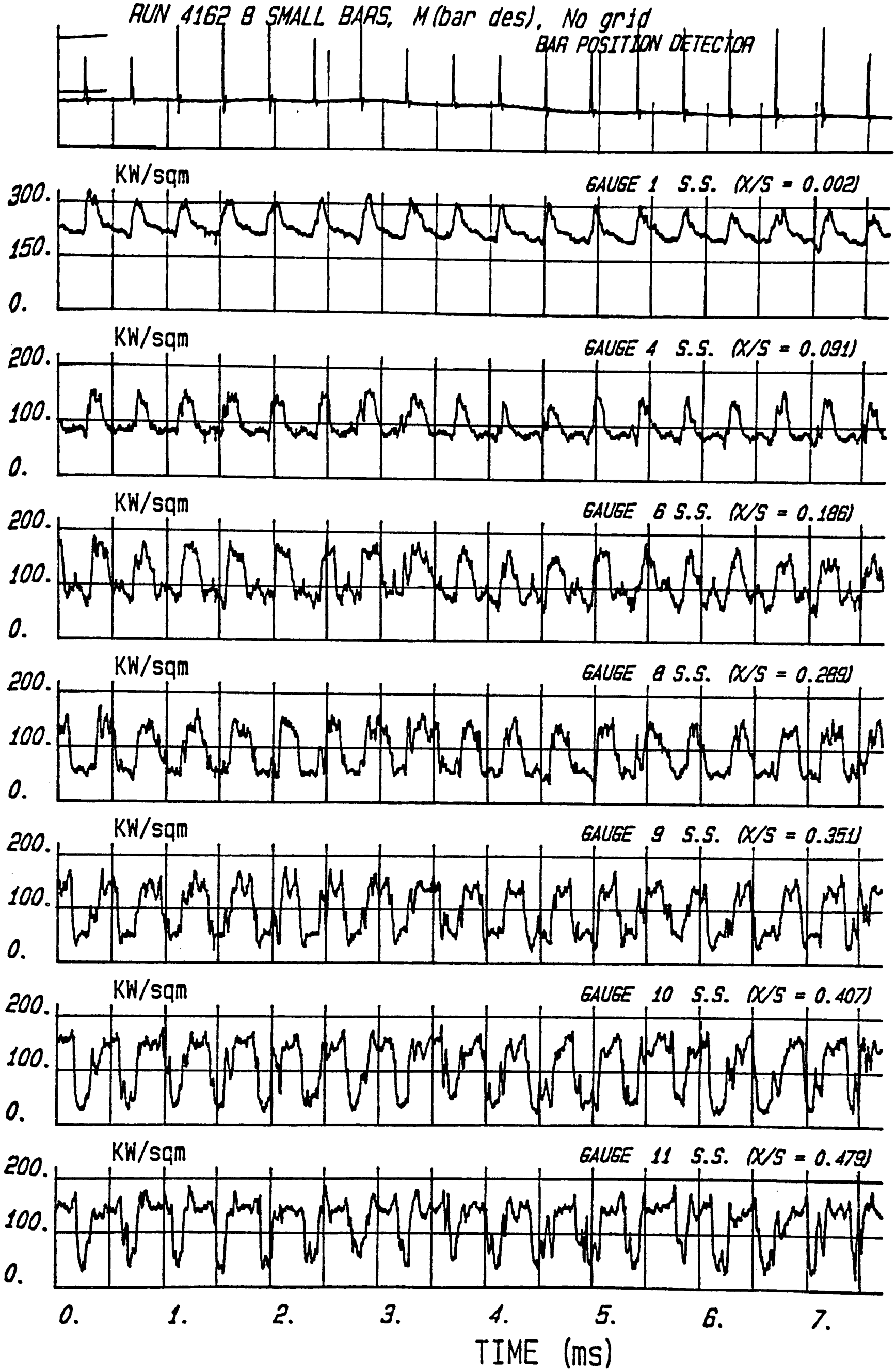

Figure 8.52: Results from Bar Passing Experiment - Unsteady Heat Transfer Rate to Suction Surface - Eight 0.9mm Bars, 0.2% Turbulence, (From **Doorly, 1984**)

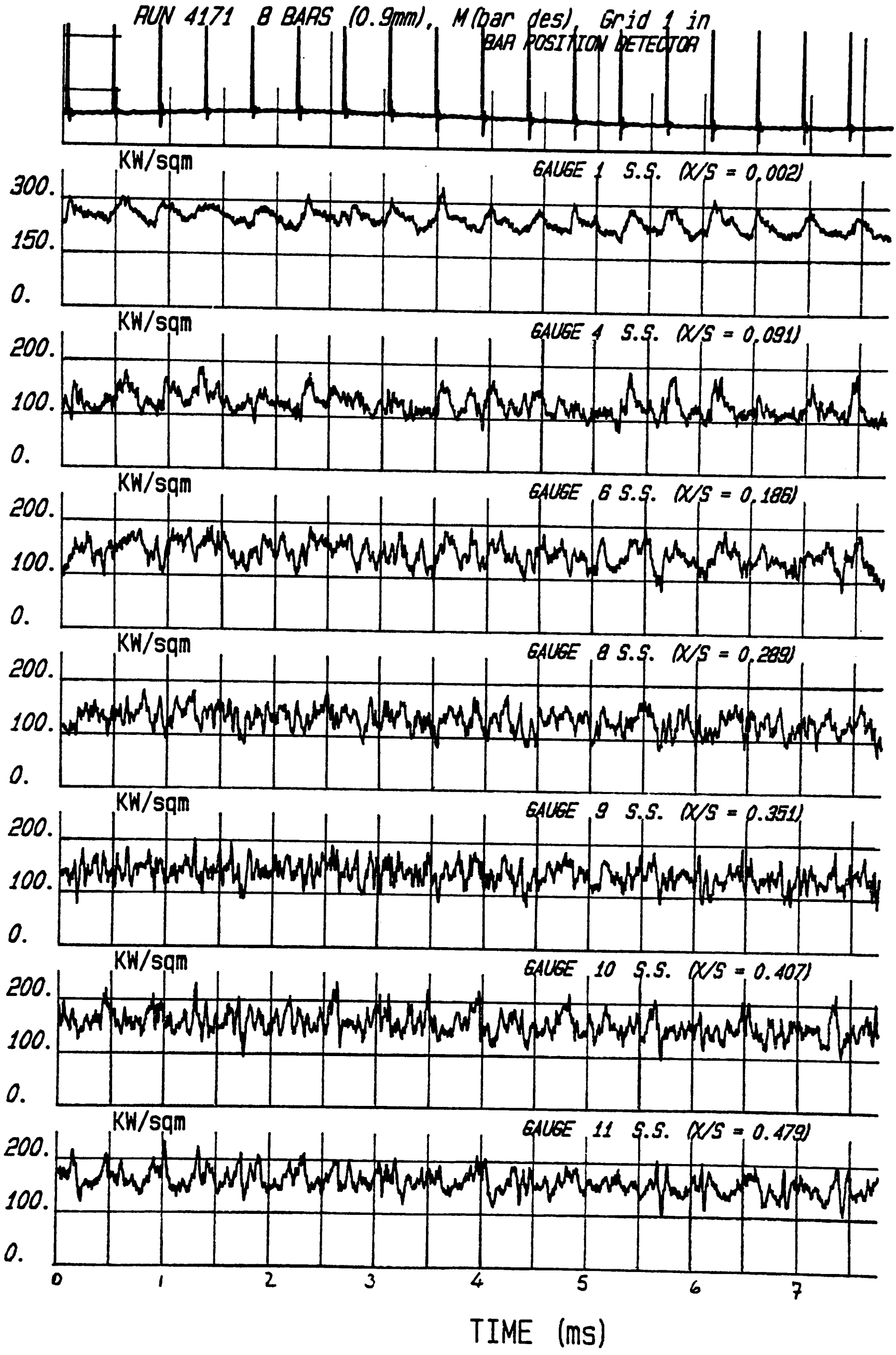

Figure 8.53: Results from Bar Passing Experiment - Unsteady Heat Transfer Rate to Suction Surface - Eight 0.9mm Bars, 5% Turbulence, (From **Doorly, 1984**)

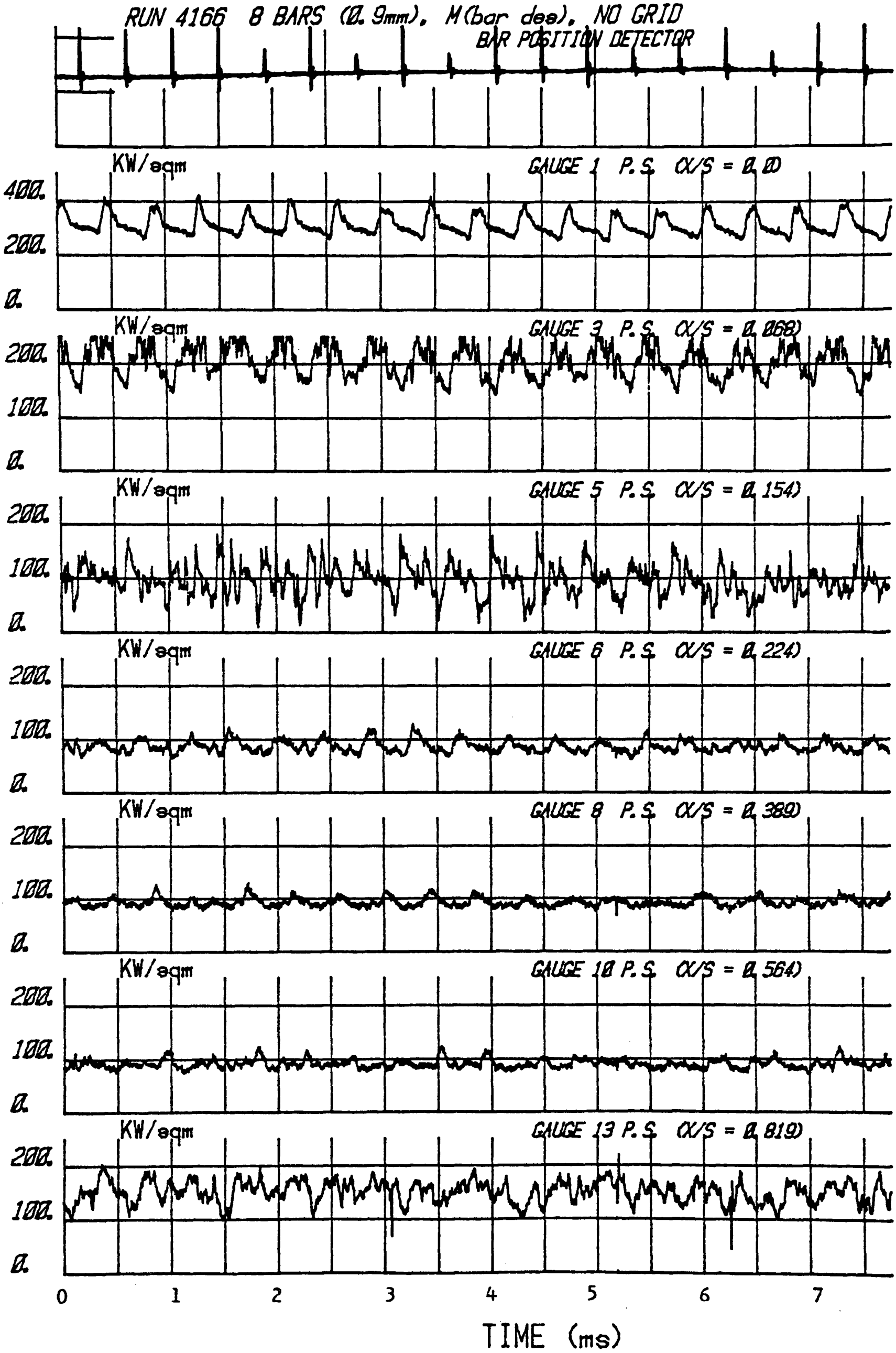

Figure 8.54: Results from Bar Passing Experiment - Unsteady Heat Transfer Rate to Pressure Surface - Eight 0.9mm Bars, 0.2% Turbulence, (From **Doorly, 1984**)